JAERI-Review
2001-010

NUCLEAR ENERGY SYSTEM DEPARTMENT ANNUAL REPORT
(APRIL 1, 1999 – MARCH 31, 2000)

March 2001

Department of Nuclear Energy System

日本原子力研究所
Japan Atomic Energy Research Institute

本レポートは、日本原子力研究所が不定期に公刊している研究報告書です。
入手の問合わせは、日本原子力研究所研究情報部研究情報課（〒319-1195　茨城県那珂郡東海村）あて、お申し越し下さい。なお、このほかに財団法人原子力弘済会資料センター（〒319-1195　茨城県那珂郡東海村日本原子力研究所内）で複写による実費頒布を行っております。

This report is issued irregularly.
Inquiries about availability of the reports should be addressed to Research Information Division, Department of Intellectual Resources, Japan Atomic Energy Research Institute, Tokai-mura, Naka-gun, Ibaraki-ken 〒319-1195, Japan.

編集兼発行　日本原子力研究所

JAERI－Review 2001－010

Nuclear Energy System Department Annual Report
(April 1, 1999 – March 31, 2000)

Department of Nuclear Energy System

Tokai Research Establishment
Japan Atomic Energy Research Institute
Tokai-mura, Naka-gun, Ibaraki-ken

(Received February 5, 2001)

This report summarizes the research and development activities in the Department of Nuclear Energy System during the fiscal year of 1999 (April 1, 1999 - March 31, 2000).

The Department has been organized from April 1998. The main research activity is aimed to build the basis of the development of a future nuclear energy system. The research activities of the fiscal year cover basic nuclear and atomic & molecular data evaluation, conceptual design of a reduced-moderation water reactor, reactor physics experiments and development of the reactor analysis codes, experiment and analysis of thermal-hydrodynamics, development of advanced materials for a reactor, lifetime reliability assessment on structural material, development of advanced nuclear fuel, design of a marine reactor and the research for a nuclear ship system. The maintenance and operation of reactor engineering facilities belonging to the Department are undertaken.

The activities of the research committee to which the Department takes a role of secretariat are also summarized in this report.

Keywords: Nuclear Energy System Department Annual Report, Nuclear Data, Reactor Physics, Thermal Hydraulics, Advanced Material, Advanced Nuclear Fuel, Marine Reactor

---

JAERI－Review 2001－010

平成１１年度エネルギーシステム研究部年報

日本原子力研究所東海研究所
エネルギーシステム研究部

（2001年 2月 5日受理）

本報告書は、平成１１年度におけるエネルギーシステム研究部の研究活動状況をとりまとめたものである。

エネルギーシステム研究部は、平成 10 年度より新たに編成された部であり、将来型炉等新たなエネルギーシステムを視野に入れた基礎基盤的な研究を進めている。エネルギーシステム研究部の研究分野は、核及び原子分子データの評価や低減速スペクトル炉の概念設計研究、炉物理実験及び炉特性解析コードの開発、伝熱流動実験及び解析、原子力用新材料の開発及び経年挙動研究、新型燃料の研究、舶用炉及び原子力船システムの研究等の研究開発に亘っている。この他、エネルギーシステム研究部の各種炉工学施設の維持・管理も行っている。

本報告では、エネルギーシステム研究部が運営を担当する研究委員会の活動報告もとりまとめられている。

東海研究所：〒319-1195　茨城県那珂郡東海村白方白根２－４

Contents

This is a blank page.

Preface

The research activities of the Department of Nuclear Energy System, Japan Atomic Energy Research Institute, during the fiscal year 1999 (April 1999 - March 2000) are presented in this report. The Department of Nuclear Energy System was newly organized in April 1998 as the course of the reorganization in Japan Atomic Energy Research Institute. The Department is expected to do the work relating to the development and utilization of an advanced nuclear energy system. The research activities cover such fields as reactor physics, thermal-hydraulics, material science including research for advanced fuel and R&D for nuclear ship.

The total number of permanent staff working in the department during the year was 127 including the clerical service staff. The Department was funded from JAERI expenditure amounting to 820 million yen for FY 1999, excluding nuclear fuel cost and personnel expense. About 350 million yen was provided by the research contracts with external organizations; Science and Technology Agency (STA) for non-destructive measurement technology of trans-uranic elements (TRU) , for demonstration test on lifetime reliability of structural materials for an advanced prototype power reactor and for demonstration of reliability of new materials used in nuclear fuel reprocessing plant, Japan Nuclear Cycle Development Institute (JNC) for reactor physics constants of a fast breeder reactor and covariances of major actinide data, and Mitsubishi Research Institute, Inc. (MRI) for investigation of the development and research on cladding required for high burn-up. The Department has served as the secretariat of Japanese Nuclear Data Committee, the Research Committee on Reactor Physics and the Research Committee on Marine Reactors.

The research activities have been conducted in ten research groups with the support of two divisions.

Nuclear Data Center

This center has two main research themes; one is nuclear data and the other is atomic & molecular data. As to the nuclear data, the research activities consist of nuclear data evaluation of JENDL files (including Special Purpose Files as well as General Purpose File) for the general applications and nuclear data measurements to enrich the fundamental database. Reevaluation work for JENDL-3.3 has finished, and file editing has started. Wide range of benchmark test is forseen in the next fiscal year. Some progresses are also made for JENDL high-energy files. As to the atomic & molecular data, main efforts are devoted to compilation and evaluation of atomic and molecular collision data for JAEMDL-5. Fundamental database having been developed so far including atomic & molecular data as well as nuclear data are available through WWW

(http://wwwndc.tokai.jaeri.go.jp) of our home page.

This center has a function of the National Center that disseminates the nuclear and atomic & molecular data to Japanese customers, contacts the foreign and international centers and coordinates the international collaboration. This center also serves as a secretariat of Japanese Nuclear Data Committee. We are going to hold an International Conference on Nuclear Data for Science and Technology (ND-2001) at October 2001 in Tsukuba City. Official organizing committees are set up and preparation work has started.

Research Group for Energy System Assessment

In the development of analytical tools, a macro-economy model was developed in order to analyze possible economic impacts of nuclear moratorium. In the analysis of energy systems, long-term scenarios were developed for the evolution of power reactors and fuel cycle systems of Japan, and their implications were analyzed from various viewpoints. In addition, detailed analysis was made on the effect of changing conversion ratios and/or initial plutonium loadings of reduced moderation water reactors to natural uranium requirement of nuclear energy systems.

Research Group for Advanced Reactor System

Main research activity of this group is the study of reduced-moderation water reactor (RMWR), which includes core design study, basic thermal hydraulic investigation and evaluation of introduction effect of RMWR. Another research area is development of diagnosis system of nuclear power plants based on the neural networks, and new reactor instrumentation by utilizing optical fiber.

Research Group for Reactor Physics

Research field of this group covers very wide range of fundamental studies on reactor physics and their applications to nuclear fuel cycle systems. Main areas are development of calculation code systems, reactor physics experiments using critical assemblies FCA and TCA, new reactor concepts and non-destructive assay of TRU content in radioactive waste package. The code development work has been continued for high speed and high accuracy Monte Carlo codes and nodal codes to construct a comprehensive code system for reactor core design including thermal-hydraulics, core management and kinetics. The experimental studies have been concentrated on the accelerator-driven sub-critical systems, reduced-moderation water reactors, gas-cooled fast reactors and so on.

Research Group for Thermal and Fluid Engineering

Design studies were widely performed to check the feasibility of the proposed concepts of reduced moderation water reactors (RMWRs) under normal operation and several abnormal events, as well as a model experiment for critical heat flux (CHF) in a tight lattice core. Construction of a new test facility for the simulation of the ingress of the coolant event (ICE) in the ITER was completed to obtain data for the assessment of the safety analysis codes.

Research Group for Reactor Structural Materials

This research group carries out irradiation assisted stress corrosion cracking (IASCC) study, demonstration test on lifetime reliability of structural materials for advanced prototype power reactors (STA commissioned research), and development of material performance database.

Research Group for Compatible Materials

R&D on the advanced materials have been extensively carried out aiming at the establishment of new techniques for material evaluation and the development of advanced materials on the basis of the results of the material evaluation. The mechanisms of SCC of zirconium and local attacks of steels in nitric acids were analyzed and modeled. On the demonstration test of material performance for Rokkasho reprocessing plant sponsored by the STA, the acid recovery evaporator and dissolver mock-ups were operated.

Research Group for Advanced Fuel

The activities of the group focus on R&D of advanced fuels from the viewpoint of proposing and realizing a flexible fuel cycle system in the coming century. Rock-like fuel has been developed for burning excess plutonium in existing LWRs coupled with direct depository of spent fuel as a short-term subject. As a long-term subject, nitride fuel has been investigated for the transmutation of long-lived minor actinides and also advanced fast reactors, which shall be coupled with pyrochemical reprocessing in a molten salt.

Advanced Marine Reactor Laboratory

Designs of very small-scale and highly compact reactors having passive safety systems have studied, aiming use for an under-sea research vessel and for heat supply at an office building. The cores were designed so as to provide a long life period, 12 years for the former reactor with 1.25 MWt and 10 years for the latter reactor with 1 MWt, with a load factor of 50 %. The development of the in-vessel type CRDM as one of key components in the marine reactor was completed.

Nuclear Ship System Laboratory

In R&D related to nuclear ship systems, advanced automatic control foe nuclear ships and nuclear engineering simulation system development has been studied. Operator's knowledge for the advanced automatic operation system has been revised using the new graphical tool. Start-up and shutdown operations of the integral-type nuclear ship reactor has been examined for an stable manual operation and control system design.

Reactor Engineering Facility Operation Division

This division operated three large-scale engineering facilities; FCA, TCA and Heat Transfer Fluid Flow Test Facilities in accordance with each experiment program and maintained in the monthly or the annual inspection. Consequently safety operations of these facilities were achieved and contributed sufficiently to the execution of each experimental study. Furthermore the maintenance work for VHTRC was put into practice as scheduled.

The Department is involved in the following project-oriented program in JAERI;

(1) Design Studies of Advanced Reactors

(2) Development of High Temperature Gas-Cooled Reactor

(3) Engineering Research for a Fusion Reactor

The activities of the Department in FY 1999 have contributed to the essential progress in the field of reactor engineering.

Masayuki Nakagawa, Director
Department of Nuclear Energy System
September 30, 2000

1. Nuclear Data, and Atomic and Molecular Data

Both evaluation for JENDL3.3 General Purpose File and JENDL Special Purpose Files have been progressed significantly with the cooperation of JNDC (Japanese Nuclear Data Committee).

As to the JENDL3.3 General Purpose File, two groups are worked out for the revision, one is for heavy actinides group concerning U and Pu evaluations, and the other is medium-heavy nuclides like structural/coolant materials. Re-evaluation work is finished and file editing and benchmark tests are foreseen.

As to the Intermediate Energy File, which is important for new applications emerging recently such as Accelerator Driven System in the Neutron Science Research, much effort are made for the file developments of JENDL High Energy File, JENDL PKA/KERMA File and JENDL Photonuclear Data File. The evaluation work for the neutron and proton files up to 3GeV is progressed for about 40 second-priority nuclei succeeding the first priority ones, which is finished last year.

As to the Covariance File development, evaluations of covariances for neutron nuclear data important for FBR applications was made for the JENDL-3.2 evaluated data. U-233 covariances are newly estimated and re-evaluation work is also made to improve the data for the one already evaluated.

As to the data dissemination, we are opening all of our data through our home page (http://wwwndc.tokai.jaeri.go.jp). To enhance the data use in the astro-physics research especially in stellar evolution or nucleothynthesis, Maxwellian averaged cross sections are calculated and tabled out from JENDL-3.2 data file. A program of generating Chart of the Nuclides in WEB is also developed and the code is fully utilized to reflect the latest data revision.

Mass chain evaluation has been continued within the framework of the international cooperation for the ENSDF File. The evaluation of mass chain A=119 and 125 have been made and the results are published in Nuclear Data Sheets.

For the preparation of group constants, the libraries for ORIGEN2 Code based on JENDL-3.2 data were produced for the specific MOX fuels utilized in Japan for BWR, PWR and FBR. Good performances on the PWR were confirmed.

As to the atomic and molecular data, data developments for JAEMDL-5 have been progressed. A compilation work on the cross section for electron collision with CO, CO_2 and H_2O relevant to edge plasma impurities was made, this is a very important data in the modeling of the plasma simulations. And also electron collision cross sections

with hydrocarbons such as CH_2, C_2H_6, C_3H_8, C_2H_4, C_3H_6 and C_2H_2 were obtained. All of the above stated data are presented as analytical forms for the convenience of the users. To supply fundamental data for the plasma modeling, ion production cross-sections in the collisions of $H^+ + H_2$, $H^+ + D_2$, $D + H_2$ and $D^+ + D_2$ collisions are studied. Ion production cross-sections are calculated by using a trajectory hopping method with the die-atomics-in-molecules (DIM) potential energy surfaces. Also radiation recombination cross sections in the K, L and M-shells for one-electron systems are calculated and tabulated for the element Z=1 to 112 by the exact relativistic descriptions.

1.1 Improvement of Covariance Data for Fast Reactors

K. Shibata, H. Matsuobu[*1], T. Murata[*2] and T. Kawano[*3]
(*e-mail:* shibata@ndc.tokai.jaer.go.jp)

We have revised the covariances of ^{16}O inelastic scattering cross sections, ^{23}Na total cross sections, ^{235}U fission cross sections, ^{238}U capture cross sections, and ^{238}U resonance parameters in JENDL-3.2[1]. Moreover, the covariances of ^{233}U data were newly estimated.

The covariances of the ^{16}O inelastic scattering cross sections for the second and third excited states were re-estimated by taking account of available experimental data and the uncertainties in model calculations obtained on the KALMAN system[2], because it was pointed out that the original variances seemed too small.

The standard deviations of ^{23}Na resonance parameters were evaluated[3] in 1996. However, it was found that these data yielded too small uncertainties in the total cross sections in the resonance region below 350 keV. In the present work, the covariances of the total cross sections were estimated from experimental data instead of those for the resonance parameters. The estimation was performed in the energy region from 10^{-5} eV to 20 MeV. A lest-squares fitting code GMA[4] was used after averaging measured resonance cross sections in a certain energy interval. The total cross sections and their uncertainties obtained are shown in Fig. 1.1.1.

The covariances of the fission cross section of ^{235}U were originally obtained by the simultaneous evaluation[5] taking account of absolute and ratio measurements. However, the fission cross sections measured by Lisowski et al.[6] were compiled into JENDL-3.2 above 12 MeV. The cross sections obtained from the simultaneous evaluation were discarded in this energy region, but the covariances remained unchanged. Therefore, there was inconsistency between ^{235}U fission cross sections and their covariances. The present work was undertaken to remove the inconsistency by estimating the covariances from the Lisowski data.

Above 150 keV, the covariances of the ^{238}U capture cross section in JENDL-3.2 were originally estimated from the uncertainties in nuclear model calculations on the KALMAN system, while the mean values (JENDL-3.2 capture cross sections) were obtained from available experimental data. We have a guideline[7] that covariances should be obtained by using the same methodology that was used in the evaluation of JENDL-3.2. Thus, in the present work, the covariances of the ^{238}U capture cross sections were estimated above 150

*1 Data Engineering, Inc.
*2 AITEL Corporation
*3 Kyushu University

keV from experimental data.

It was found that the covariances of ^{238}U resonance parameters yielded too small standard deviations of cross sections in the resonance region below 10 keV, because correlation was neglected among the resonance parameters. In the present work, we estimated the covariances of s-wave resonance parameters on the KALMAN system. The uncertainties in the resonance energies were neglected, since the energies were measured precisely. The ^{238}U fission cross section is very small in the resonance region, and thus the errors of fission widths are not given. The covariances obtained were adjusted so as to reproduce the uncertainties in the measured average cross sections.

The covariances of the ^{233}U data in JENEDL-3.2 were newly estimated. The quantities estimated are covariances of the total cross section, elastic and inelastic scattering cross sections, fission cross section, (n,2n) cross section, (n,3n) cross section, capture cross section, elastic angular distribution, resonance parameters, and the average number of prompt and delayed neutrons.

References:

1) Nakagawa, T, Shibata, K., Chiba, S., Fukahori, T., Nakajima, Y., Kikuchi, Y., Kawano, T., Kanda, Y., Ohsawa, T., Matsunobu, H., Kawai, M., Zukeran, A., Watanabe, T., Igarasi, S., Kosako, K., and Asami, T.: "Japanese Evaluated Nuclear Data Library Version 3 Revision-2: JENDL-3.2", J. Nucl. Sci. Technol., 32, 1259 (1995).

2) Kawano, T. and Shibata, K.: "Covariance Evaluation System", JAERI-Data/Code 97-037 (1997) [in Japanese].

3) Shibata, K., Nakajima, Y., Kawano, T., Oh, S.Y., Matsunobu, H., and Murata, T.: "Estimation of Covariances of ^{16}O, ^{23}Na, Fe, ^{235}U, ^{238}U and ^{239}Pu Neutron Nuclear Data in JENDL-3.2", JAERI-Research 97-074 (1997).

4) Poenitz, W.P.: Proc. Conf. Nuclear Data Evaluation Methods and Procedures, BNL-NCS-51363, p.249 (1981).

5) Kanda, Y., et al.: Proc. Int. Conf. Nuclear Data for Basic and Applied Science, Santa Fe 1985, p.1567 (1986).

6) Lisowski, P.W., et al.: Proc. Int. Conf. Nuclear Data for Science and Technology, Jülich 1991, p.177 (1991).

7) Oh, S.Y. and Shibata, K.: "Evaluation of Covariance Data for Chromium, Iron and Nickel Contained in JENDL-3.2", J. Nucl. Sci. Technol., 35, 66 (1998).

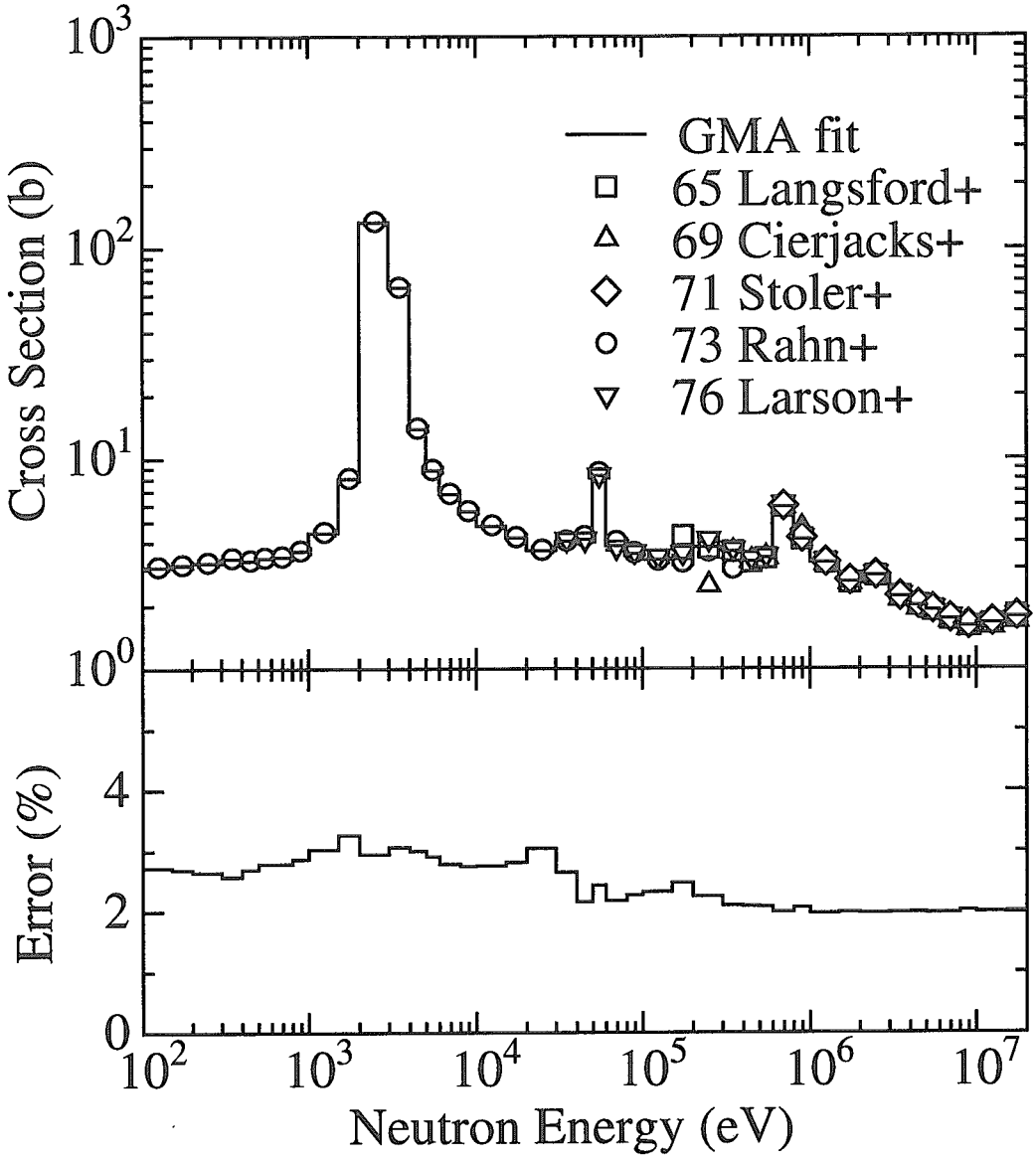

Fig. 1.1.1 ^{23}Na total cross section and its standard deviation

1.2 Evaluation of Medium-Heavy Nuclide Data for JENDL-3.3

K. Shibata and Medium-Heavy Nuclide Data Evaluation Working Group* of Japanese Nuclear Data Committee
(*e-mail:* shibata@ndc.tokai.jaer.go.jp)

Neutron nuclear data for medium-heavy nuclei have been evaluated for JENDL-3.3 in the energy region from 10^{-5} eV to 20 MeV. The evaluated nuclides are ^{46,47,48,49,50}Ti, V, ^{50,52,53,54}Cr, ^{54,56,57,58}Fe, ^{59}Co, ^{58,60,61,62,64}Ni, ^{93}Nb, ^{182,183,184,186}W. The data for V are regarded as elemental data, while no elemental data were constructed for other nuclides. Except for ^{61,62,64}Ni, emitted neutron and charged-particle spectra were taken form the JENDL Fusion File 99[1] in the form of the ENDF-6 format File 6.

For Ti isotopes, the upper limits of the resonance regions were extended to higher energies. New optical model calculations removed an anomaly found in the elastic angular distribution for elemental Ti around 60 deg. at 14MeV. The cross sections for threshold reactions on Ti isotopes were also revised by considering new calculations and other libraries.

The resonance parameters for ^{51}V were modified so as to reproduce experimental data with the Reich-Moore formula. The contribution from ^{50}V was compiled into the background cross section. The total cross section of V was evaluated on the basis of the data measured by Rohr et al.[2] above 100 keV. Moreover, the capture cross section of V was calculated by the direct and semi-direct model above 1.5 MeV.

The resonance parameters of Cr isotopes were updated with the Reich-Moore formula. Gamma-ray production cross sections were evaluated for each isotope by using the EGNASH code[3].

The resonance parameters of ^{54}Fe and ^{56}Fe were taken from ENDF/B-VI and JEF-2.2, respectively. The upper limits of the resonance region for ^{54}Fe and ^{56}Fe (250 keV for both isotopes in JENDL-3.2) were extended to 700 keV and 850 keV, respectively. The total cross section of ^{54}Fe was based on the data measured by Carlton et al.[4] and Cornelis et al.[5] The total cross section of elemental Fe was evaluated on the basis of Berthold et al.[6], Carlson et al.[7], and Perey et al.[8] The total cross section of ^{56}Fe was obtained by subtracting the contributions of other isotopes from the elemental cross section. The ^{56}Fe(n,2n) cross section was calculated by using the TNG code[9]. Above 5 MeV, the capture cross sections of

* Members are K. Shibata, T. Asami (Data Engineerging, Inc.), Y. Harima (CRC), M. Igashira (Tokyo Institute of Technology), H. Kitazawa (National Defense Academy), T. Watanabe (Kawasaki Heavy Industry), Y. Watanabe (Kyushu University), N. Yamamuro (Tokyo Institute of Technology).

$^{54, 56, 57}$Fe were modified by considering the pre-equilibrium capture cross sections calculated by the TNG code.

The resonance parameters of ^{59}Co were modified with the Reich-Moore formula. The ^{59}Co(n,2n) cross section was taken from the JENDL Activation Cross Section File 96[10]. The total cross section of ^{59}Co was also modified.

The cross sections for the threshold reactions on Ni isotopes were evaluated by using the EGNASH code. Gamma-ray production data for $^{61, 62, 64}$Ni were obtained from the EGNASH calculations. The capture gamma-ray spectra for ^{93}Nb were modified in the MeV region by considering the direct and semi-direct capture effects.

The resonance parameters of $^{182, 186}$W were re-evaluated. As a result, we could solve the problem related to small resonance integrals for the ^{186}W(n,γ) cross sections.

References:

1) Chiba, S., Fukahori, T., Shibata, K., Yu, B., and Kosako, K.: "Status and Evaluation Methods of JENDL Fusion File and JENDL PKA/KERMA File", Fusion Eng. Des., 37, 175 (1997).
2) Rohr, G., et al.: Taken from EXFOR (1995).
3) Yamamuro, N.: "A Nuclear Cross Section Calculation System with Simplified Input-Format Version II (SICROS-II)", JAERI-M 90-006 (1990).
4) Carlton, R.F., Harvey, J.A., and Castel, B.: Bull. Am. Phys. Soc., 30, 1252 (1985).
5) Cornelis, E., Mewissen, L., and Poortmans, F.: Proc. Int. Conf. Nuclear Data for Science and Technology, Antwerp 1982, p.125 (1983).
6) Berthold, K., Nazareth, C., Rohr, G., and Weigmann: Taken from EXFOR (1995).
7) Carlson, A.D. and Cerbone, R.J.: Nucl. Sci. Eng., 42, 28 (1970).
8) Perey, F.G., Love, T.A., and Kinney, W.E.: ORNL-4283 (1972).
9) Shibata, K. and Fu, C.Y.: "Recent Improvements of the TNG Statistical Model Code", ORNL/TM-10093 (1986).
10) Nakajima, Y., et al.: To be published as a JAERI report.

1.3 Nuclear Data Evaluation and Compilation for JENDL Intermediate Energy Files in 1999

T. Fukahori and Japanese Nuclear Data Committee (High Energy Nuclear Data Evaluation WG)
(*E-mail*: fukahori@ndc.tokai.jaeri.go.jp)

The JAERI Nuclear Data Center started evaluation work in cooperation with Japanese Nuclear Data Committee (JNDC) to produce files related intermediate energy, which are JENDL High Energy File, JENDL PKA/KERMA File and JENDL Photonuclear Data File.

The JENDL High Energy File includes nuclear data for proton- and neutron-induced reactions. Below 20 MeV, the data of JENDL Fusion File[1] or JENDL-3.2[2] are adopted. The neutron file for IFMIF[3] in the energy range up to 50 MeV has been merged with files below 20 MeV. The evaluation work for the neutron and proton files energy range up to 3 GeV is performed for the second-priority 42 nuclei by mainly using the "quick-GNASH system"[4] and JQMD code[5]. The target isotopes included in the JENDL High Energy File are summarized in Table 1.3.1 as well as priorities. The semi-empirical formulae derived by Pearlstein[6], Wellisch[7] and NASA[8] were examined to calculate total, elastic scattering and non-elastic scattering cross sections in the intermediate energy region for the target nuclei having less experimental data. The Pearlstein's systematics has been modified to reproduce experimental data much better than before (Figs.1.3.1-2). The angular distribution of elastic scattering has also been included. Those results have been summarized into the code TOTELA.

The JENDL Photonuclear Data File is being developed for gamma-ray induced reaction data up to 140 MeV. The photon absorption cross section is evaluated with the giant dipole resonance model and quasi-deuteron model, and the decaying processes are estimated with the statistical model with preequilibrium correction by using MCPHOTO[10] and ALICE-F[11] codes. Evaluated results for the 26 target nuclides were compared with the other photonuclear data files evaluated at Los Alamos, Beijing, Moscow and Obninsk as well as experimental data (Figs.1.3.3-4). The evaluated results were compiled in ENDF-6 format and those preliminary review was performed.

The JENDL PKA/KERMA File is generated to supply primary knock-on atom (PKA) spectra, damage energy spectra, DPA (displacement per atom) cross sections and kerma factors by neutron-induced reactions in the energy region up to 50 MeV. A processing code system, ESPERANT[11] was developed to calculate above quantities from evaluated nuclear data file by using effective single particle emission approximation (ESPEA). For light mass nuclei, SCINFUL/DDX code, which considers break-up reactions with PKA spectra is used as well as EXIFON code which can calculate with correction of preequilibrium process.

References:

1) Baosheng, Y., et al.: J. Nucl. Sci. Technol., 29 677 (1992).
2) Nakagawa, T., et al.: ibid., 32 1259 (1995).
3) Noda, K.: Proc. of 1994 Symposium on Nuclear Data, Tokai, Japan, Nov. 17-18, 1994, JAERI-Conf 95-008, p.112 (1995).
4) Chadwick, M.B. and Young, P.G.: Phys. Rev., C47, 2255 (1993).
5) Niita, K. and Chiba, S.: "JQMD: Quantum Molecular Dynamics and Statistical Decay Model Code", private communication.
6) Pearlstein, S.: J. Astrophys., 346, 1049 (1989).
7) Wellisch, H.P. and Axen, D.: Phys. Rev., C54, 1329 (1996).
8) Tripathi, R.K., Cucinotta, F.A. and Wilson, J.W.; NASA Technical Paper 3621 (1997), NASA/TP-1998-208438 (1998).
9) Kishida, N. and Kadotani, H.: private communication.
10) Fukahori, T.: Proc. Specialists' Meeting on High Energy Nuclear Data, Tokai, Ibaraki, Oct. 3-4, 1991, JAERI-M 92-039, p.114 (1992).
11) Fukahori, T., et al.: Proc. of the Third Specialists' Meeting on Nuclear Data for Fission Reactors, Tokai, Japan, Nov. 29-30, 1995, JAERI-Conf 96-005, p.130 (1996).

Table 1.3.1 Isotopes included in neutron and proton file up to 3 GeV and their priorities.

1st priority (42 nuclides)	^{1}H, ^{12}C, ^{14}N, ^{16}O, ^{23}Na, ^{27}Al, ^{50,52,53,54}Cr, ^{54,56,57,58}Fe, ^{58,60,61,62,64}Ni, ^{63,65}Cu, ^{181}Ta, ^{180,182,183,184,186}W, ^{197}Au, ^{196,198,199,200,201,202,204}Hg, ^{204,206,207,208}Pb, ^{209}Bi, ^{235,238}U
2nd priority (42 nuclides)	^{2}H, ^{9}Be, ^{24,25,26}Mg, ^{28,29,30}Si, ^{39,41}K, ^{40,42,43,44,46,48}Ca, ^{46,47,48,49,50}Ti, ^{51}V, ^{55}Mn, ^{59}Co, ^{90,91,92,94,96}Zr, ^{93}Nb, ^{92,94,95,96,97,98,100}Mo, ^{238,239,240,241,242}Pu
3rd priority (38 nuclides)	^{6,7}Li, ^{10,11}B, ^{13}C, ^{19}F, ^{35,37}Cl, ^{35,38,40}Ar, ^{64,66,67,68,70}Zn, ^{69,71}Ga, ^{70,72,73,74,76}Ge, ^{75}As, ^{89}Y, ^{232}Th, ^{233,234,236}U, ^{237}Np, ^{241,242,242m,243}Am, ^{243,244,245,246}Cm

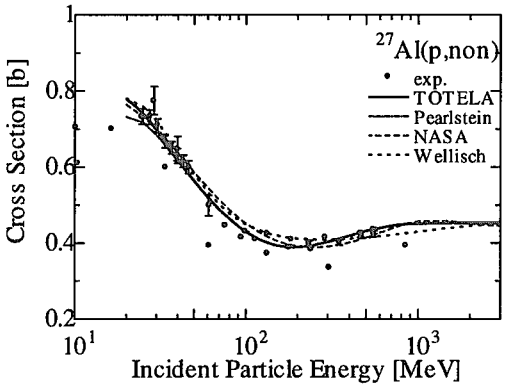

Fig. 1.3.1 Proton-induced non-elastic cross section of ^{27}Al

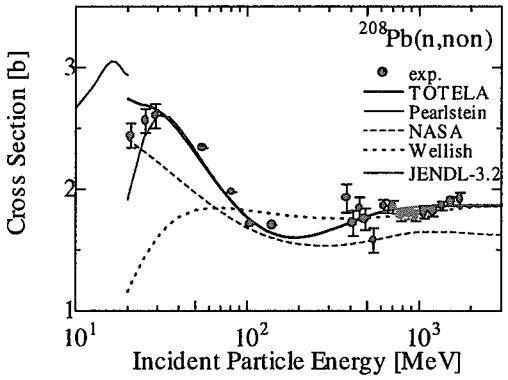

Fig. 1.3.2 Neutron-induced non-elastic cross section of ^{208}Pb

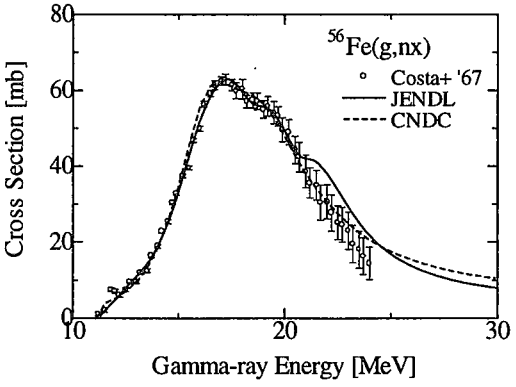

Fig. 1.3.3 Photoneutron production cross section of ^{56}Fe

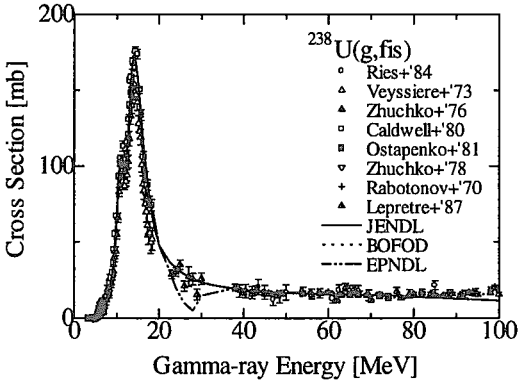

Fig. 1.3.4 Photofission cross section of ^{238}U

1.4 Maxwellian-Averaged Cross Sections Calculated from JENDL-3.2

T.Nakagawa, S.Chiba, T.Ohsaki* and M.Igashira*
(*E-mail*: nakagawa@ndc.tokai.jaeri.go.jp)

Maxwellian-averaged cross sections of the neutron capture, fission, (n,p) and (n,α) reactions of 317 nuclides were calculated from JENDL-3.2 for applications in the astrophysics. The average cross sections were calculated in the temperature range from $kT = 1$ keV to 1 MeV with the following formula:

$$\langle \sigma(kT) \rangle = \frac{2}{\sqrt{\pi}} (kT)^{-2} \int \sigma(E) E \exp\left(-\frac{E}{kT} \right) dE ,$$

where T is the temperature, k Boltzmann's constant, $\sigma(E)$ the cross section given in JENDL-3.2.

Figures 1.4.1 and 1.4.2 compare the present results at kT=30 keV for the capture cross section with the average cross sections recommended by Beer et al.[1] Large discrepancies were found for some nuclides. For example, Figure 1.4.3 shows the average capture cross section of ^{16}O. JENDL-3.2 is in very good agreement with recent experimental data measured by Igashira et al.[2] Other recommendations[1,3,4] are too small. The temperature dependence is also deferent from each other. Since JENDL-3.2 follows the energy dependence of available experimental data of the capture cross section, the shape of JENDL-3.2 average cross section might be more correct than others in the case of ^{16}O.

This work was published as JEARI-Research 2000-002.

References:

1) Beer H., Voss F. and Winters R.R.: *Astrophys. J. Suppl.*, **80**, 403 (1992).
2) Igashira M., et al.: *Astrophys. J.*, **441**, L89 (1995).
3) Bao Z.Y. and Käppeler F.: *At. Data Nucl. Data Tables*, **36**, 411 (1987).
4) Thielmann F.-K., Arnould M. and Truran J.W.: *Advances in Nuclear Astropysics*, ed. Vangiona-Flam, Editions Frontière, 525 (1987), http://isotopes.lbl.gov/isotopes/astro/friedel.html

* Research Laboratory for Nuclear Reactors, Tokyo Institute of Technology

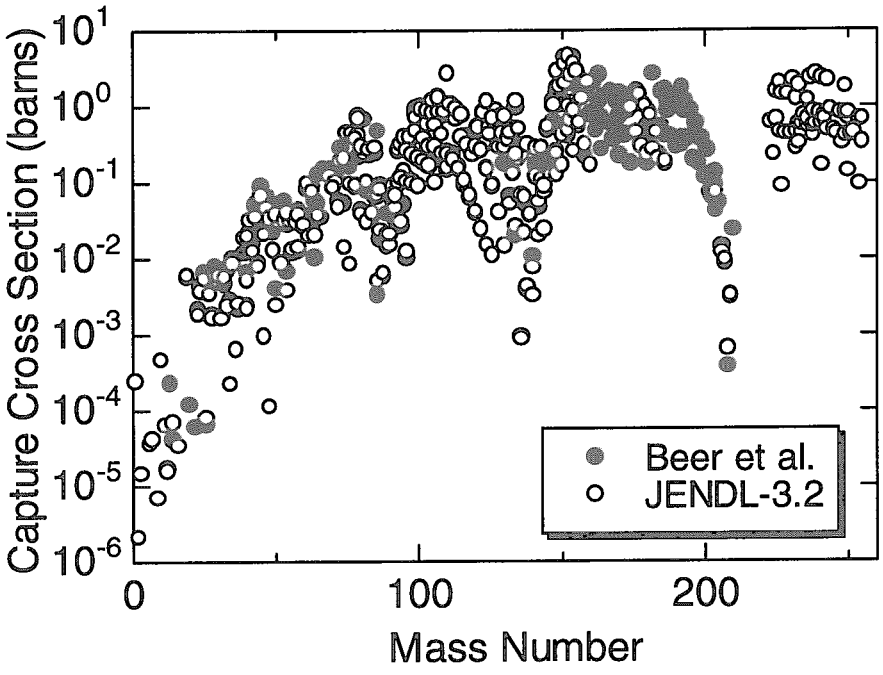

Fig. 1.4.1 Comparison of Maxwellian-averaged capture cross sections at $kT = 30$ keV

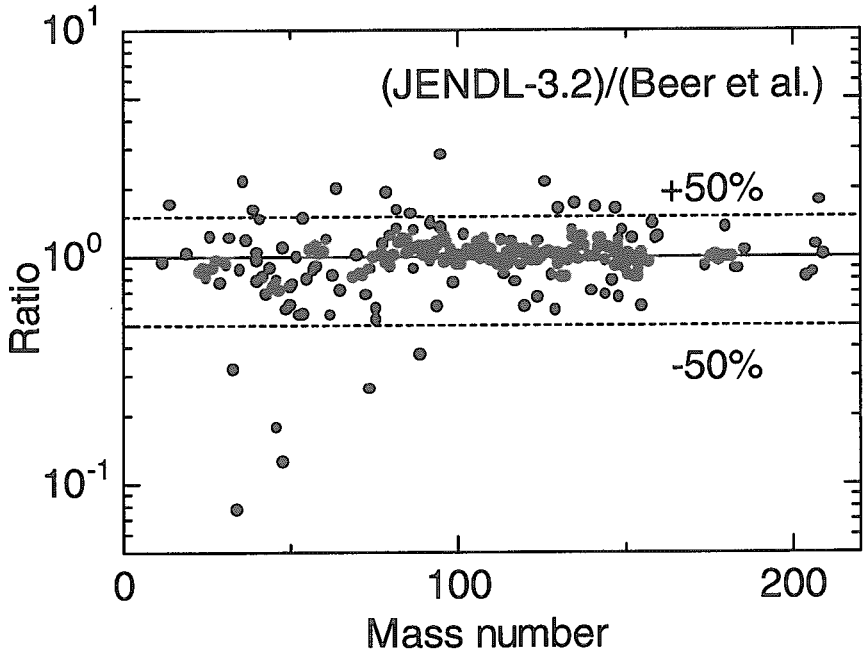

Fig.1.4.2 Comparison of Maxwellian-averaged capture cross sections at $kT = 30$ keV

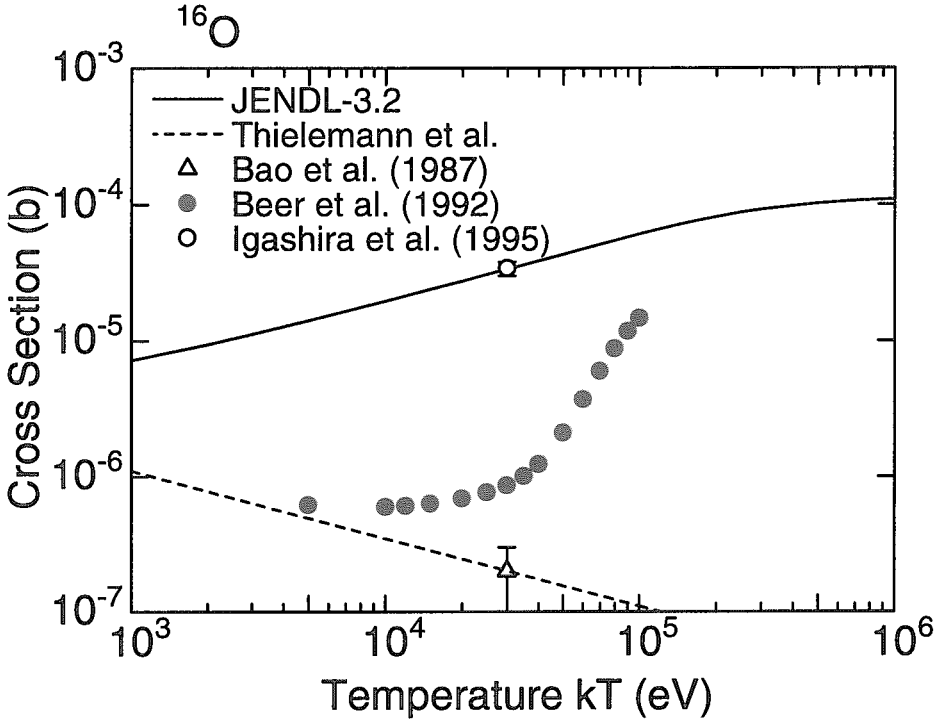

Fig.1.4.3 Maxwellian-averaged capture cross section of ^{16}O

1.5 WWW Chart of the Nuclides

T.Nakagawa, J.Katakura and T.Horiguchi[*1]
(*E-mail*: nakagawa@ndc.tokai.jaeri.go.jp)

The nuclear data center publishes "Chart of the Nuclides" every four years. A database of information on nuclides used to make the "Chart of the Nuclides" is updated every year. A computer program system[1)] has been developed to create a WWW Chart of the Nuclides, by using the database, which is a World Wide Web version of "Chart of the Nuclides".

"WWW Chart of the Nuclides 1999" has been created by using the computer program system and the database updated in 1999. This version is available from the URL of "http://wwwndc. tokai.jaeri.go.jp/CN99/index.html". The chart is divided into 29 small parts. An example of "Chart of the Nuclide 1999" is given in Fig. 1.5.1. The half-life and decay mode are distinguished by color and style of each nuclide box. The nuclide box links to various information of nuclides mainly based on the evaluated nuclear data library JENDL-3.2[2)]; a table of thermal cross sections, resonance integrals, Maxwell averaged cross sections, fission spectrum averaged cross sections, figures of cross sections, etc. Figure 1.5.2 is an example of cross section graphs.

References:

1) Nakagawa T., Katakura J. and Horiguchi T.: "Computer Programs to Make A Chart of The Nuclides for WWW," JAERI-Data/Code 99-032 (1999).
2) Nakagawa T., et al.: *J. Nucl. Sci. Technol.*, **32**, 1259 (1995).

[*1] Department of Clinical Radiology, Faculty of Health Sciences, Hiroshima International University

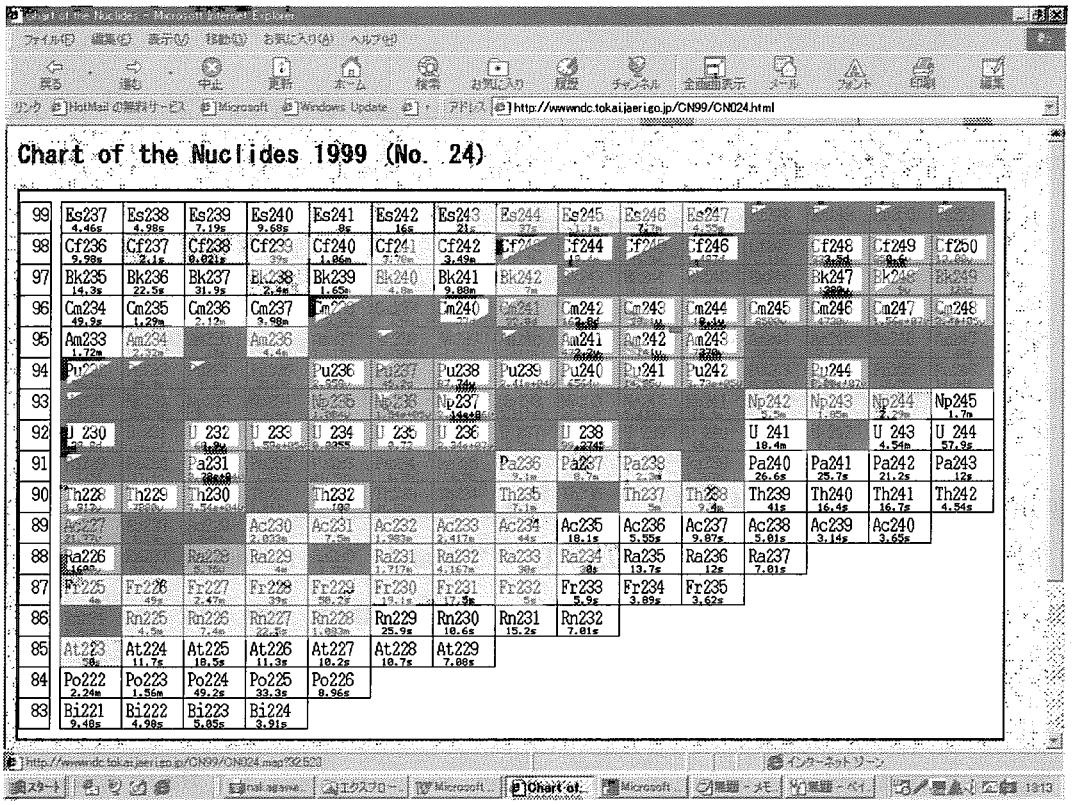

Fig. 1.5.1 Example of WWW Chart of the Nuclides 1999

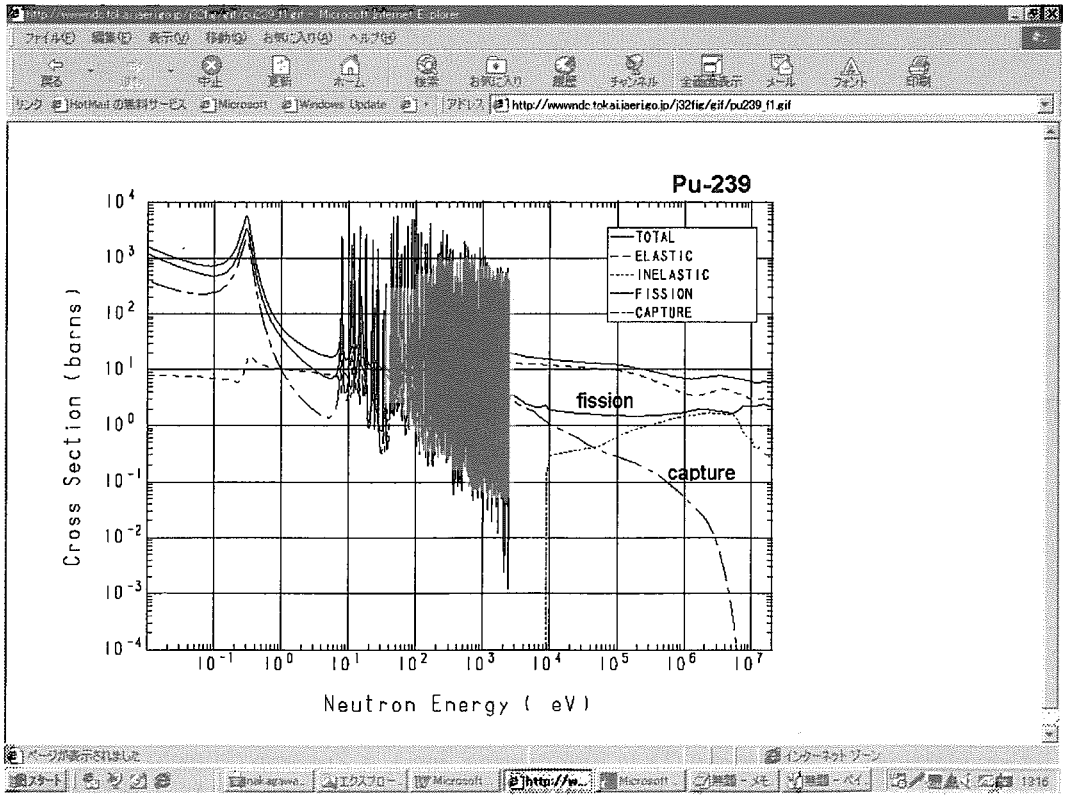

Fig. 1.5.2 Example of cross section graphs

1.6 Nuclear Data Evaluation of Heavy Nuclides for JENDL-3.3

T. Kawano[*1] and Heavy Nuclide Data Evaluation Working Group[*2] of Japanese Nuclear Data Committee

(*E-mail*: nakagawa@ndc.tokai.jaeri.go.jp)

The nuclear data of ^{233}U, ^{235}U, ^{236}U, ^{238}U, ^{239}Pu, ^{240}Pu, ^{241}Pu and ^{242}Pu have been re-evaluated for JENDL-3.3 in the neutron energy range from 10^{-5} eV to 20 MeV.

The fission cross section of ^{233}U, ^{235}U, ^{238}U, ^{239}Pu, ^{240}Pu and ^{241}Pu

The fission cross sections of ^{233}U, ^{235}U, ^{239}Pu and ^{241}Pu in the neutron energy range from 30 keV to 20 MeV, and those of ^{238}U and ^{239}Pu from 100 keV to 20 MeV were determined[1,2] by adopting the simultaneous evaluation method. For this purpose a new computer code of SOK was developed by Kawano.[2]

Experimental data of absolute and relative measurements for those nuclides were carefully selected and compiled into a database. Covariance matrices of the experimental data were constructed from the uncertainty information reported in the references. Then, a least-squares method was applied to the selected data. Figure 1.6.1 shows the results for ^{233}U.

Resonance parameters of ^{235}U, ^{240}Pu and ^{242}Pu

The resolved resonance parameters of ^{235}U and ^{240}Pu were replaced with the recent analyses by Leal et al.[3] and Bouland et al.[4] Both sets of resonance parameters were analyzed with the SAMMY code adopting the Reich-Moore formula. The upper boundary of resolved resonance region was extended up to 2.25 keV for ^{235}U and 5.682 keV for ^{240}Pu. The resonance parameters of ^{242}Pu were also reevaluated.

[*1] Kyushu University

[*2] Members are T.Kawano (Kyushu University), T.Yoshida (Musashi Institute of Technology), T.Ohsawa (Kinki University), M.Baba (Tohoku University), M.Kawai (High Energy Accelerator Research Organization), H.Matsunobu (Data Engineering, Inc.), A.Zukeran (Hitachi Ltd.), Y.Nakajima (Research Organization for Information Science & technology), T.Murata (AITEL Corporation), T.Nakagawa, K.Shibata, O.Iwamoto

Direct and semi-direct capture cross section

The capture cross section of JENDL-3.2 for those nuclides in the MeV region was not correct because the direct and semi-direct capture cross section was not considered properly. In the present work, the direct and semi-direct capture cross sections were calculated with the DSD code developed by Kawano.[5)]

Secondary neutron spectra of the (n,n'), (n,2n), (n,3n) reactions and fission

The spectra of neutrons emitted from the (n,n'), (n,2n) and (n,3n) reactions were calculated with the EGNASH code.[6)]

The neutron spectra of the ^{235}U and ^{239}Pu were calculated by Ohsawa[7)] with a new method based on the multi-mode fission model, at the incident neutron energies up to 5 MeV. The new spectra are harder than those of JENDL-3.2. It was seen by comparing calculated average cross sections in the ^{235}U thermal fission spectrum with experimental data that the present spectra are better than JENDL-3.2.

Delayed neutron data

Decay constants and abundance of 6 temporal group of ^{235}U, ^{238}U and ^{239}Pu were revised by adopting the recommendation of Delayed Neutron Data Working Group of JNDC.[8)] The spectra of delayed neutrons were replaced with the summation calculation made by Brady and England.[9)]

Other parts modified from JENDL-3.2

The number of prompt neutrons per fission of ^{233}U and ^{235}U was revised. The (n,2n), (n,3n) and (n,4n) reaction cross sections were re-evaluated for ^{233}U, ^{235}U, ^{238}U and ^{240}Pu. The inelastic scattering cross sections were re-calculated for ^{238}U, ^{240}Pu and ^{242}Pu. The angular distributions of elastically scattered neutrons of ^{238}U were re-evaluated. Those of inelastic scattering were modified for ^{238}U, ^{240}Pu and ^{242}Pu.

References:

1) Kawano T., et al.: *J. Nucl. Sci. Technol.*, **37**, 327 (2000).
2) Kawano T., et al.: "Evaluation of Fission Cross Sections and Covariances for ^{233}U, ^{235}U, ^{238}U, ^{239}Pu, ^{240}Pu and ^{241}Pu," *JAERI-Research* 2000-004 (2000).

3) Leal L.C., et al.: *Nucl. Sci. Eng.*, **131**, 230 (1999).
4) Bouland O., et al.: *Nucl. Sci. Eng.*, **127**, 105 (1997).
5) Kawano T.: private communication (1999).
6) Yamamuro N.: "A Nuclear Cross Section Calculation System with Simplified Input-Format, Version II (SINCROS-II)," JAERI-M 90-006 (1990).
7) Ohsawa T.: to be published as JAERI-Research report.
8) Yoshida T., et al.: private communication (1999).
9) Brady M.C. and England T.R.: *Nucl. Sci. Eng.*, **103**, 129 (1989).

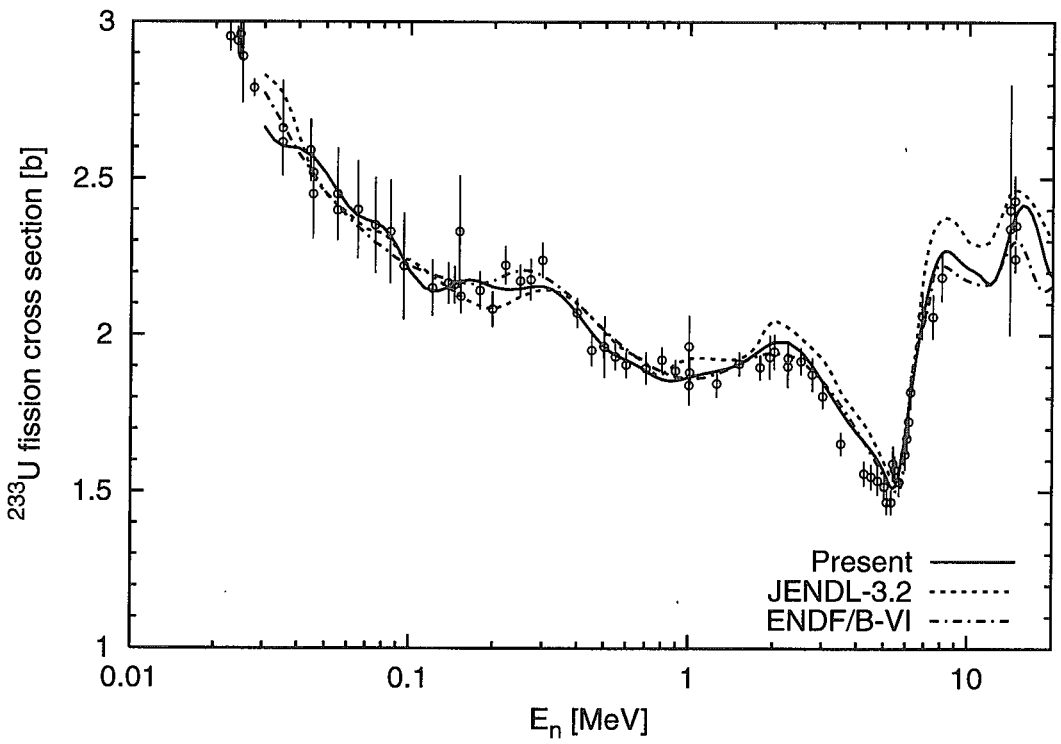

Fig.1.6.1 ^{233}U fission cross section

1.7 Evaluation and Compilation of Nuclear Structure and Decay Data in 1999

J. Katakura and ENSDF Group*
(*E-mail*: katakura@ndc.tokai.jaeri.go.jp)

The international network on nuclear structure and decay data evaluation aims at complete and continuous nuclear structure and decay data evaluation of all mass chains. The evaluated data are compiled as ENSDF (Evaluated Nuclear Struccture Data File) file. The data file is maintained and distributed by National Nuclear Data Center, Brookhaven National Laboratory (BNL), U.S.A. As a member of the network, Japanese group, whose data evaluation center is Nuclear Data Center, Japan Atomic Energy Research Institute, has responsibility for evaluating 12 mass chains with A=118-129.

In the fiscal year of 1999 (from April 1999 to March 2000), the evaluations of A=119 and 125 mass chains were published in Nuclear Data Sheets [1, 2] and the evaluation of A=121 were sent to BNL for review. The evaluation includes all experimental data available after last evaluations, 1992 for A=119, 1991 for A=121 and 1993 for A=125. The published data sets of A=119 and A=125 are listed in table 1.7.1 and 1.7.2.

The new data of other mass chains to which Japanese group has the responsibility are reviewed and being prepared for update of old mass chain evaluation.

References:

1) Katakura, J.: Nucl. Data Sheets, **86**, 955 (1999)

2) Ohya, S. and Kitao, K.: Nucl. Data Sheets, **89**, 345 (2000)

*Members are H. Iimura, M. Oshima, S. Ohya, K. Ogawa, J. Katakura, M. Kambe, K. Kitao, T. Tamura and Y. Tendow

Table 1.7.1 Updated data set of A=119

Nuclide	Data Type
^{119}Pd	Adopted Levels
^{119}Ag	Adopted Levels, Gammas
	^{119}Pd β^- Decay (0.92 s)
^{119}Cd	Adopted Levels, Gammas
	^{119}Ag β^- Decay (2.1 s)
^{119}In	Adopted Levels, Gammas
	^{119}Cd β^- Decay (2.69 min)
	^{119}Cd β^- Decay (2.20 min)
	^{119}In IT Decay
	^{120}Sn(μ^-,nγ)
	^{120}Sn(d,^{3}He)
^{119}Sn	Adopted Levels, Gammas
	^{119}In β^- Decay (2.4 min)
	^{119}In β^- Decay (18.0 min)
	^{119}Sn IT Decay
	^{119}Sb ε Decay
	^{116}Cd(α,nγ)
	^{118}Sn(n,γ) E=resonance
	^{118}Sn(d,p)
	^{118}Sn(d,pγ)
	^{118}Sn(t,d)
	^{119}Sn(p,p$'$)
	^{119}Sn(α,α'),(d,d$'$)
	Coulomb Excitation
	^{120}Sn(p,d)
	^{120}Sn(p,d),(^{3}He,α) IAS
	^{120}Sn(d,t)
	^{120}Sn(^{3}He,α)
	Sn(^{80}Se,^{80}Se$'$xnγ)

Nuclide	Data Type
^{119}Sb	Adopted Levels, Gammas
	^{119}Te ε Decay (16.05 h)
	^{119}Te ε Decay (4.70 d)
	^{116}Sn(α,p)
	^{118}Sn(p,p),(p,p$'$),(p,n) IAS
	^{118}Sn(^{3}He,d)
	^{118}Sn(^{7}Li,^{6}He)
	^{119}Sn(p,n)
	^{119}Sn(p,nγ)
	^{119}Sn(d,2nγ)
	^{119}Sn(^{3}He,t)
	(HI,xnγ)
^{119}Te	Adopted Levels, Gammas
	^{119}I ε Decay
	^{117}Sn(α,2nγ)
	^{120}Te(d,t)
	^{120}(^{3}He,α)
	(HI,xnγ)
^{119}I	Adopted Levels, Gammas
	^{119}Xe ε Decay
	(HI,xnγ)
^{119}Xe	Adopted Levels, Gammas
	^{119}Cs ε Decay (43.0 s)
	^{119}Cs ε Decay (30.4 s)
	(HI,xnγ)
^{119}Cs	Adopted Levels, Gammas
	(HI,xnγ)
^{119}Ba	Adopted Levels

Table 1.7.2 Updated data set of A=125

Nuclide	Data Type
^{125}Ag	Adopted Levels
^{125}Cd	Adopted Levels
^{125}In	Adopted Levels, Gammas ^{125}Cd β^- Decay (0.65 s) ^{125}Cd β^- Decay (0.48 s)
^{125}Sn	Adopted Levels, Gammas ^{125}In β^- Decay (12.2 s) ^{125}In β^- Decay (2.36 s) ^{124}Sn(n,γ) ^{124}Sn(d,p) ^{124}Sn(d,pγ) ^{124}Sn(α,^{3}He)
^{125}Sb	Adopted Levels, Gammas ^{125}Sn β^- Decay (9.52 min) ^{125}Sn β^- Decay (9.64 d) ^{124}Sn(pol p,p) IAR ^{124}Sn(^{3}He,d) ^{126}Te(d,^{3}He) ^{126}Te(t,α)
^{125}Te	Adopted Levels, Gammas ^{125}Sb β^- Decay ^{125}Te IT Decay ^{125}I ϵ Decay ^{124}Sn(α,3nγ) ^{124}Te(n,γ) E=thermal ^{124}Te(d,p) ^{124}Te(t,d) ^{125}Te(d,d′)
^{125}Te	Coulomb Excitation ^{126}Te(d,t) ^{126}Te(^{3}He,α) ^{127}I(μ^-,xnγ)
^{125}I	Adopted Levels, Gammas ^{125}Xe ε Decay ^{124}Te(p,p),(p,p′) IAR ^{124}Te(^{3}He,d) ^{124}Te(α,t) (HI,xnγ)
^{125}Xe	Adopted Levels, Gammas ^{125}Xe IT Decay ^{125}Cs ε Decay (HI,xnγ)
^{125}Cs	Adopted Levels, Gammas ^{125}Ba ε Decay (3.5 min) (HI,xnγ)
^{125}Ba	Adopted Levels, Gammas ^{125}La ε Decay (HI,xnγ)
^{125}La	Adopted Levels, Gammas ^{125}Ce ε Decay ^{112}Sn(^{16}O,2npγ)
^{125}Ce	Adopted Levels, Gammas ^{125}Pr ε Decay (HI,xnγ)
^{125}Pr	Adopted Levels

1.8 The Libraries for ORIGEN2 Code Based on JENDL-3.2: Development and Validation

K. Suyama, J. Katakura, Y. Ohkawachi* and M. Ishikawa*

(*E-mail*: kenya@CYCLONE.tokai.jaeri.go.jp)

A set of new libraries for ORIGEN2 code[1], ORLIBJ32[2,3] was developed based on Japanese evaluated nuclear data library JENDL-3.2[4]. Main objectives of the ORLIBJ32 are to calculate isotopic compositions averaged over a whole fuel assembly for the case of LWR, and to calculate isotopic compositions averaged over a whole core or blanket for the case of FBR.

The specifications for LWR libraries are founded on current fuel design parameters. In **Table 1**, main parameters of each library are shown. For PWR, a 17×17 fuel assembly is a target, and for BWR, 8×8 (step I and II) and 9×9 (step III) fuel assemblies are targets. For FBR libraries, as shown in **Table 2**, the parameters are chosen from request of analysts of fast reactor since no fixed specifications of FBR exist especially for a commercial fast reactor.

To validate the ORLIBJ32, Post Irradiation Examinations (PIE) data were analyzed using PWR41J32 in ORLIBJ32. In that PIE, data set named SF95 (contains five samples data, 14.7 ~38.1 GWd/t) and SF97 (contains five samples data, 31.3 ~ 48.2 GWd/t) were taken from 17×17 type fuel assembly irradiated in Japanese commercial PWR. These fuel assemblies have same initial enrichment of U-235, and the geometrical parameters are completely the same with the parameters used to make PWR libraries (PWR41J32) of ORLIBJ32. In **Figures 1.8.1 to 1.8.4**, comparison between PWR41J32, PWR-UE and PWR-US are shown. These figures present the improvement of PWR41J32 from PWR-UE.

References:

1) Croff, G.:*ORNL-5621* (1980).

* Japan Nuclear Cycle Development Institute

2) Suyama, K. et al.: *JAERI-Data/Code 99-003*(1999) (in Japanese).

3) Suyama, K. et al.: In proc. of the 2000 ANS Int. Topical Mtg. on Advances in Reactor Physics and Mathematics and Computation into the Next Millennium (PHYSOR2000), May 7-11, 2000, Pittsburgh, PA, USA.

4) Nakagawa, T. et al.: *J. Nucl. Sci. Technol.*, **32**, pp.1259-1271 (1995).

Table 1 List of LWR libraries

Libraries	Fuel Assembly	Void Ratio(%)	U-235 Enrichment(%)	Maximum Burnup (GWd/t)
BS100J32	BWR STEP-1	0	3.0	40
BS140J32	BWR STEP-1	40	3.0	40
BS170J32	BWR STEP-1	70	3.0	40
BS200J32	BWR STEP-2	0	3.8	50
BS240J32	BWR STEP-2	40	3.8	50
BS270J32	BWR STEP-2	70	3.8	50
BS300J32	BWR STEP-3	0	4.0	60
BS340J32	BWR STEP-3	40	4.0	60
BS370J32	BWR STEP-3	70	4.0	60
PWR34J32	PWR 17×17	-	3.4	60
PWR41J32	PWR 17×17	-	4.1	60
PWR47J32	PWR 17×17	-	4.7	60

Maximum burnup means that the upper burnup value for interpolation of variable actinide cross section data.

Table 2 List of FBR Libraries

Reactor Type (fuel)	Core		Blanket	
	Inner	Outer	Axial	Radial
JOYO(MOX)	JOYOM1CO		JOYOM1AX	JOYOM1RD
MONJU(MOX)	MONJMXIC	MONJMXOC	MONJMXAX	MONJMXRD
600 MWe(MOX)	600MMXIC	600MMXOC	600MMXAX	600MMXRD
600MWe(Metal)	600MMTIC	600MMTOC	600MMTAX	600MMTRD
600MWe(Nitride)	600MNIIC	600MNIOC	600MNIAX	600MNTRD
600MWe(recycled Pu)	600MRPIC	600MRPOC	600MRPAX	600MRPRD
1300MWe(MOX)	1300MXIC	1300MXOC	1300MXAX	1300MXRD
Pu Burner	PUBRMXIC	PUBRMXOC	-	-

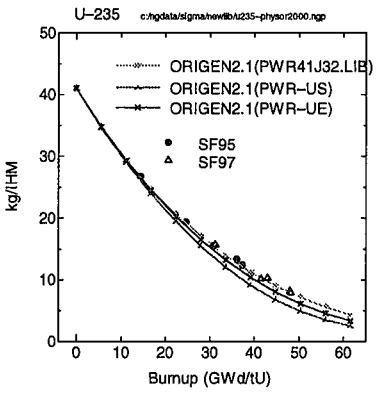

Fig.1.8.1 Calculation Results: U-235

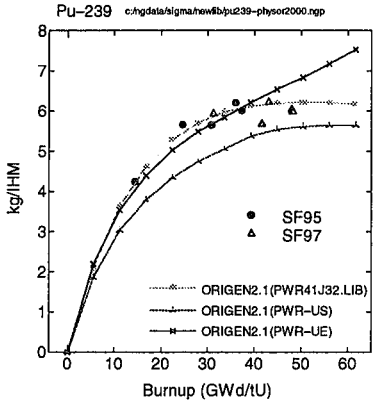

Fig. 1.8.2 Calculation Results: Pu-239

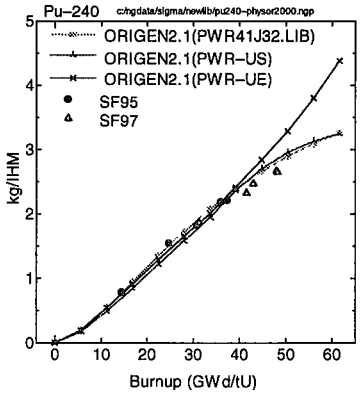

Fig.1.8.3 Calculation Results: Pu-240

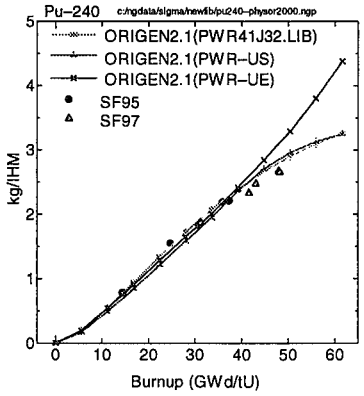

Fig. 1.8.4 Calculation Results: Pu-241

1.9 Analytic Cross Sections for Electron Collisions with Molecules Relevant to Edge Plasma impurities

T. Shirai, T. Tabata, H. Tawara and Y. Itikawa*
(E-mail: shirai@ndc.tokai.jaeri.go.jp)

The atomic and molecular data for electron collision processes with CO, CO_2, H_2O, and hydrocarbons of CH_4, C_2H_6, C_2H_4, C_2H_2, C_3H_8, and C_3H_6 are indispensable not only for modeling of planetary atmospheric behavior but also for practical application such as modeling of various discharge, plasma, and laser systems.

For the cross section data on CO and CH_4, Kanik *et al.*[1] derived the recommended data from experimental measurements for total and elastic scatterings, vibrational excitation, and total ionization. The other compilation on CO was reported by Liu and Victor[2] of the cross sections for vibrational excitation, electronic excitation, dissociation, and ionization. For electronic excitation they utilized theoretical calculations.

Two of the present authors (H.T. and Y.I) provided the comprehensive data compilation[3] of the hydrocarbons by utilizing the literature to 1990. Since then, a number of measurements have been reported. The present compilation is based on the experimental data sets except for the recommended data of CO in Ref. 1 with a revision based on recent measurement for vibrational excitation. All relevant papers published through March 2000 were collected and surveyed, and the best measurements, in our judgement, have been plotted in graphs. As far as the cross sections for electronic excitation and for photon emission are concerned, data accumulation is not enough to make a critical assessment. In cases where a single measurement is available, we have adopted it as the recommended data. In some cases where there exist large deviations among some different measurements, we have made renormalization of data sets to the most reliable one, in order to obtain its recommended data set in an energy range as wide as possible.

In the present compilation the recommended cross sections for 223 kinds of reactions have been accommodated. In order to facilitate the extraction of numerical data to practical applications we have made analytical least-squares fits to all the recommended cross sections.

The recommended cross sections in this work are given for total and elastic scatterings, as examples, in GRAPHS 1 and 2, respectively.

---

* Institute of Space and Astronautical Science

References:

1) Kanik I., Trajmar S., and Nickel J.C.: J. Geophys. Res. 98, 7447 (1993).

2) Liu W. and Victor G.A., Astrophys. J. 435, 909 (1994).

3) Tawara H., Itikawa Y., Nishimura H., Tanaka H., and Nakamura Y., Atomic and Plasma-Material Interaction Data for Fusion 2, 41 (1992).

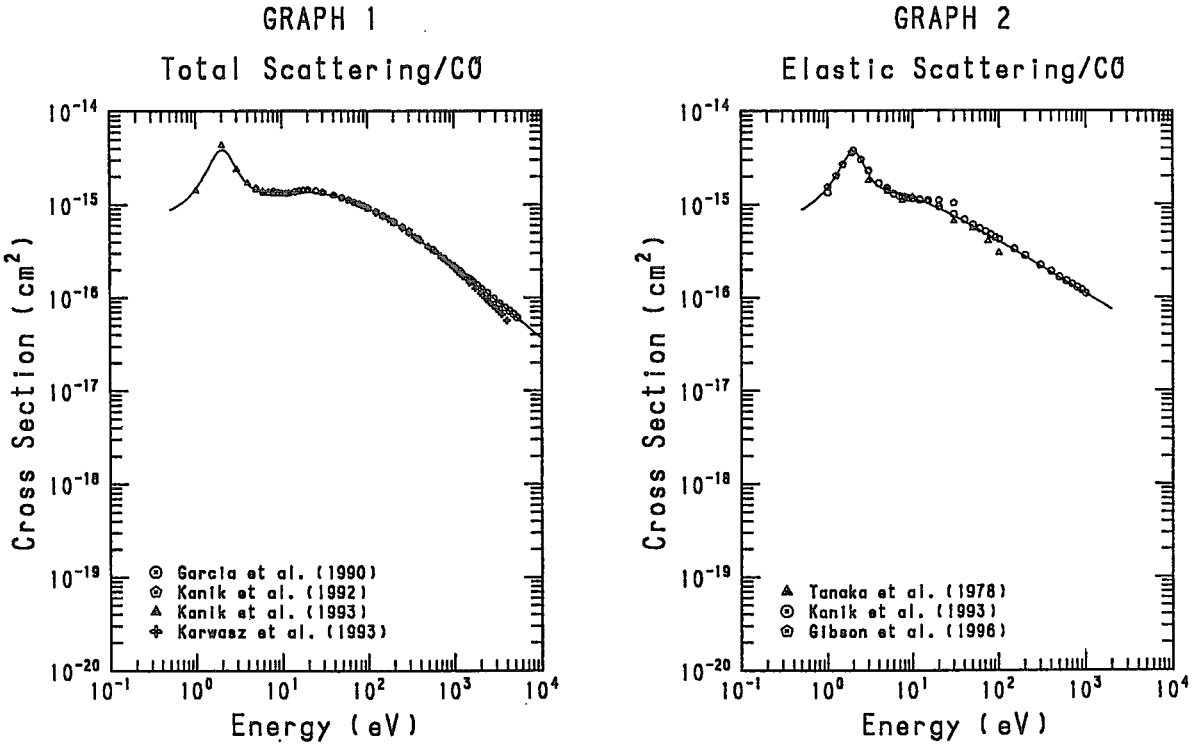

Fig. 1.9.1 Comparison of the analytic cross section (solid line) and experimental data from sources in the legends

1.10 Cross Sections for Radiative Recombination in the K, L, and M-Shells of One Electron System with 1≤Z≤112 Calculated within an Exact Relativistic Description

A.Ichihara, J.Eichler*

(*E-mail:* ichihara@ndc.tokai.jaeri.go.jp)

In radiative recombination (RR), an electron is captured into an empty shell of the bare ion, and a photon is emitted simultaneously. This reaction plays an important role in plasma physics, in particular the spectroscopic analysis of fusion plasmas. Moreover, the photoelectric effect for the high-Z hydrogen-like ions can be studied by the inverse reaction, RR, where these ions can not be easily used as targets. The importance for plasma physics as well as the methods for investigating the photoelectric effect defines the need for providing RR cross sections over a wide range of nuclear charges and electron energies.

On the basis of the need of total cross sections for RR, an extensive tabulation has been carried out for the K, L, and M ($1s_{1/2}$, $2s_{1/2}$, $2p_{1/2}$, $2p_{3/2}$, $3s_{1/2}$, $3p_{1/2}$, $3p_{3/2}$, $3d_{3/2}$, $3d_{5/2}$) shells and electron energies ranging from closely above the threshold (1.0 eV) to the relativistic regime (up to 10.0 MeV). Cross sections are obtained from complete relativistic calculations using exact Coulomb-Dirac wave functions for the bound and for the continuum states modified for the finite nuclear size. They also include all multipole orders of the photon field. The tabulated cross sections are accurate to three digits and should be considered to be the results of benchmark calculations.

In the tabulation, cross sections are given as a function of the electron energy.[1] By a simple scaling, the dependence on the projectile energy in MeV/u can be derived for accelerator experiments, and, by using elementary formulas, the cross section for the photoelectric effect can be obtained as a function of the photon energy. It is pointed out how to scale the cross sections for the capture of heavy Dirac particles. Furthermore, in order to assess the accuracy of cross sections derived from the widely used nonrelativistic dipole (ND) approximation, the ND cross sections are compared with exact relativistic results for a few representative cases. As a result, it is shown that relativistic calculations are mandatory irrespective of the electron energy for high-Z ions.

---

* Bereich Theoretische Physik, Hahn-Meitner-Institut Berlin

The cross sections have been calculated for all charge numbers between Z=1 and 112. A dense mesh of electron energies allows for comparison with all emerging data and facilitates accurate interpolation. As an example, the cross sections for K-RR of Z=92(U^{92+}) are shown in Fig.1.10.1.

References:

1)Ichihara, A. and Eichler, J.: Atomic Data and Nuclear Data Tables, 74, 1 (2000).

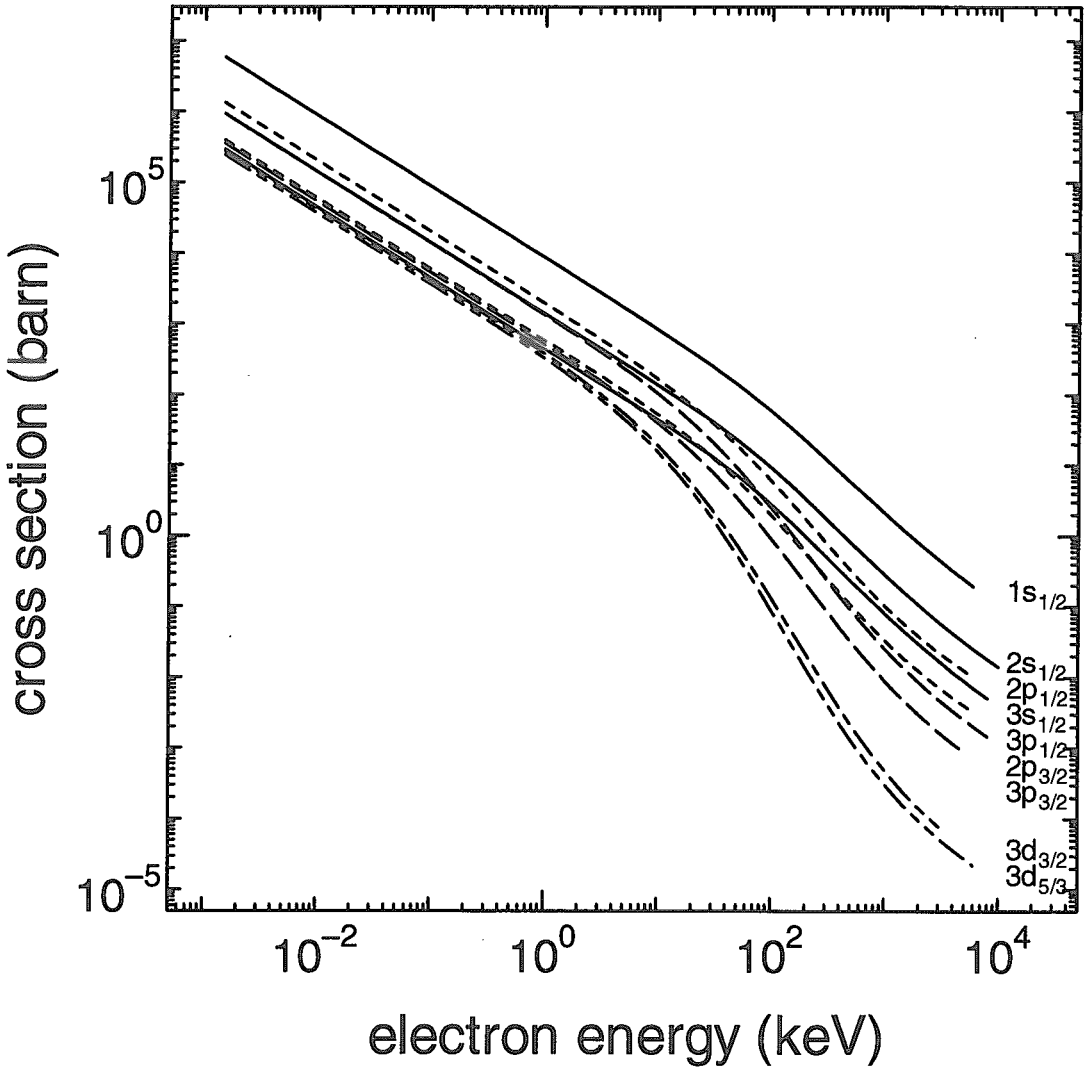

Fig.1.10.1 Total cross sections for Z=92 as a function of electron energy.

1.11 Cross Sections for Ion Production in the $H^+ + H_2$ Collisions Calculated with the Trajectory-Surface-Hopping Method

A.Ichihara, O.Iwamoto and K.Yokoyama
(*E-mail:* ichihara@ndc.tokai.jaeri.go.jp)

Ion-molecule reactions occurring in the $H^+ + H_2$ system and its isotopic variants have been attracting the interest of both experimentalists and theorists. Accurate knowledge of cross sections for these reactions is fundamental to the analysis of plasma behavior in divertors of toroidal fusion devices, where the existence of neutral atoms and molecules is supported by the low plasma temperatures (≤10-20 eV). Collision processes in this system with vibrationally and rotationally ecited H_2 in the entrance channel have significant importance, because excitation of internal states of H_2 in divertor plasmas is expected due to the effectiveness of several collision processes: vibrational excitation of H_2 by electron and proton impact, electron impact excitation followed by radiative decay, etc.

On the basis of the need for the research and development of fusion reactor, we have calculated cross sections for ion production from the $H^+ + H_2$ $H^+ + D_2$, $D^+ + H_2$, and $D^+ + D_2$ collisions in the center-of-mass collision energy range of $2.5 \leq E_{cm} \leq 8.0$ eV.[1] The vibrational and rotational quantum numbers of reactant molecules have been taken in the range ($0 \leq v \leq 6$, $j=1$) for H_2 and ($0 \leq v \leq 8$, $j=1$) for D_2, respectively, and the v dependence of cross sections have been investigated. The cross sections have also been calculated with $j=5$ and 10 for the $H^+ + D_2$ system in order to evaluate the j dependence. Furthermore, the vibrational state distribution of diatomic products has been evaluated. To obtain cross sections, the trajectory-surface-hopping (TSH) method with the ab initio three-dimensional potential energy surfaces (PES's) has been employed.[1] 9000 to 30000 trajectories were calculated for each combination of (v, j, E_{cm}).

Figure 1.11.1 shows the cross sections for the D_2^+ production from the $H^+ + D_2$($v=0$ to 7, $j=1,5,10$) collisions. It can be seen From Fig.1.11.1 that the cross section increases rapidly as v increases. The cross section also increases with increasing j, but the effect is secondary to the v effect. The increase of the D_2^+ production cross section with the increase of (v, j) can be explained from the characteristics of the H_3^+ PES's.[1] Figs.1.11.2 and 1.11.3 shows the cross sections for the HD^+ and D^+ production from the $H^+ + D_2$($v=0$ to 8, $j=1$) collisions, respectively. In the D^+ production, D^+ ions are obtained both from the HD production and dissociation. Although the HD^+

and D^+ production is affected by the internal state (v) of D_2, the v dependence is much small compared with the D_2^+ production.

In the present calculation, it has been observed that ion production occurring in other isotopic variants has the similar v dependence as the $H^+ + D_2$ system.

References:

1)Ichihara, A. et al.: Atom.Plasma-Mater. Int. Dat. For Fus.9, in press.

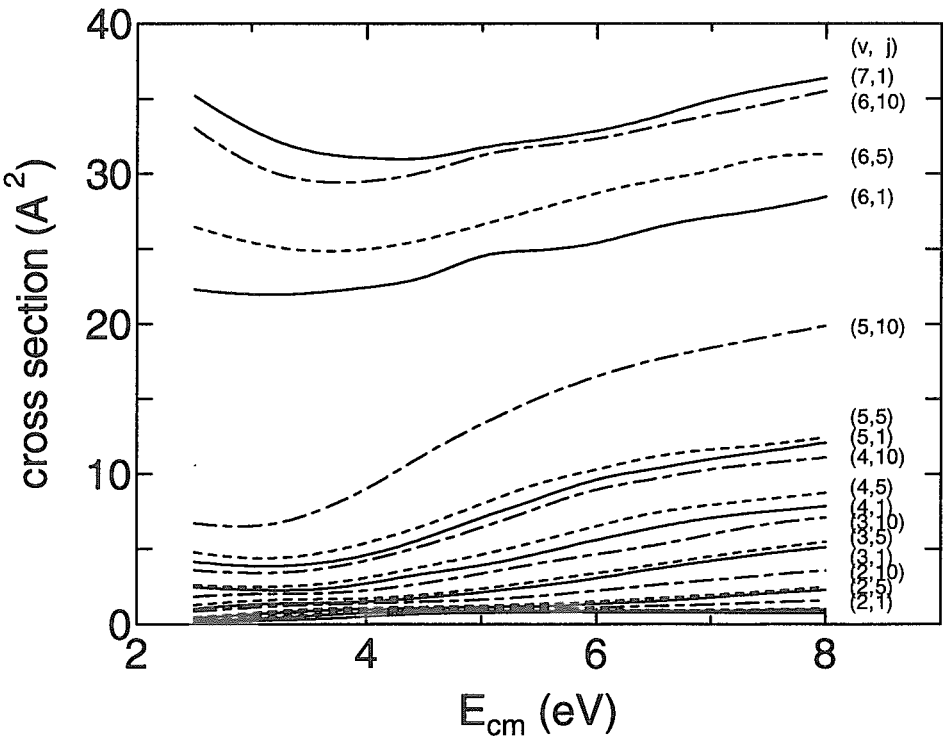

Fig.1.11.1 Cross sections for the reaction $H^+ + D_2(v=0 \text{ to } 7, j=1,5,10) \rightarrow H + D_2^+$ as a function of the center-of-mass collision energy E_{cm}.

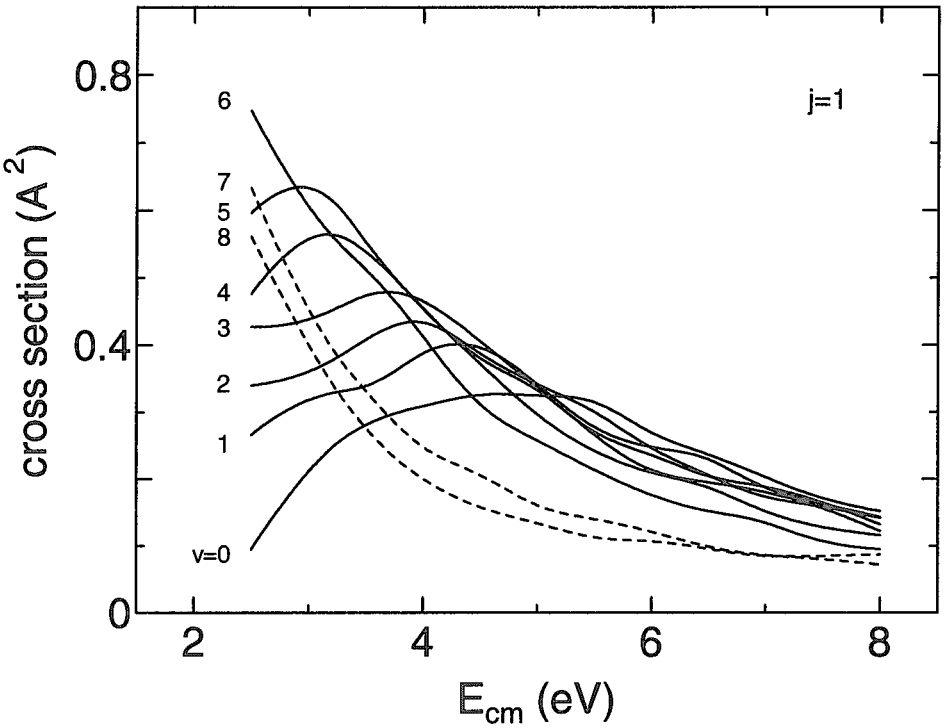

Fig.1.11.2 Cross sections for the reaction $H^+ + D_2(v=0 \text{ to } 8, j=1) \rightarrow HD^+ + D$ as a function of the center-of-mass collision energy E_{cm}.

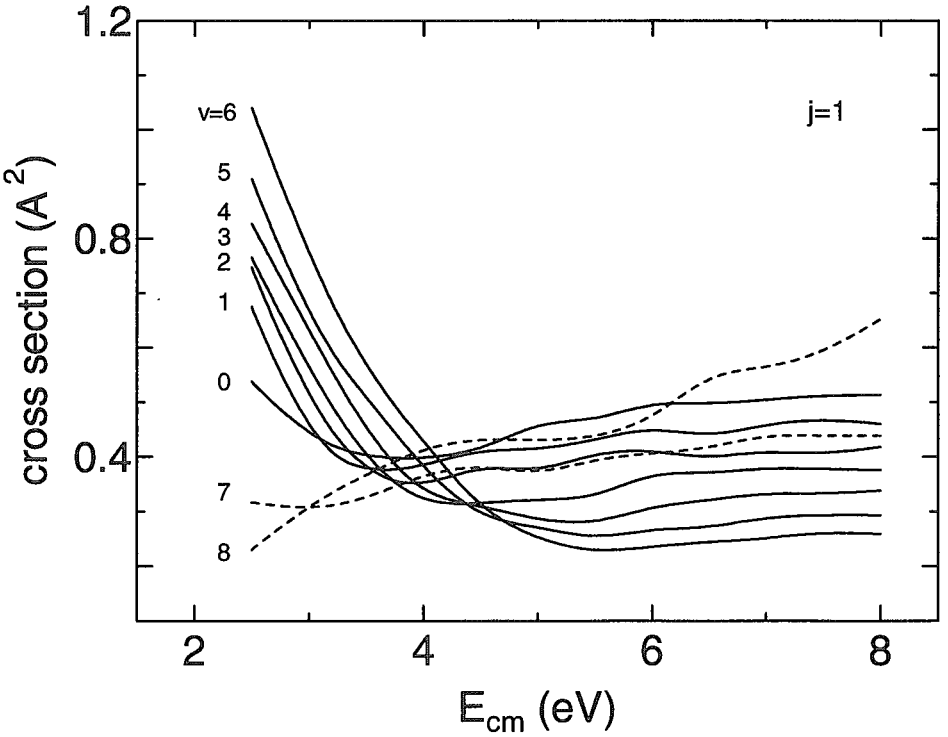

Fig.1.11.3 Cross sections for the D^+ production from the $H^+ + D_2(v=0 \text{ to } 8, j=1)$ collisions. The cross sections are given as a function of the center-of-mass collision energy E_{cm}.

2. Reactor Physics

For Monte Carlo perturbation calculations in eigenvalue problems, the method to evaluate the perturbation effect due to the fission source change has been developed on the basis of the correlation and differential sampling methods. The method has been incorporated into the MVP continuous energy code, and its applicability has been verified by several benchmark problems.

Characteristics of the Diven factor in the fast energy range have been investigated to solve two questions: (1) whether the Diven factor at thermal neutron energy is applicable to the fast system, and (2) whether the Diven factor for a specific nuclide is appropriate for use in the system where several fissionable nuclides exist. As a result, a general formula for the Diven factor, which is applicable to a multiple-fissionable-nuclides system, has been derived.

To examine the calculation accuracy for the Doppler effect of resonance materials in the rock-like oxide fuel, the Doppler reactivity worth of erbium, tungsten and thorium has been measured with a LMFBR mock-up core, FCA XX-2. The experiment has been analyzed by the two methods used for analyses of fast and thermal reactors, respectively, and the results have been compared with each other.

The external GEM reactivity worth has been measured in a mock-up core for a nitride fueled LMFBR, FCA XX-1, putting a focus on the effect of partial mock-up configuration of GEM region. In order to discuss the prediction accuracy, the measured results have been compared to calculated ones with four different methods (two S8 transport calculations with R-Z and X-Y-Z models, a multi-group Monte Carlo calculation and a continuous energy Monte Carlo calculation).

In order to clarify the limitation of the point-kinetics model for control-rod worth measurements by the rod-drop method, a rod-drop experiment has been performed at TCA and analyzed by using a 3-D reactor kinetics code MLK3D with two-group cross sections generated by the SRAC code. The strong dependence of the obtained worth on the measurement position has been observed in the experiment, ant it has been well predicted by the space-dependent kinetics calculation with MLK3D.

2.1 Evaluation of Perturbation effects for the Multiplication Factor by a Continuous-Energy Monte Carlo Code MVP

Y. Nagaya and T. Mori
(*E-mail* : nagaya@mike.tokai.jaeri.go.jp)

We have developed formulae to evaluate the fission-source change by the correlated and differential operator sampling methods in Monte Carlo eigenvalue calculations. In the previous work[1], we found that the change in the effective multiplication factor was improved by taking into account the perturbation effect due to the fission-source change for the simple 1-group problems. In the present work, we have incorporated the perturbation procedure based on the formulae into the continuous-energy Monte Carlo code MVP[2] and verified the applicability for the continuous-energy treatment by simple benchmark problems.

Firstly we calculated the effects of a density perturbation to the nominal Godiva assembly[3]. The geometry is a bare uranium sphere with a radius of 8.741 cm as illustrated in Fig. 2.1.1. The density is 18.74 g/cm^3 and the nominal composition is 94.73 wt% ^{235}U and 5.27 wt% ^{238}U. All the MVP calculations were performed with a nuclear data library JENDL-3.2[4] in this work. The effective multiplication factor is 1.00402 (1σ = 0.0097%) in the unperturbed system.

A density perturbation was introduced by increasing the density from 18.74 to 20.00 g/cm^3. The effective multiplication factor then increased to 1.05860 (1σ = 0.0098%). Table 2.1.1 shows the results for the Godiva assembly with the MCNP4C result[5]. The reference result was obtained by two independent Monte Carlo runs with a large number of histories (40 million histories). All the results without the perturbation effect due to the fission-source change underestimate the reference one by about 3% including the MCNP4C result. Taking into account the fission-source change, the Δk values obtained by both the correlated sampling and second-order differential operator methods are well improved and are in very good agreement with the reference one. However, the statistical uncertainties (1σ) are larger than those without the perturbation effect due to fission-source change by a factor of 5. As found in Table 2.1.1, the large statistical uncertainties are ascribed to the perturbation effect due to fission-source change.

We also investigated a 2-region perturbation problem for the Godiva assembly where

only the central region was perturbed to verify the present procedure for the relatively large effect due to the fission-source change. The radius of the perturbed region is 6 cm and the isotopic composition in both the regions is the same as the nominal Godiva one. The density change for the introduced perturbation is also the same as in the case of the whole region perturbation.

Table 2.1.2 shows the Δk values for the Godiva assembly in the case of the central region perturbed.

The reference solution was obtained by the 2 independent Monte Carlo runs with 40 million histories. In this case, the perturbation calculation without the effect due to the fission-source change gives a significant discrepancy, while the Δk values are in very good agreement with the reference one by both the correlated and second-order differential sampling method with the changed fission-source effect. Thus the perturbation effect due to the fission-source change is well estimated by the present procedure for the relatively large fission-source change effect of about 37%. The statistical uncertainties also become larger by taking into account the changed fission-source effect as in the case of the whole region perturbation.

In this work, the perturbation procedure has been incorporated into the MVP code and it has been shown that the formulae to evaluate the perturbation effect due to the fission-source change are applicable for the continuous-energy treatment.

References

1) Nagaya, Y. and Mori, T. : JAERI-Review 99-031, 36 (2000).
2) Mori, T., *et al.*, "Vectorization of Continuous Energy Monte Carlo Method for Neutron Transport Calculation," J. Nucl. Sci. Technol., 29, 325 (1992).
3) Whalen, D. J., *et al.*, LA-12212 "MCNP: Neutron Benchmark Problems," (1991).
4) Nakagawa, T., *et al.*, "Japanese Evaluated Nuclear Data Library, Version 3, Revision 2," J. Nucl. Sci. Technol., 32, 1259 (1995).
5) Hendricks, J. S., *et al.*, "MCNP Perturbation Capability for Monte Carlo Criticality Calculations," Proceedings of Sixth International Conference on Nuclear Criticality Safety, Palais des Congres, Versailles, France, Vol. I, 269, (Sep. 20-24, 1999).

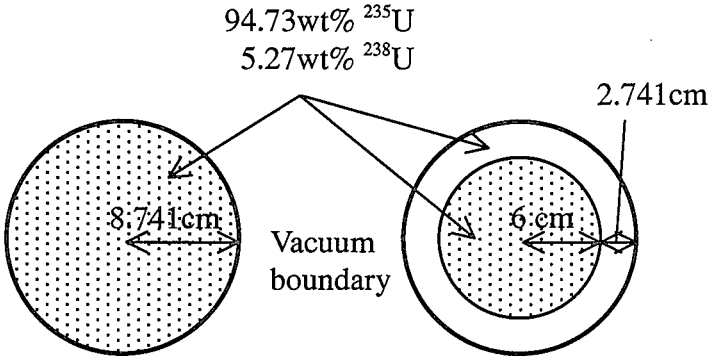

(a) Whole region perturbed (b) Central region perturbed

Fig. 2.1.1 Geometry for the Godiva assembly

Table 2.1.1 Change in the effective multiplication factor for the Godiva assembly in the case of the whole region perturbed

Method	Δk	1σ
2 Independent M. C. Runs	5.458E-2	0.014E-2
MCNP4C	5.282E-2	0.015E-2
MVP Correlated Sampling	5.448E-2	0.031E-2
MVP 2nd-Order Differential Operator Sampling	5.485E-2	0.028E-2

Table 2.1.2 Change in the effective multiplication factor for the Godiva assembly in the case of only the central region perturbed

Method	Δk	1σ
2 Independent M. C. Runs	2.980E-2	0.014E-2
MVP Correlated Sampling	2.954E-2	0.035E-2
MVP 2nd-Order Differential Operator Sampling	2.988E-2	0.028E-2

2.2 A Note on the Diven Factor in Fast Systems

S. Okajima, Y. Yamane*, Y. Takemoto* and T. Sakurai
(*E-mail*: okajima@fca001.tokai.jaeri.go.jp)

Introduction

The Diven factor is one of the most important parameters involved in the interpretation of zero power reactor noise experiments. In a fast system the fission reactions occur over a wide fast neutron energy range and arise from not only fissile but also fissionable nuclides. These conditions lead to two questions: whether or not the Diven factor at thermal neutron energy is applicable to the fast system, and whether or not the Diven factor for a specific nuclide is appropriate for use in the system where several fissionable nuclides contribute to the fission. To solve these questions, characteristics of the Diven factor in the fast neutron energy range have been investigated and a general formula for the Diven factor has been derived which is applicable to a multiple-fissionable-nuclides system.

The Diven Factor in the Fast Neutron Energy Range

The Diven factor is defined as follows [1]:

$$D_\nu \equiv \frac{\langle \nu(\nu-1)\rangle}{\langle \nu\rangle^2} \cong \frac{\langle \nu_p(\nu_p-1)\rangle}{\langle \nu_p\rangle^2} = \frac{\sum_{\nu_p} \nu_p(\nu_p-1)P(\nu_p)}{\left[\sum_{\nu_p} \nu_p P(\nu_p)\right]^2}, \qquad (1)$$

where $P(\nu_p)$ is the probability distribution function that ν_p prompt neutrons are emitted in a fission. There have been two studies [2, 3] on the $P(\nu_p)$ function for neutron energies in the MeV range. As an example, Table 2.2.1 shows the results of both $P(\nu_p)$ functions for ^{235}U, and also the first and second moments of prompt neutrons emitted in a fission and the calculated Diven factors. The $P(\nu_p)$ function evaluated by Frehaut does not satisfy the normalization condition, $\sum_{\nu_p} P(\nu_p) = 1$. Even though the function does not satisfy the normalization condition, we decided to use it in the calculation since Frehaut $P(\nu_p)$

* Department of Nuclear Engineering, Graduate School of Engineering, Nagoya University

functions give closer agreement with the Diven factors in the thermal neutron energy range [4]. When we compare the $P(\nu_p)$ functions between Zucker & Holden and Frehaut, each $P(\nu_p)$ value is slightly different even though the two functions were evaluated on the basis of the same experimental data. The difference for each ν_p was assumed to be the error of $P(\nu_p)$ and was used to estimate the error of the Diven factor by the error propagation law. To check the validity of this assumption, the calculated errors of the Diven factors at thermal energy were compared with those in Ref. 4). The calculated errors are slightly larger than the errors in Ref. 4). From these results the estimation is slightly exaggerated. Figure 2.2.1 shows the incident neutron energy dependence of the Diven factors. The results by Zucker & Holden and those by Frehaut show a similar tendency. The factor is constant below about 100 keV and shows an energy dependence above about 100 keV as shown in Fig. 2.2.1. From this result, it is concluded that the energy dependence of the Diven factor must be considered in fast systems. The values agree well within the estimated errors, except for ^{238}U in the neutron energy range below 2 MeV. The difference for ^{238}U, however, is insignificant since the fission for ^{238}U mainly occurs in the neutron energy range above ~2 MeV.

Derivation of the Diven Factor in a Multiple-Fissionable-Nuclides System

To solve the second question for the application of the Diven factor in a fast system, a new formula for it has been derived for a multiple-fissionable-nuclides system. We considered a probability $P(t_1,t_2)dt_1dt_2$ that fission events occur at time t_1 and t_2 due to different fissionable nuclides m_1 and m_2, and we derived the detection probability in the one-speed model, $X(t)dt$, as follows:

$$X(t)dt = c\,dt +$$

$$+\left[\varepsilon\frac{k_{eff}^{\,2}}{l_0^{\,2}}\frac{\left[\sum_m\int_r F_m(r)dr\right]\cdot\left[\sum_m\int_r <\nu_p(\nu_p-1)>_m F_m(r)I_m(r)^2dr\right]}{\left[\sum_m\int_r <\nu>_m F_m(r)I_m(r)dr\right]^2}\int_{t'=0}^{\infty}N(t')N(t+t')dt'\right]dt \tag{2}$$

where c is a neutron count rate, ε, the detection efficiency defined as $\varepsilon \equiv c\Big/\sum_m\int_r F_m(r)dr$, k_{eff}, the effective multiplication factor, l_0, the neutron life time, $F_m(r)$, the fission rate due to the nuclide m at position r and $I_m(r)$ means the importance function for neutrons generated by the fission of the nuclide m. When we compare Eq. (2) with the detection

probability in a single fissile nuclide system[5], we can assign the Diven factor and the spatial correction factor in the multiple-fissionable-nuclides system as follows:

$$D_\nu = \frac{\sum_m \int_r < \nu_p(\nu_p - 1) >_m F_m(r) I_m(r)^2 dr}{\sum_m \int_r < \nu_p >_m^2 F_m(r) I_m(r)^2 dr} \quad , \tag{3}$$

$$D_s = \frac{\left[\sum_m \int_r F_m(r) dr\right] \cdot \left[\sum_m \int_r < \nu >_m^2 F_m(r) I_m(r)^2 dr\right]}{\left[\sum_m \int_r < \nu >_m F_m(r) I_m(r) dr\right]^2} \quad . \tag{4}$$

Considering the neutron energy dependence, we can modify the formulae as follows:

$$D_\nu = \frac{\sum_m \int_r dr \left\{\int_E dE \left\langle \nu_p(\nu_p - 1) \right\rangle_m F_m(r,E)\right\} \cdot \left\{\int_{E'} dE' I_m(r,E')\right\}^2}{\sum_m \int_r dr \left\{\int_E dE \left\langle \nu_p \right\rangle_m^2 F_m(r,E)\right\} \cdot \left\{\int_{E'} dE' I_m(r,E')\right\}^2}, \tag{5}$$

$$D_s = \frac{\left[\sum_m \int_r dr \int_E dE F_m(r,E)\right] \cdot \left[\sum_m \int_r dr \left\{\int_E dE \langle \nu \rangle_m^2 F_m(r,E)\right\} \cdot \left\{\int_{E'} dE' I_m(r,E')\right\}^2\right]}{\left[\sum_m \int_r dr \left\{\int_E dE \langle \nu \rangle_m F_m(r,E)\right\} \cdot \left\{\int_{E'} dE' I_m(r,E')\right\}\right]^2}. \tag{6}$$

From Eq. (3) or (5), it is clear that the Diven factor is given by the first and the second moments of the prompt neutron distributions weighted with the fission rates and the squares of the neutron importances. Equations (5) and (6) are generalized formulae for the Diven factor and the spatial correction factor, which can be generally used in the interpretation of zero power reactor noise experiments.

References

1) Diven, B. C., et al.; *Phys. Rev.* 101, 1012 (1956).

2) Zucker, M. S. and Holden, N. E.; *BNL-38491* (1986).

3) Frehaut, J.; *INDC(NDS)-220* (1989).

4) Holden, N. E. and Zucker, M. S.; *Nucl. Sci. and Eng.*, 98, 174 (1988).

5) Bennett, E.F.; *ANL-81-72* (1981).

Table 2.2.1 Values of $P(\nu_p)$ functions, $\langle \nu_p \rangle$ and Diven factors, and their estimated errors

U-235 (*En*=2MeV)

$P(\nu_p)$	Holden & Zucker[2)]	Frehaut[3)*]		$\Delta P(\nu_p)$
P(0)	0.018399	0.022775		0.004376
P(1)	0.138489	0.130990		0.007499
P(2)	0.306212	0.305438		0.000774
P(3)	0.321757	0.325014		0.003257
P(4)	0.162867	0.165976		0.003116
P(5)	0.045597	0.048974		0.003377
P(6)	0.005569	0.008098		0.002529
P(7)	0.001109	0.000648		0.000461
$\Sigma P(\nu_p)$	1.000000	1.007912		
$<\nu_p>$	2.6368	2.6788	2.6578†	+/- 0.0289
$<\nu_p(\nu_p-1)>$	5.6230	5.8023	5.7567†	+/- 0.1117
Diven factor	0.8087	0.8086	0.8150†	+/- 0.0204

* The $\langle \nu_p \rangle$ value taken from the JENDL-3.2 library was used to calculate each $P(\nu_p)$ value.

† The re-normalized function was used.

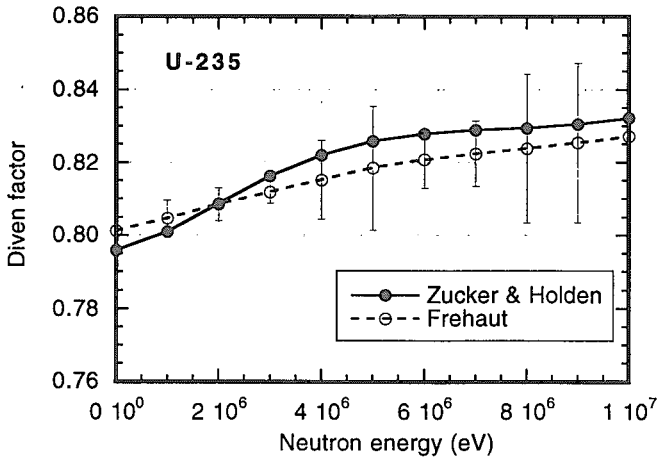

Fig. 2.2.1 Incident neutron energy dependence of the Diven factor for ^{235}U

2.3 Evaluation of Doppler Reactivity of Resonance Materials for ROX Fuels Using FCA

M. Andoh, Y. Nakano and S. Okajima
(*E-mail:* andoh@fca001.tokai.jaeri.go.jp)

To examine the calculation accuracy for the Doppler effect of resonance materials used in the rock-like oxide (ROX) fuel, we analyzed the Doppler reactivity worth of the resonance materials such as erbium, tungsten, thorium, which was measured at Fast Critical Assembly (FCA). For future experiments in softened neutron spectra, the experiment was analyzed using two different calculation methods, which are used for the analyses of fast and thermal reactors. The calculation method for the thermal system gives larger worths than that for the fast system. The prediction accuracy is relatively poor for the tungsten sample in comparison with the others.

Experiment

A series of experiments was carried out with a LMFBR mock-up core, FCA XX-2, using newly fabricated Doppler samples; cylindrical erbium metal (Er), tungsten metal (W) and thorium dioxide (ThO_2).[1] Natural uranium Doppler samples (U-metal and UO_2) were also used for references. The Doppler reactivity worth was measured up to 1073K (800°C).

Analysis

The analysis was carried out using two different schemes: one is the standard analysis method for FBR cores at FCA (the FCA method[2),3)]) and the other is the standard calculation method for thermal reactors using the SRAC system[4] (the SRAC method). The JENDL-3.2 library[5] was used in this study. Total number of neutron energy group from 10Mev to 10^{-5}eV is 70 and 101 in the FCA and SRAC methods, respectively. The difference of the group number is caused by the energy group structure below 1.86eV, while the lethergy width is 0.25 in the energy region of upper 1.86eV for the both methods.

To obtain effective cross section of the Doppler samples (except the ThO_2 and Er samples), a collision probability code with ultra-fine group structure, PEACO-X[6], was also used for the FCA method. On the other hand, a collision probability routine with ultra-fine group structure, PEACO, was used for the SRAC method. Those effective cross sections of ultra-fine energy goup structure were collapsed to the standard energy group structure of each method.

The Doppler reactivity worths were calculated by the first order perturbation theory.

The perturbation was caused by the change of the effective cross section of the Doppler sample due to the change of the sample temperature. The calculation model in the R-Z geometry with a Doppler sample is shown in Fig. 2.3.1. The real and adjoint fluxes were obtained from the two-dimensional diffusion calculation in the R-Z geometry.

Discussions

The results of the both calculations are compared for 800°C in Table 2.3.1. The following items are pointed out from Table 2.3.1:

- The SRAC method gives larger reactivity worths than the FCA method. A tendency is obserbed in the ratio between the SRAC and FCA methods; 1.05 for uranium sample and 1.08 for the other samples. It can be considered that the neutron spectrum is softened in the SRAC method caused by the difference of the effective scattering cross section.
- The C/E values of ThO_2 sample are similar to those of the UO_2 sample for both the SRAC and FCA methods.
- The prediction accuracy is relatively poor for the tungsten sample in comparison with the others.

For each calculation method, we conclude that:

a) The FCA method underestimated the experiments about 10% for the new samples; ThO_2, Er and W.

b) The SRAC method showed good agreement with the experiments for all the samples except the tungsten one.

References

1) Nakano Y., et al. : "Doppler effect experiment of resonance materials for ROX fuels", Section 9.5 in this report(2000).
2) Nakagawa M. and Tsuchihashi K. : JAERI 1294, "SLAROM: A Code for Cell Homogenization Calculation of Fast Reactor"(1984).
3) Iijima, S. : private communication.
4) Tsuchihashi K., et al. : JAERI 1302, "Revised SRAC Code System"(1986).
5) Nakagawa T., et al. : J. Nucl. Sci. and Tecnol., 32, 1259(1995).
6) Okajima S., et al. : JAERI-M 92-185, "Measurement of Doppler Effect up to 2000 °C at FCA (3) -Development of a Cell Code, PEACO-X, with Ultra-fine Group Structure-"(1992), (in Japanese).

Table 2.3.1 Comparison of the results of the analyses on the Doppler reactivity worth (for 800°C)

Doppler sample	Expt. ($-10^{-5}\Delta k/k$)	C/E				
		standard calc.[a)]		PEACO calc.[b)]		
		SRAC	FCA	SRAC	FCA	SRAC/FCA[c)]
U-metal	1.7 ± 3(%)	1.01	0.97	1.06	1.02	1.05
UO_2	0.88±7	0.96	0.92	1.03	0.99	1.05
ThO_2	0.87±6	0.98	0.90	0.99	-	1.08
W	1.1 ± 4	0.90	0.83	0.89	0.86	1.08
Er	1.4 ± 4	0.95	0.88	0.98	-	1.08

a) standard calculation method, b) ultra-fine group collision probability calculation method, c) ratio between the SRAC and FCA methods in the standard calculation.

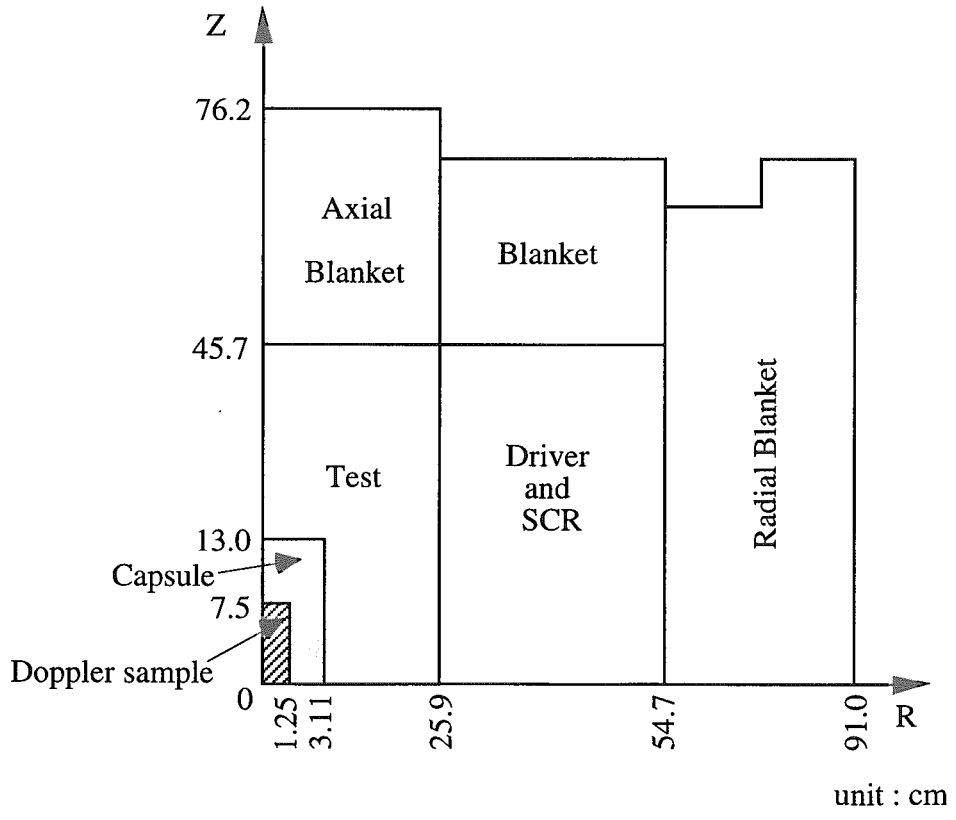

Fig. 2.3.1 The R-Z model of the XX-2 core with the Doppler sample at the core center

2.4 Experiment and Analysis on Space-Dependent Reactor Kinetics at TCA

Y. Nagaya, K. Okumura, T. Suzaki, S. Aoki* and T. Nomura**
(*E-mail* : nagaya@mike.tokai.jaeri.go.jp)

The rod-drop method is often used to measure a control-rod worth because of its simplicity. However, the measured rod worth depends on the location of a detector and thus the detector must be located at the position where the neutron flux is not largely disturbed. This is because the rod-drop method is based on the point-kinetics theory.

In order to show the limitation and the modification of the point-kinetics model for the rod-drop method we performed the rod-drop experiment at TCA[1] and analyzed it by a 3-D reactor kinetics code MLK3D[2]. The SRAC code[3] was used for few-group cross section generation.

Figure 2.4.1 shows the cross-sectional view of the experimental core configuration. 13 x 28 fuel cells are arranged in the core region and the core is surrounded by light water as a reflector. The pitch of the fuel cells is 1.956cm. Four ^{3}He counters are inserted at some detector positions from A to F in a run. Safety blades are implemented to shut down TCA and one of them was dropped at the critical state to evaluate the worth of the safety blade by the rod-drop method. During the rod-drop experiment, the time-dependent neutron counts were measured by a multi-channel scalar (MCS). The temporal change of the height of the safety blade was measured by an electromagnetic oscilloscope.

Analysis was performed by the SRAC and MLK3D codes. The 2-group cross section data was generated from the evaluated nuclear data library JENDL-3.2[4] by the following scheme. At first, 107-group homogenized cross sections were generated by the PIJ routine in SRAC with the fuel cell geometry and then the 2-D core calculation was performed by CITATION. The 2-group cross sections for the kinetics calculation were obtained by using the resultant 107-group energy spectrum. In the kinetics calculation, a fuel cell was assigned to a calculation node in the horizontal direction and the core with the reflector was divided into 21 nodes in the axial direction. The core power is almost zero and thus no feedback effect was taken into account.

---

* Mitsubishi Heavy Industries, LTD, ** Nagoya University

Figure 2.4.2 shows the comparison of the time-dependent neutron response between the measured values and the MLK3D results. The MLK3D results are in very good agreement with the measured ones. Fig. 2.4.3 shows the comparison of the worth of the safety blade between the measured and calculated values at each detector position. Both the values were evaluated by the integral counting method. As seen in Fig. 2.4.3, the dependence of the worth on the detector position is well reproduced by the space-dependent kinetics calculation except for the nearest position to the safety blade. In this work, applicability of the MLK3D code is verified for the rod-drop experiment and it is found that the dependence of the worth on the detector position in the rod-drop experiment is well analyzed by the space-dependent kinetics calculation.

References

1) Tsuruta, H., *et al.* : JAERI 1254 (1978).

2) Nagaya, Y. and Inoue, H. : JAERI-Review 98-022, pp.56-58 (1991).

3) Okumura, K., Kaneko, K. and Tsuchihashi, K. : JAERI-Data/Code 96-015 "SRAC95; General Purpose Neutronics Code System," (1996) [in Japanese].

4) Nakagawa, T., *et al.*, "Japanese Evaluated Nuclear Data Library, Version 3, Revision 2," J. Nucl. Sci. Technol., 32, 1259 (1995).

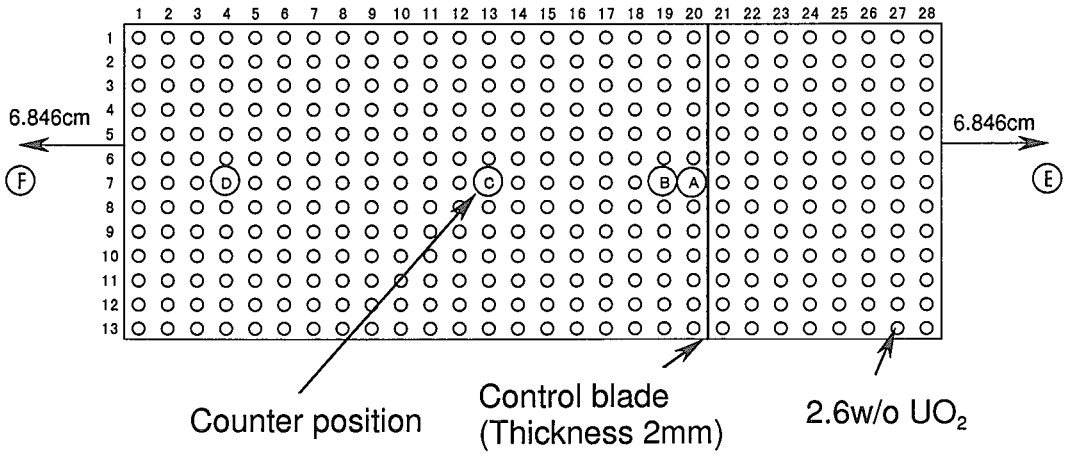

Fig. 2.4.1 Geometry for the TCA rod-drop experiment

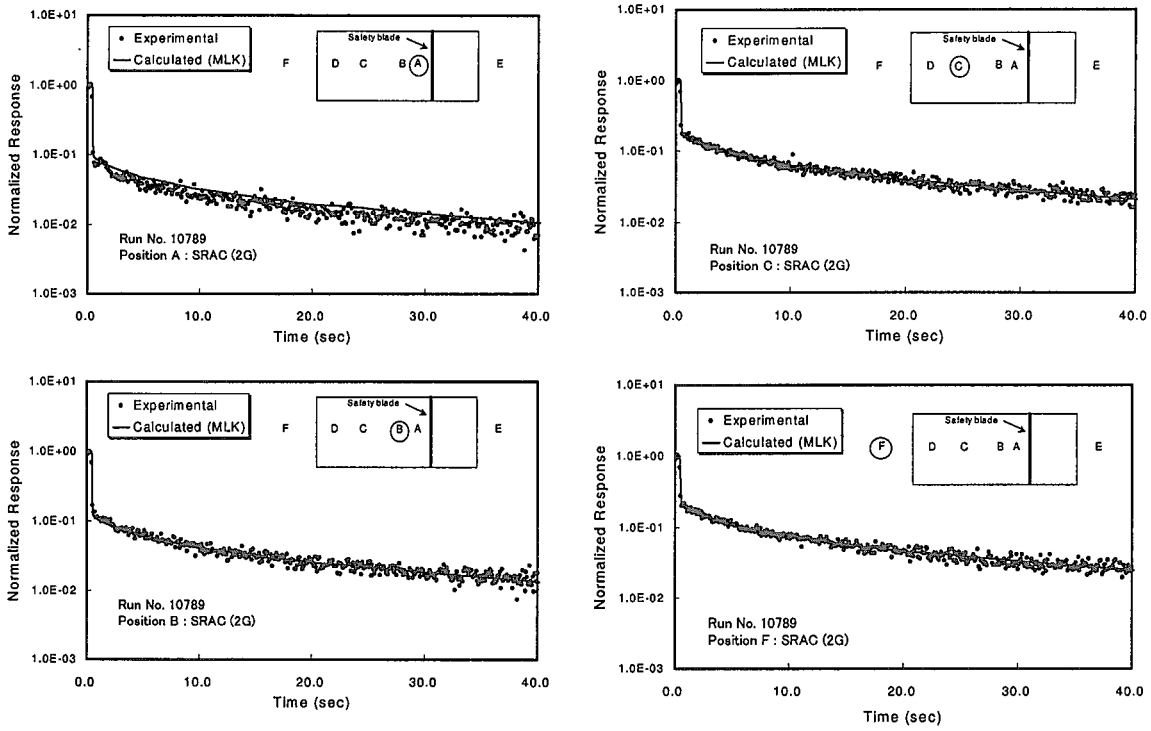

Fig. 2.4.2 Comparison of the time-dependent neutron response between the measured and MLK3D results at each detector position

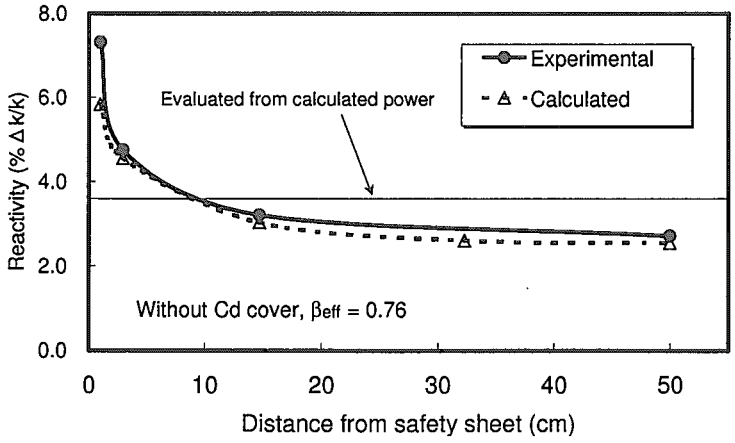

Fig. 2.4.3 Comparison of the worth of the safety blade between the measured and calculated values at each detector position

2.5 Experiments and Analyses on External GEM Reactivity Worth in FCA XX-1 core

H. Oigawa, M. Andoh and S. Iijima
(*E-mail :* oigawa@omega.tokai.jaeri.go.jp)

The Gas Expansion Module (GEM) is proposed to be installed to insert the negative reactivity in the transient of the primary pomp trip in a large scale LMFBR[1]. The GEM is divided into the external GEM and the in-core GEM; the former is installed between the core and the radial blanket and the latter is in the core region. To validate the prediction accuracy for the reactivity worth inserted by the GEM, a series of experiments has been carried out in mock-up cores at the Fast Critical Assembly (FCA)[2-4]. Since the number of sodium blocks was not enough to simulate the GEM region surrounding the whole core, a sector-type partial mock-up was applied to the external GEM experiment. In order to discuss the prediction accuracy for the GEM region surrounding the core, we changed the configuration of the GEM region and void patterns systematically. This report describes the experiments and analyses on the external GEM reactivity worth measured in a mock-up core for a nitride fueled LMFBR, FCA XX-1, putting a focus on the effect of the configuration of GEM region. The effect of the sodium level and voided area has already been reported [4].

Figure 2.5.1 shows the configuration of the GEM simulation region and the void patterns. Three kinds of GEM region, named 3-, 2- and 1-layer, were examined. In each configuration, three void patterns were measured respectively. In the case of the 3-layer, the radial width of the GEM region is about 17 cm, which corresponds to the actual design of the external GEM, though it is limited in about 1/6 sector region of the whole core. In the case of the 1-layer, on the other hand, about half of the core radial edge can be surrounded by the GEM, though its width is only 6cm.

In the experiments, the sodium-filled stainless steel cans (namely, sodium blocks) loaded in the GEM region were replaced with stainless steel void cans. Then the GEM reactivity worth was measured as the difference of the control rod positions to keep the core critical before and after the replacement.

In the analyses of the GEM reactivity worth, four kinds of calculation methods were

performed as shown in Table 2.5.1.

The calculated to experimental (*C/E*) values are shown in Table 2.5.2. The S_8 transport calculation with *RZ*-model (Method-1) shows relatively high C/E values (1.13 ～ 1.24), though no obvious dependency was found on the GEM configuration and the void pattern. The S_8 transport calculation with *XYZ*-model (Method-2) shows good agreement with the experiments for the 3-layer configuration, but about 8% overestimation is observed for the 1-layer. These tendency is possibly caused by the combination of S_n approximation and mesh effect. The Monte Carlo calculation (both Method-3 and -4) shows overestimation by approximately 10%, and no tendency on the GEM configuration and the void pattern was observed.

It is concluded that about 10% accuracy can be assured by using the Monte Carlo method for both multi-group and continuous energy methods, even if the GEM region surrounds the whole core. In the case of the deterministic transport calculation with *RZ*-model, about 20% overestimation should be taken into account. In the case of the deterministic transport calculation with *XYZ*-model, the prediction accuracy will be the same extent as that with *RZ*-model when the GEM region surrounds the core. Further investigation is desirable on the necessary S_n order and mesh width for the deterministic transport calculation.

References

1) Slovic, G. C., et al. : "Assessment of PRISM response to loss of flow events", Proc. Int. Conf. on Design and Safety of Advanced Nuclear Power Plants (ANP'92), Tokyo, Oct. 25-29, 1992, AESJ, Vol.III, 26.5-1 (1992).

2) Oigawa, H., Iijima, S. and Andoh, M. : JAERI-Review 97-011, p.63, "Measurement of In-core GEM Reactivity Worth at FCA" (1997).

3) Oigawa, H., Iijima, S. and Andoh, M. : JAERI-Review 98-022, p.78, "Measurement of External GEM Reactivity Worth at FCA" (1998).

4) Andoh, M., Oigawa, H. and Iijima, S. : JAERI-Review 99-031, p.55, "Measurement of GEM Reactivity Worth at FCA" (1999).

5) Mori, T., et al. : J. Nucl. Sci. Technol., 29, 1224 (1992).

Table 2.5.1 Calculation methods

	Method-1	Method-2	Method-3	Method-4
Base calculation	Diffusion [a] 25-group XYZ-model	Diffusion [a] 25-group XYZ-model	Diffusion [a] 25-group XYZ-model	Continuous energy Monte Carlo [c]
Transport correction	S_8 25-group RZ-model	S_8 25-group XYZ-model	Monte Carlo [b] 25-group XYZ-model	--------

a) Benoist's anisotropic diffusion coefficient was used.
b) GMVP code [5] c) MVP code [5]

Table 2.5.2 Calculated to experimental (C/E) value of external GEM reactivity worth in FCA XX-1 core

GEM region	Number of void drawers	Experimental error (relative)	C/E value [a] Method-1	Method-2	Method-3	Method-4
3-layer	18	±0.3%	1.17	0.96	1.13±2.8%	-----
	30	±1.1%	1.14	0.98	1.10±1.8%	-----
	46	±0.9%	1.24	0.99	1.09±1.2%	1.05±2.3%
2-layer	12	±3.0%	1.17	1.01	1.08±3.6%	-----
	28	±1.2%	1.18	1.00	1.03±1.7%	-----
	44	±1.6%	1.23	1.06	1.11±1.0%	1.11±1.3%
1-layer	18	±1.7%	1.15	1.09	1.11±2.3%	-----
	30	±1.0%	1.13	1.06	1.06±1.4%	-----
	46	±1.8%	1.17	1.07	1.07±0.8%	1.09±1.5%

a) Errors caused by statistical uncertainty of Monte Carlo calculation are presented for one standard deviation.

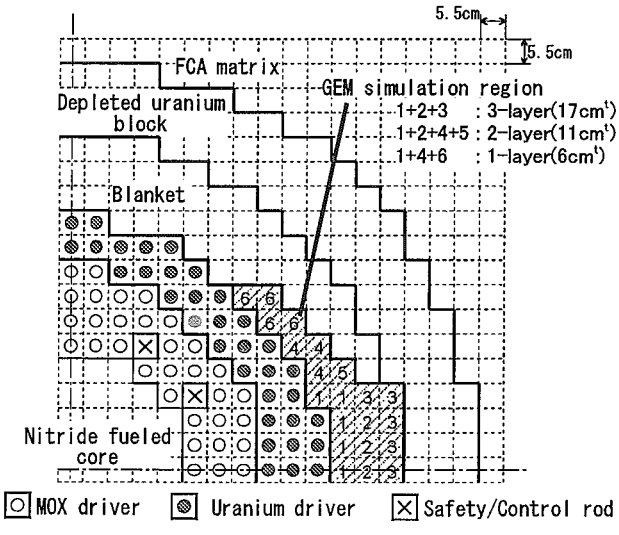

(a) GEM simulation region

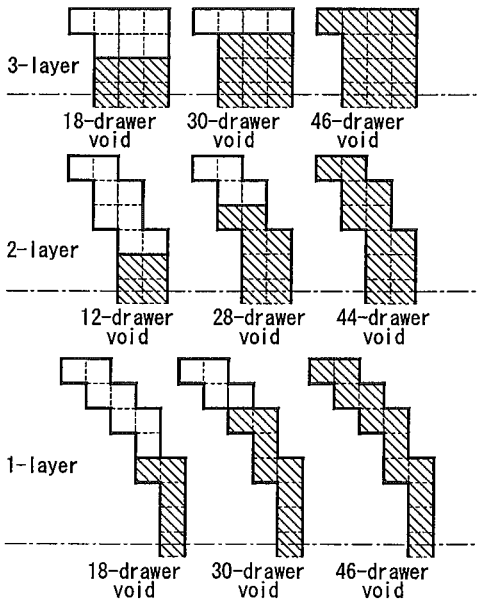

(b) Void patterns

Fig. 2.5.1 Measured region for external GEM reactivity worth at FCA XX-1

3. Advanced Reactor System Studies

The conceptual design study of Reduced-Moderation Water Reactor (RMWR) is being conducted. Five types of RMWR core design were performed. 1) The BWR type core without blanket: For increasing the reactor power, the core height is raised from the previous design. Reactor power same as that of ABWR and conversion ratio (CR) of 1.03 was attained. 2) The high conversion BWR type core: The effects of the plutonium (Pu) vector were investigated with the 10% higher fissile Pu content than that of the previous design. Same core specification such as the CR of 1.1 was attained with a little design modification. Transient analyses were also performed for demonstrating the safety of the designed core. 3) The long operation cycle BWR type core: The Pu with 8% lower fissile content than that of the previous design was utilized. The higher CR of 1.04 was attained under the same design. The characteristics of high burn-up cores ranging from 60GWd/t to 100GWd/t were also evaluated. 4) The high conversion PWR type core with heavy water coolant: The checkerboard type core configuration was adopted to reduce the radial power factor. The Pu with 10% lower fissile content was utilized. The higher CR of 1.11 was attained. 5) The PWR type core with light water coolant: The seed-blanket fuel assembly type core was adopted. To reduce the void reactivity coefficient, zirconium-hydride rods were inserted in the blanket region. The negative void reactivity coefficient and CR of 0.98 were attained. Other topics related to the RMWRs are as followings: The MOX fuel critical experiments in TCA were planned in terms of the fuel specification and facility modification. Introduction effects of RMWRs on uranium resource consumption were evaluated by the spreadsheet program. The effectiveness of introducing RMWRs was shown by comparison with the case of the LMFBR. The SUS cladding espansion under loss-of-coolant accident condition for PWR type RMWR was evaluated to determine the fuel rod condition for preventing the flow blockage under this accident.

The characterisitcs of nitride fuel type fast reactor were evaluated form the view point of the core performance and fuel cycle system. Superiority of nitride fuel core was confirmed. Transient analysis of high burn-up full MOX PWR with discharged burn-up of 100GWd/t core was performed and safty of the system was demonstrated. For the reactor instrumentation using optical technique, the irradiation effects of new type of optical fiber sensor, named fiber bragg grating (FBG), was evaluated by experiments. Nuclear power plant monitoring system with the combination of neural network and expert system was systematically integrated to enhance the usability of the system.

3.1 Conceptual Designing of Reduced-Moderation Water Reactor (1) － Study on BWR Type Core without Blanket －

T. Shirakawa, T. Okubo and T. Iwamura
(*E-mail :* shira@jpsrews1.tokai.jaeri.go.jp)

The object of the present study is to design a blanketless simple core with conversion ratio more than 1.0 and negative void reactivity coefficient, keeping the square fuel bundle configuration used in ABWR. The first core design with conversion ratio 1.1 was published in last year[1]. However, the design had disadvantages of relatively lower power (60% of ABWR power level) and lower discharged fuel burn-up(13.5GWd/t) compared with it (more than 20GWd/t) of ABWR. In order to eliminate those disadvantages, the core design was improved.

Neutronics calculations for two-dimensional XY fuel assembly lattice and three-dimensional XYZ core burn-up were performed by using JAERI's general purpose neutronics code system SRAC95[2].

In this design, the basic fuel bundle configurations are the same as the previous design; BWR type 9X9 square lattice bundle, axially distributing high and low fissile plutonium (Puf) enrichment regions to reduce axial power peaking, introducing large fuel pin diameter and adding follower on control rods to improve conversion ratio through reducing moderator to fuel volume ratio (Vm/Vf) of the bundle. The differences of the design are as follows; hollow tubes in flow channels are removed to simplify the core configuration and core height is raised to 2.6m from 1.56m to increase power level. In the low Puf enrichment region, the infinite multiplication factor (k_∞) is less than 1.0 and the void reactivity coefficient has negative value. This low enrichment region plays a rule of absorber to make void reactivity coefficient negative. With increasing the void fraction in core, the $k_\infty$of low Puf region decreases significantly, while that of high Puf enrichment region increases. Consequently, the core effective multiplication factor (k_{eff}) falls down. The fuel bundle geometry of the designed core is shown in Fig.3.1.1. The axial Puf distribution and the core refueling scheme are shown in Fig .3.1.2 and Fig .3.1.3, respectively.

Table 3.1.1 gives core neutronics specifications as well as major dimensions. The thermal power output is increased to 3925MWt and the discharged fuel burn-up is increased to 26.5GWd/t. Figure 3.1.4 shows the calculation results of the conversion ratio and k_{eff} for the equilibrium cycle. The conversion ratio is calculated to be 1.03 at the middle of the equilibrium cycle. The void reactivity coefficient was negative which was calculated from difference between k_{eff} at normal operation's void and k_{eff} at 5% higher void than that.

Maximum linear power density is 48.4kW/m at the end of cycle with all control rods withdrawn. This value is lower than that of BWR/4 7x7 fuel bundle.

Additionally, we designed core with 11x11 square fuel bundle configuration. The power level is increased to 120% of current ABWR power level. Table 3.1.1 gives core neutronics specifications.

References

1) Okubo,T., et al.: "Conceptual Designing of Reduced-Moderation Water Reactors(1)-Design for BWR-Type Reactors", Proc. of ICONE-8, ICONE-8422 (2000).
2) Okumura, K., et al.: "SRAC95: General Purpose Neutronics Code System", JAERI-Data / Code 96-015 (1996) [in Japanese].

Table 3.1.1 Major dimensions and characteristics of the core

Item	9X9fuel core	11X11fuel core
Thermal power output (MWt)	3,926	3926X1.2
Electric power output (MWe)	1,356	1,356X1.2
Fuel lattice arrangement	9 x 9 square	11 x11 square
Fuel rod length (m)	2.6	←
Fuel assembly pitch(cm)	15.5	←
Gap width between rods (mm)	1.0	1.4
Fuel outer diameter (mm)	15.2	11.8
Fuel cladding thickness (mm)	0.75	0.5
Average fissile Pu content (wt%)	6.9	7.0
Number of refueling batch	4.27	4.27
Cycle burn-up (GWd/t)	6	8
Operation cycle length (EFPM)	12.6	13.0
Discharge burn-up (GWd/t)	25.6	34.0
Conversion ratio	1.03	0.92
Void reactivity coefficient (10^{-4}dk/k/△%void)	-1.4	-6.0
Maximum linear power density (kW/m)	48.4 (EOC*)	27.9 (EOC*)

- EOC: End of cycle

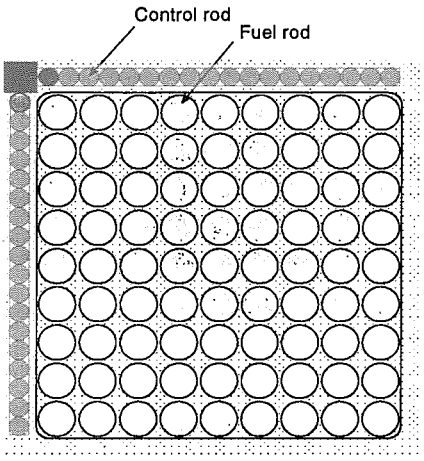

Fig. 3.1.1 Cross section of fuel rod assembly

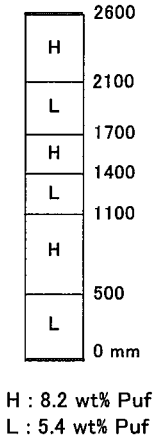

Fig.3.1.2 Axial Puf distribution

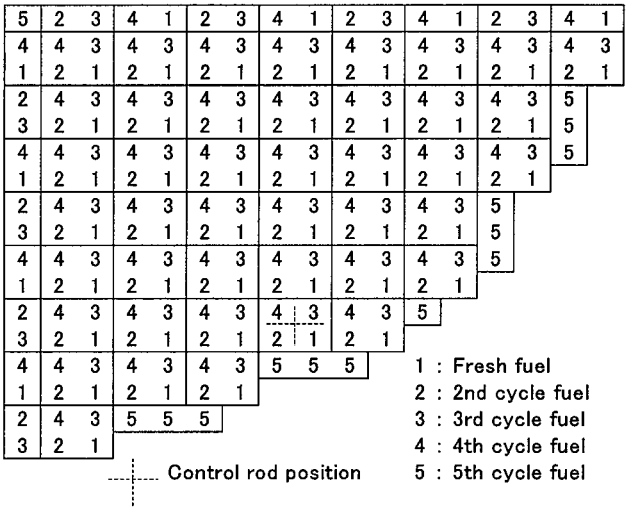

Fig.3.1.3 Core refueling scheme ((1/4) core)

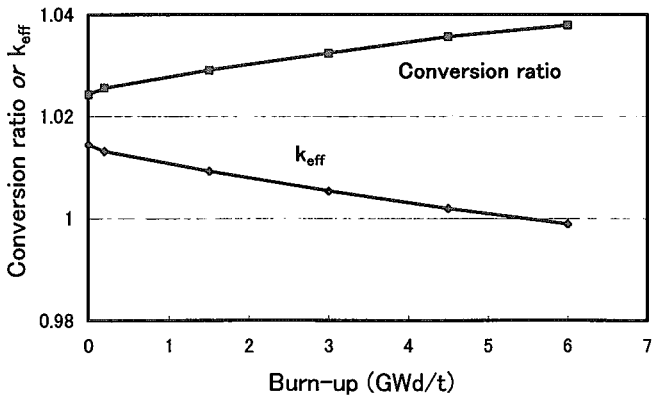

Fig. 3.1.4 Calculated conversion ratio and k_{eff} for equilibrium cycle

3.2 Conceptual Designing of Reduced-Moderation Water Reactor (2)
－ Study on High Conversion BWR Type Core －

T.Okubo, T.Iwamura, R.Takeda*[1] and S.Wada*[2]
(*E-mail:* okubo@jpsrews1.tokai.jaeri.go.jp)

A BWR type reduced-moderation water reactor (RMWR) aiming at the high conversion ratio of 1.1 has been studied in order to investigate the attainable upper limit for the conversion ratio. The reactor with such a high conversion ratio is mainly expected to be beneficial to the long-term energy supply with the uranium resources. A concept has been established achieving the conversion ratio of 1.1 and the negative void reactivity coefficients. The cross section of the fuel assembly is shown in Fig. 3.2.1. The fuel assembly and the channel box are hexagonal. Control rods are Y-shaped and with the follower for water removal. The effective moderator-to-fuel volume ratio (*Vm/Vf*) is about 0.17 under the increased core average void fraction of 70% in this design.

For this concept, the effects of the plutonium (Pu) vector on the design are investigated, since the Pu isotopic composition is expected to vary depending on many factors such as the burn-up and cooling time. For this purpose, another composition with 10 % higher fissile Pu (Pu*f*) content (see, Table 3.2.1) has been selected and investigated. The higher Pu*f* content tends to give lower conversion ratio but lower void reactivity coefficients due to the lower fraction of Pu-240, because it is the fertile for Pu-241 and its fission cross section increases but its capture cross section decreases as the neutron energy. However, it has been confirmed the same conversion ratio of 1.1 can be achieved under the same design concept with a little modification in design. Namely, the MOX fuel length is to be increased by 3 cm, and the upper and the lower blankets by 3 and 15 cm, respectively. Major characteristics of two designs with the different Pu vectors are summarized in Table 3.2.1

Analyses on the major abnormal transients and accidents have also been performed, tentatively assuming the similar system to the ABWR with some adjustment for this design. The decrease in the minimum critical power ratio (ΔMCPR) in the abnormal transients are summarized in Table 3.2.2 comparing with values for the ABWR. The pump failure event

*1 Hitachi, Ltd., *2 The Japan Atomic Power Company (JAPC)

is evaluated to give the largest ΔMCPR of 0.12, instead of the loss of feed water heating event for the ABWR case. This is corresponding to the design characteristic of this core with the small absolute value for the negative void reactivity coefficients. The value is a little smaller than the maximum value of 0.15 for the ABWR. Concerning to the design basis accidents, three major events have been analyzed. They are the trip of all recirculation pumps, the high pressure core flooder pipe break and the main steam line break. They give similar maximum cladding temperatures between 935 K and 963 K. Although the values are much higher than the maximum value of 828 K evaluated for the ABWR, they are still much lower than the licensing limit of 1,473 K. Therefore, the safety during the major abnormal transients and the accidents has been confirmed for this design.

Table 3.2.1 Comparison of major core parameters of high conversion BWR type RMWR with different Pu isotopic composition

Item		Low Puf case*1	High Puf case*2
Electric output	MWe	1,100	1,100
Thermal output	MWt	3,188	3,188
Pressure	Mpa	7.2	7.2
Core outer diameter	M	3.60	3.60
No. of fuel assembly		924	924
Discharge burn-up	GWd/t	45	45
Core height**	M	0.68*3	0.71*4
Core water flow rate	10^4t/h	1.3	1.4
Core outlet quality	%	55	50
Core void fraction	%	70	69
Average Puf content	%	10.2	10.5
Puf amount	T	12.1	13
Conversion ratio		1.10	1.10
Max. linear power	KW/ft	17	15
MCPR		1.3	1.3
Void coefficient	10^{-4} Δk/k/%void	-1	-2
Operation length	EFPM	14	13
Axial Puf content distribution	w/o cm	18 18.5	20.0
	DU cm	DU 29.5	29.5
	W/o cm	18 20.0	21.5

＊＊ : Including inner blanket region
＊ 1 : Pu-238/239/240/241/242/Am-241=2.7/47.9/30.3/9.6/8.5/1.0 wt%
＊ 2 : Pu-238/239/240/241/242/Am-241=1.9/57.5/23.3/10.0/5.4/1.9 wt%
＊ 3 : Additionally, 33 cm upper blanket and 20 cm lower blanket
＊ 4 : Additionally, 36 cm upper blanket and 35 cm lower blanket

Table 3.2.2 ΔMCPR for major abnormal transients

Event	RMWR	ABWR
Recirculation pump failure	0.12	0.08
Loss of feed water heating	0.04	0.15
Loss of load	0.01	0.11
Pressure control system failure	0.08	0.00
Feed water control system failure	0.01	0.07
Loss of feed water flow	0.00	0.00

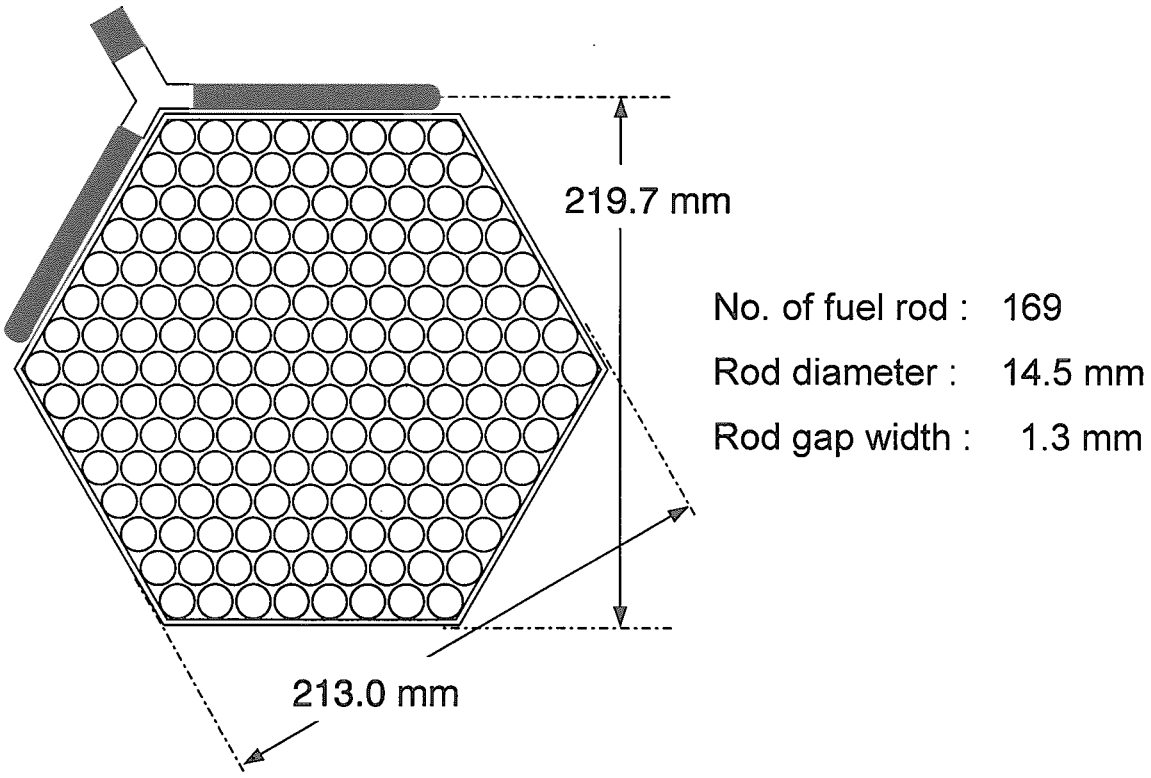

Fig. 3.2.1 Configuration of fuel rod assembly

3.3 Conceptual Designing of Reduced-Moderation Water Reactor (3)
－ Study on Long Operation Cycle BWR Type Core －

T.Okubo, T.Shirakawa, T.Iwamura, T.Yokoyama*[1] and S.Wada*[2]
(*E-mail:* okubo@jpsrews1.tokai.jaeri.go.jp)

A BWR type reduced-moderation water reactor (RMWR) has been studied, aiming at the long operation cycle more than two years and the high burn-up around 60 GWd/t under the high conversion ratio more than 1.0. The reactor with such a long operation cycle and high burn-up is mainly expected to be beneficial to reduction of radioactive waste production as well as the economical aspects with the plutonium (Pu) multiple recycling fuel cycle. A concept has been established achieving the design goals mentioned above under the negative void reactivity coefficients.

The cross section of the core is shown in Fig. 3.3.1. The core consists of three types of assembly. There are two types of fuel assembly with the different plutonium contents. The plutonium content for the outer region is 15 % higher than for the inner region, in order to reduce the radial power peaking. The resultant radial peaking factor is 1.13. The total number of the fuel assembly is 252. In the inner region, there are special assemblies named the void tube assemblies. They are introduced to reduce the void reactivity coefficients by utilizing the neutron streaming effect. The negative void reactivity coefficients have been attained with this special assembly without significantly reducing the core height, and hence, without increasing the core diameter. In the present design the void tube assemblies occupy about 20 % of all assemblies.

The fuel assembly consists of 469 fuel rods with the diameter of 11.9 mm. The gap width between rods is 1.3 mm. The cladding material is supposed to be the stainless steel. In order to reduce the local power factor, there is a Pu smear density distribution in the assembly with four smear densities. The smear density will be changed with the hollow pellet instead of the different Pu content. The resultant local peaking factor is 1.32. The control rods are Y-shaped with the follower and made with the hafnium plates. There are 138 control rods in the core.

*1 Toshiba, Co., *2 The Japan Atomic Power Company (JAPC)

For this concept, the effects of the plutonium vector on the design are investigated. Another compositions with 8 % lower in fissile Pu (Pu*f*) content are selected and investigated. Since the lower Pu*f* content tends to give higher conversion ratio due to the higher fraction of the fertile Pu-240, it has been confirmed the higher conversion ratio of 1.04 can be achieved under the same design concept.

The possibility for much longer operation cycle has been investigated. One approach to extend the operation cycle is to reduce the refueling batch number under the fixed burn-up. Another is to increase the burn-up under the fixed refueling batch number. The results are summarized in Table 3.3.1. From the results, the conversion ratio is less than 1 in any cases other than the base case with 2-year cycle and 4-batch under 60 GWd/t burn-up. However, there are some possibilities to have the conversion ratio more than 1.0 for the case with 4-year cycle and 2-batch under 60 GWd/t and the case with 2.7-year cycle and 4-batch under 80 GWd/t. There is a possibility to attain 10-year operation cycle by one batch refueling under the conversion ratio less than 0.9. This means the multiple recycling of Pu is not possible for this case. Therefore, if the conversion ratio over 1.0 is not necessarily requested, 10-year operation cycle might be possible.

Table 3.3.1 Burn-up characteristics for long operation cycle

Burn-up		60GWd／t			80GWd／t			100GWd／t		
Operation cycle	Year	2	4	8	2.67	5.33	10.67	3.33	6.67	13.3
Batch number	-	4	2	1	4	2	1	4	2	1
Average burn-up	GWd/t	61	61	60	81	80	79	100	100	97
Pu content (Inner／Outer)	%	14.5/ 16.7	15.0/ 17.1	16.2/ 18.3	15.3/ 17.7	16.1/ 18.7	17.9/ 20.1	16.2/ 18.7	16.6/ 22.6	19.7/ 22.1
Conversion ratio	-	1.01	0.99	0.94	0.98	0.95	0.89	0.95	0.92	0.85
Burn-up reactivity	%Δk/k	2.8	5.3	10.5	3.4	6.7	14.1	4.1	9.2	14.1

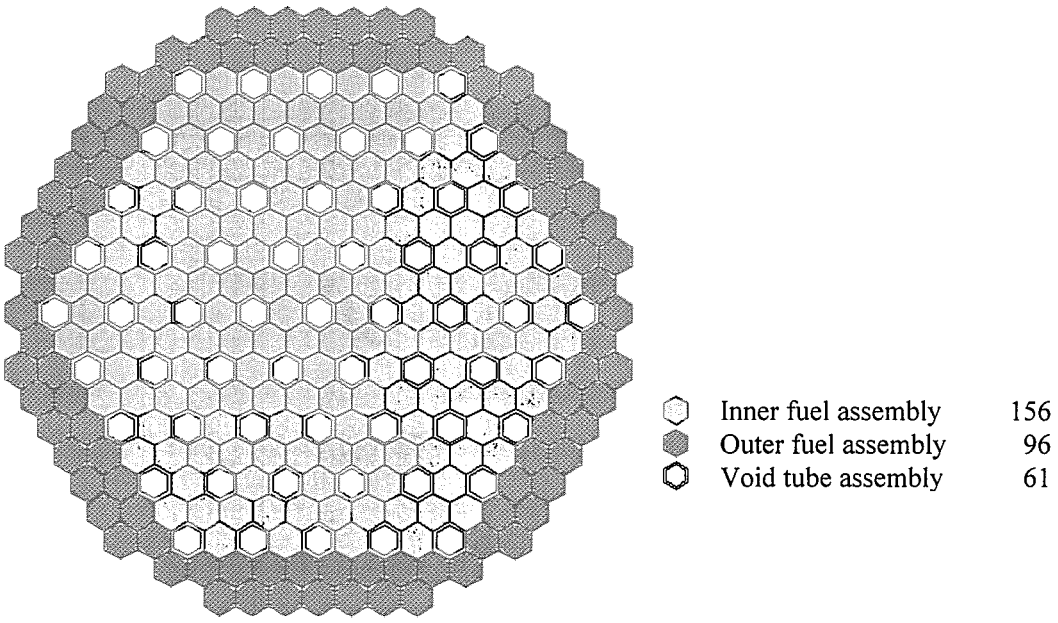

Core cross section

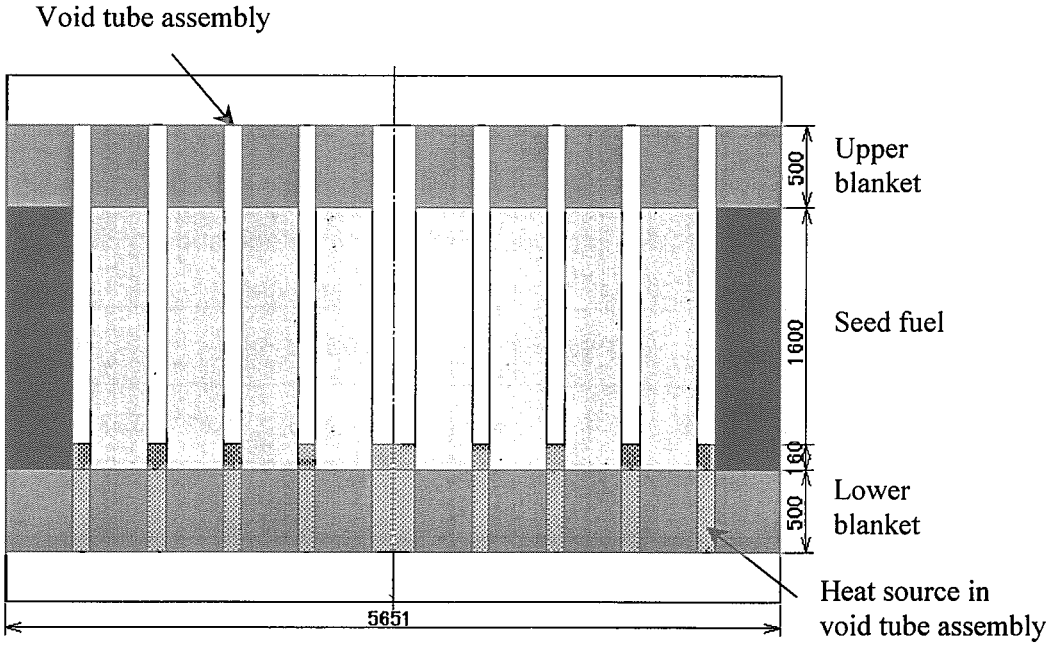

Vertical core dimensions

Fig. 3.3.1 Configuration of core

3.4 Conceptual Designing of Reduced-Moderation Water Reactor (4)
－ Study on High Conversion PWR Type Core －

T.Okubo, S.Shimada*[1], T.Kugo, T.Iwamura, K.Hibi*[2] and S.Wada*[3]
(*E-mail:* okubo@jpsrews1.tokai.jaeri.go.jp)

A PWR type reduced-moderation water reactor (RMWR) aiming at the high conversion ratio more than 1.0 has been studied. In a PWR type core, it is not easy to attain the conversion ratio more than 1.0 due to no void formation in the core. Therefore, in this study, the heavy water is introduced as the coolant and moderator. Since the design obtained in the last fiscal year[1)] had a very high radial power factor around 2.5, the improvement on this issue has been the most important point. The obtained core configuration is presented in Fig. 3.4.1. The important point is the checkerboard type distribution of the blanket assembly. That is, each blanket assembly is surrounded by six fuel assemblies. The resultant radial peaking factor is 1.54 (1.28 for only the fuel assemblies) in this design.

For the negative void reactivity coefficient, shortening of the seed region and also shortening of the radial blanket region than the fuel assemblies have been found to be effective by the survey calculations. Therefore, the length of the seed region is set to be 550 mm and the double flat core configuration with the internal blanket of 500 mm high has been adopted as shown in Fig. 3.4.2. Also, the length of the radial blanket is set to be 1,150 mm, which is shorter than the length of the fuel assemblies by 225 mm each at the top and the bottom regions as shown in the figure.

Some fuel assemblies without the internal blanket have been introduced to avoid the strong power peaking at the voided situation. That is, the length of the seed region is 1600 mm for these fuel assemblies. The number of this type of the fuel assembly is 36 and about 20 % of all the fuel assemblies in the core. In order to increase the conversion ratio, the axial blankets of 350 mm high are added both at the top and the bottom of the fuel assemblies.

---

*1 Engineering Development Co., Ltd., *2 Mitsubishi Heavy Industries, Ltd.,
*3 The Japan Atomic Power Company

Major characteristics of the core are summarized in Table 3.4.1. The conversion ratio is 1.06 and the void reactivity coefficients are negative in this core design, and hence, the design goals have been achieved.

For this concept, the effects of the plutonium (Pu) vector on the design are investigated. For this purpose, another composition with 10 % lower fissile Pu (Pu*f*) content has been selected and investigated. The lower Pu*f* content tends to give higher conversion ratio but higher void reactivity coefficients due to the higher fraction of the fertile Pu-240. Therefore, the conversion ratio is increased to 1.11 under this Pu composition. The void reactivity coefficients, however, become positive. In order to resolve this, the length of the radial blanket is reduced to 1,100 mm, aiming at increase in neutron leakage. Therefore, the design goals can be achieved for the different Pu composition under the same design concept with a little modification.

Reference

1) Research Group for Advanced Reactor System, *et al.*: "Study on Reduced-Moderation Water Reactor (RMWR) Core Design — Joint Research Report (FY1998-1999) —", JAERI-Research 2000-035 (2000) [in Japanese].

Table 3.4.1 Major characteristic of equilibrium core

Item	High Pu*f* case *1	Low Pu*f* case *2
Conversion ratio	1.06	1.11
Burn-up reactivity	2.9%Δ ρ	2.6%Δ ρ
Void reactivity coefficient (EOEC)	-0.4×10^{-4} Δ ρ /%void	-1.0×10^{-4} Δ ρ /%void
Maximum linear heat rate	38kW/m	36kW/m
Maximum assembly power	16.3MW	16.7MW
Average discharged burn-up of seed	53GWd/t	53GWd/t

EOEC : end of equilibrium cycle
* 1 : Pu-238/239/240/241/242/Am-241=1.9/57.5/23.3/10.0/5.4/1.9 wt%
* 2 : Pu-238/239/240/241/242/Am-241= 2.7/47.9/30.3/9.6/8.5/1.0 wt%

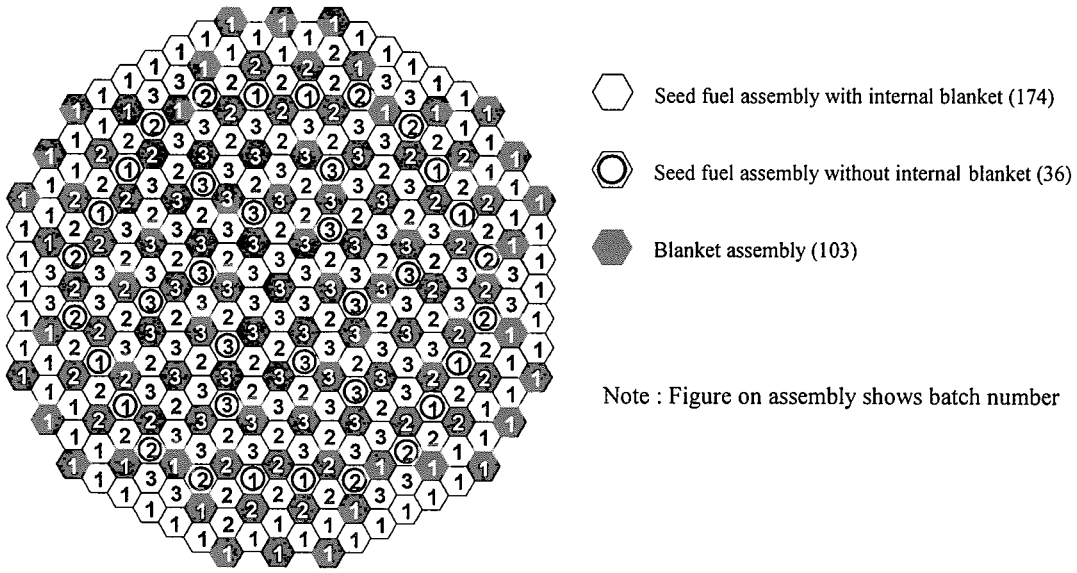

Fig. 3.4.1 Core configuration with shuffling pattern

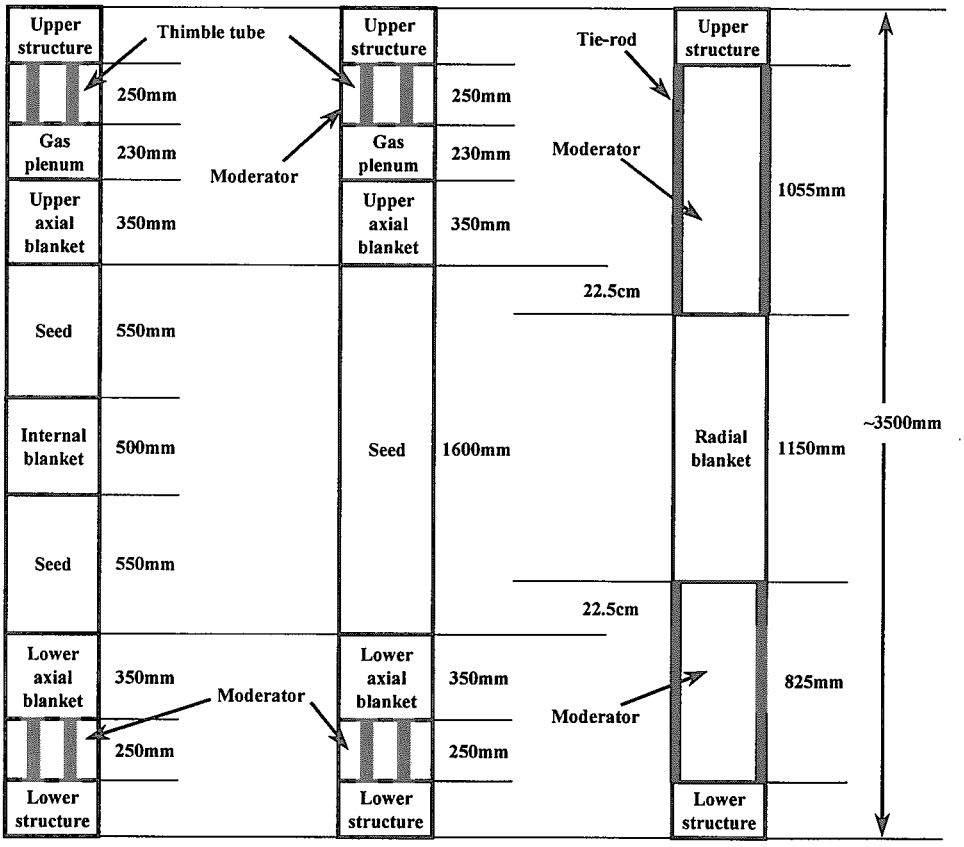

(a) Seed fuel assembly with internal blanket (b) Seed fuel assembly without internal blanket (c) Blanket assembly

Fig. 3.4.2 Vertical dimensions for three assemblies

3.5 Conceptual Designing of Reduced-Moderation Water Reactor (5)
－ Study on PWR Type Core with Light Water Coolant －

T. Kugo, S.Shimada*, T.Okubo and T.Iwamura
(*E-mail:* kugo@mike.tokai.jaeri.go.jp)

As a light water cooled reduced-moderation PWR type core, a concept with seed-blanket fuel assemblies has been investigated [1]. It has a seed fuel pin bundle surrounded by blanket fuels as shown in Fig.3.5.1. To reduce the void reactivity coefficient, some surrounding blanket fuel rods are replaced by Zirconium-hydride ($ZrH_{1.7}$) rods. Because of its complex geometry and a variety of neutron spectra, it is difficult to evaluate precisely core characteristics by conventional deterministic transport codes. In the present work, we used the continuous-energy Monte Carlo codes MVP [2] and MVP-BURN [3] as design tools. The specifications for seed and blanket fuel rods are shown in Table 3.5.1. The internal blanket divides the seed core into two parts as shown in Fig.3.5.2.

Survey calculations have been done by the MVP code with 500,000 histories employing an infinite array model of the assemblies at the initial fuel condition as a calculation model. First, survey calculations on the assembly configuration and the fissile plutonium (Puf) enrichment of the seed fuel were performed. The number of layers of the seed fuel rods is selected to be 12 or 15. The number of layers of the surrounding blanket fuel rods is 3, 3.5 and or 4 for the assemblies of 12-layer seed fuel rods. For the assemblies of 15-layer seed fuel rods, it is 4, 4.5 and or 5. A half layer means that the most outer blanket fuel rods commonly belong to neighboring assemblies. In this calculations the number of $ZrH_{1.7}$ rods is fixed to zero. Figure 3.5.3 shows the effect of assembly configuration on a relation of keff and void reactivity coefficient. From the figure, it is concluded than the best design option is 15-layers for the seed fuel rods and 4.5-layers for the blanket fuel rods, because this combination gives the lower void reactivity coefficient and higher keff compared with the other combinations. Second, survey calculations on the number of $ZrH_{1.7}$ rods in the surrounding blanket region were performed for the best design option. The number of $ZrH_{1.7}$ rods ranges from zero to 84. Figure 3.5.4 shows the effects of the number of $ZrH_{1.7}$

* Engineering Development Co., Ltd.

rods and the seed fuel Puf enrichment on the relation of keff and void reactivity coefficient. From the figure it is clarified that the introduction of $ZrH_{1.7}$ rods is more advantageous than the reduction of the seed fuel Puf enrichment to reduce the void reactivity coefficient until the number of $ZrH_{1.7}$ rods occupies approximately 15% of that of the blanket fuel rods.

From the result of the above survey calculations, we have established an assembly configuration as show in Fig.3.5.1. We choose a 15-layer for the seed fuel rods and a 4.5-layer for the blanket rods. The Puf enrichment of the seed fuel is 18wt%. The 36 $ZrH_{1.7}$ rods per the assembly are placed in the surrounding blanket region. The axial blankets of 25cm height are set on and beneath the seed core regions to increase the conversion ratio. The 3-cycle fuel loading scheme is employed. A thermal power per assembly is defined so as to generate 1,200 MWe by a whole core with an equivalent diameter of 5.0m. The burn-up characteristics have been evaluated with the infinite lattice of assemblies by the MVP-BURN code. The number of histories was taken as 500,000 per burn-up step. Figure 3.5.5 shows the burn-up characteristics. In this evaluation, we assume the reactivity loss of 2%dk for a whole core being supposed to employ an out-in fuel shuffling pattern instead of the infinite array of assemblies. From the figure, it is found that the keff value is 1.02 at 36 effective full power months (EFPMs). We assume a 3-cycle for the fuel loading in the present work. Therefore, this core will achieve 18 EFPMs as the cycle length and 54 EFPMs for the fuel loading length. Integrated conversion ratio is about 0.98 after 54 EFPMs. The reactivity increases 2%dk at the early burn-up. The void reactivity coefficient decreases by 1.5×10^{-4}dk/k/%-void during the early burn-up period. Although the void reactivity coefficient is positive at the beginning and end of life in Fig.3.5.5, it is expected that void reactivity coefficient will be kept negative through the whole operation cycle considering the 3-batch refueling scheme.

References

1) Hibi, K., et al. : "Conceptual Designing of Reduced-Moderation Water Reactors (2) –Design for PWR-Type Reactors-", ICONE-8523, Baltimore (2000).
2) Mori, T., Nakagawa, M. and Sasaki, M. : "Vectorization of Continuous Energy Monte Carlo Method for Neutron Transport Calculation", J. Nucl. Sci. Technol., 29, 325 (1992).
3) Okumura, K., et al. : "Validation of a Continuous-Energy Monte Carlo Burn-up Code

MVP-BURN and Its Application to Analysis of Post Irradiation Experiment", J. Nucl. Sci. Technol., 37, 128 (2000).

Table 3.5.1 Specification for seed-blanket fuel rods

Item	Seed Fuel Pin	Blanket Fuel Pin
Fuel Material	(Pu, U)O_2	depleted UO_2
Fuel Pellet Diameter	8.6mm	13.1
Cladding material	SS-316	SS-316
Cladding Inner Diameter	8.7mm	13.2mm
Cladding Outer Diameter	9.5mm	14.4mm
Pin Pitch	10.5mm	15.0mm
H/HM	0.81	0.45
Fuel Length	Seed:1000mm Blanket:500mm Seed:1000mm	2500mm

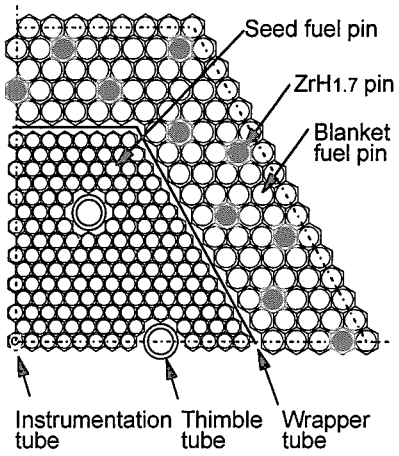

Fig.3.5.1 Configuration of seed-blanket assembly

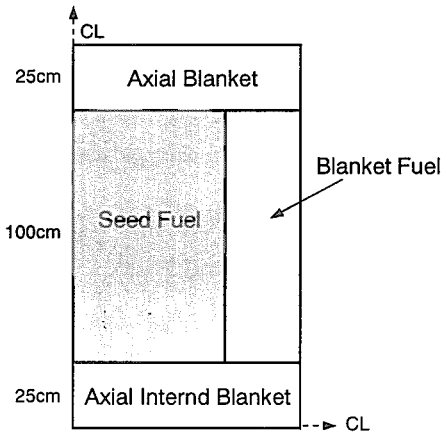

Fig.3.5.2 Axial Configuration of seed-blanket assembly

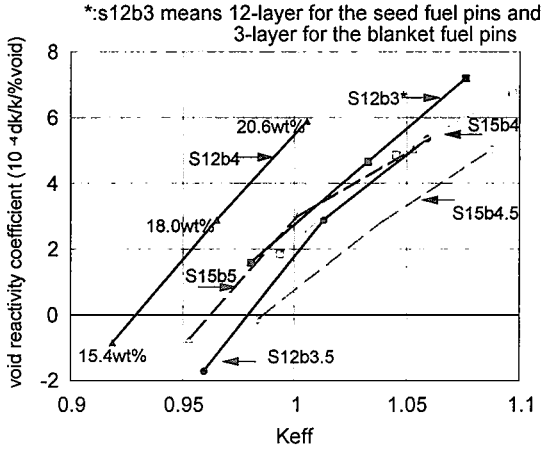

Fig.3.5.3 Relation of initial keff and void reactivity coefficient for various seed-blanket assembly configurations

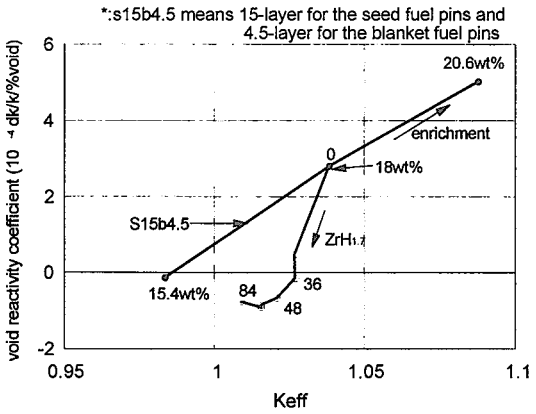

Fig.3.5.4 Relation of initial keff and void reactivity coefficient for the various number of $ZrH_{1.7}$ rods

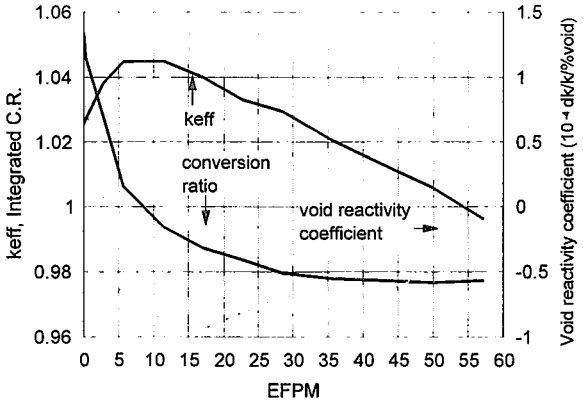

Fig.3.5.5 Burn-up characteristics of seed-blanket assembly

3.6 Plan for MOX Fuel Critical Experiments in TCA

S. Shimada*, H. Akie, T. Suzaki, T. Okubo, S. Usui, T. Shirakawa, T. Iwamura,
T. Kugo and N. Ishikawa
(*E-mail:* shimada@jpsrews1.tokai.jaeri.go.jp)

The Reduced-Moderation Water Reactor (RMWR)[1), 2)] is one of the next generation water-cooled reactors, which aims at effective utilization of uranium resources, high burn-up / long operation cycle, and multiple recycling of plutonium. For verification of the feasibility, of the RMWR the reactor physics features such as negative void reactivity coefficient and high conversion ratio beyond 1.0 must be confirmed. The review of critical experiments performed so far in Europe and Japan indicated that no useful data are available for RMWR development. Therefore, critical experiments using Tank Type Critical Assembly (TCA) in JAERI are planned[3)]. MOX fuel rods should be prepared for the experiments and some modifications of the safety-related equipment are needed for handling a large number of MOX fuel rods.

The fuel specification was determined as shown in Table 3.6.1, considering the fuel rod designs for the BWR and PWR type RMWRs[1), 2)]. The core is divided into two regions by inserting an inner tank to avoid criticality in MOX fuel test region. To determine the number of fuel rods and the size of the inner tank, preliminary calculations were performed by using the SRAC code[4)]. Calculated results are shown in Table 3.6.2. The number of fuel rods for critical experiments was determined as shown in Table 3.6.3.

Modification of TCA facility is requested to treat a large number of MOX fuels from a safety point of view. Additional safety plates and additional shielding device at the top of tank for loading the MOX fuels are needed to ensure safety. Figure 3.6.1 shows the fuel configuration. Remodeling plan of TCA for MOX critical experiments is shown in Fig.3.6.2.

The inner tanks of a cylindrical and a rectangular geometry are planed as shown in Fig.3.6.3. The test region is composed in the inner tank and driver fuels are loaded in the outer region. The criticality is controlled by only changing the water level in outer region. Three types of critical experiments for RMWR core will be performed.

---

* Engineering Development Co., Ltd.

(1) Basic experiments for simple core configuration for checking the effect of buffer region and radial blanket, estimation of void reactivity, and measurement of control rod reactivity will be performed.

(2) Experiments for simulating axial heterogeneous core configuration will be done as follow. In order to simulate the characteristics of axial heterogeneous cores with axial blanket regions, the MOX and blanket fuels are arrayed alternatively inside the rectangular inner tank and the power distribution is measured through horizontal direction instead of vertical direction.

(3) Experiments for simulating the actual RMWR core characteristics will be performed by composing the core in the inner cylindrical tank.

References

1) Hibi, K., et al. : "Conceptual Designing of Reduced-Moderation Water Reactors (2) –Design for PWR-Type Reactors-", ICONE-8423, Baltimore (2000).

2) Okubo, T., et al.: "Conceptual Designing of Reduced-Moderation Water Reactors (1) –Design for BWR-Type Reactors-", ICONE-8422, Baltimore (2000).

3) Shimada, S., et al.: "A Plan of Reactor Physics Experiments for Reduced-Moderation Water Reactors with MOX Fuel in TCA", JAERI-Research 2000-026 (2000) [in Japanese].

4) Tsuchihashi, K., et al.: "Revised SRAC Code System", JAERI 1302 (1986).

Table 3.6.1 Fuel specification

Item	MOX Fuel	Depleted UO_2 Fuel for Blanket / Buffer	UO_2 Fuel for Driver Region
Fuel Rod Dia. (mm)	11.0	11.0	11.0
Cladding Material	Zry	Zry	Zry
Cladding Thickness (mm)	0.66	0.66	0.66
Fuel	MOX	UO_2	UO_2
Enrichment (wt%)	5, 10, 15, 20 (Pu^f)	0.2	4.9
Pellet Diameter (mm)	9.6	9.6	9.6
Active Length (mm)	1,000	1,000	1,000

Table 3.6.2 Calculated results of core diameter and number of fuel rods for criticality using MOX fuels of 1m length

Pu^f Enrichment	10wt%			15wt%			20wt%		
H/HM	0.6	1.0	1.5	0.6	1.0	1.5	0.6	1.0	1.5
Critical Diameter (cm)	71.2	70.6	69.0	46.6	46.6	46.8	36.8	37.0	37.6
Number of Fuel Rods for Criticality	3630	3567	3407	1552	1557	1575	970	977	1012

Table 3.6.3 Number of fuel rods for MOX critical experiments

MOX fuels
Pu enrichment (wt%) 5 10 15 20
Number of rods 1000 1000 1500 500

Depleted UO_2 fuels for Blanket / Buffer region
Number of rods 4000

Driver fuels (4.9wt%UO_2)
Number of rods 3000

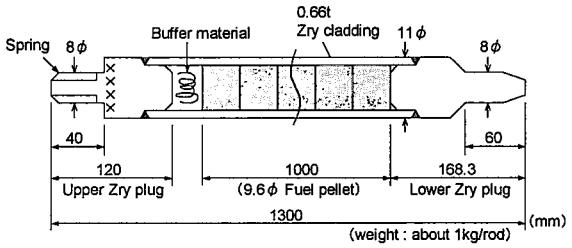

Fig.3.6.1 Fuel configuration

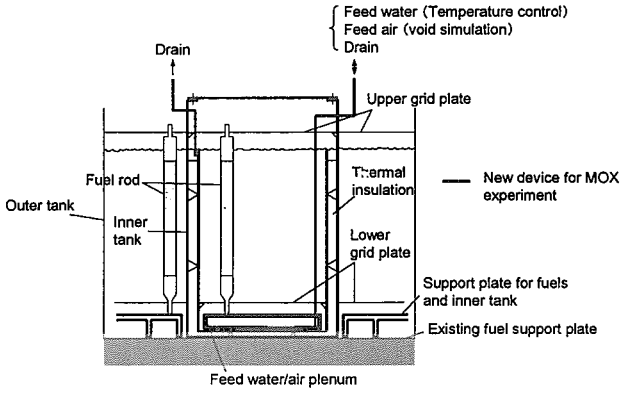

Fig.3.6.2 Remodeling of TCA for MOX critical experiments

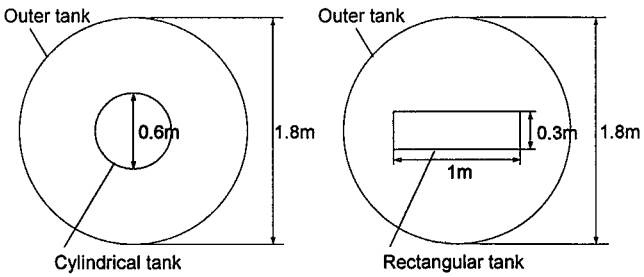

Fig.3.6.3 Installation of inner tanks

3.7 Introduction Effects of RMWRs on Uranium Resource Consumption

T. Nakatsuka, T. Okubo, T. Iwamura and O. Sato
(*E-mail:* nakatuka@jpsrews1.tokai.jaeri.go.jp)

Natural uranium cumulative consumption is one of the most important indexes in introduction effects of reduced-moderation water reactors (RMWRs). It greatly depends on reactor core characteristics such as Pu inventory, fissile Pu (Puf) surviving ratio (the ratio of the amount of discharged Puf to that of charged Puf) and plant lifetime. It is important to estimate their introduction effects quantitatively upon designing new reactors. JAERI has already developed the JALTES-II code[1), 2)] that is a detailed system analysis tool for long-term strategy on nuclear power development. In the present study, the introduction effects of the latest RMWR designs were instantly evaluated by a new spreadsheet program easier to use.

Three types of RMWR[3)] as in Table 3.7.1 were analyzed as well as conventional LWRs, the full-MOX BWR and the LMFBR. We made the following assumptions:

1) Introduction year is 2,030 for RMWRs and 2,050 for LMFBRs, respectively.
2) Future nuclear power demand finally saturates between 80 and 140 GWe.

The upper value till 2,030 is based on the national long-term program of nuclear energy[4)]. The lower value corresponds to the rather practical case considering difficulty in construction of new reactors.

Construction rate of each reactor is determined by the power demand and the amount of Pu stock. In the present calculation, new type reactors are given priority of construction. Figure 3.7.1 shows calculation results for the low inventory type RMWR with the present program and JALTES-II. Although the present program estimates the time required to saturate longer than JALTES-II, the difference in the terminal values of the natural uranium consumption is within 15%. That confirmed the validity of the present program.

Uranium cumulative consumption was calculated for the full MOX BWR, the high conversion type RMWR and the LMFBR. Fissile Pu surviving ratio is 1.06 for the RMWR and 1.20 for the LMFBR. Figure 3.7.2 shows calculation results. For the breeder type reactors, the RMWR and the LMFBR, the terminal values of natural uranium consumption saturate for both the supposed nuclear power demands, while those with the full-MOX BWR increases monotonously. Saturated values are below 1.5 mega ton which is 10% of the estimated amount of total natural uranium reserves of 15 mega ton[5)]. From this result, the high conversion ratio type RMWR is found to be one of alternatives for LMFBRs. Especially when the future nuclear power demand keeps the lowest level, the amount of uranium consumption saturates only around 0.8 mega ton for the RMWR and the LMFBR. The difference in

uranium consumption between both reactors becomes small and effectiveness of the RMWR as an alternative for LMFBRs increases. In the case of low nuclear power demand, modest conversion ratio can be acceptable and design margin increases. If economy of nuclear power is highlighted, other characteristics such as operation cycle length or plant power may have more importance.

Effects of introduction timing and core characteristics are also examined for the case of the lower electric power demand. The main core parameters are presented in Table 3.7.1. Figure 3.7.3 shows the effects of introduction timing of the high conversion type RMWR. A 10-year delay in introduction produces almost no impact on uranium consumption. As far as the high conversion ratio RMWR begins to be introduced earlier than LMFBRs, its importance as an alternative for LMFBRs will not be affected. Figure 3.7.4 shows the effects of core characteristics. At early phase when the Pu stock is little, the low inventory type is easier to be introduced than the high conversion ratio type and its uranium consumption keeps lower. As the amount of discharged Pu increases with time, the high conversion ratio type conversely becomes easier to be introduced and saturates earlier at lower level. The long operation cycle type and the low inventory type have almost the same conversion ratio. The difference between the two in uranium consumption is caused by the difference in the inventory. These results indicate some flexibility in the introduction of RMWRs depending on the demand in the future.

References

1) Sato, O. and Yasukawa, S.: "JALTES-II : A Systems Analysis Model for Long-Term Strategy on Nuclear Power Development", JAERI-M 85-129 (1985). [in Japanese]
2) Tatematsu, K., Sato, O. and Tanaka, Y.: "An Analysis on the Roles of Reduced-Moderation Water Reactors", JAERI-Research 2000-025 (2000). [in Japanese]
3) Okubo, T., et al.: "Conceptual Designing of Reduced-Moderation Water Reactors (1) - Design for BWR-Type Reactors -", Proc. of ICONE-8, ICONE-8422 (2000).
4) Atomic Energy Commission of Japan, "The long-term program of nuclear energy" (1994)
5) OECD/NEA-IAEA, "URANIUM Resources, Production and Demand 1997" (1998)

Table 3.7.1 Main core characteristics of RMWRs

	High conversion ratio type	Long operation cycle type	Low inventory type
Electric power (MWe)	1,100	1,350	1000
Puf surviving ratio	1.06	1.00	1.01
Initial Puf inventory (t)	12.1	16.4	4.4

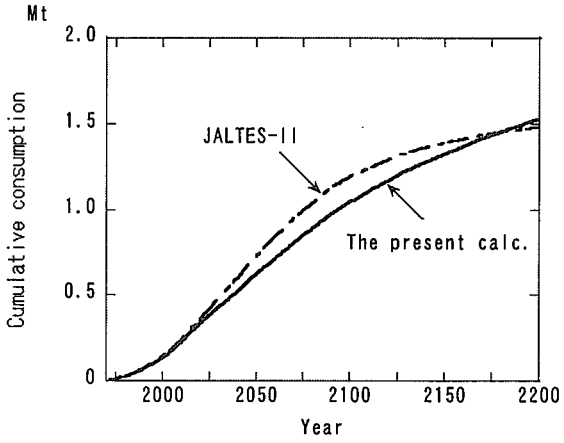

Fig. 3.7.1 Comparison of calculation results for low inventory type RMWR between the present program and JALTES-II

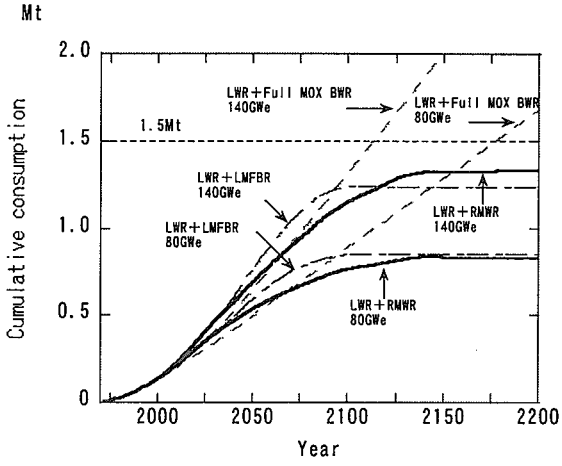

Fig. 3.7.2 Natural uranium cumulative consumption for high and low nuclear power demand with full MOX BWR, RMWR and LMFBR

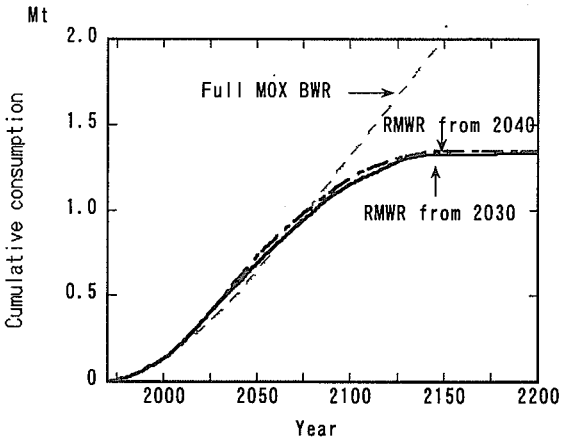

Fig. 3.7.3 Effects of introduction timing of high conversion ratio RMWR on natural uranium cumulative consumption

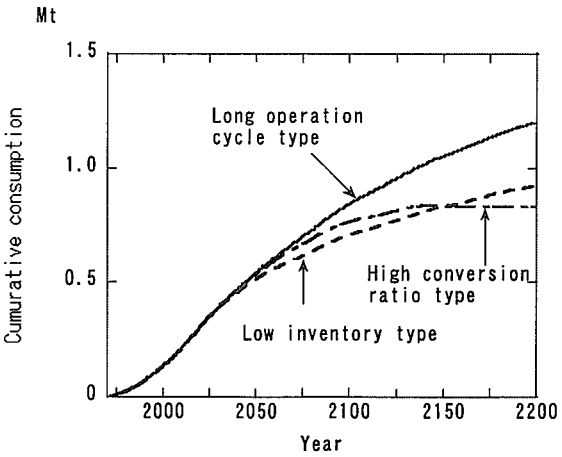

Fig. 3.7.4 Effects of RMWR core characteristics on natural uranium cumulative consumption

3.8 SUS Cladding Expansion Phenomena under LOCA Condition for PWR-Type RMWR

S.Usui, T.Iwamura and T.Okubo
(*E-mail:*iwamura@hems.jaeri.go.jp)

The Reduced-Moderation Water Reactor (RMWR) adopts triangular tight lattice fuel assemblies with the fuel rod gap width ranging from 1.0 mm to 1.3 mm in order to reduce the moderation of neutrons. For some RMWR design concepts, stainless steel (SUS) is used for the fuel cladding material because the cladding thickness can be reduced due to its high strength and therefore the effective fuel to moderator volume ratio can be increased, resulting in higher conversion ratio. Especially for PWR-type RMWR designs[1], the possibility of flow blockage caused by high temperature creep under loss-of-coolant accident (LOCA) condition should be taken into account because of the small gap width between fuel rods. Photo.3.8.1 shows the mock-up of fuel assembly of the PWR-type RMWR. In the present study, the expansion behavior of SUS cladding under high temperature environment has been investigated to determine the cladding thickness and length of fuel rod plenum for preserving the intact geometry for core cooling during the PWR-LOCA condition.

As shown in Fig.3.8.1, the LOCA analysis[2] using the REFLA/TRAC code[3] for the PWR-type RMWR indicates that the peak cladding temperature is around 980 ℃, which is lower than the current safety limit for LWRs of 1200 ℃, by injecting emergency core cooling (ECC) water into the upper plenum and the cold leg simultaneously.

The cladding expansion behavior due to high temperature creep was analyzed by using the finite-element non-linear structure analysis code FINAS[4]. In the analysis, the cladding temperature was assumed to be hold at 950, 1000, 1100 and 1200 ℃ during the whole period as shown in Fig.3.8.1. Considering the symmetric geometry, the 1/12 sector of fuel rod cladding was modeled as shown in Fig.3.8.2.

The analysis was performed for the tight lattice fuel assembly with the cladding outer diameter of 9.5 mm and the gap width between fuel rods of 1.0mm. The cladding thickness for a reference case is 0.38 mm, corresponding to the thickness to outer diameter ratio (t/d) of 0.004. For parametric study, the cladding thickness was changed to 0.475 mm (t/d: 0.05). The material of cladding is Austenitic stainless steel, which has been used for fast breeder reactors for many years. The inner pressure of fuel rod was assumed to be 3MPa, 6MPa and 9MPa, corresponding to the plenum length of 600mm, 300mm and 200mm, respectively.

Figure 3.8.3 shows the effects of inner pressure and cladding thickness on the transient of flow blockage ratio. In this case, the cladding temperature was assumed to be kept at

1000 ℃. When adjacent fuel rods contact with each other, the flow blockage ratio becomes 62.8 % for the present fuel assembly design. As shown in this figure, the adjacent rods contact within 100 sec irrespective of the t/d when the inner pressure is higher than 6MPa. On the other hand, when the inner pressure is as low as 3MPa, the flow blockage ratio remains below 40 % up to 500 sec even for the thinner cladding thickness case (t/d:0.04). Based on the analysis results, the plenum length was determined to be 600 mm to avoid contact of fuel rods during the LOCA condition. The cladding thickness was determined to be 0.38 mm because the thinner cladding is preferable from the reactor physics point of view if satisfying the criteria of material strength.

The effects of cladding temperature on cladding expansion behavior are shown in Fig.3.8.4. In this comparison, the inner pressure and t/d were set to be 3MPa and 0.04, respectively, as determined previously. As shown in this figure, the flow blockage ratio remains less than 40 % up to 500 sec for the cladding temperatures below 1000 ℃, while it exceeds 62.8 % at 30 sec and 6 sec in the cases for the cladding temperatures of 1100 ℃ and 1200 ℃, respectively. It should be noted from Fig.3.8.1 that the peak cladding temperature during the reflood phase of LOCA is slightly less than 1000 ℃ and the keeping time at high temperature is far less than 500 sec. Therefore, it is suggested that the core cooling capability is maintained during the whole LOCA sequence for the present fuel rod design with the plenum length of 600 mm and the SUS cladding thickness of 0.38 mm.

References

1) Hibi, K., et al.: "Conceptual Designing of Reduced-Moderation Water Reactors (2) - Design for PWR-Type Reactors-", ICONE-8523, Baltimore (2000).
2) Ohnuki, A., Okubo, T. and Akimoto, H.: "A Feasibility Study on Core Cooling of Pressurized Heavy Water Moderated Reactor with Tight Lattice Core", ICONE-7026, Tokyo (1999).
3) Akimoto, H., Ohnuki, A., Abe, A. and Murao, M., "Assessment of REFLA/TRAC Code for Various Postulated Accidents in PWR", Fifth Int. Topical Meeting on Reactor Thermal Hydraulics (NURETH-5), Salt Lake City, Vol. VI, 1797 (1992).
4) Power Reactor and Nuclear Fuel Development Corporation, "Universal Non-linear Structure Analysis Code FINAS Vr.13.0" (1995). [in Japanese]

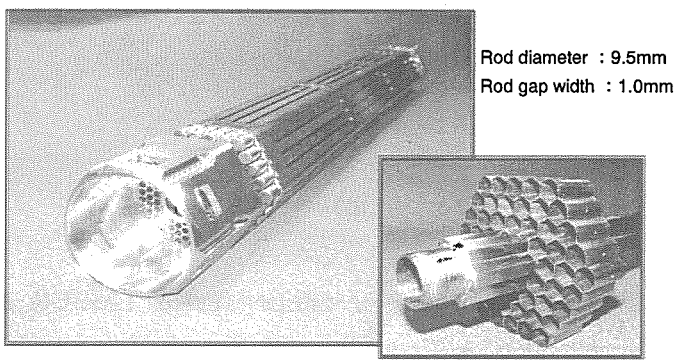

Photo 3.8.1 Mock-up of fuel assembly for PWR-type RMWR

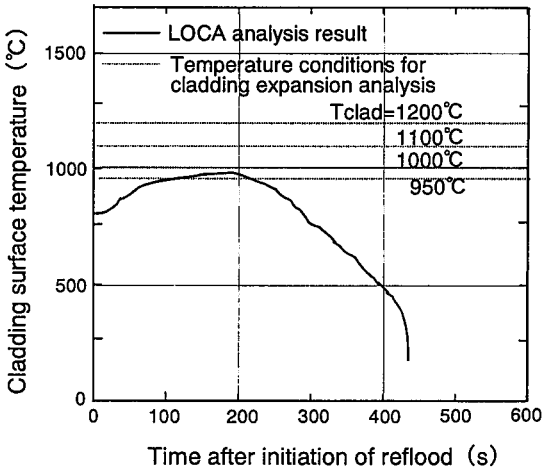

Fig.3.8.1 Cladding temperature behavior during LOCA and temperature conditions for cladding expansion analysis

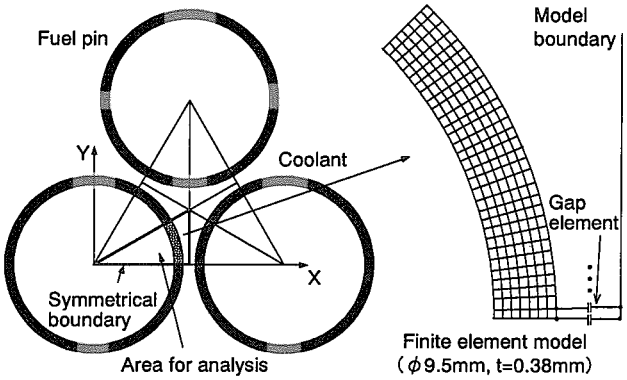

Fig.3.8.2 Calculation geometry

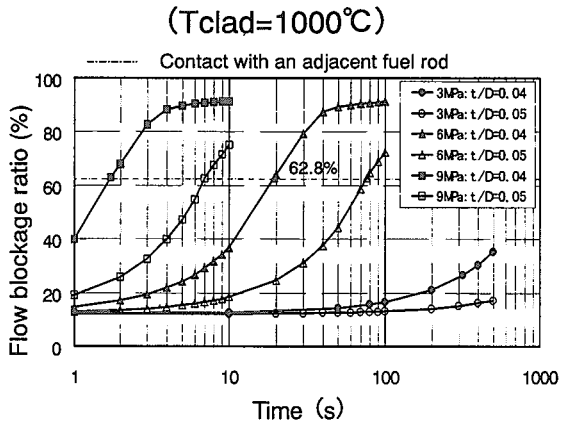

Fig.3.8.3 Effects of fuel rod inner pressure and cladding thickness to diameter ratio (t/d) on cladding expansion behavior

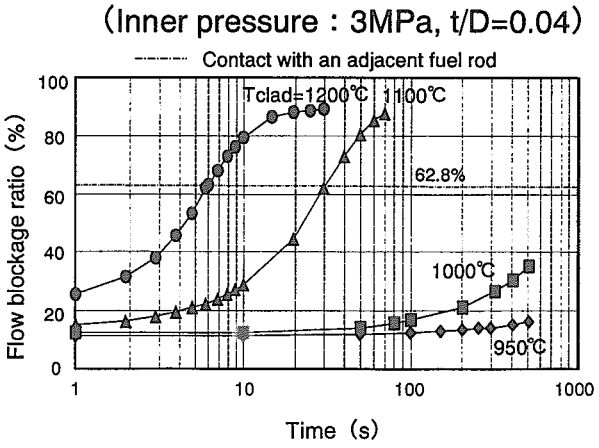

Fig.3.8.4 Effects of cladding temperature on cladding expansion behavior

3.9 Fuel Cycle System with Nitride Fuel and Pyrochemical Reprocessing for Transmutation

T. Osugi, M. Andoh and H. Takano
(*E-mail:* osugi@omega.tokai.jaeri.go.jp)

A fuel cycle system coupled with a nitride fueled LMFBR and a pyrochemical reprocessing has been investigated at Japan Atomic Energy Research Institute in order to establish a confinement / transmutation system for long-lived radioactive nuclides. [1), 2)] The pyrochemical reprocessing of nitride spent fuel is adopted for new fuel cycle systems to lower the fuel cycle cost. The main process of this fuel cycle consists of the following steps; disassembling of the nitride spent fuel, fuel element shearing, electrorefining, cathode processing, nitridation of recovered fuel metal and fabrication of nitride fuel assembly.

Core performance of the nitride fueled fast reactor was examined with parameters of bonding materials such as He or Na, and N-15 enrichment. The cost of N-15 enrichment and the possibility of recovering C-14 in the pyrochemical reprocessing were also discussed. Gaseous N-15 can be separated from argon purge gas of electrorefining cell to be recycled to nitridation process. Table 3.9.1 shows main design and performance parameters for fast reactors examined. Coolant temperatures of inlet and outlet are 380°C and 550°C, respectively.

The effect of the N-15 enrichment (100% N-14 or 100% N-15) on the nuclear performance is summarized;

* Smaller fissile inventory is required for the N-15 core than that of N-14 core by 7%.
* Excellent breeding performance is obtained for the N-15 core, and burn-up reactivity loss decreases, less than the half of that of the N-14 core.
* Larger negative Doppler coefficient and smaller positive coolant temperature coefficient (sodium void reactivity worth) are obtained for the N-14 core.

These differences in nuclear performance come from the big difference in the (n,p) reaction cross section between N-14 and N-15 in higher energy region. There may be troublesome problem of C-14 production due to the large (n,p) reaction for the N-14 core.

Takano et al. [3)] estimated the toxicity of C-14, and concluded that the problem of C-14 is not radiotoxicity but capability of recovering C-14 in reprocessing system. The recovery of C-14 is easier by pyrochemical processing in which almost of C-14 are kept in salt by chemical reactions with Zr and Mo in FP. [4)] The cost of N-15 enrichment is estimated at present as very high price of 100,000 yen/g. In order to keep the cost effect less than 10% of fuel cycle cost, the enrichment cost of N-15 should be below 4000 yen/g. These expensive gaseous N-15 can be separated from argon purge gas of electrorefining cell and be recycled to nitridation process in the case of pyrochemical reprocessing.

Table 3.9.1 Main design and performance parameters for 1300MWe fast reactor

	MOX Core	MN(He-bond) Core		MN(Na-bond) Core	
Fuel pin diameter (mm)	8.5	8.5		8.5	
Can thickness (mm)	0.48	0.48		0.48	
Gap width (mm)	0.09	0.09		0.31	
Smear density (%TD)	84	80		80	
Core height (mm)	930	800		800	
Average linear rating (W/cm)	280	330		440	
		(N-15)	(N-14)	(N-15)	(N-14)
Cycle length (Month)	13	13	13	13	13
Number of batch	5	5	5	4	4
Average burn up (GWd/t)	150	130	130	145	145
Puf enrichment (in/out)	17/19	11/15	14/16	12/17	15/20
Puf inventory (ton)	5.24	5.14	5.50	3.90	4.19
Puf generation (ton/cycle) (Puf breeding)	0.20 (1.18)	0.34 (1.33)	0.19 (1.17)	0.24 (1.24)	0.09 (1.09)
Burn up reactivity loss (%Δk/k/cycle)	3.31	0.56	2.28	1.72	3.84
Doppler coefficient* (10^{-3}T. Δk/ΔT)	-4.96	-4.69	-5.46	-4.60	-5.39
Coolant temperature coefficient (10^{-6} Δk/k/℃)	6.85	6.66	5.42	6.78	5.34
Radial expansion coefficient (10^{-6} Δk/k/℃)	-6.55	-6.95	-6.98	-7.19	-7.35

* MOX Core : 1600℃→2200℃, MN Core : 1000℃→1600℃

The transient analysis in the unprotected loss of flow (ULOF) accidents was made for each core using reactivity coefficients shown in Table 3.9.1. These cores are not optimum in point of reactivity effects, therefore, additional negative feedback equal to radial expansion effect is assumed for each core in these analyses. The variation of the coolant temperature is shown in Fig.3.9.1 as a function of time during transients. Here again, the nitride cores show good dynamic performance without sodium boiling.

We still have the various problems or unknown factors such as irradiation performance of nitride fuel, C-14 toxicity, higher cost of N-15 enrichment et al., however, the nitride core shows good core performances under normal operation and accidental condition. The pyrochemical

process can be adapted to reprocessing the nitride spent fuel of transmutor ; a new process, however, is needed to remove the actinides more efficiently from fission products in the salt.

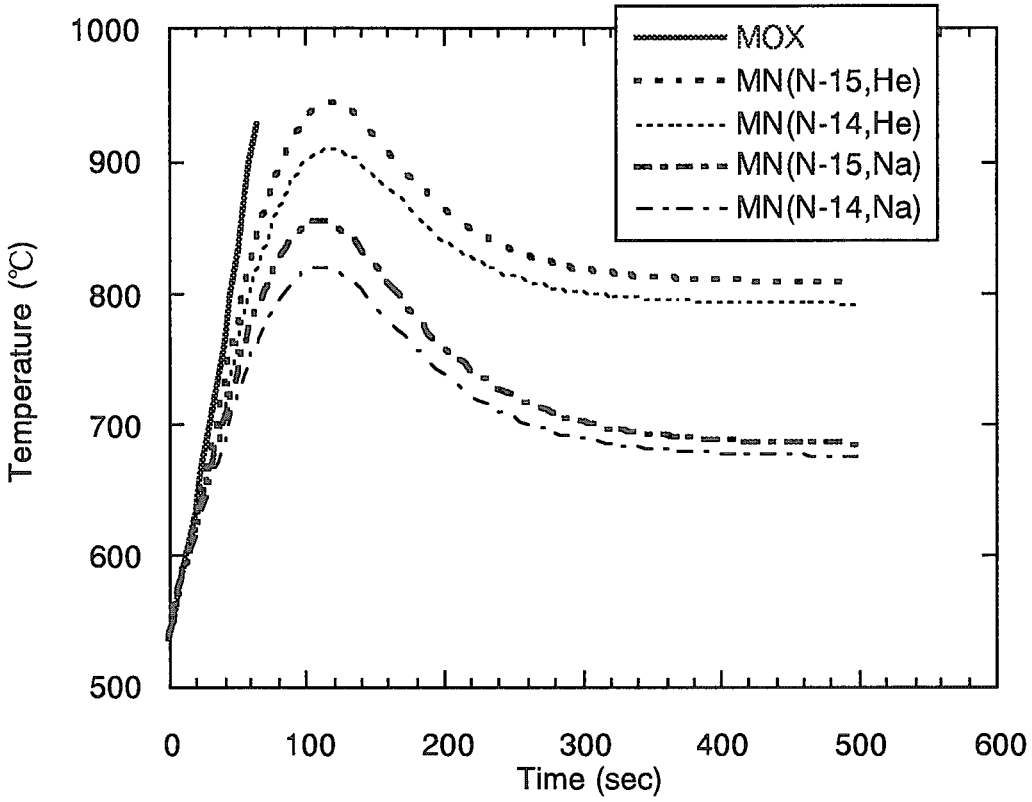

Fig.3.9.1 Coolant temperature profile at unprotected loss of flow accidents (Pump coastdown time : 20sec)

References:

1) Takano, H., Akie, H., Handa, M. et al.: " A Concept of Self-Completed Fuel Cycle Based on Nitride Fuel Lead-Cooled Fast Reactor," Proc. Seventh International Conf. on Emerging Nuclear Energy Systems, ICENES'93, p.308, World Scientific Press (1993).

2) Osugi, T., Takano, H., Ogawa, T., et al. : " A Conceptual Design Study of Self-Completed Fuel Cycle System", Proc. International Conf. on Evaluation of Emerging Nuclear Cycle Systems, Global'95, Sept. 11-14, Versailles, France, 1995, Vol.1, p.181 (1995).

3) Takano, H. and Osugi, T.: " A Concept of Nitride Fuel Actinide Recycle System Based on Pyrochemical Reprocessing," presented to Japan-Russian Seminar on Fast Breeder Reactor, 11-15 Dec. 1995, Oarai, Japan(1995).

4) Osugi, T., Andoh, M., Takano, H., Ogawa, T. and Kobayashi, T.: "Fuel Cycle Systems with Nitride Fuel for Transmutation", Proc. Workshop on Advanced Reactors with Innovative Fuels, 21-23 October 1988, Villingen, Switzerland, p333-341, OECD/NEA (1999).

3.10 Transient Analysis of High Burn-up Full MOX PWR

N. Ishikawa, F. Araya and T. Iwamura

(*E-mail:* ishikawa@clsu3a0.tokai.jaeri.go.jp)

As one of the options for future light water reactors aiming to achieve high burn-up and long cycle operation, conceptual design was performed for full MOX PWR cores with discharged burn-up of 60GWd/t and 100GWd/t [1]. Based on specification of the designed 60GWd/t core, the primary coolant and safety systems have been designed and adequacy of the systems was confirmed through transient analysis [2]. In this study, a transient analysis of the system for the 100GWd/t core was performed to confirm the feasibility of the system. Transient analysis for four representative events, namely, control rod cluster ejection accident (CREA), loss of flow accident (LOFA), loss of coolant accident (LOCA) and loss of heatsink accident (LOHS) was preformed.

Although the 60GWd/t and 100GWd/t cores are same in size, the characteristics of the nuclear dynamics and power peaking factors are different as shown in Table 3.10.1 due to the difference of fissile plutonium enrichment in both cores. This difference of nuclear dynamics and power peaking factor leads to severer results of neutronic and thermal transients for the 100GWd/t core. Absolute values of Doppler coefficient and moderator void coefficient of the 100GWd/t core are smaller than those of the 60GWd/t core, which implies a reduction of inherent ability of power suppression in the case of abnormal transients. The power peaking factor of the 100GWd/t core is about 10% larger than that of the 60GWd/t core, which causes a degradation of departure from nucleate boiling ratio (DNBR) in the LOFA event.

The transient analysis was performed by the system analysis code RETRAN-02 [3] and DNBR was evaluated by utilizing the subchannel analysis code COBRA-IV-I [4] and the EPRI critical heat flux correlation [5]. Figure 3.10.1 shows a reactor power response for the CREA event, in which case the reactivity of 1.2 $ was inserted. Although the reactor is scrammed by high power (118% of rated power) trip signal, the power is suppressed by the Doppler effect. This result reveals that the peak power for the 100GWd/t core is 1.3 times greater than that for the 60GWd/t core. The values of adiabatic enthalpy rise of the fuel for 60GWd/t and 100GWd/t cores are 74.5[kJ/kg] and 77.4[kJ/kg], respectively, which are

considered to be sufficiently low for fuel integrity.

Figure 3.10.2 shows the analysis result of LOFA event (i.e., all pumps are tripped). The moment of inertia of the pump was increased to 513.2[kg·m] which is one and half times larger than the previous design so as to maintain the value of DNBR being greater than 1.3. The minimum value of DNBR is evaluated to be 1.33.

The result of large break LOCA analysis is depicted in Fig.3.10.3. The break area is ranging from 10% to 100% of the cold leg flow area. The maximum value of peak clad temperature (PCT) of 920℃ is attained in the case of 30% LOCA. The PCT is sufficiently lower than the allowable limit of 1200℃. The mass flow rate of accumulator is depicted in Fig.3.10.4, which indicates that the coolant injection from accumulator is successfully functioned in this event.

Also in the LOHS event, it is shown that the heat generated in the core is removed from the primary coolant system with the residual heat removal system without any safety problem. From the results derived in this study, it is concluded that the high burn-up full MOX PWR system for the 100GWd/t core is feasible from the safety analysis points of view with changing the moment of inertia of the pump from the 60GWd/t design.

References

1) Kugo, T., et al.: "Study on Nuclear Physics of High Burn-up Full MOX PWR Core", JAERI-Research 98-059 (1998) [in Japanese].
2) Araya, F., et al.: "Study on Concept for Future Light Water Reactor (18) - Transient Analyses of High Burn-up Full MOX PWR-, 1999 Annual Mtg. Atomic Engy. Sco. Jpn., F41 (1999) [in Japanese].
3) McFadden, J.H, et al.: "RETRAN-02: A Program for Transient Thermal-Hydraulic Analysis of Complex Fluid Flow System", NP-1850-CCM, Electric Power Research Institute (1984).
4) Wheeler, C.L, et al.: "COBRA-IV-I: An interim version of COBRA for thermal-hydraulic analysis of rod bundle nuclear fuel elements and cores", BNWL-1962 (1976).
5) Reddy, D. and Fighetti, C.: "Parametric Study of CHF Data Vol. 2 -A Generalized Subchannel CHF Correlation for PWR and BWR Fuel Assemblies", NP-2609, Electric Power Research Institute (1983).

Table 3.10.1 Comparison of major difference between 60 and 100GWd/t cores.

Parameter \ Discharged Burn-up	60GWd/t	100GWd/t
Power peaking factor (Fxy , Fxy*Fz)	(1.33 , 1.69)	(1.45, 1.94)
Doppler coefficient (10^{-4} Δk/k/℃)	-2.7	-2.5
Density reactivity coefficient (10^{-4} Δk/k /%void) 0~10/ 0~40/ 0~90 %void	-99/ -147/ -240	-43/ -58/ -22

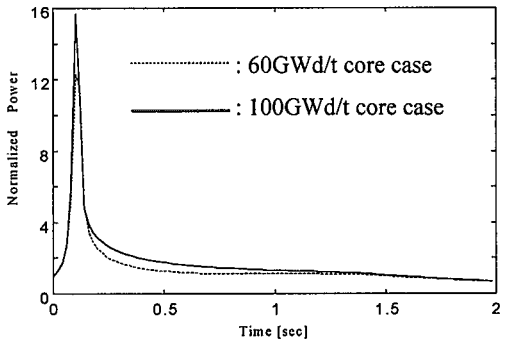

Fig. 3.10.1 Analysis result of control rod cluster ejection accident

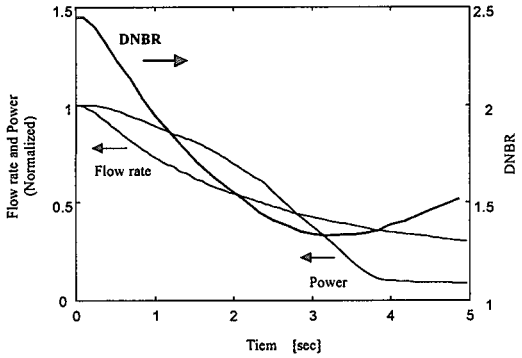

Fig. 3.10.2 Analysis result of loss of flow accident

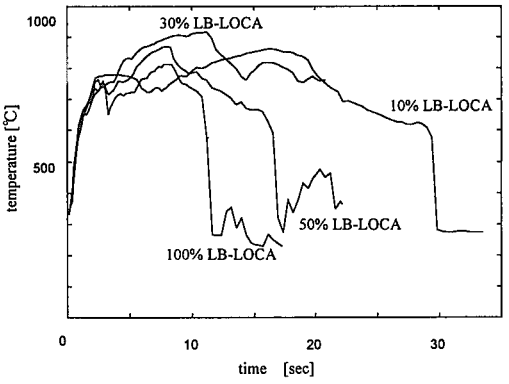

Fig. 3.10.3 Analysis result of loss of coolant accident (maximum PCT)

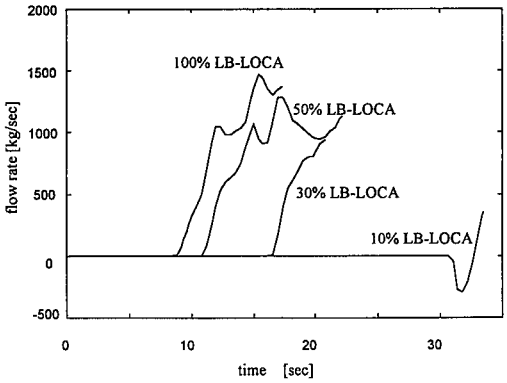

Fig. 3.10.4 Analysis result of loss of coolant accident (ACC flow rate)

3.11 Development of New Reactor Instrumentation System Using Optical Techniques -Irradiation Effects on Fiber Bragg Grating Sensors -

T. Kakuta, H. Yamagishi, T. Iwamura, and M. Urakami*
(*E-mail*:kakuta@stsp2a0.tokai.jaeri.go.jp)

A fiber bragg grating (FBG) is a kind of an optical band pass filter, and a passing wavelength will change, according to a mechanical distortion of a grating by stresses and/or temperature changes (see Fig.3.11.1). It can be used for a stress-strain monitor and for a temperature monitor in nuclear instrumentation systems. However, optical fibers are vulnerable to radiation damage in general, and especially bragg grating structures will be damaged easily by radiation. Attempts to develop radiation resistant optical fibers are showing that fused-silica core optical fibers have good radiation resistance in a wavelength range of 800-1800nm[1]. Thus, FBG sensors, working wavelength at 1550nm, were developed and their irradiation effects were examined in a Cobalt-60 gamma-ray irradiation facility and in a Japan Materials Testing Reactor (JMTR).

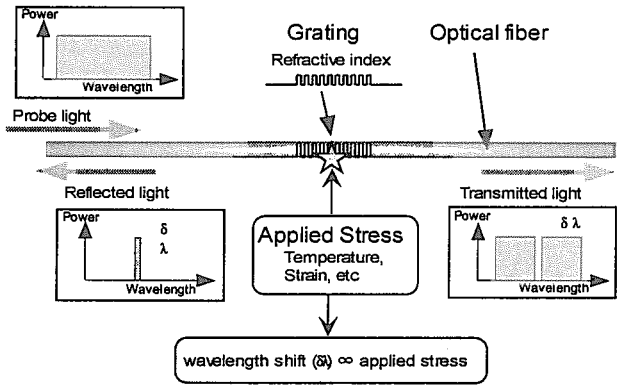

Fig. 3.11.1 Principle of fiber bragg grating sensor

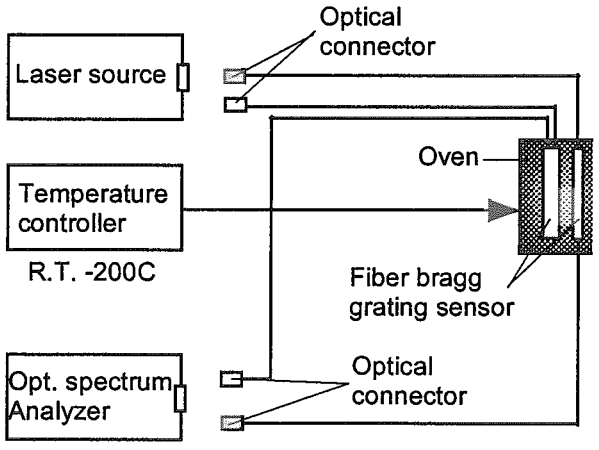

Fig. 3.11.2 Experimental setup for measuring the Reflection and transmission type FBGs

Two types of FBG sensors, a reflection and a transmition type, were tested. An experimental setup is schematically shown in Fig.3.11.2. FBG sensors were heated in an electric oven. Both wavelength of reflect and transmit light from FBG sensors were monitored by an optical

* The Japan Atomic Power Company

spectrum analyzer during irradiation. A light source was a wide-band laser of 1550±20nm.

A gamma-ray irradiation was carried out up to an ionization dose of 1.5 x 10^6Gy, with a dose rate of a few Gy/s. In the JMTR irradiation, a total ionization dose was in the range of 10^9Gy and a total fast neutron fluence(E>1MeV) was in the range of 10^{24}n/m^2 with an ionization dose rate of a few kGy/s and a neutron flux of about 10^{17}n/m^{2}s, at about 600K.

Both FBG sensors showed good radiation resistance under a gamma-ray irradiation. Figure 3.11.3 shows a passing wavelength of a reflection type FBG sensor as a function of a temperature. An irradiation up to 1.5x10^6Gy did not affect a temperature dependence of a reflected wavelength. Similar results were obtained on transmission type FBG sensor. The results indicate that FBGs could survive a gamma-ray dose of 1.5x10^6Gy at temperatures up to 670K. Thus, FBGs could be used in primary systems in nuclear power reactor, in a periphery of reactor core regions where a neutron flux is marginal. There, a total gamma ray dose of life span will be range of a 10^6Gy and FBGs will survive for a operating span of power reactor.

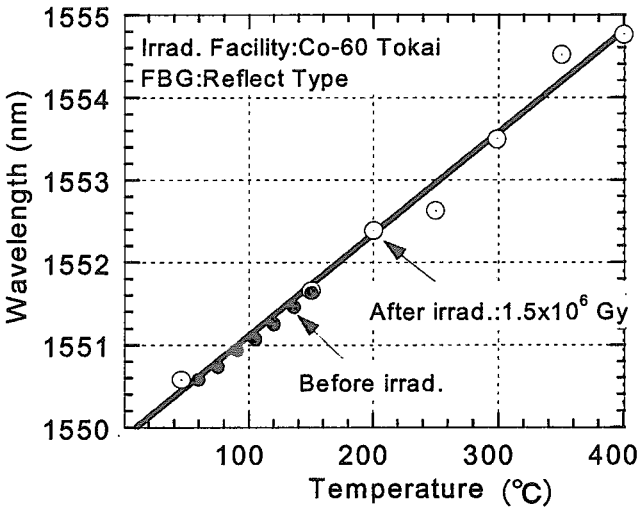

Fig. 3.11.3 Passing wavelength as a function of a temperature, in a refrection type FBGsensor

In the meantime, optical signals could be detected up to a fast neutron fluence of 10^{24}n/m^2, but a substantial drift of a passing wavelength was observed. Also, intensity of optical signals decreased substantially in the course of a reactor irradiation. As optical transmission loss in a fused silica core optical fibers are small in this wavelength up to the present neutron fluence, structural modifications of a Bragg grating will be responsible for these degradation phenomena. Further improvements of radiation resistance of FBG sensors are needed for application to reactor core region.

Reference

1) Kakuta, T., et al. : "Behavior of optical fibers under heavy irradiation", Fusion Engineering and Design, 41, 201-205 (1998).

3.12 Nuclear Power Plant Monitoring with the Combination of Recurrent Neural Network and Real-time Expert System

K. Nabeshima, T. Suzudo, T. Ohno*, and K. Kudo*
(*E-mail:* nabe@clsu3a0.tokai.jaeri.go.jp)

One of the goals of nuclear power plant (NPP) monitoring is to identify the current state of the operational plant using observed signals in real-time. Especially, it is critical to find the symptoms of small anomalies earlier than the conventional alarm system, to diagnose the cause of failures, and to give optimal advice to the operators before the anomalies develop to significant accidents.

In this study, we have developed the hybrid monitoring system for nuclear power plant utilizing recurrent neural network (RNN) and rule-based real-time expert system. The integration of them is expected to enhance the functionality of each part as an operator support. The whole monitoring system including data acquisition part and the advisory displays has been tested by the simulation codes for a high temperature gas cooling reactor (HTGR) dynamics and an on-line simulator of PWR. These are connected in series through local area network (LAN), as shown in Fig. 3.12.1.

The data acquisition controller is a software module embedded in a personal computer (PC), and can set the parameters of the data acquisition, such as the source of data, total number of signal channels, and sampling period. The controller treats the digital signals calculated by simulation code on another computer or sensory analog signals from NPPs (PWR plant simulator in this case). In case of analog data source, at most 87 analog signals are digitized at the AD conversion board inserted in the PC which is connected to the PWR simulator. The digitized data is sent to the host computer of the monitoring system every second through LAN.

Amongst various types of neural network we selected the RNN for plant modeling because of the high capability of modeling for dynamic behavior. The RNN is trained by the current and past system inputs and outputs, so that it can predict the outputs at the next time step of the system. This one-step-ahead prediction can be effectively implemented by RNN,

* Graduate School of Engineering, Kyushu University

and applied to dynamic tracking. The basic principle of the anomaly detection is to monitor the deviation between process signals measured from the actual plant and the corresponding values predicted by the plant model, i.e., the RNN. In different reactor operation mode, different RNN is used; this selection is automatically done by the expert system.

The expert system is used as a decision agent which works on the information space of both the RNN and the human operators. The information of other sensory signals is also fed to the expert system, together with the outputs which the RNN generates from the real-time plant signals. A major advantage of expert system is to process a lot of operator's knowledge and to derive useful information for complex decision environments. The expert systems can treat almost all known correlation between plant status patterns and operation modes as a priori set of rules. Especially, the real-time expert system can treat the information of time in the rules.

The graphical advisory displays are programmed by Java language and the monitoring results can be displayed on any computers connected to the computer network. Java is useful also to construct user-friendly man-machine interface. Figure 3.12.2 shows the main display of this monitoring system. In this display, the schematic plant figures are shown with some important signals, the trend graph of the reactor outlet temperature signal and the messages from the expert system. The error messages and the diagnostic results are popped up on the screen when the monitoring system detects anomalies. The table of all measured signals and the trend graphs are also displayed on different pages.

Using the simulation code and the simulator, many kinds of malfunctions caused by equipment failure during steady state and transient operations were simulated here. Those malfunctions are much lighter than the usual accident cases. From the off-line test results using the codes, it was shown that the monitoring system with the RNN successfully detected the symptoms of anomalies in the early stage. The rule-based real-time expert system also worked satisfactorily in diagnosing and displaying the system status by using the outputs of the RNN and a priori knowledge base. The future direction of this study will be the on-site test of the monitoring system at the actual plants.

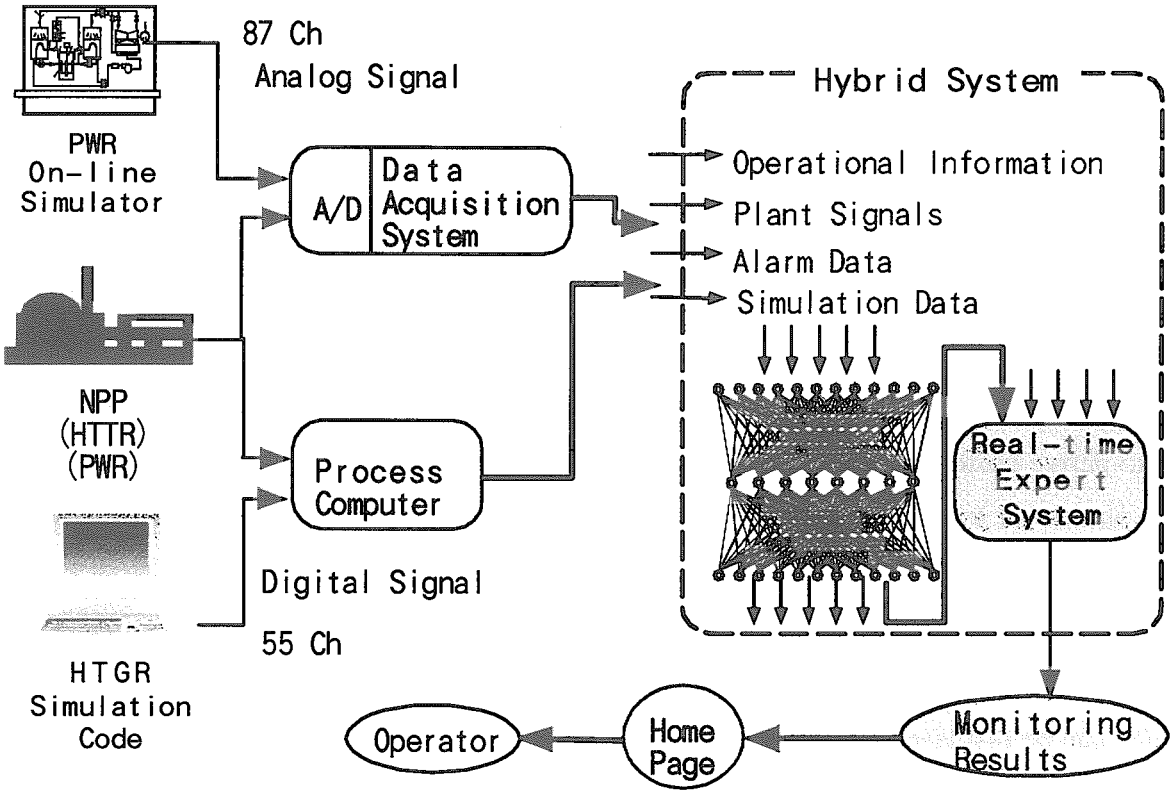

Fig. 3.12.1 Monitoring system overview

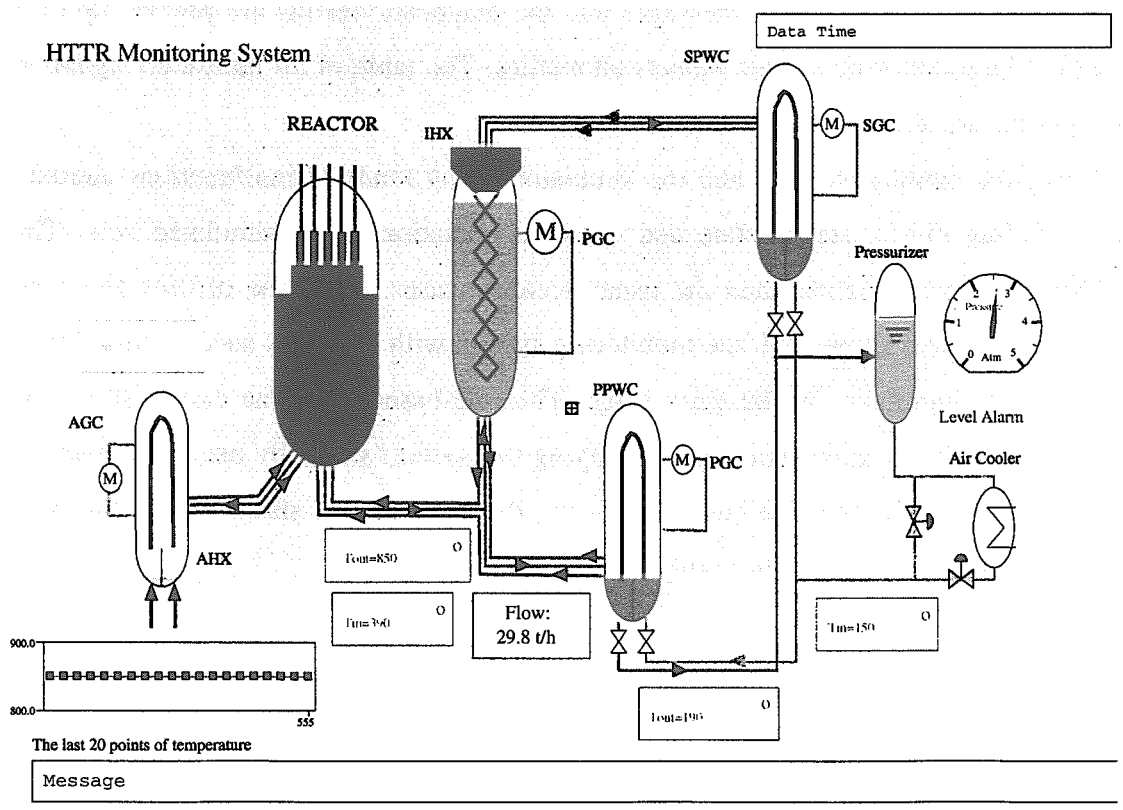

Fig. 3.12.2 Main advisory display

4. Thermal and Fluid Engineering

In Fy 1999, design studies were widely performed to check the feasibility of the proposed concept of reduced moderation water reactors (RMWRs) under normal operation and several abnormal events. Through the analytical evaluation with three dimensional thermal-hydraulic analysis codes, the feasibility was confirmed for the proposed four RMWRs, or high conversion ratio BWR type core, long operation cycle BWR type core, BWR type core without blanket, and high conversion ratio heavy water cooled PWR type core.

A critical heat flux (CHF) experiment was performed using the tight-lattice fuel assemblies including seven heater rods arranged in the triangular array with 1.0 or 1.5 mm rod gap size in order to validate the CHF correlation used in the design study of the PWR type core. The test results showed that the CHF correlation predicts the conservative CHF for the tight-lattice core. To validate the TRAC code for the reflood under combined injection condition, an assessment study was performed using data from the slab core test facility. A multidimensional two-phase flow analysis code, named ACE-3D, was applied to the analysis of steam-blanket effect in passive containment cooling system (PCCS) with horizontal heat exchanger. Coupling of TRAC codes with three-dimensional neutronics code was also continued as a cooperative work with the reactor physics research group.

A series of experiments on thermal-hydraulic safety in a fusion reactor was performed to get validation data for safety analysis codes of fusion reactors as one of International Thermonuclear Experimental Reactors (ITER) subtasks. In Fy 1999, construction of a new test facility for the simulation of the ingress of coolant event (ICE) in the ITER was completed. Numerical simulation study was also performed to support the design of the facility using the TRAC code focusing on the parameter effect on the pressure transient during the ICE. A new code was developed to evaluate the dust transport phenomena during the loss of vacuum accident (LOVA) in the ITER and assessed using the test data of the preliminary LOVA experiments.

A model experiment of critical heat flux was also performed to understand the burnout under subcooled conditions with extremely high heat flux. A measuring technique of void fraction changes in a subcooled flow was developed using the thermal neutron radiography.

4.1 Thermal-Hydraulic Feasibility Study for BWR-Type Reduced Moderation Water Reactor

F. Araya, M. Kureta and H. Akimoto

(*E-mail:* araya@jpsrews1.tokai.jaeri.go.jp)

The feasibility of BWR-type reduced moderation water reactors (RMWRs) have been studied in view points of the thermal-hydraulics. Three BWR-type RMWR cores have been proposed by the nuclear design studies[1]. All of these have extremely tight lattice cores for high conversion ratio by reducing moderation of neutron energy. Therefore, the evaluation of therma-hydraulic feasibility is important. In the present study, the feasibility evaluations were performed with the thermal-hydraulic transient analysis code TRAC-BF1[2] introducing the Biasi CHF correlation modified by Arai et al.[3] for tight lattice fuel bundle. In the evaluation for each concept, the feasibility in the steady-state nominal operating condition and flow reduction transients were evaluated. Namely, an occurrence of the boiling transition (BT) and the maximum cladding temperature were focused in the analyses.

The first design concept of the core named " simple core without blanket" aims at square lattice core based on the current ABWR fuel assembly without blanket. The core consists of 9x9square lattice fuel assemblies with large rod diameter of 15.2mm and the gap width of 1.0mm between fuel rods. There are two versions of the concept. One is a high conversion ratio type core and the other is a high power type. A single channel model was used for each version, which simulated single fuel assembly having highest bundle power. The minimum critical power ratios (MCPRs) were determined by searching the channel power input so that the BT would occur under the nominal core inlet flow condition. The calculated results for steady-state showed that the MCPRs were 1.46 for the high conversion ratio type and 1.38 for the high power type, respectively. As for the transient calculations, the time histories of core inlet flow, core pressure and core power were assumed based on the

results of safety analysis of the all recirculation pump trip accident in ABWR. The calculated results are shown in Fig. 4.1.1 for the high conversion type, showing no BT occurrence. On the other hand, BT is calculated to occur in the high power version as shown in Fig.4.1.2. This is caused by the assumption of the high power at the top of the active fuel region. The maximum cladding temperature is, however, very low comparing to the safety limit.

The second concept named " high burn-up and long cycle core" aims at the high burn-up around 60 GWd/t and long operation cycle length about 2 years which are tentatively set target. The core consists of 252 hexagonal fuel assemblies and 61 void tube assemblies. The fuel assembly consists of 469 fuel rod with diameter of 11.9 mm and gap width of 1.3 mm between rods. The void tube assembly is a new device to realize negative void reactivity coefficient by neutron streaming through the void tube assembly. In order to evaluate the feasibility, the 252 fuel assemblies in the core were lumped into 10 channels and 61 void tube assemblies into one channel by TRAC-BF1. The steady-state operating condition was achieved for the nominal condition in the calculation by adjusting the inlet pressure loss coefficient of each channel so that the void fraction distribution at the core exit becomes flat. As the results, the average channel exit void fraction was set at about 90%. The BT was not experienced in all channels. As for the transient condition, the same transient was analyzed using the samen assumptions as the first concept. The calculated results show that the BT is not occur in the transient as shown in Fig. 4.1.3.

The last concept named " high conversion ratio core" aims at as high conversion ratio as possible. Although the several version of the concept have been studied, a version which has a relatively low core power output was focused here. The core consists of 720 hexagonal fuel assemblies which contain 169 fuel rods with diameter of 14.5 mm and gap width of 1.3 mm between fuel rods. In order to evaluate the feasibility of this core concept, a 25 channel model was developed. The boundary conditions were set based on the ongoing design study of the plant coolant system. The steady-state nominal operating condition was achieved by adjusting the pressure loss coefficients at the core inlet so that the flow

distribution became flat. No boiling transition was appeared in the core. As for the transient condition, one pump trip and all three pumps trip transients were analyzed. The calculated results of the former case showed no boiling transition would occur during the event. For the latter case, though the boiling transition was calculated to occur, the maximum cladding temperature was evaluated to be low enough than the safety limit, as shown in Fig. 4.1.4.

As described above, the calculated results showed that all concepts could be feasible.

References

1) Iwamura, T., et al., JAERI-Research 99-058 (1999)[in Japanese].

2) Giles, M.M., et al., NUREG/CR-4356, EGG-2626 (1992).

3) Arai, K., et al., IAEA-TECDOC-638.332,139-147 (1992).

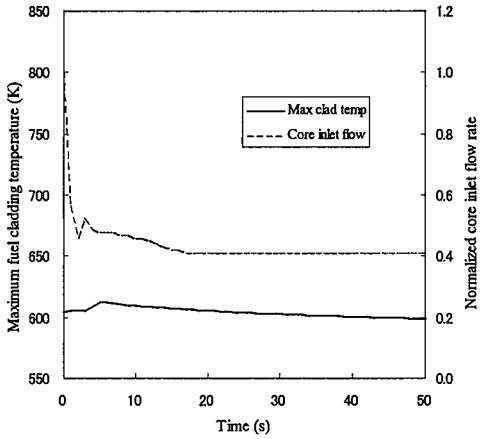

Fig. 4.1.1 Maximum fuel cladding temperature for high conversion version

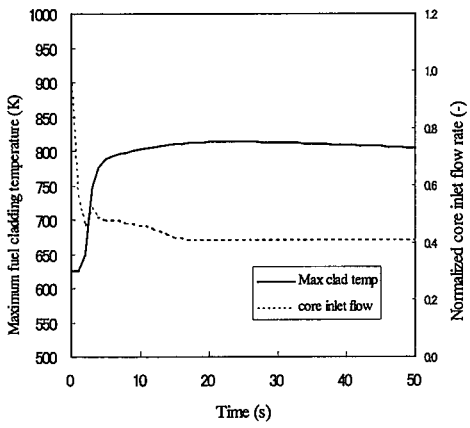

Fig. 4.1.2 Maximum fuel cladding temperature in high power version

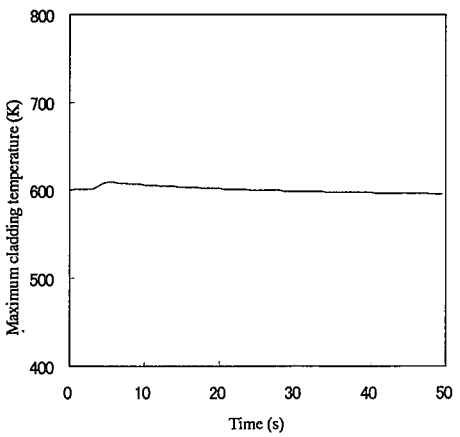

Fig. 4.1.3 Calculated cladding temperature of flow reduction accident

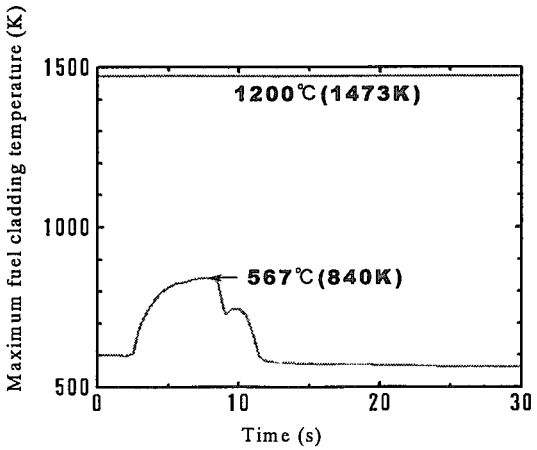

Fig. 4.1.4 Calculated maximum fuel cladding temperature

4.2 CHF Experiments and Subchannel Analysis for Reduced Moderation Water Reactor

F. Araya, T. Yoritsune, T. Nakatsuka, T. Okubo, H. Watanabe, T. Satoh
and H. Akimoto
(*E-mail:* araya@jpsrews1.tokai.jaeri.go.jp)

The critical heat flux (CHF) experiments were performed to construct a data base for an evaluation of the thermal margin of the reduced moderation water reactor (RMWR) core which consisted of highly tight-lattice fuel assemblies with gap widths around 1.0 mm. The experiments have been completed on the gap widths between heater rods, 1.5 and 1.0 mm under PWR thermal-hydraulic conditions. Since the experiments on the gap width of 0.6 mm are on going, the data presented here are in a preliminary stage. The previous reports[1),2)] have presented the experimental data on g=1.5 and 1.0mm and analyzed results on g=1.5mm with the sub-channel analysis code COBRA-IV-I. Here, progresses after the previous reports are shown. Namely, characteristics of the experimental data of all gap cases are discussed and analytical results on the gap widths of 1.0 mm are shown together with the g=1.5mm cases.

The experimental conditions in all gap cases are as follows,

1) for g=1.5mm; Mass velocity :1,100 ～ 4,400 kg/m^2-s, Inlet temperature: 533 ～ 593 K,
2) for g=1.0mm; Mass velocity : 1,100 ～ 3,100 kg/m^2-s, Inlet temperature: 513 ～ 593 K,
3) for g=0.6mm; Mass velocity : 1,375 ～ 4,585 kg/m^2-s, Inlet temperature: 513 ～ 593 K.

The pressure is set to 15.5MPa for all cases, considering the PWR-type RMWRs conditions.

The CHF data, as experimental results, are shown in Fig. 4.2.1 in relation to the inlet mass velocity. Only the data for the inlet temperatures of 553 K and 573 K are shown for simplicity. In the lower mass velocity region, linear relations are observed. However, in the higher mass velocity region, the linearity becomes weaken and CHF becomes higher. This characteristics are resulted from the following experimental fact. The most of positions of

CHF onset are in top areas of heated region, in the lower mass velocity. As increasing mass velocity, the position moves to the upstream side, i.e., downward. Since a chopped cosine shape for the power distribution is used, the CHF values become higher and scattered.

The following facts look like implications of the phenomena of CHF not the departure from nucleate boiling (DNB) but CHF even in the PWR pressure condition.

- The onset of CHF occurs in the top end area having relatively lower heat flux.
- The temperature increase after the onset of CHF is moderate.

Based on the above reason, the critical power is studied. The same experimental cases are re-plotted on the plane of critical power vs. inlet mass velocity as shown in Fig. 4.2.2. It is shown that the critical power are linearly changing with the mass velocity without scattering as observed in Fig. 4.2.1. These figures strongly imply that the transition boiling observed in the present experiment is so called CHF even in the PWR pressure condition.

The subchannel analysis has been performed on the g=1.0mm cases. The calculation tools and input models used in the calculations are almost same as the previous calculations. Namely, the subchannel analysis code COBRA-IV-I and the KfK correlation were used.

The calculated results on the g=1.0 mm are compared with the experimental data in Fig. 4.2.3 together with the g=1.5 mm cases previously reported. In the figure, the calculated CHFs are shown in a form divided by the experimental data (ECHFR). All ECHFRs are much lower than the unity. The ECHFR values for g=1.0mm ranging from 0.4 to 0.7 are lower than those for g=1.5mm ranging from 0.6 to 0.9. These results show that the combination of the KfK correlation and the COBRA-IV-I gives lower CHF. This means that this combination has large conservatism in the CHF calculation. As for the large differences between the analysis and the experiment, more precise analysis is needed.

References

1) Yoshida, H., et al.: JAERI Review 99-031, 4.5 (2000).

2) Yoritsune T., et al.: JAERI Review 99-031, 4.6 (2000).

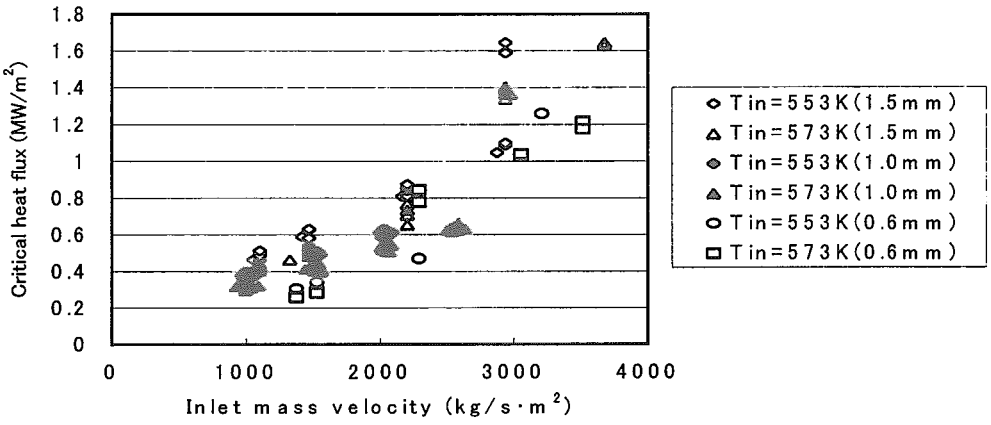

Fig. 4.2.1 Comparison of critical heat flux

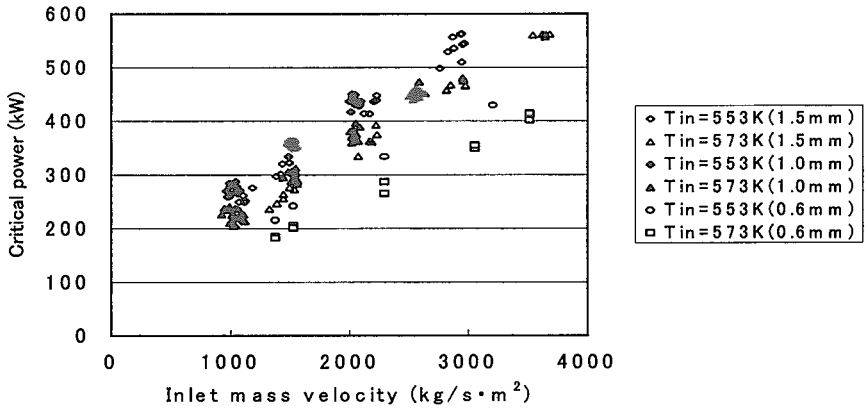

Fig. 4.2.2 Comparison of critical power

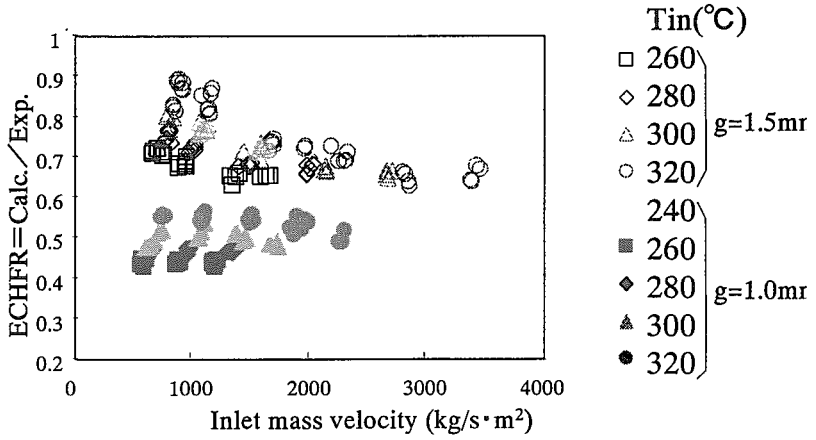

Fig. 4.2.3 Comparisons of ECHFRs between g=1.5 mm and g=1.0 mm cases

4.3 Study on Thermal Hydraulic Design of RM-PWR Core

H. Yoshida, A. Ohnuki, and H. Akimoto
E-mail: yoshida@jpsrews1.tokai.jaeri.go.jp

At present, reduced-moderation pressurized water reactor (RM-PWR) with tight lattice core is developed as one candidate for the RMWR concepts[1]. To achieve a conversion ratio greater than unity, the tight lattice core is used. Under such tight configuration, the core thermal margin becomes smaller and should be evaluated in a normal operation. In this study, we have performed a feasibility evaluation on core cooling under normal operation of RM-PWR.

The present design adopts seed assemblies and several blanket assemblies. There are two types of seed assemblies. One has internal, upper and lower axial blanket regions, and the other has no internal axial blanket region. In the blanket regions (internal, upper and lower axial blanket regions and blanket assemblies), power density is lower than that of the seed regions. Prior to detailed analysis, we performed preliminary analysis of the RM-PWR, however, boiling of coolant heavy water was occurred in the seed assemblies. This was caused by a radial flow of the coolant between the seed and blanket fuel assemblies. Then, we set a channel box to each fuel assembly in order to restrict the movement of the coolant and adjust the flow rate in each assembly.

In the feasibility evaluations for a normal operation, subchannel code COBRA-IV-I[2] was used in combination with KfK DNB correlation[3] for a tight lattice bundle. Table 4.3.1 shows calculation parameters of the subchannel analysis. .

Table 4.3.1 Calculation parameters

Bulk void model	EPRI bulk void correlation
Subcool void model	Levy's subcool void model
Spacer loss coefficient	1.0
Turbulent mixing coefficients	0.003 (single and two phase)
CHF correlation	KfK DNB correlation
Solution algorithm	Implicit

The seed blanket assemblies are located under one-sixth symmetric arrangement in RM-PWR core. Figure 4.3.1 shows radial power ratio of RM-PWR core at beginning of

cycle (BOC) for the one-sixth sector. Each fuel assembly has channel box, and heat and mass transfer between fuel assemblies are not occurred. Then, analyses for the each assembly were performed. In RM-PWR core, three types of fuel assembly exist. We selected three assemblies (see Fig. 4.3.1) as analyzed assembly.

Figure 4.3.2 shows subchannel node model for seed and blanket fuel assembly. The gap between adjacent fuel rods is 1 mm and the fuel assembly is supported using grid spacers with hexagonal shape. The outer diameter of rod for the seed and blanket fuel assemblies are 9.5mm and 17.7mm, respectively.

The most important parameters of this analysis are flow rate ratio of the blanket fuel assembly (F_b=mass flow rate of blanket fuel assembly/average mass flow rate). The number of the axial direction divisions is 40, and uniform coolant velocity and temperature are applied at inlet of each assembly.

Figure 4.3.3 shows maximum void fraction of each assembly at assembly exit. The subchannel analyses are performed at BOC and EOC condition for each assembly. If mass flow rate of coolant to

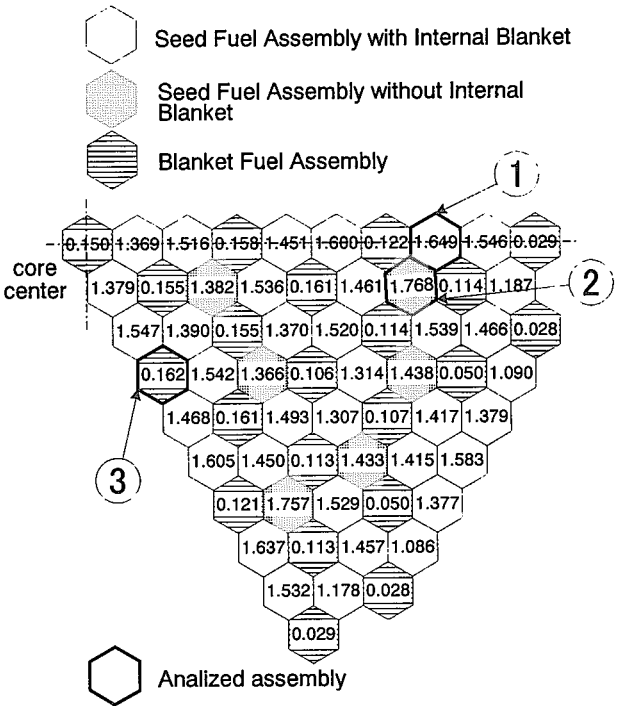

Fig.4.3.1 Radial power ratio of Core

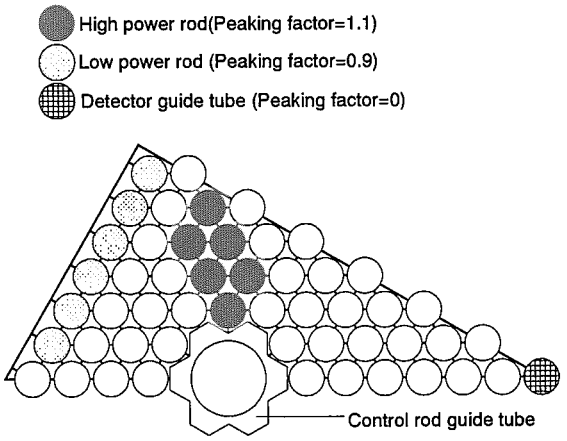

(a) Seed fuel assembly

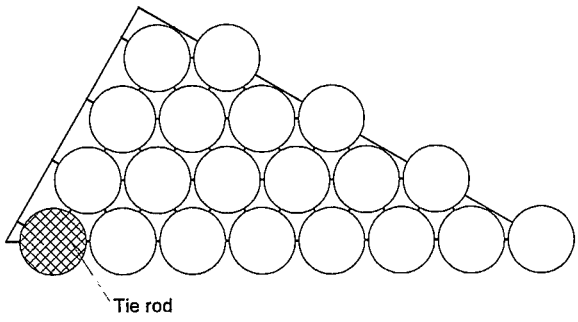

(b) Blanket fuel assembly

Fig. 4.3.2 COBRA-IV-I Subchannel node model

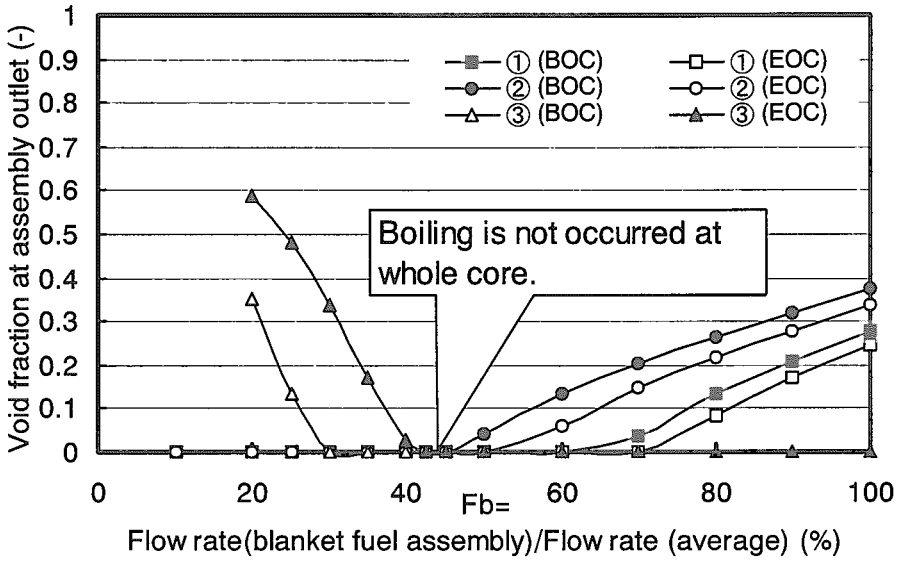

Fig. 4.3.3 Maximum void fraction at exit of assembly

the blanket fuel assembly is not reduced (it means that F_b=100%), coolant is boiling in the seed fuel blanket. The void fraction records maximum values near the control rod guide tube and high power rod. On the other hand, a coolant boils at the blanket fuel assembly when F_b is set less than 40%. It is understood that boiling doesn't occur in the whole core if mass flow rate of the blanket fuel assembly is restricted to about 45% of averaged value. In this case, minimum DNBR in the core is 1.3, and this value is larger than the value being used in the design of the current PWR (1.3).

References:

1) Hibi, K. et al., Conceptual designing of reduced-moderation water reactors (2) -Design for PWR-type reactors-, Proc. 8th Int. Conf. of Nuclear Engineering (ICONE8), Baltimore, April 2000.

2) Stewart, C.W. et al., COBRA-IV: The model and the method, BNWL-2214, 1977.

3) Donne, M. D. et al., Critical Heat Flux Correlation for Triangular Arrays of Rod Bundles with Tight Lattices, including the Spiral Spacer Effect, Nuclear Technology V0l.71 October 1985.

4.4 Study on Predictability of REFLA-TRAC Code for Reflood Phase with an Upper Plenum Injection

H. Yoshida, A. Ohnuki, and H. Akimoto
E-mail: yoshida@jpsrews1.tokai.jaeri.go.jp

The RM-PWR core has a relatively tight lattice core, and, in the reflooding problem, it is demonstrated that a combined injection with an upper plenum injection of ECC water is significantly effective[1]. In this Study, we will clarify the validity of R-TRAC2000 simulations using the Slab Core Test Facility (SCTF) data with an upper plenum injection[2].

The SCTF was designed to properly simulate the two-dimensional core heat transfer and hydraulic behaviors during refill-reflood phase. The pressure vessel is of slab geometry as shown in Fig. 4.4.1. The simulated core consists of 8 bundles arranged in a row. Bundle 1 corresponds to the center bundle and Bundle 8 to the peripheral bundle of a PWR.

In the SCTF test referred to in this study, each bundle has 236 electrically heated rods and 20 non-heated rods. The dimensions of the heater rods are based on a 15×15-type fuel assembly and the heated length and the outer diameter of each heater rod are 3.613 m and 10.7 mm, respectively.

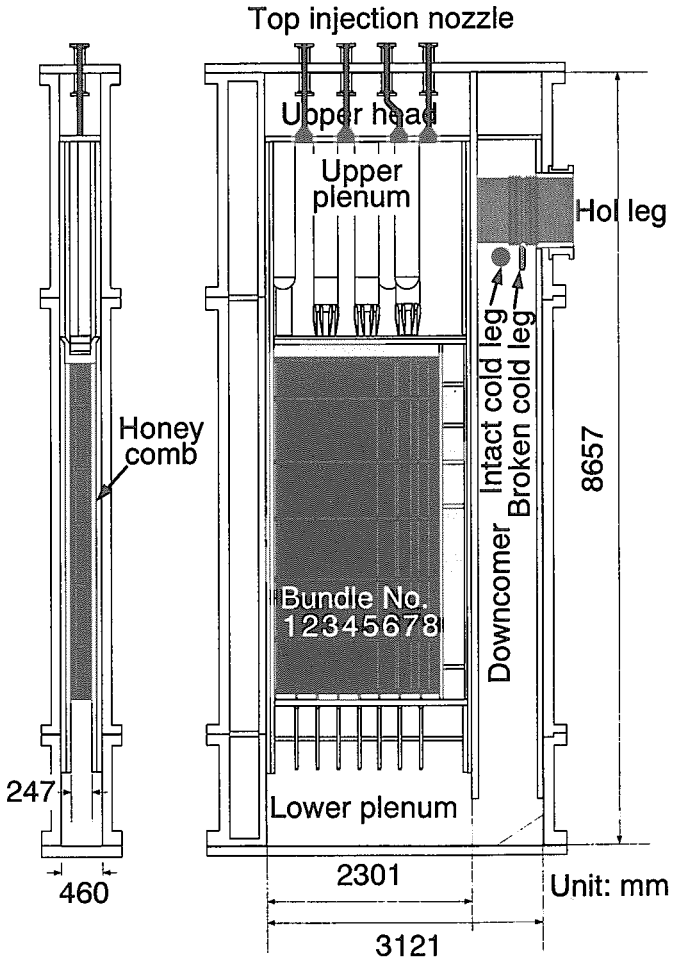

Fig. 4.4.1 Vertical cross section of SCTF pressure vessel.

The SCTF test referred to in this study was performed under an flat radial power distribution in order to investigate the effect of the upper plenum injection on the

two-dimensional thermal-hydraulic behaviors in the core. The ECC water was injected into the lower plenum and from the upper injection nozzles.

Figure 4.4.2 shows the input nodalization. Modeled were the pressure vessel, ECC injection piping and a hot leg of the SCTF. The two-dimensional input of VESSEL component consists of 63 axial levels and 11 sections in lateral direction. Levels 4 through 59 and lateral sections 1 through 8 represent the heated core.

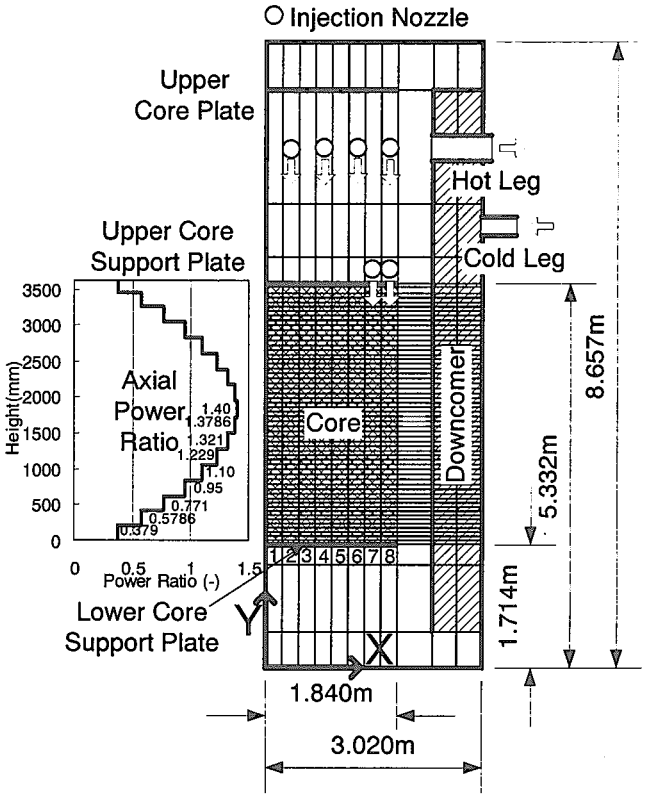

Fig. 4.4.2 Nodalization of SCTF.

Figure 4.4.3 shows the comparison of maximum clad surface temperature of the core. Measured PCT (Peak Clad Temperature) was realized as well as in the calculation, and no significant differences are existed during almost the whole period.

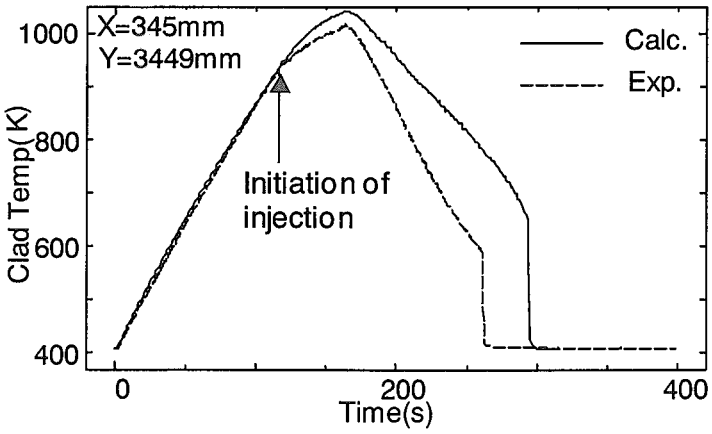

Fig. 4.4.3 Comparison of Clad Surface Temperature

Reference:

1) Ohnuki, A. Annual Meeting of the Atomic Energy Society of Japan, F40 (1999) (in Japanese)

2) Iwamura, T. et al. JAERI-M88-125 (1988).

4.5 Development of Analytical Method for Steam-Blanket Effect in PCCS with Horizontal Heat Exchanger

A. Ohnuki, H. Nakamura and Y. Anoda
(*E-mail*: ohnuki@hflwing.tokai.jaeri.go.jp)

A passive containment cooling system (PCCS) is under planning to use in a next-generation-type BWR for long-term cooling by condensing steam using horizontal heat exchangers.[1] Figure 4.5.1 shows the outline of the PCCS. Horizontal U-tubes are submerged in a water pool. Steam from the upper head is condensed in the U-tubes and condensate and non-condensable gases are drained from the lower head. Heat transfer behavior in the secondary water pool is one of important phenomena governing heat removal performance of the PCCS. It was concerned that the heat transfer tubes are covered by steam under high heat flux regions and the heat transfer is degraded in the region (Steam-blanket effect). In this study, an analytical method for the steam-blanket effect was developed based on multi-dimensional two-fluid model code ACE-3D[2].

In order to develop the analytical tool, we incorporated a turbulent heat flux model and heat conduction structures into ACE-3D. Preliminary analyses indicated that the turbulent Prandtl number in the turbulent heat flux model governs boiling-condensation phenomena in water pool. Thus, we optimized the turbulent Prandtl number using data from steam jet experiments in water pool[3].

The ACE-3D was then applied to the analysis of the secondary water pool in the PCCS. Two-dimensional analyses were carried out, focusing on the area adjacent to the header where heat flux is the highest. Figure 4.5.2 shows the analytical configuration and conditions. Modeled is a half of one unit from symmetric property. Square obstacles with equal cross section simulate the heat transfer tubes and a one-dimensional heat conduction module is set to each side. The boundary conditions for inner wall of the heat conduction module were derived from single U-tube experiments[1].

Figure 4.5.3(a) indicates the liquid velocity distribution and void fraction contour line when boiling and condensation were occurred inside the tube bundle. A vortex builds up at upper right in the pool. A high void fraction region exists locally near center in the upper side of tube bundle. In the high void fraction region, the liquid velocity is high and the direction of liquid flow was fluctuated. Upward liquid flow is dominant near the central region in the tube bundle, and however cross flow velocity was almost the same order as the

upward one in the outer region than 5th row.

Figure 4.5.3(b) indicates the distribution of heat flux by bar chart. The heat flux is higher in the upper side than that in the lower one and the highest heat flux is occurred in the high void fraction region. In the high void fraction region, a local variation of heat flux is recognized: a higher heat flux was attained by a higher upward flow velocity, and the heat flux at the region under only cross flow with a low velocity was about half to the high value. On the other hand, such a local variation is very small in the right side of tube bundle where the cross flow velocity was almost the same order as the upward one.

It was found from the steam-blanket analyses that no any heat transfer tubes are covered only by steam and no significant heat transfer degradation is occurred.

References

1) Nakamura, H. et al.: NTHAS2, Fukuoka, Oct. 15-18 (2000).
2) Ohnuki, A. et al.: JAERI-Data/Code 96-033 (1996) in Japanese.
3) Ohnuki, A. et al.: JAERI-Data/Code 99-038 (1999) in Japanese.

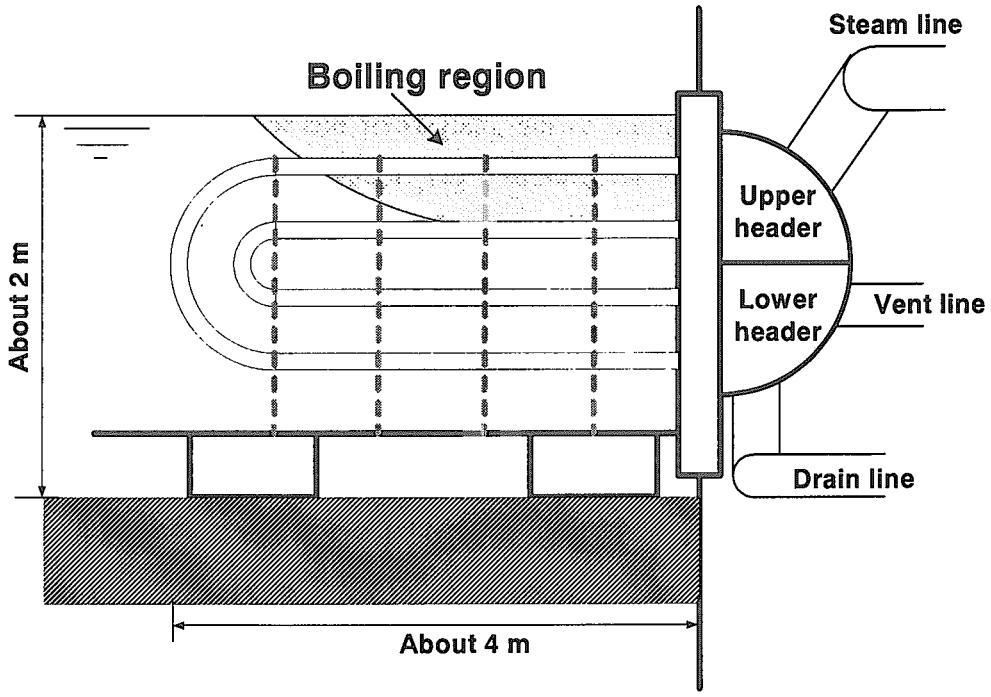

Fig. 4.5.1 Side view of horizontal PCCS

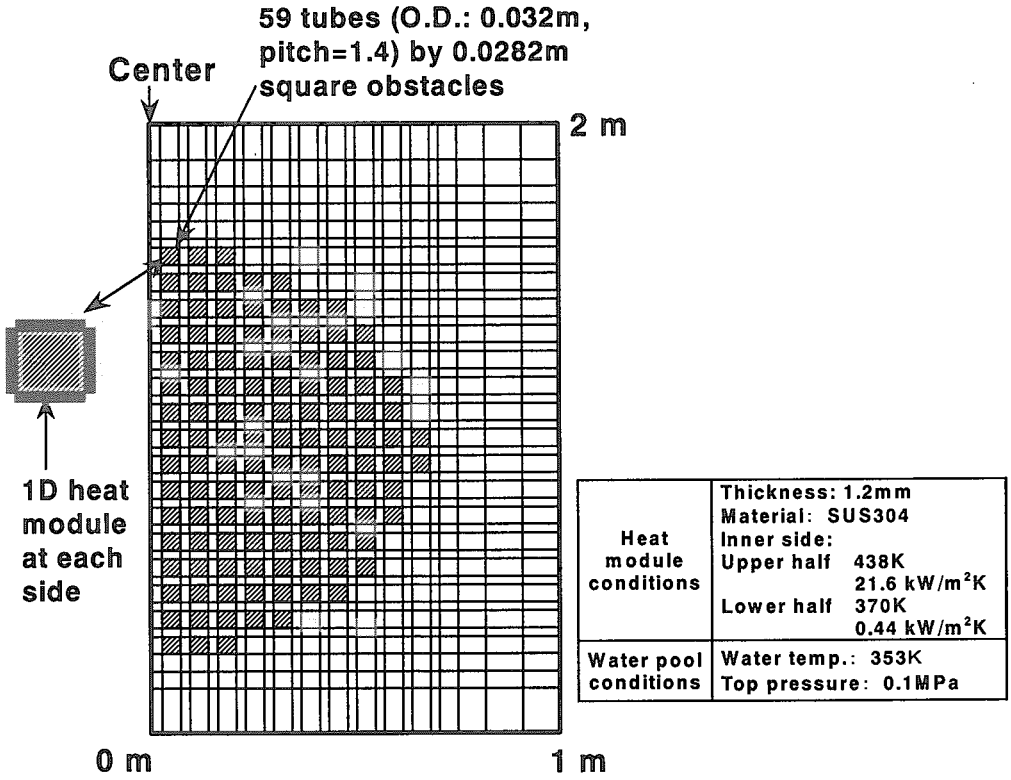

Fig. 4.5.2 Analytical configuration and conditions

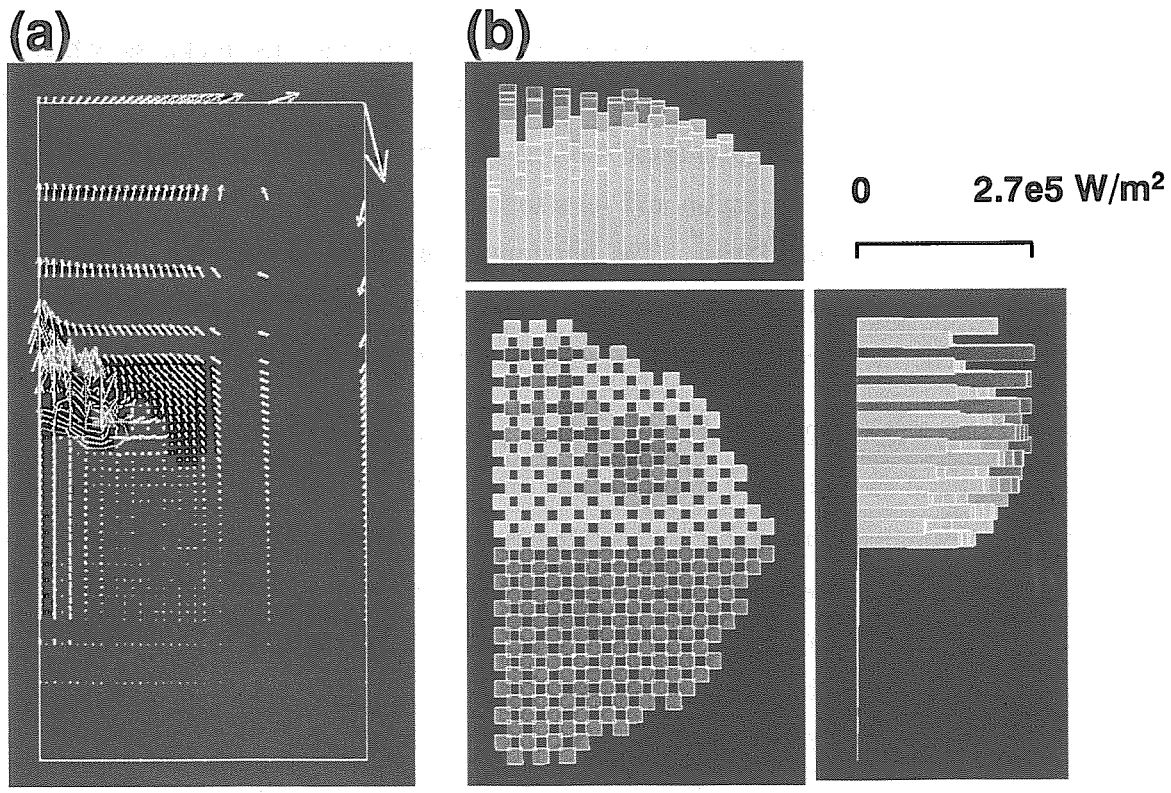

Fig. 4.5.3 Calculated results ((a) Liquid velocity distribution and void fraction contour line, (b) Distribution of heat flux)

4.6 Application of Neutron Radiography to Burnout Phenomena

M. Kureta and H. Akimoto
(*E-mail*: kureta@hflwing.tokai.jaeri.go.jp)

The high-frame-rate dynamic neutron radiography has been conducted for understanding of high-heat-flux burnout phenomena. In this report, we focus on (1) the measurement accuracy of the dynamic neutron radiography, (2) the discussion of the burnout phenomena on the basis of consecutive images of instantaneous void fraction distributions, and (3) the discussion of the point of net vapor generation (PNVG).

The test channels used in the experiment were rectangular channels heated from one side with gap thickness of 3 mm and 5 mm, channel width of 30 mm, heated width of 20 mm and heated length of 100 mm. The test channel was installed at the thermal neutron radiography port of the JRR-3M of Japan Atomic Energy Research Institute. Purified water flowed through the channel upwardly to be heated and boiled in the heated section. The pressure at the exit of the heated section was kept near the atmospheric pressure. Measurement error on instantaneous and time-averaged void fraction was evaluated experimentally and analytically. Figure 4.6.1 shows the schematic view of the test section for the error estimation experiment. Polystyrene plates with various thickness, which were used as substitutes for the mixture of water and steam with various void fraction, were mounted on an aluminum plate. Figure 4.6.2 shows the time-averaged local void fraction profile α in the transversal direction and its standard deviation σ for the case of which the recording speed was set at 0.89ms. The horizontal solid line denotes the designed value. The measurement error of void fraction E [%] was evaluated here by the following equation: $E[\%]=\frac{\langle\sigma\rangle}{\langle\bar{\alpha}\rangle}\times 100$. The measurement error E in the instantaneous void fraction was 17.2 % for the case shown in Fig. 4.6.2. Causes of the measurement errors were considered analytically. In this experimental condition, the measurement error of 50-80% due to statistical variation of neutrons. Measurement errors due to discrete gray level, due to blurry images, due to vapor bubble motion, and total measurement error were also discussed. Measurement error would be within 18% and 2% for instantaneous void fraction, and time-averaged void fraction, respectively in the present boiling-flow experiment.

Void fraction distribution of subcooled-boiling flow was measured using atmospheric-pressure water, inlet water subcooling from 10 to 30K and mass velocity ranging from 240 to 2000 kg/(m^2s). Figure 4.6.3 shows the images of the instantaneous void

fraction distribution taken by dynamic neutron radiography. The images were taken under the near critical heat flux condition: heat flux =0.9MW/m^2 (q/q_{CHF}=0.99) for gap =5mm, mass velocity =600kg/(m^{2}s) and inlet water temperature =90 ℃. The behavior of subcooled-boiling steam bubbles was observed by translating it into an animation of 2-dimentional and 3-dimenational instantaneous profiles of void fraction at every 0.89ms. From this observation, the following were suggested: (1) PNVG was located at the distance =5-10mm from the centerline, i.e. near the side edge of the heated region. (2) Bubble size and moving velocity could be measured with the use of consecutive instantaneous void fraction images. (3) A burnout was observed when a slug bubble expanded to its maximum to cover a wide area of the heated section near the exit. The liquid film thickness around the slug bubble section became very thin (for example, 0.1mm for the case shown in Fig. 4.6.3) at the center of the bubble near burnout condition. Based on this observation, the mechanism of burnout in subcooled boiling is discussed as follows. As shown in Fig. 4.6.3, the local instantaneous void fraction can be as high as α~0.95 near burnout condition even if the bulk flow is subcooled. At such a high local void fraction condition, the bubble-crowding burnout model[1] may not be applicable. The idea of liquid sublayer dryout appears to be applicable to the high void fraction region. However, it was found that the liquid-sublayer dryout model[2] overestimates CHF more than 10 times higher than experimental result. Comparing the instantaneous void fraction measured by the present experiment and the void fraction calculated by the model, it was found that the model overestimates the void fraction, and this is a main reason of the lowering of predicting CHF. We have investigated the void fraction profile along the flow direction and PNVG using the present dataset. The PNVG was determined approximately from the slop of the void fraction against the thermal equilibrium quality. Figure 4.6.4 shows the comparison between the PNVG determined from the experimental data and the prediction by existing models. It was found that the net vapor generation point seemed to be a weak function of the heat flux. No correlations proposed by Saha-Zuber[3], Ahmad[4], Levy[5], and Bowling[6] give reasonable predictions on the PNVG. This discrepancy may be due to the database, which was used to develop the correlations. The length of the heater used in the present experiment is so short that the thermal boundary layer was not well developed over the entire heated length, resulting in heat transfer coefficient higher than in the thermally developed flow.

Because neutron radiography is an innovative technique for the thermal-hydraulic measurement, we have continually developed it to get the bubble and/or liquid film information and to study the burnout mechanism.

References

1) Weisman, J. and Pei, B. S. : Int. J. Heat Mass Transf., 26, 1463(1983).

2) Katto, Y. : Int. J. Heat Mass Transf., 35, 1115(1992).

3) Saha, P. and Zuber, N. : "Proc. 5th, Int. Heat Transfer Conf.", Tokyo, Japan, 4, 175(1974).

4) Ahmad, S. Y. : Trans. ASME, J. Heat Transfer, 92, 595(1970).

5) Levy, S. : Int. J. Heat Mass Transfer, 10-7, 951(1967).

6) Bowring, R. W. : Report HPR10, OECD Halden Reactor Project, (1962).

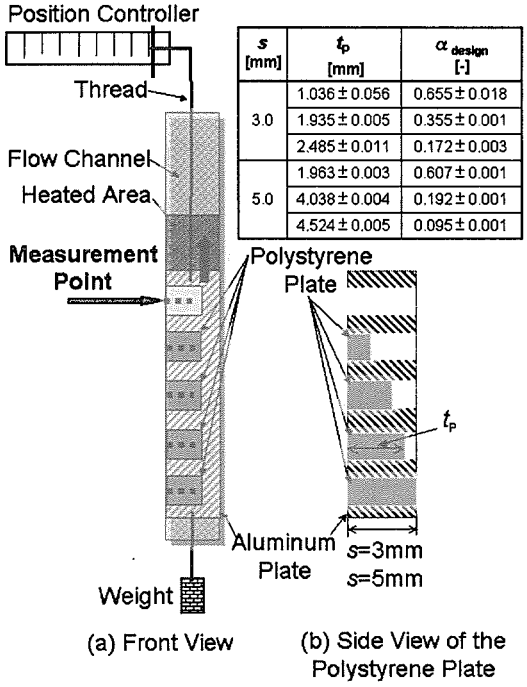

s [mm]	t_p [mm]	α_{design} [-]
3.0	1.036±0.056	0.655±0.018
	1.935±0.005	0.355±0.001
	2.485±0.011	0.172±0.003
5.0	1.963±0.003	0.607±0.001
	4.038±0.004	0.192±0.001
	4.524±0.005	0.095±0.001

Fig. 4.6.1 Schematic view of the test section for the error estimation experiment

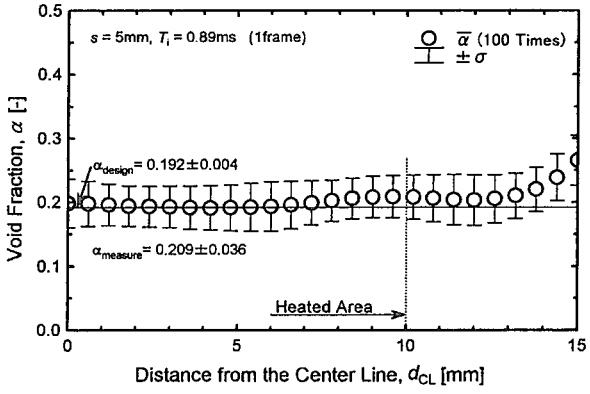

Fig. 4.6.2 Comparison the measured void fraction with the designed one

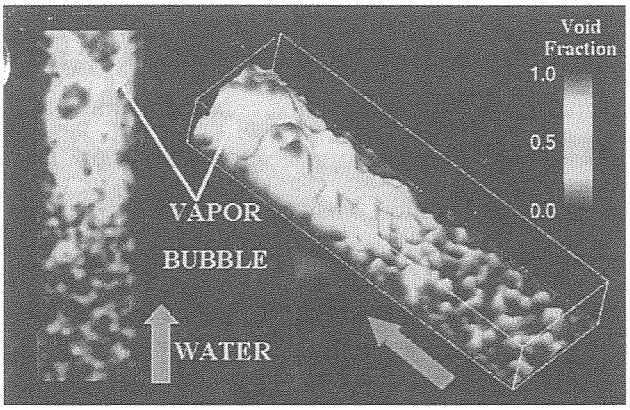

Fig. 4.6.3 Instantaneous void fraction distribution near burnout condition taken by dynamic neutron radiography

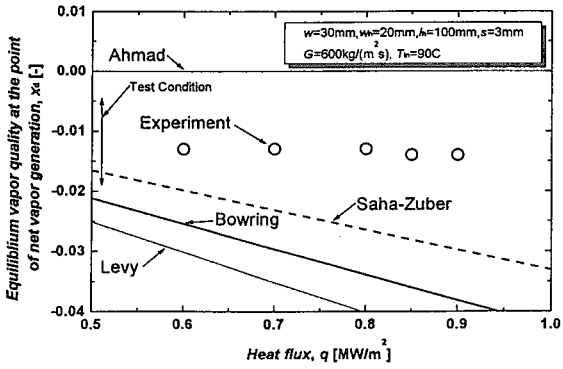

Fig. 4.6.4 Comparison between the experimental result of PNVG and correlations

4.7 Construction of an Integrated ICE Test Facility

K. Takase, M. Shibata, T. Takahashi, H. Watanabe and H. Akimoto

(*E-mail*: takase@popsvr.tokai.jaeri.go.jp)

An integrated ICE (Ingress-of-Coolant Event) experiments were planned so as to obtain verifying data for ITER (International Thermonuclear Experimental Reactor)[1] safety analysis codes during an ICE event. An integrated ICE test facility[2] was constructed to carry out the integrated ICE experiments. Objectives for the integrated ICE test facility are:

- To demonstrate that the ITER safety design approach and design parameters are adequate for mitigation of the ICE events; and
- To provide experimental data for validation of safety analysis codes and methodologies.

For demonstration of the adequacy of safety design approach and design parameters, the test conditions were focussed on the multiple in-vessel pipes break case[3] which is considered as the severest ICE condition in ITER. More detailed experimental objectives are to obtain integrated test data to make sure that the code-predicted accidental over-pressure is correct including the effect of steam generation in the plasma chamber (PC) and vacuum vessel (VV), two-phase pressure drop through the divertor and the condensation in the suppression tank. Major test items are:

- Pressure rise characteristics inside the VV
- Two-phase flow characteristics and pressure drop through the divertor;
- Direct-contact condensation effcet in the suppression tank and condensation on VV wall;
- Functional performance of the ITER pressure suppression system.

The basic policy of the scaling of the integrated ICE test facility is to functionally simulate the ICE phenomena, such as by scaling based on volume and mass, without modeling the actual shape of ITER machine. The proposed basic scaling laws between the test facility and ITER are: the volume size is about 1/1600; and flow velocity, pressure and temperature are simulated by the scaling factor of 1/1, respectively. Here, the current volume size was determined on the basis of the total coolant flow rate discharged into the plasma chamber during the double-ended pipe break condition in ITER.

Figure 4.7.1 shows a schematic drawing of the integrated ICE test facility. The test facility mainly consists of a PC, divertor, VV, relief pipe and suppression tank. The PC is a

cylindrical tank with a diameter of 600 mm and length of 2100 mm. The volume is 0.59 m^3 and corresponds to 1/1600 of ITER volume (914 m^3). The PC wall can be heated to the specified temperature with electrical heaters. The maximum wall temperature is set to be 250°C to cover the specified range in the ICE events of ITER. The maximum pressure at the plasma chamber is 1 MPa.

Three sets of water injection mechanisms are attached to the side wall of the PC for the simulation of the break conditions of the primary coolant system. Each water injection mechanism consists of a water injection nozzle, flowmeter and valve. The water injection nozzle is installed into the PC. The break size can be changed by replacing the nozzle. The maximum nozzle size is 10 mm and was determined by the condition of the multiple in-vessel pipes break case.

The water simulating the primary coolant is supplied from the boiler. The boiler consists of a cylindrical tank and electric heaters. The tank volume is 0.63 m^3. The boiler can be pressurized by nitrogen gas up to 4.3 MPa. The water can be heated up to 250°C so as to cover the fluid temperature range in ITER.

The divertor simulates an orifice plate with multiple slits as can be seen in Fig. 4.7.2. The orifice plate can be replaced to obtain the reasonable simulation of the divertor. The multiple slits at the orifice plate simulate the evacuation slits which is settled at the divertor cassette in order to evacuate the internal impurity gas to the outside. The choking effects on the two-phase flow behavior through the divertor can be investigated systematically.

The VV is settled to the bottom of the plasma chamber through the orifice plate with multiple slits and simulates the bottom part of the VV in ITER. The wall temperature is controlled separately from the plasma chamber to make test conditions. Observation windows are attached to the simplified VV to understand visually the two-phase flow behavior. The volume of the simplified VV is around 0.34 m^3. The maximum pressure and wall temperature are 1 MPa and 250 °C, respectively.

The suppression system consists of a cylindrical tank, relief pipe, and organ pipes. The volume of the suppression tank is 0.93 m^3. The initial water volume stored in the tank is 0.4-0.5 m^3. The suppression tank is connected with theVV by the relief pipe and organ pipes.

Construction of the integrated ICE test facility was completed by the end of December, 1999. Scoping tests were performed from january, 2000 to investigate the functional performance of the integrated ICE test facility and clarify the experimental ranges.

References

1) ITER Final Design Report, June, (1998).

2) K. Takase, et al., Nuclear Fusion, Vol.40, No.3Y, 527(2000).

3) ITER NON-SITE SPECIFIC SAFETY REPORT (NSRR-2), Executive Summary, December, (1997).

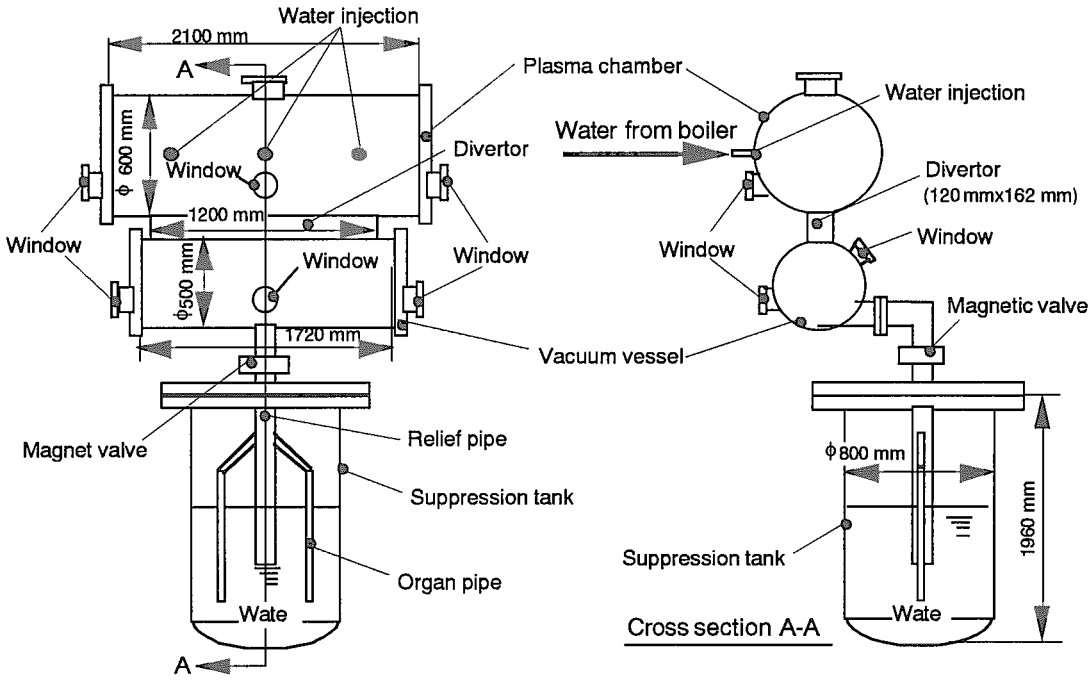

Fig. 4.7.1 Dimensions of the integrated ICE test facility

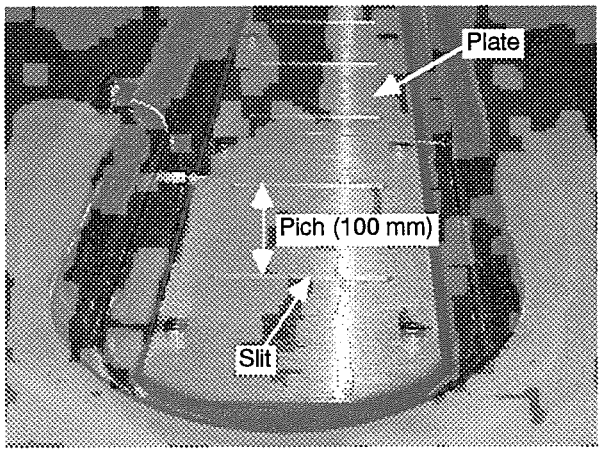

Fig. 4.7.2 Outline of an orifice plate set to the divertor

4.8 Numerical Analysis on Two-Phase Flow Characteristics in Fusion Reactors During Ingress-of-Coolant Events with TRAC Code

K. Takase, Y. Ose and H. Akimoto

(*E-mail*: takase@popsvr.tokai.jaeri.go.jp)

If cooling tubes installed into plasma-facing components (PFCs) in a Tokamak vacuum vessel of the International Thermonuclear Experimental Reactor (ITER)[1] are broken by some damage, water under high temperature and pressure in the cooling tubes will be discharged into a plasma chamber (PC) and vacuum vessel (VV), and the discharged water will impinge on a hot surface of the PFCs and evaporate. As a result, the VV will be filled with steam and the pressure in the VV will increase rapidly, and the rapid pressure rise will make a shock wave and lead to high pressurization. Furthermore, chemical reactions between the steam and PFC materials may occur. This is called an ingress-of-coolant event (ICE). The ICE event is one of the most severe accident events in ITER.

An integrated ICE test facility[2] was planned to clarify experimentally two-phase flow characteristics and adequacy of the pressure suppression system in ITER during the ICE condition. Similarly, those were predicted numerically before the experiments with the integrated ICE test facility. The Transient Reactor Analysis Code (TRAC)[3], which was originally developed for the accident analysis in light water reactors, was used in the present numerical study. The predicted results of the TRAC code were already verified with the results of the fundamental ICE experiments[4].

Figure 4.8.1 shows the predicted pressure transients in the PC under the nonheated wall condition (i.e., T_v=T_w). Here, T_v=160°C, T_w=160°C and d and N were varied and t shows the time from the start of the experiment. The injection time of water is 10 s. The injected flow rate at d=10 mm and N=3 corresponds to the severest ICE case of the ITER design (i.e., multiple in-vessel leakage case) and the injected flow rate at d=5mm and N=3 corresponds to the normal ICE case of that[5]. The pressure increases with increasing d and N (i.e., the injected water flow rates). From the results the pressurization due to the flashing can be predicted by the following equation based on an equation of state of water.

$$p(t) = \frac{c_p mR}{M} \int_0^t \frac{T_{sat}(t)\{T_w - T_{sat}(t)\}}{V_v(t) h_{lg}(t)} dt$$

Figure 4.8.2 shows the depressurization effect due to the suppression tank under the condition that a large amount of water is injected into the PC (i.e., the severest ICE condition). Here, T_v =160°C, T_w=160°C, d=10 mm and N=3 and R_D was varied. The solid, dashed, dotted and one-pointed dashed lines represent the predicted pressure transients at the PC when R_D=0, 100, 150 and 200 mm, respectively. A magnetic valve at the relief pipe was opened at 0.2 MPa. The effect of depressurization due to the suppression tank is remarkable when R_D=200 mm. From the results it was concluded that the relief pipe diameter is one of the most important factors to suppress the pressure rise during the ICE events.

The following conclusions were given from the present numerical results.

1) The pressure increases with increasing the injected water flow rate;

2) The pressure changes the orifice size and pitches at the divertor;

3) The pressure receives the effect of the wall and water temperatures;

4) The suppression tank is effective to reduce the high pressure.

Nomenclature

c_p specific heat capacity

d water nozzle diameter

h_{lg} latent heat of evaporation

M molecular weight of vapor

m injected water flow rate

N water nozzle number

p pressure

R universal gas constant

R_D relief pipe diameter

t time

T_{sat} saturation temperature

T_v wall temperature

T_w injected water temperature

V_v volume of vapor

References

1) ITER, ITER Final Design Report, June 1998.

2) Takase, K., et al., ISFNT-5, Rome, September (1999).

3) Liles, R., at al., NUREG/CR-5069 (LA-11208-MS R4), (1988).

4) Takase, K., et al., ICONE-6, San Diego, (1996).

5) ITER, Study of Options for the Reduced Thechnical Objectives/Reduced Cost ITER, February, (1999).

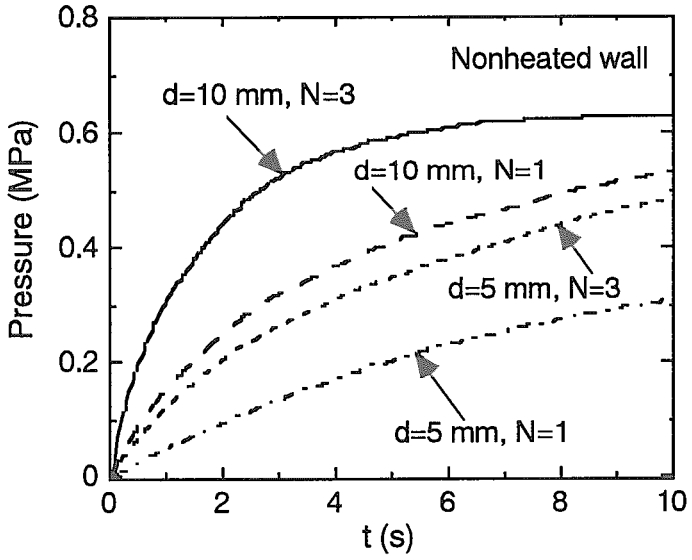

Fig. 4.8.1 Predicted pressure transients at T_v=160°C and T_w=160°C

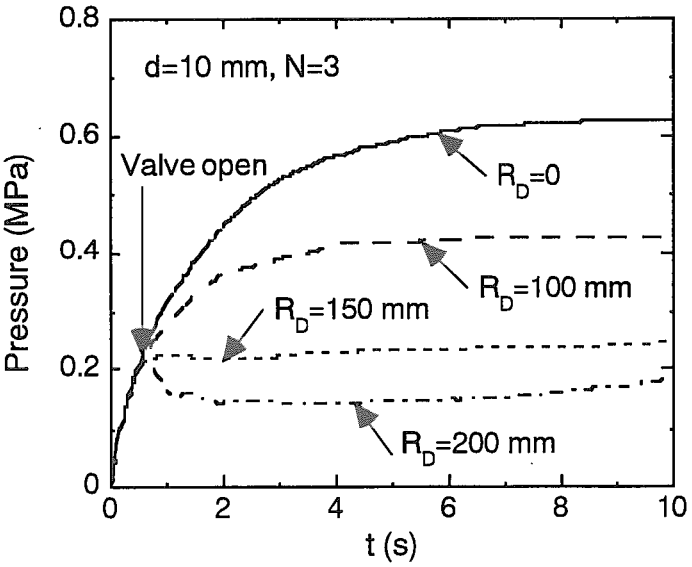

Fig. 4.8.2 Effect of depressurization due to the suppression tank and R_D at d=10 mm and N=3

4.9 Numerical Simulations on Thermal-Hydraulic Phenomena in Fusion Reactors at Loss-of-Vacuum Events

K. Takase and H. Akimoto

(*E-mail*: takase@popsvr.tokai.jaeri.go.jp)

If a loss-of-vacuum accident (LOVA) event occurs in a fusion reactor, an external fluid may flow into the inside of a vacuum vessel (VV) through breaches. In the International Thermonuclear Experimental Reactor (ITER) design[1], air is considered as the external fluid. After the inside pressure of the VV equalizes with the outside pressure, the buoyancy-driven exchange flows will take place through the breaches due to the temperature difference between the inside and outside of the VV. At the same time, the activated dust accumulated in the VV may be entrained with the exchange flows from the inside of the VV through the breaches to the outside.

Exchange flow characteristics were investigated using a preliminary LOVA apparatus[2]. The results indicated that since the exchange flow receives a large flow resistance depending on the breach diameter and length, its velocity drops considerably. Thus, it can be expected that the dust mobilized from the VV walls during the LOVA event will settle on the floor if the dust is heavy or be entrained in the exchange flows if it is not heavy. Therefore, it is very important to investigate the dust mobilization characteristics at the LOVA event from the viewpoint of the thermofluid safety design of ITER.

Thus, a newly thermofluid analysis code[3] for a compressible flow was developed and three-dimensional numerical simulations were carried out to evaluate quantitatively the dust mobilization and air ingress characteristics in the fusion reactors during the LOVA events. The newly analysis code consists of the three-dimensional continuity equation, Reynolds-averaged Naiver-Stokes equation and energy equation. The two-equation k-ε turbulence model was applied to simulate the large flow disturbance inside the VV due to the air ingress through the breaches after the LOVA event occurred.

Major assumptions regarding to the dust mobilization simulation are:

1) Dust particles are spherical in shape;

2) All dust particles have the same size and specific heat;

3) Motion of the dust particles is governed by their inertia and drag forces in the fluid;

4) Phase transformation does not occur;

5) Dust particles are isothermal having no temperature gradients in the radial direction;

6) No surface forces such as van der Waals force, particle wetness and electrostatic charges are considered that would limit the mobilization of dust.

The analytical region and boundary conditions are shown in Fig. 4.9.1. The analytical region simulates a room where the preliminary LOVA apparatus[2] is located and its diameter and height are 2500 mm each. The no-slip and adiabatic boundary conditions were adopted for the side and bottom walls, and the free-slip boundary condition was set at the top wall. At the top of the analytical region, the initial temperature gradient and pressure were set to zero and 0.1 MPa, respectively. The breach is positioned at the top, side and bottom of the VV and its cross-sectional area is almost equal to the experimental conditions.

Figure 4.9.2 shows the case in which the breach is at the top of the VV and this is named as the top-breach case. In Fig. 4.9.2(a) the dust accumulated on the bottom of the VV begins to mobilize and the horseshoe-shaped vortex appears at the opposite of the breached side. As can be seen in Figs. 4.9.2(b)-(d) the dust moves to the upper side in the VV and then is widely mobilized inside the VV. With the time the most of the moving dust drop down to the bottom and adhere the side wall of the VV.

The present numerical results are summarized as follows:

1. The predicted average pressures in the VV agree well with the experimental results within an error of 10 %;

2. The dust mobilization depends on the flow configurations of the buoyancy-driven exchange flows through breaches and the dust density;

3. The rate of dust released from the inside of the VV through the breaches to the outside depends on the breach positions on the VV; and,

4. The present numerical approach is very effective to estimate the thermal-hydraulic phenomena in the VV at the LOVA event.

References

1) G. Saji, et al., Non-Site Specific Safety Report (NSSR-2) Executive Summary, ITER report, 1997, p.III-28.

2) K. Takase, et al., Nuclear Science and Engineering, Vol.125, 223 (1997).

3) K. Takase, 5th ASME/JSME Joint Thermal Eng. Conf., San Diego, AJTE99-6428 (1999).

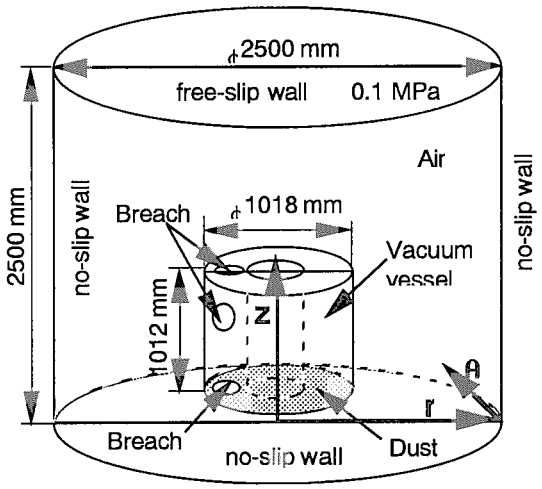

Fig. 4.9.1 Analytical region and boundary

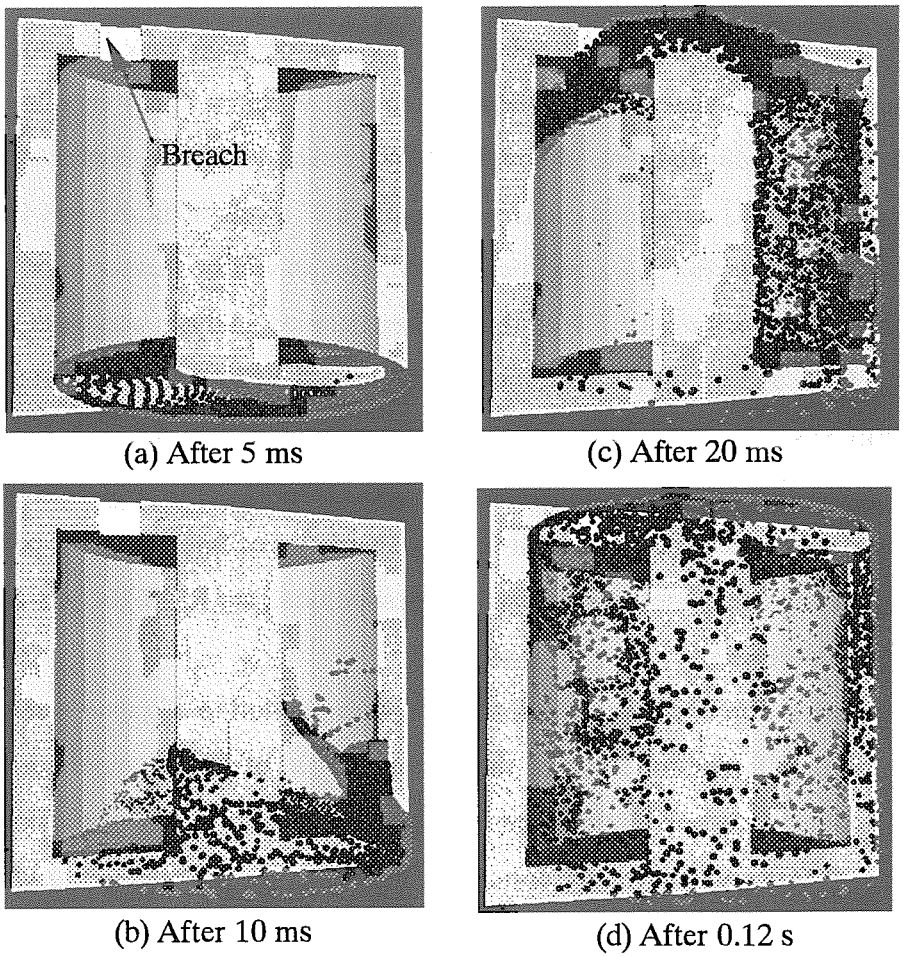

(a) After 5 ms (c) After 20 ms

(b) After 10 ms (d) After 0.12 s

Fig. 4.9.2 Predicted dust mobilization behavior in the VV at the top-breach case

5. Energy System Analysis and Assessment

In order to assess the roles of nuclear energy and its relevant technologies in Japan's future energy systems, analytical tools have been developed, and studies applying them have been made so far. Major development and analyses made in the fiscal year 1998 are summarized below.

In the development of analytical tools, a macro-economy model was developed in order to analyze possible economic impacts of nuclear moratorium. The model is of neo-classical type based on the Turnpike theory. The basic structure of the model was completed, and favorable behaviors were observed through test analysis.

In the analysis of power reactors and nuclear fuel cycle systems, a set of long-term scenarios was developed focusing the availability of breeder reactors. In analyzing consequences of these scenarios, the role of reduced moderation water reactors (RMWRs) was assessed from the viewpoint of reducing natural uranium (NU) consumption of the system. The results indicated that, although RMWRs even with a modest conversion ratios (CRs) might reduce NU consumption to sufficiently low levels if future growths of nuclear power capacity are low, the characteristics of RMWRs should be further improved in order to employ them as substitutes of FBRs. In addition, detailed analysis was made on the effect of changing CRs and/or initial plutonium loadings of RMWRs to NU requirement of nuclear energy systems. The results indicated that the both factors are very sensitive to NU consumption, and that slight improvement of CRs is very effective around 1.0. Beside these analyses, the database was developed on the characteristics of future nuclear power reactors and relevant fuel cycle technologies. Reactor types included are RMWRs, gas-cooled FBRs, and sodium-cooled FBRs.

In the analysis on energy systems, the long-term evolution of Japan's energy systems was investigated in order to evaluate the potential role of high temperature gas-cooled reactors in reducing carbon dioxide emissions. The results of the preliminary analysis indicated that HTGRs will possibly contribute to lower emission reduction costs through application of process heat in a variety of purposes. In addition to this, price elasticity of energy consumption in Japan was analyzed based on the results obtained in the last year's analysis. By applying advanced methods of statistical analysis, significant improvements were observed in the estimated results.

5.1 Long-term Scenarios of Power Reactors and Nuclear Fuel Cycle Development

O. Sato
(*E-mail*: sato@ruby.tokai.jaeri.go.jp)

Nuclear energy is one of the most promising options to cope with the climate change problem. However, current nuclear systems do not assure energy production over a very long time period such as more than hundred years because less than one percent of natural uranium (NU) can be used effectively by LWRs with enriched uranium (EU) fuel. We need to develop new technologies in order to solve the resource problem associated with nuclear energy utilization. In this study, long-term scenarios were generated on the development of power reactors and fuel cycle systems in Japan focusing on the availability of breeder reactors, and their implications were analyzed.

In developing the scenarios, two cases were considered for future capacity of nuclear power generation. High case assumes rapid growth; 120GWe in 2050, 140GWe in 2100, and constant thereafter, while low case assumes much lower growth; 80GWe in 2050 and constant thereafter. Reactor types considered are LWRs with EU fuel, LWRs with MOX fuel (in partial core or full core), reduced moderation water reactors (RMWRs) with a conversion ratio 1.01, and FBRs. It is also assumed that plutonium (Pu) recycling requires 3 years for reprocessing and re-fabrication with 1% Pu loss. The scenarios are defined as listed in Table 5.1.1 with different combinations of reactor types. The outline of these scenarios is described below together with implications in NU consumption.

In the scenario D1 and D2 where breeders are not employed, NU consumption increases with time exceeding 1.5 million ton (high case) or 1.0 million ton (low case) before the year 2100. These scenarios are feasible only if large-scale recovery of uranium from seawater can be implemented. In the scenario B1 where FBRs are used from 2050, LWRs are replaced by FBRs completely around the year 2115. However, since the amount of Pu necessary to feed FBRs is not large, about 90 thousands ton of LWR spent fuel will remain un-reprocessed.

In the scenario B2 (Fig. 5.1.1), where fully MOX fueled LWRs are added to B1, the excess spent fuel is reprocessed to recover Pu. Instead of fully MOX fueled LWRs, RMWRs can be used for this purpose (scenario A). If FBRs are available from 2030 (scenario B3), LWRs can be completely replaced before 2100, resulting in the drastic reduction of NU consumption. In the scenario C where RMWRs are introduced as substitutes of FBRs (Fig. 5.1.2), RMWRs replace LWRs completely around the year 2050, much later than the case of FBRs because of its low conversion ratio.

Fig. 5.1.3 compares NU consumption of these scenarios. In the high capacity case, B1 requires more than 1.5 million ton, of NU, higher than B3 by approximately 0.5 million ton. But even when FBRs are available only from 2050, the consumption can be reduced by using fully MOX fueled LWRs (B2), or more significantly by RMWRs (A). Without using FBRs, RMWRs alone can also limit NU consumption at some finite levels (C), although highest in all scenarios. In the low capacity case, since

ultimate capacity level is much lower than the high case, the total amount of Pu necessary for breeder reactors is much less than the high case. This condition favors the use of RMWRs. The scenario C requires less NU than B1, and also the requirement by the scenario A is as low as that of B3.

Summarizing the above, if FBRs are available only from 2050, RMWRs are effective in reducing NU consumption by using excess Pu that is recovered by reprocessing spent fuel of LWRs. When introduced as substitutes of FBRs, RMWRs with modest conversion ratios can control NU consumption at enough low levels if future capacity of nuclear power generation is rather small such as the low case in this study. However, further improvements are necessary on their characteristics in order to make them a steady option for substituting FBRs at any conditions in the future.

Table 5.1.1 Long-term scenarios and reactor types adopted in them

Scenario	LWR		MOX Fuel LWR		RMWR	FBR
	~45GWd/t	60GWd/t	Partial Core	Full Core		
Without Breeders						
D1	○	○	○	One Unit *		
D2	○	○	○	○		
FBR Scenario						
B1	○	○	○	One Unit *		○(2050)
B2	○	○	○	○		○(2050)
B3	○	○	○	One Unit *		○(2030)
RMWR Scenario						
A	○		○	One Unit *	○	○(2050)
C	○		○	One Unit *	○	

* Ohma Nuclear Power Station

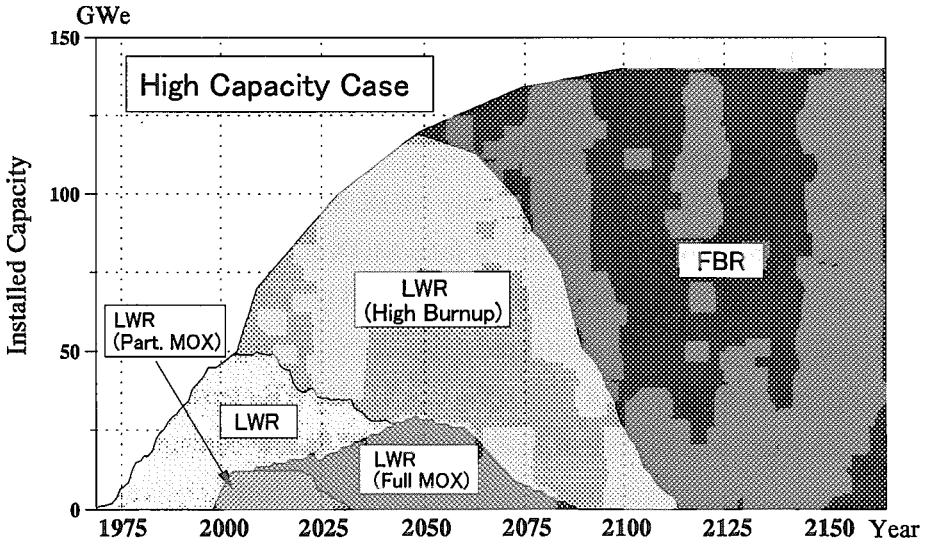

Fig. 5.1.1 FBR scenario (B2) - FBR (2050)+LWR (full MOX core)

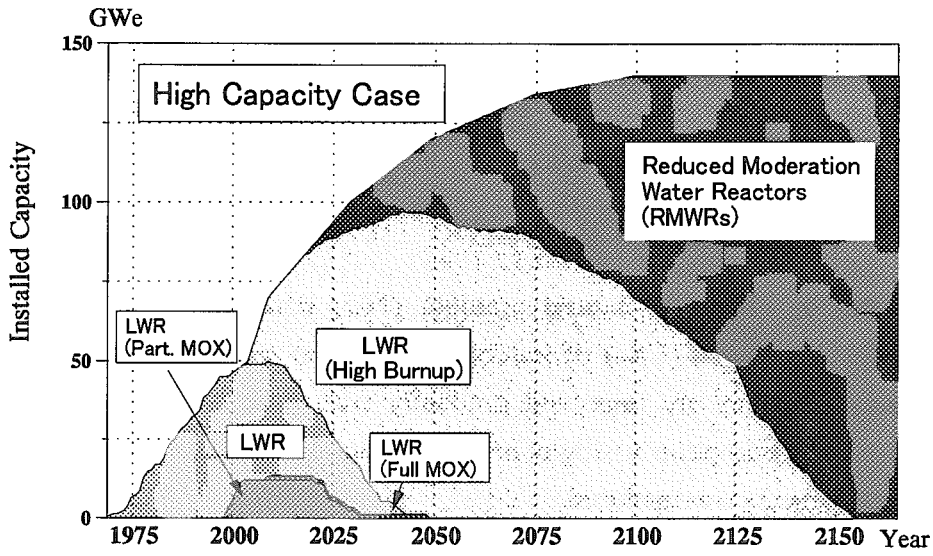

Fig. 5.1.2 RMWR scenario (C) - RMWR as substitute of FBR

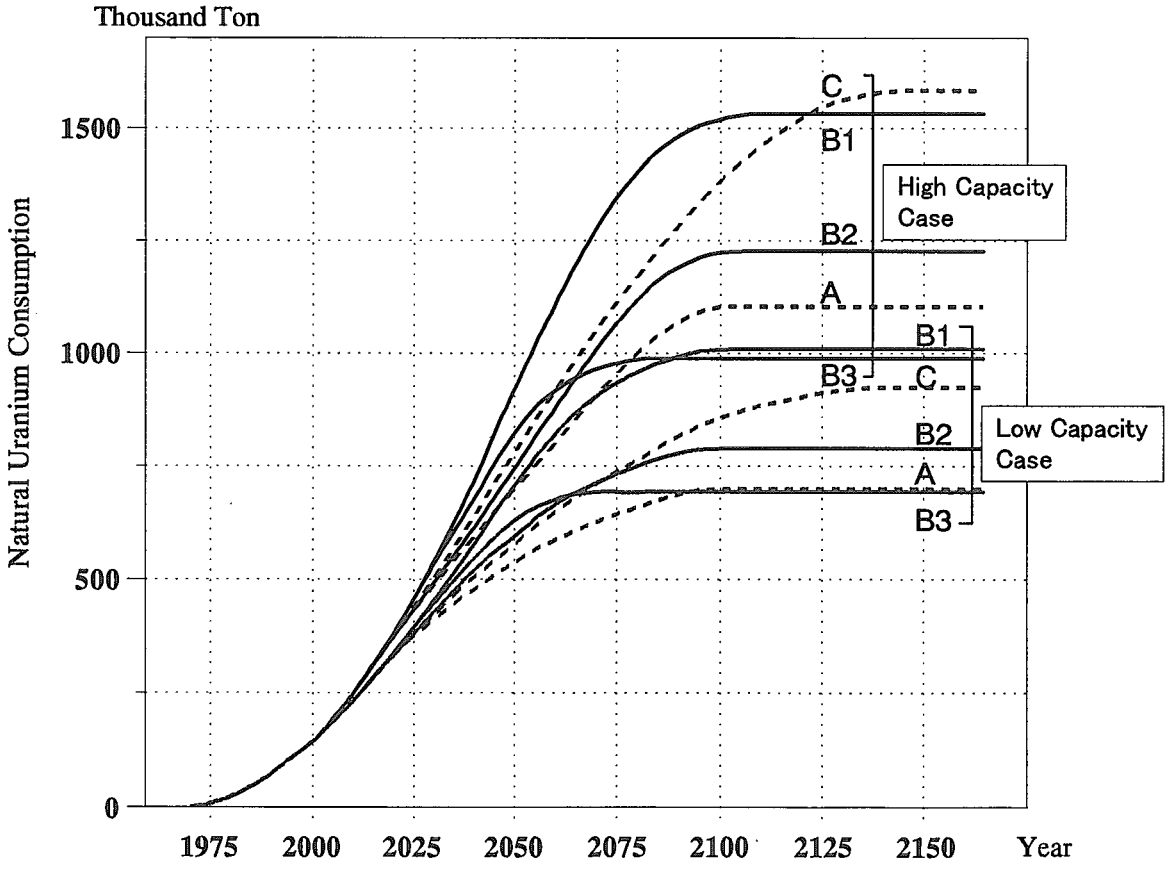

Fig. 5.1.3 Cumulative consumption of natural uranium in each scenario

5.2 An Analysis on the Characteristics and Roles of Reduced-Moderation Water Reactors

K. Tatematsu, O. Sato and Y. Tanaka
(*E-mail*: ktate@ruby.tokai.jaeri.go.jp)

We studied the effect on natural uranium (NU) consumption of nuclear power systems when conversion ratios (CRs) of reduced moderation water reactors (RMWRs) are changed, and also when they are improved gradually with time last year. In this study[1], sensitivity of the NU consumption to slight improvements of CRs around 1.0 and to initial plutonium (Pu) requirements was analyzed.

The PC version of JALTES-II was used for the analysis. The time horizon was set as 1970-2300. Total nuclear power capacity was assumed to be 100, 120 and 140GWe in 2030, 2050 and 2100 respectively, and constant thereafter. Nuclear power systems are assumed to consist of LWRs with enriched uranium fuel, LWRs with MOX fuel, and RMWRs. Several designs of RMWRs, either PWR type or BWR type, were selected in order to analyze the effect of different CRs and/or Pu requirements. It was assumed that RMWRs will be available from the year 2020. For the purpose of comparison, the NU consumption was also calculated for the case where FBRs are available from the year 2050 instead of RMWRs. The installed capacity of individual reactor types in each analytical case was determined by minimizing NU consumption with the assumption of total nuclear power capacity over the time horizon.

The NU consumption is compared for the three cases where BWR type RMWRs with net CRs excluding material loss in recycling 0.99, 1.00 and 1.005 are utilized (Fig. 5.2.1). It is shown that the NU consumption can be remarkably reduced even with a slight improvement of CRs in the vicinity of 1.0.

The comparison of the NU consumption of PWR and BWR types RMWRs is made in Fig. 5.2.2. In spite of the higher CR of PWR-2 as compared with BWR-1, the NU consumption of the case utilizing PWR-2 is larger. This is because much higher Pu requirements of PWR-2 offset its advantage in CRs.

Regarding the effect of Pu requirements, comparison was made also for the two cases utilizing RMWRs with the same CRs but different Pu requirements as shown in Fig. 5.2.3. BWR-1 requires less Pu than BWR-2 for initial loading, but requires more for annual replacement. Since there is no self-recycling of Pu for initial several years due to lag time of recycling, the total amount of Pu that must be provided by LWRs, 'initial requirement' in Fig. 5.2.3, is the sum of the amount for initial loading and for annual replacement of initial several years. In this regard, BWR-1 needs slightly more Pu from LWRs than BWR-2. Accordingly,

the NU consumption in the BWR-1 case is larger as shown in Fig. 5.2.3. Without lag time of recycling the NU consumption is affected only by the difference of Pu required for initial loading, therefore it is much lower in the BWR-1 case as indicated by dotted lines in the same figure.

In summary, it was found that the NU consumption of nuclear power systems can be significantly reduced with a small improvement of CRs of RMWRs when they are close to 1.0. Also, the effect of improving CRs is expected to follow the law of 'diminishing return on scale', although this was not adequately confirmed in this study. On the other hand, initial Pu requirements of RMWRs affect also much on the NU consumption. Accordingly, it is suggested to design RMWRs with CRs a little higher than 1.0 while controlling initial Pu requirement as low as possible.

Reference

1) Tatematsu, K., Sato, O. and Tanaka, Y.: "An Analysis on the Roles of Reduced-Moderation Water Reactors", JAERI-Research 2000-025 (2000).

Characteristics of RMWRs

Case	A	B	C
Conver. Ratio	1.01	1.01	1.015
Fuel Cycle Loss	2%	1%	1%
Net Conver. Ratio	0.99	1.00	1.005

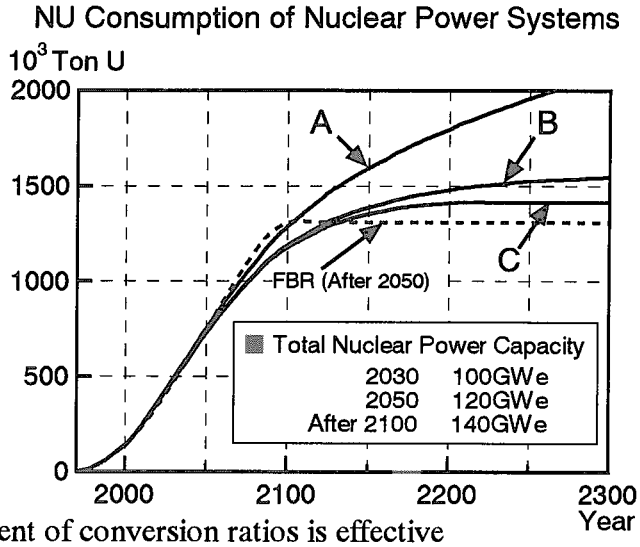

Fig. 5.2.1 In the vicinity of 1.0, the improvement of conversion ratios is effective in the saving of natural uranium.

Characteristics of RMWRs

Case	PWR–2	BWR–1
Conver. Ratio	1.03	1.01
Fissile Plutonium		
Initial Loading (t/GWe)	10.2	4.4
Annual Replacement (t/y/GWe)	2.54	1.69
Annual Discharge (t/y/GWe)	2.62	1.71

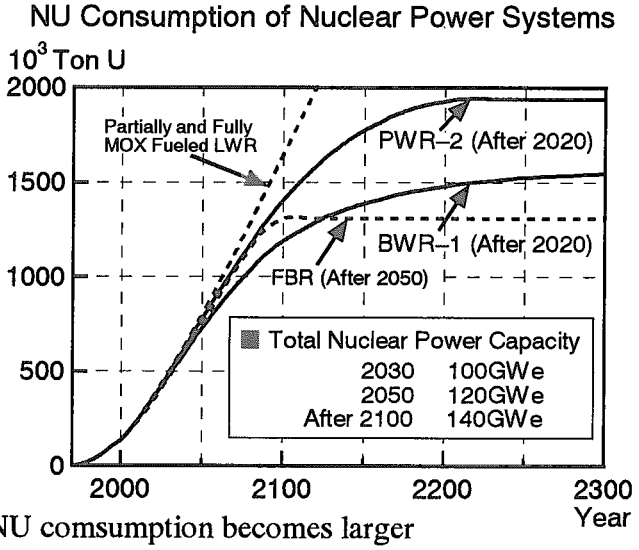

Fig. 5.2.2 Despite higher CR of PWR–2, the NU comsumption becomes larger because of larger Pu requirement.

Characteristics of RMWRs

Case	BWR–1	BWR–2
Conver. Ratio	1.01	1.01
Fissile Plutonium		
Initial Loading (t/GWe)	4.4	5.8
Annual Replacement (t/y/GWe)	1.69	1.07
Initial Requirement (t/GWe)	9.47	9.01

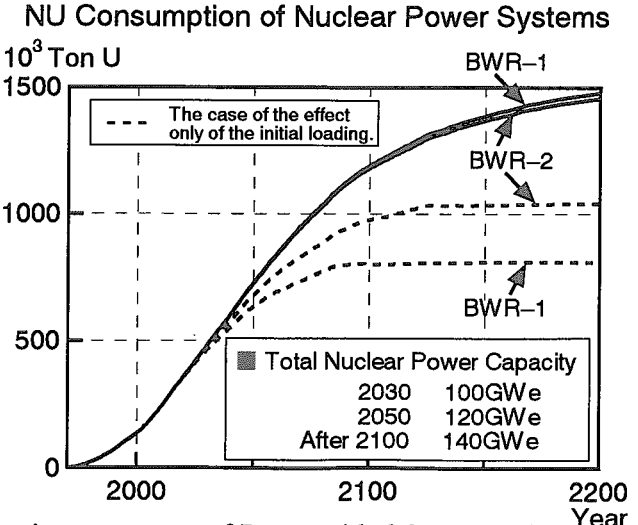

Fig. 5.2.3 It is necessary to reduce initial Pu requirement, sum of Pu provided from outside before self–recycling starts.

5.3 Price Elasticity of Energy Consumption - Historical Analysis -

K. Kunii, T. Sato, T. Yuyama* and T. Shiba*
(*E-mail*: kunii@jpsrews1.tokai.jaeri.go.jp)

The analysis was made on income and price elasticities of final energy consumption in Japan, particularly focusing on price elasticity, by applying advanced statistical methods based on the results in the previous analysis[1]. The objective of this analysis is to search for more significant information on the price elasticity.

Framework and Statistical Analysis Method The framework of the analysis is as follows : (see the previous analysis[1] for the basic procedures on elasticity analysis)

- Time period : 1969-1996
- Sources of statistical data : EDMC-Handbook of Energy and Economic Statistics in Japan (1998), Annual Report on National Accounts (1998), Energy Balance Tables in Japan (1998), Industrial Statistics Monthly (in Japanese, respectively)
- Statistical analysis method[2] : Some methods were applied in order to remove the serial correlation of error terms significantly in the estimation of elasticity. The point is to modify the estimation equation by introducing additional error terms explicitly. Three methods were applied to the present analysis, the Cochrane-Orcutt, maximum likelihood, and regression analysis including lagged dependent variables. For both Cochrane-Orcutt and maximum likelihood methods, additional cases with a time trend term were analyzed.

Moreover, in order to estimate long-term price elasticity, two methods of a distributed lag model, the Almon-lag and Coick-lag models, were applied. Here, long-term price elasticity takes into account not only prompt effects of price changes but also delayed effects. While, short-time price elasticity considers only prompt effects of price changes. It was assumed for the Almon-lag model that delayed effects can be estimated effectively in four years consisting of the current year and the next three years.

---

* Mitsubishi Research Institute, Inc.

Results and Findings The following are obtained :

- The serial correlation was almost removed in the estimation by using the methods, the Cochrane-Orcutt, maximum likelihood, and regression analysis including lagged dependent variables. Including a time trend term was, however, not effective to remove the serial correlation.
- Statistical significance over the whole sectors is summarized as follows: the estimated income elasticity was significant, while the short-term and long-term price elasticity was less significant.
- No significant difference was found on estimated price elasticity between electricity and non-electricity energy consumption.
- Table 5.3.1 shows the estimated short-term price elasticity in the whole sectors. The approximate values are -0.1 in industry, -0.1 in the resid. & commer. sector, and nearly zero in the transportation sector. The result indicates that the short-term effects of price changes are much smaller than those of income changes.
- On the long-term price elasticity ;

  The values are 2 to 5 times larger than those of short-term elasticity, depending on the used methods described above. This implies that the delayed effects of price changes are much larger than the prompt effects. The estimated elasticity by the Almon-lag model in the whole sectors is shown in Table 5.3.2.

Finally, it can be said that this analysis improved significance of the price elasticity of energy consumption, providing the important information for the future energy economic analyses.

References

1) Kunii, K. and Sato, O.: JAERI-Review 99-031, 130 (2000) .
2) Wago, H. and Pan, K.: "Analyzing econometric data by TSP (2nd Edition)" , Tokyo-Univ. Publishing (1996) (in Japanese).

Table 5.3.1 Short-term price elasticity estimated for 1969-1996 years

Sector		Price elasticity
Industry	Iron & Steel	0.0 to - 0.2 (dependent on analytical method)
	Chemicals	- 0.2
	Cement, etc.	- 0.1
	Pulp, Paper	- 0.1 to - 0.3 (dependent on analytical method)
	Others	- 0.1
	Total	- 0.1
Resid.& Commer.	Commercial	- 0.1 to - 0.2 (dependent on analytical method)
	Residential	- 0.1 to - 0.2 (//)
	Total	- 0.1
Transport	Passenger	- - - (nearly zero , t-value insignificant)
	Freight	- - - (//)
	Total	- - - (//)

Applied indices both of income and price are for the sum of electricity and non-electricity fields.

Table 5.3.2 Short and long term price elasticity estimated for 1969-1996 years

Sector		Price elasticity		
		short-term	,	long-term
Industry	Iron & Steel	- 0.12	,	- 0.30
	Chemicals	0.07	,	- 0.05
	Cement, etc.	0.06	,	0.04
	Pulp, Paper	- 0.08	,	- 0.25
	Others	- 0.06	,	- 0.14
	Total	- 0.02	,	- 0.16
Resid.& Commer.	Commercial	- 0.09	,	- 0.25
	Residential	- 0.13	,	- 0.27
	Total	- 0.17	,	- 0.27
Transport	Passenger	- 0.06	,	- 0.20
	Freight	- 0.22	,	- 0.44
	Total	0.23	,	0.20

where, short-term ; in the current year,
long-term ; in four years consisting of the current year and the next three years.
Applied indices both of income and price are for the sum of electricity and non-electricity fields.
Long-term price elasticity was estimated by the Almon-lag model.

5.4 Japan's Very Long-term Energy Demand and Supply – A Preliminary Study

O. Sato
(*E-mail*: sato@ruby.tokai.jaeri.go.jp)

Nuclear energy is already used significantly in Japan for generating electricity. A large amount of fossil fuel is still used, however, to meet non-electric energy demand such as industrial heating or transportation. High temperature gas-cooled reactors (HTGRs) and heat application systems have been developed by JAERI in order to apply nuclear energy for various purposes. In this study, the long-term evolution of Japan's energy systems was investigated and the role of HTGRs was analyzed from the viewpoint of reducing carbon dioxide (CO_2) emissions.

The analytical procedures are as follows. First, a reference energy system was established by incorporating HTGRs and heat application systems. Second, future demand for energy services was estimated by assuming growths of population and GDP. Third, prices and availability were assumed for imported fuels. And finally, four analytical cases were defined (Table 5.4.1). Here, two cases were assumed for future CO_2 emission levels, a stabilization case and a drastic reduction case (Fig. 5.4.1). For each analytical case an optimum set of energy sources and technologies was determined by minimizing system cost under the constraint on CO_2 emissions.

In the results of optimization, HTGRs were introduced to their upper limit on capacity (140 GWt in 2100) in the case A4, but did not reach the upper limit after 2080 in the case A2. This implies that economic competitiveness of HTGRs is enough only in the case where CO_2 emissions are reduced substantially lower than the 1990 levels.

Cost of reducing CO_2 emissions depends generally on the level of reduction and availability of technical measures. Fig.5.4.2 compares marginal costs of emission reduction in the four cases. In the both stabilization case (A2 and B2) and drastic reduction case (A4 and B4), the use of HTGRs contributes significantly to the decrease of CO_2 emission reduction cost.

The structure of primary energy supply is compared in Fig. 5.4.3. In the stabilization case, a lot of coal is used in the latter half of the time period, and utilization of natural gas decreases with time after the year 2030. Because of no HTGRs, utilization of renewable energy and oil in B2 becomes larger than in A2. In the drastic reduction case, coal is replaced by natural gas and renewable energy. The amount of natural gas and renewable energy is particularly large in B4 where HTGRs are not employed.

Hydrogen is produced currently by reforming oil products. In the future it can be produced by using high temperature heat from HTGRs. In this study, most of hydrogen is produced by reforming natural gas, and it is used as transportation fuel either directly or in the form of methanol (Fig.5.4.4).

The above results indicate the potential role of HTGRs in reducing CO_2 emissions from Japan's future energy systems. It is planned to make more detailed analysis with refined assumptions on imported fuel prices and dynamics of fuel change in the transportation sector.

Table 5.4.1 Analytical cases

Case	HTGRs	Constraints on CO_2 Emissions
A2	Yes	Stabilize (Case 2)
A4	Yes	Reduction (Case 4)
B2	No	Stabilize (Case 2)
B4	No	Reduction (Case 4)

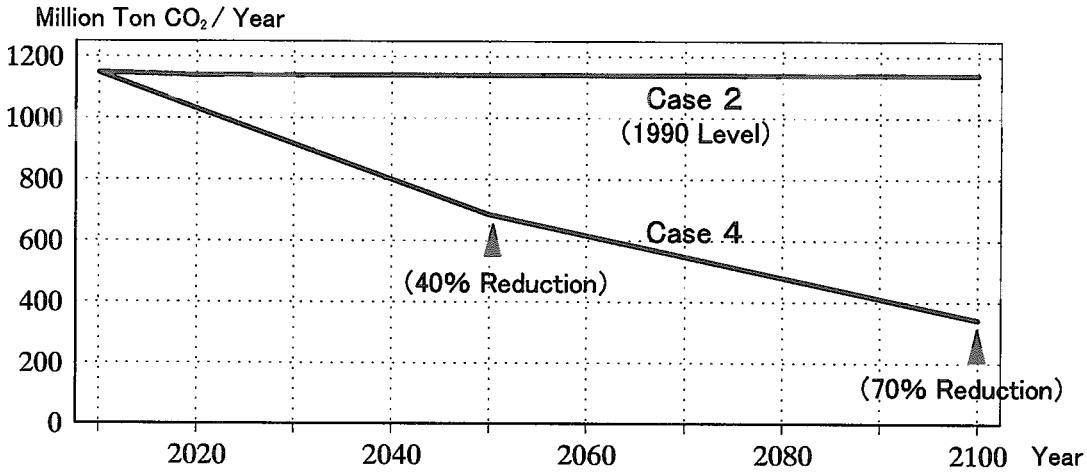

Fig. 5.4.1 Constraints on annual emissions of CO_2

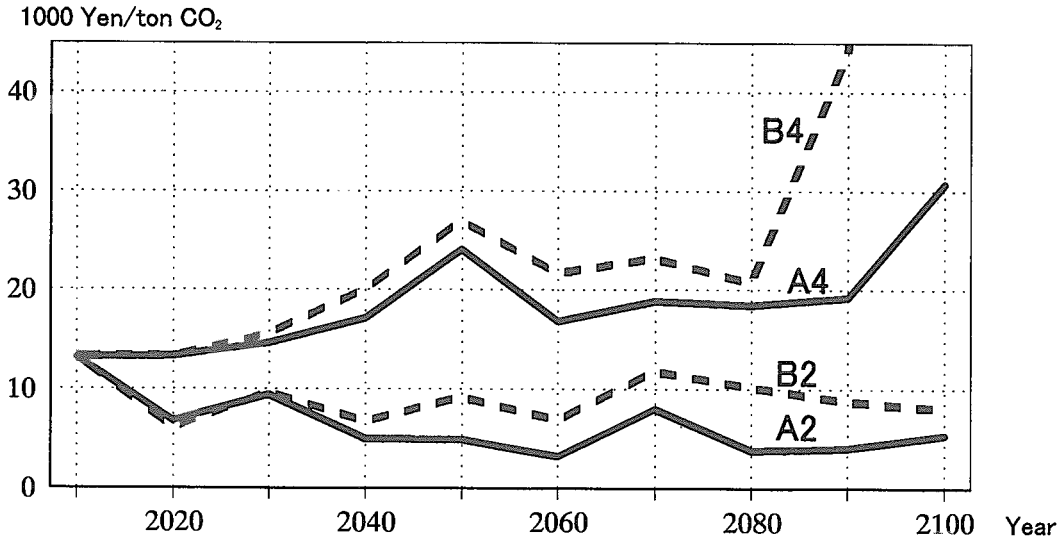

Fig. 5.4.2 Marginal costs of CO_2 emission reduction in each analytical case

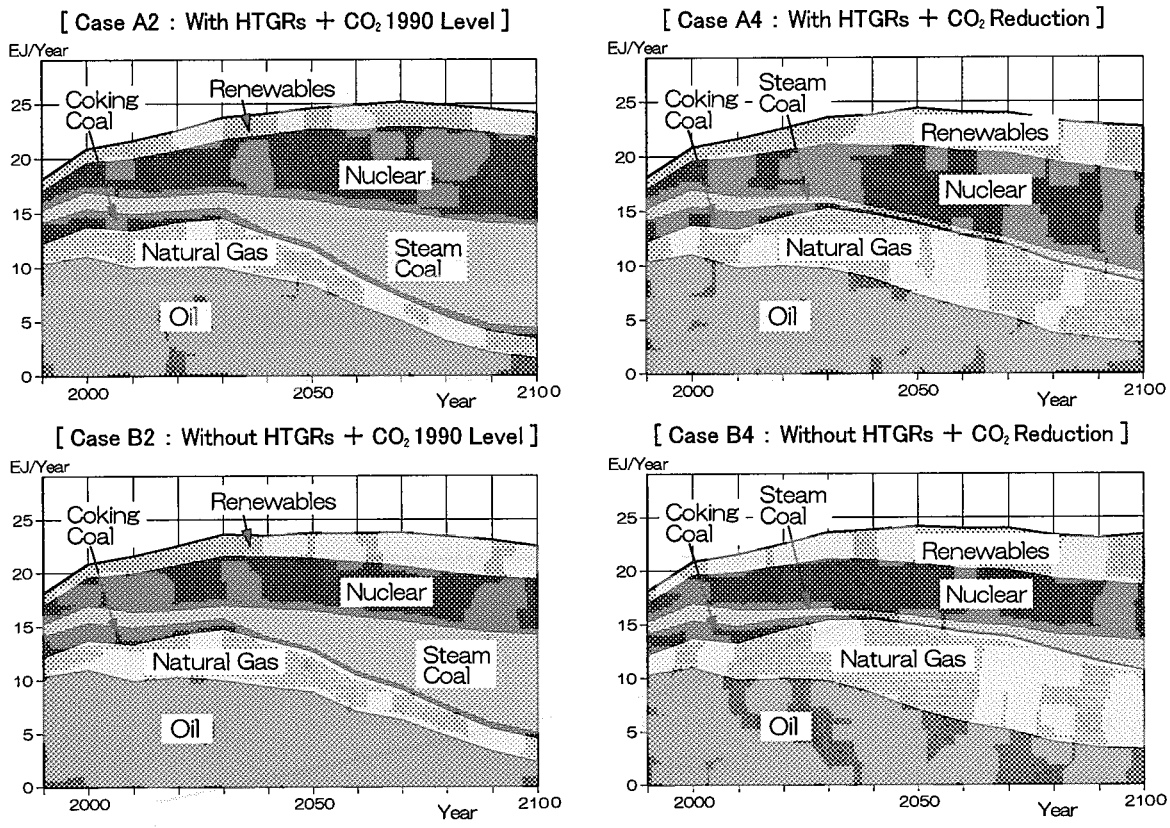

Fig. 5.4.3 Primary energy supply in each analytical case

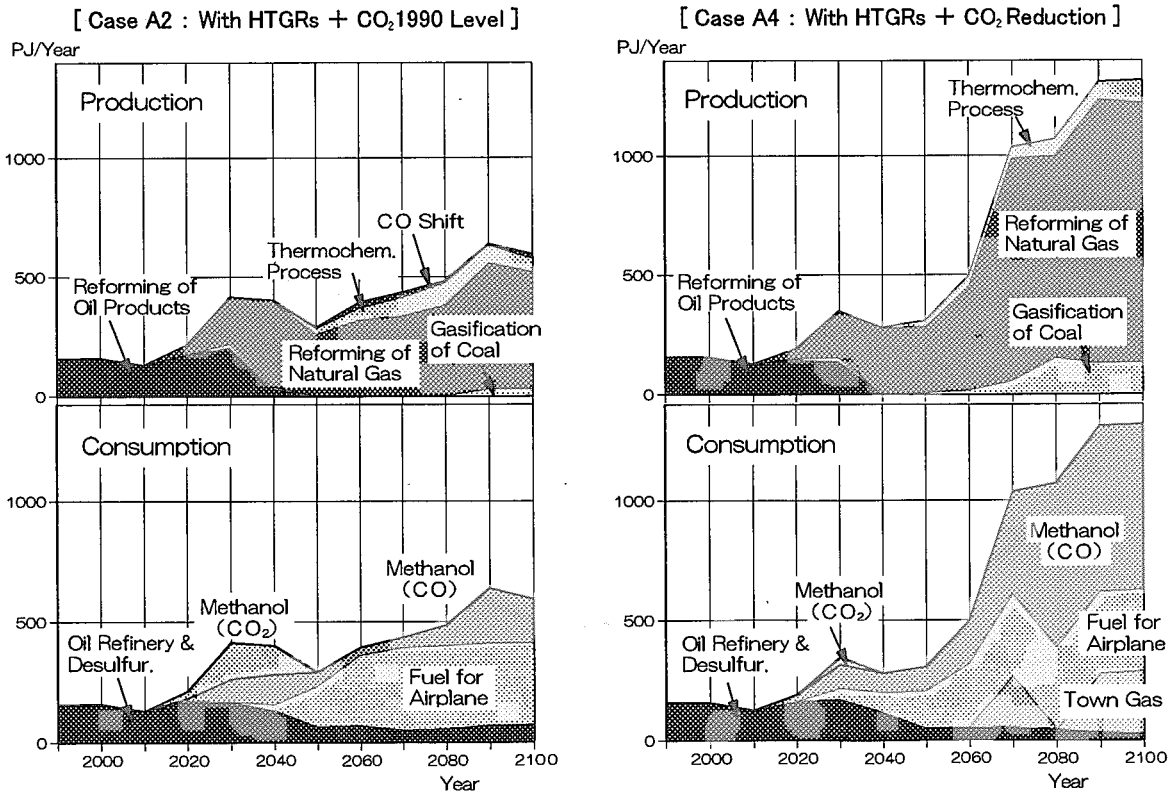

Fig. 5.4.4 Hydrogen production and consumption in analytical case A2 and A4

5.5 Development of Database on Fuel Cycle of Future Nuclear Reactors

Y. Tanaka and O. Sato
(*E-mail:* ytanaka@ruby.tokai.jaeri.go.jp)

In order to make a study on the development of future nuclear energy systems in Japan by using the JALTES model, (abbreviated as JALTES study), the database for future nuclear power plants and relevant fuel cycle facilities was developed. The reactor types selected for the database are reduced moderation water reactors (RMWRs), sodium-cooled fast breeder reactors and gas-cooled fast breeder reactors. RMWRs are expected to take a complementary role to FBRs before the era of FBR, or to substitute FBR , since it would take long time to reduce high capital cost and to enhance maintainability of FBRs. The primary design objective of RMWR is its early introduction into nuclear electric generation system with capability of plutonium breeding based on the present water reactor technology. Introduction of the first of the kind of RMWR is expected to be around the year 2020.

As a summary of the database on the future nuclear power plants, basic design specifications and annual fuel charge/discharge data are described in the Table 5.5.1. Two types of FBR with different discharge burn-ups are considered taking into account the progress of cladding materials that allow the target average discharge burn-up of 100 and 150 GWd/t. Two types of RMWR, i.e., the boiling water reactor type and the pressurized water reactor type with heavy water coolant are under a conceptual design study. The annual amount of fissile plutonium charge/discharge of RMWR tends to be larger by factor 2.5 - 3.0 than that of two FBRs.

As a summary of the database on the fuel cycle facilities, basic specifications of those supporting the present UO_2 fueled LWR, MOX fueled LWR and of the conceptual fuel cycle facility to support sodium cooled FBR are indicated in the Table 5.5.2. The table shows the capacity and the design requirement of relevant fuel fabrication, interim storage, reprocessing and radioactive-waste disposal. At present, the reprocessing facility for the UO_2 fueled LWR, is under construction and will begin its operation in July 2005. The concept of the interim spent fuel storage facility[1] and the storage and disposal facility of high level radioactive waste[2] recently have been reported from the national investigation committees. A conceptual design study for the fuel fabrication and reprocessing facility for MOX fueled FBR is being

performed at JNC under the title of "Feasibility Studies on Commercialized Fast Reactor Cycle System"[3].

The JALTES study involves an economic analysis on long term scenarios of nuclear power generation, so that the database is being expanded to include the cost of whole nuclear energy systems, primarily composed of reactor construction cost, operation & maintenance cost and fuel cycle cost. The fuel cycle cost data were compiled by both evaluation and investigation of the previous study performed in Japan. The summary of fuel cycle cost data is also shown in Table 5.5.2. Furthermore the fuel cycle cost data evaluated by OECD/NEA working group[4] and the target values the of JNC's feasibility study[3] are quoted in the table for the sake of comparison.

By applying these database of the reactors and their fuel cycle in the further JALTES study, the role of RMWR and its limitation in the future nuclear energy system in Japan will be clarified from the viewpoints of natural uranium consumption, plutonium balances and cost of nuclear energy systems.

References

1) Advisory Committee for Energy, Atomic Energy Subcommittee (Interim Report): "For the Realization of the Transitional Storage of Recycling Fuel Resources" (1998)(in Japanese).

2) ibid. : "The Ideal Way of the Institutionalization of High-level Radioactive Waste Disposal Business" (1999) (in Japanese).

3) Noda H. (Japan Nucl. Cycle Develop. Inst.): "Current Status of Feasibility Studies on Commercialized Fast Reactor Cycle System", Journal of the AESJ, 427-7(2000).

4) OECD/NEA : "The Economics of the Nuclear Fuel Cycle"(1994).

Table 5.5.1 Summary database for fuel balances and core specifications of the future nuclear reactors

Reactor	RMWR^{B}	RMWR^{P}	FBR	FBR	FBR
Coolant	Light Water	Heavy Water	Sodium	Sodium	Helium
Fuel	MOX	MOX	MOX	MOX	MN
Fuel Type	Pellet	Pellet	Pellet/Granular	Pellet/Granular	Pellet/Granular
Conversion Ratio	1.06	1.03	1.23	1.21	1.37
Average Discharge Burnup (GWd/t)	45	52	100	150	100
Fuel Charge (tHM/y/GWe)					
Uranium	28.51	33.04	19.03	9.62	23.96
Plutonium (including Am)	3.12	3.71	1.34	0.95	1.3
Fissile Plutonium	1.81	2.51	0.9	0.64	0.87
Fuel Discharge (tHM/y/GWe)					
Uranium	27.29	31.84	17.93	8.53	22.61
Plutonium (including Am)	3.29	3.84	1.59	1.14	1.64
Fissile Plutonium	1.95	2.58	1.11	0.79	1.2
Electric Power (MWe)	1100	1000	1000	1000	1000
Thermal Power (MWt)	3188	2900	2420	2420	2900
Thermal Efficiency (%)	34	34	40	40	38
Cylcle Length of Operation (months)	15	15	17	17	15
No. Fuel Exchange Batchs	4	3	3	3	3

Note: The super script B stands for BWR type and the super script P for PWR type.

Table 5.5.2 Summary database for the fuel cycle facilties, their status and the unit fuel cycle costs that're supporting the present-day reactors and the future nuclear reactors

Reactor	LWR	MOX-LWR	FBR	RMWR
Fuel	UO2	Low-Pu MOX	High-Pu MOX	High-Pu MOX
Fuel Fabrication Facility	Commercial	Planning (JNFL)	Design Study[3]	TBD
Capacity	～1500tU/y	100tHM/y	50 or 200tHM/y[3]	>32^{B}-37^{P}tHM/y/GWe
Pu-Enrichment	-	<4.4^{B}-8.5^{P}wt%	<25wt%	29^{B}-25^{P}wt%
Fabrication Cost ($/kgHM)				
This Compilation	610～900	1000～2090	1400[3]	1000～2100
OECD data	200～350[4]	800～1400[4]	-	-
Spent Fuel Interim Storage Facility	Planning[1]	Undecided	Unnecessary	Unnecessary
Capacity	5000tHM[1]			
Storage Cost ($/kgHM)				
This Compilation	270～450			
OECD data	(51+5/y)[4]			
Reprocessing Facility	Rokkasho(JNFL)	Undecided	Design Study[3]	TBD
Capacity	800tU/y		50 or 200tHM/y[3]	>32^{B}-37^{P}tHM/y/GWe
Burnup	≦55GWd/t		≒150GWd/t	45^{B}-52^{P}GWd/t
Fissile Concentration	U-235≦3.5wt%			18.0^{B}-17.0^{P}wt%
VHLW Production Rate	1.2VHLW/tHM			
Reprocessing. Cost ($/kgHM)				
This Compilation	1740～2610	-	2500[3]	1740～3750
OECD data	540～720[4]	500～1000[4]	-	-
VHLW Disposal Facility	Planning[2]	Undecided	Undecided	Undecided
Capacity	40000[2]		-	-
Disposal Cost ($/kgHM)				
This Compilation	110～1000		-	-
OECD data	90～580[4]		-	-

Note: The super script B stands for BWR type and the super script P for PWR type.

6. Reactor Structural Materials

Research items carried out were classified into three different categories,. i.e., irradiation assisted stress corrosion cracking (IASCC) study, demonstration test on lifetime reliability of structural materials for advanced prototype power reactors (STA commissioned research), and development of material performance database.

In the field of IASCC study, effects of irradiation temperature and cold working on IASCC behavior of model austenitic stainless steels were investigated. The results can be summarized as follows: (1) Solution-annealed specimens irradiated at 323 K showed susceptibilities to IGSCC in oxygenated water. (2) Addition of carbon enhanced IASCC accompanied by a change in the fracture morphology and increased radiation hardening after irradiation at 513 K, while it seems to increase an uniform elongation of specimens after irradiation at 323 K. (3) Cold working before irradiation is effective to suppress IASCC susceptibility. In the field of IASCC study, in-pile crack initiation detection technique, in-pile crack length measurement techniques, in-pile strain measurement techniques, etc. also have been tried to be developed aiming at performing in-pile IASCC tests using JMTR.

In the demonstration test on lifetime reliability of structural materials for advanced prototype power reactors, a series of mechanical tests was performed on the pre- and post irradiation type 304 stainless steel which is used as the structural material of Japanese prototype fast breeder reactor "Monju". Mechanical properties of neutron irradiated materials are affected by both the displacement damage level and the amount of gaseous ingredient such as H and He produced by nuclear transmutation. Three types of neutron irradiation capsules, therefore, were specially designed, namely thermal neutron shielding, normal, and thermal neutron trapping types, in order to examine the effect of He production level on mechanical properties of type 304 stainless steel using JMTR. As for creep properties, in-pile tests were also carried out. Based on the test results, it was confirmed that the material of Monju has reliability and integrity after neutron irradiation corresponding to 30 year operation.

In the field of material performance database, JAERI material performance database (JMPD) and the distributed database named "Data-Free-Way" have been developed. Based on the experience of development of JMPD, Data-Free-Way was constructed under the collaboration of JAERI, the National Research Institute for Metals, the Japan Nuclear Cycle Development Institute and the Japan Science and Technology Corporation in order to share fresh and stimulating information as well as accumulated information for the development of advanced materials, for the design of structural components, etc.

6.1 Effect of Irradiation Temperature on IASCC Behavior of Model Stainless Steels

T. Tsukada, H. Yamamoto, F. Takada and H. Tsuji
(*E-mail:* ttsukada@popsvr.tokai.jaeri.go.jp)

The irradiation assisted stress corrosion cracking (IASCC) has been investigated in the last decade mainly from a view point of the aging of LWR core components. On the other hand, it is recently concerned as one of the possible degradation phenomena of structural materials of the water-cooled components of ITER.[1] However, a temperature range of concern for ITER design, which is below about 473 K, is lower than that for LWRs, and the experimental result on IASCC in the lower temperature range is very limited. Therefore, the effect of irradiation temperature on IASCC behavior was examined in the present study from both viewpoints of understanding IASCC mechanism and the fusion reactor design.

Chemical compositions of two materials of type 304 austenitic stainless steels used for the present study are shown in Table 6.1.1, where alloy HP is a high purity type base alloy and alloy HP+C is doped with carbon into the alloy HP. Solution annealed materials of both alloys were machined into the round bar type tensile specimens. Those specimens were irradiated at 513 K in the Japan Research Reactor No.3 (JRR-3) and at 323 K in JMTR. In JRR-3, the specimens were irradiated in an inert gas environment and exposed in a primary coolant water in JMTR. Fast neutron fluence and irradiation period were 6.7×10^{24} n/m^2 (E>1MeV), 3925 h in JRR-3 and 9.0×10^{24} n/m^2 (E>1MeV), 1187 h in JMTR, respectively.

After the irradiation, susceptibilities to SCC of specimens were examined by the slow strain rate testing (SSRT) at 573 K in the water saturated with pure-oxygen at room temperature where the dissolved oxygen (DO) level was 42 ppm. A flow rate of water was 5 l/h and conductivity was below 0.2 mS/cm at the inlet of the autoclave and in the range from 1.0 to 1.7 mS/cm at the outlet. Specimens were strained up to failure at a strain rate of 1.7×10^{-7} s^{-1}. Fracture surfaces of SSRT specimens were examined with a scanning electron microscope (SEM) to evaluate the susceptibility to IASCC.

In Fig. 6.1.1, the engineering stress-strain (S-S) curves during SSRTs of alloys HP and HP+C irradiated at 513 K or at 323 K and unirradiated specimens are compared. Specimens irradiated at 513 K showed high susceptibilities to IASCC and the dominant fracture modes were intergranular type (IG) in alloy HP and transgranular type (TG) in alloy HP+C. In

addition, the maximum stress level of alloy HP+C was higher than that of alloy HP. The addition of carbon had affected both the fracture mode and radiation hardening. In case of the alloys irradiated at 323 K, as shown in Fig.6.1.1, total elongation of both alloys HP and HP+C are larger and the yield stress levels are lower than those of specimens irradiated at 513 K. The effect of carbon addition on the total elongation by SSRT were different between two irradiation temperature levels; at 513 K the carbon addition enhanced a reduction of the total elongation, while at 323 K the carbon addition increased the total elongation

SEM photographs in Fig. 6.1.2 show the fracture surfaces of SSRT specimens of alloy HP. Although fractions of diametrical reduction and IGSCC area are different for each irradiation temperature, the similar morphologies are observed in both specimens. On the other hand, as shown in Fig. 6.1.3, the fracture surface morphologies of alloy HP+C are remarkably different between the specimens irradiated at 513 K and 323 K; at 513 K a cracking initiated as IGSCC and then propagated as TGSCC, and at 323 K the specimen failed by IGSCC. Here, it must be noticed that the failure of the latter specimen occurred at a portion of the specimen shoulder where a diameter is 6 mm comparing with 4 mm at gauge section. Loaded stress concentrated at this portion during SSRT can be estimated as about 260 MPa from a ratio of the cross sections and maximum stress during SSRT. This stress level is nearly half of the yield stress level of irradiated HP+C alloy as seen in Fig. 6.1.1, therefore a strain rate at this failed portion is negligibly small.

As seen in Fig. 6.1.1, the specimen of alloy HP+C showed work hardening with a large elongation and then cracked at the shoulder portion in a short time. It may imply that an addition of carbon did not reduce IASCC susceptibility, but it increased a durability to localized deformation and consequently suppressed IASCC at the gauge section. Katsura et al.[2] performed the uniaxial constant load (UCL) tests on neutron irradiated stainless steels and some of their specimens failed at the pinhole sections outside the gauge section. The reason of those irregular fractures of specimens might be inferred as radiolysis of water in a crevice due to gamma radiation from the specimen itself. High susceptibility to IGSCC of their specimens failed at the pinhole section is similar to the present specimen of alloy HP+C. However, in our experiments no other SSRT specimens irradiated at higher temperatures in the past had shown such irregular cracking, so that it is difficult to attribute the cracking to the radiolysis. On the present specimen the gauge section was deformed under a relatively large strain rate, while the cracking portion was not deformed and under the nearly constant loading condition. These

situations appear to be a cause of cracking at the shoulder portion of specimen.

The conclusions are summarized as follows:

(1) Solution-annealed specimens of both alloys irradiated at 323 K showed susceptibilities to IGSCC in oxygenated water.

(2) Addition of carbon enhanced IASCC accompanied by a change in the fracture morphology and increased radiation hardening after irradiation at 513 K, while it seems to increase an uniform elongation of specimens after irradiation at 323 K.

References

1) ITER Interim Design Report (San Diego, Garching, Naka, 1995)

2) R. Katsura, J. Morisawa, M. Kodama, S. Nishimura, S. Suzuki, S. Shima and M. Yamamoto, Proc. 6th Int. Symp. on Environmental Degradation of Materials in Nuclear Power Systems - Water Reactors. (TMS, 1994) p.625.

Table 6.1.1 Chemical compositions of specimen materials tested (mass%)

Alloy	C	Si	Mn	P	S	Cr	Ni	Ti	Al	N	Fe
HP	0.003	0.01	1.36	0.001	0.0014	18.17	12.27	0.01	0.16	0.0014	bal.
HP+C	0.098	0.03	1.39	0.001	0.0020	18.30	12.50	<0.01	0.11	0.0016	bal.

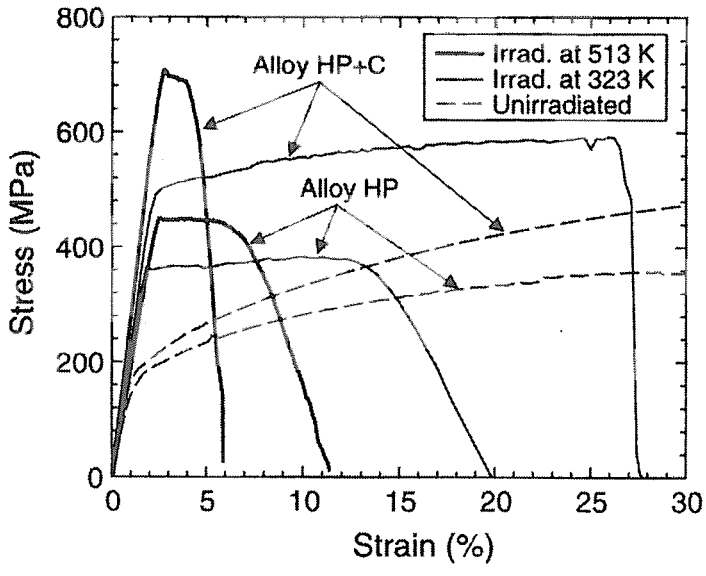

Fig. 6.1.1 Stress-strain curves for SSRT on the specimens irradiated at 513 K and 323 K

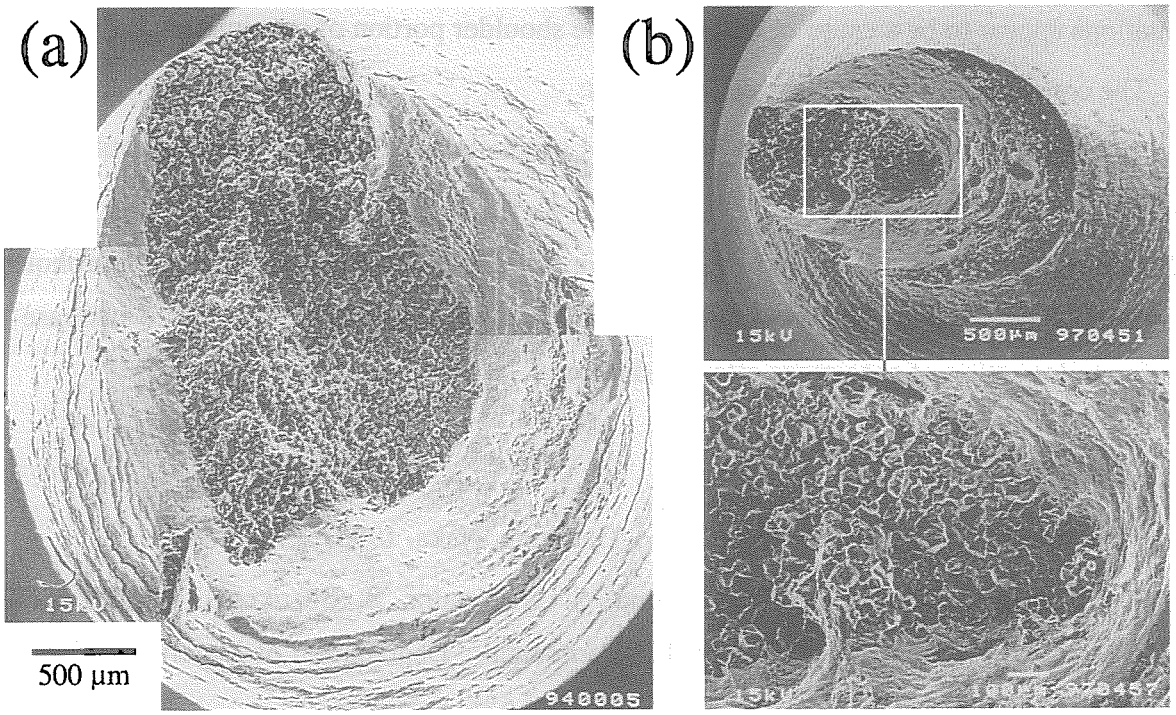

Fig. 6.1.2 Fracture surfaces of SSRT specimens of alloy HP
Irradiated at (a) 513 K and (b) 323 K

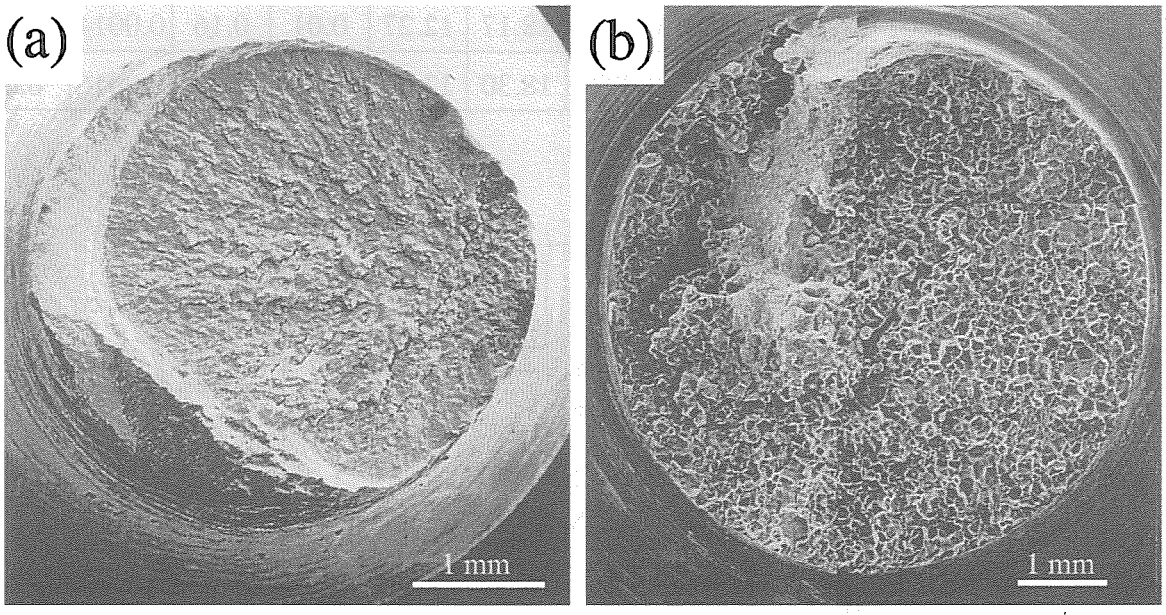

Fig. 6.1.3 Fracture surfaces of SSRT specimens of alloy HP+C
Irradiated at (a) 513 K and (b) 323 K

6.2 IASCC Susceptibility of Cold Worked Stainless Steels Irradiated at JRR-3

T. Tsukada, H. Yamamoto, F. Takada and H. Tsuji
(*E-mail:* ttsukada@popsvr.tokai.jaeri.go.jp)

One of the concerns about IASCC behavior of austenitic alloys is an effect of cold-working from viewpoints of industrial application and mechanistic understanding. It is known that the cold working sometimes induces a susceptibility to stress corrosion cracking. On the other hand, the cold working is the usual method to improve the strength of materials and is known as the effective way to diminish void swelling of in-core materials[1]. In addition, the authors had found prominent effects of carbon addition into the model stainless steels on IASCC fracture morphology, radiation hardening[2] and on microstructural evolution by neutron irradiation[3]. The aim of the present study is to examine the effects of cold working and carbon addition on IASCC behavior.

Two types of 304 austenitic stainless steels used in the present study have the chemical compositions shown in Table 6.2.1, where alloy HP is a high purity type base alloy and alloy HP+C is doped with carbon into the alloy HP. 50 % cold-worked materials of both alloys were machined into the round bar type tensile specimens with a diameter of 4 mm at the gauge portion. Specimens were irradiated at 513 K in the Japan Research Reactor No.3 (JRR-3). Fast neutron fluence and irradiation period were 6.7×10^{24} n/m^2 (E>1MeV) and 3925 h, respectively. After the irradiation, susceptibilities to SCC of specimens were examined by the slow strain rate testing (SSRT) in high-temperature water using the test machine installed in a hot-cell. SSRTs were carried out at 573 K in the water saturated with pure-oxygen at room temperature where a dissolved oxygen (DO) level was 42 ppm. A flow rate of water was 5 l/h and conductivity was below 0.2 mS/cm at the inlet of the autoclave and in a range from 1.0 to 1.7 mS/cm at the outlet. Specimens were strained up to failures at a strain rate of 1.7×10^{-7} s^{-1}. Fracture surfaces of SSRT specimens were examined with a scanning electron microscope (SEM) to evaluate the susceptibility to IASCC.

The stress-strain curves obtained at 513 K are shown in Fig. 6.2.1 which includes the results of both irradiated and unirradiated specimens. Although the maximum stresses increased by radiation hardening, basically stress-strain behavior of the specimens was not changed by irradiation. Fig. 6.2.2 shows SEM photographs of fracture surfaces of the cold-

worked and irradiated specimens. Neither alloys HP nor HP+C showed appearance of SCC.

Cold working is known as one of the effective methods to suppress a void swelling in a higher neutron fluence region. Dumbill et al. [4] suggested that cold working could suppress RIS (Radiation Induced Segregation), e.g., chromium depletion, and consequently susceptibility to IASCC. They analyzed RIS on the ion irradiated specimens and found that chromium depletion was reduced by 5 % cold-working. Kodama et al. [5] reported that the 20 % cold worked type 304 stainless steels showed no susceptibility to IGSCC at 1.7×10^{25} n/m^2 (E>1MeV). In the present study, no IGSCC was observed in the cold-worked alloys HP or HP+C and it can be concluded that 50% cold-working suppressed IASCC. This effect of cold working may be attributed to an increase in a density of dislocation network and therefore the number of sink of radiation induced point defects. As seen in Fig. 6.2.1, a fracture elongation of alloy HP decreased after irradiation but that of alloy HP+C decreased slightly, therefore addition of carbon seems to retard a fracture of irradiated specimen.

As a result of the present study, it can be concluded that the cold working before irradiation is effective to suppress IASCC susceptibility. However, it should be noted that a loading condition by SSRT is very intensive for specimens and it may modify the initial microstructure induced by cold working and this situation may be different from that under a loading condition in actual components. Therefore, further studies are necessary to examine the cold working on IASCC applying SCC testing techniques that reproduce more realistic loading conditions expected in core components.

References

1) F.A. Garner, Proc. Symp. Phase Stability During Irradiation (AIME, 1981) p.165.

2) T. Tsukada, Y. Miwa and H. Nakajima, Proc. 7th Int. Symp. on Environmental Degradation of Materials in Nuclear Power Systems - Water Reactors. (NACE, 1995) p.1009.

3) Y. Miwa, T. Tsukada, S. Jitsukawa, S. Kita, S. Hamada, Y. Matsui and M. Shindo, J. Nucl. Mater. 233-237 (1996) 1393.

4) S. Dumbill and W. Hanks, Proc. 6th Int. Symp. on Environmental Degradation of Materials in Nuclear Power Systems - Water Reactors. (TMS, 1994) p.521.

5) M. Kodama, J. Morisawa, S. Nishimura, K. Asano, S. Shima and K. Nakata, J. Nucl. Mater. 212-215 (1994) 1509.

Table 6.2.1 Chemical compositions of specimen materials tested (mass%)

Alloy	C	Si	Mn	P	S	Cr	Ni	Ti	Al	N	Fe
HP	0.003	0.01	1.36	0.001	0.0014	18.17	12.27	0.01	0.16	0.0014	bal.
HP+C	0.098	0.03	1.39	0.001	0.0020	18.30	12.50	<0.01	0.11	0.0016	bal.

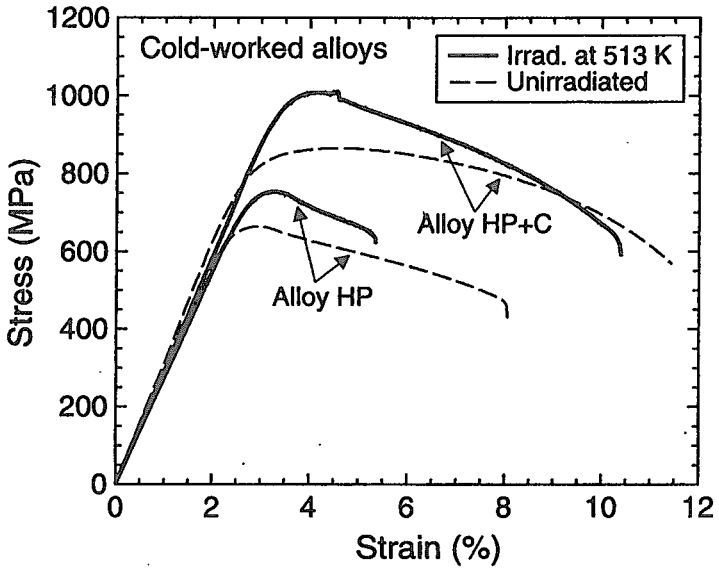

Fig. 6.2.1 Stress-strain curves from SSRT on the cold-worked specimens irradiated at 513 K and unirradiated specimens

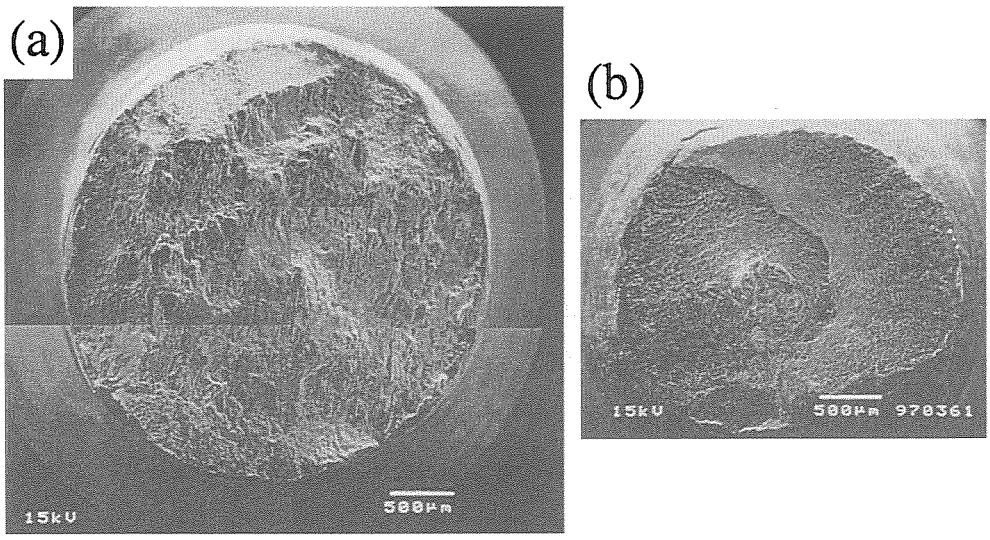

Fig. 6.2.2 Fracture surfaces of SSRT specimens of cold-worked alloys (a) HP and (b) HP+C irradiated at 513 K

6.3 Four-point Bent Beam SCC Test of Austenitic Stainless Steels in High Temperature Water

H. Ugachi, T. Tsukada, Y. Matsui, A. Maeda, Y. Kaji, M. Kikuchi, S. Kita and H. Tsuji
(*E-mail:* ugachi@cat.tokai.jaeri.go.jp)

Irradiation assisted stress corrosion cracking (IASCC) is caused by the synergistic effects of irradiation, stress and corrosion by high temperature water. It is, therefore, essential to perform in-pile SCC tests, which are material tests under the conditions simulating those of actual LWR operation, in order to clarify the precise mechanism of the phenomenon, though mainly out-of-pile SCC tests for irradiated materials have been carried out in this research field. There are, however, many difficulties to perform in-pile SCC tests. Performing in-pile SCC tests, essential techniques must be developed. Hence as a part of development of the essential techniques for in-pile SCC tests, four-point bent beam SCC tests were performed on sensitized austenitic stainless steels under the out-of-pile condition, and an irradiation capsule was produced by way of trial for in-pile SCC test using Japan Materials Testing Reactor (JMTR). Four-point bent beam SCC test technique was adopted among some SCC test methods for the following reasons in the present study.

1. Relatively many test units can be installed in the limited test space in the case of bent beam test method.
2. Independent load or strain level can be applied for each specimen in the case of bent beam test method.
3. Initial load or displacement can be applied at a constant value in longer portion in the four-point bent beam test method than that in the three-point one.

The materials tested are four heats of sensitized type 304 stainless steel. The chemical compositions, the heat treatment conditions and the Electrochemical Potentiokinetic Reactivation (EPR) test results of the materials tested are shown in Tables 6.3.1 and 6.3.2, respectively. The geometry of the test unit used in this study is shown in Fig. 6.3.1. Two types of specimens were used for out-of-pile SCC tests. They are the specimens with and without holes, the diameter of which is 1 mm, which introduce the stress concentration. The applied stress levels range from 191 MPa to 276 MPa, which roughly correspond to 0.2% proof stress levels of the specimen materials. It was attempted to detect the initiation of cracks with potential drop technique. In the first run, only the specimens without holes were exposed to

288 ℃ water for 960 h. In the second run, additional specimens with holes were exposed to 288 ℃ water for 2400 h. During the tests, no obvious signal of crack initiation was detected. After the tests, the specimens were examined with an optical microscope and a scanning electron microscope (SEM). Though some corrosion pits were observed near the hole, no cracks were detected.

Based on the above-mentioned experience, an irradiation capsule was produced by way of trial for in-pile SCC test using JMTR. Figure 6.3.2 shows the specimen portion of the capsule, which will be irradiated in the first half of 2000.

Table 6.3.1 Chemical compositions of materials tested (mass%)

Alloy	C	Si	Mn	P	S	Ni	Cr	Mo
11A	0.051	0.52	1.51	0.021	0.002	10.19	18.40	0.01
13								
22A	0.019	0.51	1.47	0.021	0.002	9.99	18.39	0.01
23A								
31A	0.079	0.50	1.47	0.021	0.001	10.00	18.47	0.01
33								
41A	0.056	1.42	1.48	0.017	0.002	9.93	18.35	<0.01

Alloy	C	Si	Mn	P	S	Ni	Cr	Mo	Alloy
11A	0.051	0.52	1.51	0.021	0.002	10.19	18.40	0.01	11A
13									13
22A	0.019	0.51	1.47	0.021	0.002	9.99	18.39	0.01	22A
23A									23A
31A	0.079	0.50	1.47	0.021	0.001	10.00	18.47	0.01	31A
33									33
41A	0.056	1.42	1.48	0.017	0.002	9.93	18.35	<0.01	41A

Table 6.3.2 EPR test results and heat treatment conditions of materials tested

Alloy	EPR(%)	Heat treatment condition (℃×min)
11A	15	600×5
13	21	600×30
22A	0.5	650×10
23A	1.7	650×30
31A	27	600×5
33	22	600×15
41A	15	600×5

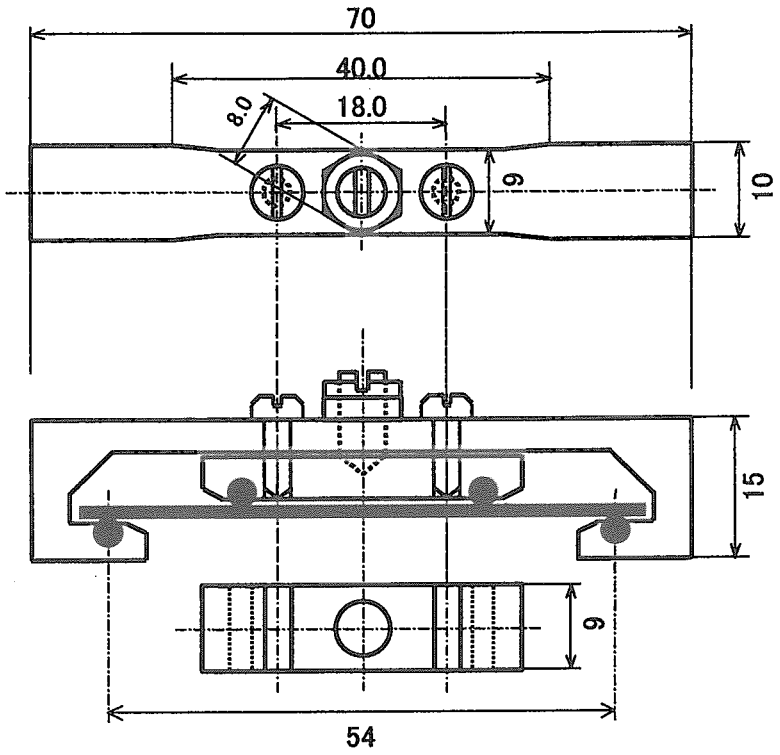

Fig. 6.3.1 Geometry of test unit

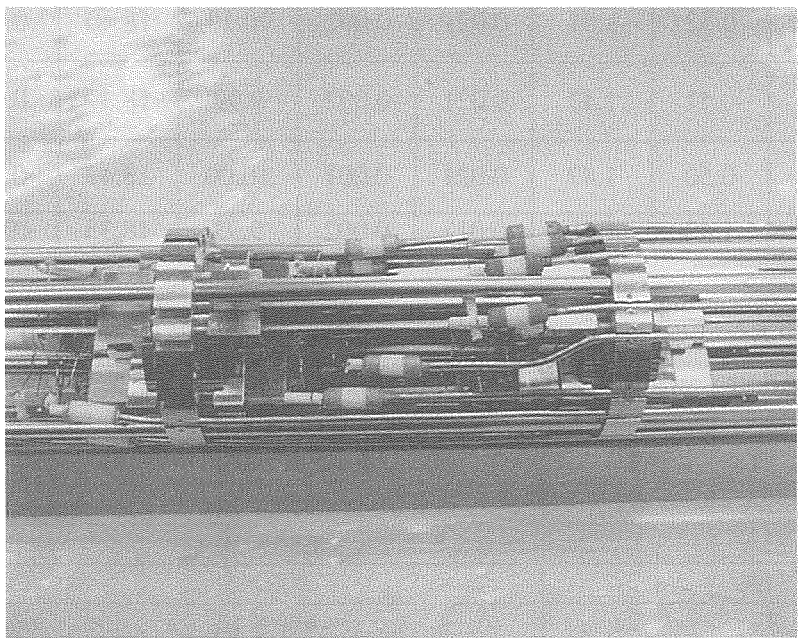

Fig. 6.3.2 Specimen portion of irradiation capsule produced by way of trial for in-pile SCC test.

6.4 Evaluation of DCPD and ACPD Methods for Monitoring of Crack Length

Y. Kaji and H. Tsuji

(E-mail: kaji@popsvr.tokai.jaeri.go.jp)

In order to evaluate the characteristics of direct current potential drop (DCPD) and alternating current potential drop (ACPD) methods, the crack growth tests were performed at room temperature in air for monitoring crack length of austenitic stainless steels by both DCPD and ACPD methods.

The fatigue crack growth tests were carried out for 0.5TCT specimens and the stress ratio and frequency of the tests were 0.1 and 20Hz, respectively. The potential drop was measured in every 0.2mm crack length at the maximum load value. The surface crack length was measured by optical methods and final crack length was measured on the fracture surface of the 0.5TCT specimen.

Fig. 6.4.1 shows relation between potential drop of ACPD method and crack length for two specimens. This figure shows the results of two crack growth tests performed in the same experimental conditions in order to confirm the scatter of the

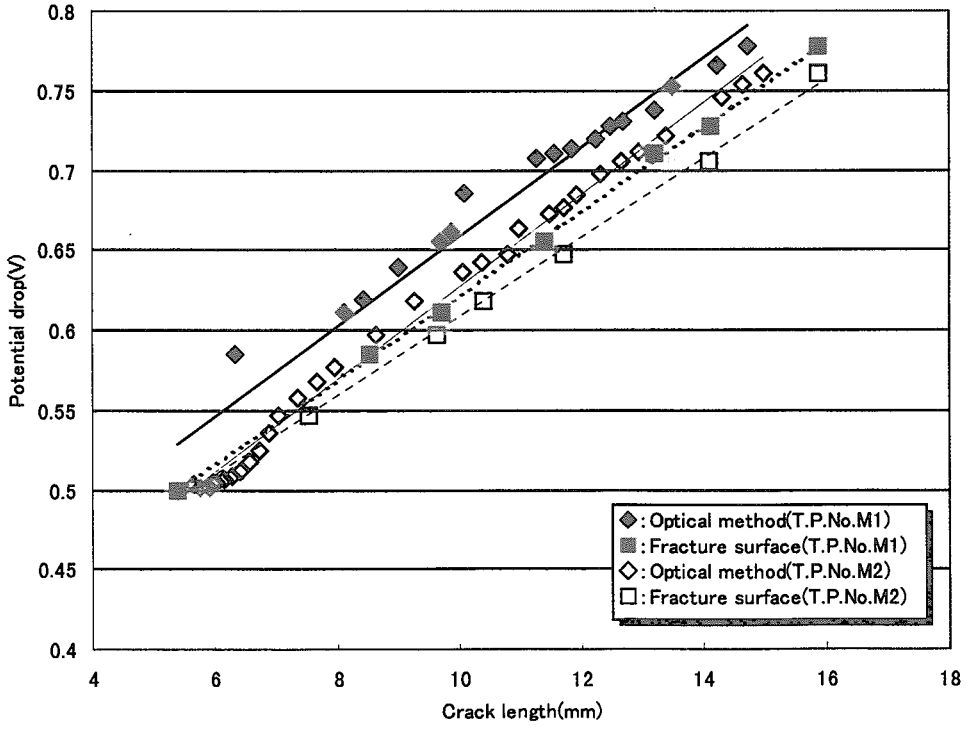

Fig. 6.4.1 Relation between potential drop and crack length in ACPD method

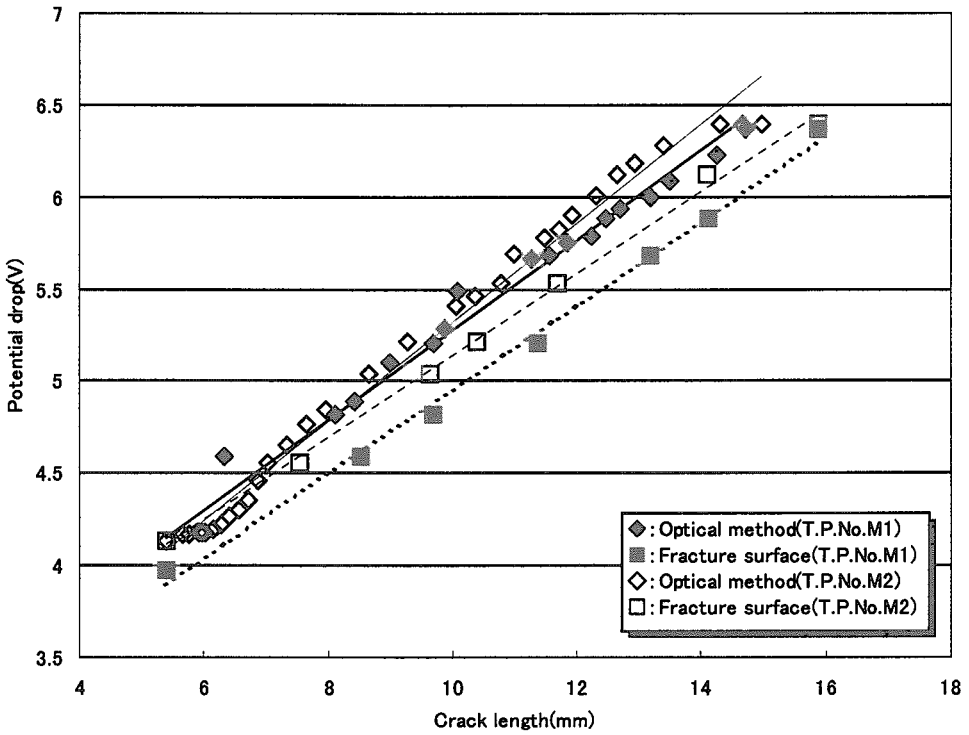

Fig. 6.4.2 Relation between potential drop and crack length in DCPD method

data. Good correlation was observed between potential drop and crack length. The reproducibility of the relation was good and the scatter of the data was relatively small. Fig. 6.4.2 shows relation between potential drop of DCPD method and crack length for two specimens. Good correlation was observed between potential drop of DCPD method and crack length in the same way as the ACPD method. Therefore the difference between ACPD and DCPD methods was not observed in these fatigue crack growth tests for type 304 stainless steels in air. It is possible to measure the crack length of the 0.5TCT specimens for type 304 stainless steels by both ACPD and DCPD methods.

6.5 Application of Capsule Type Strain Gage and Fiber Optic Grating Strain Sensor for Measurement of Strain under Irradiation Environment

Y. Kaji, Y. Matsui, S. Kita, H. Ide, T. Tsukada and H. Tsuji
(E-mail: kaji@popsvr.tokai.jaeri.go.jp)

In order to evaluate the performance of capsule type strain gage and fiber optic grating sensor under irradiation environment, the performance tests at elevated temperature before irradiation for fiber optic grating sensor and in-pile tests for both sensors were performed.

As for capsule type strain gage, it is found that gage factor almost didn't change and both its electric resistance and strain output decreased by irradiation effect. Fig. 6.5.1 shows relation between ratio of electric resistance and fast neutron fluence (E>1MeV) for capsule type strain gage in in-pile tests. A correlation was found between the change ratio of the electric resistance of the capsule type strain gage and fast neutron fluence as shown in Fig. 6.5.1.

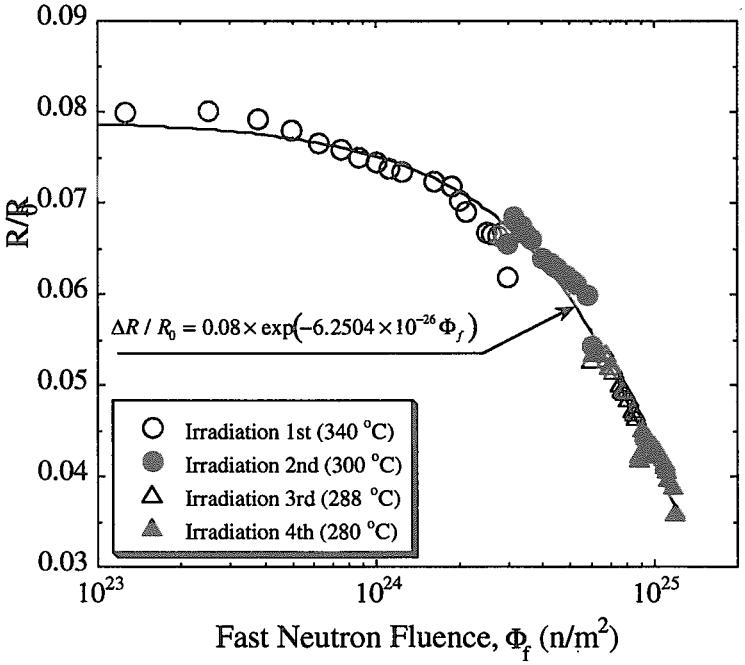

Fig. 6.5.1 Relation between ratio of electric resistance and fast neutron fluence

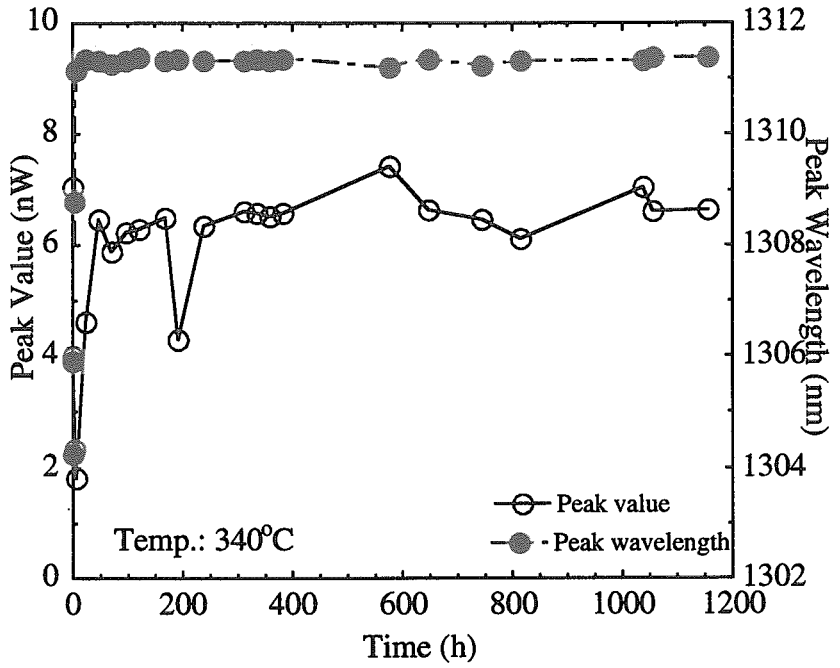

Fig. 6.5.2 Change of peak value and peak wavelength of Bragg reflected wave at 340°C

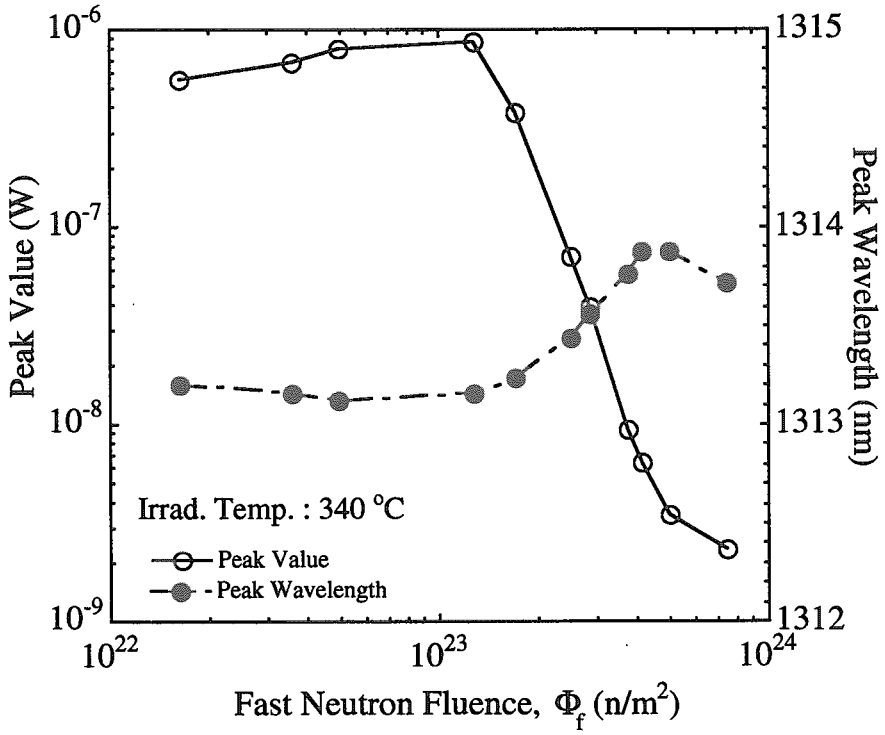

Fig. 6.5.3 In-pile test results for fiber grating optic sensor

As for the performance tests results at elevated temperature before irradiation, Fig. 6.5.2 shows relation between peak wavelength of Bragg reflected wave and time for fiber optic grating sensor. The performance tests at elevated temperature (340°C) were carried out for 1000 h. And it was found that the peak wavelength and peak value were almost constant for 1000 h as shown in Fig.6.5.2.

As the in-pile test results for fiber optic grating sensor, change of peak value and peak wavelength against fast neutron fluence are shown in Fig. 6.5.3. As in-pile characteristic of the fiber optic grating sensor agrees with out-of-pile test results, it may be applicable for measuring strain under irradiation environment below $1x10^{23}n/m^2$ (E>1MeV).

6.6 Analysis of Stress Corrosion Cracking (SCC) Data Using JAERI Material Performance Database (JMPD)

Y. Kaji, Y. Miwa, T. Tsukada, H. Tsuji and H. Nakajima
(*E-mail:* kaji@popsvr.tokai.jaeri.go.jp)

Fundamental studies of structural materials have been performed at JAERI regarding practical applications for nuclear plants. For the evaluation of reliability and safety of structural materials, various material tests have been conducted. The JMPD was designed for mechanical properties data such as fatigue crack growth, creep, tensile, low-cycle fatigue, SSRT, etc.

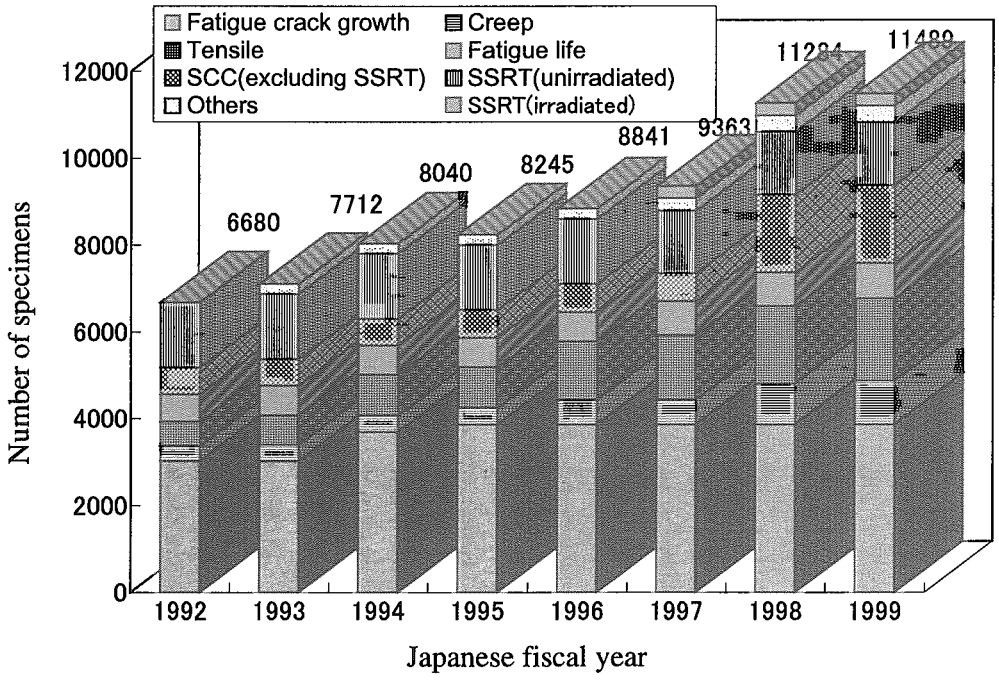

Fig. 6.6.1 Transition of data stored in JMPD

The data stored in the JMPD by the end of March 2000 are listed in Fig.6.6.1, in which the data from around 11,000 test pieces are prepared for data evaluation. Only the data of the materials whose origin such as chemical compositions and heat treatment conditions as well as experimental methods are clear have been stored.

As for the part of the SCC database, about 1000 data of SCC growth rate from 21 published papers were input. The SCC growth rate data consist of those of thermally

sensitized type 304 and 316 alloys under constant load condition at 403-561K in high temperature water containing various concentration levels of dissolved oxygen.

Figure 6.6.2 shows the relationship between da/dt and electrical conductivity of the water. The data are classified into three groups by the level of dissolved oxygen and alloy type. The SCC growth rate da/dt in lower DO environment is found to be lower for type 304 alloys. The rate for type 316 alloys is lower than that for type 304 alloys under the same DO condition.

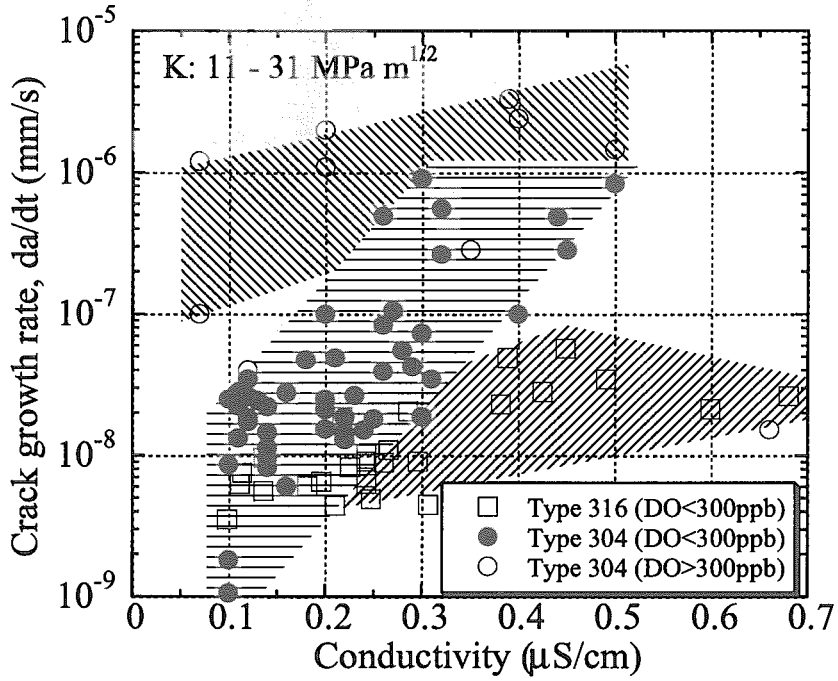

Fig. 6.6.2 Relationship between da/dt and electrical conductivity

Since the DO content in high temperature water is an essential factor for SCC growth rate, all data are classified into three groups by the level of DO content and alloy type on da/dt-K relationship in Fig. 6.6.3. A tendency observed is that the SCC growth rate of both type 304 and 316 alloys tested in lower DO environment is lower than that in higher DO environment in Fig. 6.6.3. It is difficult to deduce any relation between type 304 and 316 alloys regarding da/dt-K relationship under lower DO condition, because the data are scattered over a wide range of da/dt through the K for type 304 alloys.

In Fig. 6.6.4, therefore, the rates from type 304 alloys are plotted separately to confirm the effect of dissolved hydrogen (DH) on the da/dt-K relationship. The range of DH is from 50 to 500ppb for BWR condition in Fig. 6.6.4. As shown in Fig. 6.6.4, the rates in lower DO

and DH environments show lower values than those under normal DO environments. This can be attributed to the DH addition.

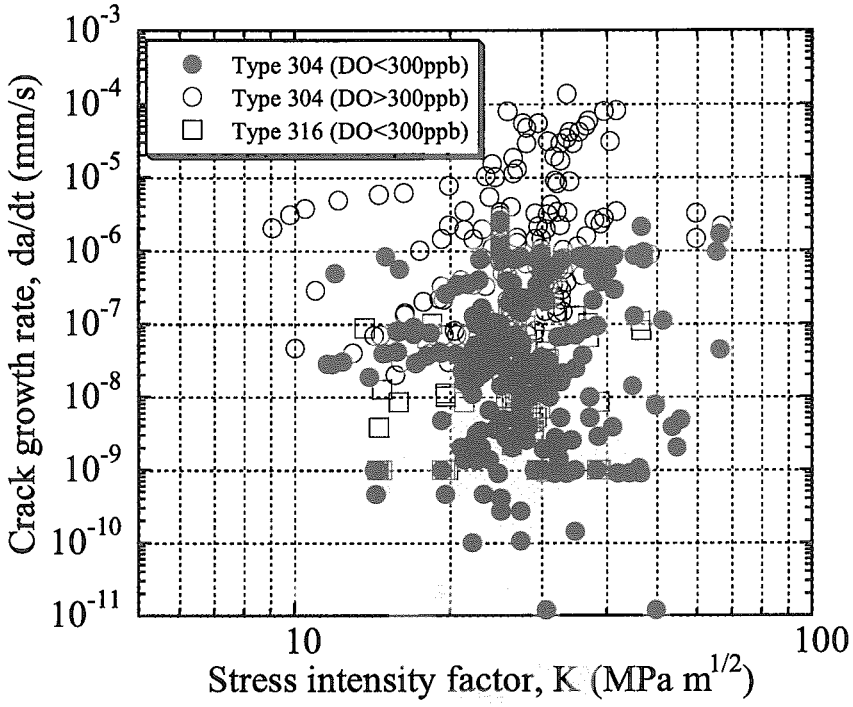

Fig. 6.6.3 Effect of dissolved oxygen on da/dt-K relationship

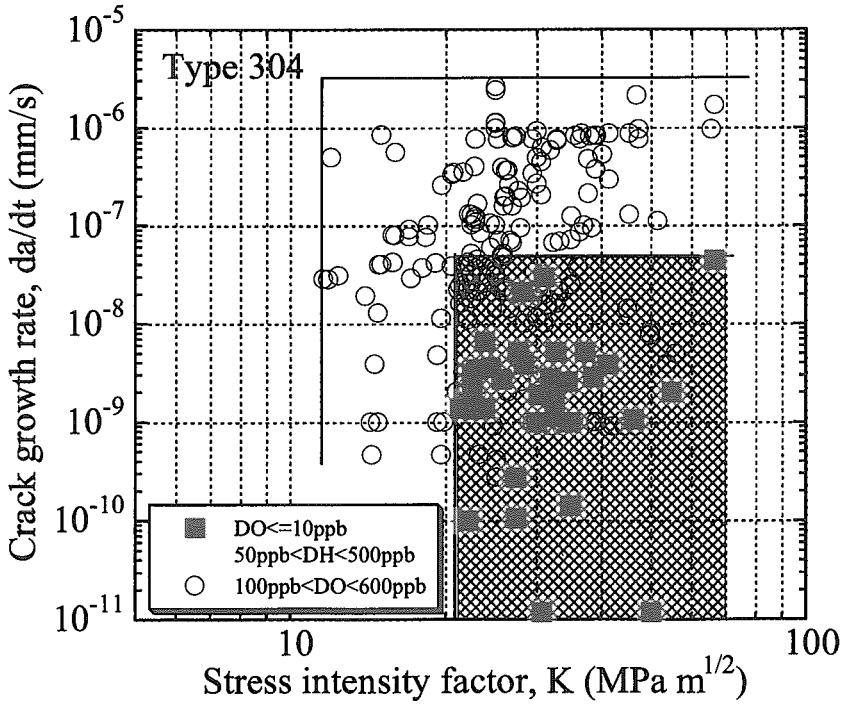

Fig. 6.6.4 Effect of hydrogen addition on da/dt-K relationship

6.7 Improvement of Users' Friendliness of JAERI Material Performance Database (JMPD)

T.Sakino, Y.Kaji and H.Tsuji
(*E-mail:* sakino@jmpdsun.tokai.jaeri.go.jp)

The JAERI Material Performance Database (JMPD) was developed with a view to utilizing such material performance data efficiently[1)-3)]. The database structure for metallic materials in the JMPD was originally determined in a three-level hierarchy. Six categories such as data source, material, specimen, test method & data reduction, test condition, and test result, were classified into the primary level. Twenty-five tables were considered to be in the secondary level. More than 420 data items were prepared for the final level. The JMPD is implemented with Oracle, which is a relational database system on a workstation. A data entry supporting system is implemented with spreadsheet-type software on a personal computer and is connected with the JMPD by middle software through Ethernet.

The main feature of this system is (a) to design the input sheet by extracting the data item from the data dictionary of the JMPD, (b) to enter the data by using the guide function. Users can access the Internet through their own computers in the WWW browser, retrieve the required data from JMPD and output the graph.

The original interface of the JMPD has been replaced by the newly developed one in order to improve the user-friendliness. Figure 6.7.1 shows the flow diagram of narrowing the retrieval conditions. Users can start the data search from any screens of reference, material, test type, description, or test condition as shown in Fig. 6.7.1. Using the new interface, the searched results can be saved as the file. Users, therefore, can easily extract various kinds of graphic output using commercial graphic software.

Figure 6.7.2 shows the flow diagram of an example of searching the creep data of Alloy 800H. When a user selects "creep test" and "Alloy 800H" as the test type and as the material, respectively, the retrieval condition and the list of retrieval results are displayed. In order to obtain the graphic output, the items of X-axis and Y-axis as well as the symbols of the plotting points will be selected. On the screen, the number of the data for each symbol is also displayed. On the graph, the test condition for each plotting point is easily checked by clicking the point.

References

1) N. Yokoyama, T. Tsukada, and H. Nakajima, JAERI-M90-237 (in Japanese) (1987).

2) H. Tsuji, N. Yokoyama, T. Tsukada and H. Nakajima, J. Nucl. Sci. Technol., Vol. 30, No. 12, pp.1234-1242 (1993).

3) N. Yokoyama, H. Tsuji, T. Tsukada and M. Shindo, ASTM STP 1311, pp.261-272 (1997).

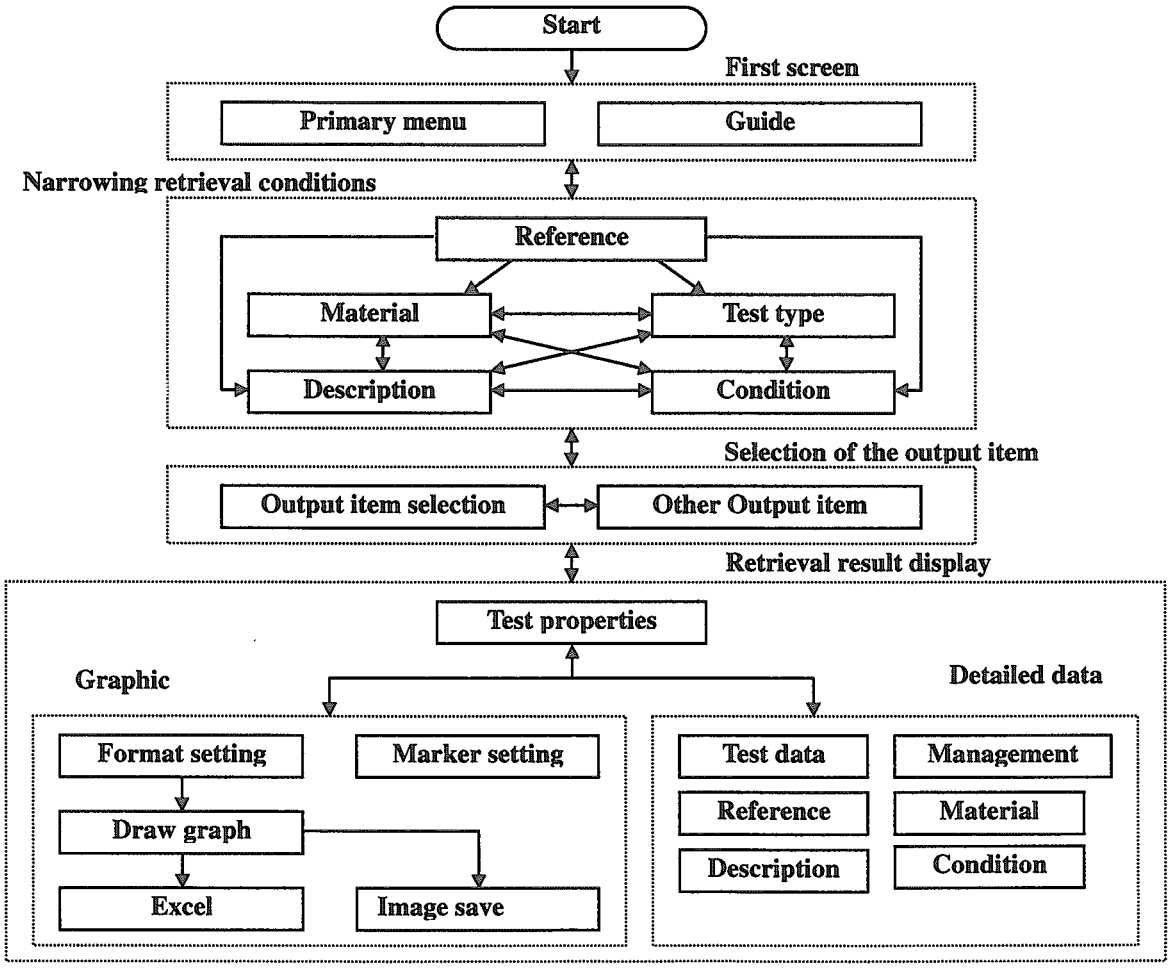

Fig. 6.7.1 Flow diagram of narrowing the retrieval conditions

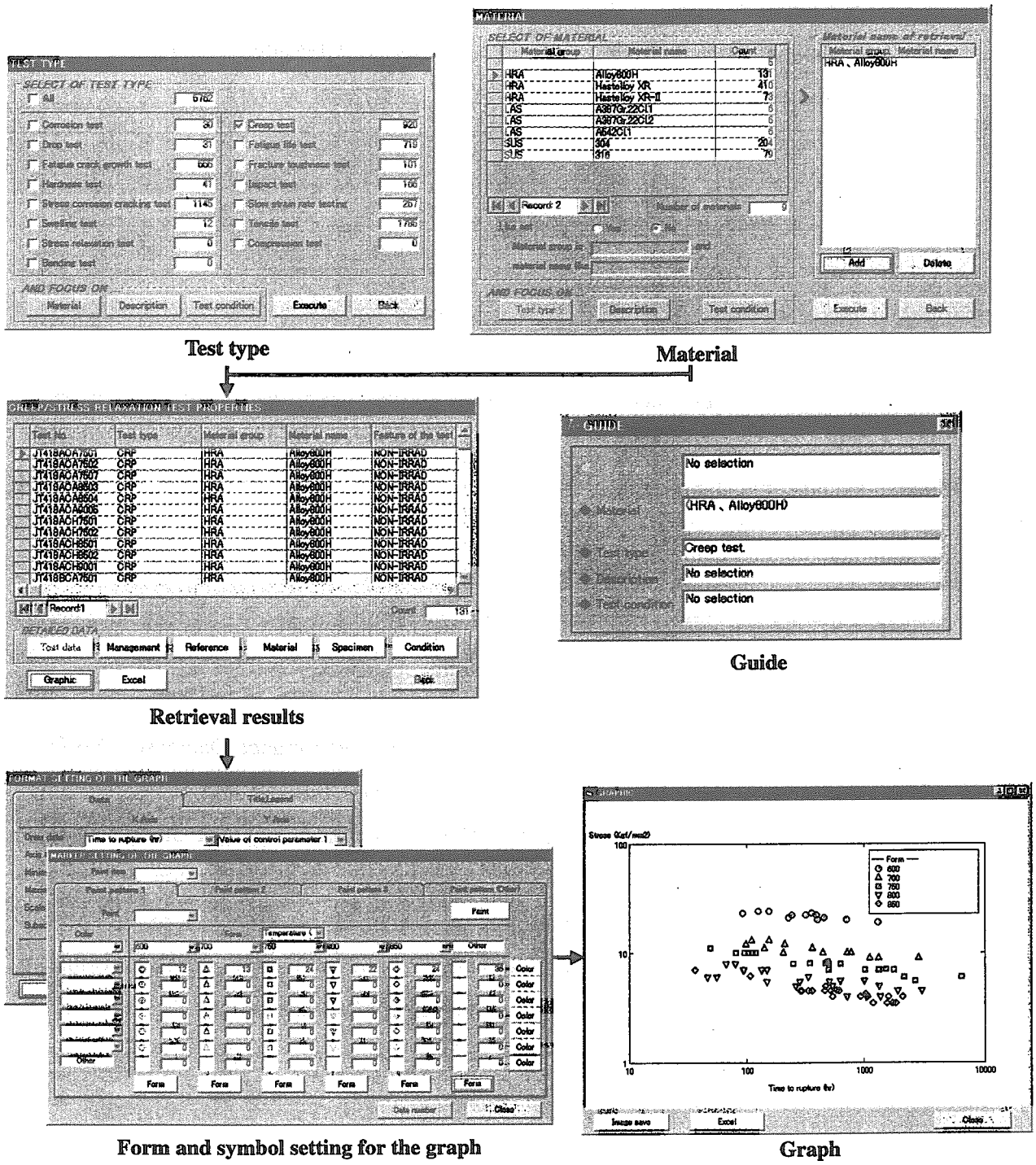

Fig. 6.7.2 Flow diagram of searching the creep data of Alloy 800H

6.8 Construction of Material Database System through Demonstration Test on Life Time Reliability of Structural Materials for Advanced Prototype Power Reactors

T.Sakino, Y.Kaji and H.Tsuji
(*E-mail:* sakino@jmpdsun.tokai.jaeri.go.jp)

In the demonstration test on lifetime reliability of structural materials for advanced prototype power reactors, a series of mechanical tests was performed on the pre- and post irradiation type 304 stainless steel which is used as the structural material of Japanese prototype fast breeder reactor "Monju". Mechanical properties of neutron irradiated materials are affected by both the displacement damage level and the amount of gaseous ingredient such as H and He produced by nuclear transmutation. Three types of neutron irradiation capsules, therefore, were specially designed, namely thermal neutron shielding, normal, and thermal neutron trapping types, in order to examine the effect of He production level on mechanical properties of type 304 stainless steel using JMTR. As for creep properties, in-pile tests were also carried out.

A new database system as a part of the JAERI Material Performance Database (JMPD)[1)2)] was constructed with a view to utilizing the data obtained through the above-mentioned demonstration test. The system works under the Windows environment. The database and the interface are Microsoft Access and Microsoft Visual Basic, respectively. On the basis of database structure of JMPD, the database structure were extended to store the detailed information concerning the irradiation condition such as the irradiation capsule information, the irradiation portion and the operation cycle of the Japan Materials Testing Reactor (JMTR), etc. The irradiation capsule information includes irradiation time, temperature, fast neutron fluence, thermal neutron fluence in each operation cycle. The data of the specimens irradiated in 9 capsules were stored. The number of data stored by the end of March 2000 are as follows. Tensile test data are from 107 specimens, creep data from 66 specimens, and low cycle fatigue Data number stored in the database are irradiation capsule of 9, creep test of 66, low cycle fatigue data from 43 specimens.

Figure 6.8.1 shows the flow diagram of the data retrieval procedure. Main menu and information screen are displayed when the system is started. Information of irradiation cycle and information of core arrangement of JMTR are displayed in the information screen. Main

menu is the entrance of narrowing retrieval condition, and users can start to search the data from test type, material, fast neutron fluence, thermal neutron fluence , description, irradiation temperature, capsule as shown in Fig 6.8.1. From the irradiation temperature screen, users can reach the irradiation temperature history figure in each cycle of the designated capsule. In the specimen screen, the geometry of the specimen and the photograph of fracture surface of the tested specimen can be displayed.

Figure 6.8.2 shows the examples of data retrieval screens. The capsule screen shows irradiation type, cycle count, etc. of every capsule, and it also shows material information and irradiation cycle history of the selected capsule. The fast neutron fluence screen can show both the nominal and estimated fast neutron fluence values. The thermal neutron screen has also the same function. Irradiation cycle information screen displays the irradiation history. Core arrangement screen shows the irradiation position of the selected capsule.

References

1) H. Tsuji, N. Yokoyama, T. Tsukada and H. Nakajima, J. Nucl. Sci. Technol., Vol. 30, No. 12, pp.1234-1242 (1993).

2) N. Yokoyama, H. Tsuji, T. Tsukada and M. Shindo, ASTM STP 1311, pp.261-272 (1997).

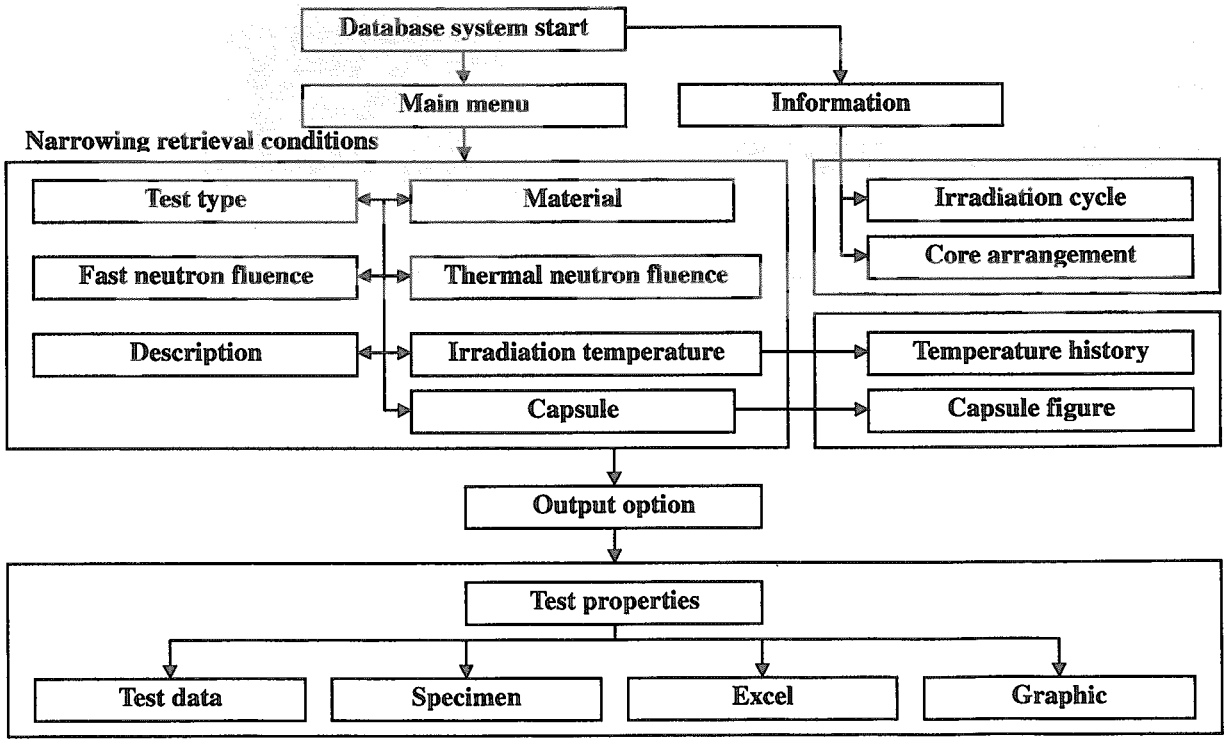

Fig. 6.8.1 Flow diagram of data retrieval procedure

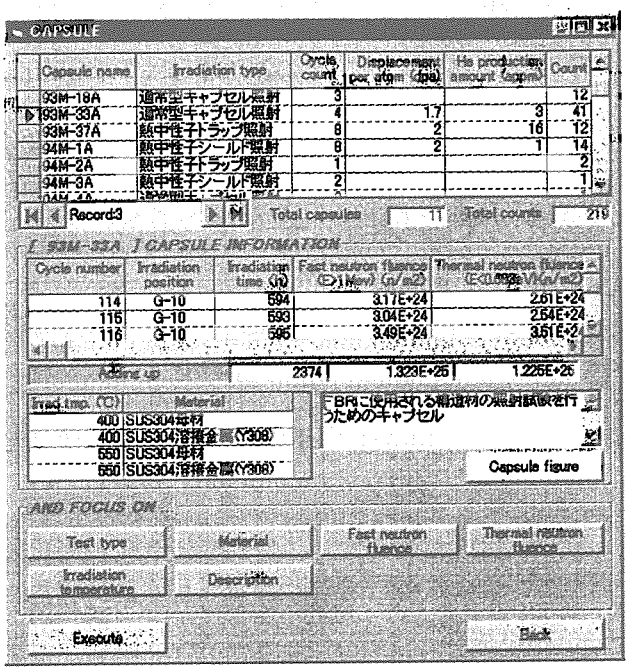

Capsule

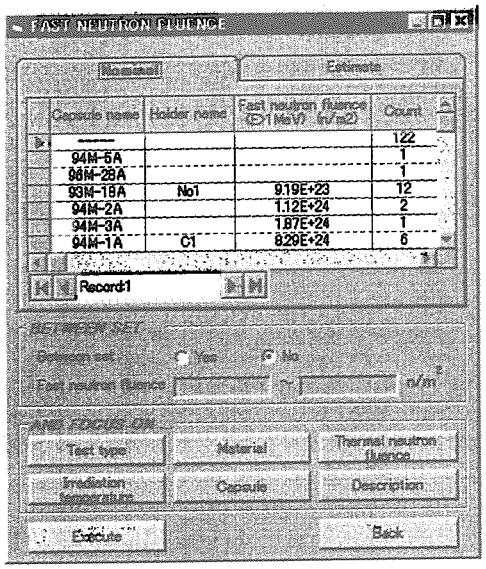

Fast neutron fluence

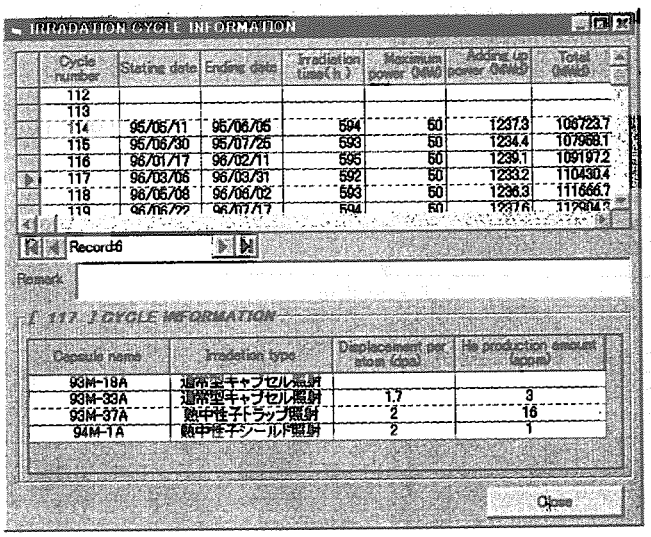

Irradiation cycle information

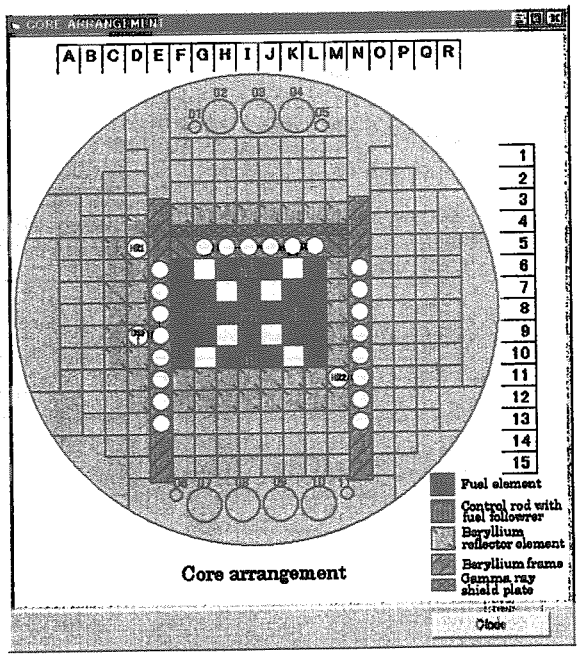

Core arrangement

Core arrangement

Fig. 6.8.2 Examples of data retrieval screens

6.9 Distributed Database System for Advanced Nuclear Materials (Data-Free-Way) - Present Status and Example of Utilization -

H. Tsuji, Y. Kaji, T. Sakino, M. Fujita[*1], J. Kinugawa[*1], S. Mashiko[*2], K. Shimura[*3], R. Nakajima[*3] and S. Iwata[*4]
(*E-mail:* hts89@popsvr.tokai.jaeri.go.jp)

Material behavior under the service conditions in the nuclear field can be little understood without practical examination. An easily accessible material information system with a huge material database using effective computers is, therefore, necessary for the design of new materials and the analyses or the simulations of the phenomena occurring in the materials of the nuclear plants under the service conditions, especially neutron irradiation relevant phenomena.

Hence, the distributed database system for advanced materials named "Data Free-Way" was constructed under the collaboration of the National Research Institute for Metals (NRIM), the Japan Atomic Energy Research Institute (JAERI) and the Japan Nuclear Cycle Development Institute (JNC) in order to share fresh and stimulating information as well as accumulated information for the development of advanced materials, for the design of structural components, etc[1)-5)].

In order to make the system more substantial, the second stage joint research in which the main objective was to develop the utilization techniques for the Data-Free-Way was performed among NRIM, JAERI, JNC and the Japan Science and Technology Corporation (JST) which joined the collaborative research group from the second stage.

The system consists of a common database and a generic database. Evaluated, selected and edited data in each in-house database, which has been developed by each organization, are stored in the common database. For easy comparison of the relevant data sets from one organization with those of the others, a common data model is adopted.

Contents of the common database have already been shown in the previous reports[1)-5)]. NRIM prepares physical properties and ion irradiation data, JAERI prepares corrosion data, thermal neutron irradiation data and mixed spectrum neutron irradiation data, JNC prepares

---

*1 National Research Institute for Metals, *2 Japan Nuclear Cycle Development Institute
*3 Japan Science and Technology Corporation, *4 University of Tokyo

high temperature data and fast neutron irradiation data, and JST prepares public fact data. At present, the data of more than 35,000 specimens in various kinds of materials are stored in the common database. The generic database contains a meta directory, a data dictionary and sets of generic materials data for smooth communication. Both the common database and the generic database can be exchanged mutually among the participating organizations through the network. The user interface of the system plays an important role in developing a useful system, especially to extract information from the complex mixture of material data. Concepts of the user interface including a graphic analytical model and application programs for analysis and evaluation of data are adopted to the system. The system can be easily accessed by engineers and scientists in the advanced power engineering field.

The world wide web (WWW) home page and the WWW server have been prepared. The URLs of NRIM, JAERI and JST sites are "http://inaba.nrim.go.jp/," "http://jmpdsun.tokai.jaeri.go.jp/dfw-e/dfw-e.html" and "http://dfw.jst.go.jp/," respectively. As the data input output supporting system, the additional functions have been prepared to reinforce the linkage function between the database and the WWW, such as the retrieval-layout function of image data, the simple graph preparation function, the linkage function between numerical data and image data, the preparation function of a fixed retrieval screen, the saving-reproducing function of retrieval conditions, etc. The dictionary on data items and unit conversion function have been prepared as a users' supporting system.

An example of data handling for type 316 stainless steels using the Data Free-Way is described in the part that follows.

Fig. 6.9.1 shows the relation between the total elongation (TE) and the uniform elongation (UE) under the various tension test conditions for type 316 stainless steels[6)-11)]. Approximately 290 points are indicated in this figure. The displacement damage ranges from 0.3 to 121 dpa.

Interesting trend is recognized that the data points are divided into three groups of A, B and C. In the group A, the values of TE and UE are almost equivalent. The values of UE are almost constant despite increase of UE in the groups B and C. The values of UE in the group B are larger than those in the group C. Both of unirradiated and irradiated data are included in the group A. On the other hand, almost all the data in the group B are unirradiated ones and those in the group C are irradiated ones. Paying attention to the test temperature, the data obtained at lower than 600℃ belong to the group A and those at higher than 600℃ belong to the group B or C.

References

1) Nakajima H. et al.: J. Nucl. Mater. 212-215, 1711 (1994).

2) Fujita M. et al.: "Computerization and Networking of Materials Databases V, ASTM-STP 1311", American Society for Testing and Materials, Philadelphia, USA, 249 (1997).

3) Tsuji H. et al.: "Materials for Advanced Power Engineering 1998, Part III", Forschungs zentrum Jülich, Jülich, Germany, 1739 (1998).

4) Tsuji H. et al.: "Innovative Materials in Advanced Energy Technologies", TECHNA Srl, Faenza, Italy, 417 (1999).

5) Tsuji H. et al.: J. Nucl. Mater. 271&272, 486 (1999).

6) Bloom E. E. and Wiffen F. W. : J. Nucl. Mater. 58, 171 (1975).

7) Grossbeck M. L. and Maziasz P. J.: J. Nucl. Mater. 85 & 86, 883 (1979).

8) Shiraishi H., Nagata N. and Watanabe R. : J. Nucl. Mater. 87, 157 (1979).

9) Jacobs A. J. et al.: Proc. of Third Inter. Symp. on Environmental Degradation of Materials in Nuclear Power Systems - Water Reactors (The Metallurgical Society) 673 (1988).

10) Jitsukawa S., Grossbeck M. L. and Hishinuma A.: J. Nucl. Mater. 191-194, 790 (1992).

11) Josefsson B. and Bergenlid U.: J. Nucl. Mater. 212-215, 525 (1994) (1994).

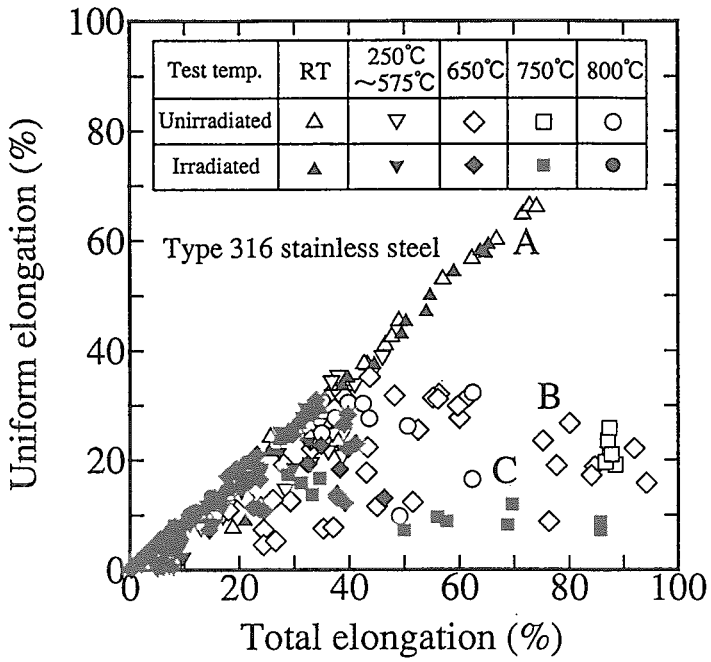

Fig. 6.9.1 Relation between total elongation and uniform elongation under various tension test conditions for type 316 stainless steels[6)-11)]. Displacement damage ranges from 0.3 to 121 dpa.

6.10 Evaluation of In-pile and Post-irradiation Creep Properties of Type 304 Stainless Steel under Different Neutron Spectra

Y. Kurata, Y. Itabashi, H. Mimura, T. Kikuchi, H. Amezawa,
S. Shimakawa, H. Tsuji and M. Shindo
(*E-mail:* ykurata@popsvr.tokai.jaeri.go.jp)

The study of irradiation creep is essential for the core structures of fast breeder reactors and for first wall and blanket structures of fusion reactors. The effect of irradiation on creep properties has been investigated by means of in-pile/post-irradiation creep tests. The objectives of this study are to estimate the effect of irradiation on creep properties of materials for the core structures of fast breeder reactors and to contribute to the understanding of the neutron spectral effect on creep behavior. For this purpose, in-pile creep capsules with uni-axial creep specimens to be irradiated under different neutron spectra were developed for irradiation in Japan Materials Testing Reactor, JMTR. [1)]

The tested material was type 304 stainless steel for fast breeder reactor internals such as a core barrel and support plate. The weld metal specimens were also used. Table 6.10.1 lists the irradiation conditions. Values of dpa and helium production were calculated by analysis of fluence monitor wires. Normal irradiation without spectral tailoring in a fuel zone was performed for (1)93M-33A. Under the conditions of (3)94M-1A and (5)94M-3A, thermal neutrons were shielded using cadmium. In contrast, a high thermal neutron flux was obtained using graphite under the conditions of (2)93M-37A and (4)94M-2A.

Table 6.10.1 Irradiation conditions

Capsule name	Damage by thermal neutron (dpa)	Total damage (dpa)	Helium production (appm)
(1)93M-33A, Post-irradiation test (Normal irradiation, fuel zone)	2.87×10^{-3}	2.19	2.93
(2)93M-37A, Post-irradiation test (High thermal neutron flux)	1.78×10^{-2}	1.51	11.0
(3)94M-1A, Post-irradiation test (Thermal neutron shield)	1.09×10^{-5}	0.97	0.9
(4)94M-2A, In-pile creep (High thermal neutron flux)	Upper 7.34×10^{-4} Lower 2.18×10^{-4}	5.62×10^{-2} 1.67×10^{-2}	0.64 0.21
(5)94M-3A, In-pile creep (Thermal neutron shield)	2.74×10^{-6}	0.21	0.20

Figure 6.10.1 shows a comparison of rupture time among post-irradiation creep, in-pile creep under different neutron spectra and creep of the unirradiated material. In this figure, the design allowable creep-rupture stress (S_R)[2,3] for the structural material of Japanese prototype fast breeder reactor "Monju" is also indicated. Irradiation effects were taken into consideration to generate S_R.[3] The relative order is in-pile creep under a high thermal neutron flux condition(94M-2A), post-irradiation creep under different neutron spectra(93M-33A, 93M-37A and 94M-1A), in-pile creep under a thermal neutron shield condition(94M-3A) and creep of the unirradiated material, in increasing order. It is found that all rupture time data of in-pile and post-irradiation creep are longer than values shown by S_R. Figure 6.10.2 shows a comparison of creep curves obtained by in-pile creep under different neutron spectra, post-irradiation creep and creep of the unirradiated material. The creep curve after normal irradiation is shown as a typical example of the creep curve of post-irradiation. The acceleration of creep deformation is observed in post-irradiation creep and in-pile creep under a high thermal neutron flux condition. Figure 6.10.3 compares the rupture time data of the unirradiated and post-irradiated weld metal with S_R. In case of the weld metal, the creep rupture strength obtained from post-irradiation creep is also higher than that shown by S_R.

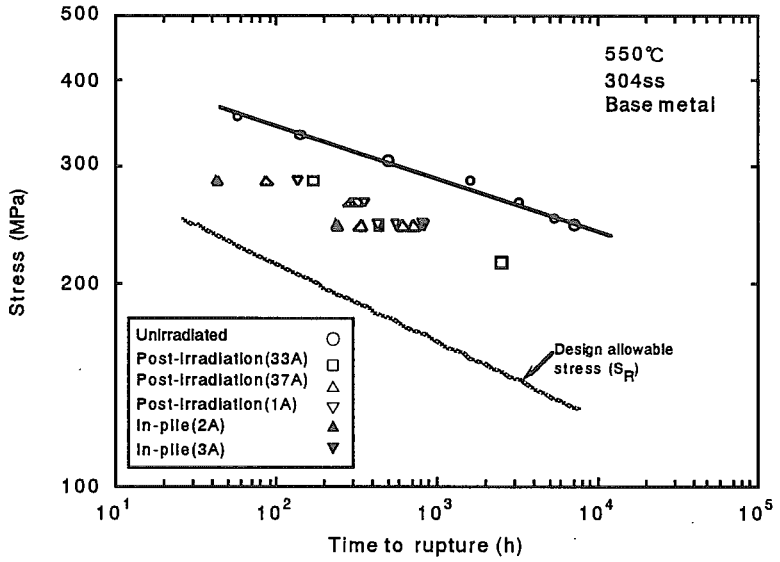

Fig. 6.10.1 Comparison of creep rupture time of the base metal among post-irradiation creep, in-pile creep, creep of unirradiated material. The design allowable creep-rupture stress (S_R) for the structural material of Japanese prototype fast breeder reactor "Monju" is also indicated.

References

1) Kurata Y., Itabashi Y., Mimura H., Kikuchi T., Amezawa H., Shimakawa S., Tsuji H. and Shindo M. :JAERI-Conf 99-006, 201(1999).

2) Yoshitake A. et al.:Int. Conf. on Creep, Tokyo,441(1986).
3)Systems and Components Division, O-arai Engineering Center, Fuels and Materials Division, Power Reactor and Nuclear Fuel Development Corporation, PNC Technical Report, 73, 81 (1990)[in Japanese].

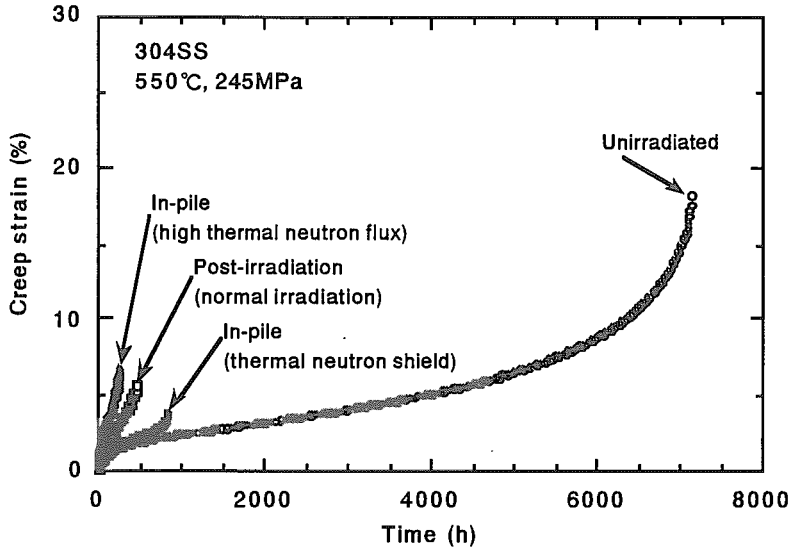

Fig. 6.10.2 Effect of neutron irradiation on creep curves of type 304 stainless steel.

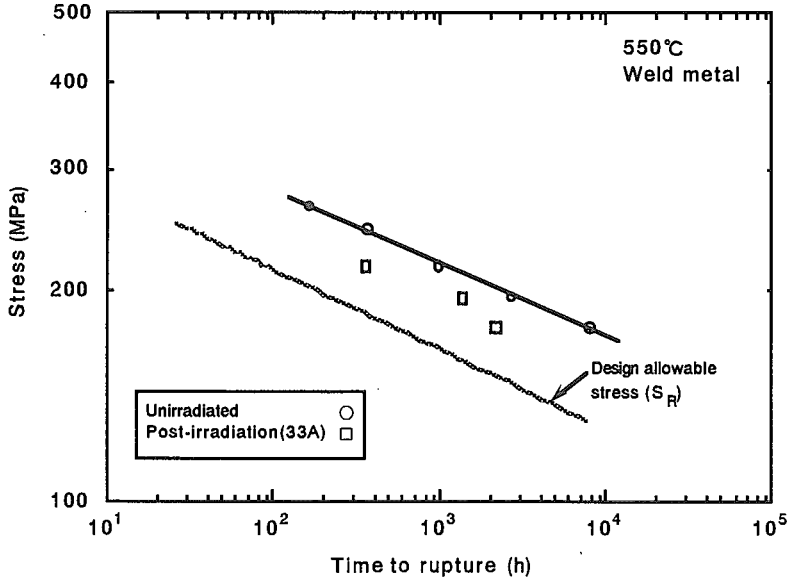

Fig.6.10.3 Comparison of the rupture time of the weld metal between post-irradiation creep and creep of unirradiated material. The design allowable creep-rupture stress (S_R) is also indicated.

6.11 Effect of Helium to dpa Ratio on Fatigue behavior of Austenitic Stainless Steel Irradiated to 2dpa

I. Ioka, M. Yonekawa, Y. Miwa, H. Mimura, H. Tsuji and T. Hoshiya

(*E-mail:* ioka@popsvr.tokai.jaeri.go.jp)

Stainless steels have been widely used as structural and core component materials of light and fast breeder reactors. The main purpose of the present investigation is to evaluate the effect of helium to displacement damage ratio (He/dpa) on high-temperature fatigue life of type 304 stainless steel used as the structural material of Japanese prototype fast breeder reactor, Monju.

The material tested was commercially manufactured type 304 stainless steel. The material was prepared by hot rolling followed by solution annealing at 1323K for 12 minute and rapid cooling. The material was machined into bottom-ended test specimens with gauge section of 4 mm in diameter and 6 mm in length with the length-axis parallel to the final rolling direction. Specimens were irradiated in the fuel or beryllium reflector regions of the Japan Materials Testing Reactor (JMTR) at 823K. Irradiation utilizing neutron spectrum tailoring method was carried out in the JMTR in order to control the He/dpa level of the specimen. Three types of capsules were specially designed, namely thermal neutron shielding, normal and thermal neutron trapping types. Details of the normal, thermal shielding and thermal trapping irradiation conditions can be found in Table 1. Uniaxial strain-controlled fatigue tests were performed on a computer-controlled servohydraulic fatigue testing machine installed in a hot cell. All tests were performed at the irradiation temperature of 823K. Total axial strain ranges used were 0.8, 1.0 and 1.6%. The fatigue life of the specimen was defined as a number of cycles at which a tensile stress reduced to 75% of maximum stress during cyclic stress testing.

Fatigue life of unirradiated and irradiated specimens are plotted in Fig. 1 as the total strain range versus the number of cycles to failure on log-log scale. The difference between unirradiated and irradiated specimens is quite clear and appears to be a reduction by a factor of 2 to 4 in fatigue life. In the preliminary test, the thermally aged specimens, which were aged under the same thermal condition as the irradiated specimens, showed no discernible

difference in fatigue life from the solution annealed specimens. Murty and Holland[1] examined the effect of radiation on fatigue characteristics of type 304 stainless steel irradiated to fluence level of $8x10^{26}n/m^2$ (E>0.1MeV) at 673K. They also showed irradiation was detrimental in fatigue life at low cycle fatigue testing. On the other hand, de Vries[1] and Elen et al.[2] reported the different results, that is, there is no significant effect on the fatigue life after irradiation at 823K. It seems that the difference between their results and the present results were attributed to lower fluence; a low density of irradiation induced defects. Because the fatigue life-shortening mechanism of the irradiated type 316 stainless steel is believed to be a high density of faulted loops[2]. Moreover, fatigue life depends on the ductility of the materials. The irradiation caused the decrease in the elongation of the material at the same irradiation and test conditions[3]. It is considered that the high density of irradiation defects and the loss of ductility can explain a degradation of fatigue life in Fig. 1. Further study is being conducted to determine the reason for this effect. Figure 1 also shows the effect of helium concentration on fatigue life. Significant degradation of fatigue life was not observed in irradiated specimens with different levels of helium concentration. The similar trend was shown by Sonnenberg et al.[4] using He-implanted type 316 stainless steel. It has been speculated that the cyclic motion of dislocations associated with fatigue could sweep helium atom clusters to sinks such as grain boundaries where they will accumulate until sufficient concentration can cause failure[5]. It is believed that the mechanism could be depending on the fatigue testing temperature. Tavassoli et al.[6] reported the irradiation influences fatigue life of type 304 stainless steel over 973K. It is concluded that helium concentration of the specimen is not main factor to shorten fatigue life in the present experimental condition. The results of this work were summarized as follow:

(1)The influence of helium concentration on cyclic stress-strain relationship is not observed.

(2)The stress amplitude of irradiated specimen was saturated at lower cycle, though the stress amplitude of both unirradiated and irradiated specimens was almost same.

(3)The irradiation caused a reduction by a factor of 2 to 4 in fatigue life of the specimen.

(4)A helium concentration of the specimen is not main factor to shorten fatigue life in the present experimental condition.

References

1) K. L. Murty and J. R. Holland, Nucl. Technol. 58(1982)530.

2) J. D. Elen et al., ECN-39(1978).

3) H.Tsuji et al., in: Proc. 9th CIMTEE-World Forum on New Materials Symposium VII-Innovative Materials in Advanced Energy Technologies, Ed. P. Vincenzini (1999)483.

4) K. Sonnenberg and H. Ullmaier, J. Nucl. Mater. 103&104(1981)859.

5) M. L. Grossbeck and K. C. Liu, Nucl. Technol. 58(1982)538.

6) A. A. Tavassoli et al., in: Proc. 17th Conf. On Effects of Radiation on Materials, ASTM-STP 1270, American Society for testing and Materials, Philadelphia, (1999)995.

Table 1 Irradiation conditions of normal, thermal shield and thermal trap capsules in the experiment.

Irradiation capsule	Fluence(n/m^2)		Dose(dpa)	Helium(appm)
	Fast(E>1MeV)	Thermal(E<0.683eV)		
Normal	$1.0x10^{25}$	$5.1x10^{24}$	1.8	2.5
Thermal shielding	$0.5x10^{25}$	$5.8x10^{22}$	0.9	0.8
Thermal trapping	$0.7x10^{25}$	$2.3x10^{25}$	1.3	8.1

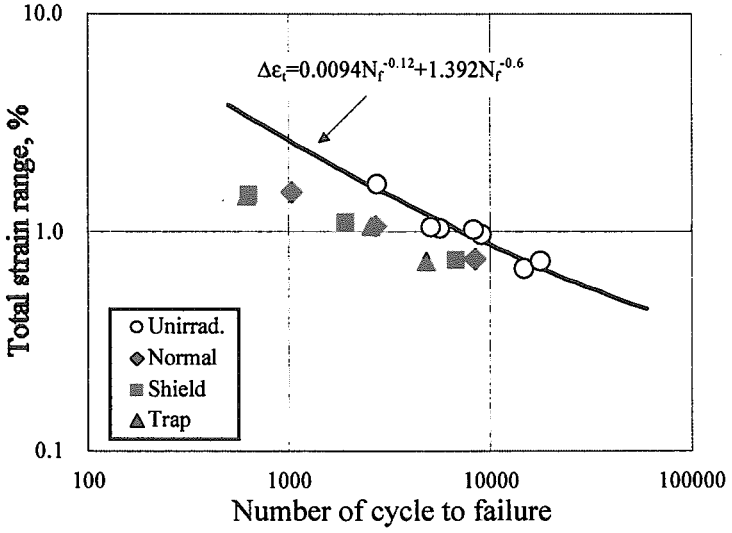

Fig. 1 Fatigue life of unirradiated and irradiated specimens as the total strain range

7. Advanced Materials for Nuclear Applications

The research was mainly carried out in the following fields: (1) corrosion-resistant materials for IS(Iodine-Sulfur) hydrogen production process, (2) evaluation of the vacuum vessel welding structure of ITER and bonding techniques for the fusion reactor components, and (3) advanced materials for HTGR and spallation neutron source. These above research subjects include the development of advanced techniques for materials evaluation as well.

As for the research on the IS process materials, the corrosion tests of 10 iron-base and nickel-base alloys were carried out in H_2O+SO_3 atmosphere at 850 C up to 1000h. The corrosion behavior in the atmosphere was evaluated through microstructure observation on the corroded specimens with optical microscope, EPMA and X-ray diffraction. The metal-ceramic composites, metallic materials coated with these corrosion-resistant materials, are considered as candidate structural materials. In such composite materials, residual mismatch stresses develop. These stresses influence on the service life of the materials. In order to precisely evaluate the residual stress, the novel technique, i.e. the indentation technique combined with in-situ bending, was developed and applied to the evaluation of the residual stress of the glass which is one of the candidate materials for the IS process.

On the 316 SS, TIG, MAG and EB welded joints used for the vacuum vessel in ITER, neutron irradiation effect on the mechanical properties were investigated through tensile and Charpy impact tests. As for a bonding technology for DS Cu to stainless steel, low cycle fatigue tests on the direct diffusion bonded joint, the Au interlayer joint, the stainless steel and the DS Cu were performed to investigate their fatigue strength and fracture behavior, which were associated with the microscopic features.

Creep behavior of pure Ni-Cr alloy and the alloy with the third solution element was investigated through microscopic observation using creep-interrupted specimens and in-situ observation using a specially designed mechanical testing machine with SEM. The novel indentation technique combined with an inverse analysis using an FEM code and with different apex angle indenters was proposed to characterize mechanical properties of material surfaces and applied to the H^+, He^+ and Ni^{3+} ions-implanted thin surface layer, simulating irradiation effect in the spallation neutron source.

7.1 Neutron Irradiation Effect on Mechanical Properties of Type 316L Stainless Steel Welded Joint for Vacuum Vessel of ITER

S. Saito, K. Fukaya, S. Ishiyama, H. Amezawa, M. Yonekawa, F. Takada, Y. Kato, H. Takahashi and K. Koizumi
(*E-mail* : sai@popsvr.tokai.jaeri.go.jp)

In design activity of International Thermonuclear Experimental Reactor (ITER)[1,2], the vacuum vessel (VV) is designed as double walled structure so that some parts of them are not qualified in the conventional design standards. JAERI has executed the preparation activity of the new design standards[3] and the technical data to support them[4]. In this study, neutron irradiation effect on the mechanical properties of 316L SS welded joint were investigated.

316L SS and its TIG, MAG and EB welded joint are used. The tensile and Charpy impact specimens were cut from base metal and these welded joints. The test pieces were $\phi 3\times$ 30mm G.L. for tensile tests and half-size specimens for Charpy impact tests. The neutron irradiation tests were performed at Japan Material Testing Reactor (JMTR). The irradiation temperature were 473K and neutron fluence were $1.2\sim3.4\times10^{22}$n/m^2 (0.2～0.5dpa). The post irradiation experiments were performed at Hot Laboratory of JMTR. Tensile tests were done in air at temperatures from R.T. to 473K. Charpy impact tests were done in air at R.T..

Figure 7.1.1 shows load-displacement curve of tensile tests on the irradiated specimens with those unirradiated materials. In case of base metal, yield strength was increased with neutron fluence. It is said that yield strength increases with neutron fluence up to 1～3dpa[5] in the low temperature (～523K) irradiation. In case of deposited metal, no fluence dependence was seen. Probably, yield strength increase was already reached to a saturation value. For each specimen, elongation and strain-hardening were decreased. Though, sufficient ductility for a structural materials were still maintained. The appearance of yield point is the typical phenomenon to a low temperature (～573K) irradiation of austenitic steel[6]. Figure 7.1.2 shows the results of Charpy impact tests. Base metal, deposited metal and heat affected zone (HAZ) of TIG and EB welded joint showed enough ductility after irradiation. On the other hand, deposited metal of MAG showed extremely low impact value and lateral expansion like a brittle material. SEM photographs of fracture surface after Charpy impact tests are shown in Fig.7.1.3. For MAG specimen, there are a number of fine non-metallic inclusions in the bottom of small dimples. Maybe, some fine ceramics particles added to welding rod as a flux were left in deposited metal. Consequently, base metal of 316L SS and its TIG and EB welded joint were kept these soundness after 0.2～0.5dpa neutron irradiation.

References

1) ITER General Design Requirements, (ITER, 1996).
2) ITER Design Description Document, (ITER, 1996).
3) The Japan Welding Society, JWES-AE-9803, p.122-123.
4) Saito, S., Fukaya, K., Ishiyama, S., Takahashi, H. and Koizumi, K., JAERI-Tech to be published.
5) J.E.Powel, A. F. Rowcliffe, G. E. Lucas and S. J. Zinkle, J. Nucl. Mater., 239(1996)126-131.
6) H.R.Higgy and F. H. Hammand, J. Nucl. Mater., 55(1975)177-186.

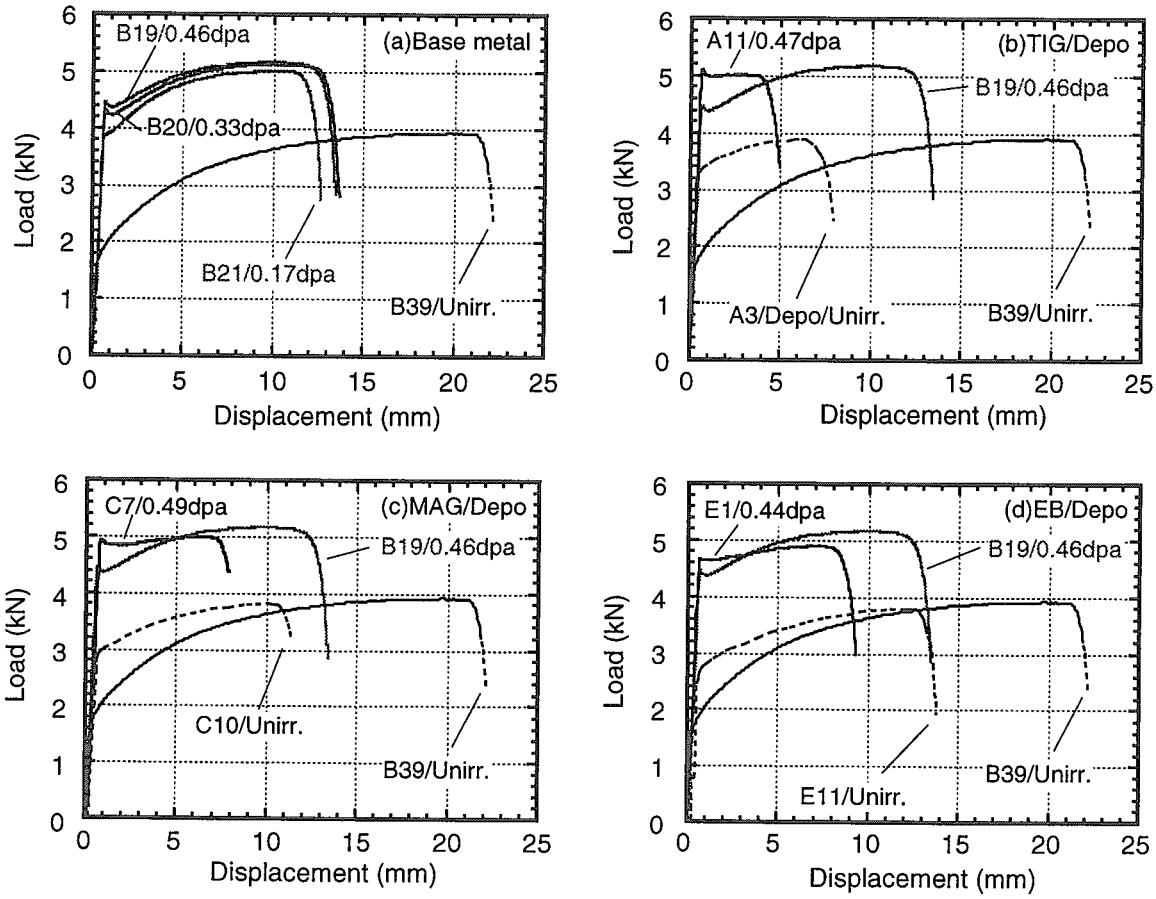

Fig. 7. 1. 1 Load-displacement curve of tensile test on 316L (a)Base metal, (b)TIG, (c)TIG+MAG and (d)EB welded joint deposited metal (Ttest =R.T.).

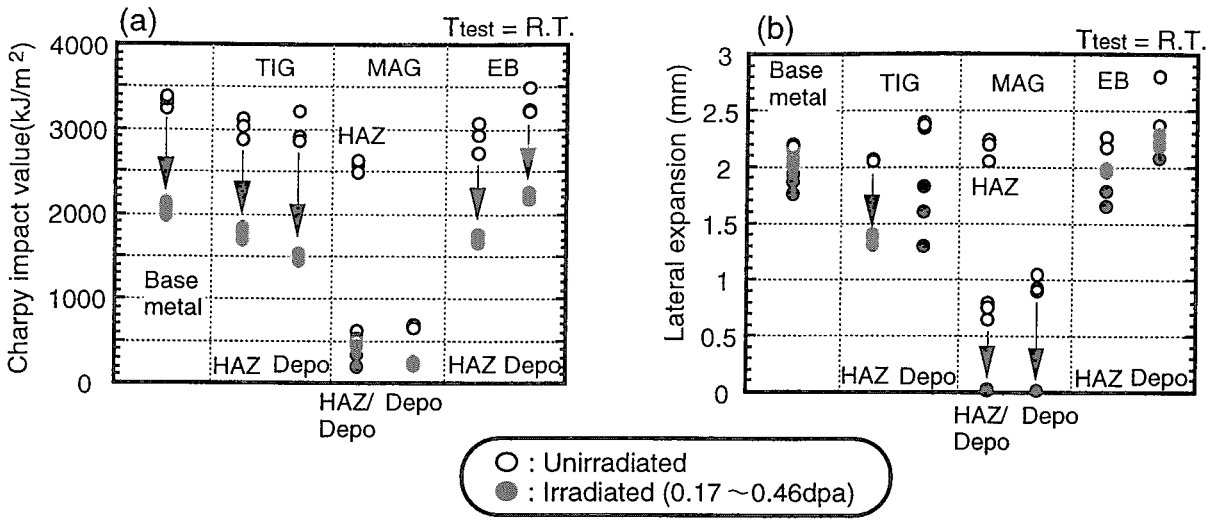

Fig. 7. 1. 2 Changes in (a) Charpy impact value and (b)lateral expansion between the unirradiated and the irradiated specimens.

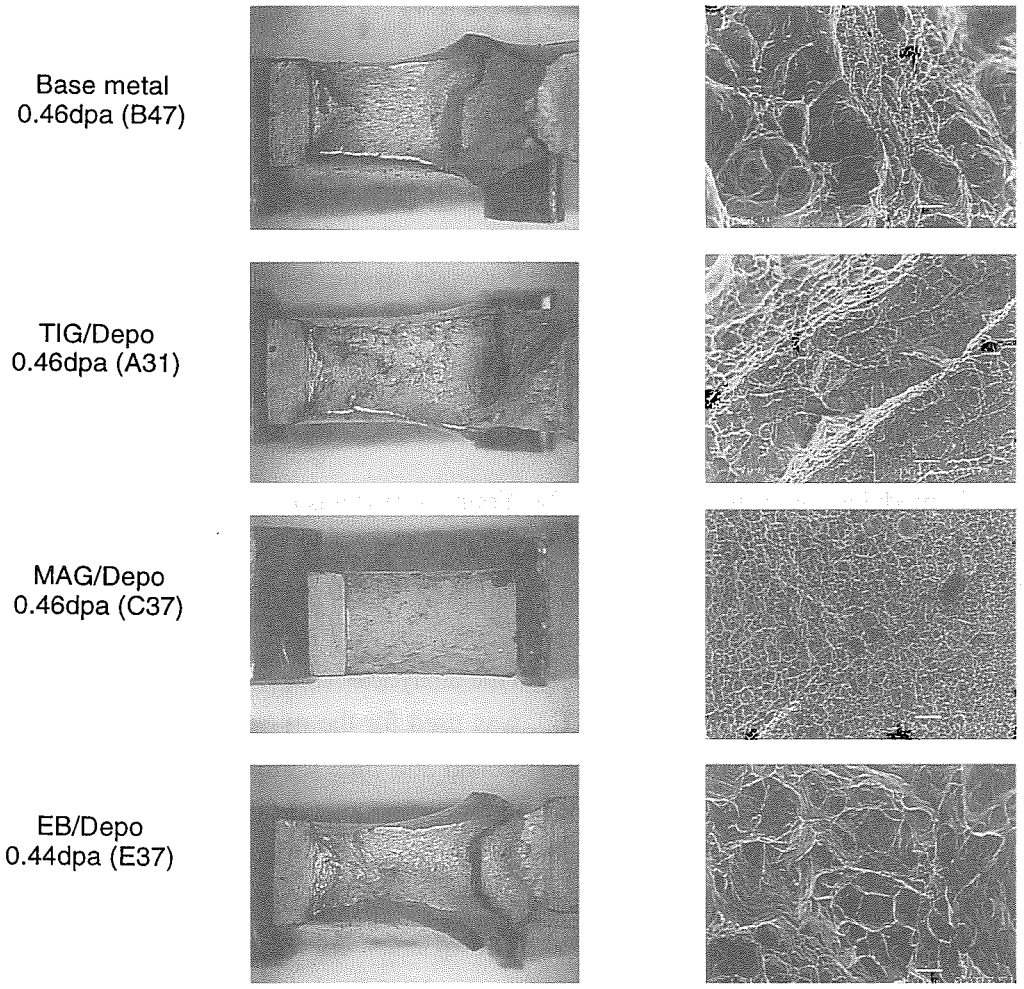

Fig. 7. 1. 3 SEM photograph of fracture surface after Charpy impact tests on 316L SS base metal and welded joint deposited metal.

7.2 Mechanical Characterization of Ion Implanted Layer by Micro-indentation Test Using Different Apex Angle Indenters

I.Ioka, M.Futakawa, T.Wakui* and A.Naito**
(E-mail:ioka@popsvr.tokai.jaeri.go.jp)

A triple ion beam facility at JAERI can be used to simulate a spallation neutron environment[1] by producing displacement damage in the material by simultaneously implanting H^+ and He^+ ions. However, the ion implanted area is limited to the very shallow surface layer of the specimen so that the irradiation damage is distributed around the thin layer. In previous report[2], we proposed a technique for deriving constants of the Swift's power low constitutive equation[3] ($\sigma=A(\varepsilon_0+\varepsilon)^n$, A: strength coefficient, ε_0: equivalent strain by cold rolling, n: strain hardening exponent) of the damaged parts by a microindentation test combined with an inverse analysis using a finite element method (FEM). It was assumed that the values of A and n were almost equal to those of the base material in the technique. The value of ε_0 was decided so that the analytical result by FEM may agree with the result of microindentation test.

In this study, the values of A, n and ε_0 were simultaneously obtained from the result of microindentation test using three kinds of trigonal pyramid indenters. The constitutive equation of nickel superalloy with high yield stress was deduced by the new technique in order to confirm the validity of the technique. Moreover, the constitutive equation of the ion implanted layer was estimated using the new technique.

By the microindentation test with the different apex angle, the gradient (S_{exp}) during loading was obtained from Load/Depth-Depth curve (P/h-h curve) of nickel superalloy shown in Fig.7.2.1.

The constitutive equation assumed the following Swift's power low curve.

$\sigma=E\varepsilon, \quad \sigma\leq\sigma_y$ (1)

$\sigma=A(\varepsilon_0+\varepsilon)^n, \varepsilon_0=(\sigma_y/A)^{1/n}-(\sigma_y/E), \quad \sigma>\sigma_y$ (2)

where E is Young's modulus and σ_y is yield stress. The Young's modulus is calculated from unloading part in the Load-Depth curve (P-h curve) of the microindentation test.

Relationships between the remainder of constitutive equation (A, n, σ_y) and the gradient (S) of the P/h-h curve on each indenter are obtained by the FEM analysis. A, n and σ_y are decided from the comparison of the result of the microindentation test with the analytical results[4].

A testing machine, DUH-200 (Shimadzu Co.), was used for the microindentation test. A load was applied with a loading speed of 2.6mN/s, held 1 second and then removed. During loading and unloading, the load was continuously monitored along with the displacement with a resolution of 2mN and 0.01_ m, respectively. Three kinds of indenter were selected so that the apex angle may become A_p/h^2=12.2, 24.5, 49.0. A_p and h are the projected area and the depth from the surface, respectively. The indenter with A_p/h^2=24.5 is correspondent to the Birkovich indenter. In the microindentation test, the maximum load was set to be 98mN, and the test frequency was 10 times for each.

The tensile test was carried out in order to confirm the constitutive equation obtained. Nickel superalloy used in the micro-indentation test was also used for the tensile test. The specimen is round bar type of 6mm in diameter and 32mm in length of gauge section. The tensile test was conducted at room temperature in air with strain rate of 4×10^{-4} 1/s.

The material for ion implantation is type 316L SS. Specimens are disks 3 mm in diameter with 0.2 mm thickness. The electrochemically polished disk specimens were irradiated in triple (12 MeV Ni^{3+}, 750 keV He^{+} and 290 keV H^{+}) ion beam modes at a temperature of 473 K. The ion fluence and the displacement dose as a function of depth under the specimen surface were computed by the SRIM97 code formerly known as TRIM[5]. The displacement damage in the disk specimen is mainly attributed to Ni^{3+} ion implantation. The peak dose is about 22 dpa around 2 μm. The peak values of concentration of Ni, He and H atoms are about 6000, 2000, and 20000 appm, respectively. The peak positions of implanted He^{+} and H^{+} ions are controlled so that the effect of implanted Ni^{3+} ions can be neglected. The He/dpa and H/dpa ratios of the disk specimens are about 250 and 2400 at the depth of approximately 1.3 μm.

The P-h curves by the FEM analysis using the constitutive equation obtained and by tensile test are shown in Fig.7.2.1. Each constant of the constitutive equation is also shown in Fig.7.2.2. The analytical result showed good agreement with the experimental one. They also agreed with each other with deformation at failure as shown in Fig.7.2.3.

The P/h-h curves of the ion implanted specimen obtained from the microindentation test with different apex angle indenters are shown in Fig.7.2.4. The inflection point appears in each curve as shown in Fig.7.2.4, and it is possible to divide each curve into two regions. The curve in region I reflects the change in properties of the ion implanted layer. In region II, the properties of the base metal become more prominent rather than those of the ion implanted layer. Therefore, the constitutive equation of ion implanted layer was deduced by the gradient ($S_{exp.}$) in region I.

The micro-indentation test with a spherical indenter was carried out for examining the validity of the constitutive equation deduced. The radius of the hemisphere apex of the spherical indenter is 5 μm. The P-h curves obtained from the microindentation test with the spherical indenter and the analytical result are shown in Fig.7.2.5. The experimental result almost agreed with the analytical one using the constitutive equation deduced. From this fact, it was confirmed that this technique could apply to the derivation of the constitutive equation of the ion implanted layer.

For the ion implantation layer, the constitutive equation was deduced by the new technique that combined the microindentation test using different apex angle indenters with the FEM analysis. The validity of the constitutive equation deduced was confirmed by the comparison between the analytical result and the result of the micro-indention test using the spherical indenter.

References

1) M.S.Wechsler, et al., Proc. of Sympo. on Materials for Spallation Neutron Sources, Florida, 23(1997).
2) I.Ioka et al., JAERI-Review 99-025, (1999) 140
3) P.B.Mellor, J. Mech. Phys. Solids, 5(1956)5.
4) T.Wakui et al., Ibaraki-kouennkai, (1999)7-8.
5) J.F.Ziegler et al., "The Stopping and Range of Ion in Solids", vol.1, Pergamon Press, New York(1985).

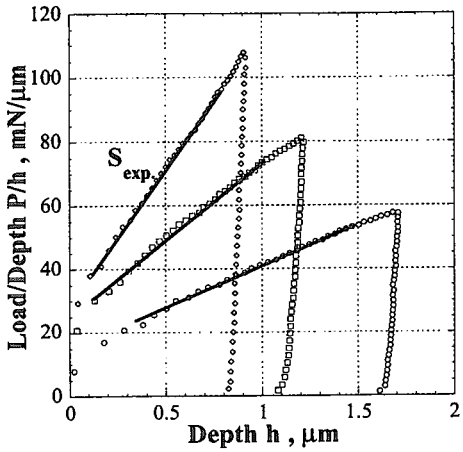

Fig.7.2.1 P/h-h curves of nickel superalloy

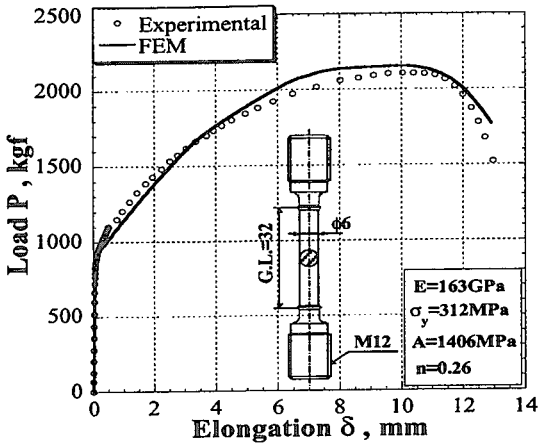

Fig.7.2.2 Load-Elongation curve of nickel superalloy

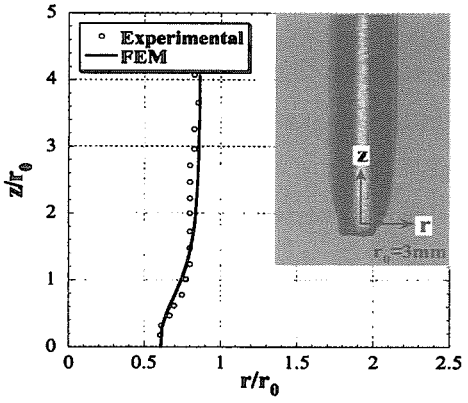

Fig.7.2.3 Deformation at failure from the analytical and experimental results

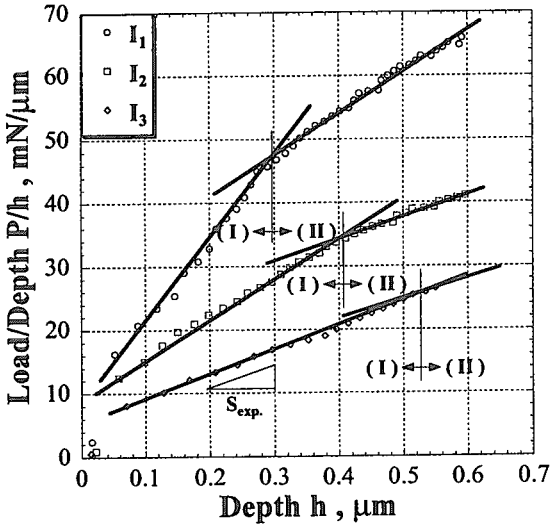

Fig.7.2.4 Load/Depth-Depth curves of ion implanted specimen using trigonal pyramid indenters

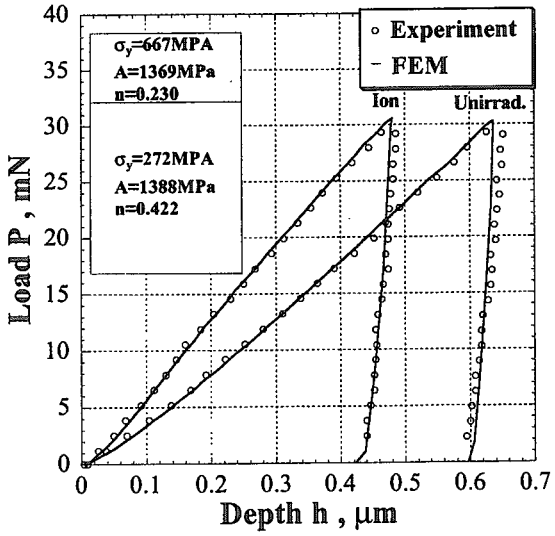

Fig.7.2.5 Experimental and analyzed Load-Depth curves using a spherical indenter.

7.3 Residual Stress Evaluation in Brittle Coating Using Indentation Technique Combined with In-situ Bending

M. Futakawa, T. Wakui* and R. W. Steinbrech

(*E-mail* : futakawa@popsvr.tokai.jaeri.go.jp)

Thermochemical hydrogen production system, IS (Iodine- Sulfur) process investigated by Japan Atomic Energy Institute[1], consists of chemically active environments, i.e., boiling sulfuric acid, halogen gasses, in which most of the conventional structural materials corrode. It is a key issue to find appropriate corrosion-resistant materials for proceeding to a next stage, the scaled-up IS process. Some brittle materials, ceramics, glass or high silicon iron are expected to be usable as corrosion-resistant structural materials for very severe corrosive environments[2].

The inherent brittleness of these materials reduces their attractive extent for application. As promising alternative, structural metallic materials coated with the corrosion-resistant materials as ceramics are increasingly exploited. In such metal-ceramic composites typically residual mismatch stresses develop. In particular, in the case of low expansion glass coatings substantial compressive stresses build up during cooling to room temperature. These stresses are favorable to hindering crack initiation while unfavorable to de-bonding due to buckling. As a result, the service life of the coated materials is strongly dependent on these residual stresses. Thereby, the evaluation of the residual stress of the glass coating which is one of the candidate materials for IS process was carried out by using the indentation technique combined with in-situ bending. The technique allowed us to more precisely evaluate the residual stress rather than the conventional indentation crack arrest method[3].

The condition of the crack arrest is given by

$$K_R = K_{total} \quad (1)$$

where, K_R is the inherent material toughness. If imposing an additional stress due to bending load, K_{total} is

$$K_{total} = K_{res,IND} + K_{res,MM} + K_{app} \quad (2)$$

where, $K_{res,IND}$, $K_{res,MM}$ and K_{app} are the stress intensities introduced by indentation, thermal expansion mismatch and bending load, respectively. The following equations are given from eqs (1) and (2) to express the crack length and stresses explicitly,

$$K_R = \chi P c^{-3/2} + \psi (\sigma_{app} + \sigma_{res,MM}) c^{1/2} \quad (3)$$

$$P c^{-3/2} = K_R/\chi - (\psi/\chi)(\sigma_{app} + \sigma_{res,MM}) c^{1/2} \quad (4)$$

*Niigata University

where P is indent load, χ residual stress parameter for indent ($\chi=\zeta\,(E/H)^{1/2} \approx 0.057$, $\zeta=0.016$[3]), E: Young's modulus, H: Hardness), ψ a dimensionless geometry parameter for a crack shape ($\psi \approx 1$[4]), σ_{app} applied stress due to bending load, $\sigma_{res,MM}$ residual stress due to thermal expansion mismatch. According to eq (4), graphical representation on the relationship between $Pc^{-3/2}$ and $c^{1/2}$ is given. If the data were plotted linearly, the implicit assumption that χ and ψ are independent on the crack length is confirmed. In the graph to describe the relationship of eq (4), the toughness was determined from the value of $Pc^{-3/2}$ at $c^{1/2}=0$, i.e. the intersection between the extrapolation of the apparent toughness curves and the $Pc^{-3/2}$ axis. The residual stress in the coatings is determined from the relationship between the bending load and the slope m ($= (\psi/\chi)(\sigma_{app} + \sigma_{res,MM})$) of the curves.

The indentation test combined with in-situ bending was carried out a miniaturized 4-point bending machine mounted on the translation stage of the micro-hardness tester, as shown in Fig.7.3.1. Steel specimen (5x5x50 mm^3) was dip-coated with glass. The average thickness of the coasting layer is about 0.5 mm. Figure 7.3.2 displays as an example a crack propagation pattern on the coatings imposed with bending load. The superposition of uni-axial bending stress and bi-axial residual mismatch stress cerates an asymmetric stress field, which the crack branches visualize by exhibiting different length. Figure 7.3.3 shows the relationship between $Pc^{-3/2}$ and $c^{1/2}$, where the c is the crack length normal to the bending stress direction. All plots demonstrate that an increasing tensile bending stress reduces the residual compressive stress and the slope becomes smaller with higher bending load. The toughness evaluated from the mean intersection value is 0.5 $MPam^{1/2}$, which agrees with the toughness of balk glass without any residual stress. Figure 7.3.4 shows the relationship between the slope m and the bending load P_{bend}. The residual stress determined using the values of slope m at $P_{bend}=0$ and ψ/χ is 108 MPa, which agrees very well with the value evaluated by a thermoelastic calculation.

References

1) Onuki, K., Nakajima, H., Ioka, I., Futakawa, M., and Shimizu, S. : "IS-process for thermochemical hydrogen production", JAERI-Review 94-006 (1994).

2) Futakawa, M., Wakui, T., Ioka, I., and Eto, M. : "Mechanical-property evaluation of thin corroded surface layers of ceramic materials by the microindentation technique", Jour. Euro. Ceram. Soc., 20(2000) 1135-1143.

3) Anstis, G.R., Chantikul,P., Lawn,B.R. and Marshall, D.B.: A critical evaluation of indentation techniques for measuring fracture toughness" , J. Am. Ceram. Soc.,64-9(1981), 533-538.

4) Lawn, B. R. and Fuller, E.R.,Measurement of thin-layer surface stresses by indentation fracture, J. Mat. Sci., 19(1984), 4061-4067.

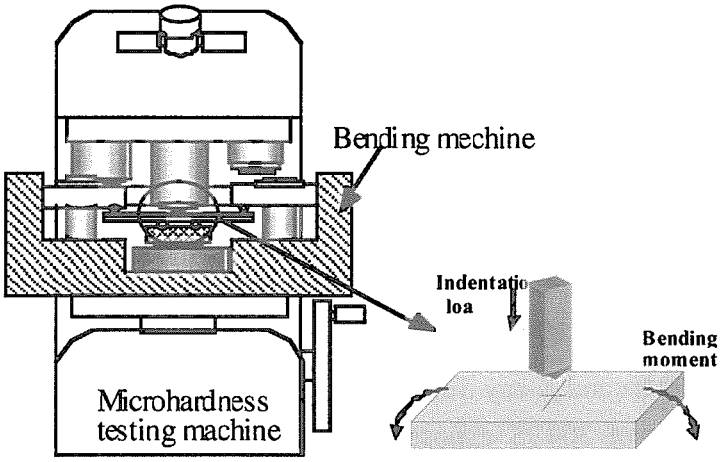

Fig.7.3.1 The indentation test combined with in-situ bending.

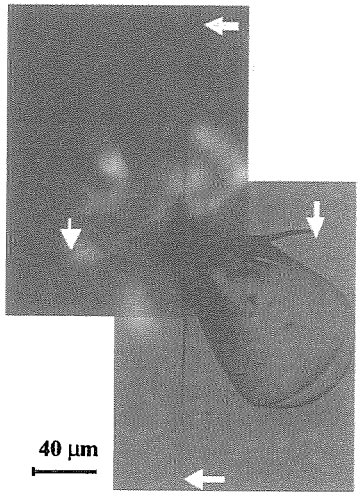

Fig.7.3.2 A crack propagation pattern on the coatings.

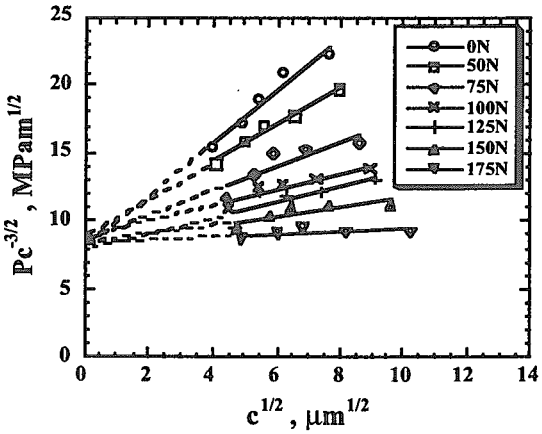

Fig.7.3.3 shows the relationship between $Pc^{-3/2}$ and $c^{1/2}$

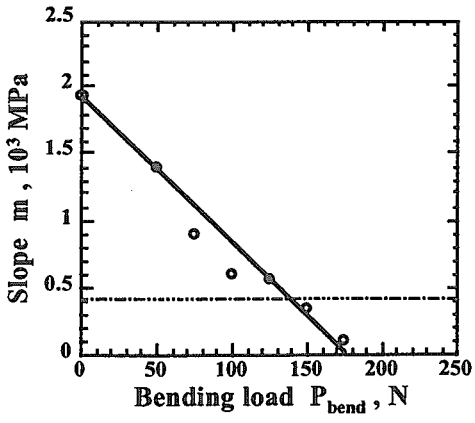

Fig.7.3.4 The relationship between the slope m and the bending load P_{bend}

7.4 High Temperature Corrosion of Equipment Materials Applied to Thermochemical Hydrogen Production Process in $H_2O + SO_3$ atmosphere

Y. Kurata, T. Suzuki and S. Shimizu
(*E-mail:* ykurata@popsvr.tokai.jaeri.go.jp)

The thermochemical hydrogen production process developed at Japan Atomic Energy Research Institute has severely corrosive environments such as boiling sulfuric acid, sulfuric acid decomposition gases and halogen gasses. Therefore, it is important to study corrosion-resistant materials in these environments in order to put this process to practical use. In this study[1], corrosion tests of 10 iron-base and nickel-base alloys were carried out in $H_2O + SO_3$ atmosphere.

The tested alloys were Alloy 800H, Hastelloy XR, Hastelloy C276, 304SS, Ni-18.5Cr, Ni-18.5Cr-21W, 316SS, Fe-25Cr-7Ni, Inconel 600 and Alloy 800. Corrosion tests were performed in $H_2O + SO_3$ atmosphere at 850℃ for 1000h. Microstructure of corroded specimens was analyzed using optical microscope, EPMA and X-ray diffraction.

Figure 7.4.1 shows EPMA analysis of 304SS exposed to $H_2O + SO_3$ atmosphere at 850℃ for 1000h. As shown in this figure, oxide films of alloys containing iron and chromium are mostly composed of outer iron-oxide and inner chromium-oxide. Internal oxidation is also recognized. Sulfur concentrates at the scale/metal interfaces and grain boundary penetration regions.

Figure 7.4.2 shows schematic diagram of high temperature corrosion in $H_2O + SO_3$ atmosphere. Surface oxidation, spallation of corrosion film, uniform corrosion and grain boundary penetration composed of internal oxidation and sulphuration occur in this atmosphere and the corrosion proceeds by grain boundary penetration.

Relationship between grain boundary penetration depth and time is shown in Fig.7.4.3. 304SS, 316SS and Hastelloy C276 are inferior in corrosion resistance and Fe-25Cr-7Ni steel is superior among 10 alloys. Alloys such as Alloy 800H and Hastelloy XR show intermediate corrosion resistance. Corrosion in this atmosphere seems to be expressed using the parabolic law between the grain boundary penetration depth and time.

Reference

1) Kurata, Y., Suzuki, T. and Shimizu, S. : "High temperature corrosion of iron-base and nickel-base alloys for hydrogen production apparatus by thermochemical method in $H_2O + SO_3$ atmosphere", JAERI-Research 2000-011(2000) [in Japanese].

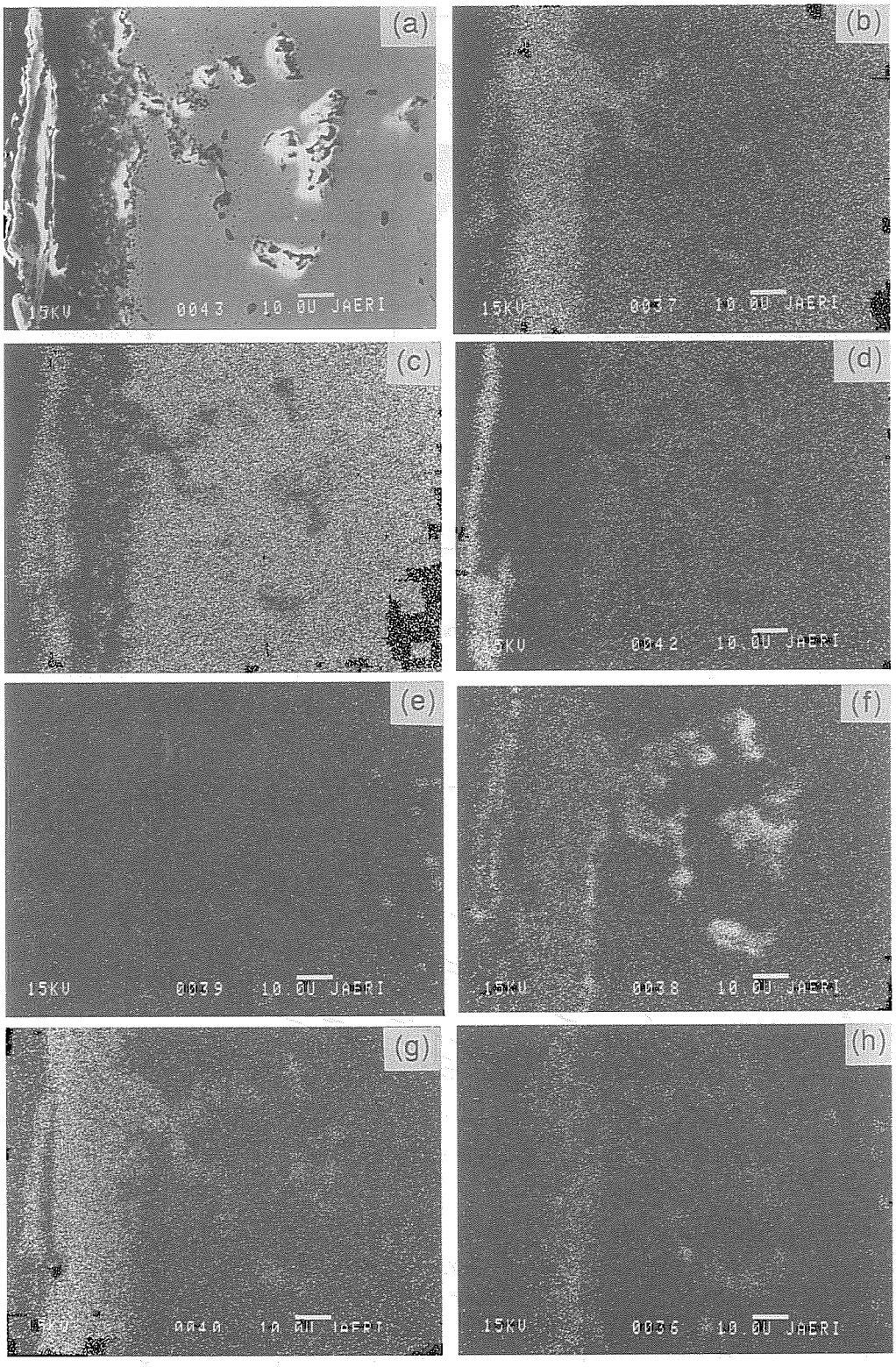

Fig.7.4.1 EPMA analysis of 304ss exposed to $H_2O + SO_3$ atmosphere at 850℃ for 1000h, (a) SEI, (b) Cr, (c) Fe, (d) Ni, (e) Mn, (f) Si, (g) O and (h) S.

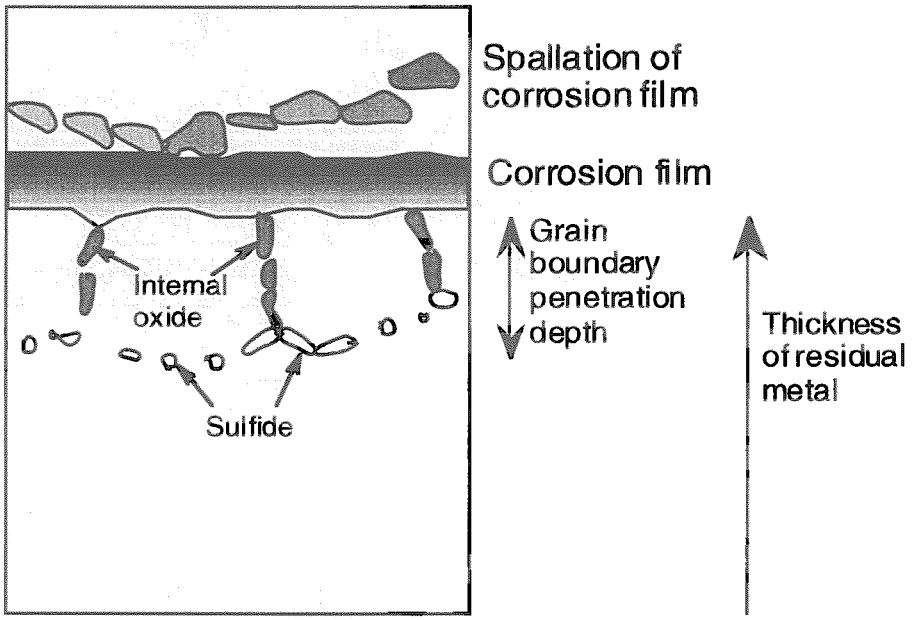

Fig. 7.4.2 Schematic diagram of high temperature corrosion in $H_2O + SO_3$ atmosphere.

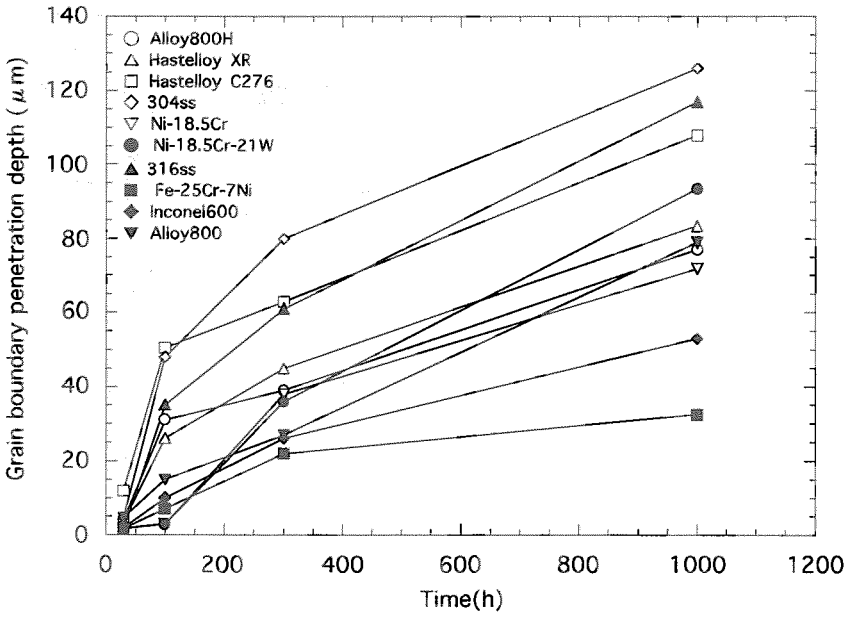

Fig.7.4.3 Relationship between grain boundary penetration depth and time.

7.5 Microstructural Evolution during Creep of Ni-base Solid Solution Alloys and In-situ Observation at High Temperatures

Y.Kurata, H.Utsumi*, K.Kikuchi, T.Suzuki and T.Miura**
(*E-mail:* ykurata@popsvr.tokai.jaeri.go.jp)

It is essential to study creep behavior and microstructural evolution during creep of pure Ni-Cr alloy and the alloy with the third solution element to understand creep and fracture behavior of practical alloys. In this study[1], changes of creep curves and microstructure during creep were studied using Ni-18.5Cr and Ni-18.5Cr-16W alloys. In addition, in-situ observation of specimen surface during creep was made.

The materials tested in this study were Ni-18.5Cr and Ni-18.5Cr-16W alloys, and supplied in the form of plates 15 mm thick and under solution-treated condition. Creep tests under constant load were carried out at 700 to 900℃ in air environment. Creep-interrupted specimens were prepared at 700 and 900℃ for microstructure observation using an optical microscope (OM) and transmission electron microscope (TEM). A specially designed mechanical testing machine with SEM[2] was used to make in-situ observation of specimen surface during creep at 700℃.

At 700 and 800℃, Ni-18.5Cr alloy exhibits a normal type creep curve consisting of primary (transient), steady-state and tertiary creep stages. On the other hand, oscillation of creep rates is recognized in creep curves of Ni-18.5Cr alloy at 900℃ as shown in Fig.7.5.1. Ni-18.5Cr-16W alloy exhibits a tertiary creep dominant curve with an inverse transient creep stage at 700 to 900℃. Figure 7.5.2 shows creep curves of Ni-18.5Cr-16W alloy at 700℃.

According to OM and TEM observations, a characteristic subgrain structure of class II alloys[3] forms in Ni-18.5Cr alloy during creep at 700℃. In contrast, dislocations distribute uniformly without forming subgrains in Ni-18.5Cr-16W alloy. This dislocation structure of Ni-18.5Cr-16W alloy is a characteristic one of class I alloys[3]. It is found that addition of W to Ni-18.5Cr alloy brings about change of creep behavior of a solid solution from class II to class I.

Creep rupture at grain boundaries usually proceeds by the following steps; (i) nucleation of voids, (ii) growth of voids and (iii) coalescence of voids. Figure 7.5.3 shows grain boundary damage as a function of time fraction for void-nucleated grain boundaries and for void-coalesced grain boundaries. This result is obtained from in-situ observation during creep at 700℃. As

---

* Tohoku University , **Muroran Institute of Technology

shown in this figure, voids form and coalesce in Ni-18.5Cr alloy at an earlier stage of time fraction than in Ni-18.5Cr-16W alloy. Nevertheless, fine grains form at grain boundaries and development of voids occur at new grain boundaries until fracture in Ni-18.5Cr alloy.

References

1) Kurata. Y., Utsumi. H., Kikuchi. K., Suzuki. T. and Miura. T.: "Proc. of 4th Inter, Conf. on Recrystallization and Related Phenomena", The Japan Institute of Metals, 283(1999).
2) Kikuchi. K., ASME-PVP, 315 , 229 (1995).
3) Sherby. O.D. and Burke. P.M., Prog. Mat. Sci., 13, 325 (1967).

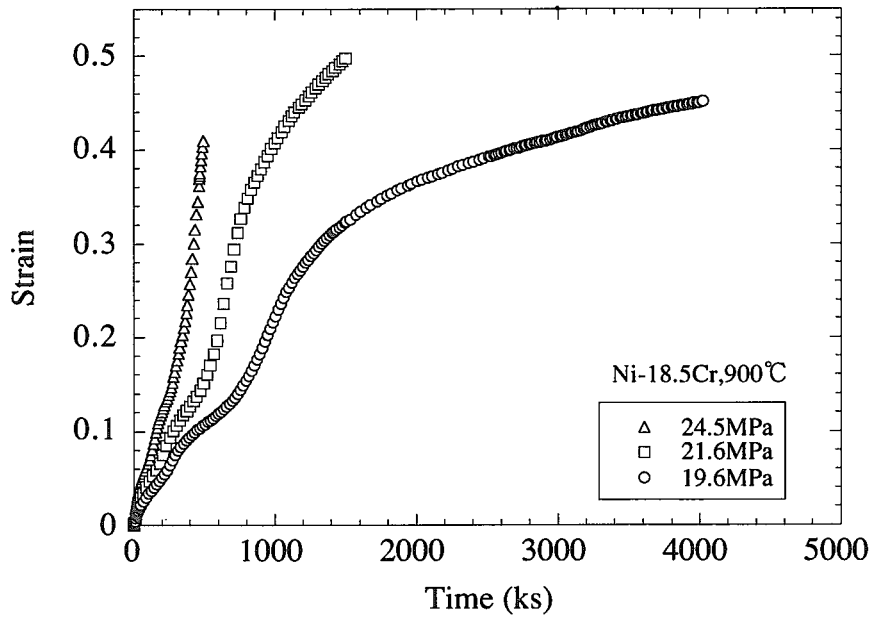

Fig.7.5.1 Creep curves of Ni-18.5Cr alloy at 900℃.

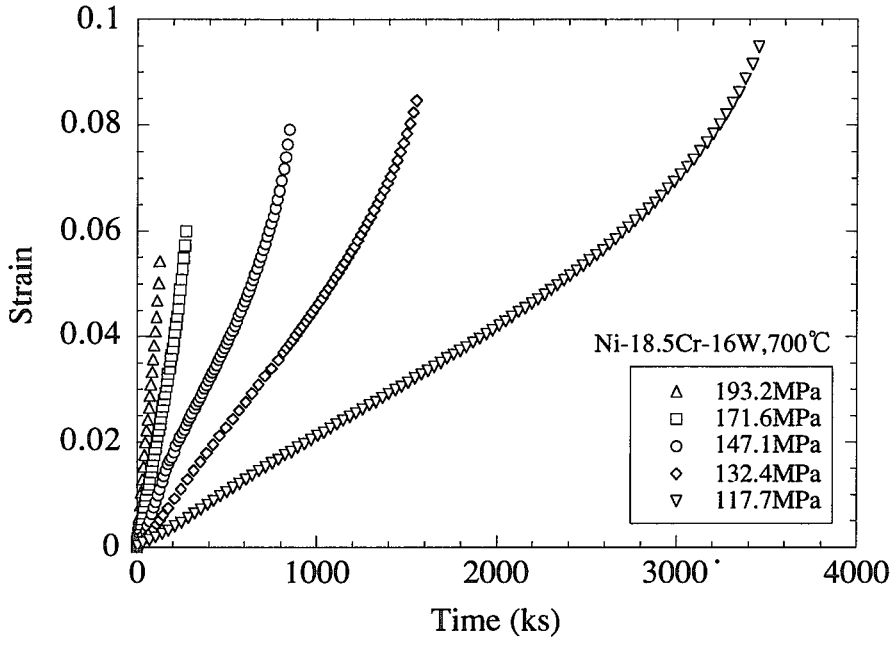

Fig.7.5.2 Creep curves of Ni-18.5Cr-16W alloy at 700℃.

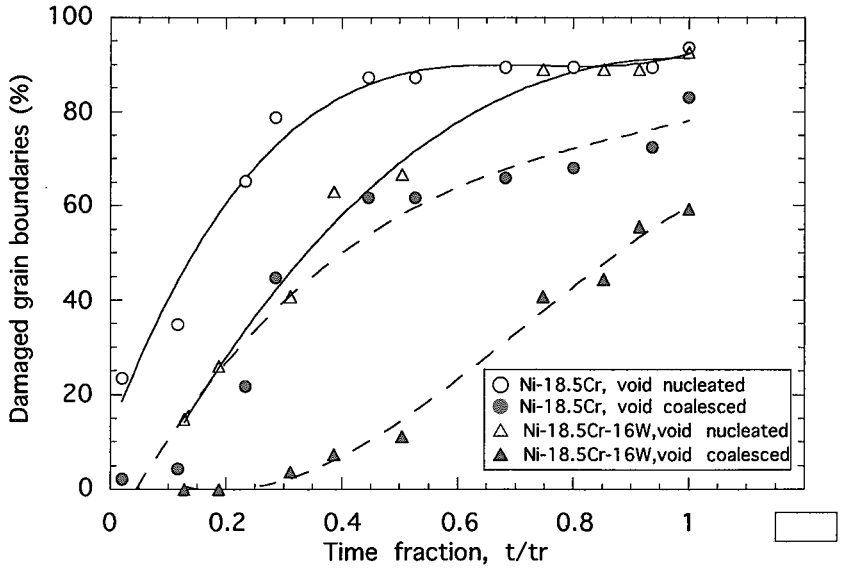

Fig.7.5.3 Grain boundary damage as a function of time fraction.

7.6 Low Cycle Fatigue Strength of Diffusion-Bonded Joints of Alumina Dispersion-Strengthened Copper to Stainless Steel

H. Nishi and T. Araki*

(*E-mail*: nishi@popsvr.tokai.jaeri.go.jp)

It is proposed that the first wall and divertor components of ITER are made of alumina dispersion-strengthened copper (DS Cu) bonded to austenitic stainless steel, since the DS Cu has excellent thermal conductivity and strength at elevated temperatures. Therefore, a bonding technology for DS Cu to stainless steel has been investigated and improved[1, 2]. The authors have studied the strength of the joint using direct diffusion bonding and diffusion bonding with an interlayer. For direct diffusion bonded joints, recrystallization and intermetallic compounds consisting of B, Fe and Cr developed in the DS Cu near the bonding interface. Its Charpy impact strength was 20% of that of DS Cu, though the tensile specimen fractured at the DS Cu and the joint had strength similar to DS Cu. Diffusion bonding with interlayer foils, such as Au, Cu and Ni, was subsequently carried out to avoid recrystallization and the formation of intermetallic compounds near the interface. The tensile strength of the joint with Au interlayer was superior to those with Cu and Ni interlayers and similar to that of DS Cu. The Charpy impact strength of the Au interlayer joint was 50% of that of DS Cu.

It is also important to evaluate the fatigue strength of the joints, because the first wall and the divertor components are subjected to severe stress caused by thermal expansion and electromagnetic forces. In this work, low cycle fatigue tests were performed on the direct diffusion bonded joint, the Au interlayer joint, stainless steel and DS Cu in order to investigate their fatigue strength and fracture behavior. The bonding conditions of the direct bonded joint were 1273K for 1 hour. For the Au interlayer joint, the thickness of Au interlayer was 20 μ m and the bonding was done at 1123K for 2 hours.

Low cycle fatigue strengths are summarized in Fig.7.6.1. The low cycle fatigue life of 316 stainless steel was large enough compared with the DS Cu and the joints. For the direct bonded joint, the fatigue life in the small strain range was considerably lower than that of the DS Cu annealed at 1273K, while the fatigue life in the large strain range was almost the same as that of the DS Cu. In the Au interlayer joint, however, low cycle

*Kawasaki Heavy Industories, Ltd

fatigue strength was larger than the direct bonded joint and similar to the DS Cu annealed at 1123K. The fatigue strength of the DS Cu annealed at 1123K was larger than that at 1273K. This is attributed to difference in the microstructure caused by recovery.

The direct bonded joint specimen fractured at the interface in the case of small strain range, whereas fracture occurred at the DS Cu approximately 6 mm from the interface for specimens corresponding to $\Delta \varepsilon_t$ =1.5, 1.2%. As for the Au interlayer joint, the specimen fractured in the 316 stainless steel in the case of small strain range (less than $\Delta \varepsilon_t$ =1%). On the other hand, in the case of large strain range the fracture location was in the DS Cu similar to behavior for the large strain range for the direct bonded joint.

As mentioned above, the fracture locations of the joint specimens varied depending on the strain range. Figure 7.6.2 shows the cyclic stress-strain curves of both joints as well as the stainless steel and DS Cu obtained at half of the number of cycles to failure. Comparing the cyclic stress-strain curves of the stainless steel and the DS Cu, the strain hardening of the stainless steel was larger than that of DS Cu annealed at 1273K and 1123K. The stress-strain curve of stainless steel intersected those of DS Cu at a strain amplitude of approximately 0.55% for DS Cu annealed at 1273K and 0.65% for 1123K. The deformation stress of the stainless steel was smaller than DS Cu at small strain amplitudes (less than the strain at the crossover points). Hence, the strain distribution in the joint specimen was not uniform. In the case of large strain range, the strain in the DS Cu was larger than that in the stainless steel, because the deformation stress of the DS Cu was smaller than that of the stainless steel. Therefore, the specimen fractured at the DS Cu in the case of large strain range. On the contrary, for the small strain range the strain in the stainless steel was larger than that in the DS Cu. The fracture location of the joint corresponded with its strain distribution except for the small strain range of the direct diffusion bonded joint. Since this had both recrystallization and intermetallic compounds near the interface, it fractured at the interface.

References :

1) Nishi, H., Muto, Y. and Sato, K.:"Solid-state Diffusion Bonding of Alumina Dispersion-strengthened Copper to 316 Stainless Steel", J. Nucl. Mater., 212-215, p1585-1589(1994)

2) Nishi, H., Araki, T. and Eto, M.:"Diffusion bonding of alumina dispersion-strengthened copper to 316 stainless steel with interlayer metals", Fusion Engineering and Design, 39-40, p.505-511(1998)

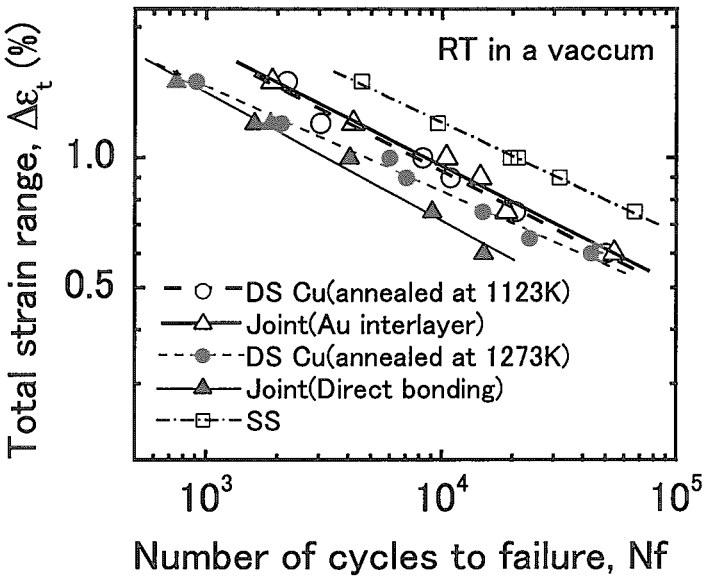

Fig. 7.6.1 Low cycle fatigue strength for all specimens.

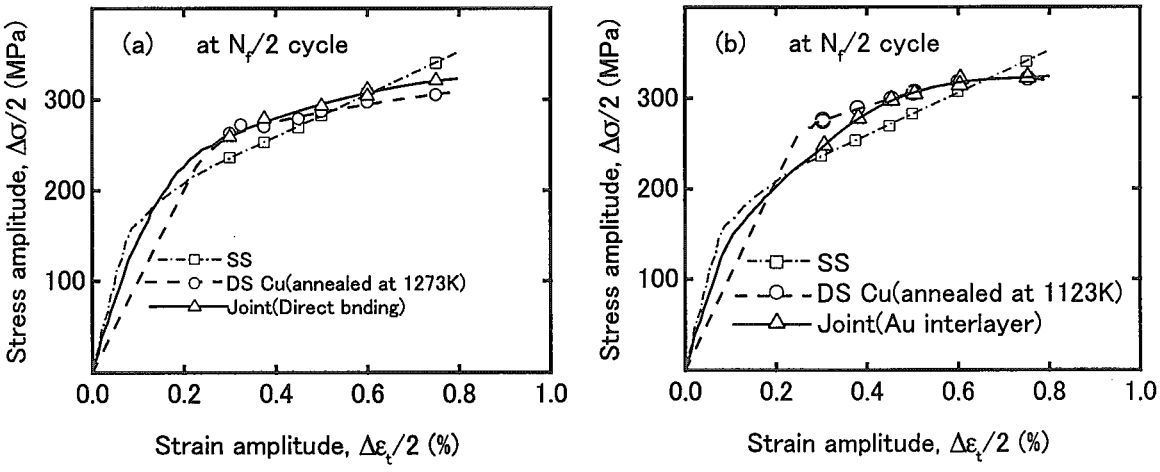

Fig.7.6.2 Comparison of cyclic stress-strain curves.
(a) direct bonded joint (b) Au interlayer joint.

8. Interfacial Studies for Reprocessing Materials and Reactor Core Materials

The life prediction study of spent fuel reprocessing equipment materials have been carried out in relation to the STA projects for the safety research on the RRP (Rokkasho Reprocessing Plant). The corrosion behavior of the mock-ups of nitric acid recovery evaporator made of type 304ULC and dissolver made of zirconium was minutely examined by nondestructive inspection methods as second ISI and first ISI respectively after operated during one year. In the former, the enhancement effect on the wall thinning rates was clearly observed in both top side and bottom side of heat conducting tubes. The reason was clarified with the effects of the surface temperature and the formation rate of oxidizer ions like V^{5+} and RuO4. V was added in the mock-up nitric acid solution as a dummy of Np contained in it of the practical device. The corrosiveness of V at heat conducting surfaces was coincident with it of Np, as the results of corrosion tests using radioactive isotopes of Np. On the other hand, the reliability of zirconium on a dissolver was examined with respect to the susceptibility to SCC. It is clarified that the susceptibility to SCC on the thermal jacket depends on the characteristics of the surface oxide films with the low thermal conductivity formed by the deposition of Ru etc. The AE detection method as one of the promising techniques for monitoring the SCC was modified with removing noises arisen from boiling and mechanical wear. The important role of the SCC was observed in the crack growth rate of corrosion fatigue as functions of the stress intensity factor range and the wave pattern. The modified stainless steel with immunity to intergranular attacks so-called the EB-SAR and a new Cr-W-Si nickel base superalloy enriched with passive film former elements showed the high resistance to corrosion on heat conducting surfaces in the mock-up nitric acid solution. On the other hand, the purified Nb-5W alloy developed as alternative materials of zirconium showed the high resistance against SCC and high mechanical strength.

The development of new cladding materials was carried out focusing on the selection

of candidate alloys according to the requirements for the advanced nuclear power plants aiming at the ultra-high burnup more than 100GWd/t MOX and the fast neutron spectrum tailoring. On the point of view, the major characteristics among candidate materials were examined with the neutron adsorption, mechanical properties, the corrosion resistance against high temperature water, the compatibility to MOX fuels etc. Stable austenitic stainless steels and niobium alloys were selected for candidate cladding alloys of the ultra-high burnup ABWRs. The former was modified by the adjustment of alloying elements, the purification by the EB-CHR melting process and the modification of metallographic structures by the SAR thermo-mechanical treatment. The corrosion test device with a pair of sapphire windows installed in a critical temperature water loop was arranged for evaluating the corrosion resistance at cladding surfaces of candidate alloys. The new experimental corrosion apparatus simulated by the low temperature RF plasma was arranged for analyzing the surface reaction mechanisms on the heat conducting surfaces in high temperature water. A new developed austenitic stainless steels type 25Cr - 25-35Ni showed the excellent corrosion resistance. The corrosion resistance of Nb was modified by addition of Mo up to that of zircaloy-2. The usefulness of Nb alloys as a PCI liner was evaluated with respect to the high mechanical strength and high hydrogen solubility.

8.1 Outline of Research on Advanced Cladding Materials Applied for Ultra-high Burnup and Reduced Moderation Water Reactors

I.Ioka, S.Kanbara, Y.Inohara, K.Fukaya, K.Tachibana and K.Kiuchi
(*E-mail:* ioka@popsvr.tokai.jaeri.go.jp)

The development of the cladding tube with excellent durability is an essential problem in ultra-high burnup of the power reactor. The research of advanced cladding tubes for ultra-high burn-up reactor and for the reduced moderation water reactor has been carried out. The progress of the research is described as follows:

(1)Evaluation of the Zircaloy for ultra-high burnup

The development history of the zirconium alloy including the Zircaloy shows that it is hard to estimate the results of in-pile test from that of the conventional corrosion test (out-pile test). Therefore, the development of the new testing method that can simulated the actual environment and the elucidation of the corrosion-controlling factor of the cladding tube are desired. In the development of zirconium alloy by adjustment of Fe, Ni, Cr and Nb, the optimized Zircaloy-2 was the most protective material in the BWR's environment. However, the effect of Nb on the corrosion-resistant mechanism of zirconium alloy may be different from other additive elements. It is necessary to evaluate the effect of Nb in detail. In case of RIA and LOCA, it seems that the loss of ductility in zirconium alloy under heavy irradiation and boiling restricted extended fuel burnup. Therefore, the extended burnup in zirconium alloy seems to be about 70 GWd/t even in the maximum.

(2)Primary determination of advanced cladding materials

A preliminary evaluation to select the advanced cladding materials was carried out on the practical materials, such as austenitic stainless steel, iron or nickel base superalloys, titanium alloy, niobium alloy and ferritic stainless steel. In the austenitic stainless steel, the loss of the ductility by irradiation at the light water reactor coolant temperature and irradiation induced stress corrosion cracking are a largest problem. High Cr and Ni austenitic stainless steel with the _ phase at practical temperature range seems to be a most powerful candidate at the point of the irradiation resistance for void swelling and the improvement on corrosion resistance. Though they have a technical problem in the

weldability, the high-pure technique removed the problem.

In the iron or nickel base superalloys, there is little research on high-temperature and high-pressure water corrosion under the light water reactor condition. Especially, the mechanical properties of nickel base superalloys are degraded by hydrogen and helium that are created by the nuclear transmutation of the element in the superalloy. Enrichment of helium and impurity at the grain boundary is severe problems in the high temperature irradiation field.

The titanium alloy under the light water reactor condition is expected to the good corrosion resistance. It is necessary to sufficiently clarify the corrosion action under the irradiation environment. The titanium alloy resembles the zirconium alloy in the physical property (phase transformation, lattice structure, protective film structure). However, the titanium alloy has low thermal neutron economical efficiency. Therefore, it is hard to expect large improvement as new material of ultra-high burn-up cladding tube.

In the niobium alloy, the development of new material by ultra-high purity technique is related to the improvement of ductility and DBTT. The improvement of corrosion resistance on high temperature water is being tried by the addition of V, Cr and W. However, it is necessary to acquire the wide data for corrosion and irradiation under the light water reactor condition. The effective utilization as liner material in the fuel side is also considered because the solution range of the hydrogen in middle low temperature is big.

The corrosion resistance and DBTT rise seem to be problems in the vanadium alloy, though the many data of the V-Cr-Ti alloy are accumulated for a fusion reactor. However, it is chemically the activity metal. The superiority is lower than the niobium alloy.

Though the wide research is carried out in the zirconium alloy in a past, it is necessary to confirm material data that utilized the latest purification technology because the impurity seems to give large effect in the characteristics. The corrosion-resistant mechanism of Zr-Nb alloy may be different from the Zircaloy. Therefore, there is a room of the examination including the fraction of Nb and the heat treatment.

In ferrite stainless steel, the storage of the data is widely attempted as a material for the fusion reactor. The data under the light water reactor condition is little. Though high Cr

(>12%) is necessary in ferritic stainless steel in view of the corrosion resistance, high Cr caused the DBTT rise and the 475℃ brittleness. It is hard to improve the properties of ferritic stainless steel in high temperature water condition.

From the above, high-pure niobium alloy which could expect the good corrosion resistance and stable austenitic stainless steel with a capability of future development and improvement were selected as candidate materials of ultra-high burnup cladding tube.

(3)Trial manufacture and basic evaluation test of the candidate materials

High Cr and Ni austenitic stainless steels (25Cr-20Ni, 20Cr-35Ni) with the stable _ phase at middle temperature was manufactured by the electron beam melting because of the reduction of impurity. The materials were thermomechanically treated in order to give a fine grain with uniformly dispersed precipitation. Though gas impurity O and N in the materials can be reduced 30 ppm or less, impurity C remained over 100 ppm. It is considered that high C in the material is attributed to TaC in the raw material. The distribution of element in the materials axially fluctuated the range of 2 %. It was proven that a vacuum arc melting was necessary in order to achieve homogenization of the element after the electron beam melting. Nd-10Mo alloy was experimentally manufactured using the electron beam melting. The impurity O, N and C in the alloy was 10 ppm or less. The hardness and the grain size of the alloy were almost uniform.

(4)Cold/hot test equipment

Test equipment was manufactured in order to evaluate the temperature dependency of corrosion rate of candidate materials including zirconium alloy. The equipment realized the condition to the supercritical water (25MPa and 450℃). Sapphire windows for the laser Raman spectroscopy analyzer were installed in respect of the in-situ observation of the generation of oxide film.

(5)Simulated ion irradiation test

Chemical species, such as active H^+ and O^{2-}, were produced in the primary cooling water of light water reactor by radiation. They diffuse in the material inside, and bring about the change of properties. In addition, the diffusion may be promoted under the irradiation environment. The ion irradiation was carried out in zirconium alloy and austenitic stainless steel in order to clarify this phenomenon. Microstructure observation and microhardness test were carried out in the ion-irradiated material.

8.2 Evaluation of Fundamental Properties Required to Candidate Alloys of Fuel Cladding Materials Applied for Ultra-high Burnup and Fast Neutron Spectrum Reactors

K.Kiuchi, M.Takizawa, H. Ogawa and T. Sabri
(*E-mail:* kkiuchi@popsvr.tokai.jaeri.go.jp)

The candidate materials for MOX fuel cladding of advanced power reactors aiming at the ultra-high burnup and/or fast neutron spectrum control were investigated with respect to the neutron economy and technological fusibility. The fissile plutonium in MOX fuels is possible to enrich up to 20% as same as it of FBR fuels. It was clarified that the neutron economy is not the predominant factor on the selection of candidate materials, compared with irradiation properties and mechanical properties. Stable austenitic stainless steels and niobium alloys were selected for candidate materials instead of zirconium alloys like zircaloys with based on these properties. In ABWR, the displacement rate of cladding alloys at 100GWd/t of MOX fuels with the low excess reactivity is 40% lower than that of uranium fuels. The infinite multiplication factor of above candidate alloys is almost same on the calculation with a pin cell model of ABWRs with nearly half thickness of zircaloy cladding as shown in Fig.8.2.1. However, stainless steels are the most promising alloy for the fast neutron spectrum reactor, because refractory metals like Nb, V, Ti etc., have the high resonance neutron absorption in the high neutron energy region.

The critical issues on the long performance of candidate materials were examined with respect to the water side corrosion. The improvement of corrosion resistance is required to niobium alloys as well as zirconium alloys. The degradation in metal matrix is expected to control with the irradiation defect-gaseous impurity interactions. The maximum enrichment of gaseous impurities like H(T) and O in candidate alloys during 100GWd/t was calculated by the computer simulation method. The surface reaction is expected to control with the amount of exited atoms at metal–high temperature steam interfaces under heavy irradiation as shown in Fig.8.2.2. The hydrogen penetration rate in metal matrix is proportional to that of oxidation rate. The oxidation of N-type semiconductor like ZrO_2 accompanies with the penetration of oxygen in metal matrix.

The protectiveness of ZrO_2 is going on poor with increasing oxygen solubility in metal matrix. Accordingly, the steady state oxidation rate obeys with Arrhenius relationship with dependent on the metal surface temperature as described in the previous report.

On the other hand, austenitic stainless steels form the protective oxide film composed of P/N dual semiconductor layer like spinel type oxide/Cr_2O_3. The enrichment of Cr is effective to form the inner layer of Cr_2O_3. The formation of a series of different type semiconductors on metal surfaces is possible to inhibit the migration of different type of point defects and to decrease the oxidation rate, even if that under irradiation. However, the important factor on reliability of stainless steels is considered to be to increase the contents of hydrogen formed by transmutation reactions of Ni under heavy neutron irradiation. It is affected to enhance the susceptibility to IASCC by the interactions of hydrogen with irradiation defects and another impurities. The degradation rate due to the interaction in austenitic stainless steels is controlled with the austenite phase stability. Therefore, the chemical composition of candidate materials was selected by considering the balance among austenite phase stability, corrosion resistance and nickel contents as shown in Fig.8.2.3. The appropriate chemical composition range is very limited. However, the resisitance against IASCC would be improved by purifying impurities through electron beam melting and by modifying the metallographic structure through thermo-mechanical treatment so-called SAR. One of the other effective means is to decrease hydrogen contents by cladding a thin metallic layer with high hydrogen solubility at the practical temperature. On this purpose, niobium with the body centered cubic structure is considered to be one of the most promising metals. Niobium alloy cladding on austenitic stainless steels is possible to make with economical means by a new melting method using the difference of melting points between these alloys. The metal-hydrogen interaction in cladding alloy is controlled kinetically with the boundary conditions both high temperature water side and fuel side (tritium formation by nuclear reactions) as shown in Fig.8.2.4. On the practical conditions、the degradation of cladding materials accompanied with hydrogen absorption is expected to occur at the low temperature range, because of decreasing hydrogen solubility in metal matrix and increasing metal–hydrogen interactions with exo-thermally chemical reactions. The effectiveness of niobium cladding on stainless steels as a scavenger for removing hydrogen is required to clarify theoretically and

experimentally, by considering the effect of heat transfer. The acceleration mechanism on the oxidation and hydrogen permeation on heat conducting surfaces should be solved with new testing methods like the low energy plasma corrosion.

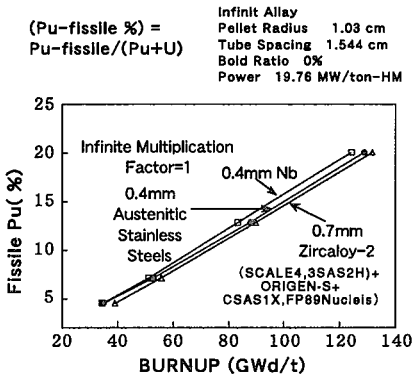

Fig.8.2.1 The enrichment rate of fissile Pu in MOX for satisfying the infinite multiplication factor higher than 1, as a function of the burnup rate.

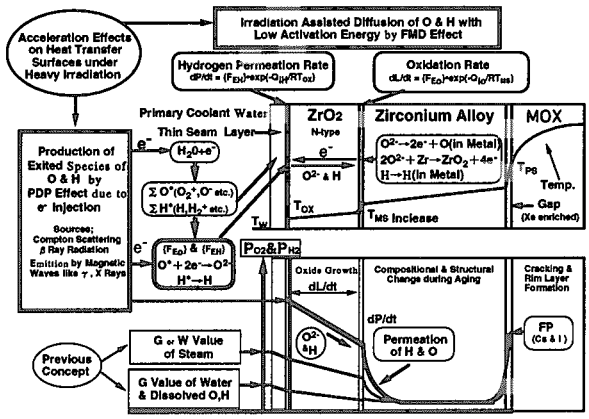

Fig.8.2.2 A schematic model for surface reactions on heat conducting surfaces. Oxidation and hydrogen permeation are accelerated by exited species.

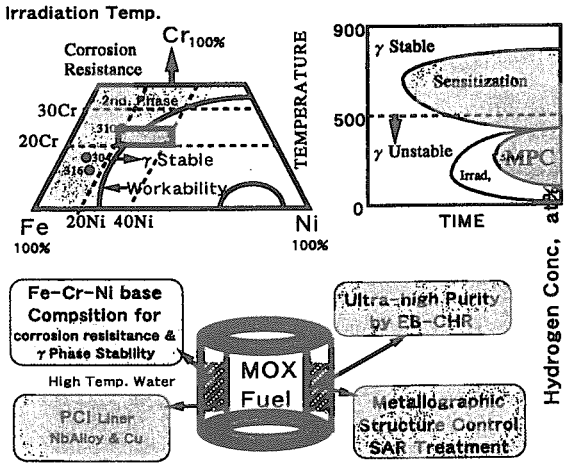

Fig.8.2.3 A schematic diagram on the modification process of stainless steels for inhibiting the resistance to IASCC

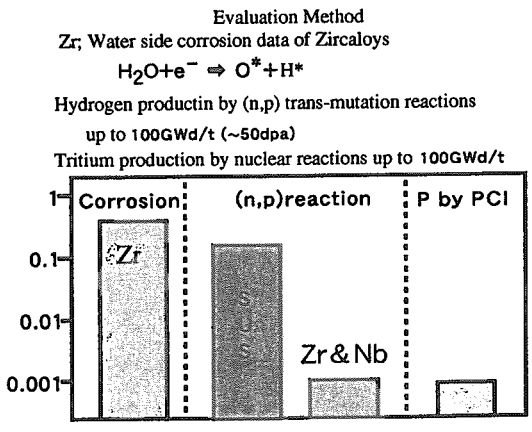

Fig.8.2.4 The maximum contents of hydrogen expected in candidate alloys for fuel cladding after 100GWd/t burnup of ABWRs

8.3 Development of New Cladding Materials for Advanced Light Water Reactors Aimed at Ultra-high Burnup and Fast Neutron Spectrum

S. Kambara, Y. Inohara, I. Ioka and K. Kiuchi

(E-mail: kambara@galileo.tokai.jaeri.go.jp*)*

The development of new cladding tube materials for advanced light water reactors aimed at ultra-high burnup and fast neutron spectrum is important. It is also significant to clarify the dependence of purity and cleanliness on the characterization like chemical, mechanical and physical properties of the developed materials.

In this research, we obtained ultra-high purity and cleanliness materials and evaluated and/or established the best forging, rolling and heat treating process. The materials are austenitic stainless steels with high Cr and Ni concentration which ratios are 20Ni-25Cr and 35Ni-25Cr, and Nb-10Mo alloy purified by electron beam melting (EB melting).

Table 8.3.1 presents the chemical composition of the stainless steels. Oxygen was remarkably decreased to 10 ppm or less. Nitrogen was decreased to 30 ppm. Carbon remained over 100 ppm. It may be estimated that residual carbon and nitrogen combined with tantalum to form TaC, TaN and Ta(C-N). Nickel and iron are deviated to some degree in casting direction. However chromium is not deviated in the same direction. By the way, deviation of the horizontal plane is at most within 0.2% to all metallic elements. So, it may be considered that these ingots have homogeneous property.

Table 8.3.2 presents chemical composition of Nb-10wt%Mo alloy. It is obvious that gaseous elements are extremely evaporated to 10 ppm or less and the alloy is sound due to little deviation of metallic elements.

Figure 8.3.1 shows as rolled stainless steel plates and a Nb-Mo alloy bar. The rolled stainless steels had different colors, the difference is attributed to their oxide scales. However, no cracks and cleavages at edge part of the plates and bar are found from visual examination

Figure 8.3.2 shows vickers hardness of the stainless steels and Nb-Mo alloy plate. Hardness perpendicular to rolling direction is equal in the same materials. Nb-Mo alloy is harder than the stainless steels. Adding 10 % molybdenum into niobium metal makes Nb alloy hard by forming solid solutions expectedly.

Figure 8.3.3 shows a microstructure as annealed stainless steels and Nb-Mo alloy at half

depth of the plate measured with an optical microscope. Especially, the stainless steels are undergone thermomechanically treatment[1] to obtain fine grain with uniformly distributed precipitation. The grain size of the stainless is almost uniform, however Nb-Mo alloy is not uniform for increased yield strength. The smaller this structure is forced to do under the best condition, the stronger the material becomes through hall peach principles.

From this study, we are able to obtain the suitable procedure both of the stable austenitic stainless steels and Nb-Mo alloy, which possesses high purity, clean, segregation free, high resistance and mechanically strong materials for future advanced reactors.

Reference

1) K. Kiuchi , et al., : J. Nuclear Materials, 212-215, 554(1994).

Table 8.3.1 Chemical composition of 2 types of stainless steels

Material	Ni	Cr	Fe	O	N	C
	(wt%)			*(ppm)*		
aimed spec.	*20±2*	*25±2*	*55±2*	*<30*	*<30*	*<30*
20Ni-25Cr	22.7	24.7	0.5	10.2	23.9	117.2
aimed spec.	*35±2*	*25±2*	*40±2*	*<30*	*<30*	*<30*
35Ni-25Cr	36.7	25.3	38.0	12.6	32.8	62.8

Table 8.3.2 Chemical composition of Nb-10wt%Mo alloy

Material	Nb	Mo	O	N	C
	(wt%)		*(ppm)*		
aimed spec.	*90.0*	*10.0*	*<15*	*<10*	*<10*
Nb-10Mo	90.7	9.3	11	10	5

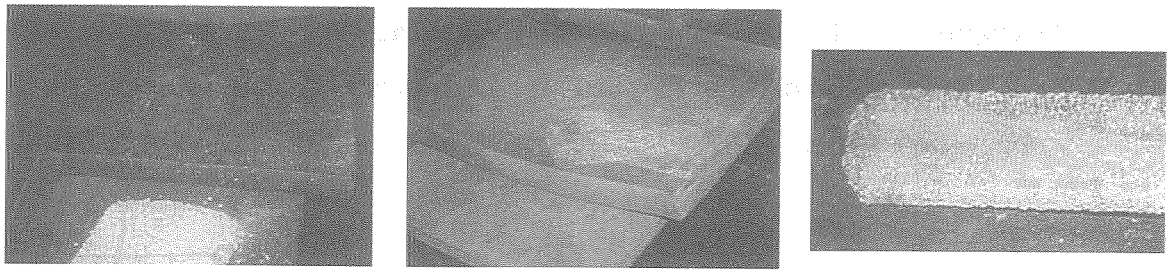

a). 20Ni-25Cr (31^{t} x 202^{w} x 300^{L})

b).35Ni-25Cr (32^{t} x 205^{w} x 297^{L})

c).Nb-10Mo (10^{t} x 114^{w} x 677^{L})

Fig. 8.3.1 As Rolled SUS steels plate and Nb-Mo alloy bar

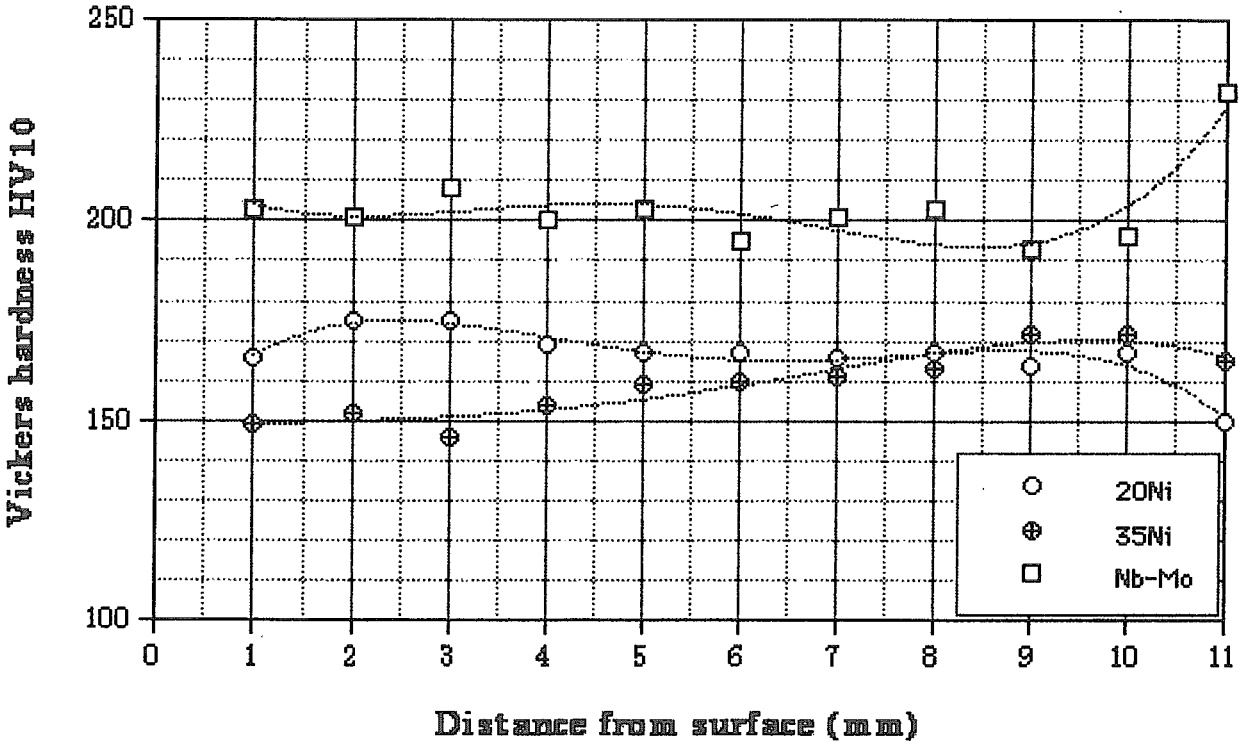

Fig. 8.3.2 Vickrers hardness result in SUS steels and Nb-Mo alloy plate

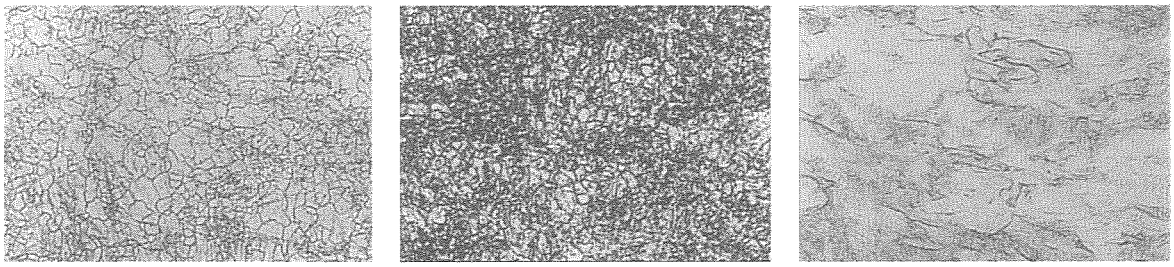

a). 20Ni-25Cr b).35Ni-25Cr c).Nb-10Mo

Fig. 8.3.3 Micro structure as annealed SUS steels and Nb-Mo alloy

8.4 Development of Testing Apparatus for Evaluating Corrosion Resistance of New Fuel Cladding Materials Applied for Advanced Water Reactor to High Temperature Water

Y. Inohara, I. Ioka, K. Fukaya and K. Kiuchi
(*E-mail:* yinohara@galileo.tokai.jaeri.go.jp)

On the developments of new fuel cladding materials applied for advanced water reactor, it is important to evaluate the corrosion resistance of the materials under an advanced water reactor condition. So the testing apparatus for evaluating corrosion resistance under high temperature and high pressure water was developed. The specification of the testing apparatus is shown in Table 8.4.1. The apparatus can control the temperature up to 450°C and the pressure up to 25MPa.

The apparatus consists of the testing part (autoclave), the circulating part (pump and filter) and the control and recording part (thermocouple and flow meter). The flow-sheet of the apparatus is shown in Fig.8.4.1. The autoclave is made of Inconel 625, and it had two sapphire windows for in-situ observation of specimen. Standard size of specimen is 45mm in length, 20mm in width and 2mm in thickness. And the 4 specimens can be tested at one time.

Controlling capability of this apparatus at high temperatures and high pressures was tested. The results of the test were summarized in Table 8.4.2. Temperature fluctuations are controlled in the range of -1 to 1℃ at tested temperatures and pressure fluctuations are controlled in the range of -0.2 to 0.2MPa at tested pressures. The dissolved oxygen (DO) in water can decrease less than 0.6ppb and DO fluctuations are controlled in the range of -2 to 2% at tested DO.

Table 8.4.1 Main specification of the testing apparatus

autoclave capacity	780cc	
autoclave material	Inconel 625	
autoclave seal	edge type (Ni seal ring)	
control range	temperature	R.T.～450℃
	pressure	～25.0MPa
	DO (dissolved oxygen)	>0.4ppb
	flow rate	1L/hr

Table 8.4.2 Capability of controlling operation parameters

temperature	±1℃(at 330℃)
	±1℃(at 420℃)
pressure	±0.2MPa(at 16.0MPa)
	±0.2MPa(at 23.0MPa)
DO (dissolved oxygen)	0.4～0.6ppb (on pure N_2 bubbling)
	±1%(at 1ppm)
	±2%(at 10ppm)

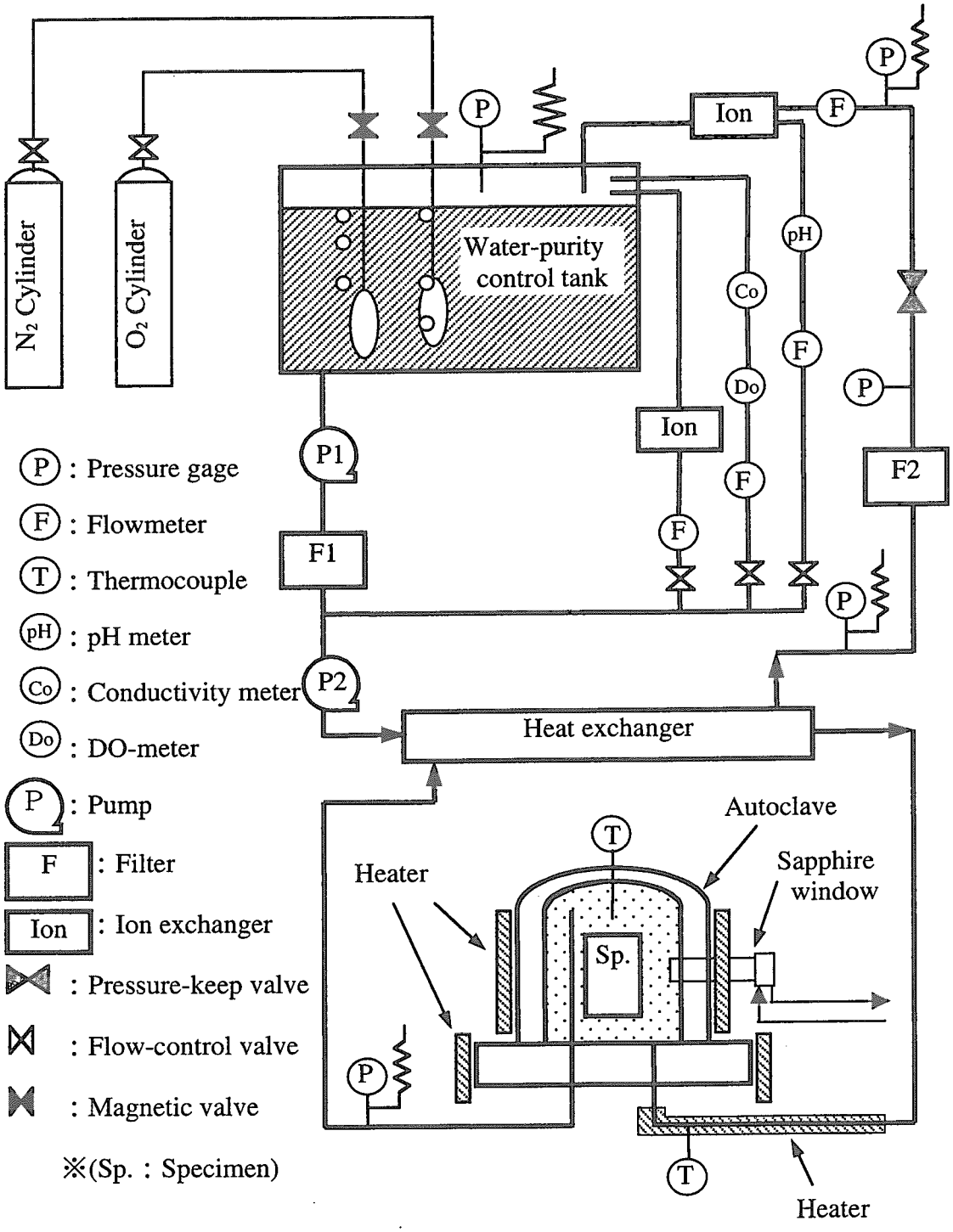

Fig. 8.4.1 Flow-sheet of the testing apparatus

8.5 Development of Corrosion Testing Methods with Low Temperature Plasma Source for Simulating Irradiation on Heat Transfer Surfaces in Environment

T.Saburi and K.Kiuchi
(*E-mail:* saburi@galileo.tokai.jaeri.go.jp)

In considering the corrosion of metals in nuclear facilities, it has been clear that the analysis method and countermeasurement based on the usual aqueous chemical and electrochemical understanding cannot be adhibited. Because the corrosion rate and the change of material property at heat transfer surfaces in the corrosive solution such as cladding tubes of power plants[1] and evaporator tubes of a spent fuel reprocessing equipment[2] are accelerated one order higher than those expected from the simple immersion condition. Authors have been pointed out the new corrosion mechanism for interpreting the phenomena, namely, the direct surface reactions with the activated oxygen and hydrogen species formed at specimen surfaces by the low temperature plasma excitation[3),4)]. This report deals with the development of corrosion test devices under the low temperature plasma excitation[5] for clarifying the detail corrosion mechanism.

The developed device as shown Fig.8.5.1, is composed of the inductively coupled RF plasma source system for generating the activated particles, measurement and control systems for estimating the condition of the excited species, and a corrosion cell system for the quantitative evaluation of the elementary process of reaction for corrosion and permeation into materials. The incident flux of ions and electrons is controlled by bias potential, gas pressure and so on. The measurement of the weight change or permeation rate is also possible for detail analysis of the surface reaction mechanism under the low temperature plasma condition. The surface morphology and analysis of specimen are conducted by SEM (Fig 8.5.2), Laser Raman, XPS and so on. From the standpoint of the simulation assessment of actual environment, the analysis condition of the dominant factor of the surface reaction and the surface analysis method of the specimen were estimated and selected.

References

1) M.Takizawa, K.Kiuchi, M.Yano and S.Shibata.: "The Life Prediction Study of Rokkasho Reprocessing Plant Materials.", RECOD'98, 3, pp. 859, (1998).
2) K.Kiuchi et al.: "Development of Advanced Cladding Material for Burnup Extension.", IAEA Technical Committee Meeting on Technical and Economic Limit to Fuel Burnup Extension, 8,15 (1999).
3) M.Takizawa, K.Kiuchi, H.Ishizuka, Y.Sougawa, T.Endo and Y.Fujii.: "Hydrogen Permeation Through Metal Enhanced by Low Temperature Plasma. ", J. Plasma. Fusion. Res., 75,pp 432-443,(1999).
4) M.Takizawa, K.Kiuchi, M.Okamoto and Y.Fujii.: "Surface Condition Effects on Plasma Driven Permeation.", J. Nucl. Mater., 248,pp 15-18,(1997)
5) T.Saburi, H.Ogawa, S.Ueda and K.Kiuchi.:"Development of Testing Device for Analyzing Low Temperature Plasma Surface Reaction.", JAERI-Tech 2000-057.

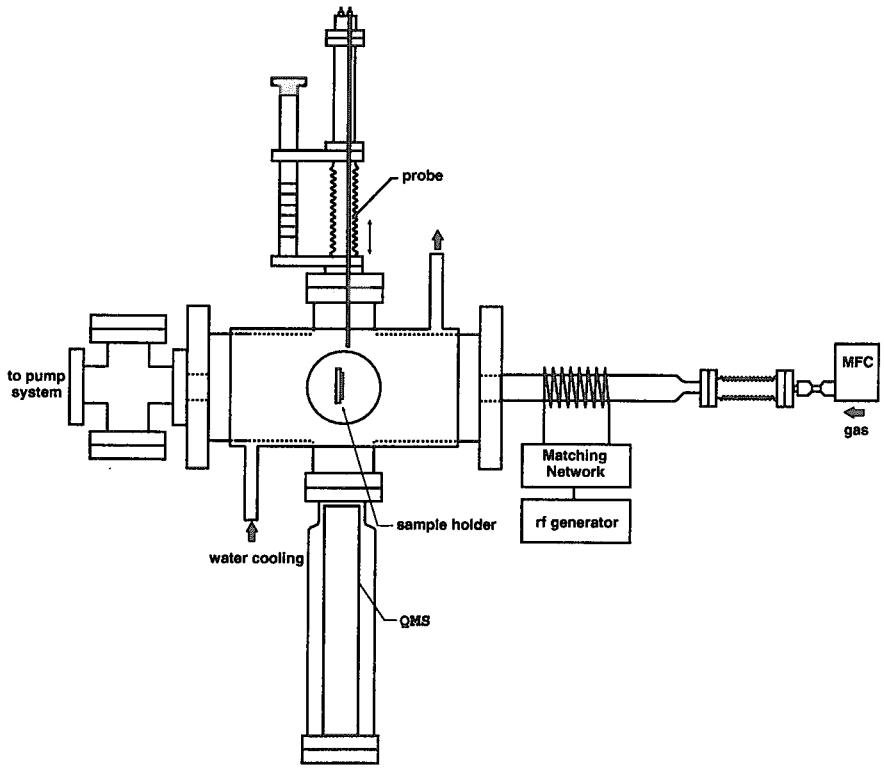

Fig 8.5.1 (a) A Schimatic of The Experimental Setup of Low Temperature Plasma Testing Device.

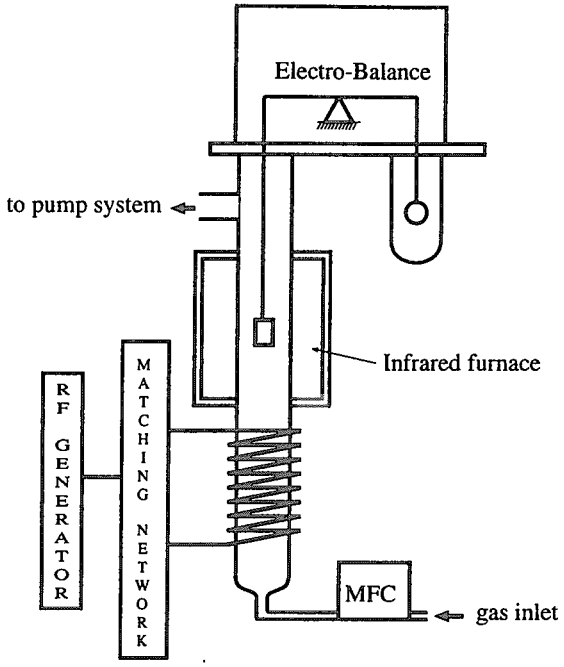

Fig 8.5.1 (b) A Schematic of The Experimental Setup of Chan Type Low Temperature Plasma Testing Device.

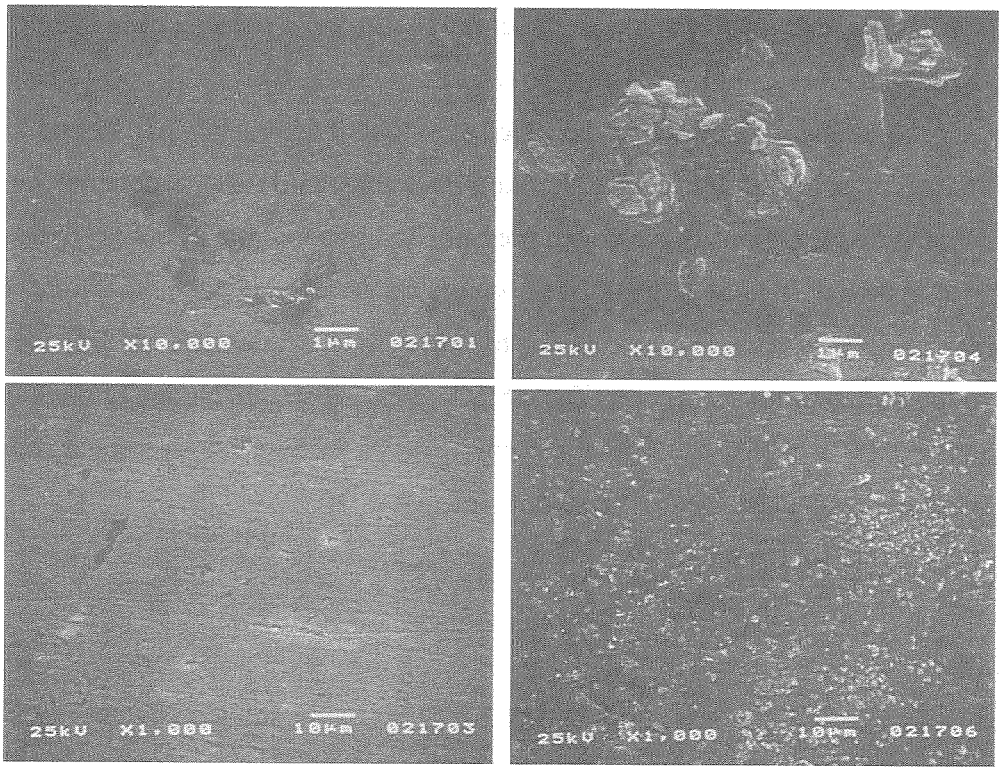

(before plasma oxidation) (after plasma oxidation)

Fig.8.5.2 Example of the surface morphology of Ti by SEM.

8.6 Effect of Crystal Structure and Imperfection on Metal-Hydrogen Interactions with Viewpoint of Hydrogen Permeation and Hydrogen Embrittlement.

H.Ogawa, T.Saburi and, K.Kiuchi
(*E-mail:*hiroaki@galileo.tokai.jaeri.go.jp)

The development of new cladding materials is required for the advanced water cooling reactors aiming at the fast spectrum tailoring and burn-up extension more than 100GWd/t with respect to the economical demand and spent fuel management. One of the critical issues on reliability of cladding materials is the compatibility to high temperature water. The degradation is promoted by the permeation of hydrogen and oxygen excited at cladding surfaces by heavy irradiation[1].

On this study, the interaction of representative metals with hydrogen was examined for selecting the candidate materials of claddings and liners with the high resistance to hydrogen embrittlement. The resistance is strongly controlled in the solubility limit without forming hydrides at the practical temperature. The solubility is essentially dependent on the crystal structure like hcp < fcc < bcc as shown in Fig.8.6.1. The mutual correlation is observed between the solubility and the diffusion coefficient of hydrogen as shown in Fig.8.6.2[2]. The resistance to hydrogen embrittlement of bcc type refractory metals like V, Nb and Ta purified in the low impurity contents is anticipated to be superior to that of hcp metals like Zr and Ti as shown in Fig.8.6.3. The solubility of fcc metals like Ni and austenitic alloys depends on statistical thermodynamics as functions of hydrogen pressure and temperature. However, the maximum solubility of hydrogen is smaller than that of bcc metals at the practical temperature. The excess hydrogen forms crystal imperfections leading to hydrogen embrittlement. Nb with the low cross-section to thermal neutron adsorption (Table 8.6.1) is considered to be one of the most promising liner materials for claddings made of austenitic alloys, with respect to trapping effects of the excess hydrogen formed by the transmutation reaction of Ni.

References:

1)Takizawa,T., Kiuchi,K., Okamoto,M. and Fujii,Y.: "Surface condition effects on plasma driven permeation", J. Nucl. Mater. 284, pp15-18,(1997).

2)Ogawa,H., Saburi,T. and Kiuchi,K.: "Basic Evaluation on Metal-Hydrogen Interactions for Selecting Cladding Materials", JAERI-Research(to be published in 2000 year).

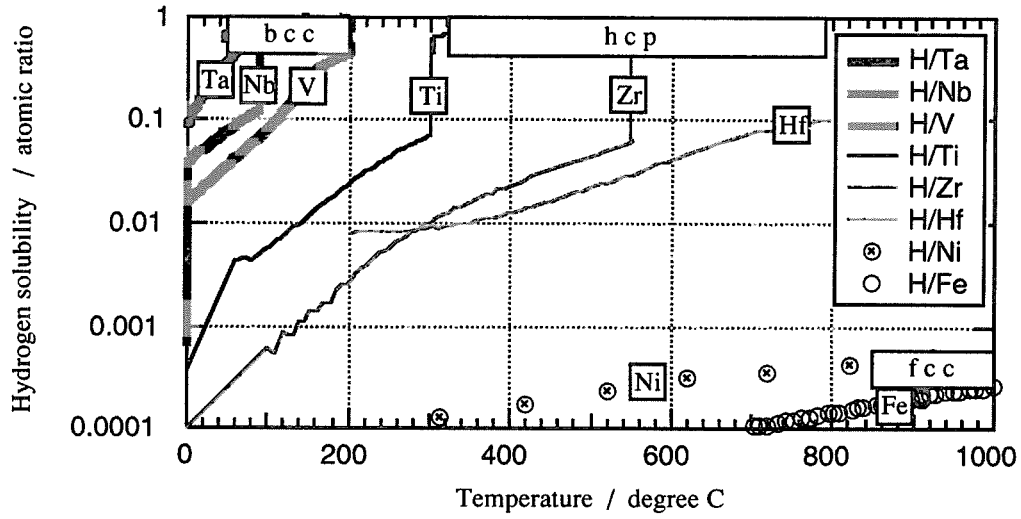

Fig.8.6.1 Comparison concerning solid solubility limit of hydrogen among representative metals

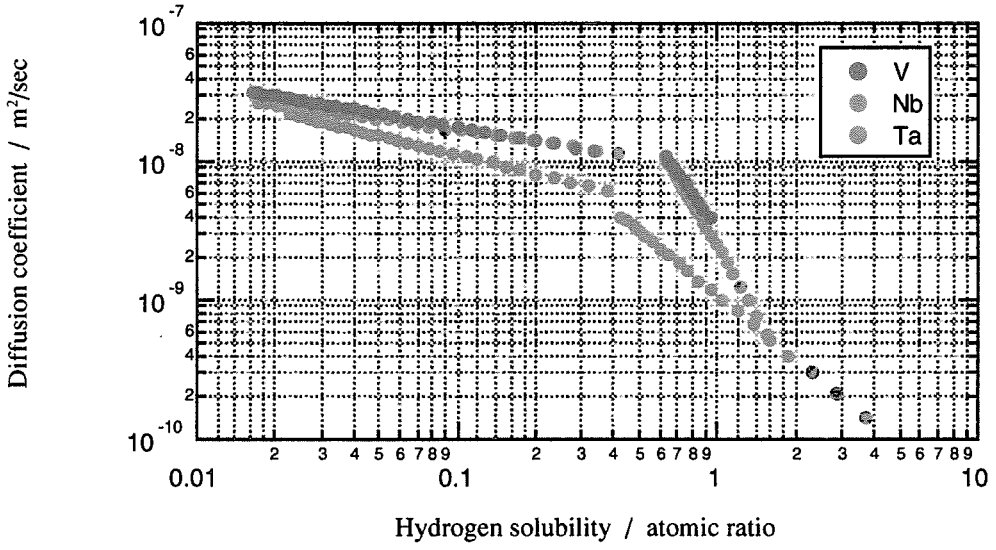

Fig.8.6.2 Relationship between hydrogen solubility (solid solubility) and the diffusion coefficient on metal-hydrogen systems of Nb-H, Ta-H, and V-H

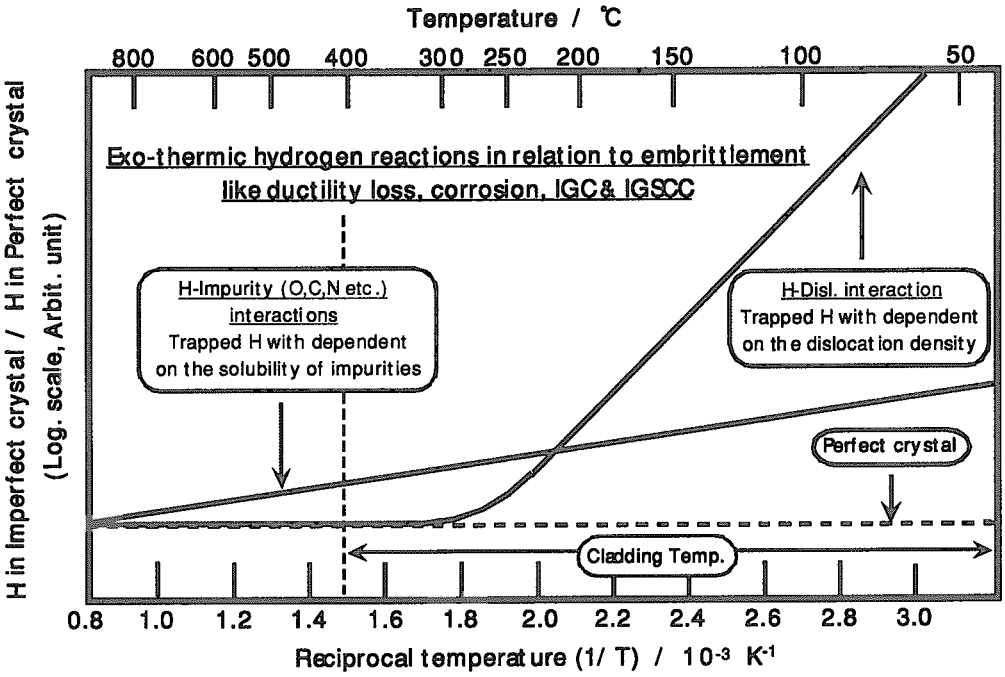

Fig.8.6.3 A schematic model on the enhancement effect of hydrogen solubilities by the interaction with impurities and dislocation at the practical temperature

Table 8.6.1 Neutron economically for the crystal structure

Contents \ Crystal structure	hcp			bcc			fcc	
Metallic element	Zr	Ti	Hf	V	Nb	Ta	Fe	Ni
Thermal neutron cross section / barn	◎	○	×	○	○	×	○	○
	0.2	6	105	5	1	21	2.6	4.4
Formation of hydride	△	△	△	○	○	○	*	*

* : Thermal equilibrium

8.7 Outline of Reliability Tests of Equipment Materials Used in Rokkasho Reprocessing Plant and Development of Testing Methods for Clarifying Irradiation Effects

S. Hamada ,T. Motooka and K. Kiuchi

(*E-mail:* shamada@popsvr.tokai.jaeri.go.jp)

The project of the demonstration test for a nitric acid evaporator made of AISI 304 steel and a dissolver of zirconium in Rokkasho reprocessing plant started in 1995 and so far, the mock-up tests, the reference tests in the laboratories and service of database have been making progress on schedule. These tasks before 1999 have been carried out under un-radioactive environment to evaluate reliability for corrosion and lifetime of the materials used in these equipment. A lot of radioactive materials, however, are included in the nitric acid solution and radiolysis of the nitric acid solution produces active chemical species under the environment of practical reprocessing plants. So the effect of them on reliability for corrosion and lifetime of these materials should be considered in the near term. Therefore, evaluation ways on the corrosion test in a fuel dissolved nitric acid solution, ion irradiation experiment and numerical analysis of activity levels by various radiation were developed in 1999.

On the corrosion test for zirconium in a fuel dissolved nitric acid solution, the spent fuel and gamma ray radiation source (^{60}Co), which is employed to provide additional gamma radiation toward zirconium, were used. This apparatus was basically made of zirconium and settled in the No. 3 hot cell in Waste Safety Test Facility (WASTEF). The spent fuel used in this experiment was the type for PWR and had been employed in Ohi electric power generation plant of Kansai Electric Power Corporation. The average burnup of this fuel was 44.7GWd/t. The fuel rod which was stored in Reactor Fuel Examination Facility (RFEF) was partially cut 18 mm in length and a part of them were moved from RFEF to WASTEF in order to carry out dissolution and corrosion test. Figure 8.7.1 shows the schematic diagram of the apparatus for corrosion on the heat conducting surface. Dissolution test of the spent fuel was performed in the No. 3 cell in WASTEF. Off gas like ^{85}Kr mainly generated from the spent fuel was checked during solution and the activity level of off gas in

air was confirmed to be within regularity value. Total spent fuel of 9.2 g was dissolved in nitric acid solution of 8 normality (N) and the dissolved nitric acid solution of Uranium concentration 239 gU/L and free nitric acid concentration 3 N was finally obtained by vaporizing and adding water. The heat conducting corrosion test that used this nitric acid solution for zirconium started and the continuous corrosion test of 700 hours was achieved at the end of March in 2000. This test will finally be continued until 1000 hours

In the environment of reprocessing plants, their materials and the nitric acid solution were exposed under radiation by radioactive materials. Active chemical species like H_2, O_2, H^+ and O^{2-} were induced by radiolysis of the nitric acid solution. It is reported that hydrogen of them permeates into materials by Plasma Driven Permeation (PDP) effect at lower temperature[1]. Further, oxygen might have similar trend to hydrogen. Atoms that could permeate into materials by PDP effect would deposit at any sites like grain boundaries. As a result, it is predicted that this would lead to decrease corrosion resistance during long term usage of the materials. So far, the mechanism of such phenomena has been not shown. In order to clarify this, ion irradiation experiment would be applied. Hydrogen and oxygen ions were irradiated with the accelerators in TIARA to simulate permeated atoms of hydrogen and oxygen. Figure 8.7.2 shows a schematic diagram of multi beam irradiation experimental apparatus in TIARA. These atoms with various energies were used to provide wider distribution of incident atoms in depth. Figure 8.7.3 shows depth profiles of hydrogen atoms in stainless steel calculated by TRIM code[2]. Microstructural observation with a transmission electron microscope and corrosion test are planed in the near future.

References

1) Takizawa, M., Kiuchi, K., Ishizuka, H., Sougawa, Y., Endo, T., and Fujii, Y.: "Hydrogen Permeation through Metal Enhanced by Low Temperature Plasma", Journal of Plasma and Fusion Research, 75(4), pp. 432-443 (1999).

2) Ziegler, J.F., Biersack, J.P. and Littmark, U.: "The Stopping and Range of Ion in Solids" Vol. 1, PERGAMON PRESS, New York, (1985).

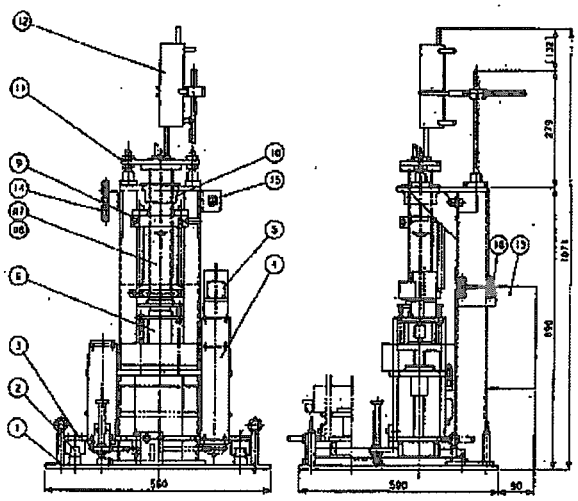

Fig. 8.7.1 the Schematic diagram of the corrosion test apparatus for heat conducting surface.

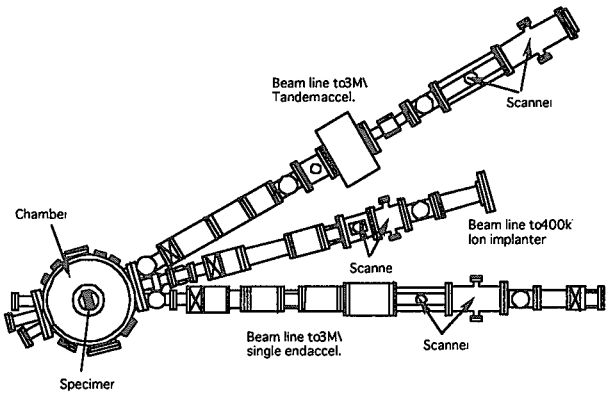

Fig. 8.7.2 The schematic diagram of the multi beam irradiation facility in TIARA

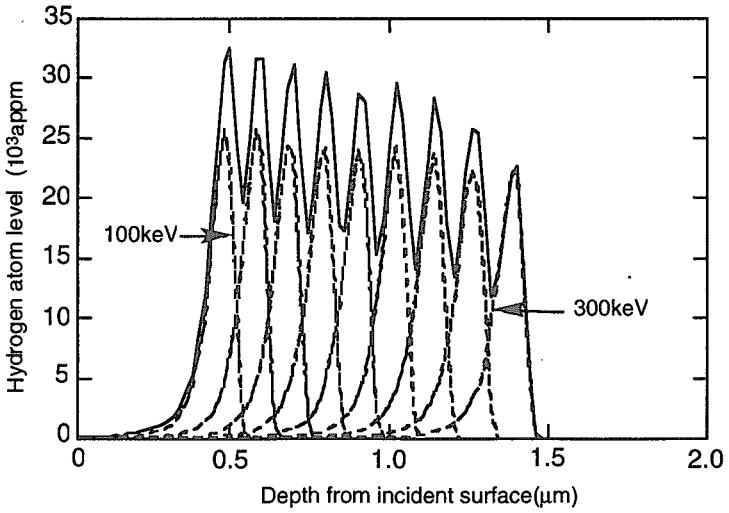

Fig. 8.7.3 Depth profiles of hydrogen atoms implanted to stainless steel (1_ A·hr/cm^2)

8.8 Major Results Obtained by In-service Inspection of Demonstration Testing Equipments for Acid Recovery Evaporator and Dissolver after Operated one Year of 1999

T. Yanagihara and K. Kiuchi
(*E-mail* : yanagi@galileo.tokai.jaeri.go.jp)

The demonstration testing equipments for the Rokkasho Reprocessing Plant (RRP) have been operated at Ehime Works of Sumitomo Chemical Co., Ltd. They have an acid recovery evopolator and a dissolver. The operation of the acid recovery evaporator and the dissolver were started on Mar. 27, 1998 and Mar. 23, 1999 respectively. The reliability of the equipments was evaluated by in-service inspection.

The in-service inspections using nondestructive testing methods for the equipments were carried out from Jan. 24, to Feb. 4, 2000. The second in-service inspection of the acid recovery evaporator was done after 7180 hour operation from the first in-service inspection. The first in-service inspection of the dissolver was done after 7280 hour operation.

Acid Recovery Evaporator

The thermo-siphon type acid recovery evaporator made of type R-SUS304ULC SS was designed to concentrate 9N nitric acid solution from the supplied 1.8N nitric acid solution at a boiling point of 68℃ under 0.016MPa pressure control. The chemical composition of nitric acid solution in the evaporator was controlled as following: 9N HNO_3, 1200mg/L Fe^{3+}, 300mg/L Cr^{3+}, 5mg/L Ru^{3+} and 50mg/L V^{3+} for simulating the solution of RRP. This evaporator consists of an evaporator portion made of seven heat conducting tubes and a gas-liquid separator portion as shown in Fig.8.8.1. The length and diameter of the heat conducting tubes are equal to these of RRP's equipment. The maximum capacity of the evaporator in design is 150kg/h in the flow rate of feed solution and/or 100℃ of a steam temperature at heater side. The measured flow rates of at a steam temperature of 100℃ is 178kg/h, with the circulation flow rate of 860kg/h in the thermo-siphon tube. At this condition, the by-pass flow rate from the top of the heat conducting tubes is 21kg/h, the flow rate of concentrate acid is 5.4kg/h and the flow rate of distillated acid is 172.6kg/h. The feed solution is concentrated 40 times by this thermo-siphon. In the second in-service inspection, a deposit of 176g was found inside of the bottom cap of gas-liquid separator. In the first in-service inspection after 8120 hour operation, it was 68g. These deposits are identified as grains detached from heat

conducting tube walls due to grain-boundary attack.

The wall thickness of 7 heat conducting tubes was measured by the ultrasonic immersion measurement with 10MHz UT sensor along the vertical and radius axis. The accuracy in this measurement is maintained within ±0.01mm. The wall thinning was observed in two different parts in each heat conducting tube. One part is nearly 1m apart from the foot of the heat conducting tube and the other part is the upper of it as shown in Fig.8.8.2. The maximum corrosion rate of heat conducting tubes is higher than that designed. The corrosion was not observed in the other parts like separator. The corrosion of the lower part of heat conducting tubes is controlled with the surface temperature of the tube. On the other hand, the corrosion of the upper part is enhanced by the oxidizing ions like V^{5+} formed at the high oxidizing atmosphere due to the evaporation and thermal-decomposition of nitric acid at heat transfer surfaces inside the tube.

The operation parameter of the evaporator was examined for estimating the testing conditions at steady-state operation. The steam temperature of evaporator was controlled at 98, 96,94 and 92℃ for a short time respectively. The relationship between the feed flow rate and steam temperature is shown in Fig.8.8.3. By decreasing the feed flow rate from 178 to 112kg/h, the circulation flow rate was decreased from 860 to 790kg/h, and the flow rate in by-pass tube was increased from 21 to 667kg/h.

Dissolver

The dissolver has a steam jacket ($0.19m^2$) made of reprocessing grade zirconium with 8mm in thickness as shown in Fig.8.8.4. The liquid volume of the dissolver is 170L. The dissolver was operated at a boiling point of testing solution of 107℃. The steam temperature is 165℃ under 0.71MPa. The steam flow rate is ca. 30kg/h. The nitric acid evaporated from the dissolver is cooled in a condenser and dropped in the dissolver. The testing solution is 3N nitric acid solution containing 142g/L $Al(NO_3)_3$, 1200mg/L V^{5+}, 1000mg/L Ce^{4+} and 1500mg/L Ru^{3+} for simulating the dissolver solution of RRP. The solution was replaced every three months. The compositional change of the solution was little through the three months. After 7280 hour operation, the inside wall surface was covered with an adhered film and some deposits. These were identified as a mixture of ruthenium oxide and vanadium oxide deposited from the dissolver solution. In the first in-service inspection, Radiographic test and dye penetrating test were carried out along the welding lines for detecting defects such as cracking. There are no defects in tested parts. The wall thickness of the dissolver was measured by ultrasonic testing using 10MHz sensor. The wall thinning was not observed.

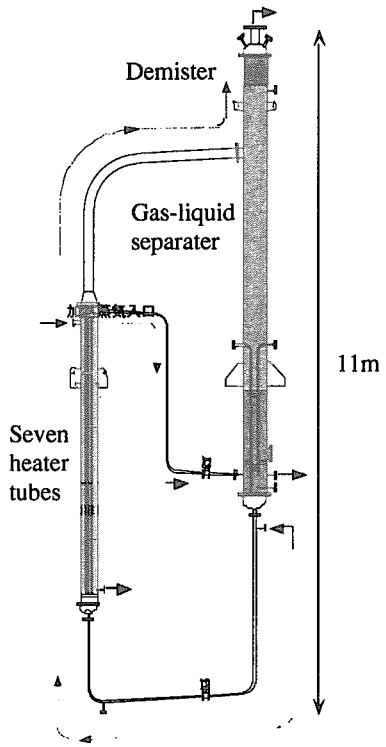

Fig. 8.8.1 A schematic view of demonstration testing equipment for the evaporator.

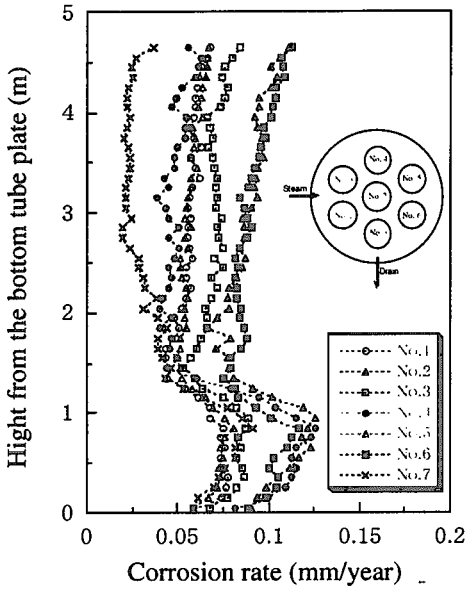

Fig. 8.8.2 The corrosion rate of 7 heat conducting tubes obtained by UT measurements

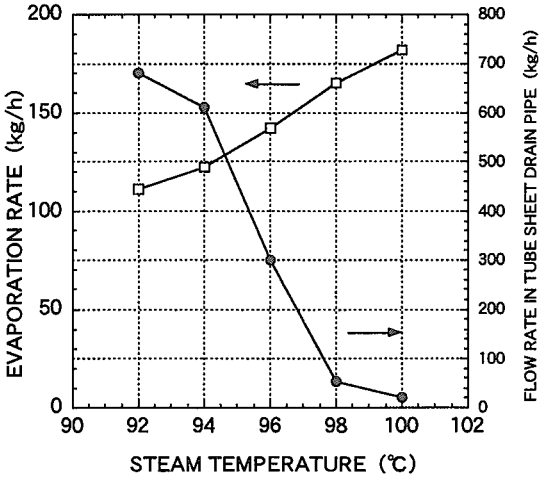

Fig. 8.8.3 The relationship between the feed flow rate and steam temperature obtained by mock-up tests for evaluating the operation parameters of evaporator.

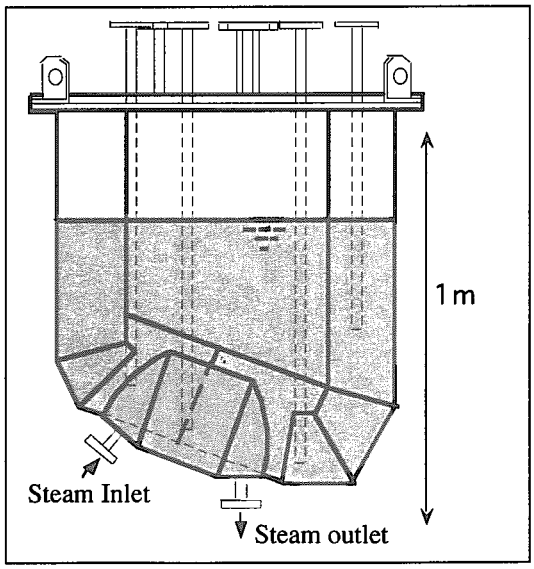

Fig. 8.8.4 A schematic view of demonstration testing equipment for the dissolver.

8.9 Development of Corrosion Model for Heat Conducting Tubes Used in Reprocessing Nitric Acid Environments

K.Kiuchi, T. Yanagihara, T.Kato and M.Takizawa
(*E-mail:* kkiuchi@popsvr.tokai.jaeri.go.jp)

The enhancement effect on corrosion rates at heat conductor surfaces is one of the most important issues on reliability of equipment materials like an acid recovery evaporator made of type 304ULC stainless steel used in the commercial reprocessing plants. From the fundamental research, this acceleration mechanism is supposed to be control mainly with the metal surface temperature and the evaporation rate accompanied with the thermal decomposition of nitric acid. Under boiling conditions, the formation rate of oxidizing ions like Ce(4+), Cr(6+), RuO_4, Pt(6+) ,Np(6+) from the reduced species of these ions is promoted with the high oxidization atmosphere corresponding to the decomposed NOx gas potential, because the solubility of nitrous acid with the low oxidation potential is low. From the laboratory tests, it is clarified that the intermediate oxidizer ions like RuO_4, Pt(6+) , Np(6+) with the low redox potential up to nearly 1.3V are possible to form at heat conducting surfaces in low boiling point under the reduced pressure control. The corrosion rate at heat conducting surfaces of plate and tube specimens obtained by laboratory tests is plotted to the surface temperature as shown in Fig.8.9.1. The corrosion rate is higher than it of immersion test data corresponding to the metal surface temperature. And it depends on the contents of oxidizer former elements like V added instead of Np. These results is coincident with above corrosion mechanism expected in heat conducting surfaces. The Arrhenius dependency shows the low activation energy, compared with as described in another paper in this report, the wall thickness of heat conductor tubes of mock-up equipment was minutely evaluated by UT thickness measurement method on ISI. The corrosion parameters were clarified with analyzing the mock-up data, by considering the boundary conditions concerning thermo-fluid dynamics as shown in Fig.8.9.2. The tendency in the average wall thinning rate of seven heat conducting tubes shows the maximum values at two different locations along the longitudinal direction. In no-boiling region at the bottom side, the maximum corrosion rate corresponds to the region with the

maximum metal surface temperature. On the other band, the corrosion rate at boiling region increases with the evaporation rate and the flow rate of gaseous nitric acid. These parameters control the corrosion rate at boiling region as the supply rate of oxidizer ions possible to attack at each position. As shown in Fig.8.9.3, the overall corrosion rate is possible to explain as functions of these corrosion acceleration parameters, namely, the surface temperature, the evaporation rate (heat flux) and the flow rate of nitric acid steam.

The corrosion rate of heat conducting tubes in the mock-up of acid recovery evaporator increases with the operation time. This acceleration mechanism is analyzed with the graphical computer simulation method, by considering the initiation and propagation of grainboundary attack. As reported in the previous report, the change in corrosion rates due to the initiation of grainboundary attack is possible to explain by simulating the difference in the local corrosion rate between grainboundary and intragrain. However, the acceleration tendency in corrosion rates had been observed at the steady state of grainboundary attack after 10,000hrs. The similar tendency was observed in the corrosion data obtained from heat conducting tubes made of type 310Nb stainless steels used in the mock-up equipment of nitric acid recovery evaporator operated at normal pressure. The acceleration is not able to explain based on the grainboundary attack model. Therefore, the cracking mode was incorporated in the corrosion model based on the observation results experienced as tunnel corrosion along longitudinal direction. The acceleration behavior in corrosion rate of heat conducting tubes observed in mock-up equipment was dependent on the modified model(Fig.8.9.4).

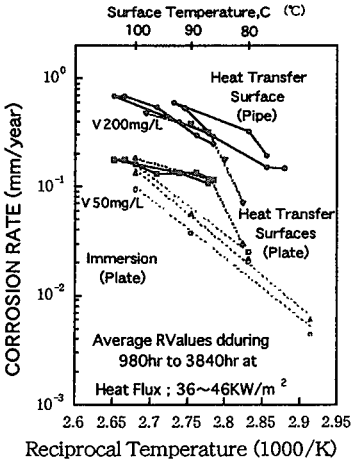

Fig.8.9.1 Arrhenius relationship of the Corrosion rate on heat conducting surfaces of plate and tube specimens as a function of metal surface temperature.

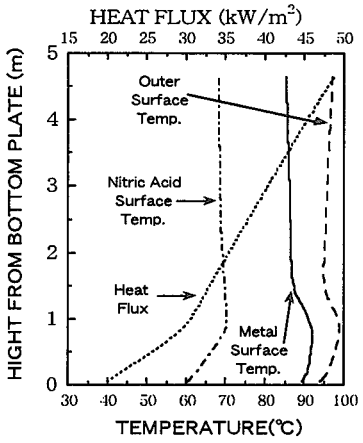

Fig.8.9.2 The distribution of major corrosion parameters at heat conducting surfaces along longitudinal direction obtained by considering experimental and theoretical data based on thermo-fluid dynamics

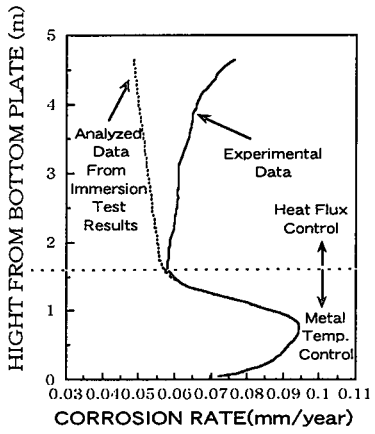

Fig.8.9.3 The tendency in the average wall thinning rate of seven heat conducting tubes along longitudinal direction. The rate is exhibited with sum of the predominant corrosion factors.

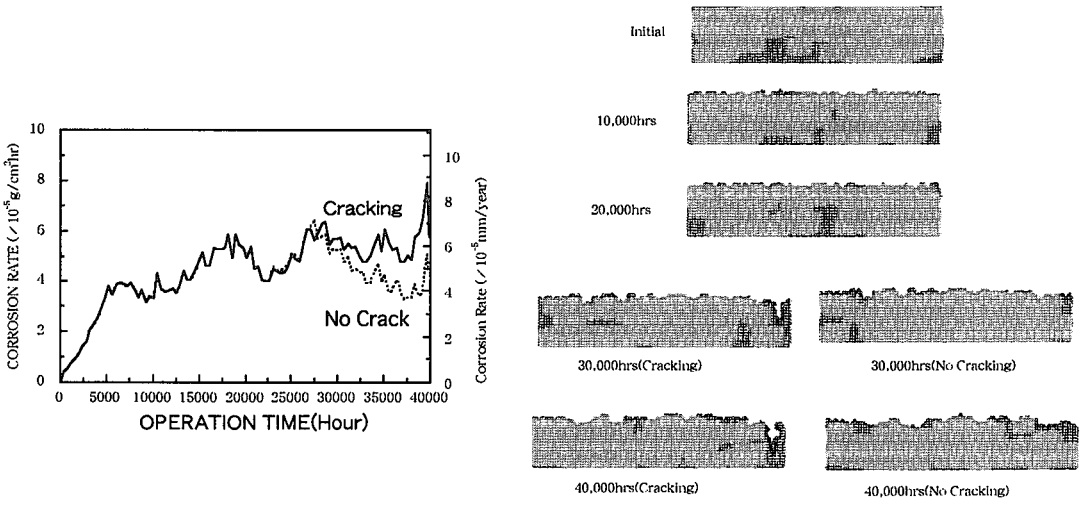

Fig.8.9.4 The graphic simulation model for analyzing the corrosion acceleration behavior on heat conducting tubes after long operation time.

8.10 Corrosion Tests under Heat-flux Control of Type 304 ULC Stainless Steel in Nitric Acid Solution Containing Np Ions for Simulating Nitric Acid Recovery Evaporators

T. Motooka, S.Hamada and K.Kiuchi
(*E-mail:* motooka@popsvr.tokai.jaeri.go.jp)

A remarkably accelerated corrosion of type 304 L stainless steel (304 ULC SS) was found in the mock-up test using small-scaled nitric acid recovery evaporator in a reprocessing plant. In this test, 50 mg/L vanadium ion is added in nitric acid solution to corrode type 304 ULC SS with the same corrosiveness as 900 mg/L neptunium ion for simulating the environment in nitric acid recovery evaporator. The above concentration of neptunium in nitric acid solution is 4 times higher than that of vanadium. To verify the corrosiveness of neptunium ion in nitric acid solution, the corrosion of type 304 ULC SS in neptunium nitrate solution under heat-transfer condition was examined by weight loss measurement and ICP analysis using 9 mol/dm^3 nitric acid solution containing only neptunium ion.

The test specimens were corroded for a total of 930 hr in the 900 mg/L of neptunium nitrate solution and in 9 mol/dm^3 nitric acid solution containing 50 mg/L vanadium ion, respectively. The testing solutions were renewed every 310 hr. The ratio of solution volume to surface area of specimen was about 18 mL/cm^2. The corrosion tests were conducted with an equipement as shown in Fig.8.10.1. The inner pressure of test-cell was controlled under 120 mmHg by a vacuum controller and the heat-flux of specimen had been 60 kW/m^2 during the tests.

As shown in Fig.8.10.2, corrosion rates increased with test time. The corrosion rate of type 304 ULC SS in the testing solution with Np content of 900 mg/L was approximately 3 times higher than that in the nitric acid solution containing 50 mg/L vanadium ion. According to this result, the assumption that corrosiveness of vanadium ion in nitric acid solution is about 4 times higher than that of neptunium ion is not suitable. The corrosiveness of vanadium ion may be equal to that of neptunium ion in case of equal molarity.

Photo.8.10.1 shows the specimen surface after corrosion tests. The type of corrosion was intergranular corrosion in neptunium nitrate solution, whereas a little intergranular corrosion was displayed on the surface tested in 9 mol/dm^3 nitric acid solution containing vanadium ion.

From above results, we should carry out the corrosion test to verify the corrosiveness of neptunium ion in the nitric acid solution containing other corrosive metallic ion, i.e. iron or chromium ion.

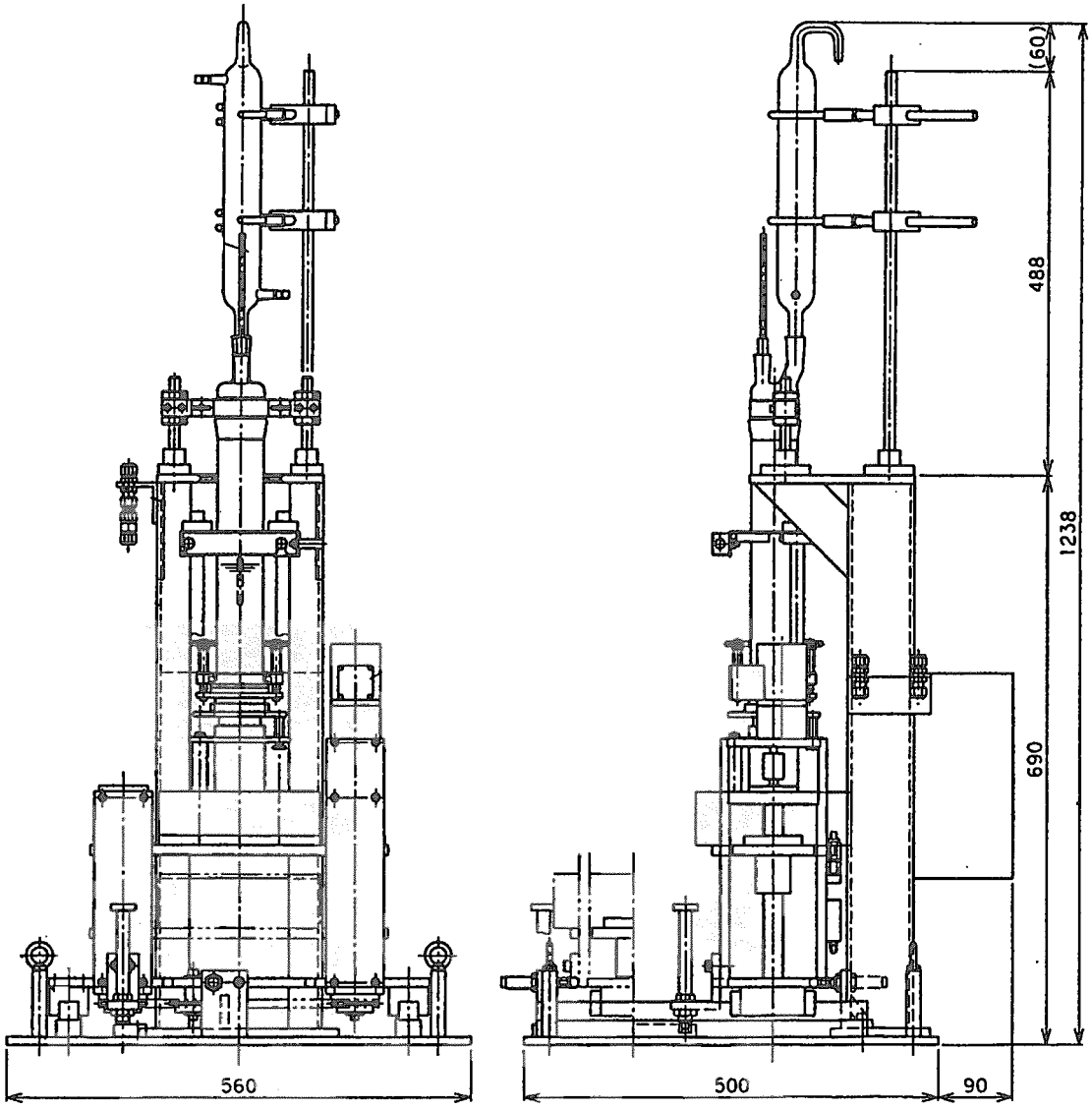

Fig.8.10.1 Equipement used for corrosion tests under heat-flux control.

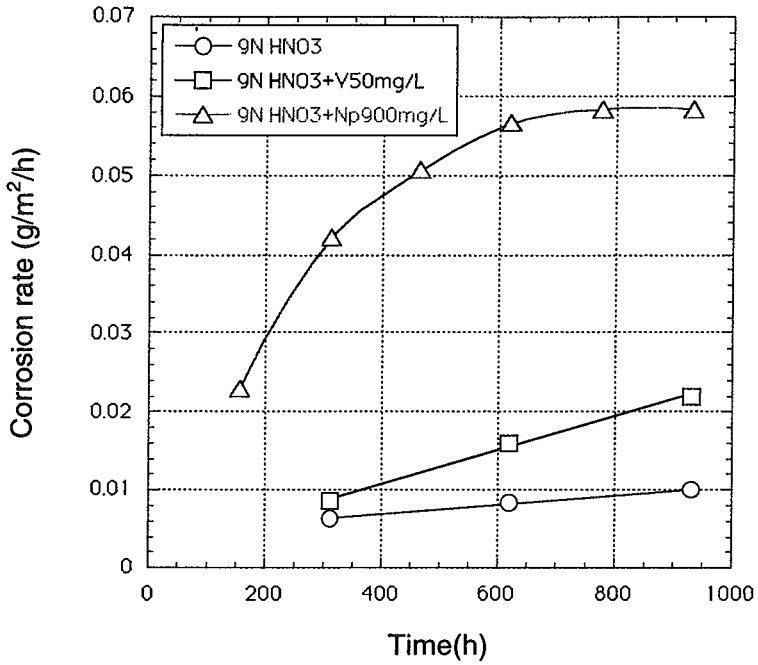

Fig.8.10.2 Corrosion rates of type 304 ULC SS under heat transfer condition

	9N HNO3 + Np 900 mg/L	9N HNO3 + V50 mg/L
Heat transfer		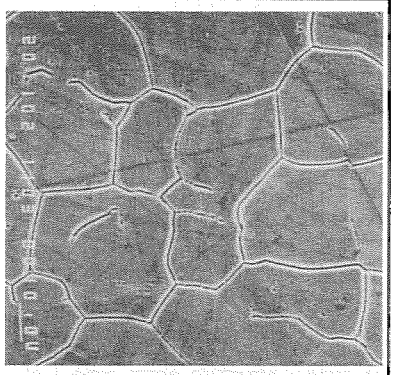
Immersion	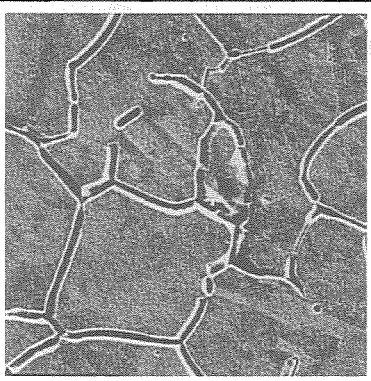	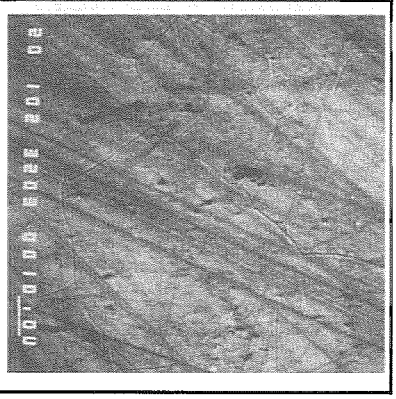

Photo.8.10.1 SEM photographs of specimens after corrosion tests

8.11 Development of AE Monitoring Method for Detecting Stress Corrosion Cracking of Reprocessing Grade Zirconium in Nitric Acid Solutions

C. Kato and K. Kiuchi

(*E-mail:* multi@popsvr.tokai.jaeri.go.jp)

Structural materials used in the Purex type nuclear fuel reprocessing devices are required to have the sufficient corrosion resistance against boiling nitric acid solutions including oxidizer ions derived from spent nuclear fuels[1]. Zirconium has been used as one of the alternative materials applied for devices operated under the normal pressure like a dissolver and Pu evaporator. However, it shows the high susceptibility to stress corrosion cracking (SCC)[2]. We have considered that the SCC can detect by the acoustic emission (AE) monitoring technique. In this study, the applicability of AE technique for monitoring the initiation and propagation of SCC of reprocessing grade zirconium was examined using the slow strain rate tensile test (SSRT) in boiling nitric acid solution.

Figure 8.11.1 shows the histogram of AE events of zirconium plotted to the stress-time (strain) curves obtained by SSRT in boiling 8N and 12N HNO_3 and in silicone oil at 115°C respectively. In comparison with silicone oil, the time to failure of zirconium is reduced with increase of the nitric acid concentration as expected from the previous reports[3]. The rate of reduction in nitric acids compared with reference data obtained in silicone oil is 22% and 25% in 8N and 12N HNO_3 respectively. In the present experimental conditions, the AE signals were only detected in nitric acid solutions. This indicates that the AE signal due to the plastic deformation is not included in the analyzed data. The AE signals were detected in wide range of stress–strain curves, even if the stress level is low. It was assumed that the AE signals include the bubbling noise. The difference of the initial AE counting rates between in 8N and 12N HNO_3 would be dependent on the boiling condition and the initial AE counting rate as a background.

In 8N HNO_3, the incubation time up to generate AE signal is about 55 hours and the stress level is 320 MPa. On the other hand, these are about 34 hours and 205 MPa respectively in 12N HNO_3. The incubation time clearly shortened with increase of the nitric acid concentration. It seems to correspond to the difference of the susceptibility to SCC between in 8N and 12N HNO_3. The stress level at first AE signal generation in 12N HNO_3 is lower than 0.2 % proof stress of zirconium. This indicates that the low temperature creep during SSRT plays an important role on initiation of SCC. The optical photographs of the fracture surface of specimens are shown in Fig.8.11.2. SEM photographs of the fracture surfaces of SSRT specimens are shown in Fig.8.11.3. The morphology of specimen surfaces fractured in silicone oil showed the metallic luster and ductile fracture. On the other hand, the morphology in boiling 8N and 12N HNO_3 showed the black color and quasi-cleavage type fracture along circumference of notch groove surfaces. The center in specimen surfaces fractured in boiling nitric acid and silicone oil showed the ductile fracture mechanically teared at the final stage on SSRT. The ratio of the quasi-cleavage type fracture area to the total fracture area was 65% and 80% in 8N and 12N respectively. The area with quasi-cleavage fracture is significant to estimate the susceptibility to TGSCC.

References:

1) K.Kiuchi : J.Atomic Energy Society of Japan, 31, 229(1989).

2) J.A.Beavers, J.C.Griess and W.K.Boyd : Corrosion, 36, 292(1981),.

3) C.Kato, Y.Takagi and K.Kiuci : Proceeding of International Symposium on Plant Aging and Life Predictions of Corrodible Structures, p883(1995), Japan.

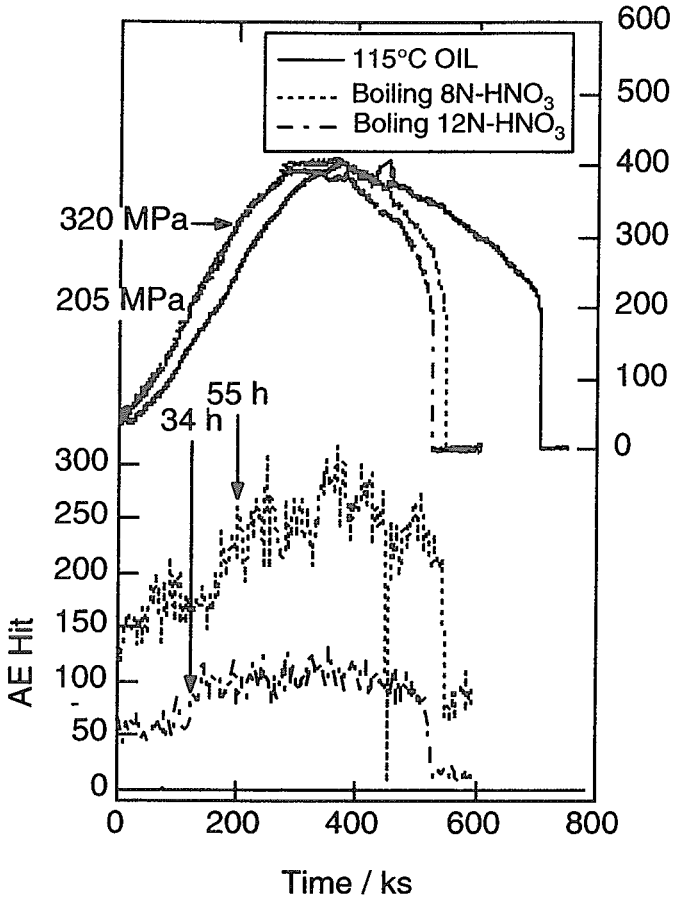

Fig.8.11.1 The histgram of AE event plotted to stress-time(strain) curves of SSRT.

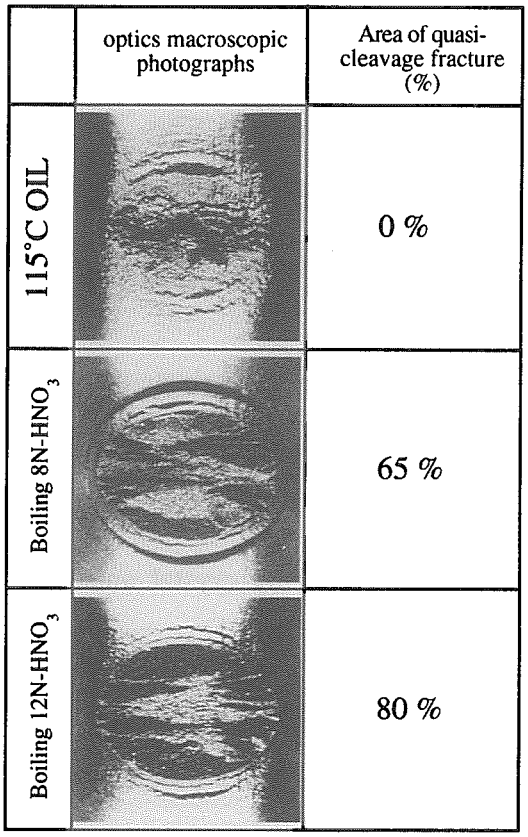

Fig.8.11.2 Optical photographs and the cleavage fracture area after SSRT.

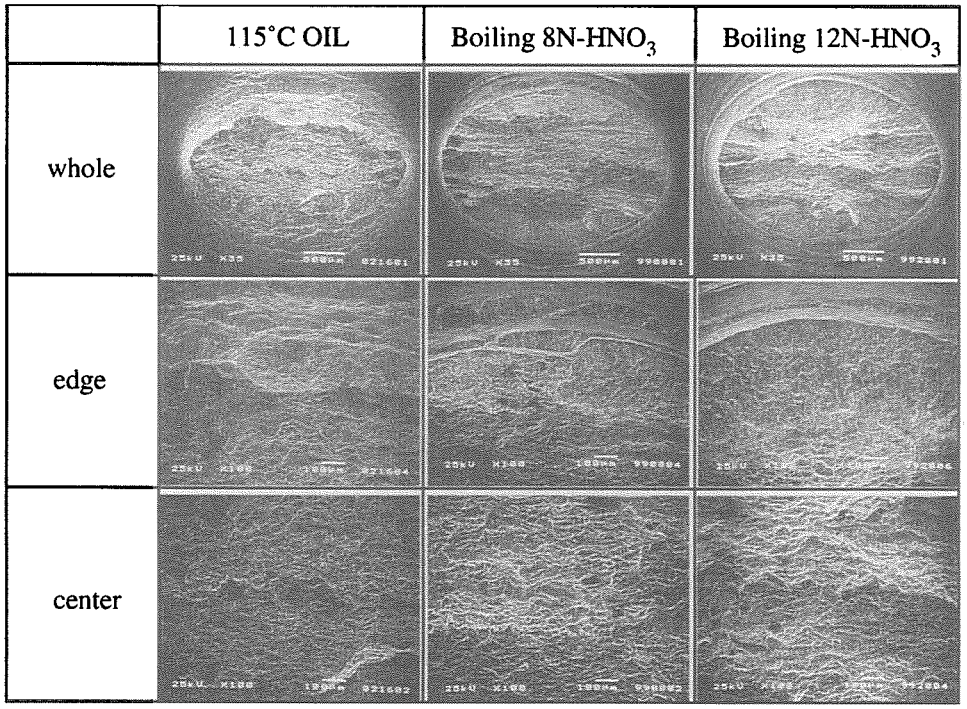

Fig.8.11.3 SEM photographs of the fracture surfaces of zirconium after SSRT.

8.12 Effect of HCP Type Crystal Texture on Fatigue Crack Propagation Rate of Zirconium in Boiling Nitric Acid Solution

T. Motooka, S.Hamada and K.Kiuchi

(*E-mail :* motooka@popsvr.tokai.jaeri.go.jp)

In order to evaluate the durability of the nuclear fuel reprocessing equipment made of Zr, we have been investigated the crack propagation behavior of Zr in boiling nitric acid solution by fatigue test. We have found that crack propagation rate and SCC susceptibility of Zr are affected by crystal anisotropy of zirconium[1, 2]. Zircaloy, (0001) plane is oriented parallel to the rolling direction, has less susceptibility to SCC than Zircaloy which is not texture-controlled. In this work, the effect of texture-controlling was investigated by the measurement of crack propagation rate and the observation of fracture surface using 2 kinds of texture-controlled zirconium, Zr-A and Zr-B.

The fatigue crack of specimen was propagated in air at room temperature and in boiling 3 mol/dm^3 nitric acid solution. Test specimens were machined out longitudinal (L-type) and transverse (T-type) to the rolling direction of plate. Tests were conducted with an electro-hydraulic servo-type fatigue testing machine at a frequency of 0.1 Hz with a stress ratio R=0.1. Measurement of crack propagation rate was conducted by optical microscope observation and fracture surface was observed with a scanning electron microscope.

Fig.8.12.1 illustrates textures of Zr-A and Zr-B. In Zr-A, (0001) plane is oriented parallel to rolling direction. In Zr-B, (0001) plane inclined about 35° . Fig.8.12.2 shows the fatigue crack growth rate (da/dN) as a function of stress intensity factor range (ΔK) in air at room temperature. In L-type specimen, the da/dN of Zr-A is higher than that of Zr-B. The crack growth rate of Zr is decreased by texture-controlling. Fig.8.12.3 shows the comparison of crack propagation rate in boiling 3 mol/dm^3 nitric acid solution. There is no

significant difference between da/dN of Zr-A and Zr-B. Crack propagation behaviors are similar each other. There is no remarkable texture controlling effect on crack propagation in boiling nitric acid environment.

References

1) T.Motooka and K.Kiuchi : JAERI-Research 99-031 (1999), in Japanese.

2) T.Motooka and K.Kiuchi : Zairyo-to-Kankyo, 48, 320 (1999) , in Japanese.

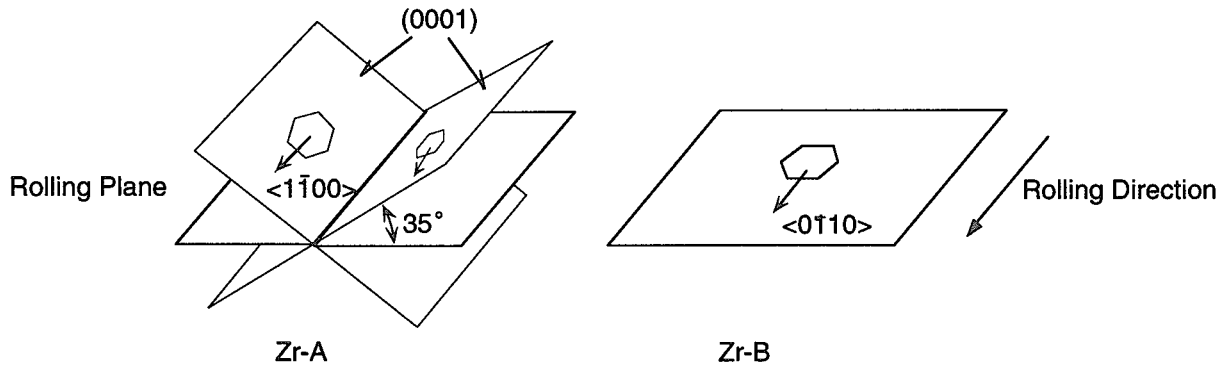

Fig.8.12.1 Illustration of texture of Zr-A and Zr-B.

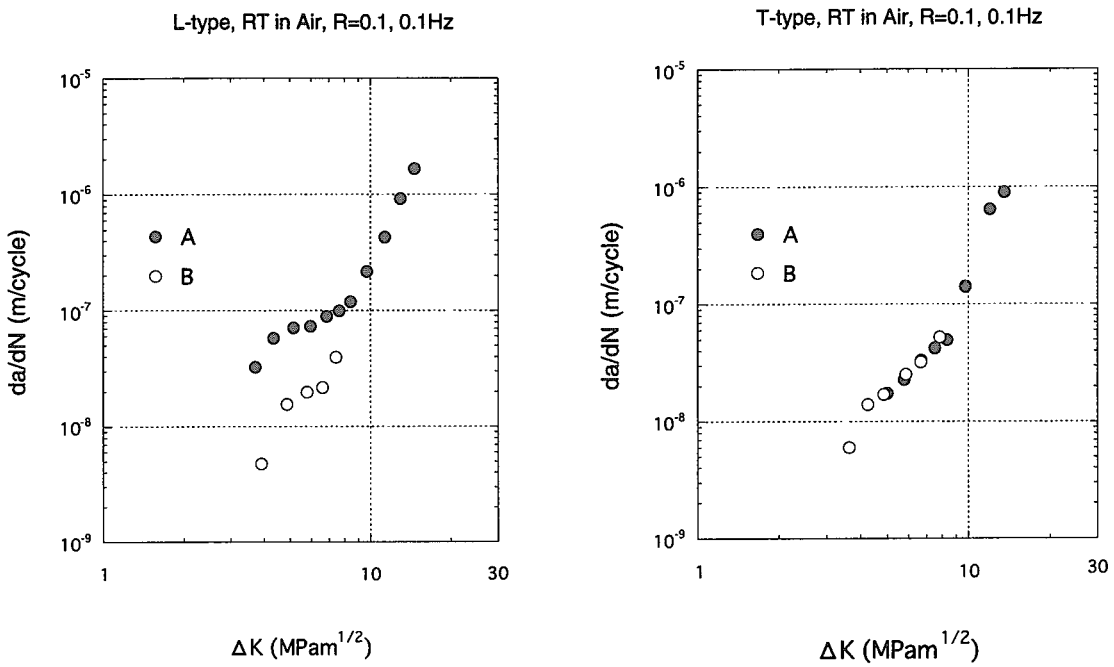

Fig.8.12.2 Crack propagation rates of Zr in air at room temperature and in boiling 3 mol/dm^3 nitric acid solution.

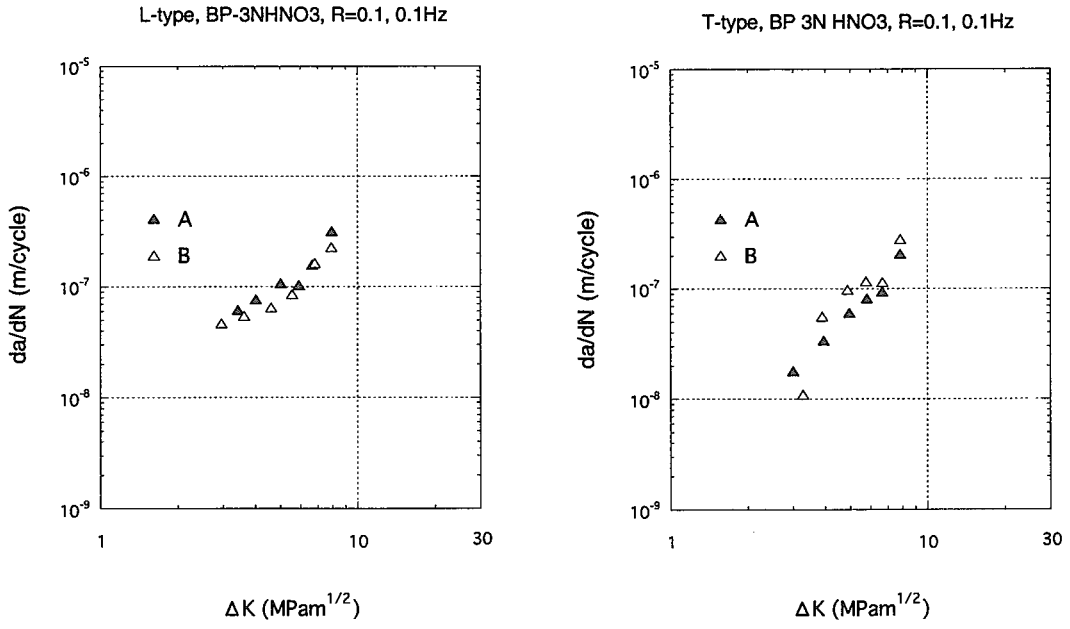

Fig.8.12.3 Comparison of crack propagation rates in boiling 3 mol/dm^3 nitric acid solution.

8.13 Basic Analysis of Corrosion Factors on Heat Conducting Surfaces in Nitric Acid Solutions Expected in Reprocessing Equipment Materials

M. Doi and K. Kiuchi
(*E-mail*: mdoi@galileo.tokai.jaeri.go.jp)

In the advanced purex reprocessing equipment, the higher corrosion resistance is required for materials because of the high corrosive environment caused from the thermodynamic decomposition of boiling nitric acid. The authors group has been developed the two types of new corrosion resistant materials for application to the reprocessing equipment [1]. One is the type 304ULC stainless steel with controlled microstructure and decreased minor elements (EB-SAR). The other is the nickel base alloy with the ability of forming stable oxide film (RW alloy).

In this study, the dominant factors of heat conducting corrosion by the nitric acid solution, the effect of the heat flux and the concentration of the corrosive vanadium ions were investigated by corrosion tests. The materials used are shown in Table 8.13.1. EB-SAR and RW alloy are developed materials. Reference steel I is the present type 304ULC stainless steel for the reprocessing equipment. The testing solution was 9N nitric acid solution containing vanadium, 300mg/L chromium, 1200mg/L iron, and 5mg/L ruthenium. The corrosion tests were conducted with heat flux (20 to 128kW/m^2) and vanadium content (50-200mg/L).

The following results were obtained from this study :

(1) The corrosion rate of the reprocessing type 304ULC stainless steel is increased with the heat flux and vanadium content increase (Fig. 8.13.2).

(2) The reprocessing type 304ULC steel shows the severe attack at the grain boundaries, and the intergranular corrosion propagates in the depth direction. On the other hand the developed materials (EB-SAR, RW-alloy) shows the uniform corrosion (Fig. 8.13.3).

(3) The developed materials show superior corrosion resistance on the point of total corrosion depth (Fig. 8.13.4).

It is confirmed that the controlling microstructure in EB-SAR and the addition of elements, the stable oxide film former, Cr, W, and Si in the RW alloy restrain the intergranular corrosion.

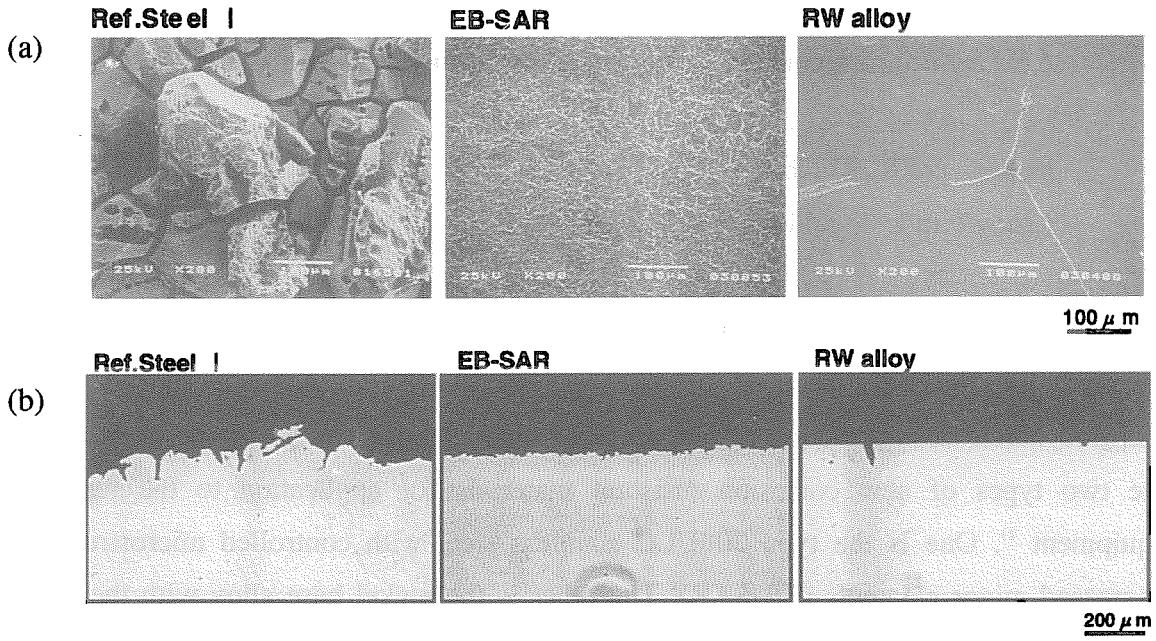

Fig.8.13.3 (a) SEM observation result of the specimen surface after corrosion test
(b) Cross-sectional observation result of the specimen

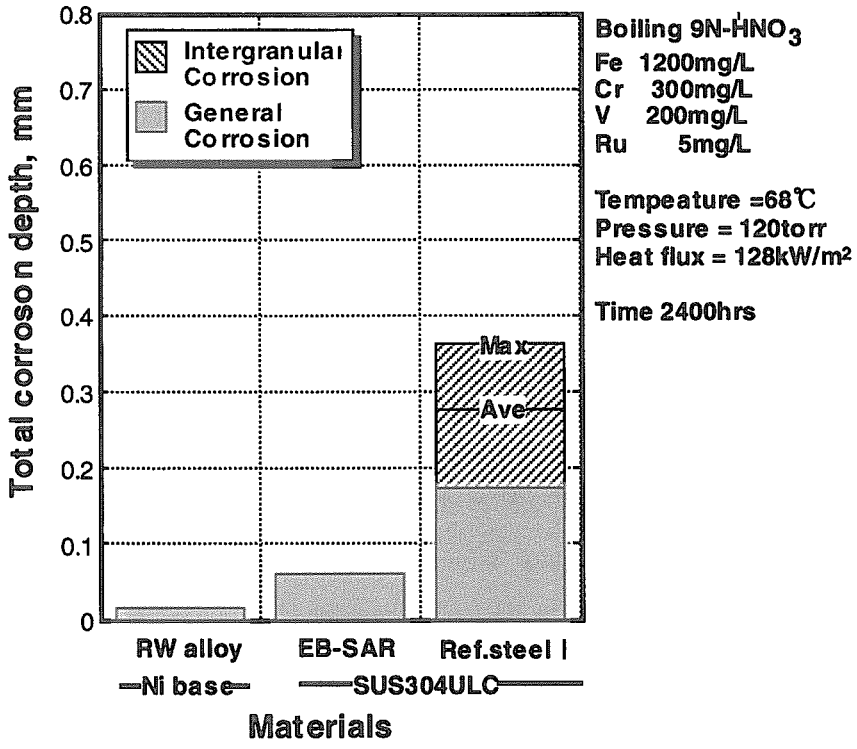

Fig.8.13.4 The total corrosion depth of specimen after 2400hrs test

Reference:

1) K.kiuchi et. al.; Proceeding of Inter. Conference of RECOD 98,Nice France, 859-867 (1998)

Table 8.13.1 Chemical composition of the material used (wt%)

No.	Material		C	Si	Mn	Ni	Cr	Fe	Others	
EB-SAR	304ULC SS	Developed	0.015	0.14	0.10	12.7	19.3	Bal.	0.26Ti	SAR*
Ref. Steel I		Reprocessing	0.011	0.34	1.71	10.8	19.0	Bal.		MA**
RW alloy	Ni base	Developed	0.005	2.70	0.10	Bal.	30.1	Tr.	10W	ST***

* SAR Strained Aged Recrystallized
** MA Mill annealed
*** ST Solution treatment

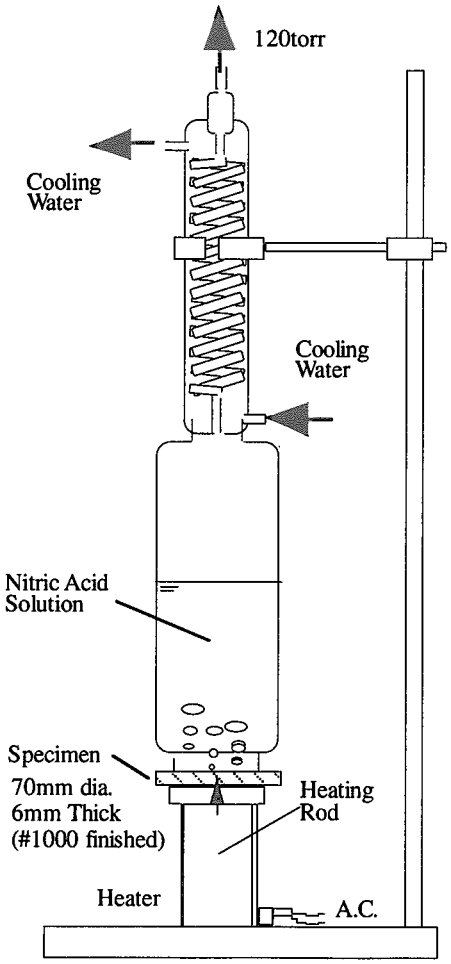

Fig.8.13.1 The schematic view of the corrosion test apparatus

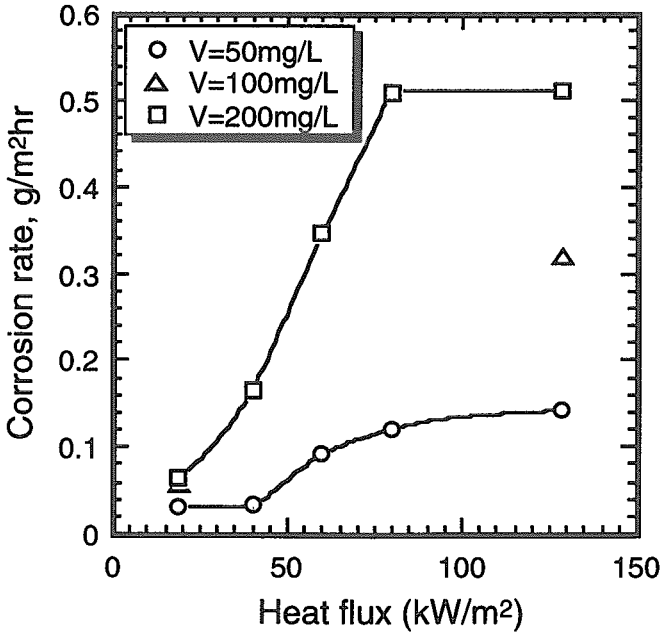

Fig.8.13.2 The effect of heat flux and vanadium content on the corrosion rate (Ref.steel Ⅰ)

9. Rock-Like Oxide Fuel for Plutonium Burning in LWRs

Research on plutonium rock–like oxide (ROX) fuel and its once-through burning in LWRs has been carried out in order to establish a new option for the optimum use of excess plutonium. Features of the ROX-LWR system are almost complete burning of plutonium and the direct disposal of spent ROX fuels without reprocessing.

New particle dispersed type ROX fuels were prepared and irradiated in JRR-3 to the thermal neutron fluence of about 7 x 10^{24} m^{-2} in order to clarify their irradiation behavior. Non-destructive post-irradiation examinations of these fuels were performed for such items as visual inspection, profilometry, X-ray photography and γ scanning. These results indicated that ROX fuels showed a similar irradiation behavior as the conventional UO_2 fuel: cracks in fuel pellets and a volatile Cs migration to cooler regions. As fundamental researches on the ROX fuel, reactions between PuO_{2-x} and yttria-stabilized zirconia (YSZ) were investigated. Chemical state of irradiated ROX fuels was also evaluated using a thermodynamic calculation code SOLGASMIX-PV.

As for the reactor physics area, two important experiments were performed: pulse irradiation tests in NSRR and a Doppler reactivity measurement in FCA. The YSZ single-phase ROX fuel test pins were irradiated by a short pulse simulated reactivity initiated accident condition to investigate a transient fuel behavior. Test results showed that the threshold energy of the fuel pin failure for the ROX fuel was nearly the same as that of the conventional UO_2 fuel when the deposit energy was expressed in term of unit volume energy. The Doppler reactivity measurements were carried out for such elements as Th, Er and W which were possible additives to improve the small Doppler reactivity of ROX fuel. Experimental results showed that these elements had comparable Doppler effect to ^{238}U. Effects of these additives on the core characteristics, minor actinides transmutation and long life fission products production were extensively investigated by using SRAC code system. Radiotoxicity hazard of spent ROX fuel was shown to be lower than spent MOX fuel. From core burnup calculations of Th-ROX fuel, Th-ROX fueled core was found to have preferable physics characteristics from reactor safety and Pu transmutation points of view, although it produced some new fissile ^{233}U.

9.1 Post-Irradiation Examination of Uranium-based Rock-like Oxide Fuels

K. Kuramoto, T. Yamashita, T. Shiratori and N. Nitani
(*E-mail*: kura1@nucef.tokai.jaeri.go.jp)

On the use of surplus Pu, JAERI has been promoting a basic research for once-through type fuels, rock-like oxide (ROX) fuel. The concept consists of fabrication of chemically stable ROX fuels in conventional fuel facilities, almost complete Pu burning in LWR and disposal of chemically stable spent fuels without further processing. To investigate irradiation behavior of ROX fuels, five kinds of fuels were prepared using 20% enriched ^{235}U instead of Pu. The first one is a single phase fuel of an yttria-stabilized zirconia containing UO_2 (U-YSZ), next two are particle-dispersed type fuels of U-YSZ particles + $MgAl_2O_4/Al_2O_3$ powder, the other two are homogeneously-blended type fuels of U-YSZ powder + $MgAl_2O_4/Al_2O_3$ powder. The fuel composition and estimated thermal condition of the irradiation are listed in Table 9.1.1. The fuels were irradiated in JRR-3 for 100 days and estimated thermal neutron fluence was 7 x 10^{24} m^{-2}. We are performing post-irradiation examinations including non-destructive examinations, destructive examinations and leaching tests for the evaluation of irradiation behavior of the fuels and the geochemical stability of the irradiated fuels. In this report, the results for the non-destructive examinations of ROX fuels, visual inspection, profilometry, X-ray photograph and γ scanning, will be described and discussed.

Table 9.1.1 Composition of cation (mol%) and estimated irradiation condition of fuels.

Fuels	Single phase of	Particle-dispersed type of		Homogeneous-blended type of	
	UO_2-based YSZ (Z)	UO_2-YSZ + $MgAl_2O_4$ (SD)	UO_2-YSZ + Al_2O_3 (CD)	UO_2-YSZ + $MgAl_2O_4$ (SH)	UO_2-YSZ + Al_2O_3 (CH)
YSZ*	81.75	11.90	11.93	11.90	11.93
UO_2	18.25	19.71	19.76	19.71	19.76
$AlO_{1.5}$	------	45.60	68.31	45.60	68.31
MgO	------	22.79	------	22.79	------
	Average/Maximum				
Linear power ($kW \cdot m^{-1}$)	6.2/10.6	10.0/14.9	12.0/14.1	13.7/18.3	8.7/10.8
Temperature at (K) Near surface of cladding	609/690	477/757	732/768	761/834	678/719
Surface of pellet	740/890	880/1030	950/1010	1130/1280	900/980
Center of pellet	970/1290	1070/1350	1180/1310	1430/1700	1060/1200

*The ratio of ZrO_2 : $YO_{1.5}$ is 78.57 : 21.43 in mol% in all fuels.

Figure 9.1.1 shows appearances of Z, SD and SH fuel pins. No apparent deformation, for example crack and swelling, is observed as seen in Fig. 9.1.1. Stainless steel cladding surfaces are partially discolored by the oxidation, and the oxidized "dark" area coincides with the location of the fuel pellets. The spot oxidation will be caused by partial contact with the cladding and pellets. For CD and CH fuel pins, similar results were obtained. From the precise size measurement using an electronic micrometer, no significant but ~ 10 μm of slight swelling was observed in the fuel pins.

X-ray photographs revealed that significant pellet fragmentation was not observed for all fuels. In Z, SH and CH fuels, crack formations in the horizontal and vertical directions are observed as in irradiated LWR UO_2 fuels as shown in Fig. 9.1.2 (a) and (b), but clear cracks were not observed in the particle-dispersed type fuels, SD (see Fig. 9.1.2 (c)) and CD. Additionally, for the SD fuel, "dark" parts reveal lack of the particles and the gap between pellets. These lines are not cracks caused by the irradiation, because the lines have existed in the photographs examined before the irradiation.

From γ spectrum measurement at the center of each fuel, FPs with short lives such as ^{95}Zr, ^{103}Ru, $^{106}Ru(^{106}Rh)$, ^{134}Cs, $^{144}Ce(^{144}Pr)$ and ^{154}Eu etc. were identified. Additionally activation products of stainless steel cladding such as ^{58}Co, ^{59}Fe and ^{60}Co were also detected. From the γ scanning, the neutron fluence distribution causes the gradual increase of ^{95}Zr counts from the bottom to the top of fuel pin in Z fuel. The sharp dents of the peaks coincide well with pellet-pellet gaps in Z and SH as well as CH fuels as shown in Fig. 9.1.2 (a) and (b). In Fig. 9.1.2 (c), the dark lines of the particle lack and pellet-pellet gaps coincide with the

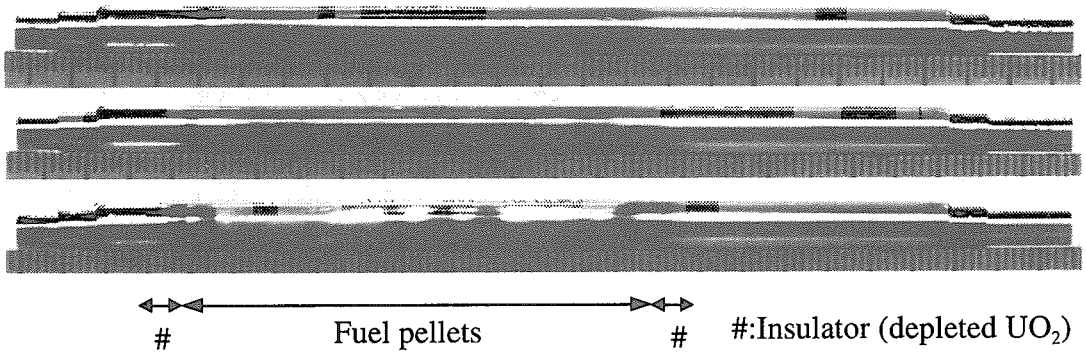

Fig. 9.1.1 Appearances of irradiated Z, SD and SH fuel pins.
Top: Z (UO_2-based YSZ)
Middle: SD(Particle-dispersed type of UO_2-YSZ + $MgAl_2O_4$)
Bottom: SH(Homogeneously-blended type of UO_2-YSZ + $MgAl_2O_4$)

sharp dents of ^{95}Zr peaks. A similar tendency can be seen in CD fuel. For the migration behavior of FPs, the nonvolatile nuclides of ^{95}Zr as well as ^{144}Ce and ^{106}Ru were observed only between the location of fuel pellets in all the irradiated fuels. In the Z fuel, the volatile ^{137}Cs is observed only between fuel pellets as shown in Fig. 9.1.2 (a). On the other hand, a small amount of Cs moved to the bottom of the insulator in the SD fuels as shown in Fig. 9.1.2 (c). For CD and CH fuels, the amount of released Cs were the same grade, several percent, as that of SD fuel. About 10 % of Cs produced in fuel pellets is released not only to the edge of fuel pellet and the bottom of the insulator but also to the plenum in SH fuel as shown in Fig. 9.1.2 (b). The pellet surface temperature (T_s) of SD, CD and CH fuels are the same grade as Cs boiling temperature (~ 950 K), and that of SH fuel is beyond it greatly. These T_ss are remarkably higher than that of LWR UO_2 (~ 720 K). It is obvious that T_s controls amounts of Cs release when it is near and beyond the Cs boiling temperature. Therefore Cs release will be suppressed by the cooling around the fuel pin to the same grade as Z fuel and LWR UO_2. From these non-destructive examinations, no significant difference in macroscopic irradiation behavior was distinguished among 5 fuels and LWR UO_2.

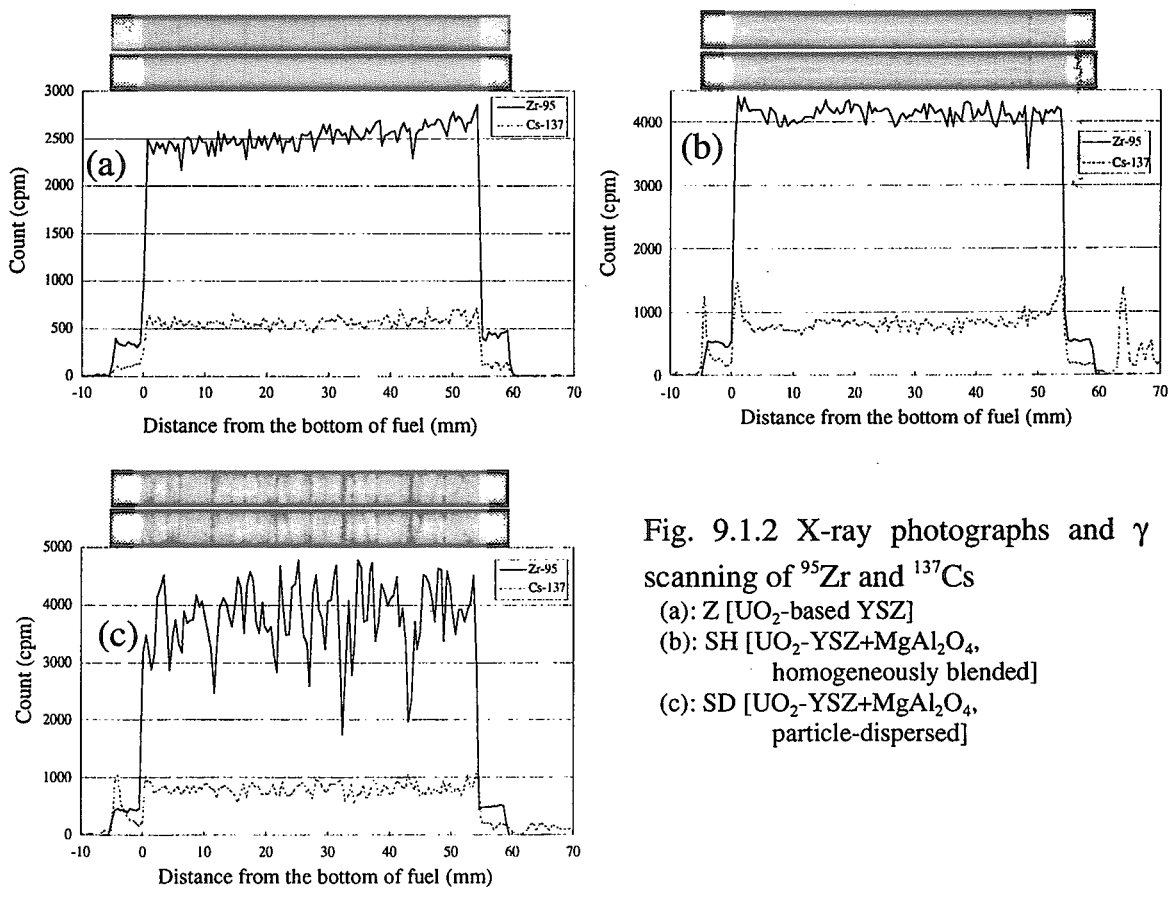

Fig. 9.1.2 X-ray photographs and γ scanning of ^{95}Zr and ^{137}Cs
(a): Z [UO_2-based YSZ]
(b): SH [UO_2-YSZ+$MgAl_2O_4$, homogeneously blended]
(c): SD [UO_2-YSZ+$MgAl_2O_4$, particle-dispersed]

9.2 Solid Solubility of PuO_{2-x} in Yttria Stabilized Zirconia

T. Yamashita
(*E-mail:* yamasita@popsvr.tokai.jaeri.go.jp)

Yttria stabilized zirconia (YSZ) is one of important inert matrix candidates because of its high chemical/physical stability and high resistance against irradiation. YSZ has a fluorite-type structure and is presumed to have an excellent capability to accommodate actinides/lanthanides elements in its lattice. However, few reports were available on the solid solubility of actinides in YSZ/ZrO_2. Cohen and Schaner reported that the solubility limit of UO_2 in tetragonal ZrO_2 was about 20 mol% at 2073 K.[1] Muromura et al. claimed that a single phase solid solution was formed in the whole range of YSZ and UO_2 system.[2] No report was available on the YSZ and PuO_2 system. In the present work, reactions between PuO_2 and YSZ were investigated in various atmospheres and lattice parameters of the solid solutions were determined in terms of compositions.

YSZ was prepared by heating a mixture of $ZrO(NO_3)_2{\cdot}2H_2O$, Y_2O_3 and Gd_2O_3 in molar ratio of 88.8:11.0:0.2 in vacuum at 1673 K. PuO_2 and YSZ powders were mixed in the ratio of Pu/(Pu+YSZ)=0-0.5 and were heated at 1773 K in air, vacuum and H_2. Powder X-ray diffraction analysis (XRD) was performed on the reaction products and lattice parameters of the products were determined using the standard Nelson-Riley extrapolation method. Thermo-gravimetric analysis was carried out for samples prepared in H_2 in order to determine oxygen contents.

Reaction between PuO_2 and YSZ in air was found to be very slow: Reaction products after twice heating at 1773 K for 10 h were found to be three-phase mixture of PuO_2, YSZ and a small amount of the solid solution. Samples heated at 1773 K in vacuum and H_2, however, were single-phase solid solutions with the fluorite structure. After XRD, samples heated in vacuum were heat-treated in air at 1173 K. The resultant products showed single-phase fluorite solid solutions. Lattice parameters of the Pu-YSZ solid solutions are plotted in Fig. 9.2.1 against Pu contents. The lattice parameter of the solid solution increases straightly with increasing Pu content, which is reasonable because large Pu ions substitute for small Zr ions. In the figure the dotted line and solid line indicate expected lattice parameters of a PuO_2-YSZ solid solution and a Pu_2O_3-YSZ solid solution, respectively. Lattice

parameters of the air-heated solid solution are exactly on the dotted line, indicating that the solid solution is formed from PuO_2 and YSZ: The oxidation state of Pu in the solid solution is tetravalent. Lattice parameters of the solid solutions heated in reducing atmospheres are larger than those heated in air as a result of formation of oxygen vacancies and Pu^{3+} ions. The lattice parameter of the solid solution $(Pu_yYSZ_{1-y})O_{2-x}$ can be expressed as:

$a = 0.51468 + 0.0258y$, for samples heated in air,

$a = 0.51472 + 0.0280y$, for samples heated in vacuum,

$a = 0.51450 + 0.0337y$, for samples heated in H_2.

From these results, it is confirmed that the Pu solubility in YSZ is at least 50 at%.

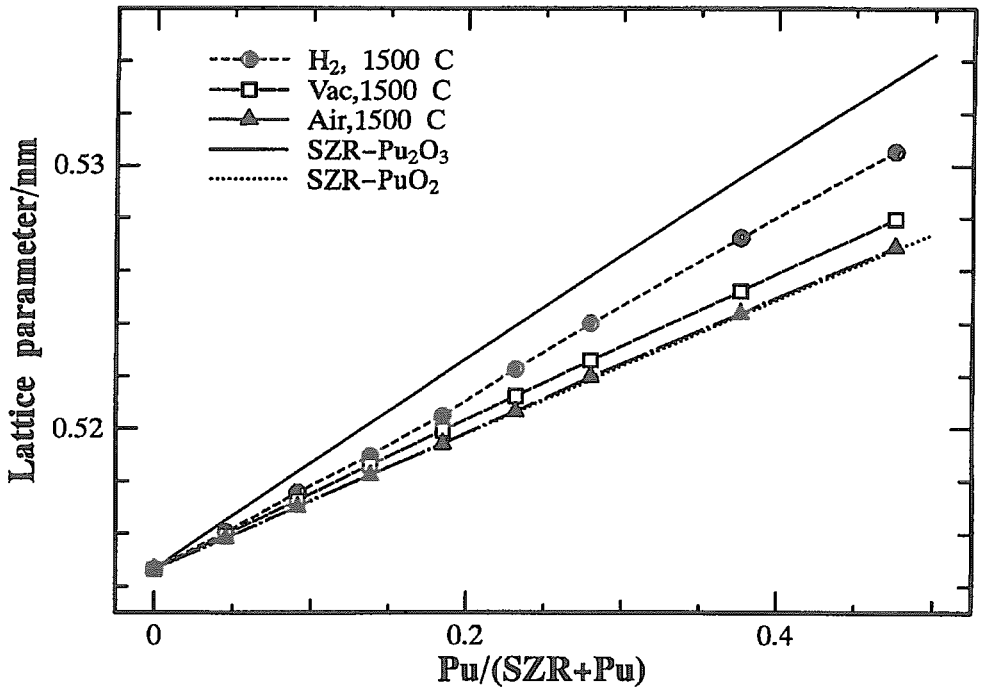

Fig. 9.2.1 Lattice parameters of Pu-YSZ solid solutions

Thermogravimetric analysis was performed for the samples prepared in H_2 using a Sartorius MP7 microbalance in order to determine oxidation states of Pu in the solid solutions. Analyzed results are summarized in Table 9.2.1. In this analysis it was assumed that the weight changes were attributed to oxidation state change of Pu in the solid solutions. Although some scattering are observed in the Pu^{3+} content in the table, about 2/3 of Pu is

reduced to Pu^{3+} in the reaction at 1773 K in H_2 for 10 h, which is consistent with the fact that the lattice parameter of the sample prepared in H_2 does not reach to the expected value of the Pu_2O_3-YSZ solid solution (the solid line in Fig. 10.2.1).

Table 9.2.1 Oxidation states of Pu in the Pu-YSZ solid solutions prepared in H_2

Composition	0.045	0.091	0.137	0.184	0.230	0.278	0.474
O/Pu ratio	1.75	1.71	1.68	1.67	1.67	1.67	1.74
Oxidation state	3.5	3.42	3.36	3.34	3.34	3.34	3.48
Pu^{3+} content	0.5	0.58	0.64	0.66	0.66	0.66	0.52

Kim proposed an empirical equation to calculate lattice parameters of ZrO_2-base solid solutions.[3] Calculated lattice parameters obtained by applying his equation to the present solid solutions showed large deviations from the experimental values, especially for samples with high Pu content and prepared in H_2. This may be attributed mainly from neglecting the effect of oxygen vacancies which are introduced by Pu^{3+} substitution for Zr^{4+}.

Crystallochemical behavior of YSZ may be very different from that of similar fluorite compounds such as ThO_2 and UO_2. When trivalent cations are introduced to ThO_2, oxygen vacancies are formed. The oxygen vacancies will be distributed randomly over the available sites in the solid solution. On the other hand, formed oxygen vacancies might be localized around Zr^{4+} sites and stabilize the oxygen deficient fluorite structure. A small ionic radius of Zr^{4+} (0.085 nm)[4] compared with that of Th^{4+} (0.105 nm)[4] may cause this behavior. Mössbour spectroscopy and X-ray absorption fine structure (XAFS) analysis will help to clarify the detailed structure of the YSZ solid solution. With combination of the detailed structure and experimentally determined lattice parameters, it will be possible to establish a reliable relation between lattice parameter and composition of the YSZ solid solution.

References:

1) Cohen I. and Schaner B.E.: J. Nucl. Mater., 9, 18 (1963).
2) Muromura T. and Hinatsu Y.: J. Nucl. Mater., 151, 55 (1987).
3) Kim D.J.: J Am. Ceram. Soc., 72, 1415 (1989).
4) Schannon R.D.: Acta Cryst. A32, 751 (1976).

9.3 Evaluation on chemical state of irradiated rock-like oxide fuels by SOLGASMIX-PV code

N. Nitani, K. Kuramoto, T. Yamashita and T. Ohmichi *
(*E-mail* : nitani@analchem.tokai.jaeri.go.jp)

In order to evaluate the changes of chemical forms of the actinides and FPs under irradiation, the thermodynamic equilibrium calculations of the ROX fuels of yttria stabilized zirconia (YSZ)-$MgAl_2O_4$ composite system were carried out using the SOLGASMIX-PV code[1]. The chemical forms and distribution between phases of FPs were obtained. Further, the relation between oxygen potential and phase equilibrium were discussed.

The compositions of fuels used in the calculations are shown in Table 9.3.1 and 9.3.2. Two isotopic ratios of plutonium were used: reactor grade plutonium (R-Pu) and weapon grade plutonium (W-Pu). The isotopic ratio of R-Pu is determined for 1 year of cooling time after reprocessing. Americium accumulated in this interval is also considered. The changes of actinides and FPs contents in the fuels under irradiation were obtained using the ORIGEN2 code[2]. The fuels were assumed to burn in LWR under thermal neutron flux of 2.5 x $10^{14}/cm^2$ for 1000 days. Using obtained yields, the thermodynamic equilibrium calculation at 1000K in constant volume was carried out using the SOLGASMIX-PV code.

Table 9.3.1 Pu composition (mol%)

	Reactor Grade Pu	Weapon Grade Pu
^{238}Pu	1.6	0
^{239}Pu	58.3	94.3
^{240}Pu	22.4	5.3
^{241}Pu	11.3	0.4
^{242}Pu	5.8	0
^{241}Am	0.6	0

Table 9.3.2 Fuel composition (mol%)

	Reactor Grade Pu	Weapon Grade Pu
$MgAl_2O_4$	56.00	56.00
PuO_2	15.23	11.19
YSZ	19.17	23.23
UO_2	9.60	9.58

Elements used in the calculation and stand-in role of each element are shown in Table 9.3.3. The representative elements for the calculation were chosen based on the consideration of the yields and chemical properties. The chemical species considered in the calculation are

*Research Organization for Information Science and Technology

shown in Table 9.3.4. The phases such as gas, fluorite, spinel, perovskite, hibonite and metal were regarded as forming ideal solid solutions, respectively, and the other chemical compounds, shown as 'others' in Table 9.3.4, were regarded as forming each separated phase.

Table 9.3.3
Elements under consideration

Element	Stand-in role
U	Th, Pa, U, Np
Pu	Pu
Zr	Zr
Y	Y
Mo	Mo, Tc
Cs	Rb, Cs
Ba	Sr, Ba
I	I
Nd	La, Nd, Gd, Pm, Sm,Eu, Am, Cm
Ce	Ce, Pr
Ru	Ru, Rh, Pd, Ag
O	O
He	He

Table 9.3.4 Compounds under consideration

Gas	Fluorite	Spinel	Alloy	Perovskite	Others
He	UO_2	Al_2O_3	U	$BaZrO_3$	Cs(L)
O_2	PuO_2	$MgAl_2O_4$	Pu	$BaPuO_3$	MoO_2
I_2	Pu_2O_3	$BaAl_2O_4$	Zr	$PuAlO_3$	MoI_2
I	ZrO_2		Y	$CeAlO_3$	CsI
Cs	Y_2O_3		Mo		RuO_2
CsI	Ce_2O_3		Ba	Hibonite	U_3O_8
Cs_2I_2	CeO_2		Ru	$BaAl_{12}O_{19}$	Cs_2ZrO_3
	Nd_2O_3		Ce	$Cs_2Al_{11}O_{17}$	Cs_2UO_4
	BaO		Nd	$CeAl_{11}O_{18}$	$BaUO_4$
	MgO		Al		Cs_2MoO_4
			Mg		$BaMoO_4$

The phase relations, distribution between phases of each element and oxygen potential change with the irradiation at 1000K were obtained from the calculated thermal equilibrium. The oxygen potential of R-Pu ROX fuel approached about -140 $kJ \cdot mol^{-1}$ by the irradiation. This result indicates that the irradiation could lead to undesirable behavior for the fuel: Oxidation of the cladding tube, etc. The oxygen, which was liberated by fission of Pu, oxidizes the FPs. Molybdenum oxidized to the hexavalent state formed molybdate phases with Cs and Ba: Cs_2MoO_4 and $BaMoO_4$. Iodine initially formed CsI with Cs. However after all the Cs formed molybdate, iodine formed I_2 whose chemical property and behavior are undesirable. The occurrence of I_2 formation is due to the high oxygen potential. Therefore, for safety reasons it is necessary to decrease the oxygen potential of the R-Pu ROX fuel.

A part of the initial Pu was reduced to the trivalent state, in order to consume the excess oxygen. The relation between composition of initial Pu valence and oxygen potential change is shown in Fig. 9.3.1. In the case of 10% Pu reduced to the trivalent state, the oxygen potential increase is suppressed to about –400 $kJ \cdot mol^{-1}$ at EOL (shown by mark '△' in Fig. 9.3.1). The value

is nearly the same as that of the conventional UO_2 fuel. The equilibrium between metallic Mo and MoO_2 controls the oxygen potential at about –400 $kJ \cdot mol^{-1}$. Under this condition in which the metallic Mo exists, iodine presents as CsI, which is a desirable result for the irradiation behavior. On the other hand, the oxygen potential of W-Pu ROX fuel was about –400 $kJ \cdot mol^{-1}$ at EOL, even if all the initial Pu were tetravalent. It is because the proportion of conversion of Pu to Am for W-Pu is less than that for R-Pu, due to the difference in isotopic ratios. The consumption of oxygen by trivalent Am is less than that by Pu or FPs, whereas the existence of large amounts of Am causes the generation of excess oxygen and increase of oxygen potential.

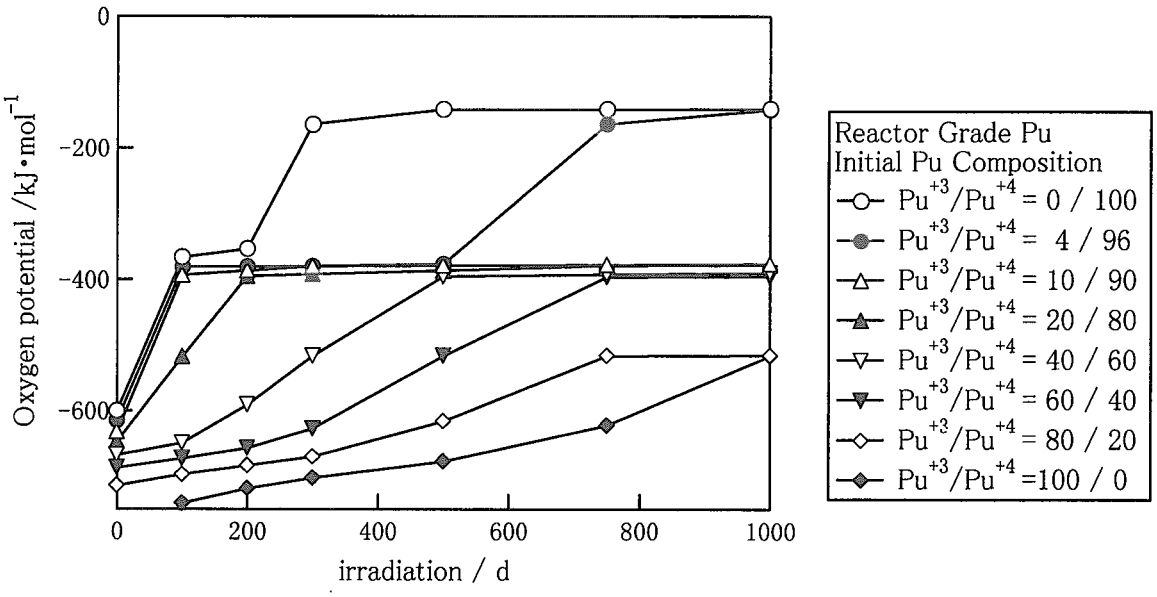

Fig. 9.3.1 Oxygen potentials of reactor grade Pu ROX fuels at 1000K

References:

1) Eriksson, G. and Rosen, E. Chem. Scr. 4 (1973) 193.

2) Croff, A. G.: ORNL/TM-7175, "A User's Manual for the ORIGEN2 Computer Code" (1980).

9.4 Pulse Irradiation Tests of Yttria Stabilized Zirconia Single-phase Type Rock-Like Oxide Fuel

T. Nakamura, K. Kusagaya, M. Yoshinaga, H. Uetsuka, T. Yamashita and H. Akie
(*E-mail:* akie@mike.tokai.jaeri.go.jp)

The transient characteristics of the ROX-LWR core tends to be more dynamic than that of the UO_2 core, having smaller fuel temperature feedback due to the absence of ^{238}U.[1] Thus, the fuel safety under the reactivity-initiated accident (RIA) condition is one of the key issues for the ROX fuel development. In order to investigate the fuel performance under the RIA conditions, pulse irradiation tests were conducted in the Nuclear Safety Research Reactor (NSRR) for two types of ROX fuels, i.e. yttria stabilized zirconia (YSZ) and YSZ/Spinel composite. The behavior of the YSZ/Spinel-ROX fuel was reported earlier[2], and the results of the pulse irradiation experiment are shown here for the YSZ single-phase type ROX fuel.

A short test fuel rod with a 17x17 PWR type design, containing 14 ROX pellets, was pulse irradiated in an experimental capsule filled with water. The specifications of the test fuel rod are listed in Table 9.4.1. The plutonium in the ROX test fuel was replaced by U for easier fuel handing. The thermal and mechanical properties of U-ROX were examined[3], and there was found no considerable difference to those of Pu-ROX. In the tests, the irradiation was carried out three times at different peak energy depositions of 0.5 MJ/kg (125 cal/g), 1.5 MJ/kg (350 cal/g) and 1.9 MJ/kg (450 cal/g), respectively, by natural pulse operation of half widths of 4.4 - 10 ms.

Table 9.4.1 Specifications of YSZ-ROX test fuel rod for NSRR pulse irradiation test

Element	Over all / stack length	279 mm / 135 mm
Pellet	Material composition	UO_2:YSZ=20:80 mol% YSZ=ZrO_2:Y_2O_3=0.81:0.19 mol%
	U-235 Enrichment	20 w/o
	Diameter / length	8.05 mm / 9 mm (P/C radial gap = 0.085 mm)
Cladding	Material	Zry-4
	Outer / Inner diameter	9.5 mm / 8.22 mm (thickness = 0.64 mm)

As a result of the pulse irradiation tests, the YSZ-ROX fuel remained intact at peak fuel enthalpy of up to 1.5 MJ/kg, although 15 % of the fuel was calculated to be molten. The failure occurred at peak fuel enthalpy of 1.9 MJ/kg, in which 40 % of the fuel was calculated to be molten. The cross section of the failed rod is shown in Fig. 9.4.1, and compared with that of UO_2 fuel rod. The failure of UO_2 fuel rod occurs at the part of once molten and embrittled cladding, and the fuel itself remains solid. The failure of the ROX fuel, on the other hand, occurs due to cladding burst with considerable fuel melting. Then about 50 % of partly molten fuel was dispersed out to the surrounding water. The behavior is rather similar to that of YSZ/Spinel-ROX, but the cladding damage of YSZ/Spinel rod was quite limited except for the burst opening. Lower fuel melting temperature of ROX fuels, 2820 K for YSZ-ROX and 2210 K for YSZ/Spinel-ROX, respectively, than that (3110 K) of UO_2 should have contributed to the different failure modes.

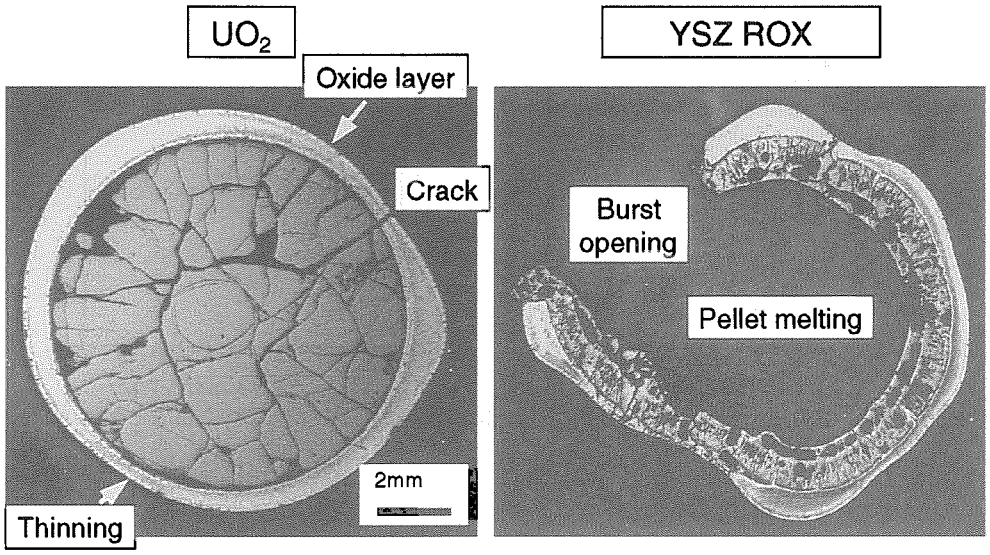

Fig. 9.4.1 Cross section of the failed UO_2 and YSZ-ROX fuel rods

When the ROX fuel rod fails, in spite of the large fraction of fuel dispersion into the surrounding water, generation of pressure pulse and water hammer due to molten fuel/water interaction was negligible either by the capsule pressure sensor or the water column movement sensor. Relatively mild fuel dispersion during the high temperature burst might have prevented the mechanical energy generation, which could threaten the reactor safety in

RIAs.

The results of the YSZ- and YSZ/Spinel-ROX fuels pulse irradiation experiments are summarized in Fig. 9.4.2. The failure threshold of ROX fuel rods in Fig. 9.4.2 (a) is more than 1.5 MJ/kg, and seems higher than that of UO_2 rod of about 1 MJ/kg. By taking into account the difference in fuel densities between ROX fuels and UO_2 fuel, the failure threshold of ROX fuels in terms of volumetric enthalpy is rather similar to that (10 GJ/m^3) of UO_2 fuel in Fig. 9.4.2 (b). Even though the failure mode of the ROX fuels was quite different from that of UO_2 fuel, the current UO_2 fuel rod failure limit seems possible to be adopted for ROX fuels.

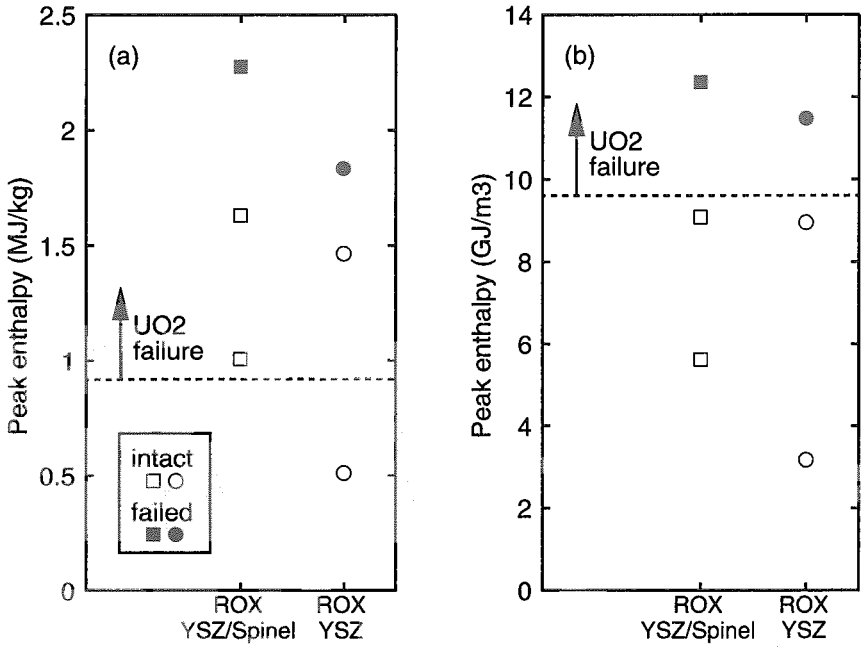

Fig. 9.4.2 ROX fuel rod failure threshold enthalpy in terms of (a) MJ/kg and (b) GJ/m^3

References:

1) Akie, H., Takano, H. and Anoda, Y. : J. Nucl. Mater., 274, 139 (1999).

2) Okonogi, K., et al. : J. Nucl. Mater., 274, 167 (1999).

3) Matsuda, T., et al. : JAERI-Research 97-083 "Thermal Expansion and Thermal Conductivity of Rock-like Fuel" (1997) [in Japanese].

9.5 Doppler Effect Experiment of Resonance Materials for ROX Fuels

Y. Nakano, M. Andoh, S. Okajima and H. Takano
(*E-mail:* nakano@jrr3fep2.tokai.jaeri.go.jp)

As the rock like oxide (ROX) fuel contains very small amount of fertile materials in itself, the Doppler effect of the reactor becomes small. It affects increase in the fuel temperature when the reactivity initiated accident (RIA) occurs. Akie showed that addition of some resonance materials into the fuels improves the Doppler effect successfully.[1] Erbium, tungsten and thorium are considered as candidates of additives. To obtain the Doppler reactivity data of them, a series of experiments was carried out in the FCA Assembly XX-2[2]. The Doppler reactivities of natural uranium metal and its dioxide samples were also measured for the reference data.

Experiment:

Doppler samples of erbium metal, tungsten metal and thorium dioxide were newly fabricated for the experiment. Natural uranium metal and its dioxide samples, which have been used for the Doppler effect measurements in various mock-up cores in FCA[3], were also measured to obtain the reference data. They are cylindrical shaped with 150 mm in stack length and 23 mm in diameter. It is enclosed in a thin-walled stainless steel can. The can is inserted in an evacuated stainless tube (vacuum capsule) and is surrounded by an electric heater that is on the inside wall of the capsule. The vacuum capsule is contained in an outer stainless capsule (cooling capsule). The forced airflow through the gap between the vacuum and cooling capsules removes the heat, which escapes from the sample. The capsule is set in the Doppler drawer, which is 5 cm square and 2 m long. The drawer is inserted in the center of the core. Temperature of the sample is raised up to 1073 K. The Doppler effect is derived from the difference in the reactivities between unheated and heated sample at the center of the core. Since the measured Doppler reactivity is so small, the reactivity-oscillator technique[4] is used to minimize a reactivity drift effect of the core which is caused by a slight temperature change of the core.

The Doppler effect experiment was conducted on a mock-up core of a nitride fueled fast reactor, FCA Assembly XX-2. Figure 9.5.1 shows the dimensions and the regions of the core. The center part of the core is the test region consists of plutonium, natural uranium,

nitrogen, sodium and other structural materials, which simulates a mixed nitride fuel. The test region does not contain sample materials such as erbium, tungsten and thorium in itself. The test region is surrounded by a driver region that makes the system critical.

Results:

Table 9.5.1 shows the results of the experiment. The erbium and tungsten metal samples have comparable Doppler reactivities to uranium metal's one. Thorium dioxide has almost the same value as uranium dioxide. From the table, erbium, tungsten and thorium are estimated to be good candidates for resonance absorbers to improve the Doppler effect of the ROX fueled core.

Table 9.5.2 shows the Doppler reactivities per unit mole of the sample materials. One mole erbium atoms have the largest Doppler reactivity than that of the other sample atoms. Uranium dioxide has larger value than that of uranium for its lower atom density in the sample.

Conclusion:

Experimental data of erbium, tungsten and thorium on the Doppler reactivity have been obtained. It has been found that they have comparable Doppler effect to uranium-238 and are good candidates for the additives of the ROX fuels.

References:

1) Akie, H., Takano, H., Anoda, Y., : J. Nucl. Mater., 274, 139 (1999).
2) Andoh, M. et. Al., : Private Communication (1999).
3) Okajima, S., Oigawa, H., Mukaiyama, T., Andoh, M., : J. Nucl. Sci. Technol., 33, 202 (1996).
4) Foell, W. K., : "Small-Sample Reactivity Measurements in Nuclear Reactors", Am. Nucl. Soc. (1972).

Table 9.5.1 Measured Doppler Reactivities* of the Samples (Δk/k)

Sample	Er	W	ThO_2	U	UO_2
Doppler Reactivity	-1.44×10^{-5}	-1.13×10^{-5}	-8.70×10^{-6}	-1.67×10^{-5}	-8.83×10^{-6}
(error)	(3.8%)	(4.1%)	(6.3%)	(3.1%)	(7.2%)

*Temperature change: room temp. => 1073 K

Table 9.5.2 Measured Doppler Reactivities* per Unit Mole of the Samples (Δk/k/mol)

Sample	Er	W	ThO_2	U	UO_2
Reactivity	-4.41×10^{-6}	-1.81×10^{-6}	-4.28×10^{-6}	-2.95×10^{-6}	-3.94×10^{-6}

*Temperature change: room temp. => 1073 K

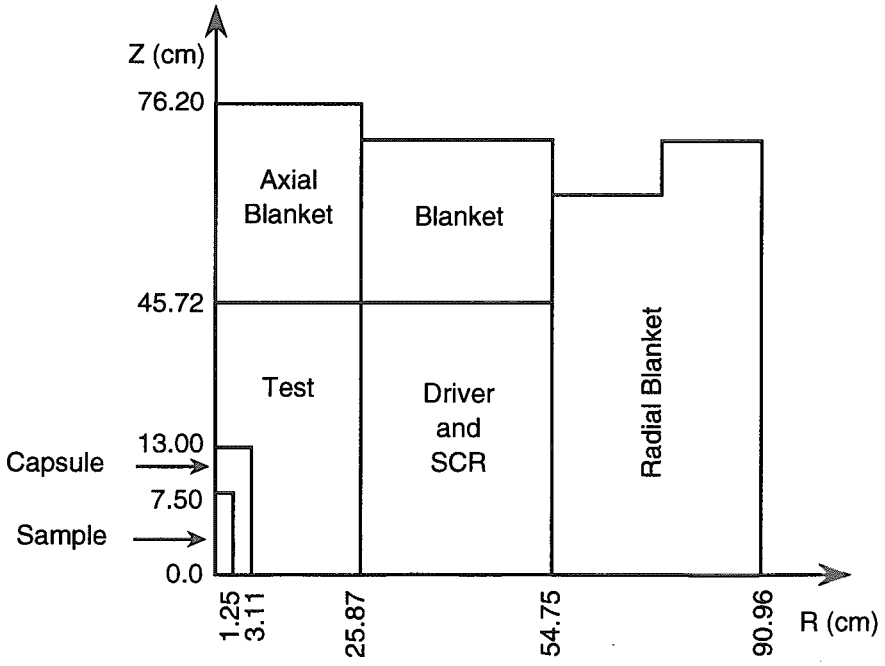

Fig. 9.5.1 R-Z Model of Doppler Experiment Core

9.6 Effect of Different Types of Additives on the Thermal Neutron Spectrum and Fuel Temperature Coefficient of Rock-like Oxide Fuel

A. Shelley*, H. Akie, H. Takano and H. Sekimoto*

(*E-mail:* shelley@popsvr.tokai.jaeri.go.jp)

A rock-like oxide (ROX: PuO_2-ZrO_2) fueled LWR cell has a small negative fuel temperature coefficient (FTC). It becomes even positive at EOL, mainly due to a large thermal spectrum shift with fuel temperature increase[1]. For the adequate improvement of FTC of ROX fuel, it is effective to add some fertile or poison additives[2]. Here, the effect of different types of additives on the FTC and thermal neutron spectrum change has been studied.

Cell burnup calculations were done on a pin cell model based on 1150 MW electric class 17×17 type PWR for 887 EFPD. The temperatures of fuel, cladding and moderator are assumed to be 600 °C, 350 °C and 300 °C, respectively. Cell calculations have been performed by the SRAC95 system based on JENDL-3.2 nuclear data library. As an additive, ThO_2, UO_2 or Er_2O_3 is considered. The content of additives UO_2 and ThO_2 are considered to be from 10 to 20 a/o for weapons-grade Pu (W-Pu) and from 5 to 15 a/o for reactor-grade Pu (R-Pu) ROX fuels. Additive Er_2O_3 is considered from 3 to 10 a/o for W-Pu and from 2 to 5 a/o for R-Pu ROX fuels. These additive contents were decided so that the ROX fueled cell has sufficiently negative FTC[2].

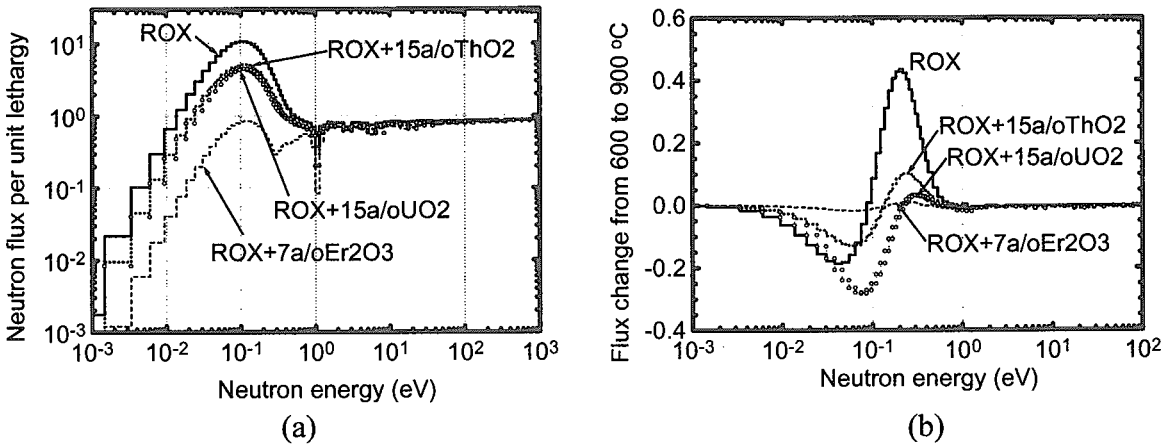

Fig.9.6.1 Neutron spectra and its change with fuel temperature in W-Pu fuels at EOL

* Tokyo Institute of Technology

Figures 9.6.1 (a) and (b) respectively show the neutron spectra and its change with the increase of the fuel temperature at EOL in the W-Pu ROX fueled cells with and without additives. It can be seen from Fig.9.6.1 (a) that the soft spectrum of ROX fuel becomes harder at EOL after adding the additive ThO_2, UO_2 or Er_2O_3. In consequence, the spectrum changes with fuel temperature increase become smaller in Fig.9.6.1 (b). Additive UO_2 increases the negative side change of thermal neutron spectrum of ROX fuel more than that with the other additives. Additive Er_2O_3 is most effective to decrease the spectrum change of ROX fuel. As a result, the smaller FTC value of ROX fuel is improved by these additives. Figure 9.6.2 shows the effect of additives ThO_2, UO_2 or Er_2O_3 on the FTC of ROX fuel cell. This figure shows that all of these additives make the FTC of ROX fuel negative from BOL to EOL.

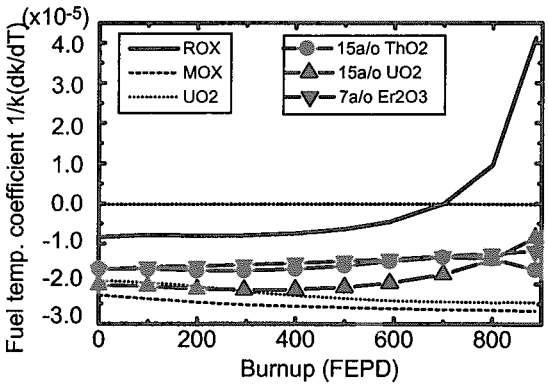

Fig. 9.6.2 Burnup dependent fuel temp. coefficient of W-Pu ROX fuel with additives

Thermal neutron spectrum becomes hard, if neutron is absorbed by a resonance or a thermal absorber, such as Th, U or Er. Furthermore in the ROX fuel with such an additive, the density of Pu becomes more than that in the additive free ROX fuel at EOL. Pu has also a large thermal neutron absorption cross section. Consequently, not only the additives themselves but also Pu may contributed to the thermal spectrum hardening as well as to the decrease in the spectrum shift with the fuel temperature increase. It is therefore studied the independent effect of the additive and Pu isotopes on the thermal neutron spectrum and FTC of ROX fueled cell.

The densities of nuclides in W-Pu ROX fuel cell at EOL is considered as a reference case to compare the density effect of Pu and additives on the neutron spectrum and FTC. From the reference case, the density of ^{239}Pu is increased up to 1.0E-3 atom/cm^3, which is nearly equivalent to the initial loaded density of ^{239}Pu in ROX fuel. The density of ^{241}Pu is increased up to 5.0E-4 atom/cm^3. The ^{241}Pu density in the W-Pu ROX fuel is initially very low, and it increases with burnup. Especially in the 7 a/o Er_2O_3 added ROX fuel, the ^{241}Pu density becomes very high at EOL to be about 5.0E-4 atoms/cm^3. The density of ^{232}Th and ^{238}U is increased up to 1.0E-2 atom/cm^3, which is nearly equal to the initial loaded density of these

isotopes in TOX and MOX fuels, respectively. The density of Er is increased up to the equivalent amount to the initial loaded density in 7 a/o Er added ROX fuel.

Figure 9.6.3 compares effect of ^{239}Pu, ^{241}Pu, ^{232}Th, ^{238}U and ^{166}Er + ^{167}Er on the thermal neutron spectrum change with the fuel temperature increase, when their densities are the same (1.0E-4 atom/cm^3). It is seen by this figure that fertile nuclides ^{232}Th and ^{238}U have nearly the same and a small effect on the thermal neutron spectrum shift in ROX fuel. Poison additive Er is more effective to decrease the spectrum shift than the fertile additives ^{232}Th and ^{238}U. This figure shows clearly that ^{239}Pu and ^{241}Pu are more effective than the fertile and poison additives to decrease the thermal neutron spectrum shift.

Figure 9.6.4 shows the independent density effect of ^{239}Pu, ^{241}Pu, ^{238}U, ^{232}Th and Er on the FTC of ROX fuel cell. This figure shows that ^{232}Th and ^{238}U does not improve the positive FTC values of ROX fuel in comparison with the other isotopes. Erbium can improve the FTC of ROX fuel especially when the density is more than 1.0E-4 atom/cm^3. With this amount of Er in ROX fuel, however, the value of k-eff becomes unrealistically low. To keep the criticality, it is essential to increase the Pu enrichment of ROX-Er fuel largely.

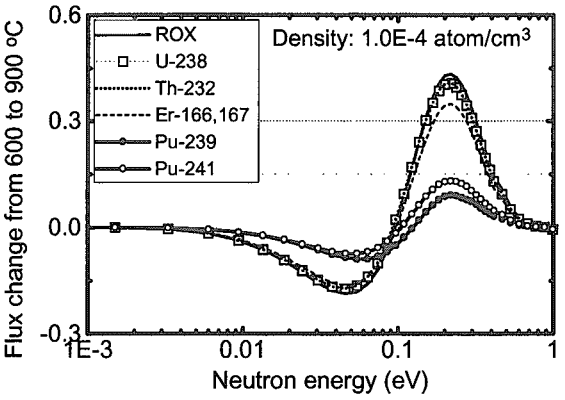

Fig. 9.6.3 Effect of nuclides addition of 10^{-4} atoms/cm^3 on the thermal spectrum change with fuel temperature (W-Pu ROX, EOL)

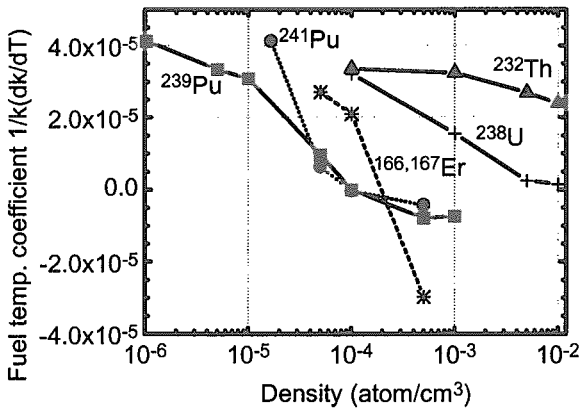

Fig. 9.6.4 Density effect of some nuclides on the FTC of W-Pu ROX fuel at EOL

References

1) Shelley, A., et al. : JAERI-Review, 99-031 "Nuclear Energy System Department Annual Report (April 1, 1998 – March 31, 1999)", p.238 (1999).

2) Akie, H., Takano, H., and Y. Anoda : J. Nucl. Mater., 274, 139 (1999).

9.7 Effect of Additives on the Plutonium Transmutation and Minor Actinide and Long Life FP production Characteristics in a ROX fueled LWR

A. Shelley*, H. Akie, H. Takano and H. Sekimoto*

(*E-mail:* shelley@popsvr.tokai.jaeri.go.jp)

A Rock like oxide, ROX (PuO_2+ZrO_2) fueled LWR has lower fuel temperature coefficients values, which can be improved by some additives such as ThO_2, UO_2 or Er_2O_3. The effect of these additives on the transmutation of Pu and production rate of minor actinides (MAs) and long life fission products (LLFP) of ROX fueled LWR are studied. A typical MOX fueled LWR is considered as the reference case.

Burnup calculations were performed on a pin cell model based on 1150 MW (electric)-class 17×17 type PWR. These fuel cells are burnt for 887 EFPD. As an additive, 15a/o of ThO_2 or UO_2 and 7a/o Er_2O_3 were considered in W-Pu ROX fuel. These additive contents were decided so that the ROX fueled cell has sufficiently negative FTC[1]. The enrichment of fissile plutonium was adjusted to keep criticality for 887 EFPD by three batch refueling scheme. The cell calculations were performed by the SRAC95 system with JENDL-3.2 nuclear data except Er, which was adopted from ENDF/B-VI nuclear data library.

Figure 9.7.1 shows the inventory of net W-Pu as a function of burnup time in EFPD. Fertile additives UO_2 and ThO_2 decrease the initial content of Pu of ROX fuel by increasing new fissile nuclides production during burnup, while the poison Er_2O_3 increases the initial Pu inventory. The transmutation rate of Pu (kg/GWe/day) in ROX fuel decreases with fertile additives by the newly produced fissile nuclides. On the other hand, the poison Er_2O_3 does not change the transmutation rate of Pu. The transmutation percentage of Pu in W-Pu ROX fuel is 87.1 %. Considering 15 a/o ThO_2, 15 a/o UO_2 or 7 a/o Er_2O_3 additive, this percentage becomes 85.3 %, 73.6 % or

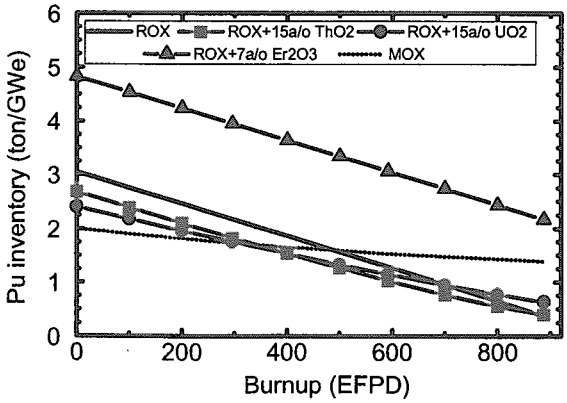

Fig. 9.7.1: Effect of additive on net Pu inventory of W-Pu ROX fuels.

* Tokyo Institute of Technology

55.1 %, respectively. There is a negligible change of ^{239}Pu transmutation percentage in ROX fuel by adding ThO_2. But additive 15 a/o UO_2 and 7 a/o Er_2O_3 largely decrease it[2]. The net Pu transmutation amount (kg/GWe) in ROX-Er_2O_3 fuel is nearly equal to that in ROX fuel, but the transmutation percentage of Pu is less than that in ROX-ThO_2 and ROX-UO_2 fuels because of large initial Pu inventory.

Table 9.7.1 compares the production amount of MAs in W-Pu ROX fuel with the additives ThO_2, UO_2 and Er_2O_3. The production amount of MAs in ROX-additive fuels decreases due to lower production of ^{243}Am and ^{244}Cm. The major source of ^{243}Am is based on (n,γ) reaction of ^{242}Pu and succeeding β-decay, which increases with burnup by the (n, γ) reaction of ^{241}Pu. In ROX fuel, fission rate of ^{239}Pu decreases very rapidly with burnup time due to absence of fertile nuclides. As a result, ^{241}Pu becomes the major contributor of fission reaction at EOL. The additives UO_2 and ThO_2 produce new fissile nuclides ^{239}Pu and ^{233}U, respectively, and decrease the fission contribution of ^{241}Pu. In Er_2O_3 added fuel, the density of ^{239}Pu is very high even at EOL, which also decreases the fission contribution of ^{241}Pu. As well as fission rate, neutron capture rate of ^{241}Pu also decreases, which decreases the production of ^{242}Pu as well as ^{243}Am and ^{244}Cm, especially in Er_2O_3 added ROX fuel. On the other hand, the production of ^{241}Am is increased by the increase of β-decay rate of ^{241}Pu in the ROX additive fuels in comparison with that in the additive-free ROX fuel. However, the increasing amount of ^{241}Am in ROX-additive fuel is less than the decreasing amount of ^{243}Am.

Table 9.7.2 compares the effect of additives on the production amount of LLFP in the W-Pu ROX fuels. As LLFP, ^{79}Se, ^{93}Zr, ^{99}Tc, ^{107}Pd, ^{126}Sn, ^{129}I and ^{135}Cs were considered. It can be seen net LLFP production in ThO_2 or UO_2 added ROX fuel is nearly the same as that in the ROX fuel. However, with the additive Er_2O_3, the production amount of ^{135}Cs increases largely. The main sources of ^{135}Cs are β-decays of ^{135}I and ^{135}Xe. The effective capture cross-section of ^{135}Xe becomes very small in Er_2O_3 added ROX fuel, because Er and ^{135}Xe both have very large capture cross-section at low neutron energy region. It is expected that smaller neutron capture cross-section of ^{135}Xe in ROX-Er_2O_3 fuel increases its β-decay rate.

In conclusion, ROX-ThO_2 fuel shows very similar tendencies to ROX fuel compare to ROX-UO_2 or ROX-Er_2O_3 fuels, from the points of view of Pu transmutation and MA and LLFP productions.

References:

1) Akie, H., Takano, H. and Anoda, Y. : J. Nucl. Mater., 274, 139 (1999).

2) Shelley, A., et al. : to be published in J. Nucl. Sci. Technol.

Table 9.7.1: Production amount (kg/GWe) of MAs in ROX and ROX-additives fuels.

	ROX	ROX-ThO_2 (15 a/o)	ROX-UO_2 (15 a/o)	ROX-Er_2O_3 (7 a/o)	MOX
^{241}Am	1.38	2.77	3.43	17.97	8.63
^{242g}Am	3.24E-2	2.46E-2	2.67E-2	3.48E-2	2.24E-2
^{242m}Am	1.80E-2	3.80E-2	4.63E-2	3.22E-1	1.34E-2
^{243}Am	44.71	34.85	34.47	18.96	19.94
Net Am	46.14	37.69	37.97	37.28	28.72
^{242}Cm	5.36	4.29	4.20	4.14	3.08
^{243}Cm	1.49E-1	1.17E-1	1.13E-1	9.17E-2	7.23E-2
^{244}Cm	24.76	16.30	15.63	6.75	6.82
^{245}Cm	1.06	7.98E-1	8.01E-1	5.54E-1	4.43E-1
^{246}Cm	3.79E-1	2.00E-1	1.82E-1	2.91E-2	3.84E-2
Net Cm	31.71	21.70	20.92	11.56	9.46
^{237}Np	1.66E-2	6.32E-2	1.67	3.78E-2	7.57
Total MA	77.86	59.45	60.56	48.88	46.75

Table 9.7.2: Production amount (kg/GWe) of LLFP in ROX and ROX-additives fuels.

	^{79}Se	^{93}Zr	^{99}Tc	^{107}Pd	^{126}Sn	^{129}I	^{135}Cs	Net LLFP
ROX	0.28	37.01	54.44	43.10	2.94	15.69	32.73	186.18
ROX-15 a/o ThO_2	0.43	42.67	55.14	36.81	3.04	16.84	29.01	184.03
ROX-15 a/o UO_2	0.31	38.01	56.34	41.40	2.98	16.36	29.10	184.40
ROX-7 a/o Er_2O_3	0.36	38.33	59.68	40.32	3.33	18.07	56.11	216.19
MOX	0.34	40.10	60.18	37.69	2.99	17.13	33.50	191.91

9.8 Ingestion Radiotoxicity Hazard of U-free Spent Fuels from LWR

A. Shelley*, H. Akie, H. Takano and H. Sekimoto*

(*E-mail:* shelley@popsvr.tokai.jaeri.go.jp)

Radiotoxicity hazard of U-free rock-like oxide: ROX (PuO_2+ZrO_2) and thorium oxide: TOX (PuO_2+ThO_2) LWR spent fuels are investigated in comparison with the radiotoxicity hazard of MOX spent fuel. Ingestion radioactivity concentration limit of nuclides, which has been approved by ICRP[1], is used to calculate the toxicity index of the nuclides for the period up to 10^7 years cooling. The radiotoxicity hazards of ROX and TOX fuel are considered in terms of fresh fuel volume equivalent to one metric ton MOX.

Figure 9.8.1 compares the total ingestion radiotoxicity hazard of weapons-grade Pu (W-Pu) ROX, TOX and MOX spent fuels. At the cooling of 10 years, the total toxicity hazard of ROX spent fuel is nearly the same as that of the TOX and MOX spent fuels. At this cooling years, ROX spent fuel hazard is dominated by Cm and fission products (FP), while Pu and FP is dominant in TOX and MOX spent fuels hazard. After 10 years cooling, the toxic yield of ROX spent fuel becomes lower than that of TOX and MOX spent fuels. At the cooling of 10^3 years, the toxic yield of ROX spent fuel is one-fourth of that of TOX and MOX spent fuels. At this cooling years Am is dominant in all of these spent fuels hazard. At 10^5 years cooling, the total toxic hazard of ROX spent fuel is one-tenth and one-fourth of that of TOX and MOX spent fuels, respectively. At this cooling time, Pu is dominant in ROX and MOX spent fuels, while ^{229}Th is dominant in TOX spent fuel. At 10^7 years cooling, the total toxic yield of ROX spent fuel is one-fifth and one-third of that of MOX and TOX spent fuels, respectively. At this cooling time the main hazard contributor nuclide is Np in ROX and TOX spent fuels. On the other hand, ^{210}Pb dominates the hazard of the MOX spent fuel, which is produced by a series of α-decays from ^{234}U.

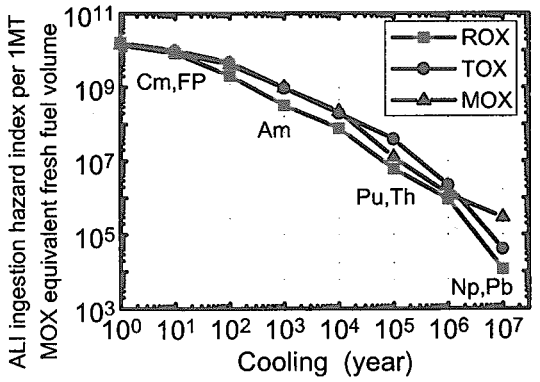

Fig. 9.8.1 Total ingestion radiotoxicity hazard of W-Pu spent fuels

*Tokyo Institute of Technology

From the discussion above, it is clear that the potential radiotoxicity of ROX, TOX and MOX spent fuel is associated mainly with isotopes particularly Pu, Am, Cm, Np etc.. The toxic hazard of these nuclides will be discussed in detail.

Figure 9.8.2 shows the radiotoxicity hazards of Pu in W-Pu ROX, TOX and MOX spent fuels. The toxicity yield of Pu in ROX spent fuel is lower than that in TOX and MOX spent fuels. This is because the discharged amount of Pu in ROX fuel is lower than that in TOX and MOX fuels. The toxic yield of ^{241}Pu (half-life 14.35 Y) dominates the hazard up to 10 years, which is one-fourth in ROX spent fuel than that in TOX and MOX spent fuels. The toxicity hazard of ^{240}Pu (half-life 6564 Y) isotope dominates in the period up to 10^4 years cooling. The toxic yield of ^{240}Pu in ROX spent fuel is one-third of TOX and MOX spent fuels. At 10^5 years cooling ^{239}Pu is the main source of Pu toxic hazard in TOX and MOX spent fuels, while in ROX fuel ^{242}Pu is the main source of Pu toxic hazard. The toxicity hazard of ^{239}Pu in ROX spent fuel is nearly one third and one tenth of that of the TOX and MOX spent fuels, respectively. At the cooling 10^6 years, the toxic yield of ^{242}Pu in ROX spent fuel is two times higher than that in TOX and MOX spent fuels.

The most important isotope of Np, ^{237}Np, is produced by (n, γ) reaction of ^{235}U, (n, 2n) reaction of ^{238}U and α-decay of ^{241}Am. Figure 9.8.3 shows the toxicity hazard of Np in W-Pu fuels. At the beginning of cooling time, the toxicity hazard of Np in TOX spent fuel is far less than that in MOX spent fuel, but after 10^2 years cooling, the toxicity hazard of Np in TOX spent fuel increases largely and becomes nearly equal to that of MOX spent fuel. This is because, the discharged ^{241}Am in TOX fuel is higher than that in ROX fuel, which is converted to ^{237}Np by α-decay.

Americium is produced by the β-decay of ^{241}Pu (^{241}Pu→^{241}Am) and (n,γ) reaction of

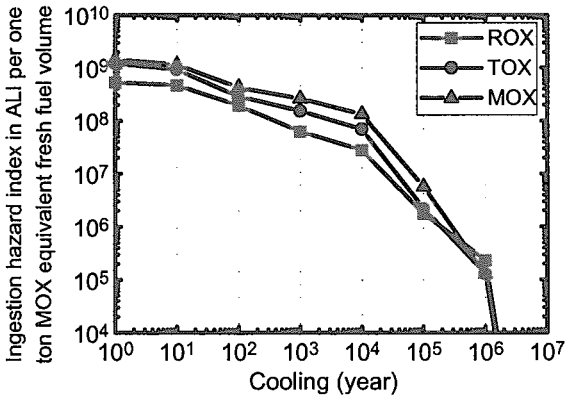

Fig. 9.8.2 Radiotoxicity hazard of Pu

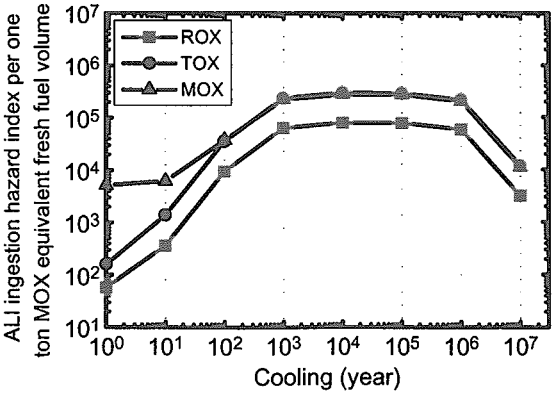

Fig. 9.8.3 Radiotoxicity hazard of Np

^{242}Pu ($^{242}Pu \rightarrow ^{243}Am$) during reactor operation. Figure 9.8.4 shows the toxicity hazard of Am in W-Pu ROX, TOX and MOX spent fuels. In the toxicity hazard of Am, ^{241}Am dominates the hazard up to 10^3 years cooling. The toxicity hazard of ^{241}Am in ROX spent fuel is one-fourth of that in TOX and MOX spent fuels. At the cooling of 10^4 years, isotope ^{243}Am is the main toxic source of Am. The toxicity yield of ^{243}Am in ROX spent fuel is double of that in TOX and MOX spent fuels.

Curium is most intensely radioactive of the actinides for both neutron emission and α-activity. The most abundant isotope is ^{244}Cm, which decays with a half-life of 18 years to form ^{240}Pu. Figure 9.8.5 shows that the toxic yield of Cm in ROX spent fuel is higher than that in TOX and MOX spent fuels.

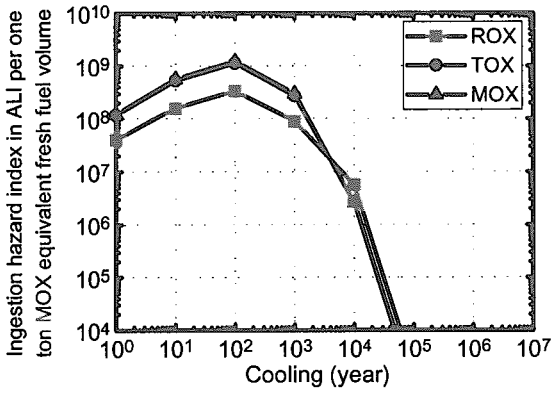

Fig. 9.8.4 Radiotoxicity hazard of Am

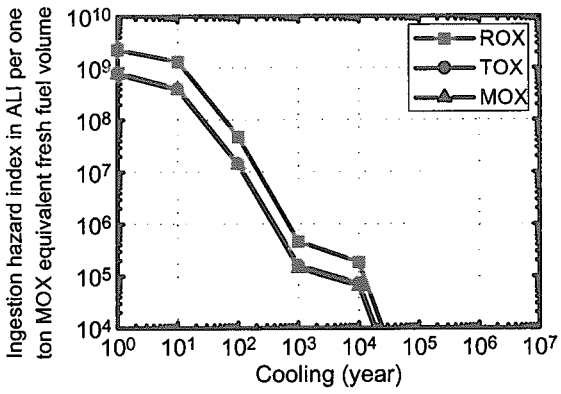

Fig.9.8.5 Radiotoxicity hazard of Cm

It is essential to add some additives such as ThO_2, UO_2 or Er_2O_3 in ROX fuel to improve small fuel temperature and void coefficients. By adding an additive, the toxic yield of ROX spent fuel increases a little, but still less than that of TOX and MOX spent fuels [2].

In conclusion, the long-term ingestion radiotoxicity hazard of ROX spent fuel is smaller than that of TOX and MOX spent fuels. Therefore, ROX fuel is better than TOX and MOX fuels to be used in LWRs as a once through Pu burning fuel.

Reference:

1) Annals of the ICRP 24(4) "ICRP Publication 68 : Dose Coefficients for Intakes of Radionuclides by Workers", Elsevier Science Ltd. Oxford (1993).
2) Shelley, A., et al. : "Proc. 3rd Int. Symp. on Global Environmental and Nuclear Energy Systems (GENES-3)", to be published in Progress in Nuclear Energy.

9.9 Core Burnup Calculation of Thoria Based Rock-like Oxide Fuel PWR

H. Akie and Y. Sugo*

(E-mail : akie@mike.tokai.jaeri.go.jp)

There were proposed two different types of rock-like oxide (ROX) fuels respectively based on yttria stabilized zirconia (YSZ : $(Zr,Y)O_2$) and thoria (ThO_2).[1] A zirconia based ROX (Zr-ROX : PuO_2-$(Zr,Y)O_2$-$MgAl_2O_4$) PWR core has problems such as a small negative fuel temperature coefficient and a large power peaking factor, which cause severe transients in accidents. For the improvement of these characteristics, it has already been found effective to use the additive of 8~25 mol% UO_2 or ThO_2 in Zr-ROX fuel.[2] As the thoria based ROX (Th-ROX : PuO_2-ThO_2-$MgAl_2O_4$) fuel contains more than 40 mol% of ThO_2, a Th-ROX fueled PWR core is expected to also have adequate core physics characteristics.

Two-dimensional X-Y core burnup calculations were carried out for weapons- and reactor-grade Pu (W-Pu and R-Pu) Th-ROX fueled PWR cores. The core specification is based on the conventional 1100 MW_e class 17×17 type PWR. In the core burnup calculations, a three batch refueling and shuffling scheme of assemblies was taken into consideration for the power distribution flattening. The Pu enrichment was adjusted to achieve the discharge burnup of about 1200 EFPD (400 EFPD × 3 batches), which corresponds to about 45 GWd/t in UO_2 and MOX fueled cores. In order to estimate the core axial power profile and the local power peaking within an assembly, one-dimensional core calculations and fuel assembly calculations were also performed. These calculations were made by using the SRAC95 system[3] with the JENDL-3.2 based data library.

The estimated core characteristics are summarized in Table 9.9.1 for W-Pu and R-Pu ROX cores at BOC. In this table, the characteristics of the Zr-ROX fueled core with and without UO_2 additive are also shown together with those of UO_2 core which were calculated with the same calculation method as the Th-ROX core. The content of UO_2 additive in the Zr-ROX fuel (15 mol% for W-Pu and 8 mol% for R-Pu) was decided so as to have a comparable transient behaviors to that of UO_2 core.[2] As shown in this table, the fuel temperature reactivity, which is the most important safety parameter in the Zr-ROX fueled cores, is

---

* Information Technologies Japan Inc.

sufficiently negative in the Th-ROX cores to the comparable level to that of the UO_2 core.

The Th-ROX fueled core also has a larger negative void reactivity in comparison with the Zr-ROX core. The radial, axial and local power peaking factors in the W-Pu Th-ROX fueled core are 1.38, 1.50 and 1.08, respectively, while the factors are 1.32, 1.50 and 1.09 in the R-Pu Th-ROX core. Consequently, the total power peaking factor becomes as low as that of UO_2 core. The delayed neutron fractions (β_{eff}s) of the Th-ROX and Zr-ROX fueled cores are the same each other, and smaller than in the UO_2 core.

Table 9.9.1 Fuel temperature and void reactivities (%Δk/k), power peaking factor and β_{eff} (%) of Th-ROX and Zr-ROX fueled cores in comparison with UO_2 core (BOC)

	weapons-Pu			reactor-Pu		
	Zr-ROX	Zr-ROX -15UO_2	Th-ROX	Zr-ROX -8UO_2	Th-ROX	UO_2
Fuel temp. reac.						
900→1200K	-0.098	-0.61	-0.82	-0.59	-0.87	-0.75
600→900K	-0.132	-0.72	-0.96	-0.72	-1.03	-0.86
Void reac.						
0→40% void	-0.32	-6.0	-3.8	-4.7	-4.3	-8.0
0→95% void	-17.7	-21	-33	-8.3	-19.5	-96.0
Peaking	2.7	2.1	2.2	2.2	2.1	2.0
β_{eff}	0.29	0.28	0.28	0.33	0.33	0.62

The Th-ROX fuel contains larger amount of fertile isotope ^{232}Th than in the Zr-ROX fuel, which produces new fissile isotope and decreases Pu transmutation rate. The Pu transmutation rate in ROX fueled cores are compared with that in the MOX fueled core in Table 9.9.2. In this table, there are shown the input and transmuted amount of Pu per 300 EFPD operation per 1 GW_e reactor power, and the transmuted percentage as a ratio of transmuted/input amount. This table shows a high Pu transmutation capability of the Th-ROX fuel for the W-Pu burning. For the R-Pu transmutation, the Th-ROX fuel has as high Pu transmutation percentage as that in the UO_2 added Zr-ROX fuel. In any case, ROX fueled cores can transmute much more Pu than the MOX core, even though Pu is recycled in the MOX core again. Besides transmuting Pu, Th-ROX produces new fissile ^{233}U. The production rate of ^{233}U in the Th-ROX fuel is about 0.14 t/300EFPD/GW_e, both in the W-Pu and R-Pu burning cases.

The Th-ROX fueled core seems to have preferable physics characteristics both from the viewpoints of reactor safety and Pu transmutation. The reactor safety during accidents should further be confirmed by performing accidents analyses.

Table 9.9.2 Input and transmuted amount (t/GW_e/300EFPD) of plutonium in ROX and MOX fueled cores (1200 EFPD discharge burnup, corresponding to 45GWd/t in MOX core)

		Weapons-Pu			Reactor-Pu		
		Input	Transmuted		Input	Transmuted	
		(t)	(t)	(%)	(t)	(t)	(%)
Th-ROX	Pu-239	0.90	0.87	97	0.82	0.73	89
	total Pu	0.96	0.76	79	1.40	0.85	61
Zr-ROX-UO_2	Pu-239	0.93	0.85	92	0.80	0.70	88
	total Pu	0.99	0.69	69	1.36	0.81	60
MOX (once-through)	Pu-239	0.88	0.56	63	0.99	0.44	45
	total Pu	0.94	0.30	32	1.69	0.41	25
(recycle once)	Pu-239	0.76	0.54	71	0.76	0.44	58
	total Pu	0.81	0.35	43	1.30	0.48	37

ROX results with 2-dimensional core calculations, and MOX results (shaded) with cell calculations.

Reference:

1) Yamashita, T., et al. : "Proc. Int. Conf. Future Nuclear Systems (GLOBAL'99)" (1999) [CD-ROM].

2) Akie, H., Takano, H. and Anoda, Y. : J.Nucl.Mater., 274, 139 (1999).

3) Okumura, K., Kaneko, K. and Tsuchihashi, K. : JAERI-Data/Code 96-015 "SRAC95 ; General Purpose Neutronics Code System" (1996) [in Japanese].

10. Nitride Fuel and Related Pyrochemical Technology

The objective of this study is to develop nitride fuel cycle for transmutation of long-lived minor actinides (MAs) and advanced fast reactors. The activity includes the fabrication and property measurements of nitride fuel, the irradiation test and the molten salt electrorefining in relation to pyrochemical reprocessing. In addition, some basic properties of actinide compounds are investigated in order to contribute to preparation of actinide database. In the fiscal year 1999, several experimental studies have been carried out as summarized below.

The irradiation of two (U,Pu)N and one (U,Pu)C fuel pins at fast test reactor JOYO was completed in September 1999 under joint research with JNC. These fuel pins were irradiated for 5 cycles from 1994 at JOYO. The maximum linear power and burnup were evaluated at 780W/cm and 40,000MWd/t, which agreed with the design study carried out preceding irradiation. On the other hand, the maximum temperature of cladding tube was evaluated at 912K. After cooling the fuel pins for a few months, non-destructive PIEs were started at JNC's hot cells.

Thermochemical measurements and thermodynamic consideration have been given to neptunium bearing nitrides. An equilibrium composition of Np(C,N) coexisting with free carbon was evaluated by both experiments and calculation. The equilibrium composition shifted to nitride rich side with increase of nitrogen partial pressure and decrease of temperature during heating. The results suggested that Np(C,N) could be treated as an ideal solid solution as is the case of Pu(C,N). Measurements of vapor pressure, heat capacity and thermal expansion of nitride fuel are underway.

In a pyrochemical reprocessing of nitride and metal fuels, liquid metal such as Cd or Bi is usually used as a cathode for recovering Pu and MAs. Here the electrode reaction of Pu at liquid Cd and Bi cathodes in LiCl-KCl eutectic melts was investigated in comparison with the solid cathode. The dissolution and deposition behavior was measured electrochemically and the results were analyzed thermodynamically by considering a lowering of activity of Pu due to the formation of intermetallic compounds. On the other hand, recovery of highly concentrated Pu of ~10wt.% was established by use of liquid Cd cathode of ~120g.

Basic properties of actinide oxides were also investigated in this fiscal year. They include high temperature heat capacity of NpO_2 and free energy of formation of gaseous UO_3. The former was carried out by high temperature X-ray diffractometry and theoretical consideration, while the latter by high temperature mass spectrometry over hyper-stoichiometric UO_2 coloaded with MgO functioning as oxygen supplier.

10.1 Completion of (U,Pu)N and (U,Pu)C Fuel Irradiation at Fast Test Reactor JOYO

Research Group for Advanced Fuel
(*E-mail: arai@popsvr.tokai.jaeri.go.jp*)

The irradiation test of He-bonded one $(U_{0.8}Pu_{0.2})C$ fuel pin and two $(U_{0.8}Pu_{0.2})N$ fuel pins at fast test reactor JOYO was started in 1994 under the joint research of JAERI and JNC named "Basic irradiation tests of carbide and nitride fuels for fast reactors". In this program JAERI were mainly in charge of fabrication of fuel pellets and fuel pins, while JNC licensing of irradiation, assembling of irradiation rig and irradiation at JOYO. Design of the fuel pins was carried out by both institutions together.

In Japan there has been no experience on the irradiation of these fuels under fast neutron circumstances. So this program aims at obtaining the fuel behavior up to medium burnup of ~40,000 MWd/t. This burnup almost corresponds to the beginning of fuel-clad mechanical interaction (FCMI). FCMI is one of the important subjects which should be investigated at higher burnup for carbide and nitride fuels.

In order to attain a linear power at ~800 W/cm following the standard design of these fuels[1] having higher thermal conductivity than oxide fuel, U-235 enriched uranium to 19.4 wt.% was used in $(U_{0.8}Pu_{0.2})C$ and $(U_{0.8}Pu_{0.2})N$ fuels. Three fuel pins, one carbide and two nitride pins, were assembled in JOYO B-type special irradiation rig where fuel pins were cooled by primary Na. The difference in two nitride fuel pins is the gap width between the pellets and cladding tube, 0.18 mm and 0.32 mm. This aims at examining the effect of smear density on the fuel behavior such as FCMI. Carbothermic reduction was applied for the synthesis of carbide and nitride and thermally stabilized low-density pellets of 85% T.D. were used in the present case. This density corresponds to 78 and 81% T.D for smear density of the fuel pins. The C/(U+Pu) and N/(U+Pu) atomic ratios in the pellets were chosen at 1.05 and 1.00, respectively. So the nitride fuel pellets had a single phase of mononitride with NaCl-type structure, while sesquicarbide phase were precipitated in addition to monocarbide for the carbide fuel pellets. For cladding tube, austenitic stainless steel of 8.5 mm in outer diameter and 0.45 mm in thickness was used.[2]

Burnup calculation showed that four or five irradiation cycles were needed to attain the burnup mentioned above. However, the irradiation schedule was substantially delayed owing to the operation cycle of JOYO. The irradiation started at 29th cycle (1994.8-1994.9) and it took about 5 years to irradiate for five cycles to 33rd cycle (1999.6-1999.9). Tables 10.1.1-10.1.3 show the typical irradiation condition of three fuel pins at each cycle evaluated. The maximum linear power and burnup were ~780W/cm and 40,000MWd/t, which almost

agree with the result of design study. The maximum temperature of cladding tube during the irradiation was evaluated at 912 K.

After cooling for a few months, non-destructive post irradiation examinations (PIEs) of the fuel pins were started at the end of 1999 in a JNC's hot cell. Any failure of the fuel pins was not observed. Destructive PIEs will begin in the latter half of 2000 in the hot cells of both JAERI and JNC. Basic irradiation behavior of carbide and nitride fuels will be obtained through the PIEs. For evaluating the feasibility of the advanced fuels for fast reactors, however, the irradiation test aiming at higher burnup, 100,000 or 150,000 MWd/t at least, is essential. In this point, the second irradiation test at JOYO should be carried out, in which the emphasis will be placed on nitride fuel.

References:

1) Blank, H.:"Materials Science and Technology", Vol. 10A, Nuclear Materials, Part I, Edited by B. R. T. Frost, VCH, Weinfeim (1994) pp. 191-363.
2) Arai, Y., Iwai, T., Sasayama, T., Okamoto, Y., Shiozawa, K. and Suzuki, Y.: JAERI-Research 96-009, "Fabrication of Uranium-Plutonium Mixed Carbide and Nitride Fuel Pins for the Irradiation Test in JOYO" (1996).

Table 10.1.1 Typical irradiation condition of (U,Pu)C fuel pin at the 29th-33rd cycle of JOYO

Cycle No.		29	30	31	32	33
Total days of irradiation (EFPD)		~24	~60	~55	~69	~68
Max. linear power (W/cm)	BOC	734	713	690	687	680
	EOC	727	698	677	670	664
Max. burnup (MWd/t)		3,743	12,680	20,610	30,450	40,090
Max. neutron fluence (n/cm^2)	total	6.71E+21	2.28E+22	3.74E+22	5.60E+22	7.46E+22
	fast	4.59E+21	1.57E+22	2.57E+22	3.85E+22	5.13E+22
Max. temperature of cladding tube (K)	BOC	638	624	619	624	632
	EOC	636	620	616	619	627

Table 10.1.2 Typical irradiation condition of (U,Pu)N fuel pin (gap width; 0.32mm) at the 29th-33rd cycle of JOYO

Cycle No.		29	30	31	32	33
Total days of irradiation (EFPD)		~24	~60	~55	~69	~68
Max. linear power (W/cm)	BOC	742	720	699	695	686
	EOC	735	705	686	678	670
Max. burnup (MWd/t)		3,682	12,480	20,300	30,000	39,460
Max. neutron fluence (n/cm^2)	total	6.89E+21	2.34E+22	3.85E+22	5.76E+22	7.66E+22
	fast	4.71E+21	1.61E+22	2.64E+22	3.96E+22	5.27E+22
Max. temperature of cladding tube (K)	BOC	639	624	620	624	632
	EOC	637	620	616	619	628

Table 10.1.3 Typical irradiation condition of (U,Pu)N fuel pin (gap width; 0.18mm) at the 29th-33rd cycle of JOYO

Cycle No.		29	30	31	32	33
Total days of irradiation (EFPD)		~24	~60	~55	~69	~68
Max. linear power (W/cm)	BOC	781	758	732	730	722
	EOC	773	742	719	713	705
Max. burnup (MWd/t)		3,679	12,460	20,240	29,920	39,380
Max. neutron fluence (n/cm^2)	total	6.88E+21	2.34E+22	3.84E+22	5.74E+22	7.65E+22
	fast	4.71E+21	1.61E+22	2.63E+22	3.95E+22	5.26E+22
Max. temperature of cladding tube (K)	BOC	639	625	620	624	633
	EOC	637	621	616	620	628

10.2 A Thermodynamic Consideration on Np(C,N) solid solution

Y. Arai and K. Nakajima
(*E-mail: arai@popsvr.tokai.jaeri.go.jp*)

Nitride fuel containing minor actinides (MA) such as Np and Am is a candidate fuel for accelerator driven system for MA transmutation.[1] In carbothermic reduction for preparing nitride fuel, an excess amount of carbon is usually added to oxide in order to lower oxygen impurities in the products. Then residual carbon existing as free carbon and/or carbonitride is removed in the final stage by heating in N_2-H_2 mixed gas stream. In this study, a thermodynamic consideration of neptunium carbonitride, Np(C,N), which is an intermediate product of carbothermic reduction, is given in order to investigate the reasonable condition for preparing high-purity NpN.

Starting materials are neptunium dioxide, $^{237}NpO_2$ and reactor-grade graphite powders. Two-phase specimen of neptunium carbonitride and free carbon, <Np(C,N)> + <C>, were prepared by heating the mixed powder of NpO_2 and graphite with a molar C/NpO_2 ratio of 2.8 in N_2 stream at 1773 K for 36 ks. Phases in the product were identified by X-ray diffraction analysis to be <Np(C,N)> + <C>.

Then the two-phase specimen was compacted again to disks for the heat-treatments at different temperatures and nitrogen partial pressures. The heat-treatments were carried out at 1723, 1823 and 1923 K in N_2, N_2/Ar=1/1 and N_2/Ar=1/99 gas streams and repeated until the significant change in lattice parameter was not observed before and after heating. The composition of Np(C,N) solid solution was calculated from the lattice parameter assuming the Vegard's law between 'NpC' and 'NpN'. In addition, the preceding tests were carried out by use of U(C,N) and Pu(C,N) solid solutions in order to check the reasonableness of the present experimental manner. A few thermodynamic characteristics of U(C,N) and Pu(C,N) solid solutions were reported previousy.[2,3]

The results of X-ray diffraction analysis after the heat-treatments to equilibrium showed that the products still had the two phases of <Np(C,N)> + <C> except one specimen. Free carbon phase disappeared and the third phase likely appeared in the specimen subjected to the heat-treatment at 1923 K under N_2/Ar=1/99 stream. So this result was excluded in the analysis described below.

The equilibrium compositions of the specimen after the heat-treatments determined from the lattice parameter were shown in Fig. 10.2.1 as the respective symbols. It is found that the composition of the Np(C,N) shifts to nitride rich side with decreasing temperature and increasing nitrogen partial pressure during the heat-treatments.

On the other hand, the equilibrium composition of Np(C,N) coexisted with free carbon was evaluated by thermodynamic calculation as a following manner. In the concerning two-phase region, the equilibrium equation can be written as

$$[NpN]_{NpC} + <C> = [NpC]_{NpN} + 0.5(N_2) \quad (1),$$

where $[NpN]_{NpC}$ and $[NpC]_{NpN}$ indicate one mole of NpN and NpC dissolved in Np(C,N) solid solution, while free carbon and nitrogen gas are indicated by <C> and (N_2). In case of ideal solid solution, the partial molar free energies of NpN and NpC dissolved in $Np(C_{1-X}N_X)$ can be written as

$$\Delta G[NpN] = \Delta G_f^\circ<NpN> + RT\bullet\ln X \quad (2)$$

$$\Delta G[NpC] = \Delta G_f^\circ<NpC> + RT\bullet\ln (1-X) \quad (3),$$

where $\Delta G_f^\circ<NpN>$ and $\Delta G_f^\circ<NpC>$ represent Gibbs free energies of formation of NpN and NpC. Accordingly, the following equation is hold in the equilibrium state,

$$\Delta G_f^\circ<NpC> + RT\bullet\ln (1-X) + 0.5\bullet\ln p(N_2) - \Delta G_f^\circ<NpN> - RT\bullet\ln X = 0 \quad (4),$$

where T and $p(N_2)$ indicate absolute temperature and nitrogen partial pressure. In calculation of equilibrium composition, Gibbs free energy of formation for NpN was cited from the value obtained by a recent vaporization experiment[4] and that for NpC was cited from the table recommended by IAEA.[5]

Accordingly, we can calculate the relationship between absolute temperature T, nitrogen partial pressure $p(N_2)$ and the composition represented by X. The solid lines in Fig. 10.2.1 show a temperature dependence of the composition of $Np(C_{1-X}N_X)$ coexisted with free carbon calculated at 1.01×10^5, 5.07×10^4 and 1.01×10^3 Pa of $p(N_2)$. The figure shows that the results of experiments (symbols) and thermodynamic calculation (solid lines) agree with each other within the experimental error in the present case. This agreement suggests that Np(C,N) solid solution could be treated as ideal solution as is the case of Pu(C,N).

When the identical condition of carbothermic reduction was applied to preparation of UN, NpN and PuN, we have observed the different carbon impurity contents remained in the products; the contents determined by chemical analysis decreased in order of UN, NpN and PuN.[6] On the other hand, the equilibrium compositions of U(C,N), Np(C,N) and Pu(C,N) coexisted with free carbon were obtained from the present experiments; they are $U(C_{0.14}N_{0.86})$, $Np(C_{0.05}N_{0.95})$ and $Pu(C_{0.01}N_{0.99})$ at 1823 K under 1.05×10^5 Pa of $P(N_2)$. Obviously, the soluble amount of carbide in mononitride decreases in order of UN, NpN and PuN. This tendency was caused by thermodynamic instability of monocarbide in higher actinides.

We assumed that the difference in carbon contents observed in UN, NpN and PuN prepared by the identical condition is related with the equilibrium composition of monocarbonitride in nitrogen atmosphere. The results of kinetic study[7] showing that the removal of excess carbon in solid solution is a rate-determined process encourages us to

support the presumption mentioned above. In this case an increase in carbon to dioxide mixing ratio will not lead to increase carbon impurity contents in mononitride of higher actinides since excess carbon existing as free carbon is likely to be removed with relative ease.

References:

1) Takizuka, T. et al.: "Studies on Accelerator –Driven Transmutation Systems", Proc. 5th OECD/NEA Information Exchange Mtg. on Actinide and Fission Product Partitioning and Transmutation, Nov. 25-27, 1998, Mol (1998) pp.383-392.
2) Katsura, M. and Sano, T.: J. Nucl. Sci. Technol., 3, 194 (1966).
3) Potter, P. E.: UK Report, AERE-M-2156 (1969).
4) Nakajima, K., Arai, Y. and Suzuki, Y.:J. Nucl. Mater., 247, 33 (1997).
5) Holley, C.E., Jr., Rand, M. H. and Storms, E. K.: "The Chemical Thermodynamics of Actinide Elements and Compounds, Part 6 The Actinide Carbides", IAEA, Vienna (1984) pp.49-52.
6) Suzuki, Y., Arai, Y., Okamoto, Y. and Ohmichi, T.: J. Nucl. Sci. Technol.: 31, 677 (1994) .
7) Muromura, T. and Tagawa: H., J. Nucl. Mater., 80, 330 (1979).

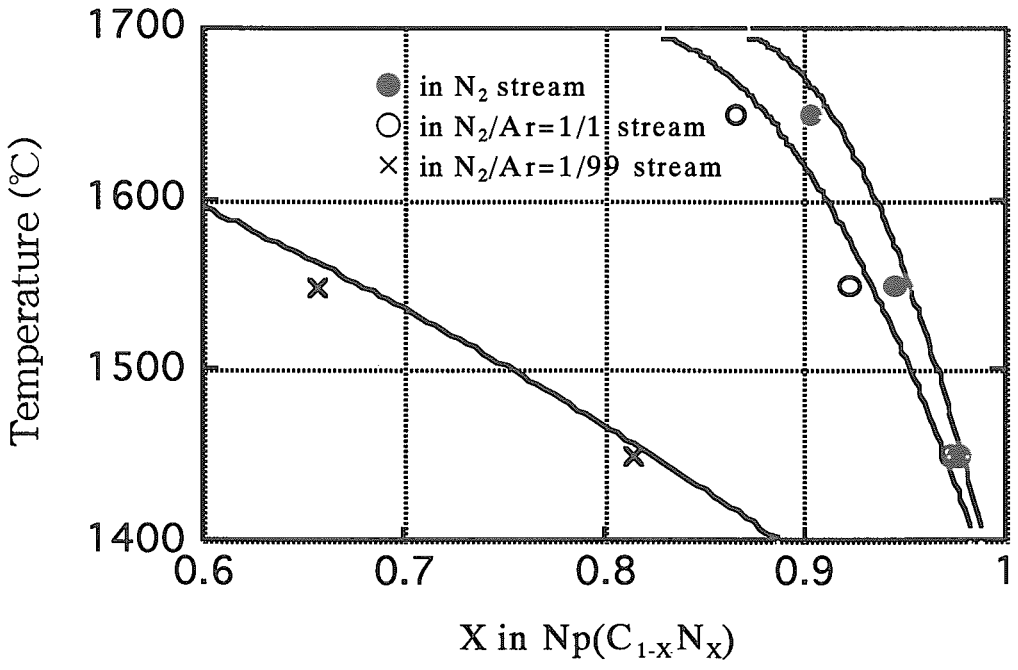

Fig. 10.2.1 Temperature dependence of equilibrium composition of $Np(C_{1-x}N_x)$ solid solution under N_2, N_2/Ar=1/1 and N_2/Ar=1/99 streams. Experimental results are compared with thermodynamic calculation applying an ideal solution model.

10.3 Specific Heat of NpO_2

H. Serizawa, Y. Arai and K. Nakajima
(*E-mail*: serizawa@popsvr.tokai.jaeri.go.jp)

The specific heat of NpO_2, C_p, was estimated for temperatures between 300 K and 1400 K. C_p was evaluated as a sum of three terms, phonon vibration, C_{ph}, dilation, C_d, and Schottky specific heat, C_s. C_{ph} and C_d were calculated using the Debye temperature, Grüneisen constant and thermal expansion data obtained by high-temperature X-ray diffractometry. The coefficient of the linear thermal expansion (LTE) for NpO_2 was given as a polynomial function up to 1573 K. The estimated C_p was compared with that of previous works. The present result at 300 K was 66.87 $JK^{-1}mol^{-1}$, which agreed well with previous data, 66.22 $JK^{-1}mol^{-1}$, measured by using calorimetry. The thermodynamic functions were given as a function of temperature.

Thermal expansion of NpO_2

Sample powder for the measurement was provided by AEA Technology, UK. The purity was more than 99.9%. The main impurities detected by ICP analysis were Ca (220 ppm) and Na (460 ppm). Prior to the measurement, the specimen was heated at 1273 K for 5 hr in Ar stream. The X-ray diffraction data were obtained using a theta-theta goniometer (Ultima, RIGAKU) with a furnace attachment unit. A Na(Tl) scintillation counter was used to detect CuKα radiation. CuKβ radiation was eliminated by Ni foil wound around the furnace attachment. The measurement was carried out at temperatures between 298 to 1573 K. The lattice parameter obtained at room temperature was (543.30 ± 0.0045) pm. The parameter obtained in this work were well fitted as a function of temperature by the equation,

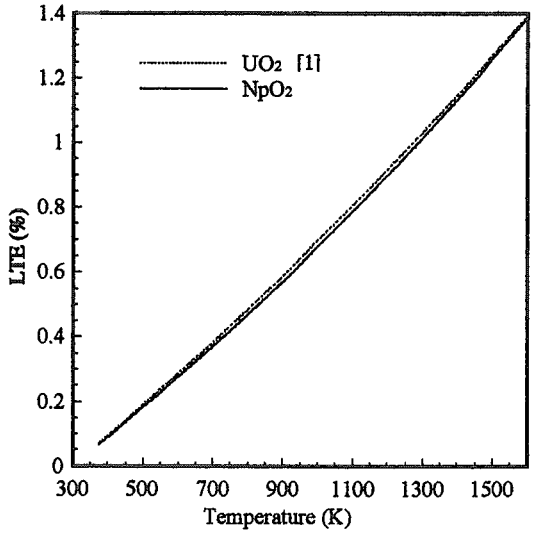

Fig. 10.3.1 Comparison of linear thermal expansion for NpO_2 and UO_2

$$a_T = 542.3 + 3.832 \times 10^{-1} T + 9.814 \times 10^{-5} T^2 - 4.209 \times 10^{3} T^{-1} \quad (298<T<1573) \quad (1)$$

where a_T is the lattice parameter at T K.

LTE for NpO_2 given by $(a_T - a_{298}) \times 100/a_{298}$ is shown in Fig. 10.3.1 with that for UO_2 calculated with the data set by Taylor [1]. As can be seen in the figure, the value of LTE for

NpO_2 was lower than that for UO_2. The corresponding coefficient of LTE (noted as α), defined as $(1/a_T)(\partial a_T/\partial T)_p$, can be readily evaluated from Eq. (1). A polynomial expression of α for NpO_2 obtained in the present study is

$$\alpha = \frac{1.96\times10^{-4}T^3 + 0.383T^2 + 4.21\times10^3}{9.81\times10^{-5}T^4 + 0.383T^3 + 542.3T^2 - 4.21\times10^3T} \qquad (298<T<1573). \qquad (2)$$

Estimation of C_p

The specific heat, C_p, can be written as a sum of several contribution terms. Previous workers showed that C_p for UO_2 from room temperature to *ca.* 1500 K can be explained satisfactorily by three or four terms. Grønvold et al. [2] attempted to quantify the specific heat in terms of separable contributions from distinct physical mechanisms. They represented C_p essentially as the following summation:

$$C_p = C_{ph} + C_d + C_m' \qquad (3)$$

where C_{ph} and C_d are the contributions of phonon and dilation, respectively. C_m' is any contribution in excess of the previous two terms. They found that they could account for the last term with the effect of the crystal magnetic field upon the U^{4+} energy level, the so-called Schottky specific heat (termed C_s). Recently, Serizawa and Arai applied this method to PuO_2 and obtained a satisfactory result [3]. The maximum error in the estimation was 8.6 % between room temperature and 1400 K. In the lower temperature range up to 900 K, the maximum error was as low as 5%.

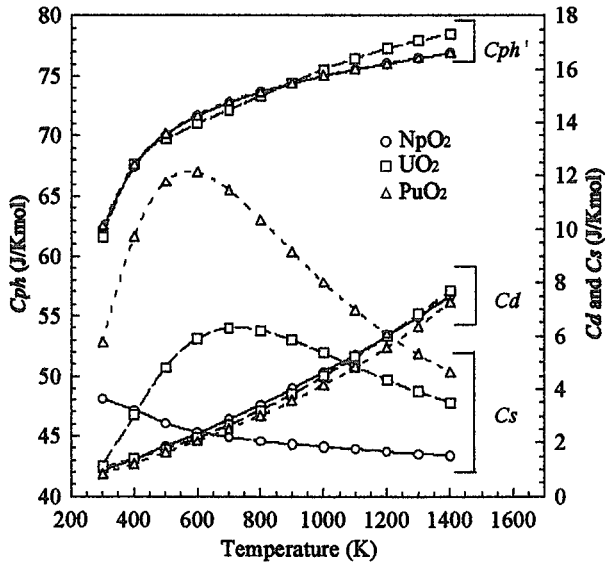

Fig. 10.3.2 Contribution terms for NpO_2, PuO_2 and UO_2

Calculated contribution terms for NpO_2 are summarized in Fig. 10.3.2. Those for UO_2 and PuO_2 are also given in the figure for comparison. C_{ph} and C_d for UO_2 and PuO_2 were calculated using the reported value of Θ_D and γ [2-4]; C_s for the oxides were evaluated with the energy level data of Krupa and Gajek [5]. Although the calculated curves of C_{ph} and C_d for NpO_2 were analogous to those for PuO_2, the temperature dependence of C_s for NpO_2 is quite different. C_s for UO_2 and PuO_2 has a maximum in the low temperature region, whereas that for NpO_2 decreases monotonously with elevating temperature. The figure indicates that the difference in C_p between NpO_2 and PuO_2 is mainly due to the Schottky specific heat that derives from the excitation of 5f-electrons.

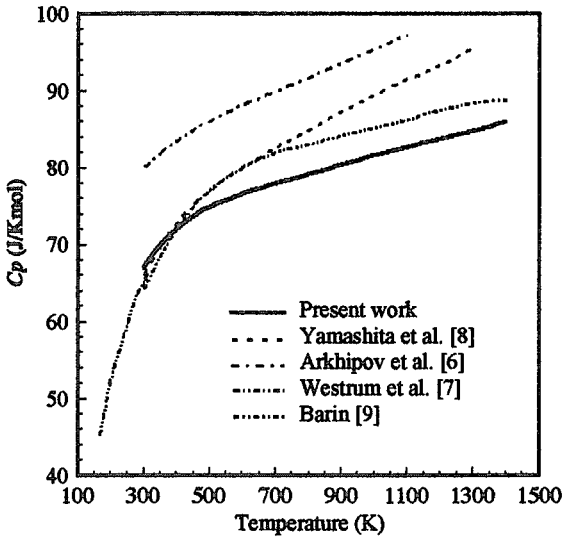

Fig. 10.3.3 Comparison of the specific heat data for NpO_2

The sum of these contribution terms for NpO_2 is given in Fig. 10.3.3 with some previous data. The value of C_p obtained in the present work increased steeply with elevating temperature up to about 900 K. At present, there are two experimental data [6,7] and two estimated ones [8,9]. As can be seen in the figure, the present data is lower than the experimental data by Arkhipov et al. [6]. Our data at 300 K is 66.86 $JK^{-1}mol^{-1}$, which is in good agreement with that by Westrum et al., 66.22 $JK^{-1}mol^{-1}$ [7]. Comparing with other estimated data, our data is lower than those of the other two workers. However, the temperature dependence of the present data is similar to that estimated by Barin [9].

References:

1) Taylor, D.: Br. Ceram. Trans. J., 83, 32 (1984).

2) Grønvold, F., Kveseth, N. J., Sveen, A. and Tichy, J.: J. Chem. Thermodynamics, 2, 665 (1970).

3) Serizawa, H. and Arai, T.: to be published in J. Alloys Comp..

4) Serizawa, H., Arai, Y., Takano, M. and Suzuki, Y.: J. Alloys Comp., 282, 17 (1999).

5) Krupa, J. C. and Gajek, Z.: Eur. J. Solid State Inorg. Chem. t., 28, 143 (1991).

6) Arkhipov, V. A., Gutina, É. A., Dobretsov, V. N. and Ustinov, V. A.: Radiokhimiya, 16, 122 (1974).

7) Westrum, Jr., Edgar F., Hatcher, J. B. and Osborne, D. W.: J. Chem. Phys, 21, 419 (1953).

8) Yamashita, T., Nitani, N., Tsuji, T. and Kato, T.: J. Nucl. Mater., 247, 90 (1997).

9) Barin, I.: "Thermochemical Data of Pure Substances", VCH: Weinheim, (1995).

10.4 Plutonium Recovery Experiments into Liquid Cadmium Cathodes

K. Uozumi*, M. Iizuka**, O. Shirai and T. Iwai
(*E-mail:* uozumi@criepi.denken.or.jp)

In the pyrometallurgical reprocessing of spent fuel, U and transuranic elements such as Np, Pu, and Am are recovered into a liquid cadmium cathode (LCC) by electrolysis, using molten LiCl-KCl eutectic salt as an electrolyte. Apparatus that can use up to 100 g of Pu has been fabricated, and a number of Pu recovery experiments were conducted.

Fig. 10.4.1 shows the newly fabricated apparatus. 1200 g of the molten eutectic salt containing 2.1 wt% of Pu is contained in a 124 mm inner diameter iron vessel. 1400 g of Cd containing dissolved Pu is placed at the bottom of the vessel and used as an anode for the electrolysis. Experiments were carried out in a high purity argon glove box. The experimental apparatus was lowered into an electric furnace that was placed in the glove box. The cell temperature was kept at 773K during the experiments.

At first, constant current electrolysis was conducted using 3 to 5 g of liquid Cd contained in small alumina crucibles (9 mm inner diameter) as cathodes. These crucibles were immersed in the salt phase. Tungsten wires sheathed by alumina tubes were connected to the LCCs and used as electrical contacts to the cathodes. A tungsten rod connected to the Cd at the bottom of the vessel was used as an anode contact. No agitation was conducted in the cathodes or the iron vessel. The current densities at the surface of the LCCs ranged between 33 and 66 mA/cm^2. The LCC potentials versus an Ag/AgCl reference electrode in the salt phase during the electrolysis are shown in Fig. 10.4.2. In order to avoid the deposition of Li, which exists as a component of the salt phase, the LCC potential should be kept above –1.6 V versus the reference electrode. With this potential limitation, 41 mA/cm^2 seemed to be the maximum cathode current density for recovering Pu in the small LCCs. With a current density of 50 mA/cm^2, the salt phase in the alumina crucible was white after the electrolysis, contrary to the cases of current densities 33 and 41 mA/cm^2, in which the salt in the crucibles was purple. The change of the salt's color to white means that Pu^{3+} in the salt was reduced by the Li that was recovered in the cathode due to the low potential of the LCC.

---

*A guest researcher from the Central Research Institute of Electric Power Industry, October, 1999～2001

**A guest researcher from the Central Research Institute of Electric Power Industry, 1998～November, 1999

Next, a Pu recovery experiment using a 120 g LCC was carried out. The cathode used in this experiment is shown schematically in Fig. 10.4.3. In this experiment, the cathode Cd was contained in an aluminum nitride (AlN) crucible, which was fabricated by Ceracom. The AlN crucible contains 0.15 wt% yttrium and less than 100 ppm of other metallic impurities. In order to remove the Cd-Pu ingot after the Pu recovery easily and use the crucible again, the inside wall of the crucible had a taper of 4 degrees. An AlN stirrer was used for mixing around the boundary of the salt and the cathode Cd. The stirrer was attached to an iron shaft. This iron shaft worked both as the cathode contact and the rotating drive of the stirrer. In order to avoid Pu deposition on the iron shaft, an AlN tube was placed on the stirrer as an electrical sheath. The diameter of the LCC was 41 mm at the surface.

At the beginning of this experiment, the LCC potential as a function of the cathode current density was measured. The result of this measurement is shown in Fig. 10.4.4. In this system, using 120 g of LCC, 23.4 mA/cm^2 was the maximum current density and the value was about 60 % of the maximum current density in the case of the small LCCs. This current density decline is considered to be due to the ratio of the volume of the salt phase versus the surface section of the cathode, which was reduced in the 120 g LCC experiment.

After these potential measurements, Pu was recovered in the cathode at a stirring rate of 40 rpm. The LCC potential versus the reference electrode during the deposition is shown in Fig. 10.4.5. During electrolysis, the LCC potential gradually became more negative and the cathode current density was reduced from 23.4 mA/cm^2 to 15.6 mA/cm^2.

After the electrolysis, the AlN crucible was pulled up from the salt phase and cooled. A Cd ingot containing Pu was recovered from the AlN crucible without breaking the crucible. No change of color was found on the surface of the AlN materials. From the weight change of the Cd cathode, the amount of Pu recovered into the cathode was calculated to be 14.6 g. This value corresponded to a Pu concentration in the Cd cathode of 10.8 wt% and a recovery efficiency versus the total coulometric amount during the electrolysis of 95 %. Our temporary target of 10 wt% Pu concentration in the LCC was achieved in this experiment.

A microscopic observation of the cathode Cd showed that a thick layer of $PuCd_6$ existed at the bottom of the Cd as is shown in Fig. 10.4.6. This indicates that the recovered Pu accumulates at the bottom of the LCC in the form of $PuCd_6$ during the deposition.

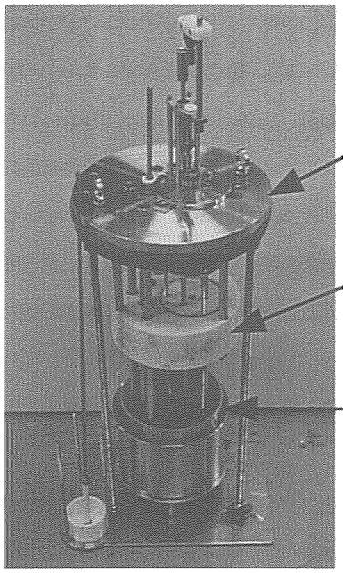

Fig. 10.4.1 The Apparatus for the Pu Recovery Experiments

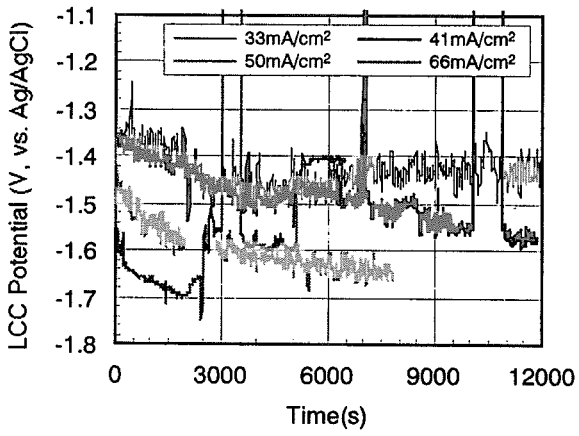

Fig. 10.4.2 LCC Potential-TimeCurves (Small LCC Experiments)

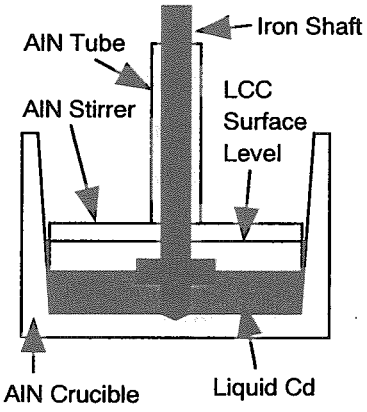

Fig. 10.4.3 A Cross Section of the 120g-LCC

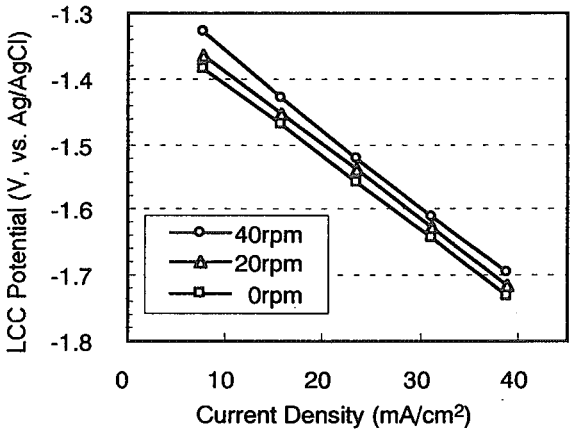

Fig. 10.4.4 LCC Potential-Current Density Curves (120g-LCC Experiment)

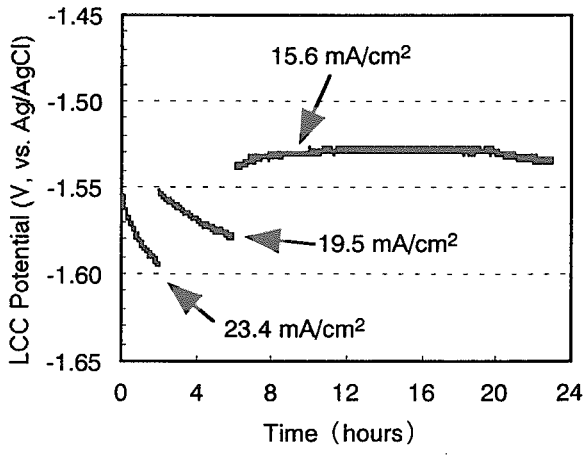

Fig. 10.4.5 LCC Potential-Time Curve (120g-LCC Experiment)

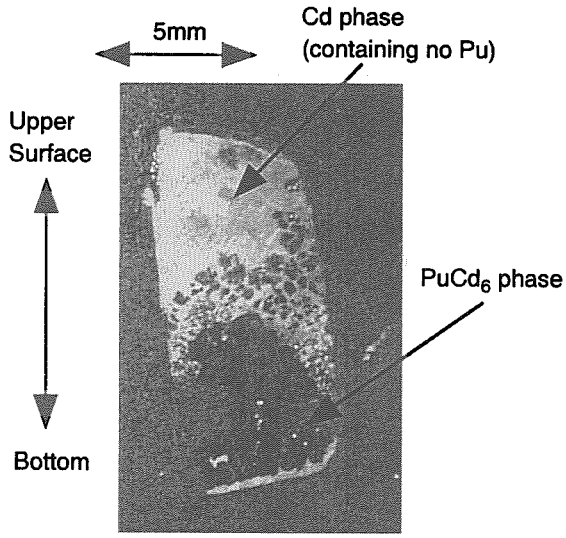

Fig. 10.4.6 A Section of the 120g-LCC Ingot

10.5 Electrode Reaction of Pu at Liquid Metal Cathode in LiCl-KCl Eutectic Melts

O. Shirai, K. Uozumi*, T. Iwai and Y. Arai
(*E-mail*: shirai@popsvr.tokai.jaeri.go.jp)

Pyrochemical reprocessing of nuclear fuels using molten salt as a solvent is expected to be very suitable for advanced nuclear engineering because of its compactness, economy, radiation resistance and nonproliferation[1]. In the electrorefining process of pyrochemical reprocessing, it has been proposed that U can be selectively recovered at the solid cathode due to the difference in the formation energies of the chlorides, and Pu and MAs at the liquid metal cathode as a mixture of U, Pu and MAs due to their small activity coefficients in liquid metals such as Cd, Bi, and so on[2].

The electrode reaction of the Pu^{3+}/Pu couple at the surface of a liquid Cd electrode was investigated by cyclic voltammetry at 723, 773 and 823 K in LiCl-KCl eutectic melt by comparison with that at the Mo electrode[3]. Cyclic voltammograms for the redox reaction of the Pu^{3+}/Pu couple are shown in Fig. 10.5.1. Curves 1 and 2 in the figure show the voltammogram for the redox reaction of the Pu^{3+}/Pu couple at the interface between the LiCl-KCl eutectic melt containing 0.87 wt. % $PuCl_3$ and the liquid Cd and that at the interface between the LiCl-KCl melt in the absence of $PuCl_3$ and the liquid Cd, respectively, at 723 K. Curve 3 in Fig.10.5.1 shows the cyclic voltammogram in the case of the Mo electrode in the $PuCl_3$-LiCl- KCl system. By the measurement of electromotive force, the standard potential of the Pu^{3+}/Pu couple vs. the Ag/AgCl electrode, $E_{Pu^{3+}/Pu}{}^0$, was obtained as denoted in eqn. (1).

$$E_{Pu^{3+}/Pu}{}^0 = -2.232 + 0.00094\,T \text{ (V vs. Ag/AgCl)} \quad (1)$$

The redox potentials of the Pu^{3+}/Pu couple at the liquid Cd electrode at 723, 773 and 823 K were observed at more positive potential by 0.299, 0.269 and 0.239 V, respectively, than those at the Mo electrode. It was supposed that this potential difference between the redox potential of the Pu^{3+}/Pu couple at the liquid Cd electrode and that at the Mo electrode was attributed to a lowering of activity of Pu in the Cd phase. Because the activities of Pu in Cd phase depend on the dissolved condition and concentration of Pu, the potential difference can be explained by assuming the formation of $PuCd_6$. Therefore, the potential shift would be transformed to the free energy of formation of $PuCd_6$, ΔG_{PuCd_6}, as eqn.(2).

---

*Central Research Institute of Electric Power Industry

$$\Delta G_{PuCd_6} = -91350 + 76.4\,T\ (\mathrm{J\ mol^{-1}}). \quad (2)$$

On the other hand, the free energies of formation of the other intermetallic compounds $PuCd_2$ and $PuCd_4$, ΔG_{PuCd_2} and ΔG_{PuCd_4}, could also be estimated by the analysis of the anodic peaks in cyclic voltammograms of the Pu^{3+}/Pu couple at a Cd-coated Mo electrode.

In analogy with the case of the liquid Cd electrode, the electrode reaction of the Pu^{3+}/Pu couple at the liquid Bi electrode can be analyzed. The redox potentials of the Pu^{3+}/Pu couple at the liquid Bi electrode in the $PuCl_3$-LiCl-KCl melt at 723, 773 and 823 K were observed to be more positive by 0.575, 0.572 and 0.566 V, respectively, than those at the Mo electrode. Since the potential shift would be caused by formation of $PuBi_2$, the free energy of formation of $PuBi_2$, ΔG_{PuBi_2}, was estimated as eqn. (3).

$$\Delta G_{PuBi_2}{}^{0} = -216400 + 64.48\,T \quad (\mathrm{J\ mol^{-1}}) \quad (3)$$

Reference:

1) Chang, Y. I.: Nucl. Technol., 88, 129 (1989).
2) Iizuka, M., Koyama, T., Kondo, N., Fujita, R. and Tanaka, H.: J. Nucl. Mater., 247, 141 (1997).
3) Shirai, O., Iizuka, M., Iwai, T., Suzuki, Y. and Arai, Y.: to be published in J. Electroanal. Chem.

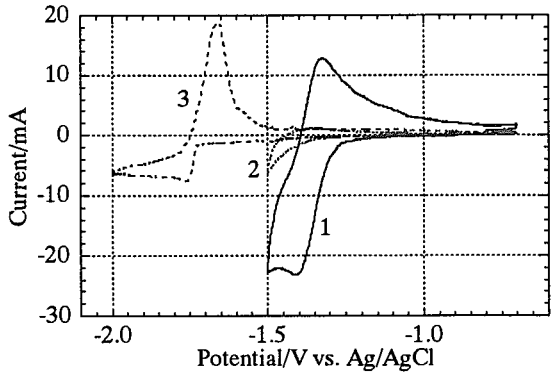

Fig. 10.5.1. Cyclic voltammograms for the Pu^{3+}/Pu couple in LiCl-KCl eutectic melt at 723 K.

10.6 Mass-spectrometric investigation of UO_3(g)

K. Nakajima and Y. Arai
(E-mail: kuni@popsvr.tokai.jaeri.go.jp)

In spite of the importance of evaluating behavior of volatile species in case of core disruptive accident, there is a discrepancy of the partial pressure over hyper-stoichiometric uranium dioxide, UO_{2+x}(s), among the literatures[1]. The reason is possibly due to inaccuracy of Gibbs free energy of formation of UO3(g), ΔGf(UO3,g). The purpose of this study is to determine the partial pressure of UO3(g) over UO_{2+x}(s) and evaluate ΔGf(UO3,g) by means of mass-spectrometry. Several mass-spectrometric studies have been conducted in the past to obtain these quantities[2]. Satisfactory results, however, have not been obtained because of the difficulties of maintaining the condensed phase sufficiently oxidized during the measurement *in vacuo* as well as the uncertainty of the ionization cross sections in mass-spectrometric measurement[3]. In this study the mass-spectrometric measurement of uranium dioxide, UO_2(s), coloaded with magnesium monoxide, MgO(s), which could function as an oxygen supplier, was carried out to overcome the former problem. For the latter problem a modified integral method was used, which does not require the ionization cross section in determining the partial pressure of vapor species from the ion current[4].

Mass-spectrometric measurement of UO_{2+x}(s) coloaded with MgO(s) was carried out in the temperature range from 1723 to 1923 K. On this experiment condition there is a possibility that magnesium dissolves into UO_2(s) because of the existence of magnesium in gaseous phase[5]. Moreover, the O/U ratio of UO_{2+x}(s) will change at each temperature under the ambient oxygen pressure in equilibrium with MgO(s). In such cases the ion currents of the species vaporized from the sample should change with time. So the time dependence of the ion currents of UO_3^+ and Mg^+ was investigated. At first the ion currents of UO_3^+ on heating stage gradually increase with time and those of Mg^+ decrease. Further, these ion currents become constant. On the other hand, these ion currents on cooling stage change in the opposite manner and come to an almost same value with those on heating stage. Therefore, it is considered that the time dependence of the ion currents of UO_3^+ and Mg^+ is resulted from the shift of O/U ratio of UO_{2+x}(s) in response to change in the ambient oxygen pressure equillibrated with MgO(s). Further, the agreement of the ion currents between on heating stage and on cooling stage suggests that the significant solution of magnesium into uranium dioxide is not likely to occur during the measurement. X-ray diffraction patterns of UO_2(s) and MgO(s) after the measurement also suggested that the significant solution of magnesium did not occur during the measurement[5].

The determined partial pressures of UO3(g), Mg(g) and O_2(g) are plotted in Fig. 10.6.1 in the temperature range of 1723-1923 K. This figure also includes the O/U ratio of UO_{2+x}(s) in

equilibrium with the oxygen pressure obtained in this study, which was calculated based on Blackburn's model[6].

For the following equilibrium reaction:

$$UO_2(s) \text{ in } UO_{2+x}(s) + 1/2O_2(g) = UO_3(g). \quad (1)$$

$\Delta_f G(UO_3,g)$ can be calculated by the following equation:

$$\Delta_f G(UO_3,g) = -RT\ln\left[\frac{P(UO_3)}{P(O_2)^{1/2} a(UO_2)}\right] + \Delta_f G(UO_2,s). \quad (2)$$

where $a(UO_2)$ is the activity of $UO_2(s)$ in $UO_{2+x}(s)$. The activity was obtained from the relationship between the partial pressure of $O_2(g)$ and the O/U ratio based on Blackburn's model by the Gibbs-Duhem equation. $\Delta_f G(UO_3,g)$ determined from eq.(2) using $\Delta_f G(UO_2,s)$ given by Cordfunke and Koning's table[7] is plotted in Fig. 10.6.2 as a function of of temperature. The least-squares treatment of the data gives the following equation:

$$\Delta_f G(T)(UO_3,g)(J/mol) = -841000 + 94.6T \text{ (1723-1923 K)}. \quad (3)$$

As shown in this figure, $\Delta_f G(UO_3,g)$ obtained in this study is a little higher than the recommended value given by Olander[1]. Most Gibbs free energies of formation of $UO_3(g)$ reported in the past have been obtained from the transpiration experiment of $U_3O_8(s)$[1,8,9]. However, the traspiration technique at higher temperature has a difficulty of establishment of the equilibrium condition due to temperature gradient in the sample region. Furthermore, the thermodynamic data of $U_3O_8(s)$ at higher temperature is not well established compared to that of $UO_2(s)$. In addition, the free energy function of $UO_3(g)$ is unreliable on account of uncertainty of contribution of the electronic partition function[7]. Therefore, it is considered that the data of $\Delta_f G(UO_3,g)$ obtained directly from the vapor pressures of $UO_3(g)$ and $O_2(g)$ over $UO_{2+x}(s)$ at high temperatures are more reliable.

References:

1) Olander, D.R. : J. Nucl. Mater. 270, 187 (1999).

2) Pattoret, A., Drowart, J., Smenove, S. : "Thermodynamics of Nuclear Materials", IAEA, Vienna, 613(1968).

3) Stolyarova, V.L., Semenove, G.A. : "Mass spectrometric Study of the Vaporization of Oxide Systems", Wiley, Chichester, 23(1994).

4) Asano, M. et al. : Bull. Chem. Soc. Jpn., 45, 82 (1972).

5) Fujino, T. et al. : J. Nucl. Mater. 246, 150 (1997).

6) Blackburn, P.E. : J. Nucl. Mater. 46, 244(1973).

7) Cordfunke, E.H.P., Koning, R.J.M. (Eds.) : "Thermodynamical Data for Materials and Fission

Products", North-Hplland, 669(1990).
8) Ackermann, R.J. et al. : J. Phys. Chem. 64, 350(1960).
9) Alexander, C.A. : Ph.D. Thesis, Ohio State University(1961).

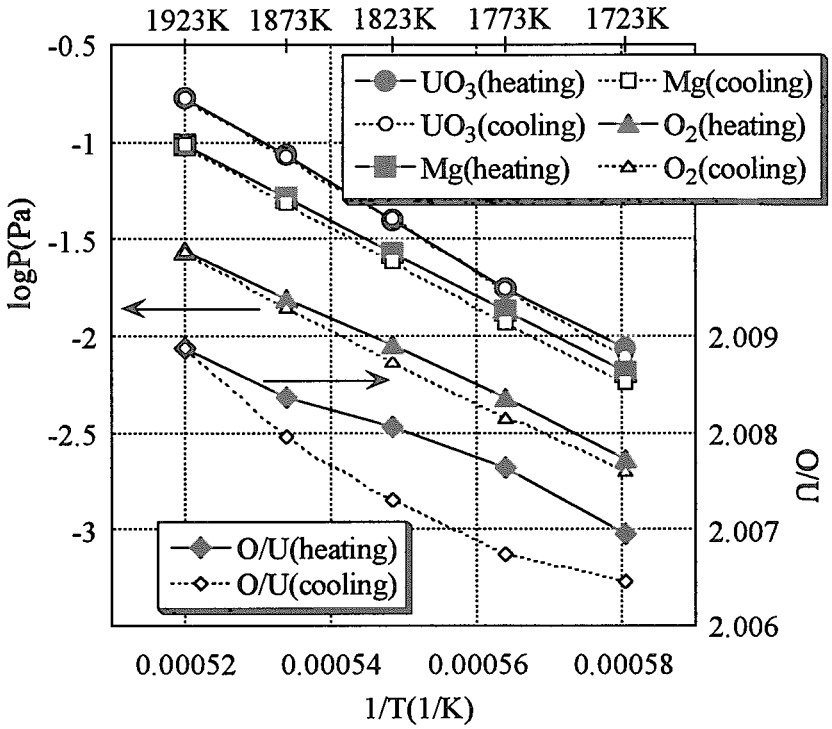

Fig.10.6.1 Vapor pressures over UO_{2+x}(s) coloaded with MgO(s) and the O/U ratio of UO_{2+x}(s) based on Blackburn's model[6]

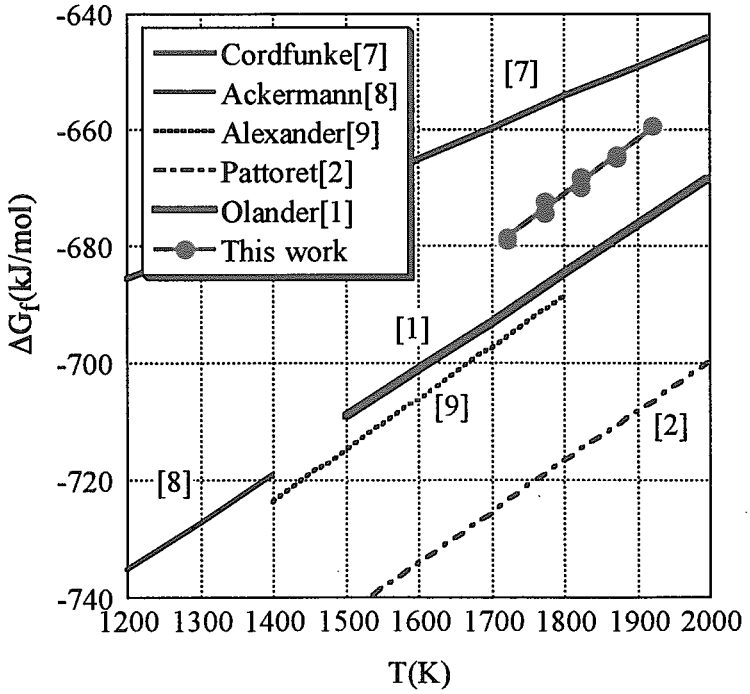

Fig.10.6.2 Gibbs free energy of formation of UO_3(g)

11. Nuclear Ship Research and Development

Design studies of two very small-scale and highly compact reactors adopting a passive safety system, a SCR and a MR-1G, have been performed. The SCR with thermal output of 1.25 MW is aiming usage for a submersible scientific research vessel especially in under-sea of the Arctic Ocean, and MR-1G with thermal output of 1 MW for heat supply at an office building.

Design requirements to the SCR such as the power size or the operation time per a research cruising were determined on the base of the need survey conducted in the previous year. This year, the reactor core was optimized for a long life operation on the enrichment of ^{235}U, the fuel pin pitch, the material and geometry of the reflector, etc. Activated corrosion products in the primary loop at the condition of no purification system were estimated for a long time operation, and it was found to be very small. Validity of function of the passive safety system was verified by safety analysis on hypothetical accidents such as LOCA.

For effective utilization of this advanced compact reactor on the ground, design study of the MR-1G was made. The reactor concept is based on the SCR or the DRX. An optimized reactor core was designed and safety analysis was conducted to verify the function of the passive safety system, which is different from the one of SCR.

These advanced reactors are designed to adopt an in-vessel type control rod driving mechanism (CRDM) for safety improvement and compactness of the system. Development of the CRDM has been performed from 1990; the final test with a prototype test assembly was finished this year. Completion of the CRDM development with a success contributes greatly to realization of these advanced reactors with a fruitful technical seed.

An advanced automatic operating system has been developed for an integral-type nuclear ship reactor under an engineering design stage based upon application of operator's knowledge. The tool for representation of operator's knowledge used at the advanced system has been made to integrating normal and abnormal operations smoothly.

Start-up and shutdown operation has been examined for an integral-type reactor using the engineering ship simulator. The manual operation was obtained of 12 hours from reactor cold state to the hot standby under heat-up constraints and nuclear heating used. Hardware replacement plan of the simulator has been discussed for the supervisory and CRT control micro-computers.

11.1 Design Study of a Submersible Compact Reactor in 1999

T. Kusunoki, N. Odano, T.Yoritune and T. Ishida
(*E-mail* tkusu@koala.tokai.jaeri.go.jp)

Advanced Marine Reactor Laboratory has conducted design study of a compact reactor, SCR, [1] to be used in a scientific research vessel for observation of the Arctic Ocean's under-sea in the medium depth region. Verification of the safety system in case of a loss-of-coolant accident (LOCA), evaluation of the activated corrosion products and radiation safety assessment in the primary loop without the purification system were carried out in 1999.

The safety system of the SCR plant consists of the water filled containment vessel, the EDRSs, the PRMSs, the containment vessel isolation valves. The water filled containment vessel passively keeps core flooding in case of a LOCA. The EDRS transfer decay heat generated in the core to water in the containment vessel. The PRMS is used to keep core flooding for long period regardless of ship posture in case of founder and abandonment. To verify the fundamental function of the safety system, the analysis in case of a EDRS pipe rupture was carried out using REALP5mod3[2]. After the EDRS pipe rupture, the pressure of the containment vessel rapidly increases and balanced with the pressure of reactor vessel, and then the pressure decrease due to heat transfer through the EDRS and the surface of containment vessel as shown in Figure 11.1.1. In the containment vessel, the water is cooled at the surface of containment vessel steadily. While the water level of the reactor vessel decreases once due to pipe rupture, it vessel keeps higher level than that of upper core with enough safety margin as shown in Figure 11.1.1. The analysis indicated that the safety system could maintain safety of the reactor plant in case of a EDRS pipe rupture.

The SCR is design to adopt no purification system. To quantitatively evaluate the validity of reactor operation without the purification system, a computer code CTAM-Ⅱ [3] has been developed. The corrosion products in the primary loops without purification system have been estimated. Figure 11.1.2 shows calculated results of activated corrosion products in the SCR and DRX, which is a compact. The accumulated corrosion products in the primary coolant in SCR are approximately 24 % of that in the Mutsu plant at the maximum reached full power days, and that in DRX are approximately 40 %. Assuming that the same

performance of the purification system as the Mutsu plant is effective, the buildup of the activated corrosion products in the primary coolant is estimated by calculation to study the effect of purification system. The analysis shows that the effect of the purification system is only 3 % for buildup of the activated corrosion products in the reactor system. It can be concluded that the purification system has no significant influence on the buildup of the activated corrosion products. During maintenance operation, however an appropriate access control and additional shields are required since the dose equivalent rate near the steam generator is rather high immediately after the core shutdown.

References:

1) Odano,N. et al., :"Submersible Compact Reactor SCR for Under-sea Research Vessel", International Workshop on utilization of Nuclear Power in Oceans, pp164-169 (2000)

2) The RELAP5 development team,: "RELAP5/mod3 code manual", NUREG/CR-5535, INEL-95/0174(1995)

3) Odano,N and Ishida,T,: "Evaluation of Buildup of activated Corrosion Products for Highly Compact Marine Reactor DRX without Primary Coolant Water Purification System", Journal of Nuclear Science and Technology, Supplement 1, pp584-588(2000)

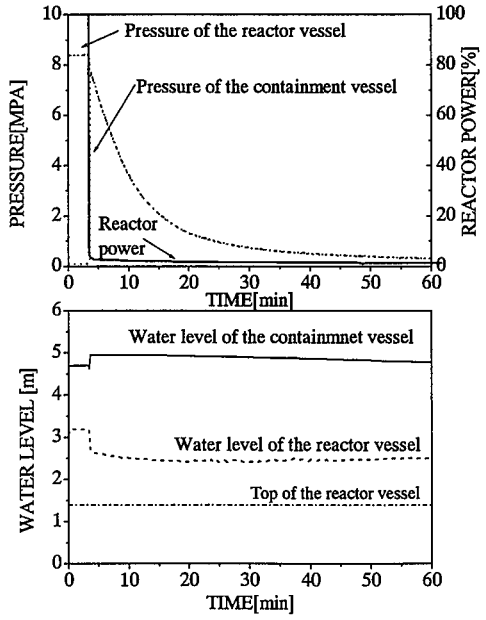

Fig. 11.1.1 Results of transient analysis in case of a EDRS pipe break accident

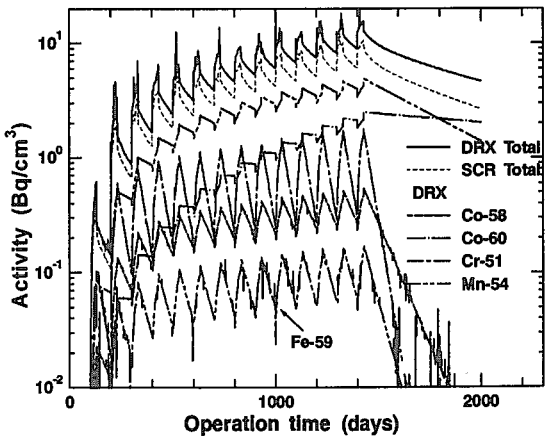

Fig.11.1.2 Calculated results of activated corrosion products in primary coolant

11.2 Core Design of a Submersible Compact Reactor

N. Odano and T. Ishida
(*E-mail:* odano@koala.tokai.jaeri.go.jp)

Nuetronic study of SCR[1] (Submersible Compact Reactor) core to be used for an undersea research vessel for scientific observation at the Arctic ocean has been carried out to establish a compact core having a long core life without fuel shuffling and refueling.

The SCR core is required to be able to operate for 10 years without refueling with 1250 kW of thermal power assuming a 50 % of effective annual load factor. The average linear heat rate is lowered to 5.9 kW/m, because more severe load should be taken into account for the SCR core than the core of ordinary PWRs. The zyrcaloy cladding UO_2 fuel rods, whose specification is the same as that used in the 17x17-type fuel assembly for current PWRs, are used for the SCR core. To realize long term burn-up of the core, the enrichment of ^{235}U and fuel pin pitch were surveyed by a general-purpose neutronic code SRAC95[2].

The dimensions of the SCR core were determined to be 45.6 in equivalent diameter and 40.7 cm in height. The ^{235}U concentration of 9.5 % is necessary to maintain an effective reactor reactivity during 23 GWd/t burn-up that corresponds to 2200 effective full power days. The pitch of fuel rods was determined to be 18 mm considering effectiveness of burn-up. Fuel rods doped with 6-weight percent of Gd_2O_3 as burnable absorber are also used to reduce the excessive reactivity at the beginning of core life. The SCR core consists of 7 fuel assemblies from a viewpoint of criticality safety. The major specifications of the SCR core are summarized in Table 11.2.1. Configuration of fuel rod assembly is shown in Fig.11.2.1.

The neutronic safety of the SCR core regarding core shutdown margin and independency of the reactor control system was assessed according to the guidelines for the safety examination of the Nuclear Safety Commission of Japan. The present analysis indicates that the SCR core satisfies the requirements of the guidelines.

Reactor physics parameters of the SCR core such as the reactivity coefficients and peaking factor were calculated for further safety and thermalhydraulics analyses of the SCR plant.

References

1) Odano, N., Kusunoki, T., Yoritsune, T., Fukuhara, Y., Saito, K., Takahashi, T. and Ishida, T.: "Submersible Compact Reactor SCR for Under-sea Research Vessel", Proc. Int. Workship on Utilization of Nuclear Power in Oceans, 164 (2000).

2) Okumura, K., Kaneko, K. and Tsuchihashi K.: "SRAC95; General Purpose Neutronics Code System", JAERI-Data/Code 96-015 (1996) [in Japanese].

Table 11.2.1 Major specifications of SCR core

Reactor	
Thermal power	1250 kW
Average linear heat rate	5.9 kW/m
Core	
Equivalent diameter	45.6 cm
Effective height	40.7 cm
Fuel	
Fuel type	UO_2 fuel
Cladding material	Zyrcaloy-4
^{235}U enrichment	9.5 wt%
Rod diameter	9.5 mm
Pin pitch	18 mm

Fuel (cnt'd)	
Number of fuel rod	523*
Burnable poison (BP)	Gd_2O_3 (6wt%)
Number of fuel assembly	7
Average burn-up	23 GWd/t
Core life	2200 EFPD
Control rod drive mechanism (CRDM)	
Type	In-vessel type
Number of CRDM	6
Number of control rod/CRDM	10

* includes 24 BP doped fuel rods

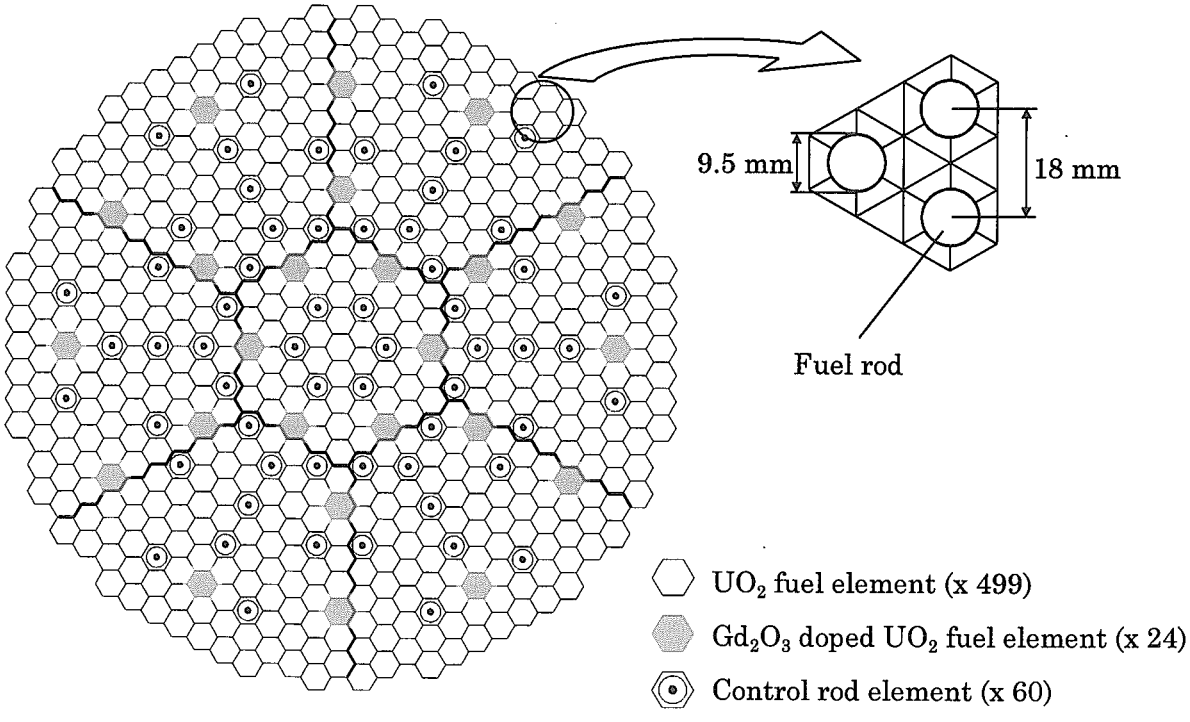

Fig. 11.2.1 Configuration of SCR core

11.3 Development of the In-vessel Type Control Rod Driving Mechanism

H.Nunokawa, T.Yoritsune and T.Ishida
(*E-mail:* hnuno@koala.tokai.jaeri.go.jp)

The advanced marine reactor laboratory has developed an unique in-vessel type control rod driving mechanism[1] (CRDM) being capable of operating under high temperature water for safety improvement and compactness of the reactor systems of Advanced Marine Reactor (MRX). Prototype test assemblies consisting of a driving motor, ball bearings, a scram mechanism etc. were manufactured and their functions under the severe condition were confirmed by several tests including movement upward and downward, and scram. After these tests, main components such as the driving motor, the separable ball-nuts, the ball bearings were overhauled and examined by the observation test and the material test. As a result, it was found that the present CRDM can satisfy the design condition required to MRX's CRDM. The test will be briefly described in following.

Overall Functioning Test

The test body of the driving motor, the latch magnet, the separable ball-nuts etc. were manufactured with the full size except for being shorter length of a driving shaft than the design of the MRX, and incorporated to the test device, as shown in Fig. 11.3.1. The air cylinder was installed at the lower part of test device to adjust the weighting load to 2.2kN equivalent to that of the MRX. Latching, or de-latching motion and up-and-down motion of the driving shaft, and scram, were repeated under condition of 310 ℃, 12MPa water.

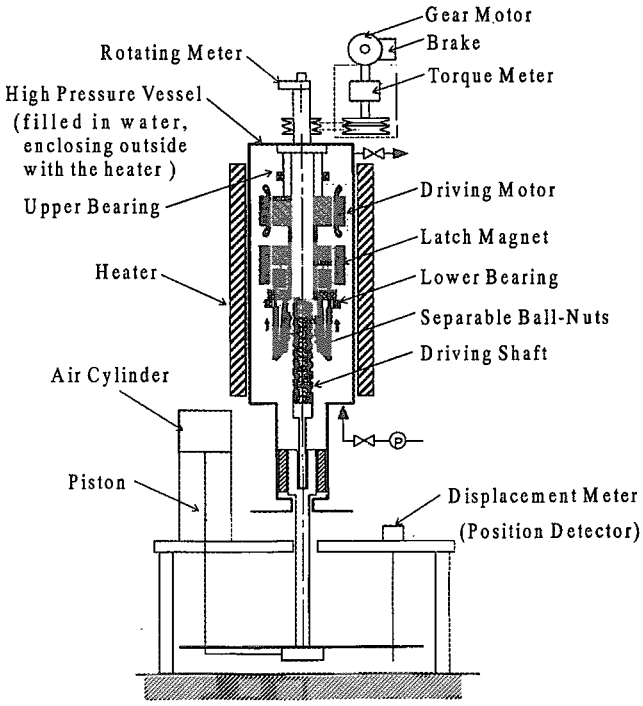

Fig. 11.3.1 Test device

In the functional test of the ball-nuts, reliable latching motion by them was confirmed at any position of the driving shaft by help of a synchronous

device. Typical pattern of the overall functioning test is shown in Fig. 11.3.2, showing latching motion, going-upward, holding, going-downward, and scram. Through the overall functioning tests repeated at many times, a smooth, stable and calm operation of the CRDM was confirmed.

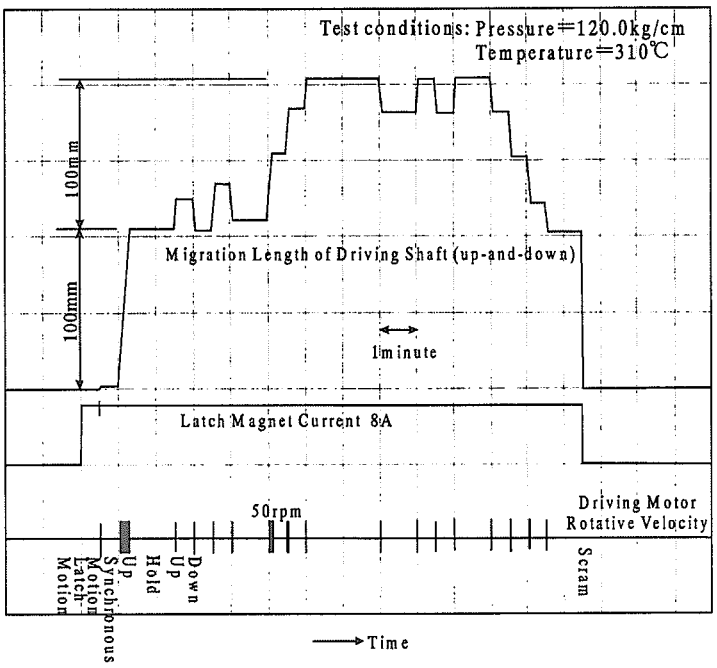

Fig. 11.3.2 Resut of overall functioning test

Driving Motor Torque Test

The maximum torque, over which the motion can not move normally, was measured as shown in Fig. 11.3.3. Reduction of the torque at the high temperature is very small. The maximum torque of the motor is shown to be higher enough than a required load torque at the operation temperature.

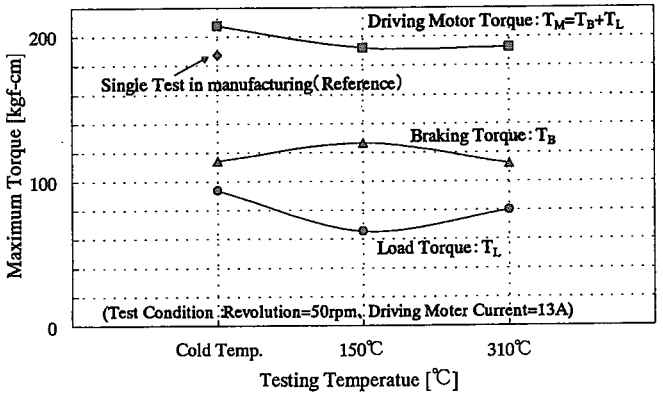

Fig. 11.3.3 Result of driving motor torque test

Scram Test

The time from cutting the latch magnet current to the start of the shaft moving, a de-latch time, was measured. The relation between the de-latch time and the latch magnet current is shown in Fig. 11.3.4. Since the design condition of scram in the MRX is to be less than 0.2 sec. and to be capable of scram at 1000 times, measurement of the de-latch time was performed at 1000 times. Through the repeated tests, all the de-latch time were found to satisfy the design

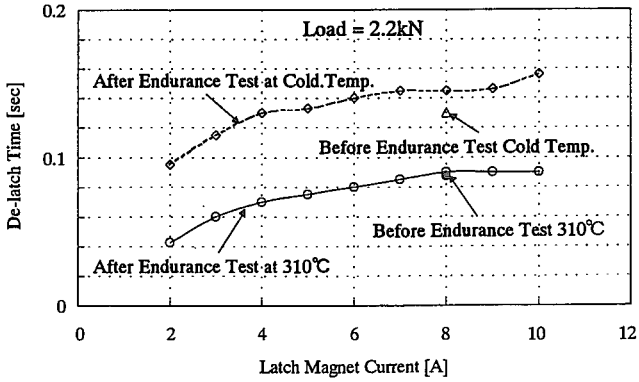

Fig. 11.3.4 Result of scram test

condition.

Endurance Test of Ball Bearings

After screening tests on the material of the ball bearings, the full size ball bearings were fabricated, shown in Table 11.3.1. Using the full size ball bearings, the endurance test was carried out at condition of high temperature water. In the endurance test, the torque and vibration of the test device installing the bearings were measured. The change of torque against the revolution of the bearings is shown in Fig. 11.3.5. Within 1,200,000 revolutions, the torque and vibration were not significantly large, although they showed a tendency to become large. The revolution of 1,250,000 is equivalent to that of the design condition for life-time of 20 years.

Table 11.3.1 Specifications of bearing

Type	Single line deep-ditch type
Dimension	
Outer/Inner Dia.	165/120mm
Material	
Race	Stellite No.1
Ball	Cermet
Retainer	Graphite

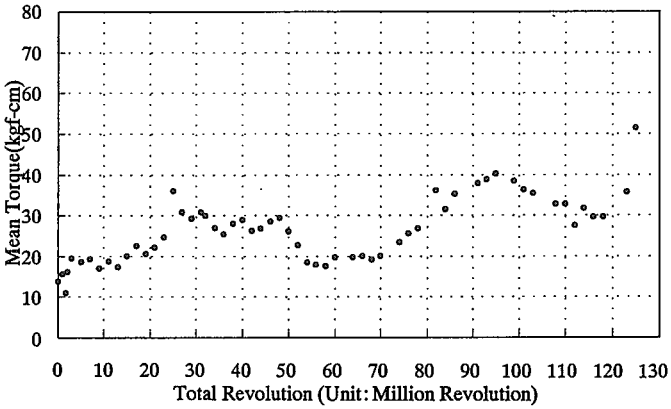

Fig. 11.3.5 Result of endurance test of bearing

Conclusions

It can be confirmed from the tests that functions of the prototype test assembly can satisfy the design condition. Development of the in-vessel type CRDM for the MRX have completed and attained the target.

Reference

1) Yoritsune, T., Nunokawa, H., Ishida, T. and Imayoshi, S.: "Development of an In-vessel Type Control Rod Drive Mechanism", Proc. Int. Workshop on Utilization of Nuclear Power in Oceans, 231 (2000).

11.4 Operator Knowledge Representation for an Advanced Automatic Control System

J.Shimazaki and N.Yabuuchi
(*E-mail:* jshima@koala.tokai.jaeri.go.jp)

An advanced automatic control system has been developed specially for nuclear ships based upon operational knowledge of "Mutsu" plant. The system was made to integrate the normal operation system[1] and the abnormal (after scram or accident) one[2]. A need for unified representation of operational knowledge occurred to develop its database easily and transparently.

A new tool for operational knowledge generation was made for this purpose. The tool is to unify knowledge of normal, abnormal and integral operations. Four fundamental functions was contained in the tool as follows,

a) fundamental elements to make operational knowledge,

b) registration and actions of its individual knowledge,

c) communication to the engineering simulator, and

d) edition and registration of execution program and G2(expert system) parameters.

The fundamental elements describe into main three hierarchical structures from its operational range. The top level is the work flow display for overall plant operations and the second is the sub-work flow display for detailed operations defined in the top level. The third level is the real action of the elements defined in the sub-work flow display.

For an example, the operational main display was shown in Fig.11.4.1 for an accident automatic operations. After the cause of the plant accident was identified to an LOCA, for example, the After-LOCA operations was selected and executed automatically in the sub-work display. The monitoring of plant state and operational actions is also made for other display suited to plant operators. The executing programs in the simulator such as valve actions, plant state monitor, control set-up and so on were written with procedure command in G2. The verification and validation of the tool is being made after completing the new operational knowledge database.

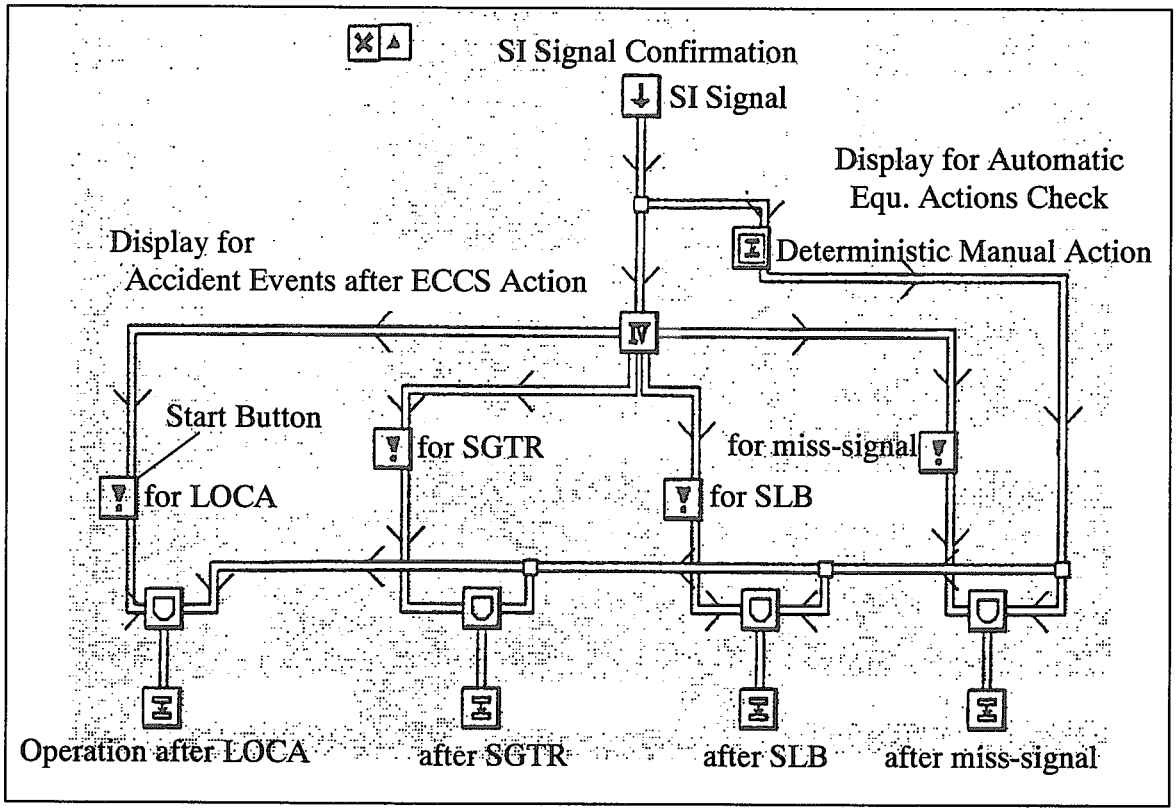

Figure 11.4.1 Main display for accident automatic operation by a new tool

References

1) Nakazawa, T., et al.: "Development of Advanced Automatic Operation System for Nuclear Ship (1) Perfect Automatic Normal Operation", JAERI-Tech 99-008 (1999) [in Japanese].

2) Yabuuchi, N., et al.: "Development of Advanced Automatic Operation System for Nuclear Ship (2) Perfect Automatic Operation After Reactor Scram Events", JAERI-Tech 97-057 (1997) [in Japanese].

11.5 Startup and Shutdown Operation for an Integral-Type Reactor Plant

N.Yabuuchi, M.Takahashi and J.Shimazaki
(*E-mail:* yabuuchi@koala.tokai.jaeri.go.jp)

We developed a real-time engineering simulator for an integral-type reactor plant[1] to confirm its fundamental design and operation performance and to utilize the study of advanced automatic operation in FY-1998. This simulator is a part of Nuclear Ship Engineering Simulation System[2] and the same hardware as "Mutsu" simulator, which was developed to simulate the first Japanese nuclear ship "Mustu". To confirm the operation performance, normal plant operation from start-up to shutdown for the integral-type reactor plant were carried out by this simulator.

Main features of the normal operation from start-up to shutdown are follows: Reactor power is controlled by control rods only. Main coolant pump, pressurizer and steam heater installed in the decay heat removal loop are used for raising temperature of the primary coolant from cold shutdown state to void generation during pressurization. After void generation, nuclear heating is used for raising the primary coolant temperature and pressure.

The plant behavior in the start-up operation is shown in Fig.11.5.1. Stable behavior was obtained within the operating limits. The start-up operation includes key manual actions: steam heating for temperature raising, void generation during pressurization and nuclear heating for temperature/pressure-raising. The heating-up rate by the steam heating was about 24℃/h with steam flow rate 4t/h and the heating-up rate by the nuclear heating was about 28℃/h with core thermal power 5MWt. The start-up time from the reactor cold shutdown to the hot stand-by state was taken about 12 hours. The primary coolant temperature at the initial state was 50℃.

The plant behavior in the shutdown operation after reactor shutdown is partly shown in Fig.11.5.2. This operation is to lower the main coolant temperature by dumping the steam from the once-through type steam generator. The carefully manual operation was required for the continuous water feed to the steam generator in order to match the feed water flow with the dumping steam flow for many hours. Finally the stable behavior obtained. Therefore, this operation requires an advanced automatic control system based on an operational skill.

References

1) Takahashi M., et al.: "Building of Nuclear Ship Engineering Simulation System, Development of the Simulator for the Integral Type Reactor", JAERI-Tech 2000-039 (2000) [in Japanese].

2) Kusunoki T., et al.: "Development of Nuclear Ship Engineering Simulation System", JAERI-M 93-223 (1993) [in Japanese].

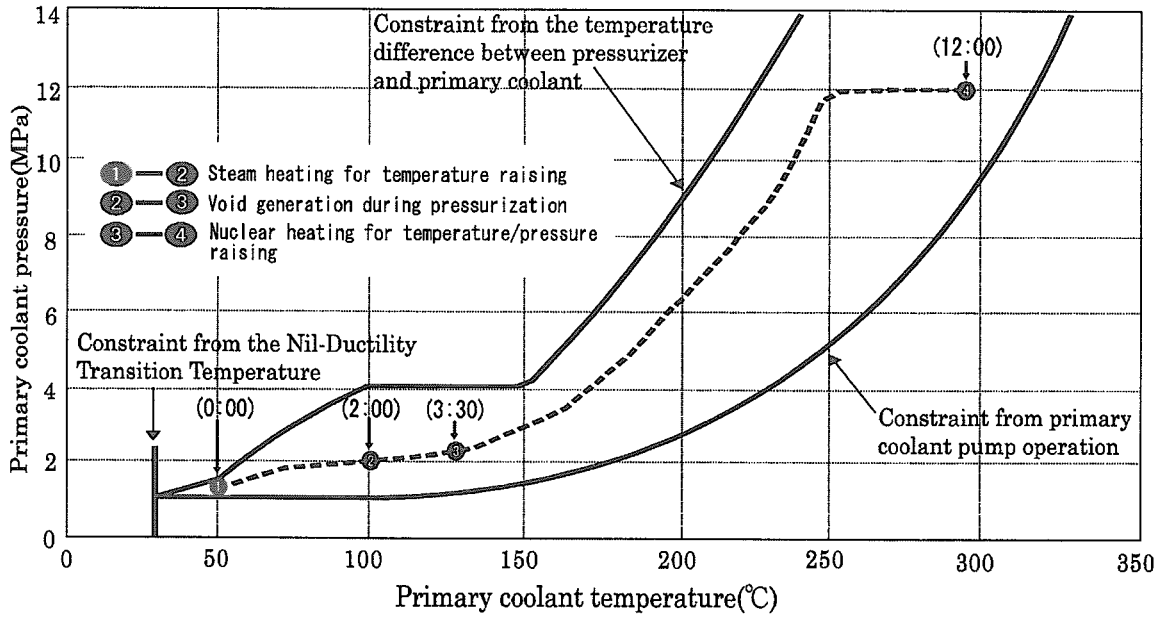

Fig.11.5.1 Plant behavior in the start-up operation for the integral-type reactor plant

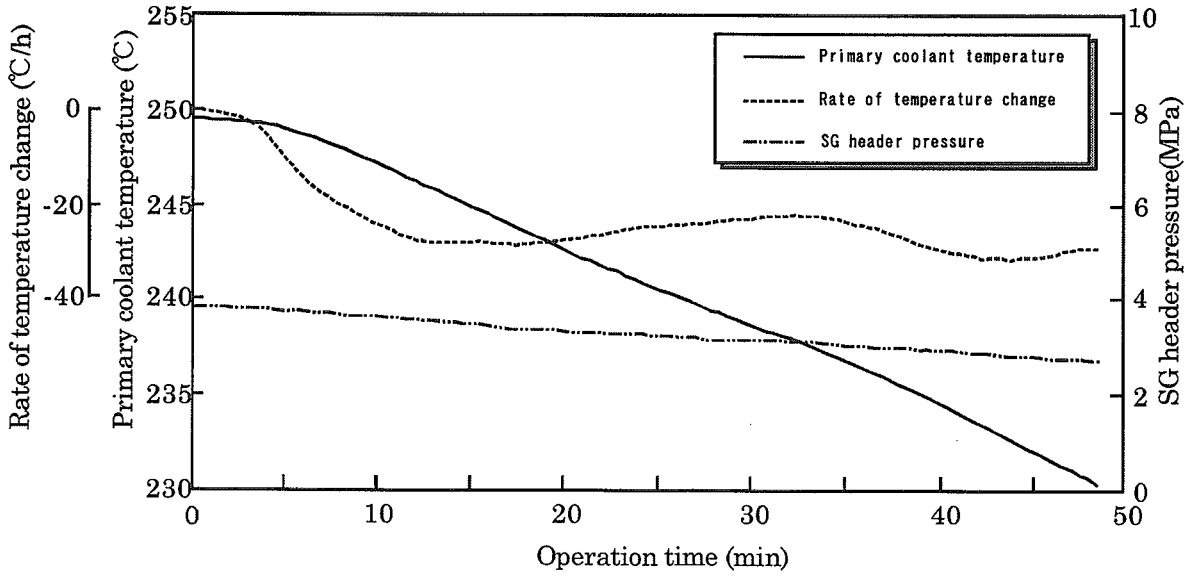

Fig.11.5.2 Plant behavior in the shutdown operation after reactor shutdown

11.6 Improvement of Supervisory and Control Functions by PC for the Integral-Type Reactor Simulator

H. Takahashi, T. Takahashi and M. Kyoya
(*E-mail:* htaka@koala.tokai.jaeri.go.jp)

JAERI had designed a light-weight and compact integral-type reactor (100MWth) with the passive safety system for a future nuclear ship. A real-time simulator for the integral-type reactor was developed to study operation performance and automatic system design. This simulator is a part of the Nuclear Ship Engineering Simulation SYstem (NESSY) and is made on the same hardware as the MUTSU simulator[1), 2)]. The simulator can be used as both MUTSU simulator and integral-type reactor simulator.

The NESSY consists of four computers used for operational supervision and control. The NESSY also has a several CRTs for the display of plant parameters and operational actions. (Fig. 11.6.1)

The hardware of the simulator was introduced about 10 years ago. It is difficult to repair due to shortage of the spare parts, when failure of the hardware elements occurs. The hardware of NESSY was changed with a modern one, and the software was improved so as to operate with higher performance. Taking account of feasibility and easiness of improvement, the new system was designed into sub-systems as simulation, supervision and operational control systems as shown in Fig.11.6.1.

Specification of hardware and software are as follows. The computers are Personal Computer (PC) (DELL 666MHz or 700MHz); OS are Windows NT Server and Windows NT Workstation (Microsoft); the supervisory and control software is InTouch (Wonderware); the program language are Visual BASIC and Visual C (Microsoft).

The new supervisory and control system consists of one PC for the data acquisition and several PCs for the supervisory and control. In case of a trouble of PC, PC can be easily exchanged with other PC because of the conventional one used.

The system of supervisory and control software adopts an HMI (Human Machine Interface) development software, InTouch. It is widely used as the system that does a real time supervisory and a control and a data acquisition in real-time operating plant. In this software, it is possible to create a screen and to use and change the screen easy to a user demand.

Visual BASIC and Visual C are adopted as the program language, which works on the Windows. They were used to make various application programs, which receive the data of the simulation computer by the data acquisition computer. Then, it is processing in the data to use with PC for the supervisory and control.

In 1999, the integrate-type reactor simulator became simple system configuration as one computer (simulation part) and two PC (supervisory and control part). The NESSY will be improved at the part of the system of the simulator control functions for the integral-type reactor. MUTSU simulator will be changed to the same structure of the integral-type reactor simulator.

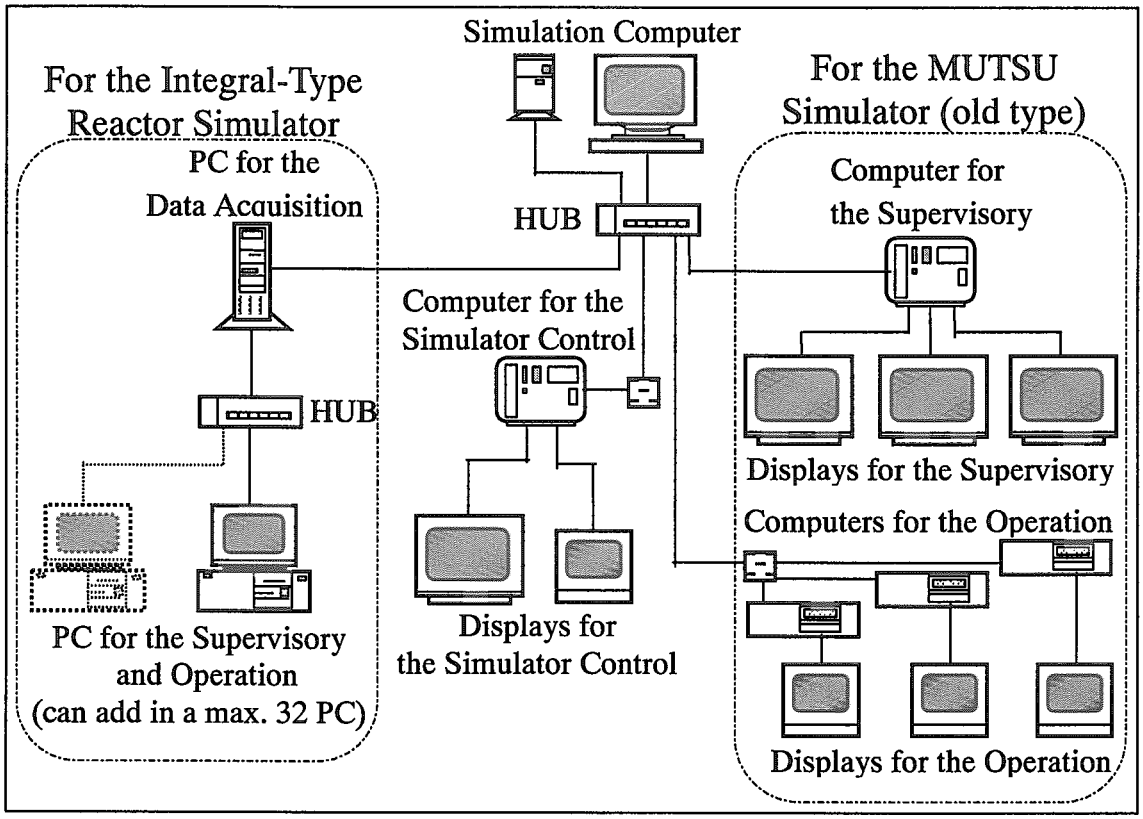

Fig.11.6.1 New hardware configuration of NESSY

References

1) Kusunoki T., et al.: "Development of Nuclear Ship Engineering Simulation system", JAERI-M 93-223 (1993) [in Japanese].

2) Takahashi T., et al.: "Building of Nuclear Ship Engineering Simulation System Development of the Simulator for the Integral Type Reactor", JAERI-Tech 2000-039 (2000) [in Japanese].

11.7 Application of a Compact Marine Reactor to the Heat Supply

T. Kusunoki, N. Odano, N.Nakajima, Y.Fukuhara and M.Ochiai
(*E-mail:* tkusu@koala.tokai.jaeri.go.jp)

A practical energy source that does not release carbon dioxide is needed in order to protect the environment of the earth. One proposed solution is use of a cassette type nuclear reactor for supplying energy for air conditioning, heating, and hot water in an office building. JAERI made clear the essential points for a cassette type nuclear reactor designed to be installed in the basement of a building, and established the concept of the nuclear reactor MR-1G [1] on the base of the compact marine reactor DRX [2] which was studied for a deep-sea research vessel. The essential points are as follows:
(1) Construction of the system in a factory and transportation to the installation site by trailer. (2) Passive safety characteristics, which do not require operation of an external electrical power source. (3) Safety characteristics for seismic activity or fire, which do not require the exceptional design of buildings for earthquake or fire. (4) Long term remote operation of the compact reactor.

The major parameters and the conceptual drawing of MR-1G are shown in Table 11.7.1 and Fig. 11.7.1. The whole plant is 2.4 m in diameter, and 6 m in height. The weight of plant is about 100 t. The reactor is very simple and compact as the circulation pump, the pressurizer, the chemical and volumetric control system, and the sampling system are not adopted. There is a small number of the dynamic machinery in the containment vessel; four control rod drive mechanisms, four motor valves in the emergency cooling system and four isolation valves in the steam and feed water line. Reactivity is controlled without soluble boron and the moderator temperature reactivity coefficient is negative even at a low temperature. Nuclear characteristics of the SCR core were analyzed by a general-purpose neutronic code SRAC95 [3]. Simplification in designing makes MR-1G highly reliable and transportable by a trailer. The concept of utilization cycle of MR-1G from assembling at the factory to transportation again to the factory is shown Fig. 11.7 2.

The concept of the district-heating reactor MR-1G was discussed and analyzed, and it was proven that the MR-1G satisfies the essential points of the conceptual design requirements.

References

1) Kusunoki, T., et al.: "Application of a compact reactor to district heating –MR-1G- ", Proc. Int. Workshop on Utilization of Nuclear Power in Oceans, 77 (2000).

2) Iida, H., et al.: "Design study of the deep-sea reactor X", Nucl. Technol., 107, 38 (1994).

3) Okumura, K., Kaneko, K. and Tsuchihashi K.: "SRAC95; General Purpose Neutronics Code System", JAERI-Data/Code 96-015 (1996) [in Japanese].

Table 11.7.1 Major Parameters of MR-1G plant

Whole Plant	
Reactor thermal output	1 MW
Supply steam temp.	180 ℃
Core	
Equivalent diameter	440 mm
Effective height	407 mm
Fuel inventory	81 kg
^{235}U concentration	8.5 %
Ave. linear heat rate	5.96 kW/m
Fuel life time / Ave. load	10 years / 44 %
No. of CRDM	4
Neutron reflector	Zry 4
Neutron absorber	Boral
Primary cooling system	
Operating pressure	3.0 MPa
Core inlet / outlet temp.	218 / 233 ℃
Circulating type	Natural circulation
Pressurization type	Self-pressurization
Secondary cooling system	
Operating pressure	0.88 MPa
Feed water / steam temp.	90 / 180 ℃
SG type	Once-through helical coil

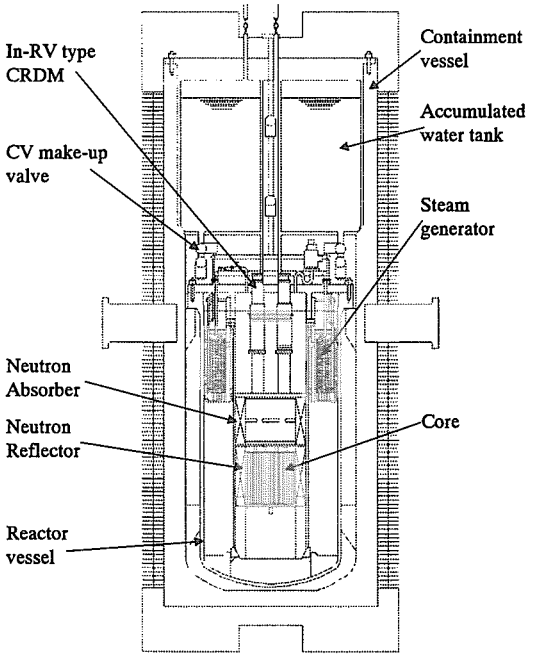

Fig. 11.7.1 Conceptual drawing of MR-1G plant

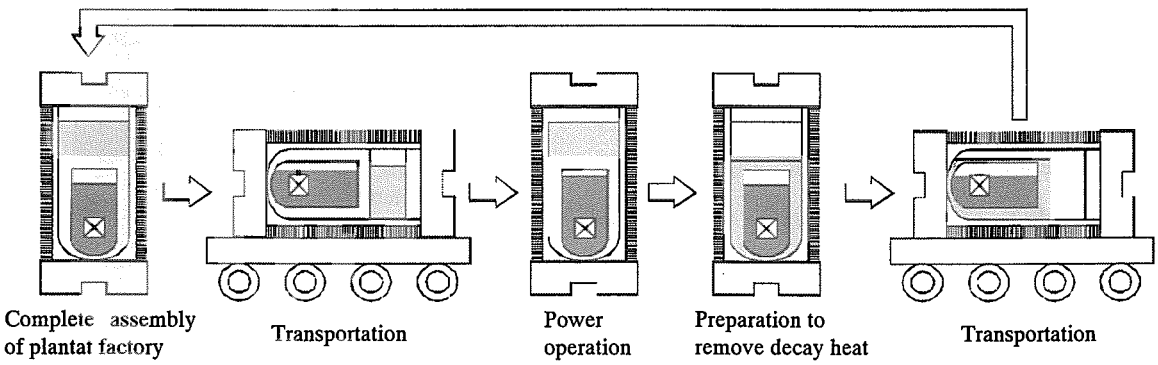

Fig. 11.7.2 Concept of utilization cycle of MR-1G

11.8 Analysis of Cooling Performance of MR-1G in Accident

T.Yoritsune, T.Kusunoki, N.Odano, H.Takahashi, N.Nakajima and M.Ochiai
(*E-mail:* tyori@koala.tokai.jaeri.go.jp)

Advanced Marine Reactor Laboratory has been conducting design studies on a very small reactor for heat supply, called MR-1G[1] which is suitable for air conditioning and hot water supply in office buildings. The MR-1G adopts the highly passive safety system to assure the safety without any operators or any emergency power generators. The safety system consists of the accumulated water tank, safety injection system and containment vessel. The safety analysis for the characteristic accidents in case of installing the MR-1G in a basement of an office building was carried out to evaluate the cooling performance in accident for MR-1G.

Transient analyses by means of the RELAP5mod3[2] program have been conducted including loss-of-coolant accident and in case of reactor buried under broken pieces of concrete due to an earthquake. These situations are important to confirm the feasibility of the MR-1G concept.

The transient analysis of loss-of-coolant accident was carried out to confirm the function of keeping core flooding and removing residual heat by natural convection. The assumed break point was a 20-mm-diam pipe of safety valve at the top of the reactor vessel on the analysis. The Fig. 11.8.1 shows the node model for transient analysis with RELAP5. The node model includes the reactor vessel, the containment vessel, the accumulated water tank and an air pipe around the containment vessel. The accumulated water tank is

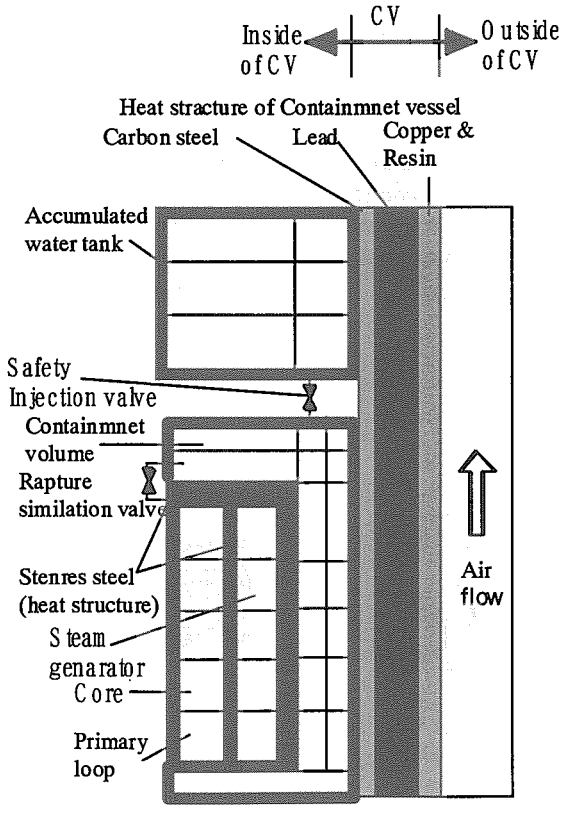

Fig. 11.8.1 Node model for transient analyses with RELAP5 code

connected to the containment vessel with two safety injection valves those are closed in normal operation. The transient behavior is shown in Fig. 11.8.2. The pipe of safety valve breaks at 10 second in the figure, and the reactor shuts down, then the safety system starts at 20 second. It is assumed that the accident is detected by water level or pressure change of the containment vessel. The pressure of the reactor vessel continues to decrease after the pipe breaks as shown in Fig. 11.8.2. The pressure of the containment vessel rise due to the flow of the water from the reactor vessel to the containment vessel, then it decrease once due to the flow of the water from the accumulated water tank to the containment vessel. The pressure of the accumulated water tank, the initial pressure was 2 MPa, decreases with the flow of water, then it becomes equal to the pressure of the reactor vessel at approximately 0.45 MPa. The pressure of the containment vessel increases as the containment vessel water is warmed at the surface of reactor vessel. The break flow of the water stopped at 450 seconds, as pressure of the reactor vessel and the containment vessel equals, then the water flow out into the RV from containment vessel. This phenomenon is considered as that the pressure of the containment vessel becomes higher than that of the reactor vessel because the pressure of the containment vessel is the sum of steam partial pressure and nitrogen partial pressure but the pressure of the reactor vessel is only steam partial pressure. As the result, the water level of the reactor vessel rapidly increases from 700 seconds and becomes full level at 2400 seconds. The remaining water level is 400 mm from the core top, it is high enough for keeping core flooding. The whole plant is cooled down after 7200 seconds as the removal heat from containment vessel exceeds decay heat. In conclusion, core damage is not expected by the safety system during the transient.

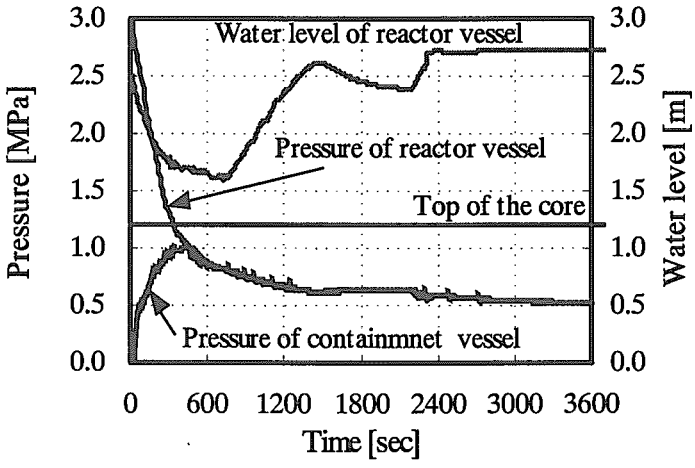

Fig. 11.8.2 Transient of pressures and water levels in case of a LOCA (20-mm-diam safety valve pipe break)

The analysis of the reactor varied under broken pieces of concrete after an earthquake was carried out by RELAP5mod3 with following assumptions; (1) The containment vessel endures the seismic load. (2) Air around the containment vessel does not flow and no

convection. (3) Heat conducts air but does not conducts concrete pieces around the containment vessel. (4) The reactor shutdown and the containment vessel are filled with emergency cooling water after the earthquake. The node model was simplified as shown in Fig. 11.8.3. Even with these severe assumptions, the analytical result shows that it takes more than 80 hours for the reactor vessel pressure to reach the design pressure as shown in Fig. 11.8.4. The detailed analysis will show the longer grace time but it is expected that repair work be done around the reactor plant for 80 hours.

As the result of this analysis, the feasibility for installing the MR-1G in a basement of an office building was obtained.

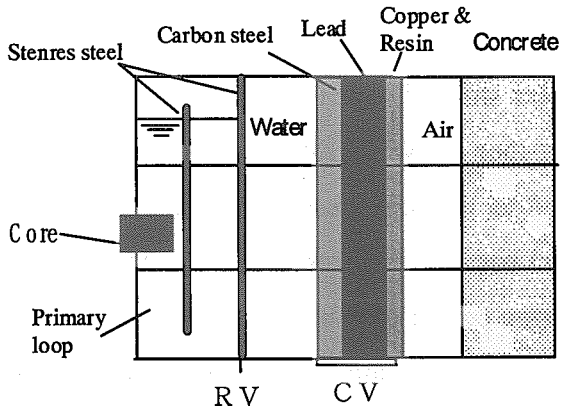

Fig. 11.8.3 Node model for analysis in case of the reactor varied under broken pieces of concrete

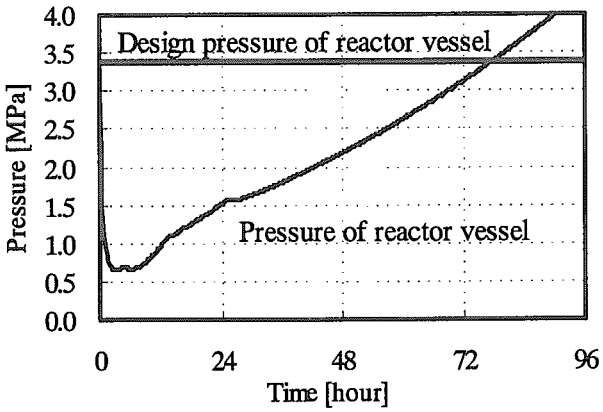

Fig. 11.8.4 Transient of pressure of the reactor vessel in case of the reactor varied under broken pieces of concrete

References

1) Kusunoki, T., et al.: "Application of a compact marine reactor to district heating –MR-1G-", Proc. Int. Workshop on Utilization of Nuclear Power in Oceans, 77 (2000).

2) The RELAP5 development team: "RELAP5/mod3 code manual", NUREG/CR-5535, INEL-95/0174 (1995).

12. Facility Operation and Techniques Development

There are four reactor-engineering facilities such as Heat Transfer Fluid Flow Test Facility, Fast Critical Assembly (FCA), Tank-type Critical Assembly (TCA) and Very High Temperature Reactor Critical Assembly (VHTRC). Maintenance work for VHTRC and operations of other facilities were carried out as scheduled. Major activities of each facility of this fiscal year are summarized briefly below.

(1) The Heat Transfer Fluid Flow Test Facility was operated for various experiments such as core thermal-hydraulic transient test for LWR, DNB Test for Advanced Reactor, Test with Two-Phase Flow Test Loop, etc. The designs and constructions for Integrated ICE/LOVA for Fusion Reactor and 500KVA DC Supply System were carried out. In addition, the R&D of the void fraction measurement system was developed.

(2) The FCA was operated according to various purposes of experiments and recorded the operation time of 380.7 hours. Maintenance activities, fuel management and physical protection were done, i.e., renewal of the nuclear instrumentation, repair for defects of coating on fuels etc. And the PIV of nuclear fuel materials was carried out.

(3) The TCA was operated for the new type control rods experiments and the training courses of the Nuclear Technology and Education Center (NuTEC). And it was recorded 155 times operation in 66 days. As for maintenance activities, various switches on the control panel were replaced. Fuel management, Physical Protection and PIV were also carried out.

(4) Maintenance works were done for VHTRC such as the monthly and annual inspections according to the safety regulation for operation. The PIT and PIV for VHTRC were also carried out as the fuel management. The planning for decommissioning VHTRC was decided. And the revised budget for dismantling was recognized by government in December 1999. The construction of dismantling will begin in 2000.

12.1 Operation Report of Heat Transfer Fluid Flow Test Facility

H. Watanabe, T. Satoh, M. Shibata, H. Watanabe and K. Nakajima
(*E-mail*: watahiro@popsvr.tokai.jaeri.go.jp)

In FY-1999, operation and maintenance of Heat Transfer and Fluid Flow Test Facilities were carried out as scheduled.

As for the maintenance of test facilities, annual official inspections of the pressure vessels and the steam generator located at both of Chemical/Mechanical Engineering Building and Thermal Engineering Test Facilities were carried out.

As for the operation of test facilities, the following six tests were performed.

1) DNB Test for Advanced Reactor
2) Core Thermal-Hydraulic Transient Test for LWRs[1)]
3) Test with Two-Phase Flow Test Loop
4) Ultra-High Heat Flux Test by the NRG
5) Thermal Fluid Safety Test (ICE/LOVA) for Fusion Reactor[2)]
6) Steam Jet Test for Assessments of Multidimensional Two-Phase Flow

As for the design and construction of test facilities, the following two test facilities were newly constructed.

1) Integrated ICE/LOVA Test Facility
2) 500KVA DC Supply System

As for the representative R&D, void fraction measurement system was developed.

References

1) Watanabe. H., et al: Core thermal-hydraulic transient test for LWRs (15) Spring Meeting of the Atomic Energy Society of Japan E29 (2000).
2) Shibata. M., et al: Dust Transport Behavior During Loss-of-Vacuum Events Fall Meeting of the Atomic Energy Society of Japan V-505 (1999).

12.2 Operation Report of FCA

K. Hayasaka, K. Satoh, H. Sodeyama, K. Kurosawa and M.Saitoh
(*E-mail*: hayasaka@fca001.tokai.jaeri.go.jp)

Operation of Fast Critical Assembly (FCA) was carried out in accordance with the experimental schedule on the FCA XX-2 assembly. Operation of 77 times was carried out in 62 days. No scram was recorded during the operation. The total operation time was 380.7 hours and the integrated power was 0.38 kWh. A total number of 5426 criticality operations has been recorded at the end of this fiscal year since the first achievement of criticality on the 29th of April 1967. For the safety regulation of operation, two days were devoted to the monthly inspection and about 8 weeks from October 1999 to the annual inspection. Routine maintenance activities were done during the inspections to provide maximum operation days for the experiments. The following instruments were renewed in this fiscal year:

- The electric circuit for electromagnet of safety／control rods:
- The position indicator of safety／control rods:
- The nuclear instrumentation for the power level monitor:

As for fuel management , the defects of coating on Enrich uranium, Natural uranium and Depleted uranium metallic fuel were repaired for about 7,500 plates and about 3,000 blocks by spraying the surface with colloidal solution of fluorocarbon in order to prevent the fuel from oxidation. Weights of the coating on the fuel plates were obtained from the difference of the weight between before and after coating.

As for the physical protection (P/P), security control of the gate was done restrictively and the system was maintained properly. In connection with safeguard, IAEA and NSB* carried out monthly inspection under the international treaty. They made the PIV (Physical Inventory Taking) from the 28th to the 30th of June. Prior to the PIV we performed item counting, weighing and non-destructive assay of the fuels from the 21st to the 25th of June.

* NSB: Nuclear Safety Bureau

12.3 Operation Report of TCA

Y.Hoshi, K.Nitta and S.Fujisaki
(*E-mail*: hoshi@melody.tokai.jaeri.go.jp)

Operation of Tank-type Critical Assembly (TCA) was carried out in accordance with the schedule on the experiments for the high-performance control rods containing highly enriched boron and the training courses of NuTEC (Nuclear Technology and Education Center) The total operation time was140 hours and integrated power was 161Wh during 155times operation in 66days. A total number of 10,882 criticality operations have been recorded at the end of this fiscal year since the first achievement of criticality on the 23rd of August 1962. For the safety regulation of operation the monthly inspection was carried out and about 24weeks from September 1999 were devoted to the annual inspection.

As for maintenance activities, various switches on the control panel were replaced during the annual inspection.

As for the physical protection (P/P), the management of the entrance and exit was done restrictively and the system was maintained properly.

In connection with safeguard the inspection of nuclear material, stored at TCA, was carried out by IAEA and NSB* under the international treaty. The Physical Inventory Taking (PIT) of the fuels was performed on the 22nd of June and IAEA and NSB made the Physical Inventory Verification (PIV) on the 23rd of June by means of item counting, and non-destructive assay.

* NSB: Nuclear Safety Bureau

12.4 Maintenance Work Report of VHTRC

T. Ono, M. Takeuchi, D. Hirayama and K. Nakajima
(*E-mail*:ono@vhtrc01.tokai.jaeri.go.jp)

The critical experiment for the establishment of measurement technique of initial criticality of HTTR was finished on September 1996 at VHTRC. Therefore, the first criticality of the HTTR was attained on November 10,1998.

Nowadays, the VHTRC is out of operation for the experiment. Then, the VHTRC is doing maintenance work only.

According to the safety regulation for operation, one day was devoted to the monthly inspection and about 12weeks to the annual inspection from March to June in 1999.

As for management, Physical Inventory Taking (PIT) was carried out from May 12 to 13 by means of item counting for fuel compact. IAEA and STA made the Physical Inventory Verification (PIV) under the international treaty on May 13. No anomaly was confirmed. The maintenance activity was also taken on the physical protection (p/p) system. The sensitivity and function of the system were examined and calibrated.

We decided the plan to decommission of the VHTRC. Therefore, government revised of budget at December 1999 recognized the cost of dismantlement of the VHTRC. So, we took the safety examination of JAERI about the method of the construction of dismantling of the VHTRC. We submitted a dismantling report of the VHTRC to the STA at March 2000. The construction of actual dismantling will begin in September 2000.

13. Activities of the Research Committee

The department of Nuclear Energy System serves as a secretariat of the following three research committees organized by JAERI; Japanese Nuclear Data Committee, Research Committee on Reactor Physics and Research Committee on Marine Reactors. The purpose and the expected task of each committee are summarized here. The detailed activities of each committee are presented in the following sections.

Japanese Nuclear Data Committee

The Committee is organized to promote the evaluation of nuclear data and the production of group constants for application fields. There are three subcommittees, six standing groups and a steering committee under the Committees. The Committee also takes a task of compiling the activities of the International Nuclear Data Committee and the Working party on International Evaluation Cooperation under OECD/NEA/NSC.

Research Committee on Reactor Physics

The Committee reviews the research activities related to reactor physics in Japan and supports the activities of Nuclear Science Committee (NSC) of OECD/NEA. Past two subcommittees were closed and three working parties were newly organized under the Committee. The expected tasks are reactor physics of accelerator driven system and LWRs loaded with next generation fuels, and conceptual study of advanced reactors.

Research Committee on Marine Reactors

The Committees is organized to review and discuss the research and development activities on marine reactors. Two subcommittees on a highly compact marine reactor and the nuclear ship Mutsu are organized under the Committee. The meeting of the Committee was held once in the fiscal year to discuss the present activities.

13.1 Activities of Japanese Nuclear Data Committee

A. Hasegawa

The Japanese Nuclear Data Committee (JNDC) consists of three subcommittees, six standing groups and a steering committee. Each subcommittee consists of several working groups (WG). The Committee Meeting of JNDC was held at July 1999 to discuss the nuclear data activity in the previous fiscal year and plans for the fiscal year 1999. Discussions were made on several topics including the planning of the 1999 Symposium on Nuclear Data as well as the international collaboration on nuclear data.

The 1999 Symposium on Nuclear Data, which is held every year in November, was held. And a specialists' meeting on Photonuclear Data, which is a topical meeting held every year on the selected hottest topics in the period, was also held together with the IAEA AGM (Advisory Group Meeting) on October.

The activities of subcommittees and standing groups are briefly summarized below.

Subcommittee on Nuclear Data

1) High Energy Nuclear Data Evaluation WG :

The evaluation is made in two phases. In the phase-I, the data up to 50 MeV for IFMIF(International Fusion Material Irradiation Facility) project is evaluated for neutron and proton induced reactions. In the phase-II, high-energy neutron/proton induced reactions up to 3GeV will be made. Data requests are very keen by the projects of JAERI Neutron Research Center and Japan Hadron Facility(KEK). Following is the status of each SWG.

- IFMIF Neutron File Compilation SWG: Neutron file compilation is the main task of this SWG. Up to now, evaluation of 42 nuclides has been finished. The files are in the reviewing stage including FORMAT check.
- MeV and GeV File compilation SWG: Compilation and evaluation of phase-II data is a main mission. Evaluations for the priority 2 nuclides (about 40 nuclides) are performed together with the code preparation inevitable as the fundamental evaluation tools in this energy range.
- Other Sub-Groups like Photonuclear Data, PKA/KERMA and High Energy Activation Cross-section, also made their progress.

2) Covariance Data Evaluation WG : Methods of covariance matrix evaluation have been investigated. A covariance matrices for U-233 have been newly made. And covariances for O-16 inelastic, Na-23 total, U-235 fission, U-238 capture, resolved resonance parameters of U-235, -238, Pu-239 and unresolved resonance parameters of U-235, Pu-239,240,241 were revised. Evaluations were made by using a least-squares program GMA for the case of rich experimental data available. For the data evaluated by model calculations, covariances were

obtained by using the KALMAN code system developed by Kyushu University. Processing system for the covariance files are also developed. Group averaged data are generated by this system.

3)Evaluation and Calculation System WG :

Recommended parameters required in the nuclear model calculations such as OMP, level density, gamma strength functions, as well as advanced methodologies like multi-modal fission, essence from the latest frontiers of theoretical calculations are discussed.

4) Charged Particle Nuclear Data WG : This WG is responsible for the JENDL (alpha,n) Reaction File. Evaluation has been progressed.

5) Delayed Neutron Data Evaluation WG: This group was set up due to the follow up work of OECD/NEA/WPEC(Working Party on Evaluation Cooperation) subgroup 13 to investigate the delayed neutron data related problems. Evaluations of delayed neutron yields and spectra for main actinides of JENDL 3.3(U-235,-238,Pu-239) are also the mission of this group. Data evaluation in 6 group time dependent scheme have been made.

6) Evaluation WG on Intermediate Mass Nuclides: This WG was set up due to the revision fork for JENDL-3.3. Re-evaluation work has been made for Na-23, V-51, Co-59, Cr, Ti, Ni, W, Nb and Er (total of 32 nuclides).

7) Evaluation WG on Heavy Mass Nuclides: This WG was set up due to the revision work for JENDL-3.3. Re-evaluation work has been made for U-233, -235,-236,-238, and Pu-236,-239,-240,-241,-242

Subcommittee of Reactor Constants

1) Reactor Integral Test WG : Benchmark test of JENDL-3.2 for fast and thermal reactors has been made.

For thermal reactors, TCA and STACY benchmark problems are defined and analyzed(4 U lattices and 4 Mox lattices). For fast reactors, some benchmark models of metallic fueled cores of FCA XVI-1&2 , one Mox fueled core of FCA XVII-1 and three benchmark models of ZPPR-9 are defined and analyzed. Inert matrix benchmarks are also defined and analyzed.

2) Shielding Integral Test WG :

This group was re-organized last year solely for the benchmark tests of JENDL up to 20 MeV data. Some benchmark tests (FNS & IPPE experiments) performed as EFF-3 tests were presented and discussed. Preparation work for JENDL-3.3 benchmark test for main shielding materials were made, because no new evaluations are available yet.

3) Dosimetry Integral Test WG : Reevaluation work for JENDL Dosimetry File 99 has been finished, and the data were distributed as CD-ROM for the publics from JAERI Nuclear Data Center.

4) Standard Group Constants WG : Revision work for JSSTDL library has been progressed. Report of the JSSTDL-300 are being prepared.

Subcommittee on Nuclear Fuel Cycle

The subcommittee on nuclear fuel cycle consists of three WGs, i.e., Decay Heat Evaluation WG, WG on Evaluation of Nuclide Generation and Depletion, and FP Mass Yield Evaluation WG.

For the First WG, JNDC FP Decay Data File has been made. A new measurement of decay heat of U-235 has been done at YAYOI U-Tokyo reactor in cooperation with JNC. For the second WG, new entry for PWR and BWR-MOX has been added to ORIGEN-2 Library. Methodology for the evaluation of sensitivity in one group cross section is discussed. For the last WG, this group was organized so as to work with IAEA CRP. To give precise mass yields data for minor actinides as well as major actinides covering the wide range of incident neutron/proton energies is the main mission. Collection of mass yields data evaluated/measured in Japan was made. The systematics made by Moriyama and Ohnishi was applied and analyzed. For high-energy fission, QMD calculation was applied to investigate the mass yields in this range.

Standing Groups

1) CINDA Group : Papers on neutron induced reaction data published in Japanese journals and reports are surveyed. Total of 137 entries were sent to the NEA Data Bank in the last one year to update the CINDA master database.

2) ENSDF Group : The evaluation of nuclear structure data is the duty of this group for nuclei with mass numbers from 118 to 129. A=125 and 121 were published as Nuclear Data Sheets.A-119 will be published in next year. Re-evaluation has been continued for A= 120, 123, 128 and 129.

3) Group on Atomic, Molecular and Nuclear Data for Medical Use : Survey work has been made for the radiopharmaceutical data needed in the field of nuclear medicine. This group was revitalized under the new group leader.

4) JENDL Compilation Group : File compilation and editing were made for the production of JENDL-3.3.

5) Editorial Group of "Nuclear Data News" : Three issues of "Nuclear Data News" (No.63-65) which is a periodic informal journal circulated in nuclear data communities of Japan (written in Japanese) were published in a year. Total of about 700 were distributed in the communities without fee.

6) High Priority Request List Group: Total of 67 entries were updated and 74 new entries added, those are mainly from ADS (Accelerator Driven System) applications. This group is a coordination group to make Japanese Requests Lists and this list is an input data for world-wide request list HPRL that is maintained at OECD/NEA/WPEC (Working Party on

Evaluation Cooperation).

The 1999 Symposium on Nuclear Data

The Symposium was held at Tokai Research Establishment of JAERI on 18-19th November 1999. Japanese Nuclear Data Committee and Nuclear Data Center of JAERI organized this symposium. In the oral sessions, presented were 18 papers on the data status for nuclear safety, data needs for fusion, precise nuclear data measurements for nuclear transmutations, measurements of intermediate energy nuclear data and international relations. In the poster session, presented were 46 papers concerning experiments, evaluations, benchmark tests and on-line database on nuclear data. Total of 157 attendees including 17 foreigners, 85 outside JAERI were gathered. The percentage of foreigners in the attendees exceeds 10 %, therefore the symposium is no longer the local one.

Specialists' Meeting on Photonuclear Data

The meeting was held on 25-26th October 1999 at JAERI Tokai site. This meeting was held together with IAEA RCM(Research Coordination Meeting) on "Compilation and Evaluation of Photonuclear Data for Applications" held 25-29th.Total of about 30 specialists including 9 foreigners were attended. Topics presented and discussed are: status of evaluation of photonuclear data in each country, problems in the evaluations and file selection for the common photonuclear data of IAEA.

13.2 Activities of the Research Committee on Reactor Physics

M. Nakagawa and T. Osugi

The committee reviews research activities related to reactor physics in Japan and supports the activities of Nuclear Science Committee (NSC) of OECD/NEA. The committee reconsidered and discussed its activities over the past two years and decided to close the past Sub-committees and to establish working parties relevant to the special tasks of reactor physics.

The 69th meeting of the Research Committee on Reactor Physics (RCRP) was held in July 1999. Documents discussed at the 10th meeting of NEA/NSC held at OECD Headquarters, Paris, June 2 - 4 1999 were distributed. The meeting was devoted to discussing the establishment of the working parties. The seven topics as the special tasks were nominated and the scopes and action plans of each topic were discussed. Three working parties were finally established and their activities were started up in FY-1999. The meetings were held twice in each working party.

1) Working Party on Reactor Physics of Accelerator Driven Systems,

Scope of activities:

- Investigation of Neutron Transport Calculations in High Energy Range,
- Investigation of Statics and Kinetics of ADS,
- Strategic Consideration of Introduction of ADS,

2) Working Party on Reactor Physics of LWRs Loaded with Next Generation Fuels,

Scope of activities:

- Proposal of Benchmark Problems for Calculation Accuracy Evaluation on LWRs Loaded with Next Generation Fuels,

3) Working Party on Conceptual Study of Advanced Reactors,

Scope of activities:

- Review of Advanced Reactor Concepts,
- Listing Problems of Reactor Physics in Development of Advanced Reactors,
- Proposal of New Research Theme in Developing Advanced Reactors.

13.3 Activities of Research Committee on Marine Reactors

T. Ishida
(*E-mail:* ishida@koala.tokai.jaeri.go.jp)

The committee is organized to review and discuss research and development (R&D) activities on marine reactor design and related technologies. The committee consists of two subcommittees: One is the subcommittee on concept design of a highly compact marine reactor for usage of submersible research vessel. The second, which is at rest now, is the subcommittee for review of Mutsu irradiated fuel and its forthcoming testing. The former subcommittee has a working group for detailed discussion on specific issues. The committee's members are from Japan Atomic Energy Research Institute (JAERI), universities, other research institutions and industries including reactor or ship manufactures and utilities.

The committee meeting is normally held once a year. The R&D plan and activities of the subcommittees for the FY 1999 were reviewed and discussed in September 1999.

Subcommittee on concept design of a highly compact marine reactor

The subcommittee meeting was held once in March 2000. The main topics were on the designs studied on the SCR for usage of the submersible research vessel and the MR-1G for heat supply at an office building. Postponement of the thermal-hydraulic experiment for the highly compact marine reactor was explained with the reason that it is effective to start the experiment when the construction of the reactor becomes clear and concrete in near future. The core designs of the SCR and the MR-1G, which were optimized to attain a high burn-up performance, were introduced. Functions of the passive safety system, of which validity were verified by safety analyses, were reviewed.

The activity from the working group consisting of the experts such as physical oceanographers, submersible designers, etc., which clarified the operation condition of submersible vessel with the SCR for cruising at undersea of the Arctic Ocean, was introduced and reviewed.

Publication List

1. Nuclear Data, and Atomic and Molecular Data

1) Kikuchi, Y., Nakagawa, T. and Nakajima, Y.: "ASREP: A Computer Program for Automatic Search of Unresolved Resonance Parameters", JAERI-Data/Code 99-025 [in Japanese].
2) Harada, M. et al.: "The $^{12}C(p,p'3\alpha)$ Breakup Reaction Induced by 14, 18 and 26 MeV Protons", J. Nucl. Sci. Technol., 36, 313 (1999).
3) Katakura, J.: "Nuclear Data Sheets for A=125", Nucl. Data Sheets, 86, 955 (1999).
4) Sukhovitskii, E. et al.: "New Options of Coupled Channels Optical Model Code OPTMAN Version 6", JAERI-Data/Code 99-028 (1999).
5) Nakagawa, T., Kikuchi, Y. and Fukahori, T.: "Auxiliary Programs for Resonance Parameter Storage and Retrieval System REPSTOR -XTOREP, ETOREP, REPTOINP, REPRENUM, REPIMRG, TREP, PASSIGN, JCONV-", JAERI-Data Code 99-030 (1999) [in Japanese].
6) Nakagawa, T., et al.: "PEGASUS: A Preequilibrium and Multi-Step Evaporation Code for Neutron Cross Section Calculation", JAERI-Data/Code 99-031 (1999).
7) Nakagawa, T. Katakura, J. and Horiguchi, T.: "Computer Programs to Make A Chart of The Nuclides for WWW", JAERI-Data/Code 99-032 (1999).
8) Sukhovitskii, E. et al.: "^{238}U Optical Potential up to 100 MeV Incident Nucleon Energies", JAERI-Research 99-040 (1999).
9) Katakura, J. (Ed.): Proc. of Specialists' Meeting on Delayed Neutron Nuclear Data, JAERI-Conf 99-007 (1999).
10) Nakagawa, T.: "Present Status of Delayed Neutron Data in the Major Evaluated Nuclear Data Libraries", p11, JAERI-Conf 99-007 (1999).
11) Katakura, J. and Fukahori, T.: "IAEA/CRP on Fission Product Yield Data and Activity of WG in Japanese Nuclear Data Committee", p121, JAERI-Conf 99-007 (1999).
12) Sugi, T. et al.: "Tables and Graphs of Cross Sections for Compound Nucleus Formation by Charged Particles", JAERI-Data/Code 99-039 (1999).
13) Nakagawa, T.: "CRECTJ: A Computer Program for Compilation of Evaluated Nuclear Data", JAERI-Data/Code 99-041 (1999).
14) Lee, Y.O., et al.: "Evaluation of Neutron- and Proton-induced Nuclear Data on Al-27 up to 2 GeV", J. Nucl. Sci. Technol., 36, 1125 (1999).
15) Katakura, J.: "Fission Yield Data -Importance for Technological Application and Problems-", Proc. of Specialists' Meeting on the Nuclear Chemistry of Heavy Elements,

p66, KURRI-KR-42 (1999).

16) Fukahori, T.: "General Activities of JAERI Nuclear Data Center and Japanese Nuclear Data Committee", Proc. 1999 Workshop on Nuclear Data Production and Evaluation, Aug. 19-20, 1999, Pohang, Accelerator Laboratory, Pohang, Korea, p129, KAERI/GP-141/99 (1999).

17) Ohya, S. and Kitao, K.: "Nuclear Data Sheets for A=119", Nucl. Data Sheets, 89, 345 (1999).

18) Nakagawa, T. et al.: "Maxwellian-Averaged Cross Sections Calculated from JENDL-3.2", JAERI-Research 2000-002 (2000).

19) Suhkovitskii, E. et al.: "Nuclear Optical Potential of Uranium-238 up to 150 MeV", J. Nucl. Sci. Technol., 37, 120 (2000).

20) Kawano, T. et al.: "Evaluation of Fission Cross Sections and Covariances for U-233, U-235, U-238, Pu-239, Pu-240 and Pu-241", JAERI-Research 2000-004 (2000).

21) Shibata, K. and OH, S.Y.: "Estimation of Covariances for Cr and Ni Neutron Nuclear Data in JENDL-3.2", JAERI-Research 2000-007 (2000).

22) Yamano, N. and Fukahori, T. (Ed.): "Proc. of the 1999 Symposium on Nuclear Data", JAERI-Conf 2000-005 (2000).

23) Donets, A.Yu et al,: "Neutron-induced Fission Cross Sections of U-233, 235, 238, Rh-232, Pu-239 and Np-237 in the Energy Range 1-200 MeV", Proc. VII International Seminar on Interaction of Neutrons with Nuclei (ISINN-7), May 25-28, 1999, Dubna, Russia, p357 (1999).

24) Suzuki, S. et al.: "Monte Carlo Simulation of Helium Atoms and Ions in JT-60U W-shaped Divertor", ECA 23J, 477 (1999).

25) Ichihara, A. and Eichler, J.: "Cross Sections for Radiative Recombination and the Photoelectric Effect in the K, L, and M Shells of one-electron systems with $1 \leqq Z \leqq 112$ Calculated within an Exact Relativistic Description", Atom. Data Nucl. Data Tables 74, 1 (2000).

26) Takayanagi, T., Kurosaki, Y. and Ichihara, A.: "Three-dimensional Quantum Reactive Scattering Calculations for the nonadiabatic $(D+H_2)^+$ Reaction System", J. Chem. Phys. 112, 2615 (2000).

27) Shirai, T. et al.: "Spectral Data for Highly Ionized Atoms: Ti, V, Cr, Mn, Fe, Co, Ni, Cu, Kr, and Mo", J. Phys. Chem. Ref. Data, Monograph No. 8 (2000), ISBN 1-56396-934-3.

28) Gulyas, L. et al.: "Origin of Structures in the Low-energy Single-electron Continuum in Calculations for Ion Collisions from Argon", Phys. Rev. A 62, 022702 (2000).

29) Zhao, Li-Bo, Ichihara, A. and Shirai T.: "Photorecombination of C^{4+} Ions in Low-lying

Resonance Energy Regions", Phys. Rev. A 62, 022706 (2000).

30) Tabata, T. and Shirai, T.: "Analytic Cross Sections for Collisions of H^+, H_2^+, H_3^+, H, H_2, and H^- with Hydrogen Molecules", Atom. Data Nucl. Data Tables 76, 1 (2000).

31) Suzuki, S. et al.: "Electron Capture Processes in Collisions between Beq+ Ions and He Atoms, J. Phys. B 33, 3307 (2000).

2. Reactor Physics

1) Petkov P., Takeda T. and Mori T.: "Comparison of the Flat and Linear Source Variants of the Method of Characteristics", Ann. Nucl. Energy, 26, 935 (1999).

2) Kugo T. and Nakagawa M.: "Application of Neural Network to Multi-Dimensional Design Window Search in Reactor Core Design", J. Nucl. Sci. Technol., 36, 332 (1999).

3) Okumura K., Mori T., Nakagawa M. and Kaneko K.: "Validation of a Continuous-Energy Monte Carlo Burn-up Code MVP-BURN and Its Application to Analysis of Post Irradiation Experiment", J. Nucl. Sci. Technol., 37, 128 (2000).

4) Ueki K., Mori T., et al.: "Present Status of Monte Carlo Simulation for Neutron and Photon Transport", J. At. En. Soc. Japan, 41, 614 (1999). [in Japanese]

5) Kobayashi K., Sugiyama N. And Nagaya Y.: "3-D Radiation Transport Benchmarks for Simple Geometries with Void Region", Proc. Int. Conf. on Mathematics and Computation, Reactor Physics and Environmental Analysis for Nuclear Applications, Madrid, Sep. 27-30, 657 (1999).

6) Mori T., Okumura K., Nagaya Y. and Nakagawa M.: "Application of Continuous Energy Monte Carlo Code MVP to Burn-up and Whole Core Calculations Using Cross Sections at Arbitrary Temperatures", *ibid.*, 987 (1999).

7) Kugo T. and Kaneko K.: "Spatially Dependent Resonance Self-Shielding Calculation Method based on the Equivalence Theory in Arbitrary Heterogeneous Systems", *ibid.*, 2113 (1999).

8) Nagaya Y. and Mori T.: "Evaluation of Perturbation Effect due to Fission-Source Change in Eigenvalue Problems by Monte Carlo Methods", PHYSOR 2000, X.A.-2, Pittsburgh, May 7-12 (2000).

9) Kugo T. and Nakagawa M.: JAERI Data/Code 2000-004, " Multi-Dimensional Design Window Search System using Neural Networks in Reactor Core Design" (2000). [in Japanese]

10) Kugo T., Tsuchihashi K., Nakagawa M. and Ido M.: JAERI Data/Code 2000-011, "Core Neutronics Module and Database Access Module for Intelligent Reactor Design System

(IRDS)", (2000). [in Japanese]

11) Sakurai T., Okayama S., Andoh M. and Osugi T.: "Experimental Cores for Benchmark Experiments of Effective Delayed Neutron Fraction β_{eff} at FCA", Progress in Nuclear Energy, 35 , 131 (1999).

12) Spriggs G. D., Sakurai T. and Okajima S.: "Rossi-α and β_{eff} Measurements in a Fast Critical Assembly", *ibid.*, 169 (1999).

13) Yamane Y., Takemoto Y., Imai T., Okajima S. and Sakurai T.: "Effective Delayed Neutron Fraction Measurements in FCA XIX Cores by using Modified Bennett Method", *ibid.*, 183 (1999).

14) Sakurai T., Okajima S., Song H. and Kim Y.: "Measurement of Effective Delayed Neutron Fraction β_{eff} by ^{252}Cf Source Method for Benchmark Experiments of β_{eff} at FCA", *ibid.*, 195 (1999).

15) Sakurai T., Sodeyama H. and Okajima S.: "Measurement of Effective Delayed Neutron Fraction β_{eff} by Covariance-to-Mean Method for Benchmark Experiments of β_{eff} at FCA", *ibid.*, 203 (1999).

16) Sakurai T. and Okajima S.: "Analysis of Benchmark Experiments of Effective Delayed Neutron Fraction β_{eff} at FCA", *ibid.*, 209 (1999).

17) Andoh M., Okayama S., Oigawa H. and Iijima S.: "Measurement of Uranium-238 Doppler Effect in a Nitride Fueled LMFBR at FCA", J. Nucl. Sci. Technol. 36, 386 (1999).

18) Sakurai T., Nemoto T., Kobayashi K. and Unesaki H.: "Measurements of Reaction Rate Ratios as Indexed of Breeding Performance in Mock-up Cores of FCA Simulating Metallic-Fueled LMFBR and MOX-fueled LMFBR", J. Nucl. Sci. Technol., 36, 661 (1999).

19) Oigawa H., Iijima S. and Bando M.: "Experiments and Analyses on Fuel Expansion and Bowing Reactivity Worth in Mock-up Cores of Metallic Fueled Fast Reactors at FCA", J. Nucl. Sci. Technol., 36, 902 (1999).

20) Oigawa H., et al.: "A Proposal of Benchmark Calculation on Reactor Physics for Metallic Fueled and MOX Fueled LMFBR Based upon Mock-up Experiment at FCA", J. Nucl. Sci. Technol., 37, 186 (2000).

21) Suzaki T., Sakurai K., Nakajima K. and Horiki O.: "Precise Determination of β_{eff} for Water-moderated U and U-Pu Cores by a Method Using Buckling Coefficient of Reactivity", Proc. 6th Int. Conf. Nucl. Criticality Safety, Versailles, France, Sep. 30, 386 (1999).

22) Suzaki T., Suyama K. and Kaneko T.: "Measurement of Criticality Properties of a BWR

Spent Fuel Assembly", *ibid.*, 1386 (1999).

23) Nakahara Y., et al.: "Experimental Verification of Availability of ($^{134}Cs/^{137}Cs)^2$/ ($^{106}Ru/^{137}Cs$) Gamma-ray Intensity Ratio as a Burn-up Monitor for LWR Fuels", *ibid.*, 1693 (1999).

24) Kaneko K., Nagao M., Yamane T. and Takeuchi M.: JAERI-Conf 99-006, 316, "Two Proposals for Determination of Large Reactivity of Reactor", Proc. 6-th Asian Symp. On Research Reactors, Mito, Japan, Mar 29-31 (1999).

25) Sakurai T. and Okajama S.: JAERI-Conf 99-007, 29, "Benchmark Experiments of Effective Delayed Neutron Fraction β_{eff} at FCA", Proc. of the Specialists' Meeting on Delayed Neutron Nuclear Data Jan. 28-29, Tokai, Japan (1999).

26) Sakurai T. and Okajama S.: *ibid.*, 85, "Analysis of Benchmark Experiments of Effective Delayed Neutron Fraction β_{eff} at MASURCA and FCA" (1999).

27) Okajima S.: *ibid.*, 124, "Action for Delayed Neutron Data Evaluation" (1999).

28) Andoh M., et al.: JAERI-Research 2000-017, "Critical Experiment and Analysis for Nitride Fuel Fast Reactor Using FCA" (2000). [in Japanese]

29) Andoh M., Iijima S. Ishikawa M. and Iwai T.: JAERI-Tech 2000-025, "Adjustment of Nuclear Data Using Criticality Data of FCA XIX-2 Core (Joint Research)" (2000). [in Japanese]

30) Okajima S.: "Study on Doppler Effect in Fast Reactor Using Critical Assembly ",(Doctor Thesis, Hokkaido University) (1999). [in Japanese]

31) Haruyama M.: "New Detection Method of Trace Amount of Fissile Material in the Waste Drum", in Series "Practice! Radiation Measurement Application Technology 「10」 Nuclear Fuel Field, Waste Management", Nuclear Viewpoints, 45 , [11], 77 (1999). [in Japanese]

3. Advanced Reactor System Studies

1) Iwamura, T., et al.: "Research on Reduced-Moderation Water Reactors (RMWR)", JAERI-Research 99-058 (1999) [in Japanese].

2) (Ed.) Iwamura, T.: "Outline of Research Proposals Selected in the Nuclear Energy Research Initiative (NERI) Program", JAERI-Review 99-017(1999) [in Japanese].

3) Iwamura, T.: "Research and Development of Future Type LWR in Japan Atomic Energy Research Institute", Genshiryoku eye, Vol. 46, No.1 (2000) [in Japanese].

4) Iwamura, T. and Minato, K.: "1999 ANS Winter Meeting", J. At. Energy Soc. Japan, Vol.42, No.1 (2000) [in Japanese].

5) Kugo, T., et al.: "Study on Core Physics Characteristics of High Burnup Full MOX PWR

Core (2)", JAERI-Research 99-057 (1999) [in Japanese].

6) Osugi, T., Andoh, M., Takano, H., Ogawa, T. and Kobayashi, T.: "Fuel Cycle Systems with Nitride Fuel for Transmutation", Proc. Workshop on Advanced Reactors with Innovative Fuels, 21-23 October 1998, Villingen, Switzerland, p333-341, OECD/NEA (1999).

7) Ishikawa, N. and Suzuki, K.: "Feasibility Study on the Application of a Human Collaborative Robot System to the Inspecting Patrol of Nuclear Power Plants", Proc. 8th Int. Conf. on Human-computer Interaction, Munich, Germany (1999).

8) Ishikawa, N. and Suzuki, K.: "Design Method for Low Order Two-Degree-of-Freedom controller Based on Pade Approximation of the Denominator Series Expansion", J. At. Energy Soc. Japan, Vol.41, No.9 (1999) [in Japanese].

9) Kakuta, T. , et al.: "Development of In-Core Monitoring System for the Advanced Fission Reactor", Proc. 10th Int. Symp. on Reactor dosimetry, Osaka, Japan (1999).

10) Syamoto, N., Shikama, T. and Kakuta, T.: "Application of Silica Core Optical Fibers to Diagnostics in Heavy Irradiation Environments", Proc. 5th Asia-Pacific conf. on Communications, and 4th Optoelectronics and Communications Conference, Beijing, China (1999).

11) Kakuta, T., et al.: "Demonstration of Optical In-Core Monitoring System for Advanced Nuclear Power Reactors", OECD Proceedings, Core Monitoring Commercial Reactor: Improvement in Systems and Methods, Stockholm, Sweden (1999).

12) Nabeshima, K., et al.: "Hybrid Monitoring System for High Temperature Gas Cooling Reactor", Proc. 8th Int. Conf. on Human-computer Interaction, Munich, Germany (1999).

13) Suzudo, T.: "The Entropy trajectory: A Perspective to Classify Complex Systems", Proc. Int. Symp. on Frontiers of Time Series Modeling, Tokyo, Japan (2000).

14) Suzudo, T. and Watanabe, N.: "Theory and State-of-the-art Technology of Software Reliability", JAERI-Review 99-027 (1999).

15) (Eds.) Nakajima, N. and Ochiai, M.: "Workshop Summary Report on Advanced Utilization of Plutonium in Water Cooled Reactors -March 2, 1999, in Tokyo -", JAERI-Conf 99-014 (1999) [in Japanese].

16) Watanabe, K.: "Analysis of Singularity in Redundant Manipulators", JAERI-Tech 2000-028 (2000) [in Japanese].

4. Heat Transfer and Fluid Flow

1) Araya, F., Yoritsune, T., Nakatsuka, T., Yoshida, H., Satoh, T., Watanabe, H. and Okubo, T.: "Study on Reduced-Moderation Water Reactors (RMWRs) (9) -CHF experiment of

triangle tight lattice bundle-", 2000 Annual Mtg. of AESJ, O9 (2000).

2) Yoshida, H., Ohnuki, A. and Akimoto, H.: "Feasibirty Study on Thermal-Hydraulic Design of Reduced-Moderation PWR-Type Core", JAERI-Tech, 2000-024 (2000).

3) Ohnuki, A., Okubo, T. & Akimoto, H.: "A Feasibility Study on Core Cooling of Pressurized Heavy Water Moderated Reactor with Tight Lattice Core", Proc. of 7th Int. Conf. on Nucl. Eng., Tokyo, Japan, April 19-23, ICONE-7026 (1999).

4) Aritomi, M., Ohnuki, A., Arai, K., Kikuta, M., Yonomoto, T., Araya, F. and Akimoto, H.: "Status and Subjects of Thermal-hydraulic Analysis for Next-generation LWRs with Passive Safety Systems", J. At. Energy Soc. Japan, 41[7], 738-757 (1999) [in Japanese].

5) Ohnuki, A., Kamo, H. and Akimoto, H.: "Improvement of Multi-dimensional Two-Fluid Model Code ACE-3D and Application to Thermal-Hydraulic Analysis of Water Pool for Passive Heat Removal", JAERI-Data/Code 99-038, (1999) [in Japanese].

6) Ohnuki, A. and Akimoto, H.: "Numerical Investigation of Heat Transfer Enhancement Phenomenon during the Reflood Phase of PWR-LOCA", J. Nucl. Sci. Technol., 36[11], 1021-1029 (1999).

7) Subcommittee on Improvement of Reactor Thermal-Hydraulic Analysis Codes: "Status and Subjects of Thermal-hydraulic Analysis for Next-Generation LWRs", JAERI-Review 2000-002, (2999) [in Japanese].

8) Ohnuki, A. and Akimoto, H.: "Experimental Study on Transition of Flow Pattern and Phase Distribution in Upward Air-Water Two-Phase Flow along a Large Vertical Pipe", Int. J. Multiphase Flow, 26[3], 367-386 (2000).

9) Kureta, M. and Akimoto, H.: "Critical Heat Flux of Subcooled Flow Boiling in Narrow Rectangular Channels", Proc. of 7th International Conference on Nuclear Engineering (ICONE-7), Tokyo, Japan, No.7016(1999).

10) Matsubayashi, M., Kureta, M., Nakamura, H., Takenaka, S., Hibiki, T. and Mishima, K.: "Application of Neutron Radiography Systems in JRR-3M to Nuclear Engineering", Proc. of 7th International Conference on Nuclear Engineering (ICONE-7), Tokyo, Japan, No.7143(1999).

11) Kureta, M., Hibiki, T., Mishima, K. and Akimoto, H.: "Void Fraction Measurement of Subcooled Boiling of Water by Using the High-Frame-Rate Neutron Radiography", Proc. of The 6th World Conference on Neutron Radiography (WCNR-6), No.144(1999).

12) Kureta, M., Hibiki, T., Mishima, K. and Akimoto, H.: "Visualization and Void Fraction Measurement of Subcooled Boiling Water Flow in a Narrow Rectangular Channel Using High-Frame-Rate Neutron Radiography", Proc. of 2nd International, Symposium on Two-Phase Flow Modeling and Experimentation, Pisa, Italy, Vol.3, 1509-1514(1999).

13) Takase, K., Kunugi, T., Seki, Y. and Akimoto, H.: "Thermal-Hydraulic Characteristics During Ingress of Coolant and Loss of vacuum Events in Fusion Reactors", Nuclear Fusion, Vol.40, No.3Y, 527(2000).

14) Takase, K., Ose, Y. and Akimoto, H.: "Numerical Prediction of Pressure Rise Characteristics in ITER at Ingress of Coolant Events", International Conference of Nuclear Engineering (ICONE-7), Tokyo, No.6422(1999).

15) Takase, K., Shibata, M. and Akimoto, H.: "Plans of Integrated Ingress-of-Coolant Event (ICE) Tests for Fusion Experimental Reactors", 5th International Symposium on Fusion Nuclear Technology (ISFNT-5), Rome, (1999).

16) Takase, K.: "Numerical Analysis on Thermal-Hydraulic and Dust Transport Behavior in Fusion Reactors at Loss-of-Vacuum Events", 5th International Symposium on Fusion Nuclear Technology (ISFNT-5), Rome, (1999).

17) Takase, K., Ose, Y. and H. Akimoto, H.: "Numerical Simulations on Pressure Rise Characteristics in an integrated ICE Test Facility For ITER Thermofluid Safety", 5th International Symposium on Fusion Nuclear Technology (ISFNT-5), Rome, (1999).

18) Takase, K.: "Thermal-Hydraulic Characteristics in Square-Ribbed Coolant Channels with Helium Gas Cooling For Fusion Power Reactors", 5th International Symposium on Fusion Nuclear Technology (ISFNT-5), Rome, (1999).

19) Seki, Y., Takase, K., et al.: "Results in ITER Engineering R&D, Chapter 11 Safety R&D, Section 11.2.2 Preliminary Experiments", J. of Plasma and Fusion Research, Vol.75 Supplement, 89(1999) [in Japanese].

20) Takase, K.: "Heat Transfer Characteristics in Square-Ribbed Fuel Channels Using Gas Cooling", 36th National Heat Transfer Symposium, B313, 543(1999) [in Japanese].

21) Takase, K. and Akimoto, H.: "Analysis of Air Ingress Behavior in Fusion Reactors under Loss-of-Vacuum Events", 1999 JSME Annual Meeting, No.99-1 (IV), 323(1999) [in Japanese].

22) Takase, K.: "Fluid Flow Analysis in a Vacuum Vessel After Loss-of-Vacuum Accident", JSME Fluid Engineering Conference '99, No.99-19, 129(1999) [in Japanese].

23) Takase, K., Ose, Y. and Akimoto, H.: "Analysis on Two-Phase Flow Behavior in Fusion Reactors at In-Vessel Loss-of-Coolant Accidents", JSME Yamanashi District Conference, No.990-3, 159(1999) [in Japanese].

24) Takase, K., Ose, Y. and Akimoto, H.: "Numerical Prediction on Transport Behavior of Cooling Water Injected into Vacuum Vessels of Fusion Reactors", JSME 12th Computational Mechanics Conference, No.99-5, 395 (1999) [in Japanese].

25) Takase, K. Ose, Y. and Akimoto, H.: "Analyses of Accident Events on Thermal-

Hydraulics in Fusion Reactor Design", JSME Kansai 75th Annual Meeting, No.004-1, 13-11(2999) [in Japanese].

26) Ose, Y., Takase, K. and Akimoto, H.: "Numerical Investigation on Pressure Rise Suppression System in Fusion Experimental Reactors", JSME Chugoku-Shikoku 38th Annual Meeting, No.005-1, 211(1999) [in Japanese].

27) Ose, Y., Takase, K. and Akimoto, H.: "Numerical Analysis on Ingress-of-Coolant Events in Fusion Reactors with TRAC-PF1 Code", JAERI-Research 99-075, (1999) [in Japanese].

28) Takase, K., Shibata, M. and Akimoto, H.: "Test Facility Specifications", ITER Task Meeting for Integrated ICE Test Facility, Jan. 31 - Feb. 2, 2000.

29) Takase, K., Shibata, M. and Akimoto, H.: "Preliminary Integrated ICE Test Results", ITER Task Meeting for Integrated ICE Test Facility, Jan. 31 - Feb. 2, 2000.

30) Takase, K., Ose, Y. and Akimoto, H.: "Results of Preliminary ICE Test Calculations with TRAC-PF1", ITER Task Meeting for Integrated ICE Test Facility, Jan. 31 - Feb. 2, 2000.

5. Energy System Analysis and Assessment

1) Gotoh, Y., et al.: "Modeling of Long-term Energy System of Japan", JAERI-Research 99-046 (1999) [in Japanese].

6. Reactor Structural Materials

1) Niimi, M., Matsui, Y., Jitsukawa, S., Hoshiya, T., Tsukada, T., Omi, M., Mimura, H., Ooka, N. and Hide, K.: "Properties of precipitation hardened steel irradiated at 323K in the Japan Materials Testing Reactor", Journal of Nuclear Materials 271-272, p.92-p.96 (1999).

2) Miwa, Y., Tsukada, T., Tsuji, H. and Nakajima, H.: "Microstructures of type 316 model alloys neutron-irradiated at 513 K to 1 dpa", Journal of Nuclear Materials 271-272, p.316-p.320 (1999).

3) Tsuji, H., Yokoyama, N., Fujita, M., Kurihara, Y., Kano, S., Tachi, Y., Shimura, K., Nakajima, R. and Iwata, S.: "Present status of Data-Free-Way (distributed database system for advanced nuclear materials)", Journal of Nuclear Materials 271-272, p.486-p.490 (1999).

4) Kurata, Y., Itabashi, Y., Mimura H., Kikuchi, T., Amezawa H., Shimakawa S., Tsuji H. and Shindo M.: "In-pile and post-irradiation creep of SUS304 with JMTR thermal neutron spectrum", JAERI-Conf 99-006, p. 201-206 (1999).

5) Tsukada, T., Miwa, Y., Tsuji, H. and Nakajima, H.: "POST IRRADIATION

EXAMINATIONS FOR IASCC STUDY AT JAERI", JAERI-Conf 99-009, p.325 (1999).

6) Tsukada, T., Miwa, Y., Tsuji, H., Mimura, H., Goto, I., Hoshiya, T. and Nakajima, H.: "STRESS CORROSION CRACKING SUSCEPTIBILITY OF NEUTRON IRRADIATED STAINLESS STEELS IN AQUEOUS ENVIRONMENT", Proceedings of 7th International Conference on Nuclear Engineering, Tokyo, Japan, April, ICONE-7207, p.19-p.23 (1999).

7) Kaji, Y., Sakino, T., Tsukada, T. and Tsuji H.: "JAERI Material Performance Database (JMPD) –Present status and examples of utilization–", Proc. CODATA '99 DSAO Workshop, p.36, Tsukuba, July 14-16(1999).

8) Kaji, Y., Arai, T., Gu, W. and Nakajima, H.: "Basic design of parallel computational program for probabilistic structural analysis", JAERI-Review 99-016, p.61 (1999)[in Japanese].

9) Kaji, Y., Matsui, Y., Kita, S., Tsukada, T. and Tsuji, H.: "Development of Strain Measurement Techniques under Irradiation Environment Capsule Type Strain Gage and Fiber Optic Grating Strain Sensor", Report of the 2nd meeting of Research and Technical Committee on Stress and Strain Analysis, The Japanese Society for Non-Destructive Inspection, p. 20 (1999) [in Japanese].

10) Tsukada, T.: "Irradiation Assisted Stress Corrosion Cracking of Austenitic Stainless Steels", Proceedings of Seminar on Water Chemistry of Nuclear Reactor Systems `99, p.26-p.32 (1999).

11) Saito, T., Kurata, Y., Takatsu, T., Tsuji, H., Shindo, M. and Nakajima, H.: "Study on Development of Filler Metal for Ni-Cr-W Superalloy (Joint Research)", JAERI-Research 99-036 (1999) [in Japanese].

12) Wakai, E., Hashimoto, N., Shiba, K., Miwa, Y., J, p, Roberston. and R, L, Klueh.: "Swelling of HFIR-irradiated F82H, F82H+^{10}B and F82H+58Ni steels", Fusion Materials 313(25), p.161-p.169 (1999).

13) Ishii, T., Ooka, N., Saito, J., Kobayashi, S., Takahashi, K., Tsukada, T., Iwai, T., Kurosawa, Y., Hoshiya, T. and Tsuji, H.: "Replacement of pressure surge thank and vent valves in JMTR", Proceedings of International Symposium on Case Histories on Integrity and Failures in Industry (CHIFI) p.227-p.236 (1999).

14) Kaji, Y., Gu, W., Ishihara, M., Arai, T. and Nakajima, H.: "Application of continuum damage mechanics for non-linear elastic deformation behaviors of brittle materials", Transactions of 15th. Conf. on Structural Mechanics in Reactor Technol.(SMiRT-15) 2, p.133-p.139 (1999).

15) Tsuji, H., Kurata, Y., Ioka, I. and Sawai, Y.: "1998 Annual Report on Demonstration Test

on Lifetime Reliability of Structural Materials for Advanced Prototype Power Reactors", STA Commissioned Research (1999) [in Japanese].

7. Advanced Materials for Nuclear Applications

1) Ioka, I., Onuki, K. Futakawa, M. et al.: "Corrosion Tests of Fe-Si Alloys in Boiling Sulfuric Acid", Ryusan to Kogyo, 52,1(1999)[in Japanese].
2) Kikuchi, K. et al.: "Non-Destructive Measurement of Residual Stress for a Superconductor Jacket Applied to the Fusion Experimental Reactor by Neutron Diffraction Method", ICONE-7, Tokyo, Japan, Apr.19-23(1999).
3) Wakui, T., Futakawa, M., Eto, M. et al.: "Rate Dependent Behaviour in Tensile Strength of SiC/SiC composites", ICONE-7, Tokyo, Japan, Apr.19-23(1999).
4) Ioka, I., Futakawa, M. and Wakui, T.:"Mechanical Characterization on Ion Irradiated Thin Surface Layer by Nanoindentation Technique with Inverse Analysis", ICONE-7, Tokyo, Japan, Apr.19-23(1999).
5) Ioka, I., Mori, J., Kato, C., Futakawa, M. and Onuki, K.: "Corrosion Resistance and Nature of Surface Film on Fe-Si Alloy in Boiling Sulfuric Acid", J. Japan Inst. Metals, 63, 609(1999)[in Japanese].
6) Nishiyama, N., Futakawa, M. Ioka, I, et al.: "Corrosion Resistance Evaluation of Brittle Materials in Boiling Sulfuric Acid", J. Soc. Mater. Sci. Japan, 48,746(1999)[in Japanese].
7) Kurata, Y., Utsumi, H., Kikuchi, K., Suzuki, T. and Miura, T.: "Microstructural Evolution during Creep of Ni-base Solid Solution Alloys and In-situ Observation at High Temperature", Proceedings of the 4th International Conference on Recrystallization and Related Phenomena, The Japan Institute of Metals, 283 (1999).
8) Futakawa, M., Wakui, T., Eto, M. et al.: "Evaluation of Mechanical Properties of Thin Corroded Surface Layer on Brittle Materials by Microindentation Technique" Proceedings in Mechanical Behavior of Materials, ICM8, Vol.II 609 (1999).
9) Saito, S., Fukaya, K., Ishiyama, S., Eto, M. and Akiba, M.: "Development of Bonding Techniques between Tungsten and Copper Alloy for Plasma Facing Components by HIP Method (1)-Bonding between Tungsten and Oxygen Free Copper-", JAERI-Research 99-049(1999)[in Japanese].
10) Ishii, T., Okamoto, Y. Ooka, N., Eto, M. and Hoshiya, T.: "Nondestructive Detection of Surface Flaws in Materials by Infrared Thermography", J. Japanese Soc. Non-destructive Inspection, 48,682(1999)[in Japanese].
11) Saito, S., Fukaya, K., Ishiyama, S., Eto, M. et al.: "Evaluation of Properties of Low Activation Mn-Cr Steel (1)-Mechanical Properties and Weldability-", JAERI-Tech 99-

076(1999)[in Japanese].

12) Ioka, I., Mori, J., Kato, C., Futakawa, M. and Onuki, K.: "The Characterization of Passive Films on Fe-Si Alloy in Boiling Sulfuric Acid", J. Mater. Sci. Letters, 18, 1497(1999)

13) Nishi, H., Eto, M., Kikuchi, K., et al.: "Material Properties on Weld Joints of 316L Stainless Steel for Vacuum Vessel", 5th International Symposium on Fusion Nuclear Technology(ISFNT-5), Roam, Italy, Sep. 19-24(1999).

14) Kurata, Y., Tanabe, T., Mutoh, I., et al.: "Creep Properties of Base Metal and Welded Joint of Hastelloy XR Produced for High-temperature Engineering Test Reactor in Simulated Primary Coolant Helium", J. Nucl. Sci. and Technol., 36, 1160(1999).

15) Saito, T., Baba, S. and Eto, M.: "Changes in Tensile Property and X-ray Parameter for Carbon Fiber after High Temperature Heat-treatment", JAERI-Research 99-070(1999)[in Japanese].

16) Wakui, T., Futakawa, M., Tanabe, Y. and Eto, M.: "Microindentation Test for Determining Mechanical Properties of Corroded Layers of Ceramics", Trans. Japan Soc. Mechanical Engineers 65, 2399(1999)[in Japanese].

17) Futakawa, M., Kikuchi, K., Conrad, H. and Stechemesser, H.: "Pressure and Stress Waves in a Spallation Neutron Source Mercury Target Generated by High-power Proton Pulses", Nuclear Instruments and Methods in Physics Research A 439, 1(2000).

18) Eto, M. and Konishi, T.: "Change in Electrical Resistivity of Nuclear Graphite and Carbon Materials during Low Cycle Fatigue", Tanso, 186, 30(1999).

19) Ishiyama, S., Akiba, M. and Eto, M.: "Thermal and Irradiation Induced Stress Analysis on Relevant Target Plate Structure of the Divertor for Fusion Experimental Reactors", J. Nucl. Sci. Technol., 37,90(2000).

20) Ishiyama, S., Fukaya, K., Eto, M. et al.: "R&D of Low Activated Fe-Mn-Cr High Strength Non-magnetic Steel (I) Screening Test for Constituent Optimization and Fundamental Characterization Test", J. At. Energy Soc. Japan, 42, 116(2000)[in Japanese].

21) Saito, S., Fukaya, K., Ishiyama, S., Eto, M. and Akiba, M.: "Development of Bonding Techniques between Tungsten and Copper Alloy for Plasma Facing Components by HIP Method (2)-Bonding between Tungsten and DS-Copper-", JAERI-Research 2000-006(2000)[in Japanese].

22) Kurata, Y., Suzuki, T. and Shimizu, S.: "High Temperature Corrosion of Iron-base and Nickel-base Alloys for Hydrogen Production Apparatus by Thermochemical Method in H_2O +SO_3 Atmosphere", JAERI-Research 2000-011(2000)[in Japanese].

23) Nishi, H. and Araki, T.: "Low Cycle Fatigue Strength of Diffusion-Bonded Joints of Alumina Dispersion-Strengthened Copper to Stainless Steel" 9th International

Confererance on Fusion Materials (ICFRM-9), Colorado Springs, USA, Oct. 10-15,1999

24) Tachibana, K., Nishi, H., Eto, M. and Muto, Y.:"Creep Strength of Hastelloy XR Welded Joints", JAERI-Tech 99-024 [in Japanease].

8. Compatible Materials Development for Advanced Nuclear Systems

1) Motooka, T. and Kiuchi, K.: "Fatigue Crack Propagation Behavior of T-5Ta Alloy in Boiling Nitric Acid Solution", JAERI-Research 99-039(1999)[In Japanese].
2) Motooka, T. and Kiuchi, K.: "Fatigue Crack Propagation Behavior of Zirconium in Boiling Nitric Acid Solution", Zairyo-to-Kankyo, 48, 320(1999)[In Japanese].
3) Kiuchi, K., et.al.: "Technological Problems and Counter-measures on Equipment Materials for Reprocessing of High Burnup Fuels", Proc.IAEA Technical Committee Meeting "Economic Limits to Fuel Burnup Extension", Argentina, Nov.15-18(1999).
4) Ioka, I., et.al, "Development of Advanced Cladding Material for Burnup Extension", Proc.IAEA Technical Committee Meeting "Economic Limits to Fuel Burnup Extension", Argentina, Nov.15-18 (1999).

9. Rock-like Oxide Fuel for Pultonium Burning in LWRs

1) Yamashita, T., et al.: IAEA-TECDOC-1122, IAEA, pp. 309-320 (1999).
2) Akie, H., et al.: OECD/NEA, pp. 199-208 (1999).
3) Yanagisawa, K., et al.: J. Nucl. Sci. Technol., 36 (1999) 1052.
4) Yanagisawa, K., et al.: J. Nucl. Sci. Technol., 36 (1999) 1153.
5) Yanagisawa, K., et al.: JAERI-Tech 99-044 (1999).
6) Shelley, A., et al.: JAERI-Research 99-051 (1999).
7) Yamashita, T., et al.: Proc. Int. Conf. Future Nuclear Systems (GLOBAL'99), ANS (1999) [CD-ROM].
8) Nakano, Y., and Takano, H.: Senda Editorial, S.A., Madrid, Spain (1999) [CD-ROM].

10. Nitride Fuel and Related Pyrochemical Technology

1) Suzuki, Y., et al.: Recent Progress of Research on Nitride Fuel Cycle in JAERI, Proc. In OECD/NEA Information Exchange Meeting on P&T, November, 1998, Mol, Belgian. p.213-222.
2) Suzuki, Y.: J. Atom. Energy Soc. Japan, 41, No. 4 (1999) 376.
3) Suzuki, Y.: Nihongenshiryokugakkai kakunennryoubukai nennpou, 31 (1999) 39.
4) Sakamura, Y., et al.: Proc. Int. Conf. on Future Nuclear Systems (GLOBAL'99), Aug. 29-Sept. 3, 1999, Jackson Hole, Wyoming (1999).

5) Arai, Y., et al.: Proc. Int. Conf. on Future Nuclear Systems (GLOBAL'99), Aug. 29-Sept. 3, 1999, Jackson Hole, Wyoming (1999).
6) Nakajima, K., et al.: J. Nucl. Mater., 275 (1999) 332.
7) Shirai, O., et al.: J. Nucl. Mater., 277 (2000) 226.
8) Hayashi, K., et al.: JAERI-Research 2000-001 (2000).
9) Iwai, T., et al.: JAERI-Research 2000-009 (2000).
10) Iwai, T., et al.: JAERI-Research 2000-010 (2000).

11. Nuclear Ship Research and Development

1) Nakajima, N.: "Crack Growth and Thermal Hydraulics", Energy Review, 19 (6), 16 (1999) [in Japanese].
2) Ishida, T. and Yoritsune, T.: "Effect of Ship Inclination and Ship Motions on Natural Circulation of Deep Sea Research Reactor DRX", Proc. EUROTHERM Seminor No. 63, Single and Two-Phase Natural Circulation, September 6-8, 1999, Genoa, Italy, p.331 (1999).
3) Odano, N., Yamaji, A. and Ishida, T.: "Shielding Design for Steam Generator of Advanced Marine Reactor", J. Nucl. Sci. Technol., Supplement 1, 78 (2000).
4) Odano, N. Ishida, T., "Evaluation of Buildup of Activated Corrosion Products for Highly Compact Marine Reactor DRX without Primary Coolant Water Purification System", J. Nucl. Sci. Technolo., Supplement 1, 584 (2000).
5) Ishida, T., Kusunoki, T., Odano, N., Yoritsune, T., Fukuhara, Y., Ochiai, M. and Hoshi, T.: "Advanced Marine Reactor MRX and Application to Nuclear Barge Supplying Electricity and Heat", Proc. Int. Workshop on Utilization of Nuclear Power in Oceans, February 21-24, Tokyo, Japan, p.55 (2000).
6) Matsuoka, T., Yamaji, A., Mitomo, N., Fukuhara, Y. and Ishida, T.: "Evaluation of the Core Damage Frequency of the Marine Reactor X", Proc. Int. Workshop on Utilization of Nuclear Power in Oceans, February 21-24, Tokyo, Japan, p.64 (2000).
7) Kusunoki, T., Odano, N., Yoritsune, T., Fukuhara, Y., Nakajima, N. and Ochiai, M.: "Application of a Compact Marine Reactor to District Heating -MR-1G-", Proc. Int. Workshop on Utilization of Nuclear Power in Oceans, February 21-24, Tokyo, Japan, p.77 (2000).
8) Shimazaki, J., Nakazawa, T. and Yabuuchi, N.: "Knowledge-Based Full-Automatic Control System for a Nuclear Ship Reactor", Proc. Int. Workshop on Utilization of Nuclear Power in Oceans, February 21-24, Tokyo, Japan, p.97 (2000).
9) Odano, N., Kusunoki, T, Yoritsune, T., Fukuhara, Y., Saito, K., Takahashi, T. and Ishida,

T.: "Submersible Compact Reactor SCR for Under-Sea Research Vessel", Proc. Int. Workshop on Utilization of Nuclear Power in Oceans, February 21-24, Tokyo, Japan, p.164 (2000).

10) Yoritsune, T., Nunokawa, H., Ishida, T. and Imayoshi, S.: "Development of an In-vessel Type Control Rod Drive Mechanism Adopted in Advanced Marine Reactor", Proc. Int. Workshop on Utilization of Nuclear Power in Oceans, February 21-24, Tokyo, Japan, p.231 (2000).

11) Takahashi, T., Shimazaki, J. and Nakazawa, T.: "Development of an Engineering Simulator for Integral Type PWR for Nuclear Ship", Proc. Int. Workshop on Utilization of Nuclear Power in Oceans, February 21-24, Tokyo, Japan, p.294 (2000).

12) Takahashi, T., Shimazaki, J., Nakazawa, T., Yabuuchi, N., Fukuhara, Y., Kusunoki, T. and Ochiai, M.: "Building of Nuclear Ship Engineering Simulation System, Development of the Simulator for the Integral Type Reactor", JAERI-Tech 2000-39 (2000) [in Japanese].

This is a blank page.

Appendix I

Department of Nuclear Energy System Organization Chart

March 2000

Department of Nuclear Energy System

Director : M. Nakagawa

Deputy Director : M. Ochiai H. Nakajima

H. Yasuda K. Fukuda H. Watanabe T. Kakuta
K. Watanabe T. Shiratori Y. Suzuki(1)

Administrative Service

T. Kimura (Administrative Manager)
T. Nogami T.Takada T. Tomita S. Hakoda

Reactor Engineering Facility Operation Division

K. Nakajima (Head)

S. Fujisaki	H. Watanabe	K. Kurosawa	Y. Hoshi
M. Takeuchi	K. Satoh	T. Satoh	T. Ono
M. Shibata	K. Hayasaka	H. Sodeyama	D. Hirayama
M. Saitoh	K. Nitta	Y. Miyoshi(2)	J. Sakurai(3)
K. Nakajima(2)			

Nuclear Data Center

A.Hasegawa (Head)

T. Shirai	Y. Nakagawa	J. Katakura	K. Shibata
T. Fukahori	A. Ichihara	O. Iwamoto	S. Chiba(4)
H. Naramoto(4)	M. Sataka(5)	H. Iimura(5)	

Research Group for Energy System Assessment

O. Sato (Head)

Y. Tadokoro	M. Yamaguchi	Y. Tanaka	K.Kunii
K. Tatematsu			

Research Group for Advanced Reactor Systems

T. Iwamura (Head)

T. Okubo	T. Shirakawa	T. Suzudo	K. Nabeshima
N. Ishikawa	T. Nakatsuka	M. Katagiri(4)	M. Kishimoto(4)

Research Group for Reactor Physics

T. Osugi (Head)

T. Mori	S. Iijima	S. Okajima	T. Fujimura
K. Okumura	T. Yamane	T. Suzaki	M. Haruyama
M. Kurosawa	T. Kugo	T. Sakurai	M. Takase
Y. Nagaya	M. Andoh	T. Hasegawa	Y. Sugimoto
H. Oigawa(6)			

Research Group for Thermal and Fluid Engineering

H. Akimoto (Head)

A. Ohnuki	K. Takase	F. Araya	H. Yoshida
M. Kureta	Y. Ose	T. Takahashi	

Research Group for Reactor Structural Materials

H. Tsuji (Head)

T. Tsukada	Y. Kaji	M. Kikuchi	H. Ugachi
Y. Miwa	S. Kita	Y. Sawai(5)	

Research Group for Compatible Materials

K. Kiuchi (Head)

Y. Kurata	M. Futakawa	T. Saito	I. Ioka
H. Nishi	S. Hamada	T. Suzuki	K. Tachibana
K. Fukaya	S. Kanbara	T. Motooka	T. Yanagihara
C. Kato	M. Doi	Y. Inohara	S. Saito
M. Eto(7)	S. Ishiyama(8)	S. Baba(8)	T. Ishiyama(5)
K. Kikuchi(6)	F. Nagase(9)		

Research Group for Advanced Fuel

Y. Arai (Head)

T. Yamashita	K. Shiozawa	K. Kikuchi	A. Inoue
T. Iwai	H. Akie	Y. Nakano	H. Serizawa
K. Kuramato	O. Shirai	N. Shirasu	K. Nakajima
T. Sasayama	H. Kimura(2)	T. Nakamura(9)	H. Otsuka(5)

Nuclear Ship Research and Development Division

M. Ochiai (Head)
N. Nakajima T. Takahashi S. Usui

Advanced Marine Reactor Laboratory

T. Ishida (Head)

Y. Fukuhara	H. Nunokawa	K. Saitoh	T. Kusunoki
N. Odano	T. Yoritsune		

Nuclear Ship System Laboratory

J. Shimazaki (Head)
N. Yabuuchi M. Kyoya H. Takahashi

Research Committee

Japanese Nuclear Data Committee
Research Committee on Reactor Physics
Research Committee on Marine Reactors

(No.) Original Organization of the Shared-Time Members
(1) Dept. of Safety Research Technical Support
(2) Dept. of Fuel Cycle Safety Research
(3) Nuclear Safety Research Center
(4) Advanced Science Research Center
(5) Dept. of Materials Science
(6) Center for Neutron Science
(7) Office of International Affairs
(8) Dept of Advanced Nuclear Heat Technology
(9) Dept. of Reactor Safety Research

Appendix Ⅱ Engineering Facilities Related to the Department

FCA : Fast Critical Assembly

The FCA is a split-table type facility of horizontal matrix structure designed for studying nuclear characteristics of fast reactor. The construction of the FCA was started in 1965 and the first core went critical on 29th April,1967. The main features of facility are summarized as follows:

Type:	Split-table type of horizontal matrix structure
Size:	2.8m×2.8m×1.3m (each half assembly)
Fuel:	Enriched uranium and plutonium (Plate type)
Other material:	Sodium, stainless steel, aluminum oxide, polystyrene etc. (Plate type)
Maximum power:	2kW
Assembly name:	FCA-I～FCA-XIX

Critical experiment using enriched uranium cores were made in 1960s investing basic characteristics of fast reactor cores. Mock-up experiments were extensively made in 1970s for the Fast Experimental Reactor JOYO and the Prototype Fast Breeder Reactor MONJU. In 1980s, the main subjects of experiments were the investigation of the core characteristics of an axially heterogeneous large fast breeder reactor and the core physics study on a high conversion light water reactor. In early 1990s, the reactor physics experiment of metallic-fueled LMFBR was carried out. Since 1995, international benchmark experiments for β_{eff} have been carried out by using FCA XIX core.

VHTRC : Very High Temperature Reactor Critical Assembly

The VHTRC is a low-enriched uranium fueled and graphite moderated / reflected critical assembly. At VHTRC, reactor physics experiments have been carried out mainly for the verification of the neutronics design of the HTTR.

Main features of VHTRC

Type:	Split table of hexagonal prism (prismatic block structure)
Size:	2.4m across the flats and 2.4m long
Fuel:	2,4 and 6wt% enriched UO_2
	Coated particle fuel compact, Pin-in-block type
Moderator/reflector:	Graphite
Core temperature:	Room temperature to 210℃ by electric heaters
Maximum power:	10W
Auxiliary equipments:	① Sample heating device (up to 800℃)
	② Pulsed neutron source

TCA: Tank-type Critical Assembly

The TCA is a light-water-moderated critical facility to provide the experimental data on light water reactor physics. The construction of the TCA was started in 1961 and the first criticality was attained on 23rd August, 1962.

Main features of TCA

Type:	Light water moderated Tank-type
Size:	Typically 0.5m×0.5m×1m
	(Core Tank 1.8m diam.×2.1m height)
Fuel:	Low-enriched UO2 and PuO2- UO2 fuel rod
Moderator:	Light Water
Maximum Power:	200W
Auxiliary equipments:	Pulsed neutron source
	Neutron absorbing materials (soluble or solid state)

国際単位系 (SI) と換算表

表1　SI基本単位および補助単位

量	名称	記号
長さ	メートル	m
質量	キログラム	kg
時間	秒	s
電流	アンペア	A
熱力学温度	ケルビン	K
物質量	モル	mol
光度	カンデラ	cd
平面角	ラジアン	rad
立体角	ステラジアン	sr

表2　SIと併用される単位

名称	記号
分，時，日	min，h，d
度，分，秒	°，′，″
リットル	l，L
トン	t
電子ボルト	eV
原子質量単位	u

1 eV=1.60218×10^{-19} J

1 u=1.66054×10^{-27} kg

表3　固有の名称をもつSI組立単位

量	名称	記号	他のSI単位による表現
周波数	ヘルツ	Hz	s^{-1}
力	ニュートン	N	m·kg/s^2
圧力，応力	パスカル	Pa	N/m^2
エネルギー，仕事，熱量	ジュール	J	N·m
工率，放射束	ワット	W	J/s
電気量，電荷	クーロン	C	A·s
電位，電圧，起電力	ボルト	V	W/A
静電容量	ファラド	F	C/V
電気抵抗	オーム	Ω	V/A
コンダクタンス	ジーメンス	S	A/V
磁束	ウェーバ	Wb	V·s
磁束密度	テスラ	T	Wb/m^2
インダクタンス	ヘンリー	H	Wb/A
セルシウス温度	セルシウス度	℃	
光束	ルーメン	lm	cd·sr
照度	ルクス	lx	lm/m^2
放射能	ベクレル	Bq	s^{-1}
吸収線量	グレイ	Gy	J/kg
線量当量	シーベルト	Sv	J/kg

表4　SIと共に暫定的に維持される単位

名称	記号
オングストローム	Å
バーン	b
バール	bar
ガル	Gal
キュリー	Ci
レントゲン	R
ラド	rad
レム	rem

1 Å=0.1 nm=10^{-10} m

1 b=100 fm^2=10^{-28} m^2

1 bar=0.1 MPa=10^5 Pa

1 Gal=1 cm/s^2=10^{-2} m/s^2

1 Ci=3.7×10^{10} Bq

1 R=2.58×10^{-4} C/kg

1 rad=1 cGy=10^{-2} Gy

1 rem=1 cSv=10^{-2} Sv

表5　SI接頭語

倍数	接頭語	記号
10^{18}	エクサ	E
10^{15}	ペタ	P
10^{12}	テラ	T
10^{9}	ギガ	G
10^{6}	メガ	M
10^{3}	キロ	k
10^{2}	ヘクト	h
10^{1}	デカ	da
10^{-1}	デシ	d
10^{-2}	センチ	c
10^{-3}	ミリ	m
10^{-6}	マイクロ	μ
10^{-9}	ナノ	n
10^{-12}	ピコ	p
10^{-15}	フェムト	f
10^{-18}	アト	a

（注）

1. 表1－5は「国際単位系」第5版，国際度量衡局 1985年刊行による。ただし，1 eVおよび1 uの値はCODATAの1986年推奨値によった。
2. 表4には海里，ノット，アール，ヘクタールも含まれているが日常の単位なのでここでは省略した。
3. barは，JISでは流体の圧力を表わす場合に限り表2のカテゴリーに分類されている。
4. EC閣僚理事会指令ではbar，barnおよび「血圧の単位」mmHgを表2のカテゴリーに入れている。

換　算　表

力	N(=10^5 dyn)	kgf	lbf
	1	0.101972	0.224809
	9.80665	1	2.20462
	4.44822	0.453592	1

粘度　1 Pa·s(N·s/m^2)=10 P(ポアズ)(g/(cm·s))

動粘度　1 m^2/s=10^4 St(ストークス)(cm^2/s)

圧力	MPa(=10 bar)	kgf/cm^2	atm	mmHg(Torr)	lbf/in^2(psi)
	1	10.1972	9.86923	7.50062×10^3	145.038
	0.0980665	1	0.967841	735.559	14.2233
	0.101325	1.03323	1	760	14.6959
	1.33322×10^{-4}	1.35951×10^{-3}	1.31579×10^{-3}	1	1.93368×10^{-2}
	6.89476×10^{-3}	7.03070×10^{-2}	6.80460×10^{-2}	51.7149	1

エネルギー・仕事・熱量	J(=10^7 erg)	kgf·m	kW·h	cal(計量法)	Btu	ft·lbf	eV
	1	0.101972	2.77778×10^{-7}	0.238889	9.47813×10^{-4}	0.737562	6.24150×10^{18}
	9.80665	1	2.72407×10^{-6}	2.34270	9.29487×10^{-3}	7.23301	6.12082×10^{19}
	3.6×10^6	3.67098×10^5	1	8.59999×10^5	3412.13	2.65522×10^6	2.24694×10^{25}
	4.18605	0.426858	1.16279×10^{-6}	1	3.96759×10^{-3}	3.08747	2.61272×10^{19}
	1055.06	107.586	2.93072×10^{-4}	252.042	1	778.172	6.58515×10^{21}
	1.35582	0.138255	3.76616×10^{-7}	0.323890	1.28506×10^{-3}	1	8.46233×10^{18}
	1.60218×10^{-19}	1.63377×10^{-20}	4.45050×10^{-26}	3.82743×10^{-20}	1.51857×10^{-22}	1.18171×10^{-19}	1

1 cal = 4.18605 J（計量法）

= 4.184 J　（熱化学）

= 4.1855 J（15 °C）

= 4.1868 J（国際蒸気表）

仕事率　1 PS（仏馬力）

= 75 kgf·m/s

= 735.499 W

放射能	Bq	Ci
	1	2.70270×10^{-11}
	3.7×10^{10}	1

吸収線量	Gy	rad
	1	100
	0.01	1

照射線量	C/kg	R
	1	3876
	2.58×10^{-4}	1

線量当量	Sv	rem
	1	100
	0.01	1

（86年12月26日現在）